NUREG/CR-5039 (1 of 2)
SAND87-2411 (1 of 2)
R3, R5, R7
Printed January 1988

Reactor Safety Research Semiannual Report January - June 1987 Volume 37

Reactor Safety Researach Department 6420

Prepared by
Sandia National Laboratories
Albuquerque, New Mexico 87185 and Livermore, California 94550
for the United States Department of Energy
under Contract DE-AC04-76DP00789

Prepared for
U. S. NUCLEAR REGULATORY COMMISSION

Available from

Superintendent of Documents
U.S. Government Printing Office
Post Office Box 37082
Washington, D.C. 20013-7082

and

National Technical Information Service
Springfield, VA 22161

NUREG/CR-5039 (1 of 2)
SAND87-2411 (1 of 2)
Vol. 37
R3, R5, R7

REACTOR SAFETY RESEARCH SEMIANNUAL REPORT
January - June 1987

Reactor Safety Research Program

Printed January 1988

Jack V. Walker, Editor
Manager, Reactor Safety Research

Sandia National Laboratories
Albuquerque, NM 87185
Operated by
Sandia Corporation
for the
U.S. Department of Energy

Prepared for
Division of Accident Evaluation
Office of Nuclear Regulatory Research
U.S. Nuclear Regulatory Commission
Washington, DC 20555
Under Memorandum of Understanding DOE 40-550-75
NRC FINs (A1016, A1019, A1030, D1124, A1181, A1218, A1246, A1335, A1336, A1342, A1389, A1390)

FOREWORD

Sandia National Laboratories is conducting, under USNRC sponsorship, phenomenological research related to the safety of commercial nuclear power reactors. The research includes experiments to simulate the phenomenology of accident conditions and the development of analytical models, verified by experiment, which can be used to predict reactor and safety systems performance behavior under abnormal conditions. The objective of this work is to provide NRC requisite data bases and analytical methods to (1) identify and define safety issues, (2) understand the progression of risk-significant accident sequences, and (3) conduct safety assessments. The collective NRC-sponsored effort at Sandia National Laboratories is directed at enhancing the technology base supporting licensing decisions.

CONTENTS

	Page
EXECUTIVE SUMMARY	1
1. CONTAINMENT LOADING AND RESPONSE	13
1.1 Ex-Vessel Core Debris Interactions	14
1.1.1 Sustained Urania-Concrete Interactions (SURC): Experiments and Analysis	14
1.1.1.1 Materials	17
1.1.1.2 Experimental Apparatus	24
1.1.1.3 Instrumentation and Calibration	32
1.1.1.4 Procedure	53
1.1.1.5 Initial Conditions, Boundary Conditions, and Posttest Observations	58
1.2 High-Pressure Melt Ejection and Direct Containment Heating	63
1.2.1 Introduction	63
1.2.2 Problem Definition and Approach	64
1.2.3 Material Properties	64
1.2.4 Modeling and Numerical Considerations	67
1.2.5 Thermal Analysis	72
1.2.6 Stress Analyses	75
1.2.7 Conclusions	84
1.3 CORCON and VANESA Code Development	87
1.3.1 Posttest CORCON Calculations for the SURC Tests	89
1.3.2 Release of the Third CORCON Correction Set	94
1.3.3 Release of the Fourth CORCON Correction Set	95
1.4 Molten Fuel-Coolant Interactions	110
1.4.1 FITS-D Experiment	111
1.4.2 Isothermal Liquid-Into-Liquid Jet Studies (IJET)	112
1.4.2.1 Introduction	112
1.4.2.2 Apparatus and Procedure	112
1.4.2.3 Test Parameters	113
1.4.2.4 Test Observations	118
1.4.2.5 Breakup Behavior	128

CONTENTS (Continued)

		Page
1.4.2.6	Conclusions, Plans, and Recommendations	139
1.4.3	Integrated Fuel-Coolant Interaction Code Development	142
1.4.3.1	Problem Setup	143
1.4.3.2	Coarse-Mixing Phase	145
1.4.3.3	Triggering and Propagation Phase	151
1.4.3.4	Discussion of Results	160
1.4.3.5	Future Work	162
1.5	Hydrogen Behavior	162
1.5.1	Oxidation of Combustible Gases in the Reactor Cavity	163
1.5.1.1	Introduction	163
1.5.1.2	No Oxidation of Combustible Gases in the Cavity	165
1.5.1.3	Influence of Steam Inerting	166
1.5.1.4	Condition With Air-Return Fans Off	172
1.5.1.5	Gas Release Rates Predicted by the CORCON Code	172
1.5.2	Heated Detonation Tube	175
1.5.2.1	Global and Local Detonations	175
1.5.2.2	Direct Containment Heating Hydrogen Problem	183
1.5.2.3	Oxidation of Combustible Gases in the Reactor Cavity	183
1.5.2.4	Effects of Diluents on Detonability	184
2.	FISSION-PRODUCT SOURCE TERM	189
2.1	High-Temperature Fission-Product Chemistry Program	189
2.1.1	Introduction	190
2.1.2	Summary and Conclusions	191
2.1.3	Vapor Pressure of Liquid CsOH	195
2.1.3.1	Introduction	195
2.1.3.2	Experimental Section	195
2.1.3.3	Results and Discussion	198

CONTENTS (Continued)

		Page
2.2	ACRR Source Term Experiments	199
2.2.1	Introduction	200
2.2.2	Description of the ST-1 Experiment	200
2.2.3	Preliminary Results of the ST-1 Posttest Analyses	208
2.2.3.1	On-line Optical Spectra	208
2.2.3.2	Gamma Spectroscopy of the ST-1 Package in the Hot Cell	215
2.2.3.3	Preliminary Results of Posttest Wet Chemical Analyses	217
2.2.3.4	Black Insoluble Material in Leachates	221
2.2.4	Comparison of ST-1 Experiment Results With Predictions From CORSOR and VICTORIA	222
2.2.5	Status of ST-1 Posttest Analyses	226
2.2.6	Status of ST-2 Experiment Preparations	226
3.	LWR DAMAGED FUEL PHENOMENOLOGY	227
3.1	DF-4 BWR Control Blade/Channel Box Fuel Damage Experiment	227
3.1.1	Introduction	227
3.1.2	Description of Experiment	231
3.1.2.1	Experiment Capsule	233
3.1.2.2	Test Section Instrumentation	236
3.1.2.3	Test Progression	236
3.1.3	Experimental Results	240
3.1.3.1	ACRR Power and Steam Flow	240
3.1.3.2	Test Bundle Thermal Response	242
3.1.3.3	CuO-H_2 Recombiner Thermal Response	248
3.1.3.4	Video Record and Test Chronology	250
3.1.3.5	Posttest X-Radiographic Examination	252
3.1.4	Experiment Analysis	254
3.1.4.1	Coupling Factors	254

CONTENTS (Concluded)

		Page
3.1.4.2	Comparison of Calculated and Measured Temperatures	256
3.1.4.3	Metal-Water Reactions	259
3.1.4.4	Melting Attack	261
3.1.4.5	Thermal Response	264
3.1.5	Discussion	266
4.	MELT PROGRESSION PHENOMENOLOGY CODE DEVELOPMENT (MELPROG)	269
4.1	MELPROG Code Development	269
4.1.1	DEBRIS Module Development	270
4.1.2	CORE Module Development-Eutectic/Mixture Treatment	275
4.2	MELPROG Code Applications	280
4.3	MELPROG Validation Experiments	282
4.3.1	Introduction	282
4.3.2	Uranium Dioxide Coupling Experiments	283
4.3.3	Magnetic Flux Characterization	292

LIST OF FIGURES

Figure		Page
1.1-1	SURC 4 Schematic	16
1.1-2	Comparison of Experiment Thermal History and Predictions of the "PROPTY" Code	20
1.1-3	"PROPTY" Thermal Conductivity Prediction for Castable MgO Material	21
1.1-4	SURC 4 Experimental Apparatus	27
1.1-5	Sealed, Water-Cooled Containment Vessel	28
1.1-6	Typical Thermocouple Array Cast Into the Concrete	31
1.1-7	Thermocouple Array Installation, MgO Annulus	33
1.1-8	Zirconium Delivery System	34
1.1-9	SURC 4 Gas Sampling Schematic	37
1.1-10	Gas Analysis Cold Trap	38
1.1-11	Grab Sample Hardware	39
1.1-12	Mass Spectrometer Hardware	41
1.1-13	CO/CO_2 Monitor Hardware	42
1.1-14	Flow Chart Illustrating How the Source Term Parameters Are Determined From Measurements Made in the SURC 4 Melt-Concrete Interaction Test	47
1.1-15	Schematic Diagram of the Sample Extraction Dilution System Showing the Configuration of the Filter, Impactor, and Cyclone Samples With Respect to the Diluters and the Aerosol Sampling Point	48
1.1-16	Power History for SURC 4	55
1.1-17	SURC 4 Initial Steel Temperature	59
1.1-18	SURC 4 Initial Concrete Temperatures	60
1.1-19	SURC 4 MgO Sidewall Temperatures	60

LIST OF FIGURES (Continued)

Figure		Page
1.1-20	SURC 4 Middle MgO Temperatures	61
1.1-21	SURC 4 Upper MgO Temperatures	62
1.1-22	SURC 4 MgO Cover Temperatures	62
1.2-1	Schematic Cross Section of an Axisymmetric Nuclear Reactor Containment Vessel	65
1.2-2	Temperature Dependent Stress-Strain Curves	67
1.2-3	Temperature Dependence of Poisson's Ratio	68
1.2-4	Temperature Dependence of Young's Modulus	68
1.2-5	Temperature Dependence of Hardening Modulus	69
1.2-6	Temperature Dependence of Yield Stress	69
1.2-7	Temperature Dependence of Thermal Expansion Coefficient	70
1.2-8	Displacement (Sag) in Spherical Sector Model	71
1.2-9	Hollow Hemispherical Finite Element Mesh	73
1.2-10	Temperature Variation Through Thickness of Vessel	74
1.2-11	Displacement (Sag) in Hemisphere - Symmetry BC	76
1.2-12	Displacement (Sag) in Hemisphere - Fixed BC	76
1.2-13	Deformed Mesh Plots of Hemisphere With Fixed BC	77
1.2-14	Deformed Mesh Near Temperature BC Discontinuity	79
1.2-15	Yield Stress Contours	79
1.2-16	Contours of Average Element Temperature	80
1.2-17	von Mises Stress Contours (psi) With Thermal Strains	81
1.2-18	Contours of Stress Ratio	81
1.2-19	von Mises Contours (psi) Without Thermal Strains	82

LIST OF FIGURES (Continued)

Figure		Page
1.2-20	Contours of Stress Ratio Without Thermal Strains	82
1.2-21	Circumferential Stress Profiles (psi) With Thermal Stress	83
1.2-22	Circumferential Stress Profiles (psi) Without Thermal Stress	83
1.2-23	Finite Element Mesh of Entire Structure	85
1.2-24	Displacement (Sag) in Full Structural Model With Thermal Strains	85
1.2-25	Comparison of Sag in Models With Thermal Strains	86
1.3-1	Comparison of Calculated and Experiment Melt Temperatures for SURC 3	92
1.3-2	Comparison of Calculated and Experiment Ablation Distance for SURC 3	92
1.3-3	Comparison of Calculated and Experiment Melt Temperatures for SURC 3A	93
1.3-4	Comparison of Calculated and Experiment Ablation Distance for SURC 3A	93
1.3-5	CORCON Version 2.02 and 2.03 Results for the CORCON Standard Problem - Melt Temperature	96
1.3-6	CORCON Version 2.02 and 2.03 Results for the CORCON Standard Problem - Gas Generation	96
1.3-7	VANESA Aerosol Source Rates Calculated for the CORCON Standard Problem	97
1.3-8	CORCON Version 2.02 and 2.03 Results for a Peach Bottom Sample Problem - Melt Temperature	97
1.3-9	CORCON Version 2.02 and 2.03 Results for a Peach Bottom Sample Problem - Gas Generation	98
1.3-10	VANESA Aerosol Source Rates Calculated for the Peach Bottom Sample Problem	98
1.3-11	CORCON Version 2.04 Results for the CORCON Standard Problem With and Without Mass Addition - Melt Temperature	101

LIST OF FIGURES (Continued)

Figure		Page
1.3-12	CORCON Version 2.04 Results for the CORCON Standard Problem With and Without Mass Addition - Ablation Distance	101
1.3-13	CORCON Version 2.04 Results for the CORCON Standard Problem With and Without Mass Addition - Gas Generation	102
1.3-14	CORCON Version 2.04 Results for a Peach Bottom Sample Problem With and Without Mass Addition - Melt Temperature	102
1.3-15	CORCON Version 2.04 Results for a Peach Bottom Sample Problem With and Without Mass Addition - Ablation Distance	103
1.3-16	CORCON Version 2.04 Results for a Peach Bottom Sample Problem With and Without Mass Addition - Gas Generation	103
1.3-17	CORCON Version 2.04 Results for a Peach Bottom Sample Problem With Addition of Core Material and Coolant - Melt Temperature	104
1.3-18	CORCON Version 2.04 Results for a Peach Bottom Sample Problem With Addition of Core Material and Coolant - Ablation Distance	104
1.3-19	CORCON Version 2.04 Results for a Peach Bottom Sample Problem With Addition of Core Material and Coolant - Gas Generation	105
1.4-1	Experimental Apparatus	114
1.4-2	Liquid Jet Breakup Regime Map	119
1.4-3	Comparison of Initial Jet Breakup Behavior for a. Carbon Tetrachloride Into Water and b. Tetrabromoethane Into Water Versus c. Laminar to Turbulent Boundary Layer Transition on an Axisymmetric Body	120
1.4-4	Modes of Jet Breakup Include a. Dripping, b. Laminar Breakup by Axisymmetric Disturbance, c. Laminar Breakup by Sinuous Wave, d. Turbulent Breakup Because of Lateral Jet Oscillations and Viscous Effects, and e. "Atomizing" Turbulent Breakup Because of Viscous Shearing Effects	122

LIST OF FIGURES (Continued)

Figure		Page
1.4-5	Composite Description of a Starting Forced Plume	123
1.4-6	Typical Penetrating Plume Development	124
1.4-7	Typical Initial Penetration Behavior Showing Vortex Formation	126
1.4-8	Vortex Ring Generation as Shown by a. Flow Visualization and b. Numerical Simulation	127
1.4-9	Schematic Definition of Frequent Terms Used in Jet Flows	131
1.4-10	Typical Penetration Data	133
1.4-11	Test Data Versus Vertical Forced Plume Starting Length Solutions Given by Abraham and Hirst	136
1.4-12	Immiscible Liquid-Into-Liquid Jet Breakup Data	140
1.4-13	IFCI Test Problem Mesh Setup	144
1.4-14	Melt Outline in FITS Experiment	146
1.4-15	Melt Volume Fraction at Time 0.02 s	147
1.4-16	Melt Volume Fraction at Time 0.2 s	148
1.4-17	Melt Volume Fraction at Time 0.3 s	149
1.4-18	Volume Fractions of Vapor, Water, and Melt Fields on Problem Center Line Versus Height at Time 0.3 s	150
1.4-19	Melt Characteristic Diameter Versus Radius at Time 0.31 s	153
1.4-20	Melt Diameter Versus Radius and Height at Time 0.31 s	153
1.4-21	Pressure Versus Radius and Height at Time 0.302 s	155
1.4-22	Pressure Versus Radius and Height at Time 0.304 s	155
1.4-23	Pressure Versus Radius and Height at Time 0.306 s	156

LIST OF FIGURES (Continued)

Figure		Page
1.4-24	Melt Size Distributions From IFCI Problem and FITS0D Posttest Debris	157
1.4-25	Melt Size Distributions From IFCI Problem and FITS2D Posttest Debris	158
1.4-26	Melt Size Distributions From IFCI Problem and FITS5D Posttest Debris	158
1.4-27	Melt Size Distributions From IFCI Problem and FITS8D Posttest Debris	159
1.5-1	Simplified Diagram of Ice-Condenser Containment	164
1.5-2	Containment Noding Systems Used in HECTR Analyses of the In-Cavity Oxidation Problem	167
1.5-3	Pressure and Temperature Responses in the Upper Compartment Predicted by HECTR	168
1.5-4	Pressure and Temperature Responses in the Upper Compartment Predicted by HECTR	169
1.5-5	Pressure Responses in the Upper Compartment Predicted by HECTR	170
1.5-6	Temperature Responses in the Upper Compartment Predicted by HECTR	171
1.5-7	Density Distributions in the Lower Compartment Predicted by HECTR	173
1.5-8	Pressure and Temperature Responses in the Upper Plenum Predicted by HECTR	174
1.5-9	Comparison of Gas Release Rates from Core-Concrete Interactions Predicted by CORCON and MAAP	176
1.5-10	Mole Fraction of Gases in the Reactor Cavity During Core-Concrete Interactions and In-Cavity Oxidation Predicted by HECTR	177
1.5-11	Pressure and Temperature Responses in the Upper Compartment Predicted by HECTR	178
1.5-12	Detonation Cell Width Dependence on Temperature for Three Equivalence Ratios, No Steam	179

LIST OF FIGURES (Continued)

Figure		Page
1.5-13	Detonation Cell Width Dependence on Temperature for Three Equivalence Ratios, 30 Percent Steam .	181
1.5-14	Detonation Cell Width Dependence on Temperature for Stoichiometric Mixtures (ER=1) and Varying Steam Concentration	182
1.5-15	Detonation Cell Width Versus Equivalence Ratio for Test Series 8	185
1.5-16	Detonation Cell Width Versus Equivalence Ratio for Test Series 9	186
1.5-17	Comparison of the Inhibiting Effect of Steam and	
2.1-1	Coupon of Boron Carbide Before and After Exposure to Steam at 1270 K for About 4.5 Hours - Test 28	192
2.1-2	Boric Acids Condensed and Completely Filled the 2.6-cm Diameter Condenser	194
2.1-3	Sketch of the Transpiration Apparatus.	196
2.1-4	Vapor Pressure of CsOH	199
2.2-1	Functional Diagram of the Gas and Aerosol Sampling System for the Source Term Experiment .	203
2.2-2	ST-1 Filter Design	204
2.2-3	ST-1: Type C Thermocouples - Channel	206
2.2-4	ST-1: Axial Temperature Profile in Channel	207
2.2-5	ST-1: Type C Thermocouples - Channel	209
2.2-6	Selected Optical Spectra Emanating From the ST-1 Test Station	211
2.2-7	Optical Spectrum Recorded at 8282 Seconds	212
2.2-8	Optical Spectrum Recorded at 8973 Seconds	213
2.2-9	Optical Spectrum Recorded at 9435 Seconds	214
2.2-10	^{137}Cs in Fuel -- Before and After ST-1	216

LIST OF FIGURES (Continued)

Figure		Page
2.2-11	^{154}Eu in Fuel -- Before and After ST-1	218
2.2-12	Source Term Experiment 1 - Filter Thimble 1	219
2.2-13	ST-1 Results	225
3.1-1	Cross-Sectional Representation of Key BWR Core Structures (Upper Left) and the DF-4 Experimental Representation (Lower Right)	229
3.1-2	The DFR Experiment Apparatus Illustrating the Steam Supply Plant, Optical Viewing Station, and the ACRR Loading	232
3.1-3	Schematic Diagram of the Ex-Capsule Flow System Showing the Steam Inlet Lines, Back Flow Preventive Features, and Other Ancillary Plumbing Features	234
3.1-4	Schematic Diagram of the In-Capsule Flow System Showing Test Section Flow Circuits, Copper Oxide Tube Manifolds, Condenser, and Holding Tank	235
3.1-5	Schematic of DF-4 Test Showing Test Bundle, Insulation, and Major Boundaries	237
3.1-6	Diagram of the Principal Test Section Instrumentation	238
3.1-7	Test Bundle Total Inlet Steam Flow Rate During the Oxidation Transient Phase of the Test	241
3.1-8	Tungsten-Rhenium Thermocouple Responses for the Fuel Rod Instrumentation	243
3.1-9	Tungsten-Rhenium Thermocouples Responses for the Channel Box Instrumentation	246
3.1-10	Platinum-Rhodium Thermocouple Responses for the Control Blade Instrumentation	247
3.1-11	Copper Oxide Recombiner Tube Behavior for Each Tube Bank	249
3.1-12	Pre- and Post- X-Radiographic Images of the DF-4 Test Bundle.	253
3.1-13	Comparison of Measured Inlet Steam (Integrated Totals) With Calculated Valve Outlet Flow	255

LIST OF FIGURES (Continued)

Figure		Page
3.1-14	Comparison of Calculated and Measured Fuel Clad Temperatures at the 9.6-cm Location	257
3.1-15	Comparison of Calculated and Measured Fuel Clad Temperatures at the 25.4-cm Location	257
3.1-16	Comparison of Calculated and Measured Fuel Clad Temperatures at the 36.8-cm Location	258
3.1-17	Comparison of Calculated and Measured Fuel Clad Temperatures at the 49.5-cm Location	258
3.1-18	MARCON-DF4 Predicted Total Hydrogen Produced	260
3.1-19	MARCON-DF4 Predicted Bundle Power Generation	260
3.1-20	Predicted Axial Distribution of Clad Oxide Fraction for the Modeled "Hot Rod"	262
3.1-21	Predicted Axial Distribution for the Channel Box Oxide Fraction	262
3.1-22	Predicted Total Oxidation Fraction of Fuel Cladding, Channel Box, and Control Blade	263
3.1-23	Predicted Fraction Melted for the Fuel Cladding, Channel Box, and Control Blade	263
3.1-24	Predicted Axial Temperature Distribution for the Modeled "Hot Rod"	265
3.1-25	Predicted Temperatures for the Modeled Structures Corresponding to the 25.4-cm Axial Location	265
4.1-1	Phase Diagram for UO_2-ZrO_2	276
4.1-2	A Typical Binary Phase Diagram With a Eutectic Reactor	277
4.1-3	A Typical Isothermal Ternary Phase Diagram	279
4.1-4	Flow Chart for the CREUTK Subroutine	281
4.3-1	Electrical Resistivity of Refractory Oxides	284
4.3-2	Nomograph for Induction Heating	285
4.3-3	Schematic of the Experimental Apparatus	286

LIST OF FIGURES (Concluded)

Figure		Page
4.3-4	Temperature History for Experiment Number 1	288
4.3-5	Power History for Experiment Number 1	289
4.3-6	Temperature History for Experiment Number 2	290
4.3-7	Power History for Experiment Number 2	291
4.3-8	Temperature Histories for Workpieces Placed In Separated Coil	294
4.3-9	Workpiece Temperature Histories in Stacked Coil Configuration Without Faraday Ring	295
4.3-10	Workpiece Temperature Histories in Stacked Coil Configuration With Faraday Ring Between Coils ...	296
4.3-11	Workpiece Temperature Histories With Only 250-kW Power Supply Operating and Without Faraday Ring .	297
4.3-12	Workpiece Temperature Histories With Only 250-kW Power Supply Operating and With Faraday Ring Between Coils	298
4.3-13	Workpiece Temperature Histories With Only 125-kW Power Supply Operating and Without Faraday Ring .	299
4.3-14	Workpiece Temperature Histories With Only 125-kW Power Supply Operating and With Faraday Ring Between Coils	300

LIST OF TABLES

Table		Page
1.1-1	Chemical Composition of K/R Cast-98 MgO Castable Refractory	18
1.1-2	Chemical Composition of Basaltic Concrete	23
1.1-3	Standard Composition of 304 Stainless Steel	25
1.1-4	Chemical Composition of the Zirconium Metal	25
1.1-5	SURC 4 Fission-Product Simulants	26
1.1-6	Location of Thermocouples Installed in the Alumina Tubes and Cast Into the Concrete Cylinder, SURC 4	30
1.1-7	Events of Test SURC 4	56
1.2-1	SA533 Temperature Dependent Elastic-Plastic Material Model Data for JAC Finite Element Code.	66
1.2-2	Material Inputs for COYOTE	70
1.3-1	Modified CORCON Input Format for Mass Addition	100
1.3-2	Modified Standard Problem Input	106
1.3-3	Modified Peach Bottom Input	108
1.3-4	Modified Peach Bottom Input With Water Added	109
1.4-1	Initial Test Parameters for R-113 Into Water Jet Test	115
1.4-2	Density and Viscosity Data	116
1.4-3	Nondimensional Parameter Groups for R-113 Into Water Jet Tests	117
1.4-4	Coefficients for Determining the Critical Velocity for Laminar-to-Turbulent Transition in Axisymmetric Jet Breakup	129
1.4-5	Breakup Length Data	134
1.4-6	Typical Transition Points for Axially Symmetric Jets	135

LIST OF TABLES (Concluded)

Table		Page
1.4-7	Immiscible Isothermal Liquid System Pairs for Which Breakup Data Are Available	141
1.4-8	Length Scales From IFCI and FITS "D" Series	160
2.1-1	CsOH Transpiration Data	197
2.2-1	ST-1 Experiment Nominal Parameters	201
2.2-2	ST-1 Experiment Fuel Characteristics	201
2.2-3	ST-1 Experiment Fission-Product Inventory	202
2.2-4	Physical Parameters Used in VICTORIA and CORSOR Calculations	223
2.2-5	Measured Versus Predicted Releases	224
4.1-1	Typical Initial Properties of a Core Rubble Bed	271
4.3-1	Experimental Parameters	287

NOMENCLATURE

ACRR	-Annular Core Research Reactor
AICC	-Adiabatic Isochoric Complete Combustion
APS	-Aerodynamic Particle Sizer
BCL	-Battelle Columbus Laboratories
BNL	-Brookhaven National Laboratories
BWR	-Boiling Water Reactor
CEA	-Commisariat a L'Energie Atomique
CDA	-Core Disruptive Accident
CMCI	-Core Melt-Coolant Interaction
CMOT	-Clad Motion Code
CORCON	-Core/Concrete Interaction Code
DCC	-Degraded Core Coolability
DCH	-Direct Containment Heating
DF	-Damaged Fuel
DFR	-Debris Formation and Relocation
ECCS	-Emergency Core Cooling System
EDX	-Energy Dispersive X-Ray
EOEC	-End of Equilibrium Core
EURATOM	-European Atomic Energy Community
EXO-FITS	-Outside of Fully Instrumented Test Sites
FCI	-Fuel-Coolant Interaction
FITS	-Fully Instrumented Test Sites
FLAME	-Flame Acceleration Measurements and Experiments
FRG	-Federal Republic of Germany
FPRF	-Fission Product Reaction Facility
HCDA	-Hypothetical Core Disruptive Accident
HDT	-Heated Detonation Tube
HECTR	-Hydrogen Event: Containment Transient Response
HEDL	-Hanford Engineering Development Laboratory
HIPS	-High-Pressure Melt Ejection and Direct Containment Heating
HPME	-High-Pressure Melt Ejection
HPIS	-High-Pressure Injection System
IC	-Ion Chromatography
IDCOR	-Industry Degraded Core Rulemaking
IFCI	-Integrated Fuel Coolant Interaction
INPO	-Institute of Nuclear Power Operation
IRIS	-Inductive Ring Susceptor Technique
ISE	-Ion Specific Electrode
KfK	-Kernforschungszentrum Karlsruhe
LANL	-Los Alamos National Laboratory
LCS	-Limestone/Common Sand
LMF	-Large Melt Facility
LMFBR	-Liquid Metal Fast Breeder Reactor
LOAC	-Loss of Coolant Accident
LOF	-Loss of Flow
LWR	-Light Water Reactor
MAAP	-Modular Accident Analysis Program
MELPROG	-Melt Progression Code

NRC	-Nuclear Regulatory Commission
NTS	-Nevada Test Site
ORNL	-Oak Ridge National Laboratory
PIE	-Postirradiation Examination
PIXE	-Photon Induced X-Ray Emission
PNC	-Power Reactor and Nuclear Fuel Development Corporation
PRA	-Probabilistic Risk Assessment
PWR	-Pressurized Water Reactor
QUEST	-Quantitative Uncertainty Evaluation for the Source Term
RCS	-Reactor Coolant System
RSR	-Reactor Safety Research
RPV	-Reactor Pressure Vessel
S/A	-Subassembly
SARRP	-Severe Accident Risk Rebaselining Program
SASA	-Severe Accident Sequence Analysis
SEALS	-Steam Explosions at Large Scale
SEM	-Scanning Electron Microscope
SFD	-Severe Fuel Damage
SHE	-Straight High Explosive
SHIP	-Small-Scale High Pressure
SPIT	-System Pressure Injection Test
ST	-Source Term
SURC	-Sustained Urania-Concrete Interactions
SWISS	-Sustained Water Interactions With Stainless Steel
TEXAS	-Thermal Explosion Analysis System
TGT	-Thermal Gradient Tube
TMBDB	-Thermal Margin Beyond Design Basis
TRAN	-Transition Phase
TURC	-Transient Urania Concrete
TWT	-Transient Water Tests
ULOF	-Unprotected Loss of Flow
UT	-Ultrasonic Thermometer
VGES	-Variable Geometry Experimental System
WDX	-Wavelength Dispersive Analysis
XRD	-X-Ray Diffraction
XRF	-X-Ray Fluorescence

EXECUTIVE SUMMARY

1. CONTAINMENT LOADING AND RESPONSE

Although U.S. commercial nuclear power plants are designed to be highly reliable and resistant to plant upsets or accidents, multiple barriers are provided to prevent the release of radioactive materials in the unlikely event of a severe reactor accident. The reactor containment building is of particular importance, since it is the last barrier preventing radionuclide release to the environment. In order to perform its function, the containment building must survive stressing phenomena that may occur during a severe accident. These include (1) interactions of core debris with structural concrete; (2) direct containment heating caused by pressure-driven expulsion of melt from the reactor vessel; (3) fuel-coolant interactions (FCIs), which may create damaging missiles, cause direct failure of containment structures (e.g., BWR MK II and III pedestal walls), or lead to rapid pressurization from the generation of hydrogen, steam, or both; and (4) hydrogen combustion, which will result in quasi-static loads from deflagrations or dynamic loads from accelerated flames and detonations. Key safety equipment must also survive high temperatures generated during hydrogen combustion. Current severe accident research is directed at understanding these phenomena to provide a sound technical basis for design and evaluation of containment systems and for the development of rational accident management procedures.

Highlights of our recent experimental research on these phenomena are described in this report.

1.1 Ex-Vessel Core Debris Interactions

The purpose of the Ex-Vessel Core Debris Interactions program is to measure, model, and assess the thermal, gas evolution, and aerosol source terms produced during core debris-concrete interactions that might occur following a severe nuclear reactor accident. These source terms are the governing phenomena in any postaccident containment integrity analysis or risk evaluation. A matrix of eight tests is being conducted as part of the program. This matrix is designated as the SURC (SUSTAINED URANIA-CONCRETE) test series.

The SURC 4 test accomplished all of its established pretest goals and was successful in observing and recording all the effects associated with both steady-state concrete erosion as well as the additional effects of Zr addition on steel-concrete attack. These effects were evident in the measured melt pool

temperatures, erosion rates, heat losses, gas flow rate, gas composition, and aerosol characterization.

The results of the experiment are not reported here because the experiment has been selected by the Committee on the Safety of Nuclear Installations as a sample problem for the validation and testing of existing models for core debris-concrete interactions. The results of the experiment have been sequestered until the study is completed. We can report, though, that the CORCON code accurately predicted the steady-state melt temperatures and concrete ablation rates observed in the experiment prior to and subsequent to the addition of zirconium. The essential input data that would be required to predict the results of SURC 4 using codes such as CORCON, WESCHEL, or INTER are provided, however. A summary of that input data is provided and includes the test geometry, the materials used in the test, the test instrumentation, test procedures, and some initial temperatures at the test boundaries. The program objectives and specific test goals are also provided.

Posttest observations of the SURC 4 containment vessel after it was opened showed that the MgO sidewalls were intact and that there was no evidence of melt pool-sidewall interaction other than thermal dehydration. The molten steel charge had completely penetrated the bottom of the interaction crucible through a gap between the MgO and the remainder of the basemat. The remainder of the basemat was not cracked and showed no signs of asymmetric erosion. Further inspection of the steel charge and the slag material remaining in the crucible showed that 100 percent of the zirconium metal had been incorporated into the melt.

1.2 High-Pressure Melt Ejection and Direct Containment Heating

The High-Pressure Melt Ejection and Direct Containment Heating program is performing experiments and analyses of the phenomena associated with the pressurized ejection of core debris into the reactor cavity. Accident analyses leading to this pressurized ejection of core debris assume localized failure of the lower reactor pressure vessel head. Experiments are being planned to investigate the potential for failure of an instrument guide tube penetration and the subsequent growth of the aperture during melt ejection. A finite element analysis was also undertaken to determine the condition of the lower head under accident conditions and the influence of thermal strains on the failure of the reactor pressure vessel.

The results of the finite element analysis show that thermal strains increase the magnitude of sag of the lower head and that the transient stress distribution is altered. Thermal strains, however, have no significant effect on the time to failure of the reactor pressure vessel where the failure mechanism is bursting of the bottom head.

1.3 CORCON and VANESA Code Development

The later stages of a severe nuclear reactor accident are marked by the deposition of molten core debris into the reactor cavity, which leads to vigorous interactions between the core melt and structural concrete. Included in these interactions are rapid ablation of the concrete with intense aerosol generation and gas and fission-product release. These phenomena are an important concern in severe accident source term evaluation, and risk and consequence assessment.

The CORCON and VANESA computer models were developed at Sandia to model these ex-vessel core debris-concrete interactions. The goals of this program are to develop and validate improved versions of CORCON and VANESA that can be used with confidence in the analysis of the source term from severe reactor accidents.

Early comparisons between experimental data and CORCON calculations indicated that the existing melt-concrete heat transfer models were inadequate. An improved melt-concrete heat transfer model was developed and included in a working version of CORCON. Subsequent comparisons between calculations made using this version of the code and the results of experiments at Sandia and Kernforschungszentrum Karlsruhe were, in general, excellent. Recent comparisons between CORCON calculations and the melt temperature and ablation results from the SURC 3, SURC 3A, and SURC 4 experiments were also excellent. The excellent comparisons for melt temperature are particularly significant since aerosol and fission-product release during core-concrete interactions are strongly dependent on the temperature of the core debris.

Two additional updates to CORCON have been released; these updates are the third and fourth correction sets to the code. The third correction set, which creates CORCON Version 2.03, was a complete replacement of the chemistry subroutine, MLTREA. The fourth correction set, which creates CORCON Version 2.04, implements the capability of accepting time-dependent input of core material, structural material, and coolant. This change was necessitated by the advent of improved, mechanistic models for

in-vessel melt progression, such as MELPROG, which calculate gradual melting of core material over a time span of several hours.

1.4 Molten Fuel-Coolant Interactions

The objective of this program is to develop an understanding of the nature of fuel-coolant interactions during a hypothetical accident in light water reactors. The understanding of these interactions achieved in this program is expected to resolve key reactor safety issues for both terminated and unterminated accidents. Experiments are being conducted to determine the influence of three classes of important independent variables: thermodynamic conditions (temperatures of the fuel and the coolant and the ambient pressure); scale variables (amount of fuel and coolant initially involved); and the boundary conditions (pour diameter and rate, shape and degree of confinement of the interaction region, presence of structures, water depth, and fuel-coolant contact mode).

The FITS-3D experiment has been conducted, completing the truncated FITS-D series. This experiment represents the first of its kind, and it yielded interesting results. Preliminary results and observations reveal that no explosive interaction occurred, as was expected. The chamber was rapidly pressurized during the experiment because of the generation of both hydrogen and steam. During the first 2 or 3 s, the chamber was pressurized from 0.7 to ~1.03 MPa and then more slowly to 1.1 MPa over the next 20 s or so. Some of the most interesting information, however, is available from the "real time" mass spectrometer data: Preliminary analysis indicates that 70 to 80 percent of the final hydrogen concentration was detected during a 2-s transient. Furthermore, both grab samples and mass spectrometer results indicated that almost complete oxidation of the metallic fuel (iron) occurred during this experiment, a result not expected and much higher than observed in past FITS experiments.

We also continued to study the coarse-mixing behavior of jets by performing and analyzing a number of isothermal jet-mixing experiments. Data obtained included information on breakup lengths, penetration behavior, and entrainment rates. Flow regimes primarily covered reactor accident scenarios, for which no data was available in the published literature.

The first preliminary calculation using the IFCI module of MELPROG was performed. The results are very encouraging in that they are qualitatively similar to experimental observations from the FITS experiments. The shape of the melt as it falls through

the water, the propagation speed of the pressure front through the mixture region, and the final melt size distribution resembles those seen in some of the previous FCI experiments. This would seem to indicate that IFCI is doing a reasonable job of simulating the major phenomena occurring during the FCI process, particularly those operative during the coarse-mixing phase.

We believe that the present calculation represents the first simulation of the complete FCI process in more than one dimension, including dynamic fragmentation. Both two dimensions and dynamic fragmentation appear necessary for a code to correctly simulate the coarse-mixing phase, and the presence of these two key features greatly aids the simulation of the propagation and expansion phases without having to make simplifying assumptions.

1.5 Hydrogen Behavior

The objectives of this program are (1) to quantify the threat, if any, to nuclear power plants (containment structure, safety equipment, and the primary system) posed by hydrogen combustion; (2) to disseminate information on hydrogen behavior, detection, control, and disposal; and (3) to provide program management and technical assistance to the NRC on hydrogen-related matters.

A sensitivity study of several parameters was conducted using HECTR for an in-cavity oxidation problem. The problem chosen was an S2HF drain-closed accident sequence in a PWR ice-condenser containment. Three parameters were studied: (1) the influence of steam inerting, (2) the operation of the air-return fans, and (3) the gas release rates predicted by the CORCON codes versus the MAAP code. Complete in-cavity oxidation is predicted using the 6-compartment model in HECTR when the steam-inerting effect is neglected. This compares to an incomplete in-cavity oxidation and a subsequent global burn when the steam-inerting effect is included. The global burn produces a larger peak pressure than the steam overpressurization for the complete in-cavity oxidation case. With the air-return fans off, a smaller amount of combustible gases will accumulate in the containment before ignition occurs and will be concentrated in the lower compartment since the air-return fans do not transport the combustible gases to the upper compartment. Therefore, the peak pressure is less for the case with the air-return fans off. Peak pressures are less when using source terms from the CORCON code versus the MAAP code.

EXECUTIVE SUMMARY

Experimental and analytical research on detonation propagation disclosed a new and important area of uncertainty in the detonability of hydrogen-air-steam mixtures at very high temperatures and high steam concentrations. Three scenarios that may be affected by this uncertainty are (1) the possibility of local and global detonations, (2) the direct containment heating problem, and (3) the in-cavity oxidation of combustible gases produced by core-concrete interactions. Analytical predictions indicate a large increase in the sensitivity of an off-stoichiometric or steam-diluted mixture to detonate with increasing initial temperature. These predictions have been experimentally verified up to 100°C.

In another area of research, the inhibiting effects of steam and carbon dioxide were quantified. A comparison of the two diluents indicates that not only is carbon dioxide a better inhibitor than steam, but it becomes more effective with increasing concentration.

2. FISSION PRODUCT SOURCE TERM

The High-Temperature Fission-Product Chemistry program provides experimental data on the thermodynamics and kinetics of chemical processes affecting the chemical form of released radionuclides, the interactions of these radionuclides with structural and aerosol surfaces, and the revaporization of deposited radionuclides. The ACRR Source Term Experiments are in-pile tests of radionuclide release under high-pressure, high-radiation intensity, and high-hydrogen concentration conditions. They supplement out-of-pile experiments of radionuclide release being conducted elsewhere in the NRC-sponsored research. Both experimental programs provide crucial data needed for accident models. The primary thrusts of the experimental programs are to provide data for the development and validation of the NRC's best-estimate model of fission-product behavior, VICTORIA.

2.1 High-Temperature Fission-Product Chemistry and Transport

The purpose of the Fission-Product Chemistry and Transport program is to obtain data on the chemistry and processes that affect the transport of fission products under accident conditions. To assist in obtaining data, an experimental facility has been built to allow the chemistry of fission products in prototypic steam-hydrogen environments to be studied. The interaction of fission products with reactor materials such as stainless steel are examined in this facility. Results of these experimental studies are compared to predictions of thermochemical models to determine if reaction kinetics play an important role in fission-product transport.

Three laboratory scale tests examined the effect of boron carbide, used for the control of some nuclear power reactors, on reactor accident conditions. The tests, conducted in steam at 1270 K in an Inconel-600 system, examined the boron carbide-steam system and then that system with an addition of either cesium hydroxide or cesium iodide vapor. Extensive reaction was demonstrated between the boron carbide and steam to produce B_2O_3 and boric acids in a two-step kinetic process. Average rates of production for the oxide and acids were calculated for the three tests. These rates were functions of time, temperature, B_4C geometry, and partial pressure of the steam and the boric acid. Significant reactions were observed between the boric oxide formed on the B_4C and both the CsOH vapor and the CsI vapor, dissociating the cesium and iodine in the latter case. The cesium reaction product in both cases was probably $CsBO_2$, with

the iodine forming HI. Surface reaction rate constants were estimated for the CsOH and the CsI reactions.

Although the JANAF thermochemical tables contain thermodynamic data from which the vapor pressure of CsOH above the pure liquid CsOH can be calculated, there has been no previous measurement of that vapor pressure. The first experimental measurements made in the temperature range of 704 to 1133 K are discussed in this report.

2.2 ACRR Source Term Experiments

The ACRR Source Term program is being conducted to provide a data base for fission-product release over a range of fuel temperatures, system pressures, and fuel damage states. Significantly, these experiments are performed in well-controlled, well-known in-pile conditions and in the presence of ionizing radiation, where little or no data currently exist. The purpose of this research is to allow development and validation of improved fission-product release models.

The ST-1 test was successfully conducted on April 28, 1987. This experiment was the first in a series of tests designed to study the release of fission products from irradiated LWR fuel elements under severe accident conditions. It was performed in a highly reducing environment at maximum fuel temperatures of about 2400 K. Six filter samplers were used to collect fission-product vapors and gases; five gas grab sample bottles were used to collect krypton and xenon and to regulate the pressure. Pretest and posttest gamma scans of the package were performed to determine fission-product relocation. The filter samplers and gas grab sample bottles were gamma scanned to measure the fission products collected (primarily cesium). The filter samplers were disassembled in the Sandia Hot Cell Facility and the filter components were gamma scanned. The filter components were leached with water and subsequently 7.5 M nitric acid. Extensive posttest analyses are under way to measure specific elements. Cesium and europium are being measured by gamma counting, iodine with an ion specific electrode, barium and strontium by ion chromatography, and tellurium by electrochemical voltammetry. Wavelength dispersive analysis is being used to identify elements that collected on deposition wires. Posttest analyses are not yet complete.

3. LWR DAMAGED FUEL PHENOMENOLOGY

The focus of the LWR Damaged Fuel Experiment program is directed toward providing separate-effects phenomenological data on important severe in-vessel fuel-damage processes to aid in the development of second generation severe accident analysis codes. The core damage configuration, hydrogen generation, and fission-product release are the primary areas of interest. The damaged fuel test series uses cinematography to record the fuel damage progression during the course of in-pile experiments in which accident conditions are simulated in a small LWR fuel bundle. Decay heating in these experiments is simulated by fission heating of the fuel in the ACRR. Steam conditions and clad preoxidation, similar to expected accidents in a local region of a degrading core, are provided. Experiment diagnostics include thermocouple measurements of the test bundle temperatures, pressure and steam flow measurements, and measurement of hydrogen production, in addition to the visual recording of the damage progression. Destructive examination of the test bundle is carried out, including metallographic characterization.

3.1 DF-4 BWR Control Blade/Channel Box Fuel Damage Experiment

The NRC-sponsored Debris Formation and Relocation experiments being performed at Sandia provide data on the effects of key variables and conditions on the progression and severity of core damage processes. In addition to steam conditions and initial clad oxidation, steam flow rates, system and rod internal pressures, and the effect of control rod materials on damage are provided.

The DF-4 experiment was the first test of this kind that used a BWR zircaloy fuel canister and stainless steel/B_4C control blade. Major uncertainties concerning BWR accident progression addressed in DF-4 included:

1. The relative heatup rate and oxidation behavior of the BWR fuel clad/canister wall/control blade structures.

2. The potential interaction between the B_4C powder in the control element and steam.

3. The timing and mode of control rod failure either by melting or eutectic liquefaction.

4. The interaction effects between the steel control structures and the zircaloy channel box wall.

5. The integrity of the channel box with respect to side wall damage.

6. The potential for tight blockage formation within the channel box.

The test bundle thermal response was characterized through the thermocouple measurements of the fuel rods, channel box, and control blade structures. The measurements indicated massive failure of the control blade and channel box structures, with failure of the B_4C filled steel control blade preceding failure of the zircaloy channel box. These major relocation events were also evident from the video record of the test bundle obtained during the damage sequence, correlating well with the on-line temperature measurements with respect to timing of failure and relocation. Radiographic examination of the posttest damage configuration confirmed the large extent of control blade and channel box failure, showing that roughly 90 percent of the axial extent of these structures failed and relocated to the base of the bundle, although the fuel rods were largely intact and standing.

A thermal analysis, using the ORNL-developed MARCON-DF4 computer code, was accomplished. An important element of the analysis was in the consistent evaluation of all of the assumed values of the test parameters, such as ACRR test bundle power coupling, test bundle inlet steam flows, and the measurable quantities such as bundle temperatures and hydrogen production rate. The results of the analysis indicate that the test data were generally absent of any inconsistent or unexplainable trends, and the thermal comparisons between calculation and experimental measurements were excellent.

Activities ongoing for this experiment include destructive examination and metallurgical characterization of the test bundle, analysis of the hydrogen production data, and analysis of the W/Re high-temperature measurements.

4. MELT PROGRESSION PHENOMENOLOGY CODE DEVELOPMENT (MELPROG)

The MELPROG computer code is being developed to provide a mechanistic computer model for analysis of in-vessel phases of severe accidents in LWRs. MELPROG is implicitly linked to the TRAC-PF1 thermal hydraulics computer code. Together, MELPROG and TRAC provide a complete and integrated treatment of an LWR primary coolant system from accident initiation through release of core materials and fission products from the reactor vessel. MELPROG is also being linked to the CONTAIN reactor analysis computer code. MELPROG provides core material transfer rates and thermodynamic conditions to CONTAIN. Currently there is no feedback from CONTAIN to MELPROG.

MELPROG has been developed as a set of modules that are coupled explicitly and share a common data structure. MELPROG consists of eight modules (FLUIDS, CORE, STRUCTURES, DEBRIS, RADIATION, VICTORIA, IFCI, and EJECT) and the implicit link to TRAC-PF1. The modular structure of MELPROG has been designed to treat tightly coupled phenomena within a module and to provide a framework that easily could be modified by changing individual models or whole modules.

4.1 MELPROG Code Development

MELPROG development is continuing and has included work on several modules; however, the major efforts have centered on the CORE and DEBRIS modules. A new treatment of eutectic formation has been added to the CORE module. This model provides for the simultaneous dissolution of UO_2 and ZrO_2 by a eutectic mixture of U-Zr-O. A new, more detailed debris-bed model is being developed to replace all or part of the current module. Development work has also continued on the IFCI and VICTORIA modules.

4.2 MELPROG Code Applications

MELPROG is currently being used in the analysis of the DF-1 and DF-2 experiments. These calculations have been carried out through significant material relocation. Also, a TMLB' accident calculation is under way for the Surry reactor. This calculation is being performed with MELPROG/TRAC and is the first full reactor calculation to use the CORE module. This calculation, also, includes coupling to CONTAIN.

4.3 MELPROG Validation Experiments

Experiments were done to determine if simulated reactor core debris could be heated directly by a magnetic field. Success of this technique would allow molten pools to be formed without interference from inductive susceptor rings. A second series of tests was completed to assess the influence of a Faraday ring on a stacked coil configuration. The results indicate that a Faraday ring is very effective in shielding a workpiece from the magnetic field. This technique will be used in experiments studying failure of instrument tube penetrations into the lower head of a reactor pressure vessel.

1. CONTAINMENT LOADING AND RESPONSE

Although U.S. commercial nuclear power plants are designed to be highly reliable and resistant to plant upsets or accidents, multiple barriers are provided to prevent the release of radioactive materials in the unlikely event of a severe reactor accident. The reactor containment building is of particular importance, since it is the last barrier preventing radionuclide release to the environment. In order to perform its function, the containment building must survive stressing phenomena that may occur during a severe accident. These include (1) interactions of core debris with structural concrete; (2) direct containment heating caused by pressure-driven expulsion of melt from the reactor vessel; (3) fuel-coolant interactions (FCIs), which may create damaging missiles, cause direct failure of containment structures (e.g., BWR MK II and III pedestal walls), or lead to rapid pressurization from the generation of hydrogen, steam, or both; and (4) hydrogen combustion, which will result in quasi-static loads from deflagrations or dynamic loads from accelerated flames and detonations. Key safety equipment must also survive high temperatures generated during hydrogen combustion. Current severe accident research is directed at understanding these phenomena to provide a sound technical basis for design and evaluation of containment systems and for the development of rational accident management procedures.

Highlights of recent experimental research on these phenomena are described in this report. The recent developments in models of core debris interactions with concrete--CORCON and VANESA--are also described. The experimental results are not only being used to support model development for CORCON and VANESA, but also for the integrated systems containment code, CONTAIN, and the melt progression code, MELPROG. FCI experiments are underway to investigate the behavior of single and multiple molten fuel jets pouring through water and to determine the rates of generation of hydrogen and steam. Based on these experiments, phenomenological models are being developed and incorporated into the MELPROG module, IFCI; development, applications, and assessment of this module is an active area of FCI research. Hydrogen detonation experiments are being completed in the Heated Detonation Tube. The ZND model is being assessed against these data and extrapolated to estimate detonability in untested regions of high temperature and high steam concentration. Work is also continuing on the development and validation of the HECTR code. HECTR combustion models are being incorporated into CONTAIN as soon as feasible.

1.1 Ex-Vessel Core Debris Interactions

(E. R. Copus, D. A. Powers, J. E. Brockmann, and R. E. Blose, 6422; D. R. Bradley, 6425)

The high-temperature ablation of concrete by molten nuclear reactor core debris has been recognized as an important aspect in radioactive source term evaluations for core meltdown accident scenarios. A core melt-concrete interaction can produce large quantities of noncondensible gases and aerosols laden with fission products. Combustible gases such as hydrogen and carbon monoxide as well as heat are liberated simultaneously. If combustion of these gases occurs, then significant pressurization of the containment can be expected, possibly even threatening containment integrity. The long-term behavior of a core melt-concrete interaction may include significant erosion of the concrete basemat, possibly even melting through the floor.

1.1.1 Sustained Urania-Concrete Interactions (SURC): Experiments and Analysis

The Ex-Vessel Core Debris Interactions program is intended to measure, model, and assess the thermal, gas evolution, and aerosol source terms produced during core debris-concrete interactions that might occur following a severe nuclear reactor accident. These source terms are the governing phenomena in any postaccident containment integrity analysis or risk evaluation. A matrix of eight tests is being conducted as part of the program. This matrix is designated as the SURC (SUSTAINED URANIA-CONCRETE) test series.

In addition to extending the existing data base to include more prototypic core debris-concrete interactions, the SURC experiments are designed to provide information necessary to validate three important aspects of ex-vessel core debris-concrete interactions models. These are (1) heat transfer mechanisms, (2) gas release chemistry, and (3) vaporization release of aerosols. Both integral tests using UO_2-ZrO_2 materials (SURC 1, SURC 2, SURC 5, and SURC 6) as well as separate effects tests using stainless steel (SURC 3, SURC 4, SURC 7, and SURC 8) will be conducted.

The first two tests in the SURC series were designed to be integral tests using a 250-kg mixture of 69 w/o UO_2-22 w/o ZrO_2-9 w/o Zr over a 40-cm diameter concrete basemat formed from either limestone concrete (SURC 1) or basaltic concrete (SURC 2). Tests 3 and 4 in the SURC series were designed to be separate effects tests using stainless steel, which investigated the additional effects of zirconium metal oxidation on sustained core debris concrete interactions. In tests SURC 3 and SURC 4, Zr metal was added to molten stainless steel to create melt pools with up to 10 percent Zr interacting with two different concrete basemats. The tests were inductively heated in order to sustain

the molten attack and lasted as long as 4 h. The molten steel charge ablated either limestone (SURC 3) or basaltic (SURC 4) concrete until steady-state erosion and gas release were established. Zirconium metal was then added to the melt pool, and its effects on gas release rates and gas chemistry were observed. Together, SURC 3 and SURC 4 are expected to provide validation data for gas release chemistry models in the CORCON code, particularly with regard to the severity and duration of any coking effects, which are predicted to produce extraordinary amounts of carbon monoxide immediately after the zirconium is fully oxidized. At present, the CORCON code calculates that the H_2O and CO_2 released from the concrete will be almost totally reduced by Zr in the melt, forming ZrO_2, H_2, and elemental carbon. Virtually no gas other than hydrogen is predicted to be released during this reduction phase. After nearly all of the Zr metal is oxidized, the residual elemental carbon is expected to react with CO_2 or H_2O to form carbon monoxide. When this occurs, the gas release rate is expected to double the steady-state value since two moles of gas are produced from each mole of gas evolved from the concrete. SURC 3 and SURC 4 were instrumented to test this predicted behavior.

The SURC 4 experiment used 200 kg of 304 stainless steel and 20 kg of Zr metal as the charge materials. It was designed to be a comprehensive test examining the additional effects of zirconium metal added to molten steel interacting with basaltic concrete. The goals of the experiment were to measure in detail the gas evolution, aerosol generation, and erosion characteristics associated with steel-zirconium-concrete interactions.

The SURC 4 experiment was conducted in a 60-cm-diameter interaction crucible constructed with a 40-cm-diameter basaltic concrete cylinder in the base of a magnesium oxide (MgO) annulus. A 10-cm thick, circular cover of MgO was fabricated and placed on top of the crucible. The interaction crucible and induction coil were housed in a sealed, water cooled, aluminum containment vessel. A schematic of this vessel and the rest of the instrumentation for the test is shown in Figure 1.1-1. The vessel was 180 cm high, 120 cm in diameter, and contained feedthroughs for the induction power leads, instrumentation leads, and an exhaust gas port connected to the flow and aerosol sampling instrumentation. The interaction crucible was instrumented with numerous thermocouple arrays cast into the concrete cylinder, MgO annulus, and MgO cover. A 280-kW induction power supply and coil were used to heat and melt the 200-kg stainless charge within the test article and to sustain the interaction for the duration of the experiment. Additionally, 6 kg of fission-product simulants were added to the melt to study fission-product release. Flow rates of generated gases were measured using a sharp edge concentric orifice, a laminar flow device, and two dry gas clocks. Gaseous effluents produced during the experiment were monitored and sampled using an infrared gas analyzer, a mass spectrometer, and an integral grab sample technique. Aerosols were captured on

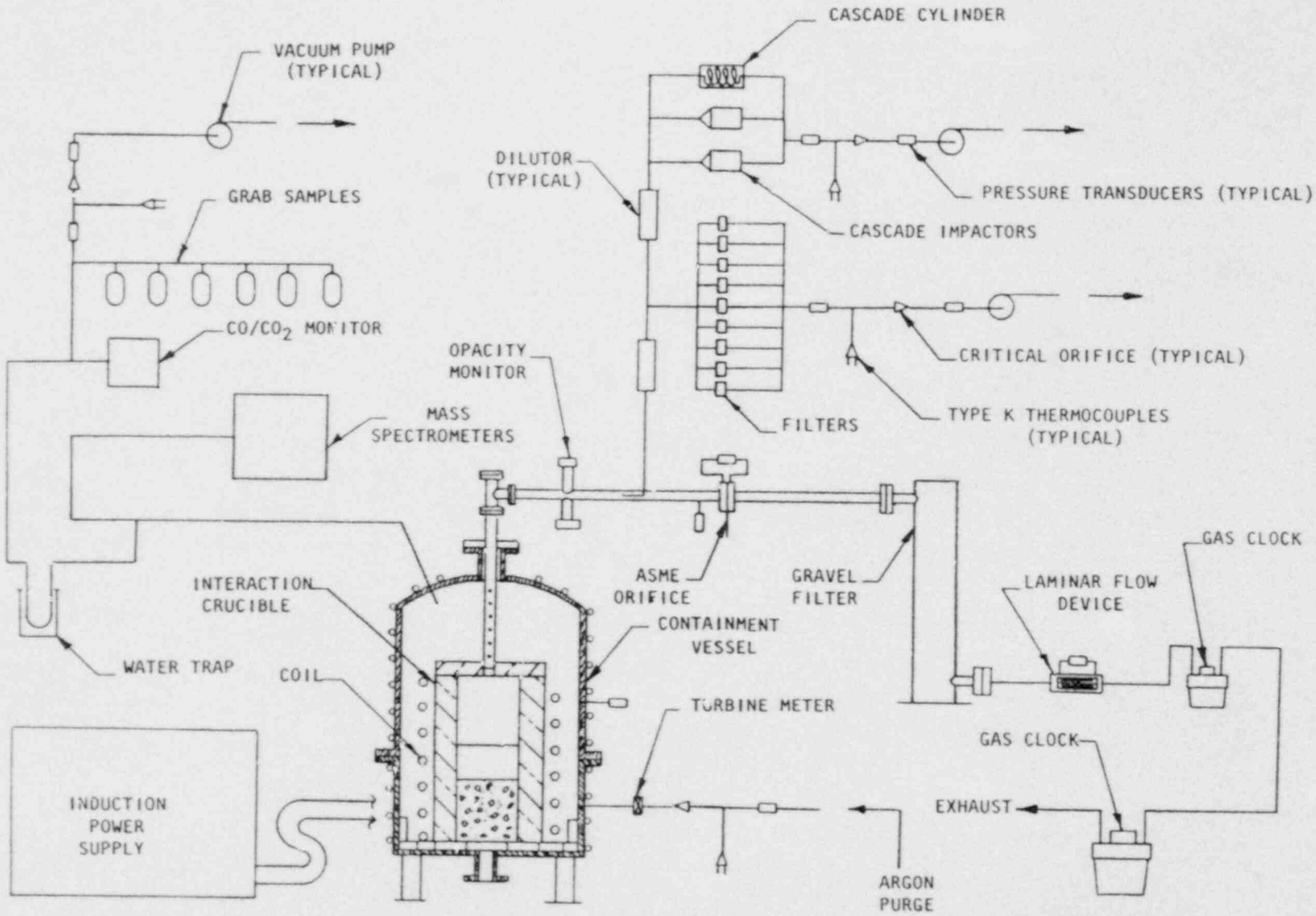

Figure 1.1-1. SURC 4 Schematic

filters, cascade impactors, and a cascade cyclone. Erosion characteristics were measured using Type K, S, and C thermocouples in order to define the melt pool temperature and overall heat balance as well as the axial erosion rate. The apparatus was sealed and purged with argon gas in order to direct the majority of the reaction gas and aerosol effluents through a 5-cm-diameter flow pipe. The SURC 4 test was run at local atmospheric pressure (0.83 atm) and at an ambient temperature of 25°C.

The zirconium metal was added to the melt pool after steady-state concrete erosion was established using a single tube, manually-actuated, delivery system attached vertically to the containment vessel. The tube contained 50 Zr cylinders each with a diameter of 3.3 cm and a length of 7.6 cm. Each cylinder weighed 400 g and the total charge weighed 20 kg. Deposition into the melt pool was accomplished by opening a ball valve to the gas flow line, dropping the Zr metal, and closing the ball valve to reestablish flow through the exit port.

The SURC 4 test was designed to provide comprehensive, redundant, and well-characterized information on the steel-zirconium-concrete interaction that would be suited for code validation efforts. The SURC 4 test ran for a total of 162 min. The data return was excellent and all of the test goals were successfully met.

1.1.1.1 Materials

The interaction crucible used in the SURC 4 experiment was of a cylindrical geometry. The crucible consisted of three major components; lower crucible, upper crucible, and cover. The annulus of upper and lower crucible and the cover were cast using a MgO castable refractory material. Basaltic concrete was cast into the base of the lower crucible. A detailed description of the interaction crucible including dimensions and thermocouple locations is discussed in Section 1.1.1.3.

- **Magnesium Oxide (MgO) Castable**

The annulus of the crucible was cast using an MgO castable material manufactured by Kaiser Refractories called K/R Cast-98. This material is a superior MgO castable produced from critically sized 98+ percent MgO periclase and bonded with a special chromate composition. K/R Cast-98 can be vibrated to exceptionally high densities. This material resists melt penetration and provides outstanding resistance to highly basic slags. This material also has excellent volume stability and is commonly used for crucibles in the steel industry. The chemical composition of K/R Cast-98 is shown in Table 1.1-1.

Table 1.1-1

Chemical Composition of K/R Cast-98[a]
MgO Castable Refractory

Oxide	Weight %
MgO	97.1
SiO_2	0.4
Al_2O_3	0.1
Fe_2O_3	0.3
CaO	1.0
Cr_2O_3	1.1

[a]K/R Cast-98 is a product of Kaiser Refractories, 300 Lakeside Drive, Oakland, CA 94643.

Data Obtained from Basic Ramming and Casting Mixes Bulletin Published by Kaiser Refractories.

The MgO castable was mixed by placing a known mass of dry material into a clean paddle-type mixer. Clean drinking water was then added, 5 percent by weight, to the castable material and mixed for at least 2 min. Once a homogeneous mixture was achieved, the mix was carefully placed into the casting forms with small scoops and shovels. Two types of vibrators, operating at 10,000 to 12,000 vibrations/min were used to densify the mix and remove entrained air. A pneumatically operated eccentric vibrator was attached to the brackets mounted to the steel casting forms. Another mechanical vibrator called a "stinger" was inserted directly into the mix to enhance densification.

After casting, the mix was cured at ambient temperature (15° to 35°C) for 24 h. Then the forms were placed in an oven and initially heated at a rate of 40°C/h to 265°C. The casting was held at temperature for 12 h. The total curing cycle took 24 h. During the baking period, two K-type thermocouples were connected to a strip chart recorder to monitor the curing temperature. One thermocouple measured the ambient oven temperature; the other thermocouples was cast into the annulus and measured the actual temperature of the annulus.

The thermal behavior of the K/R Cast-98 was characterized by thermal gravimetric analysis (TGA). This analysis was performed

with a Dupont 790 thermal analysis apparatus with a 1870 K DTA cell and Model 950 TGA attachment.

The TGA was performed in dry air with a flow rate of 50 cm^3/min. The heating rate was 10 K/min from room temperature to 1400 K. The sample had been air cured for 24 h followed by baking at 470 K for 24 h, then allowed to air cool for an additional 24 h prior to thermal analysis. Weight losses indicated in the thermogram are attributed to the release of free and bound water. This sample showed a 4.0 w/o loss due to release of free water between ambient temperature and 700 K. From 700 to 1000 K, an additional 0.2 w/o loss of bound was observed, which is probably due to the decomposition of brucite ($Mg(OH)_2$).

The thermal properties of the castable K/R Cast-98 have been extensively investigated. In addition to industry data, experiments were conducted at Sandia to study the thermal response of the MgO to intense heating conditions similar to those expected during an experiment. These experiments were carried out at the Sandia Solar Tower where a MgO specimen was subjected to incident solar fluxes in the range of 6.5×10^5 W/m^2 to 1.4×10^6 W/m^2. The test specimen was 45 cm x 45 cm x 8 cm and was cast of the K/R Cast-98 material. The test specimen was well instrumented with seventeen, 1.5-mm diameter type K thermocouples, located from 0.3 cm to 6.3 cm below the exposed surface. The test specimen was mounted in a frame compatible with the Solar Tower assemblies. The incident flux was monitored by heat flux gauges deployed along the top and side of the test specimen. The back of the test specimen was well insulated in order to approximate an adiabatic boundary condition.

A typical thermal history of the specimen is shown in Figure 1.1-2. As one can see, the temperature rise is interrupted at 373 K. This is due to the release of the free water in the castable material. The material continued to be heated until approximately 1673 K, then the solar heat flux was removed and the test specimen was allowed to cool.

The data were analyzed by the "PROPTY" code developed by J. V. Beck. The code determines the thermal conductivity of a material that fits a set of temperature response curves for specific interval and boundary conditions.

The PROPTY prediction of the thermal conductivity of the MgO is shown in Figure 1.1-3. The presence of the free water within the castable material causes minor problems in the analysis of the experimental data. As shown in Figure 1.1-3, the predicted thermal conductivity is slightly higher for "wet" or uncured material than it is for "dry" or fully dehydrated MgO castable. A check of the relative accuracy of the values of the conductivity is demonstrated by comparing the predicted thermal response with the actual experimental data. As shown in Figure 1.1-2, excellent agreement is achieved. The absolute values of thermal

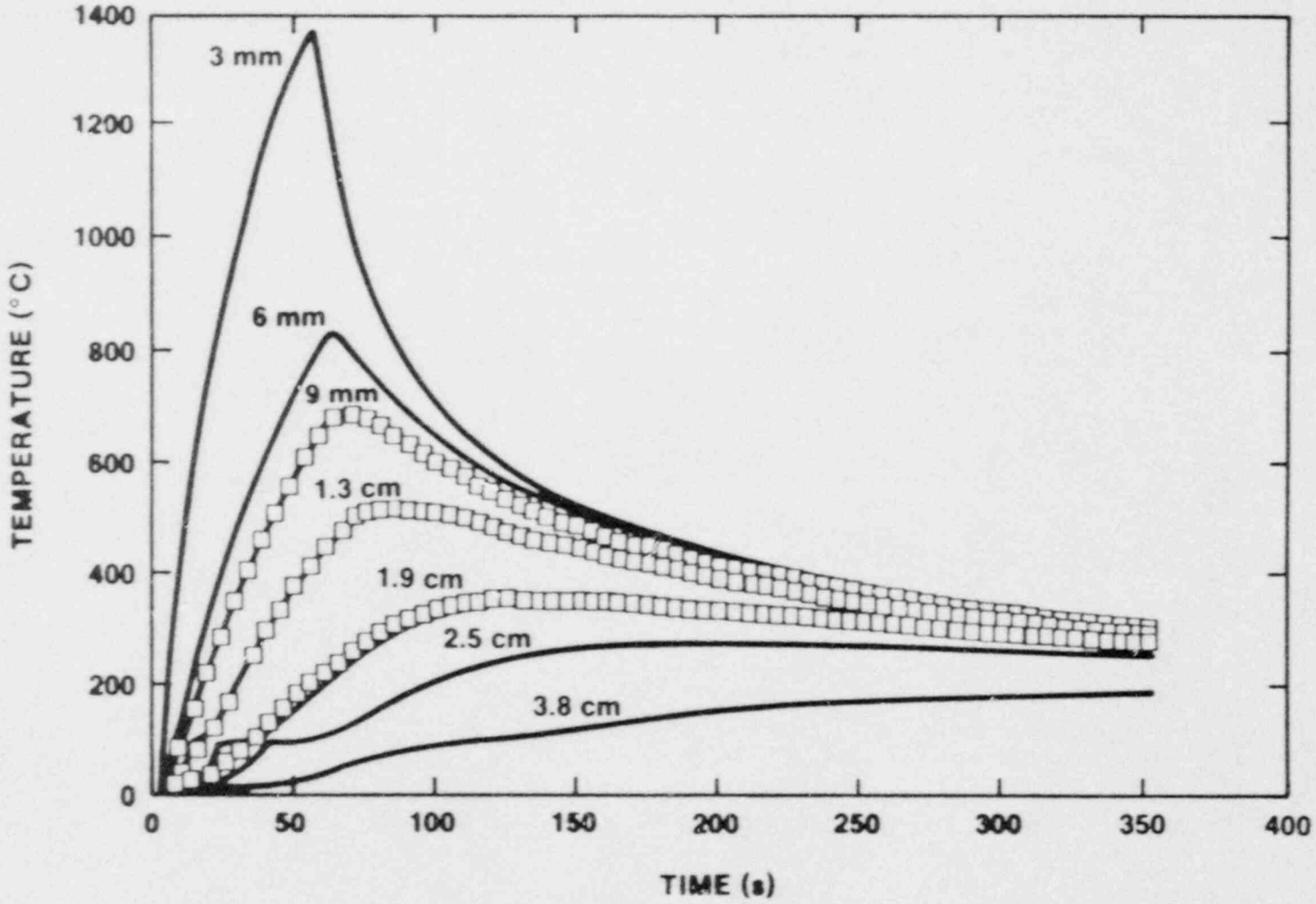

Figure 1.1-2. Comparison of Experiment Thermal History and Predictions of the "PROPTY" Code. Curves are labeled according to the depth below the surface exposed to the incident heat flux. Data obtained in the experiment are shown as open squares. Results calculated with PROPTY code are shown as solid lines.

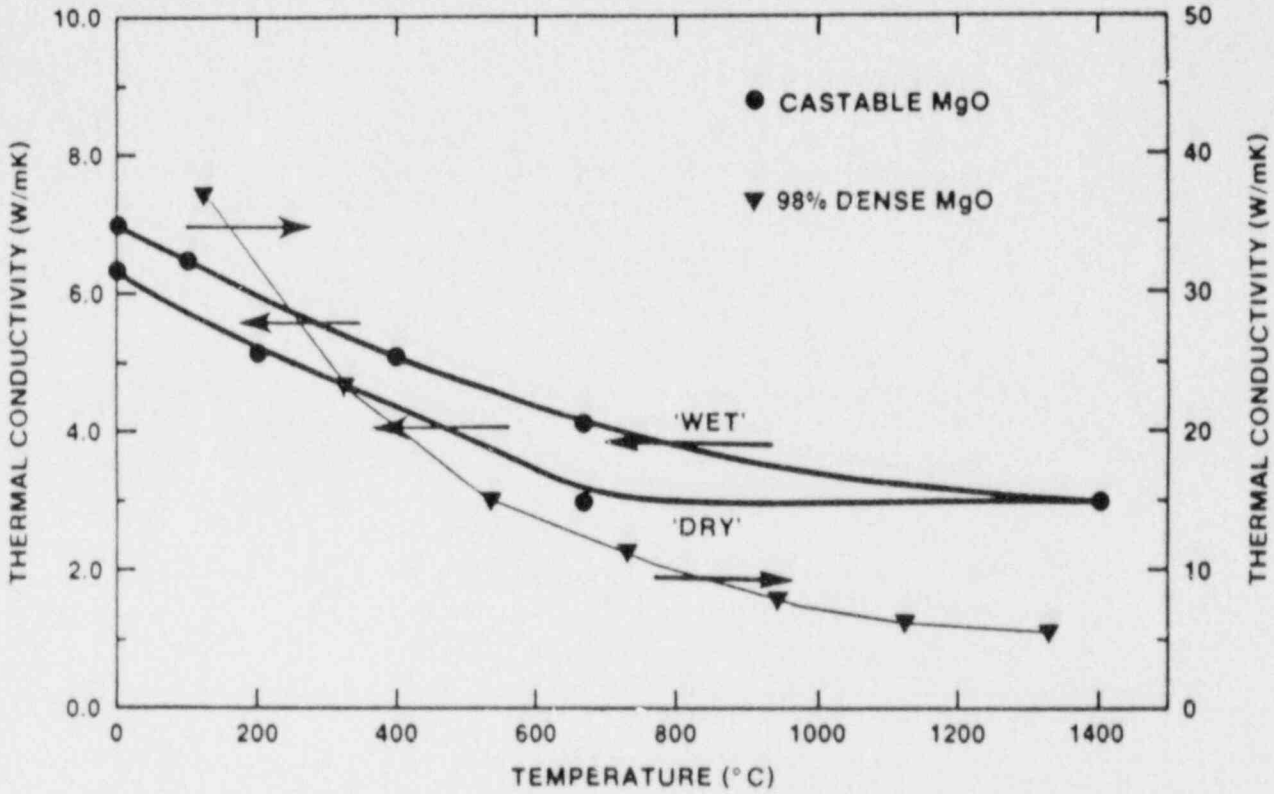

Figure 1.1-3. "PROPTY" Thermal Conductivity Prediction for Castable MgO Material. Also shown are data for 98 percent dense material. Note the significantly different scale used for the thermal conductivity of the highly dense material.

conductivity (k) are dependent on the initial value set in the PROPTY code. This value is fixed, and the values of k at other temperatures are allowed to vary in order to determine the best value of k. Thermal conductivity data for 98 percent dense magnesium oxide are also shown in Figure 1.1-2. It is readily apparent that the thermal conductivity of the K/R Cast-98 is much less than the highly densified Mgo. The conductivity of the castable material is quite dependent on density and method of preparation. Another determination of the thermophysical properties of K/R Cast-98 was performed by Purdue University.

The density of the K/R Cast-98 material was also investigated. The bulk density of the material used in SURC 4 was found to be 2680 kg/m^3 as compared to the theoretical density for MgO of 3590 kg/m^3.

• Concrete Material

The base of the interaction crucible was constructed of basaltic concrete. This concrete was used because it is typical of that used in the construction of nuclear power plants. Materials making up this type of siliceous concrete are found throughout the United States. This concrete melts over a range of 1373 K (1100°C) to 1673 K (1400°C) and typically liberates 1.5 w/o CO_2 gas and 5 w/o H_2O vapor when heated to melting.

The casting of the concrete was performed by mixing the concrete constituents in a clean paddle mixer. Once a homogeneous mixture had been achieved, the mix was carefully placed into the casting forms and vibrated as previously described.

Table 1.1-2 summarizes the chemical composition of the basaltic concrete.

Four 10.2-cm diameter x 20.3-cm long test cylinders were cast with the concrete slug to measure the compressive strength at 7, 14, 28 and 55 (day of the experiment) days. The concrete cylinder was cured at ambient temperature conditions--nominally 20° ± 10°C. Compressive strengths for the SURC 4 concrete ranged from 17 to 30 MPa, which is very typical of other basaltic-type concretes.

The thermal behavior of the concrete can be characterized by thermal gravimetric analysis (TGA), derivative thermogravimetric analysis (DTGA), and differential thermal analysis (DTA). The thermogram produced by TGA for the SURC 4 basaltic concrete indicated a free water content of 1.5 percent, a bound water content of 1.5 percent, and a CO_2 content of 3 percent. These results are also typical for basaltic concretes.

• Charge Material

The melt charge used in this experiment was a solid cylinder of 304 stainless steel having a mass of 200 kg. The cylinder was

Table 1.1-2

Chemical Composition of Basaltic Concrete

Oxide	Weight Percent
Fe_2O_3	6.3
Cr_2O_3	-
MnO	-
TiO_2	1.1
K_2O	5.4
Na_2O	1.8
CaO	8.8
MgO	6.2
SiO_2	55.2
Al_2O_3	8.3
CO_2	2.5
H_2O	4.2
SO_2	0.2

35.6 cm in diameter and 25.4 cm high. The composition of the 304 stainless steel cylinder is shown in Table 1.1-3.

Twenty (20) kg of zirconium metal were added to the melt-concrete interaction after steady-state concrete erosion was observed. The zirconium was in the form of solid cylinders, 3.3 cm in diameter and nominally 7.6 cm long. These cylinders were saw cut from a rod 3 m long. The chemical composition of the zirconium is shown in Table 1.1-4. The elemental analysis is taken from the top, middle, and bottom of the ingot from which the rod was fabricated.

- **Fission-Product Simulants**

In order to evaluate the transport of fission products during the melt-concrete interaction, various chemical species, listed in Table 1.1-5, were added to the melt prior to heating. These were added to the charge prior to initial heating as a homogeneous powdered mixture. One-third (approximately 2 cm) of the mixture was below the steel slug, one-third was in the gap between the slug and the MgO wall, and one-third was above the steel slug. Due to the porosity (50 percent), low conductivity, and high melting point of the mixture, the fission-product simulants acted as an insulator to the stainless steel slug until the charge became molten.

1.1.1.2 Experimental Apparatus

The major components of the SURC 4 experimental apparatus, as shown in Figure 1.1-4, included a sealed, water-cooled, containment vessel, interaction crucible, induction coil, and zirconium delivery tube. These components are described in the following sections. The remainder of the SURC 4 apparatus including the exit flow piping and the gravel bed filter are described in Section 1.1.1.4.

- **Containment Vessel**

An aluminum containment vessel was used in SURC 4 to ensure that nearly all of the reaction products would pass through the instrumented exit flow piping. The vessel was fabricated in two sections using 2.5-cm thick, weldable 6061-T6 aluminum alloy. The two sections were assembled using twenty-four, 1.4-cm-diameter hex head bolts and nuts to secure the mating flanges. The flange of the lower section incorporated a double O-ring for sealing. The vessel was supported by four 10-cm diameter x 45.7-cm long legs welded to the bottom of the lower section. Basic components of the vessel are shown in Figure 1.1-5. The internal volume of the vessel was calculated to be approximately 2 m^3.

Table 1.1-3

Standard Composition of
304 Stainless Steel

C Max	Mn Max	P Max	S Max	Si Max	Cr	Ni Max	Cu Max	Mo Max
0.08	2.00	0.040	0.030	1.00	18.00/20.00	8.00/11.00	0.50	0.50

Table 1.1-4

Chemical Composition of the Zirconium Metal

Trace Element	Ingot Location		
	Top (ppm)	Middle (ppm)	Bottom (ppm)
Al	150	135	125
C	150	150	150
Nb	71	76	120
Cr	110	79	62
Fe	1120	1140	1040
H	< 5	9	10
Hf[a]	0.079%	0.056%	0.055%
N	51	60	57
Ni	< 35	47	85
O	1360	1340	1300
P	10	8	10
Si	48	45	58
Sn	800	600	1100
Ta	< 100	< 100	< 100
Ti	34	27	27
W	< 25	< 25	< 25
Zr[a]	99.5%	99.5%	99.5%

[a]Composition given in percent (%) rather than parts per million (ppm).

Table 1.1-5

SURC 4 Fission-Product Simulants

Fission Product	Quantity (kg)	Category
Molybdenum	2.0	Early Transition Element
Tellurium	0.5	Chaleognes
Lanthunum Oxide	1.17	Trivalents
Cerium Oxide	1.23	Tetravalents
Barium Oxide	1.1	Alkaline Earths
TOTAL	6.0	

Aluminum (6061-T6) tubing 2.5 cm in diameter was welded to the outside and top of the vessel at a pitch of approximately 10 cm. This tubing was used to circulate a mixture of 50 v/o ethylene glycol in water to cool the vessel during the experiment. The bottom of the vessel was cooled by means of three large reservoirs welded to the bottom of the vessel. The tubing and reservoirs were connected in series to form a single cooling circuit.

Bolted, flanged ports located in the lower section of the vessel were used to provide feedthroughs for power and instrumentation leads and for mounting fittings to connect a pressure transducer and tubing for supplying argon purge gas. Another port was fitted with a spring-loaded safety diaphragm calibrated to open at 15 psig to eliminate the potential for over pressurization of the vessel. A 3-in diameter flange port located in the base of the vessel was used as a feedthrough for all crucible thermocouple terminations. The sheaths and extension wires for all the thermocouples were pulled through a mating 90-degree flanged elbow. The elbow was filled with epoxy and allowed to cure, encapsulating the instrumentation leads and thermocouple sheaths. The elbow was then bolted to the flanged port, sealing the instrumentation cabling. A flanged port in the top of the vessel was fitted with a 2-in OD x 0.062-in wall x 1-m long 304 stainless steel tube. This tube connected the interaction crucible with the flow system instrumented for sampling evolved gas and aerosols and measuring gas flow rate.

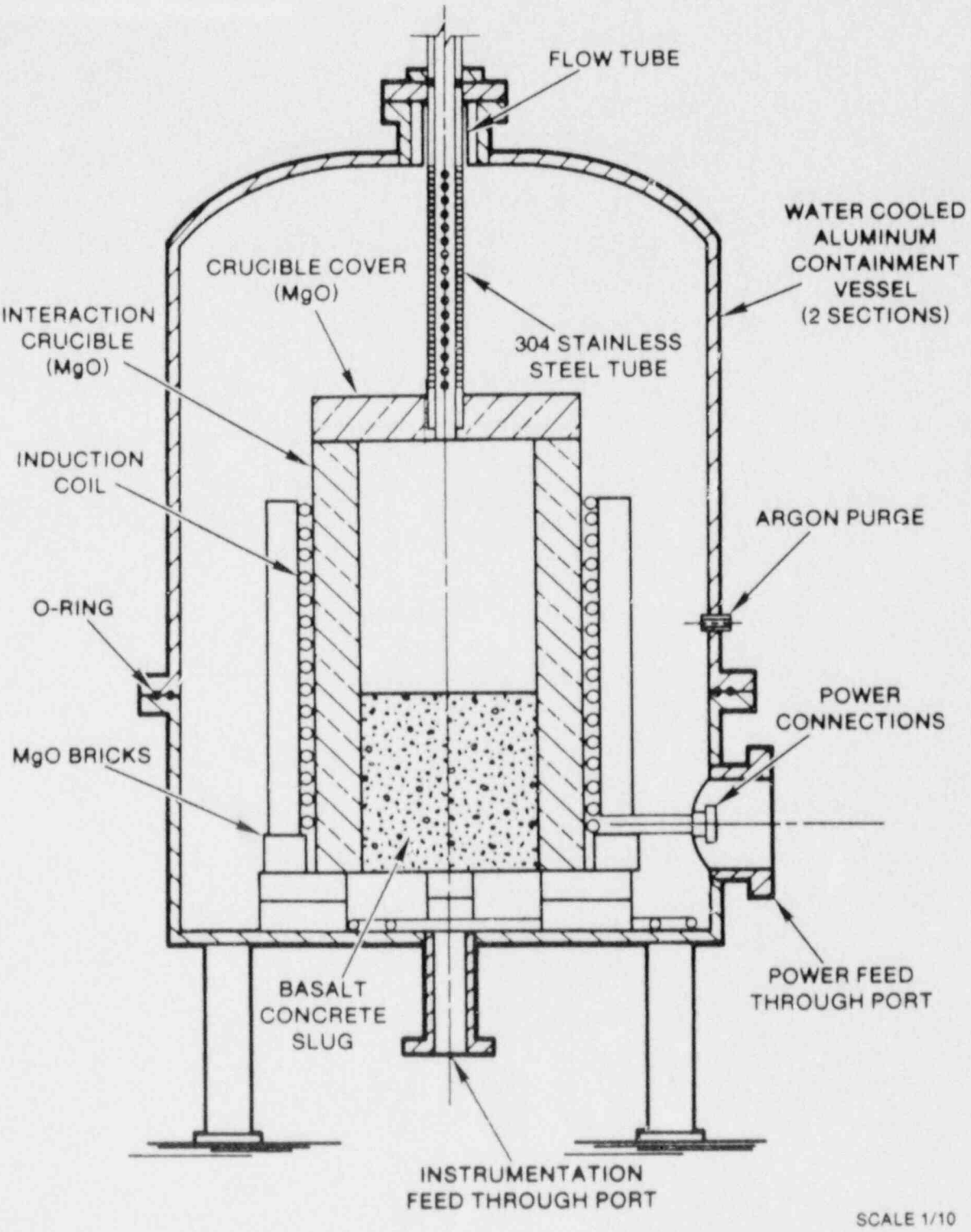

Figure 1.1-4. SURC 4 Experimental Apparatus

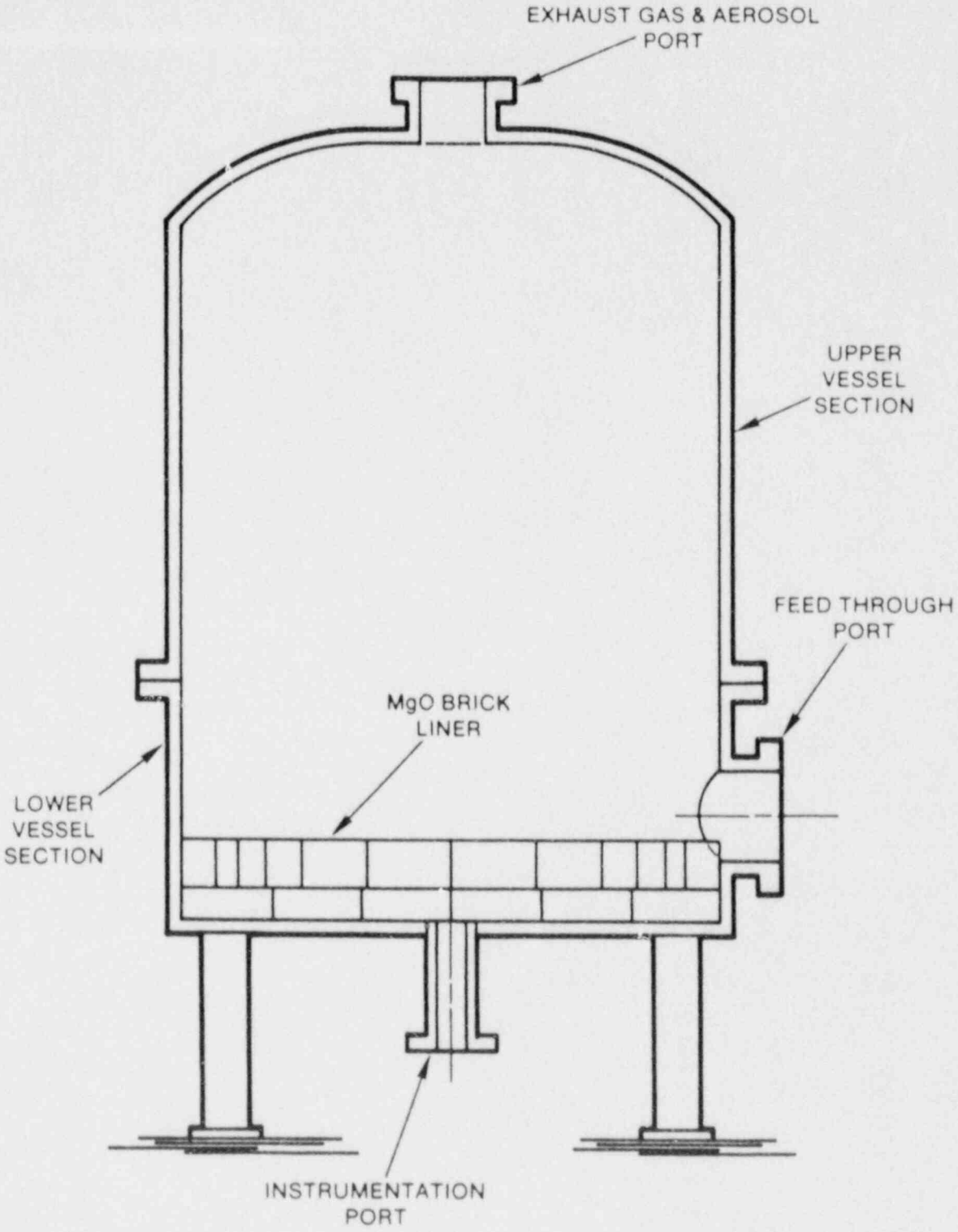

Figure 1.1-5. Sealed, Water-Cooled Containment Vessel

The inside floor of the lower vessel was lined with 6 in of standard refractory MgO brick and back filled with fine MgO powder. The perimeter of the floor was built-up with an extra layer of bricks 6 in high and 2 in thick. This was done to protect the vessel from melt attack should any molten material breach the interaction crucible during the experiment.

The vessel was pressure tested and certified to operate either in a partial vacuum or up to 20 psig.

• Interaction Crucible

The interaction crucible for SURC 4 was designed to limit concrete erosion to the downward or axial direction. The materials used in the construction of the interaction crucible have been discussed in detail in Section 1.1.1.1. The main body of the crucible was cast in two sections--namely the upper and lower crucible. The overall dimensions of the crucible were 60 cm in diameter x 100 cm high with a 40-cm diameter by 60-cm deep cavity. Cast into the bottom of the lower crucible was an instrumented basaltic concrete 40-cm diameter x 40-cm thick cylinder. The upper crucible was cast with an annular step and the lower crucible with a mating annular recess. The two crucible sections were assembled and sealed with Saureisen Cement No. 31.

The annulus of the upper and lower crucible and cover were cast using a reusable steel casting form constructed in a clam shell arrangement. Bolts were placed through the crucible cover and threaded into brass anchors cast into the upper crucible securing the cover.

Approximately 0.18 m^3 of MgO castable ceramic and 0.05 m^3 of basaltic concrete were required per crucible cast. The total estimated mass of the crucible was:

Annulus - MgO Castable
Volume - 0.15 m^3 @ 2680 kg/m^3 = 402 kg

Cover - MgO Castable
Volume - 0.03 m^3 @ 2680 kg/m^3 = 80 kg

Concrete Cylinder - Basaltic Concrete
Volume - 0.05 m^3 @ 2400 kg/m^3 = 120 kg

TOTAL MASS 602 kg

The annulus, concrete cylinder and crucible cover were instrumented with 95 Type K thermocouples cast into the crucible in 16 arrays to measure thermal response. Additionally, six Type S and six Type C thermocouples installed into six alumina tubes were cast into the basaltic concrete cylinder to measure melt temperature.

A total of 60 thermocouples were cast into the concrete in three arrays. The array containing thermocouples designated C1 through C20 was located on the axial centerline at odd (1, 3, 5, etc.) centimeter depths. The array containing thermocouples designated C21 through C40 were located on a line parallel to the center axis at a radial distance of 10 cm. These thermocouples were located at even centimeter depths. The third array was identical to the center axis array except that it was located near the perimeter of the concrete cylinder at a radial distance of 18 cm. The sheath of each thermocouple was bent at an angle of 90 degrees ten sheath diameters from the tip. This was done to minimize the errors caused by heat conduction down the metal sheath.

Six 4-hole alumina tubes were cast into the concrete slug parallel to the axial centerline, 60 degrees apart at a radial distance of 14 cm. One Type S and one Type C thermocouples located at various depths from the surface of the concrete cylinder were installed in each tube. These thermocouples were used to measure melt temperature, and their locations are tabulated in Table 1.1-6. Figure 1.1-6 shows an installation of a typical thermocouple array and alumina tube installed with the Type S and Type C thermocouples.

Table 1.1-6

Location of Thermocouples Installed in the Alumina Tubes and Cast Into the Concrete Cylinder, SURC 4

Tube Number	Thermocouple No.	Thermocouple Type	r (cm)	θ (degree)	-z (cm)
1	A1	S	14	30	1
4	A2	C	14	210	4
3	A3	S	14	150	7
6	A4	C	14	330	10
5	A5	S	14	270	13
2	A6	C	14	90	16
1	A7	S	14	30	19
4	A8	C	14	210	22
3	A9	S	14	150	25
6	A10	C	14	330	28
5	A11	S	14	270	31
2	A12	C	14	90	34

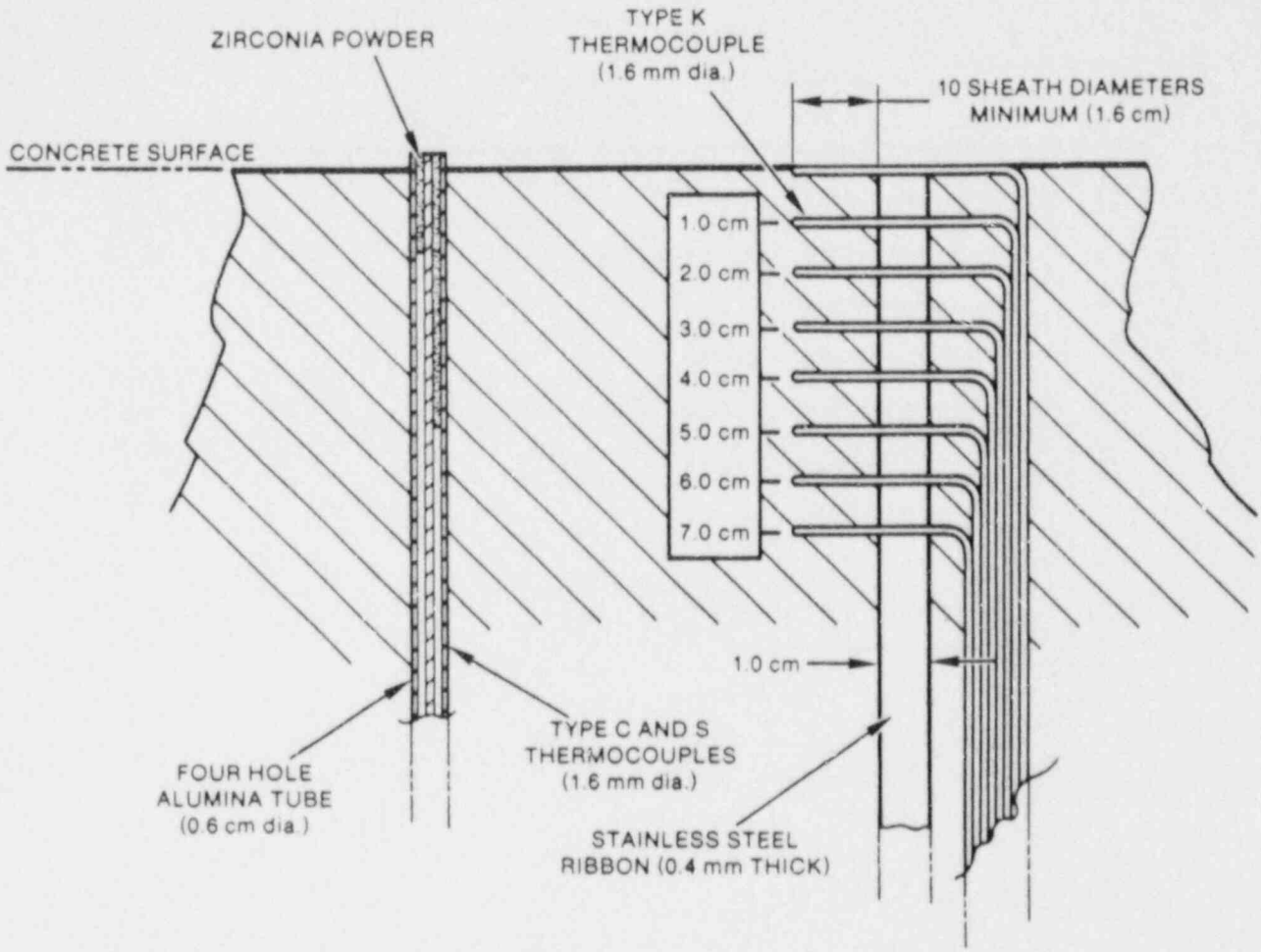

Figure 1.1-6. Typical Thermocouple Arrays Cast Into the Concrete

Thermocouples used to monitor sidewall temperatures in the MgO annulus of the crucible were installed into precast MgO cylinders prior to casting as shown in Figure 1.1-7. The ends of the cylinders, conformed to the curvature of the annulus of the casting forms, provided a good fit. The cylinders were bolted to the inside diameter of the outer steel crucible form by threading a small hex head bolt into a small brass anchor cast into the MgO cylinders. This method for installation of sidewall thermocouples accurately positioned the thermocouples, which was critical for heat flux calculations. The thermocouple tips were oriented in a horizontal plane parallel to the base of the crucible and perpendicular to the thermal front.

Two thermocouple arrays were cast into the crucible cover. The thermocouples were installed into precast MgO cylinders like the arrays cast into the annulus.

- **Induction Coil**

The induction coil used in the SURC 4 experiment was designed and built by Inductotherm Corporation. The coil was fabricated with 3.8-cm OD copper tubing having 20 turns with a pitch of 4.2 cm. The coil was supported by six equally spaced hard rock maple columns 7.5 x 5.5 x 100 cm long attached to the outside of the coil. The dimension of the coil was 61 cm ID x 71 cm high. After the coil was placed around the crucible and centered on the stainless charge inside the aluminum containment vessel, fiberglass cloth was attached to the outside of the support columns. Fine MgO powder was placed between the crucible and coil and dry K/R Cast-98 was placed between the coil and fiberglass shroud. This was done to protect the coil from contact with debris if the crucible were to fail.

- **Zirconium Delivery Tube**

The zirconium delivery tube was attached to the vertical leg of a stainless steel tee used to connect the gas and aerosol exhaust tube exiting the top of the containment vessel to the flow system. The delivery system is shown in Figure 1.1-8. Mounted to the top of the tee was a ball valve having a 3.8-cm diameter opening. Threaded to the inlet port of the ball valve was a 3.8-cm diameter black steel pipe 3 m long. Fifty zirconium metal cylinders (3.3 cm in diameter by 7.6 cm long) were stacked end-to-end in the pipe. Each cylinder weighed 400 g. At the designated time in the experiment, the ball valve was opened, delivering 20 kg of zirconium to the molten stainless steel pool.

1.1.1.3 Instrumentation and Calibration

The HP 1000 acquisition system used 166 data channels to record the results of the SURC 4 test. Of these, 135 were thermocouple

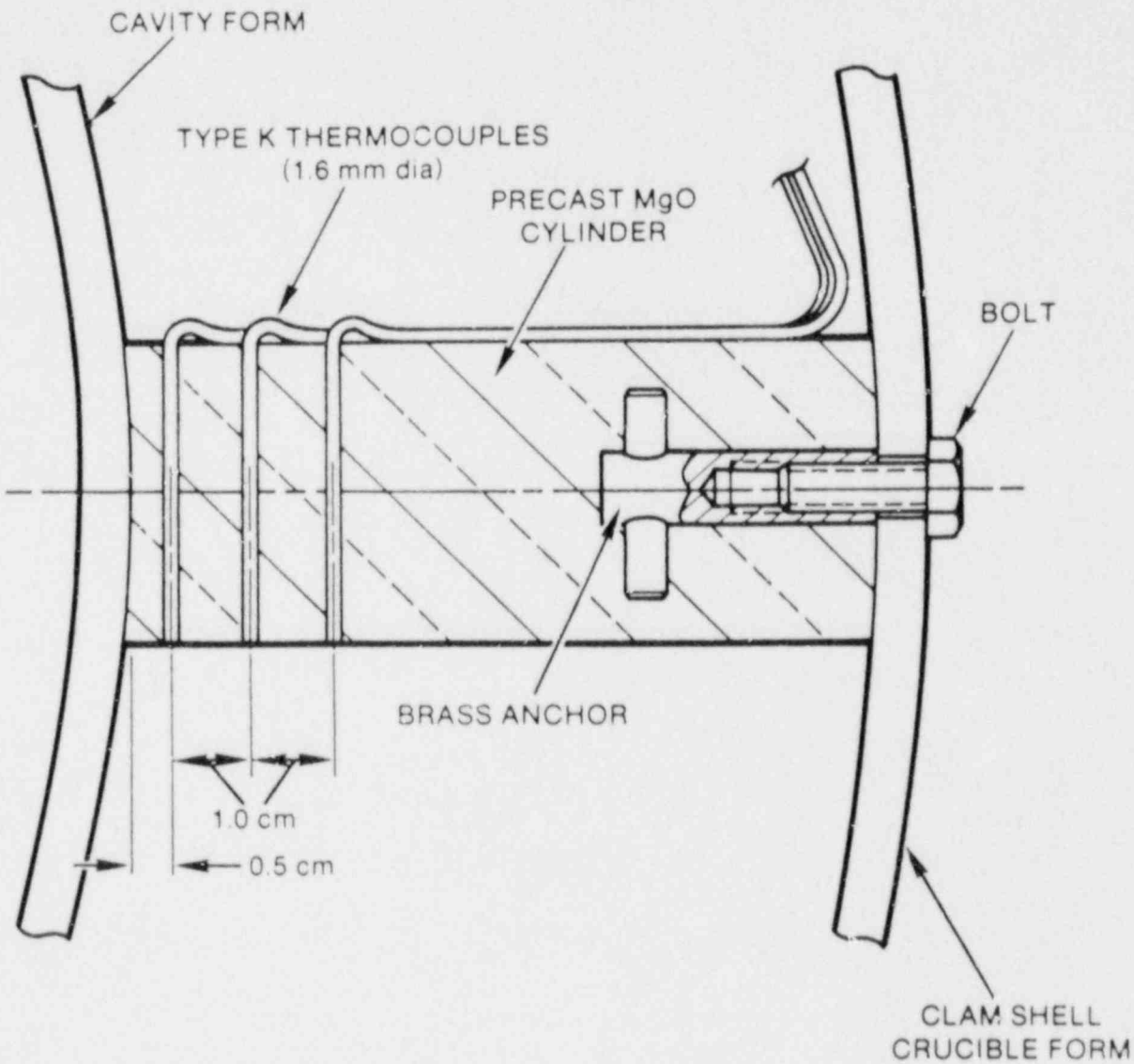

Figure 1.1-7. Thermocouple Array Installation, MgO Annulus

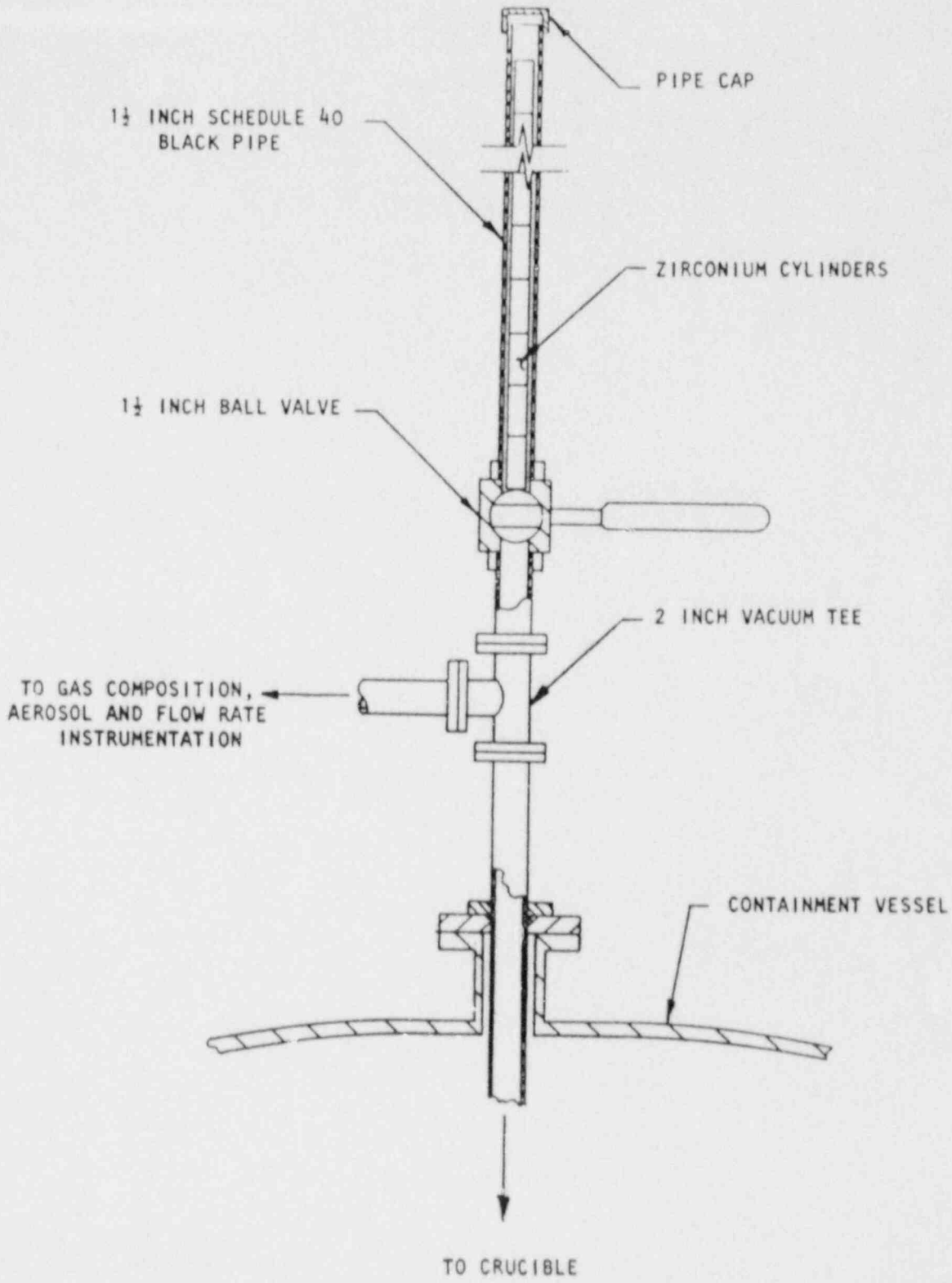

Figure 1.1-8. Zirconium Delivery System

channels. Sixty thermocouple channels were used to monitor axial erosion in the concrete. An additional 45 thermocouple channels were used to record temperatures in the crucible sidewalls and lid. Eight thermocouples were located in the flow system to monitor the temperature of the effluent gases. Eight more thermocouples were used to monitor the temperature within the aerosol collection system, and the last fourteen thermocouple channels were used to record the melt pool temperature.

Thirty-one data channels were voltage channels. Ten of these were used to monitor pressure and flow through the system. One was used to record the relative opacity of the gas stream. Five more were used to measure the induction coil power and coolant flow levels. Four were used to monitor the composition of the effluent gas and the last 11 were used to record aerosol data. All of these instrument channels were recorded using the HP 1000 data acquisition system. Each channel was recorded every 10 s for the first 90 min of the test and every 3 s thereafter.

In addition to the HP 1000 data system, data were sampled and stored with the SEDS aerosol system (14 channels), the gas grab sample system (32 channels), the Infocon Mass Spectrometer (10 channels), and a video camera and recorder system.

- **Thermocouple Instrumentation**

A total of 60 thermocouples divided into three groups were cast into the concrete slug of the interaction crucible. The relative locations of the thermocouples were discussed in Section 1.1.1.3. One typical array of 20 Type K thermocouples was located on the axial centerline. Thermocouples in this array were spaced 1 cm apart. These thermocouples had a 0.16-cm diameter, 304 stainless steel, ungrounded sheathes. The sheath of each thermocouple in the axial array was bent at an angle of 90 degrees at a minimum of 10 sheath diameters from the tip. The bent tip of the thermocouple was located in a plane parallel to the concrete surface and thus parallel to the propagating isotherm. This was done to minimize the errors caused by heat conduction down the metal sheaths. Six sets of one Type S and one Type C (Tungsten 5 percent Rhenium versus Tungsten 26 percent Rhenium) thermocouples were mounted in alumina tubes and cast into the concrete. The alumina tubes were 0.64 cm in diameter and contained four 0.2-cm diameter holes in which the thermocouples were installed. The Type S thermocouples installed in the alumina tubes were 0.16 cm in diameter and had ungrounded tantalum sheathes. The Type C thermocouples also had a 0.16-cm, ungrounded tantalum sheath. These alumina tube arrays were cast into the concrete slug on a radius of 14 cm from the axis and at 60-degree increments from an arbitrarily chosen 0 degree reference. The Type S and the Type C thermocouples were installed for measuring melt temperatures. These thermocouples also provided some data on the concrete thermal response prior to ablation which complemented data from the arrays of Type K thermocouples.

An additional 45 thermocouples were used to monitor the MgO sidewall and lid temperatures. These Type K thermocouples were similar in design to those cast in the concrete.

• Gas Composition Instrumentation

Gas sampling for the SURC 4 test was done using three techniques: an Infocon Model IQ200 mass spectrometer, an Infrared Industries Series 700 CO/CO_2 detector, and integral grab samples. The first two techniques yield real-time data that is viewed on-line and stored on computer disks. The grab samples are stored and analyzed posttest using both gas chromatography and mass spectrometry. A schematic layout of the SURC 4 gas composition sampling apparatus is shown in Figure 1.1-9

Three different sampling locations were used. Location No. 1 was downstream of the main exhaust line gravel filter, location No. 2 was between the containment vessel and the gravel filter, and location No. 3 was inside the aluminum containment vessel. All sample lines for gas collection were 6.4-mm (0.250-in) OD stainless steel with Swagelok stainless steel fittings and Nupro plug valves. The sample system manifold consisted of a normal and backup line and also a 40-psi argon source for backflushing filters. In-line filters used for SURC 4 were 0.3-μm Gelman HEPA filters with an element of acrylic copolymer.

Type K thermocouples were used to monitor sample gas temperatures in two different locations. A stainless steel cold trap with a volume of 75 cc and cooled with liquid nitrogen was used to prevent condensables from fouling the analysis equipment (Figure 1.1-10). A single Gast diaphragm type air pump was used to provide flow for the gas analysis system. Flow indication for the system was measured by self-indicating rotameters. The CO/CO_2 supply was monitored with a Dwyer 0-10 std ft^3/h air rotameter and the grab sample line was monitored using a Sierra 0-15 L/min hot wire anemoneter.

Samples from the grab sample system were analyzed by gas chromatography-mass spectrometry using a Tracor MT-150 g gas chromatograph and a Finnigan Mat 271/45 mass spectrometer. The samples were contained in 75-cm^3 stainless steel bottles with Nupro JB series regulating valves for closures. A Validyne absolute pressure transducer with a range of 1 to 1000 torr and a 0 to 10 volt output was used to mark the time of sampling events by monitoring manifold pressure. Vacuum in the bottles was maintained prior to sampling by a Welch two-stage belt drive vacuum pump with 175 L/min free air capacity. A remote control panel housed valve position indicator lights and four-position switches for controlling the multi-port valves used in acquiring grab samples (Figure 1.1-11).

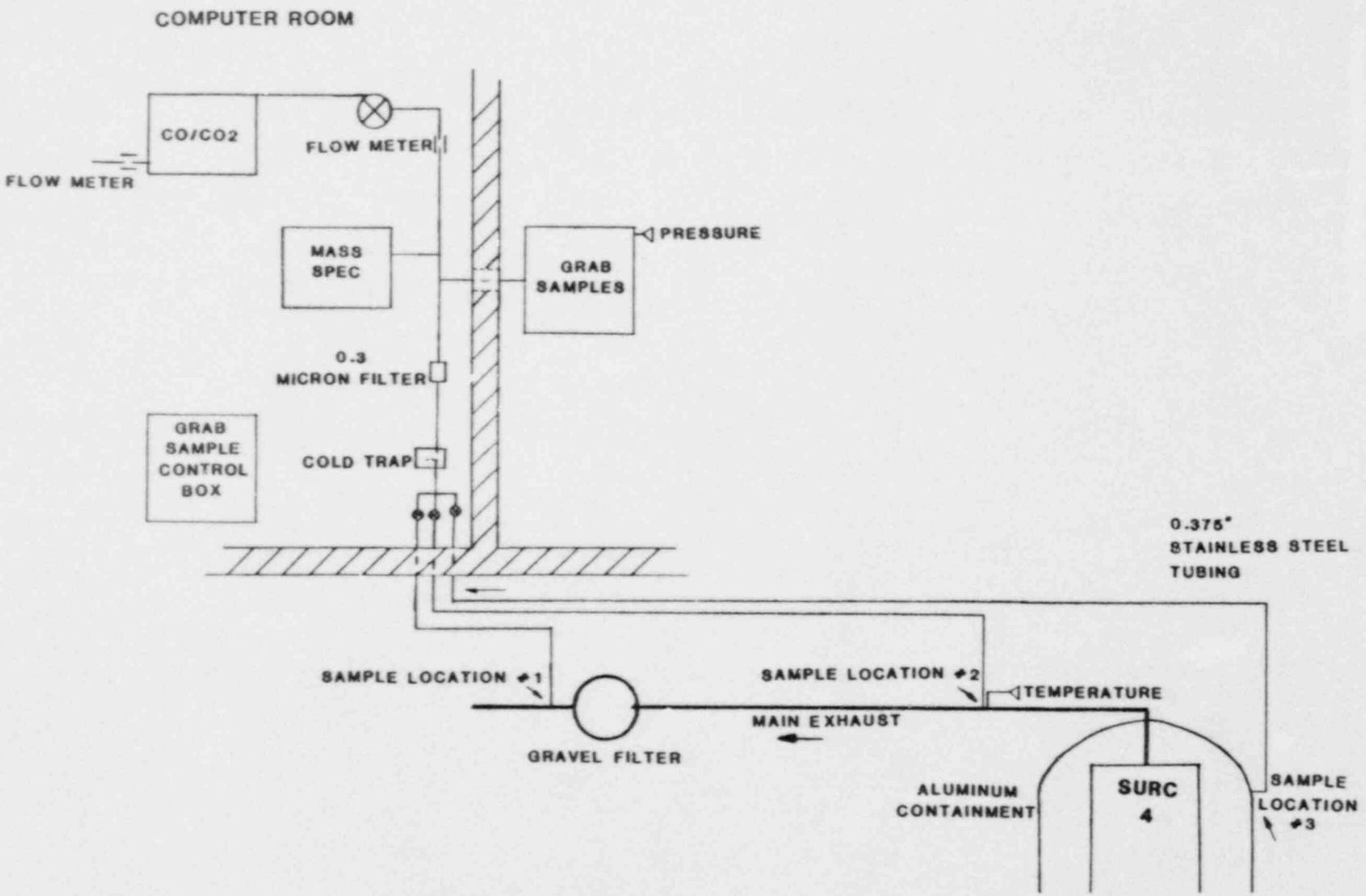

Figure 1.1-9. SURC 4 Gas Sampling Schematic

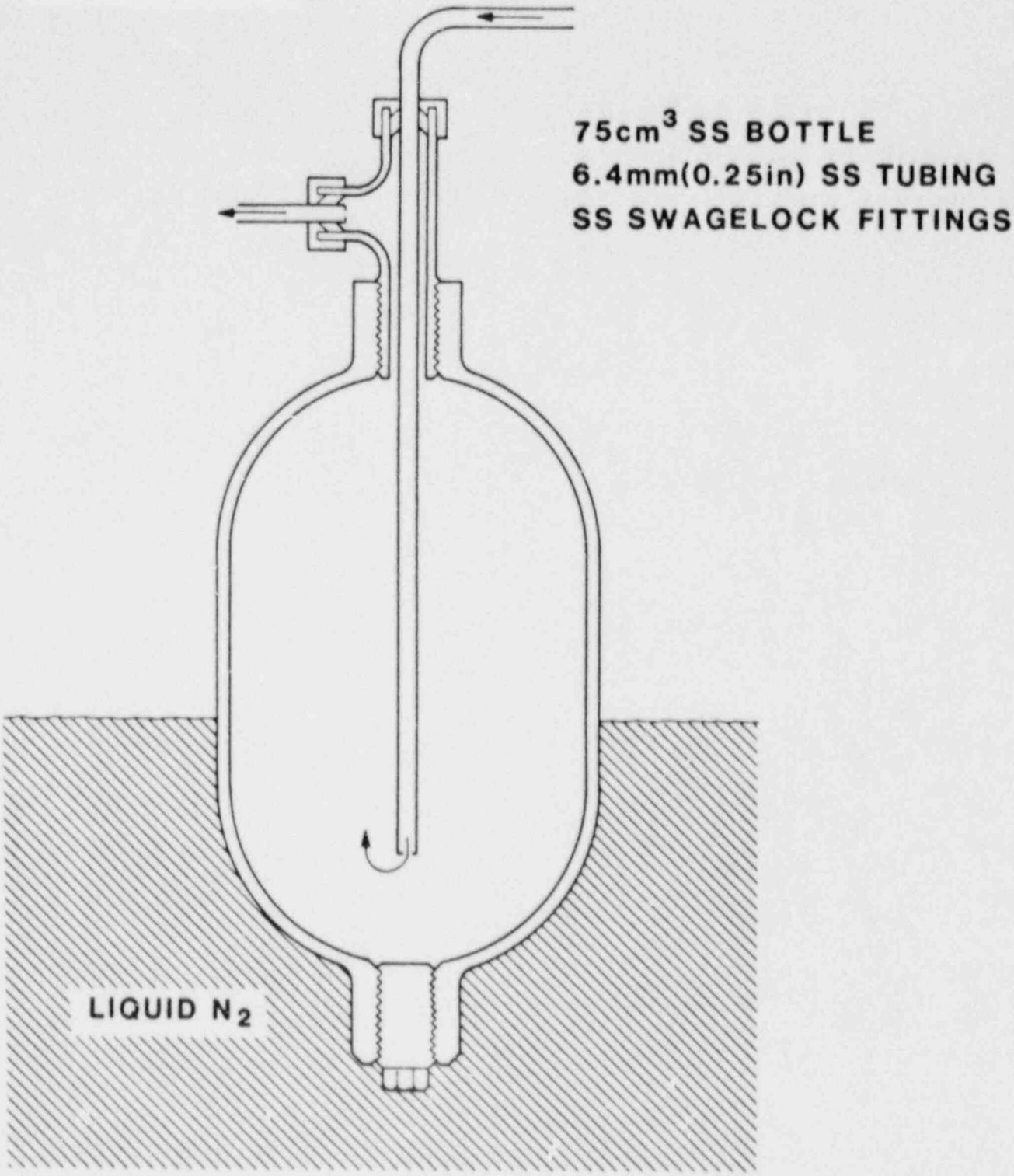

Figure 1.1-10. Gas Analysis Cold Trap

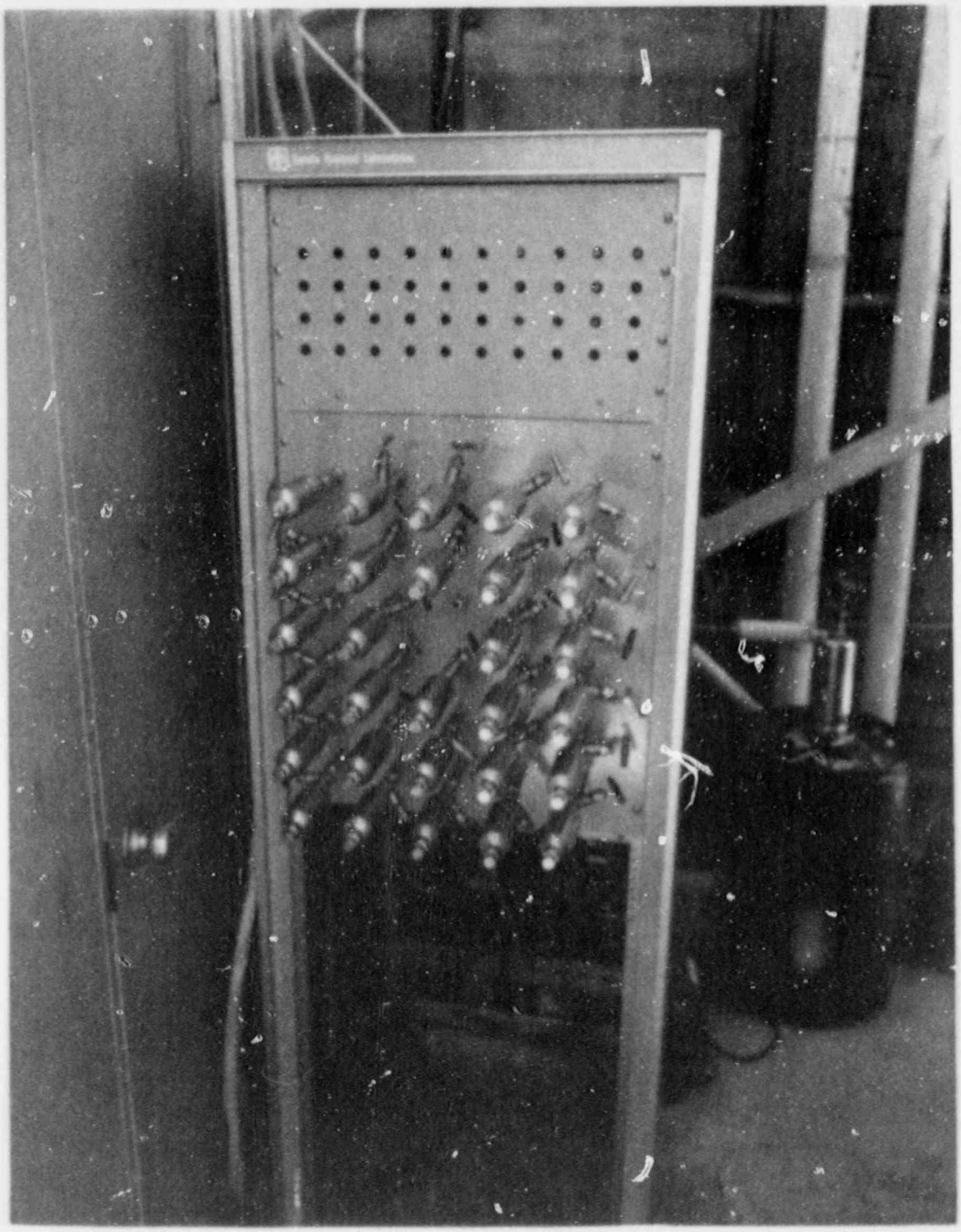

Figure 1.1-11. Grab Sample Hardware

Another diagnostic tool for gas data used for the SURC 4 test was a quadrupole residual gas analyzer, Inficon model model IQ200 (Figure 1.1-12). This instrument was set up in the table display mode for scanning specifically selected masses corresponding to the gas species of interest: H_2, H_2O, CO, O_2, Ar, and CO_2. A pressure converter manifold with a 10 torr orifice, 27 L/min vacuum pump, and 0.5-mm (0.02-in) ID capillary tube provided the ability for continuous sampling from a pressure of up to 2 atm at the sample source down to 10 torr at the analyzer supply where the associated 150 L/s turbo pump could maintain 10^{-6} torr at the analyzer head. A Faraday cup detector was used to produce the currents for analysis.

For data acquisition, a Hewlett Packard 1000 (right side - Figure 1.1-13) series computer system was used with acquisition rates of 15 s for the test warm-up and 5 s for the majority of the run where test events necessitated a faster rate. Inputs from gas composition data were temperature from the expansion chamber thermocouple, absolute pressure, percent C, and percent CO_2.

- **Flow Device Instrumentation**

Five different devices were used to measure the gas flow rate in SURC 4: a 1.02 cm orifice plate, a laminar flow element, a turbine meter, a Rockwell 450 gas clock, and a Rockwell 750 gas clock. Figure 1.1-1 is a flow train schematic of the hardware for SURC 4.

The flow system consisted of a series of piping, tubing, and a gravel filter instrumented with a variety of devices for measuring gas flow rates. The flow system started with an exhaust tube that was mounted in the top part of the containment vessel and was fitted into the crucible cover. The tube material was 304 stainless steel with an OD of 5.1 cm, a wall thickness of 0.17 cm, and a length of 1.2 m. Several 0.32-cm-diameter holes were drilled in the sidewall of the tubes in the section residing inside the containment vessel. These holes were used to provide a pathway for the argon gas used to purge the experimental chamber and provide background gas for gas composition measurements. A 5.1-cm-diameter 304 stainless steel vacuum tee was mounted to the top of the exhaust tube. The vertical flange of the tee was fitted with a 5.1-cm-diameter ball valve used to deliver the zirconium metal. The horizontal flange of the tee was connected to a 5.1-cm OD x 0.17-cm wall x 1.8-m long piece of 304 stainless steel tubing. The end of this tubing was fitted with a 5.1-cm OD, 304 stainless steel flanged cross. The center lines of all the flange ports on the cross were positioned in a parallel plane. The cross was used to mount an opacity meter and a nozzle for sampling the aerosol. The cross was adapted to a 2-m section of a 5.1-cm-diameter, 150-lb, schedule-40 black steel pipe with a 5.1-cm bolted flange. A 1.02-cm diameter, sharp-edged, concentric orifice was mounted between two flanges 1 m

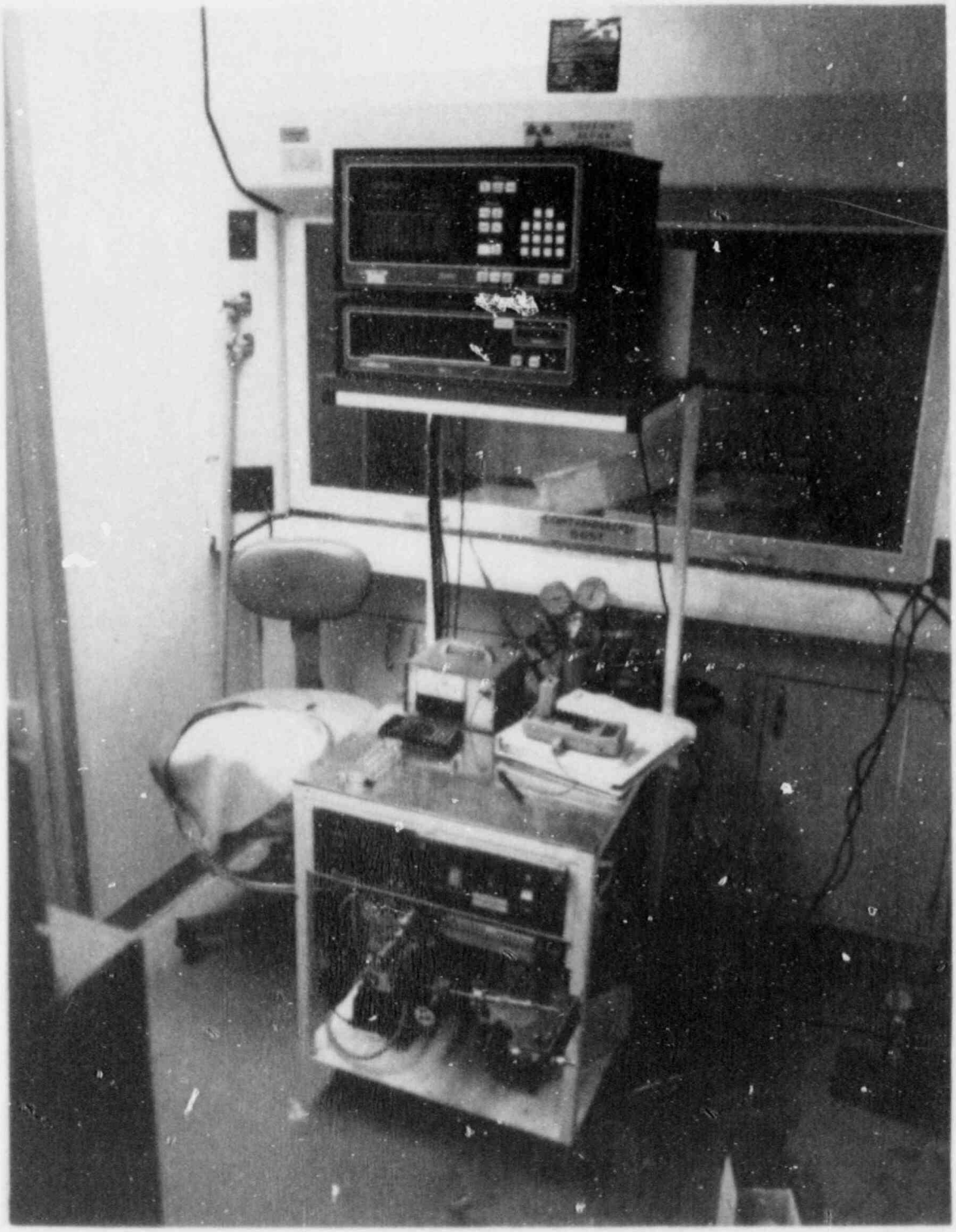

Figure 1.1-12. Mass Spectrometer Hardware

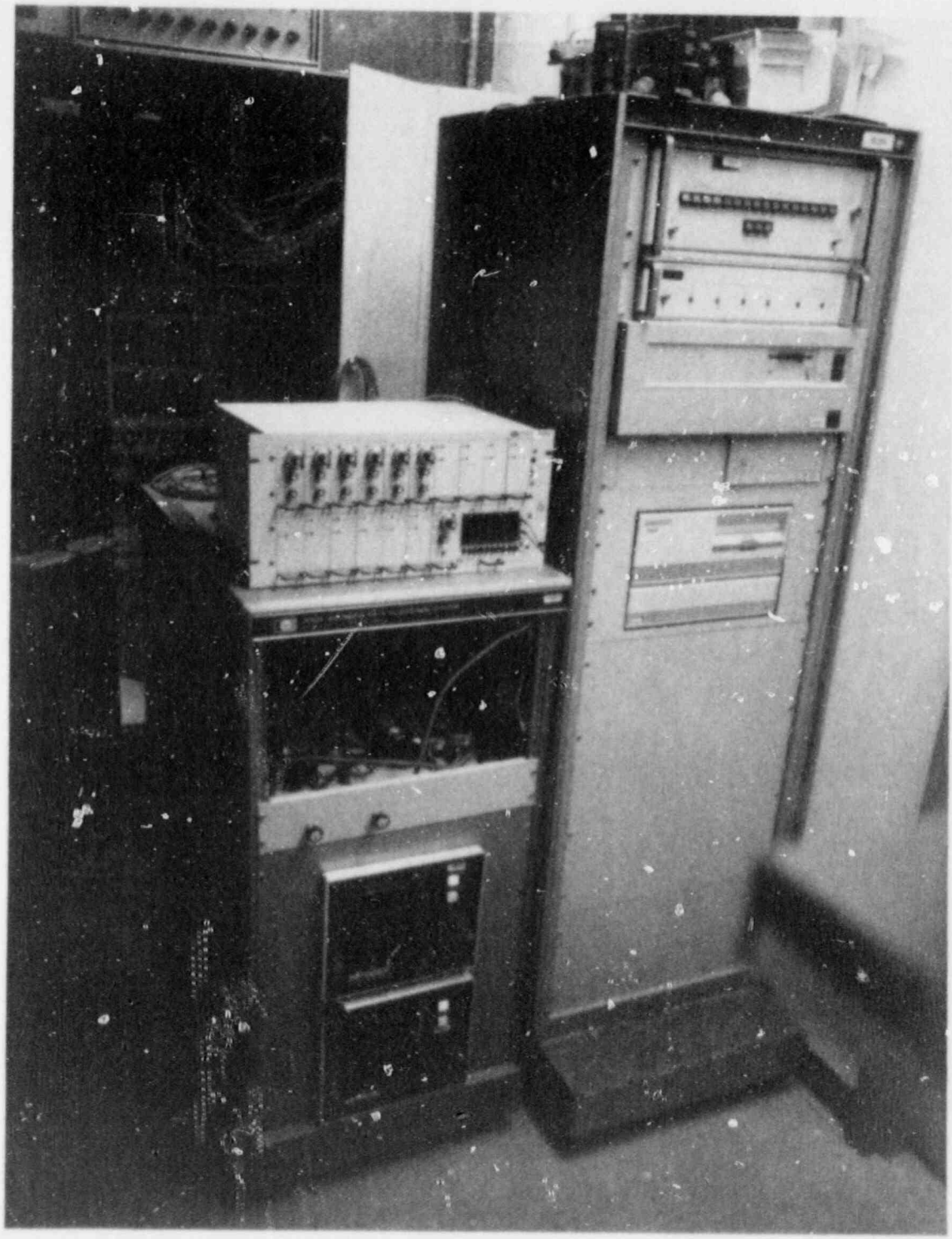

Figure 1.1-13. CO/CO_2 Monitor Hardware

from the stainless steel cross. Two Validyne pressure transducers were connected in parallel across pressure taps machined in the flanges. Another pressure transducer was connected to the flange upstream of the orifice to measure gas flow pressure.

The section of pipe containing the orifice was connected to the top of a gravel filter with a 1.1-m length of 5.1-cm black steel pipe using a combination of flanges and fittings. The gravel filter had an inside diameter of 25.4 cm and was filled with sand to a depth of 1 m. The gravel filter was used to filter aerosols, preventing them from entering the laminar flow device and the two gas clocks located downstream. The filter was designed and tested to remove 99 percent of the aerosols at flow rates of 300 std L/min with a back pressure of less than 0.25 psig. Connected to the outlet of the gravel filter were two lengths of 2.54-cm, schedule-40 black steel pipe, each 50.8 cm long. A laminar flow element (LFE) was installed between the two pipe sections. The LFE was instrumented with a Validyne differential pressure transducer. The end of the flow train was terminated by two Rockwell gas clocks mounted in series. The gas clocks were connected using 2.5 cm schedule 40 black steel pipe fittings.

The principles of operation and pertinent equations for orifice plate flow meters may be found in Reference 1. The orifice plate flow meter is probably the most widely used flow meter in service today. It is found mostly in field use and is simple, rugged, reliable, accurate, and inexpensive. Orifice plates used for gas measurement are considered to be accurate to 1 to 2 percent based on physical dimensions and published correction factors. It should be noted, however, that uncertainties in differential pressure (the measured parameter), temperature, line pressure, and gas density can easily overwhelm the uncertainty from the laboratory calibration. One disadvantage of the orifice plate is that a 10:1 change in differential pressure results from only a 3:1 change in flow due to the square root relationship between differential pressure and flow. Hence 50 percent of expected full flow is measured in 20 percent of expected differential pressure. This makes low flow rates difficult to measure accurately.

The orifice flow meter used in the SURC 4 experiment had an opening of 1.02 cm and was mounted between flanges in a 5-cm ID pipe. This pipe was mounted to the SURC 4 expansion chamber so that 80 cm of straight pipe preceded the flow device and at least 50 cm of straight pipe followed the device. Three Valdyne pressure transducers were used in conjunction with the orifice plate. Two of these were used to record the differential pressures across the plate and had operational ranges of 0 to 2 psia and 0 to 5 psia. The third pressure transducer was used to measure the system pressure and had a range of 0 to 10 psig. All of these devices were calibrated as a set--both in the laboratory

and at the test site--using several different gases and a range of flow rates.

The laminar flow element (LFE) is a group of capillary tubes bundled together to form a matrix such that the flow through each passage is laminar, even though the total flow upstream of the device may be turbulent. The LFE is not as sensitive to piping configuration as an orifice plate so that an inlet pipe length of one or two pipe diameters (instead of 5 or 10) is usually sufficient to provide a satisfactory flow pattern. The equations governing the operation of LFE devices are given in Reference 1. One advantage of an LFE is that the relationship between differential pressure (the measured parameter) and flow is linear for the range of flows for which it is designed. Calibration of the device should be done against a primary standard and is a function of gas viscosity, which is itself a function of gas composition. A potential disadvantage is that the small passages in the flow matrix are susceptible to plugging when the gas contains aerosols or water vapor.

The LFE used in the SURC 4 experiment was designed and built by Calibrating and Measuring Equipment (CME) and has a nameplate flow range of 0 to 300 L/min for air at standard conditions. The LFE is contained in a 50-cm pipe with an ID of 3.6 cm. Differential pressure is measured using a Valdyne differential transducer with a range of 0 to 2 psia. The device was calibrated both in the laboratory and at the test site. Laboratory calibration was done using a variety of gases with NBS-traceable critical orifices as the primary standard.

The turbine flow meter[1] consists of a freely rotating propeller mounted concentrically in a pipe. The force of the gas striking the propeller blades causes them to rotate at an angular velocity proportional to the gas velocity so that the volumetric gas flow is directly proportional to the rotational speed of the propeller. A magnetic pickup in the rotor causes a voltage to be generated in an external electrical coil. The magnitude of the voltage is then directly proportional to the volumetric flow rate for the designated flow range of the device. The output of the device is in actual liters per minute (AL/min) and must be corrected to standard conditions. Turbine flow meters must be calibrated to determine the coefficient of discharge, but once this is done they are considered to be accurate to about 1 percent. Some advantages of the turbine flow meter are that it is insensitive to gas composition and it produces a linear response over its design flow range. Some disadvantages are that it is susceptible to drag if the gas contains aerosols or water and that the magnetic pickup can be affected by an induction or electrical field.

The turbine meter used in SURC 4 was made by Flow Technology, Inc., and was contained in a 50-cm long pipe with an ID of 1.3 cm. The operating range of the device is 0 to 280 std L/min as

indicated by a voltage output of 0 to 10 volts dc. The turbine meter was calibrated in the laboratory and at the test site using Ag, He, air, and CO_2.

The Rockwell gas clocks used in SURC 4 were dry gas meters. These devices have four bellows-type chambers that alternately fill and empty known volumes of gas. The slide valves that control the cycle are attached to mechanical counters that totalize the volume of gas that passes through the meter. These devices are very rugged and bulky and register the total volume in actual liters per minute. They are impervious to the aerosol or water content in the gas and measure total volume independently without corrections for density or viscosity. Once the volume of the bellows is known, the accuracy of the gas clocks is within 1 percent. The major disadvantages of the dry gas meter are its size and lack of sensitivity to transient flow perturbations.

The Rockwell 415 gas clock has a stated operational range of 0 to 200 L/min at standard conditions. The device has a sensitivity of 28.3 liters per cycle. The Rockwell 750 has an operational range of 0 to 350 L/min at standard conditions. The Rockwell 750 gas clock has a sensitivity of 283 liters per cycle. Both devices were calibrated in the laboratory and at the test site with different gases and a range of flow rates.

After the experimental setup was completed for the SURC 4 test, an in situ calibration was performed using N_2 and Ar. This was done to insure that the laboratory calibrations were still valid, to evaluate the entire flow system, and to determine the system pressure as a function of flow rate. In addition, a systems leak test was performed by valving off the flow train and pressurizing the crucible and expansion chamber. Based on the in situ checks, the initial leak rate from the crucible was calculated to be 8.5 std L/min at a system pressure of 1 psig or 5 percent of the 165 std L/min flow rate.

- **Aerosol Instrumentation**

The interaction of molten material with concrete produces an aerosol. In the context of nuclear reactor accidents, the aerosol produced by the interaction of molten core debris with concrete basemat material is a potential source of radionuclide release.[2]

It is, therefore, important to characterize this aerosol with respect to its mass source rate, concentration, composition, and transport properties. The aerosol source term is defined as the mass source rate of aerosol generation, its composition, its size distribution, and additional parameters such as the dynamic shape factor, which aids in the description of the transport behavior of the aerosol, and the agglomeration shape factor, which aids in

the description of the coagulation behavior of the aerosol. Measurements of the aerosol source term resulting from the melt-concrete interaction experiments provide a data base against which to test predictive models of aerosol release and formation.[3] The SURC 4 test contained aerosol instrumentation designed to provide data that would allow calculation of the aerosol source term: aerosol mass generation rate, aerosol size distribution, and aerosol composition. Figure 1.1-14 is a flow chart illustrating how each of the three source term parameters is determined. The aerosol mass generation source rate is the product of the melt-concrete gas evolution rate and the aerosol mass concentration in the evolved gas. The gas flow train previously described measures the gas evolution rate. The aerosol mass concentration is measured primarily by filter samples; however, impactor samples and an opacity meter provide additional means of aerosol mass concentration measurement. The size distribution of the sampled aerosol is primarily determined by cascade impactor samples. The cascade cyclone gives an additional means of determining the integral aerosol size distribution over an extended sampling time.

Aerosol composition is determined from elemental analysis of the aerosol collected on the filters. A size-dependent aerosol composition is obtained from analysis of the aerosol collected by the cascade cyclone.

Brockmann et al. are developing a technique for measurement of aerosol dynamic shape factors.[4] Dynamic shape factor determination can be made by inclusion of additional instrumentation on future tests.

The sample extraction dilution system (SEDS) comprised of the filters, cascade impactors, cascade cyclone, and the necessary dilution systems and flow control is shown schematically in Figure 1.1-15. An aerosol sample is drawn into the SEDS through a gooseneck sample probe. The probe has a nozzle with an 1/8-in ID opening located coaxially in the center of the exhaust line. The nozzle expands into a 5/8-in ID tube. The cyclone samples the undiluted aerosol. The primary dilution is performed on the sample, and this is sampled by the filters. A secondary dilution is performed, and this aerosol is sampled by the impactors.

The flows are controlled by critical orifices manufactured by Millipore and calibrated at the Sandia Primary Standards Laboratory. Critical flow occurs when the ratio of upstream to downstream absolute pressure exceeds 2. The equations governing flow through a critical orifice are[5]

$$Q = Q_c \left[\frac{T}{T_c} \cdot \frac{MW_c}{MW} \right]^{1/2}$$

and

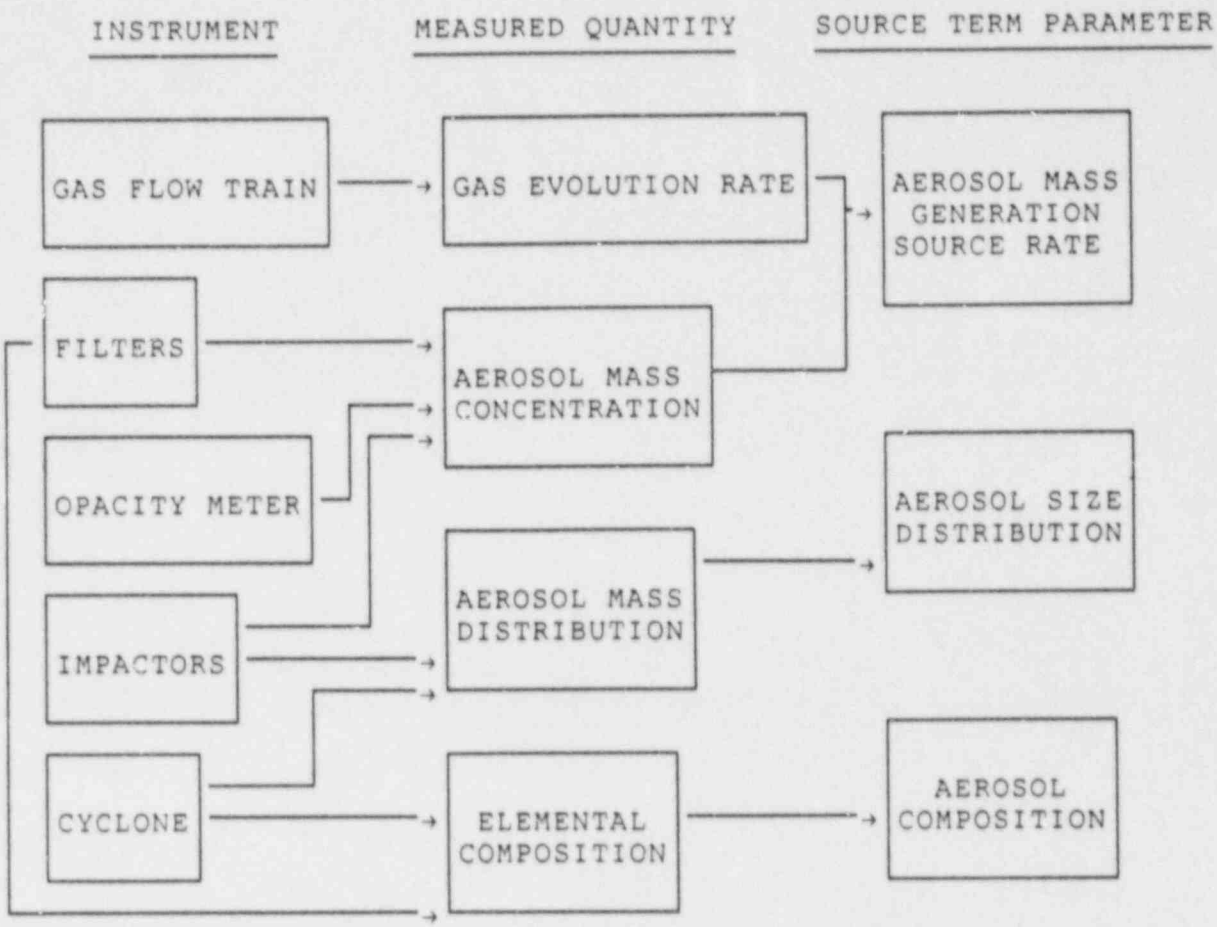

Figure 1.1-14. Flow Chart Illustrating How the Source Term Parameters Are Determined From Measurements Made in the SURC 4 Melt-Concrete Interaction Test

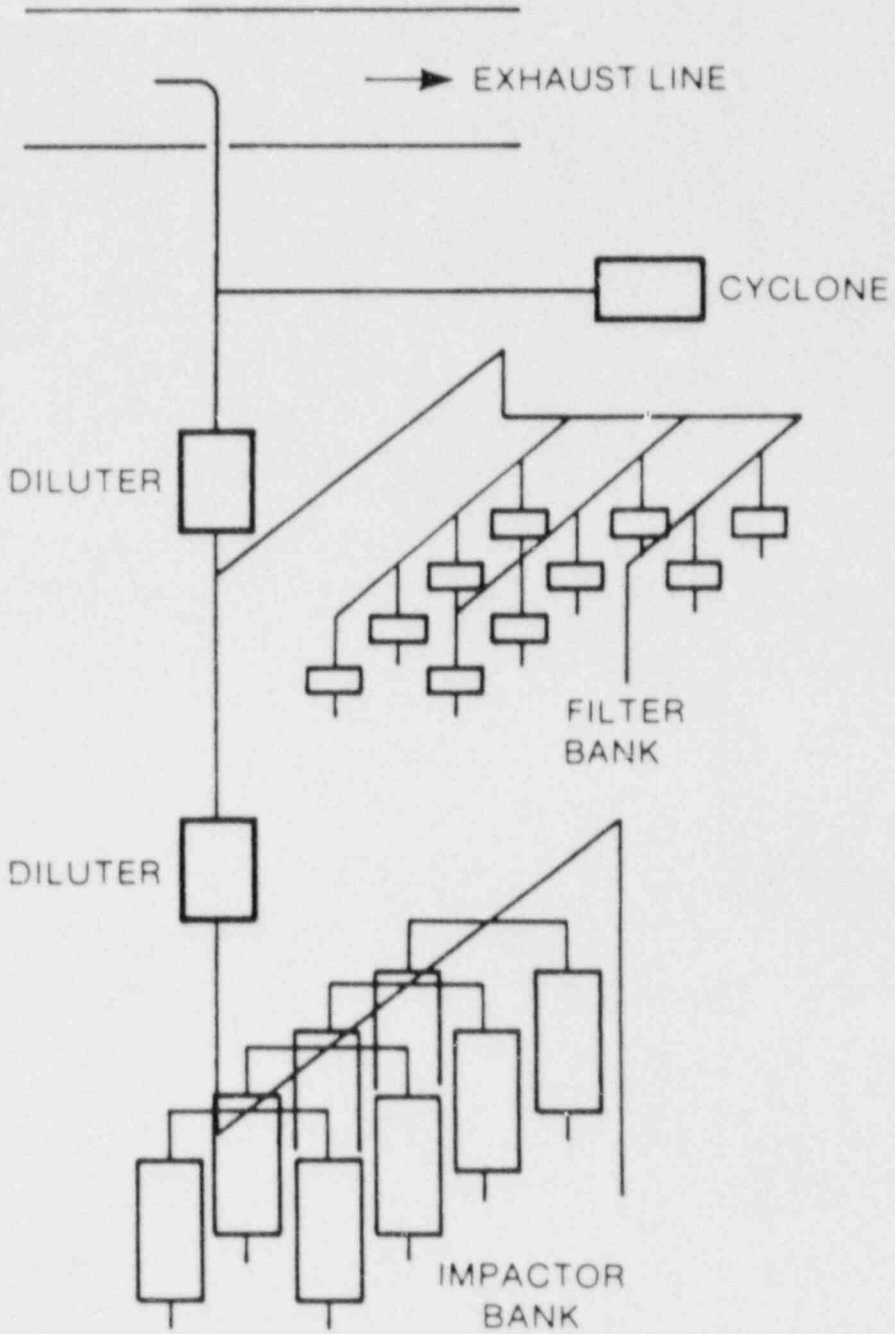

Figure 1.1-15. Schematic Diagram of the Sample Extraction Dilution System Showing the Configuration of the Filter, Impactor, and Cyclone Samples With Respect to the Diluters and the Aerosol Sampling Point

$$\dot{n} = \frac{PQ}{RT} = \frac{PQ_c}{RT_c^{1/2}T^{1/2}} \left[\frac{MW_c}{MW}\right]^{1/2} ,$$

where Q is the volumetric flow rate of gas upstream of the orifice, T is the upstream temperature, P is the upstream pressure, MW is the molecular weight of the gas, $\dot{n}$ is the molar flow rate, R is the universal gas constant, and the subscript c refers to the calibration conditions.

Temperature and pressure upstream of the orifices are measured. Where the critical orifices are located away from any heated sections of the test apparatus, such as the cyclone and dilution gas supply system, ambient temperature is assumed.

Dilution of the sample by the two diluters serves three purposes. The first is to reduce the high aerosol concentration to a level that is within the measurement range of the instrumentation (less than about 20 g/m^3 for the filters and less than about 5 g/m^3 for the impactors). The second is to cool the flow and to reduce the temperature variation of gas passing through the SEDS by the addition of the cooler dilution gas. The third is to reduce the variation in gas properties by the addition of a known dilution gas in high enough amounts to dominate the gas properties. Dilution can be used to inhibit further evolution of an aerosol size distribution resulting from coagulation and condensation.[8] In this application, however, the aerosol size distribution has evolved during transport through the crucible and exhaust line and is likely to have reached a point where the time scale of evolution is large compared to that of transport through SEDS.

The diluter for the SURC 4 SEDS consists of an aluminum outer tube that is 15 cm long with a 6.35-cm OD and a 1.9-cm OD sintered stainless steel inner tube. End caps hold the tubes in place. Dry dilution gas is passed through a 1/4-in swagelok fitting in the outer tube to the annular plenum region between the two tubes. Gas passes through the porous walls of the inner tube diluting the aerosol sample flowing through it.

The total flow out of the diluter, Q_T, and the dilution flow into the diluter, Q_D, is measured. The dilution ratio DR is then defined as Q_T divided by the difference between Q_T and Q_D. Some care in the magnitude of the dilution is necessary. The dilution ratio is calculated using the difference between two numbers and when those numbers are close, the error in the difference can become large. For example, if the uncertainty in the flows Q_T and Q_D is ± 5 percent for each, the resulting uncertainty in dilution ratio is ± 36 percent for a nominal dilution ratio of 5. This magnification of the flow uncertainties in the calculation of the dilution ratio places a practical upper limit on the

dilution ratio of about 5. For these tests, nominal dilution ratios are about 3 for each of the two diluters.

Because the system pressure in the SEDS is the same as that of the experimental apparatus, the SEDS can become pressurized (at higher gas evolution rates, the evolution gas flow train causes some back pressure in the apparatus). Each orifice controlling the dilution gas flow delivers a fixed molar flow of dilution gas by virtue of its fixed upstream temperature and pressure. The orfices controlling the sample flow draw at a fixed volumetric flow rate. The fixed volumetric flow rate yields a molar flow rate directly proportional to the system pressure. Consequently, if the dilution flow is unchanged, the dilution ratio will decrease with increasing system pressure. To maintain a consistent level of dilution in the face of a pressurizing system, the molar flow of dilution gas must be increased in proportion to the increase in molar flow of the sample produced by the increase in system pressure. This increase in dilution molar flow is accomplished in diluter 1 by selecting combinations of three orifices. These orifices are switched in and out by actuating remotely controlled valves controlling each orifice. This feature is not included in diluter 2.

The filter bank includes 12 filter samples on the SEDS. The flow through each filter is controlled by a remotely actuated valve. The 12 valves are plumbed to a single critical orifice giving a nominal filter sample flow rate of 10 L/m. The filter bank consists of 12 Gelman in-line stainless steel filter holders. These stainless steel, 5.9-cm diameter, 5.7-cm long filter holders (Gelman catalog number 2220) are designed for pressure applications of up to 200 psig. They use 47-mm diameter Durapore Membrane filtration media from Millipore (catalog designation HVLP 047). The effective filtration area is 9.67 cm^2 for each filter sample.

The inlet to the filter sample section is connected to a preseparator, which removes particles with a larger than 10 micrometer aerodynamic equivalent diameter. This preseparator is manufactured by Andersen and is of stainless steel construction, 8.2 cm in diameter and 12.8 cm long. The preseparator collects coarse material in an impaction cup, passing on the finer aerosol to the filter sample section.

The filter sample provides a collected mass of aerosol with aerodynamic equivalent particle diameters less than 15 micrometers. This sample allows calculation of the aerosol mass concentration of these smaller particles. The collected material can also be chemically analyzed. The filter sample is the principal measurement in determining aerosol mass source rate and elemental composition.

The filter sample section is mounted in an insulated box and electrically heated to avoid water condensation. The heaters are

controlled by an Omega Model 920 temperature controller with a Type K thermocouple.

The impactor sample section used Andersen Mk III cascade impactors. An Andersen Mk III cascade impactor inertially classifies aerosol particles into nine size bins. This inertial classification is accomplished by accelerating the particles through successively smaller holes (and higher velocity jets) in a stack of orifice plates. Under the jets of each plate is a glass fiber collection substrate. Particles are collected by impaction on the substrates. Those small enough to follow the gas stream lines in one stage pass on to subsequent orifice plates or stages where they may be collected. The impactor consists of eight stages and a backup filter to collect any unimpacted particles. It yields a mass distribution of aerosol with respect to the aerodynamic equivalent particle diameter. The Anderson Mk III cascade impactor is 8.2 cm in diameter and 18 cm long and is constructed of stainless steel.

A preseparator that removes particles with aerodynamic diameters nominally larger than 15 micrometers was used to avoid overloading (more than ~25 mg of material on any one stage) of the impactor by these larger particles. It effectively collects material which would otherwise be collected on the first two stages of the impactor. The preseparator collects material in an impaction cup, which is brushed out to retrieve the collected sample. The preseparator is of stainless steel construction, 8.2 cm in diameter and 12.8 cm long. It threads into the front of the impactor. The assembled preseparator-impactor is 8.2 cm in diameter and 29.8 cm long.

The box containing the impactor bank is heated in the same way as the filter sample box. Two impactor samples are taken simultaneously, one at a nominal 10 L/min and the other at a nominal 15 L/min. This provides a more detailed measurement of the aerosol size distribution.

The cascade cyclone is plumbed into the SEDS. The sample flow is controlled by two Millipore critical orifices in parallel to give a nominal sample flow of 24 L/min. A remotely actuated valve manufactured by ASCO is used to take the sample.

The cascade cyclone is manufactured by Sierra. This device inertially classifies aerosol particles and yields a mass distribution with respect to the aerodynamic equivalent particle diameter. This classification is accomplished by flowing the aerosol sample through a succession of smaller cyclones. The flow is introduced tangentially into the circular body of the cyclone where the circulating swirling flow causes larger particles to move by centrifugal force to the walls where they are collected. The smaller particles are withdrawn through the center and passed on to subsequent cyclones where they may be collected. Particles too small to be collected by the cyclones are collected by a

backup filter. A cyclone is capable of collecting much more material than an impactor and can be used to collect size classified material for bulk analyses.

The Sierra cascade cyclone is a series of six cyclones (of increasing capability to collect smaller particles) followed by a glass fiber backup filter. The aerosol sample is brushed out of the collection cup of each cyclone for weighing. The cascade cyclone is of stainless steel construction and when assembled is 12.7 cm in diameter at the widest point and about 60 cm in length.

The Dynatron Model 301 opacity meter was placed in the exhaust line of the test article upstream of the gravel filter and flow measurement devices. This device measures the attenuation of a light beam as it travels through an aerosol. Light attenuation correlates with aerosol mass concentration. Correlation of the opacity meter output with the mass measured by the filter samples provided a continuous record of mass concentration in the 3-in pipe exhausting gas and aerosol from the interaction crucible in the SURC test. The windows allowing light transmission are kept clean and free of aerosol deposition by a purge gas flow.

- **Induction Power Instrumentation**

The 200 kg of stainless steel were melted and sustained using an Inductotherm 250 kW, 1 kHz induction power supply. Power was delivered to the coils by remote control using a pair of No. 16 high current, water-cooled, flexible leads. During the melting process, the induction power supply automatically controlled voltage and frequency to deliver the desired power. Maximum efficiency was maintained throughout the experiment without the need to switch capacitors or voltage taps. The power delivered to the crucible coil was measured using a power transducer built by Inductotherm Corporation. The transducer measured coil voltage and current and converted it into a voltage equivalent of the power delivered. This transducer does not compensate for the phase angle between the current and voltage and therefore only measures gross input power.

The temperature of the cooling water was measured across the inlet and exit of each of the coils with two Omega ON-970-44008, 30,000 ohm thermistors arranged in a half-bridge circuit. The flow of water through the crucible coil was regulated manually with a 19.1-mm-diameter ball valve and measured using a Brooks Model 1110 rotameter.

- **Data Acquisition System**

All 166 instrument channels were recorded every 15 s for the first 105 min of the test and every 5 s thereafter using an HP

1000 data acquisition system. Two hundred and ten channels of data may be acquired during an experiment. Of the 210 channels, 150 are for Type K thermocouples, 20 are for either Type S or Type C thermocouples and the remaining 40 are dc voltage channels. A patch panel routes all the analog data channels from the test location to the Hewlett-Packard Model 2250 Measurement and Control Unit. This unit houses an analog to digital converter capable of multiplexing the 210 data channels. The voltage range of the data acquisition unit is ± 10 volts dc, with a programmable gain to increase sensitivity if the expected signal is small. A Hewlett-Packard Model 1000 series A-600 minicomputer is used to control all remote devices and manipulate the data received from the Measurement and Control Unit. Data are stored on a Hewlett-Packard Model 7946, 15 megabyte hard disk. A Hewlett-Packard Model 2623 terminal is used to command the minicomputer during tests and to display real time data in a tabular format as data acquisition progresses. A desk top terminal Hewlett-Packard Model 9836 is used to display real time data in both graphic and numeric format as well as to provide interrupt control over the minicomputer during a test. A Hewlett-Packard Model 9872 four color plotter and nine track magnetic tape are used for posttest data plotting and transfer.

The measurement accuracy of the 14-bit analog to digital converter is 1.56 microvolts in the most sensitive range and 1.25 millivolts at the highest range (-10 to +10 volts). With the appropriate range setting, the resolution for a Type K thermocouple is ± 1°C, and for a Type S or a Type C thermocouple, the resolution is ± 1.1°C.

The data acquisition speed can be selected from 1.25 s/point upward for 210 channels. The sample rate can be increased by reducing the number of channels sampled. For the SURC 4 test, data for the channels were sampled initially at 10 s intervals.

- **Video Monitoring Instrumentation**

The experiment was monitored remotely using a Sony Beta Model HVC 2200 video camera connected to a Sony Model SL 2000 portable Beta recorder and Model TT 2000 Tuner/Timer. The real-time camera image was displayed on a 19-in Sony model CVM 1900 color monitor. The image was passed between the video recorder and color monitor via a RG-59 coax cable.

1.1.1.4 Procedure

Initial calibration runs with the 250-kW power supply were performed using a 200-kg stainless steel slug in order to determine the coupling efficiency and overall losses for the SURC 4 geometry. Thermocouples placed in the slug indicated a temperature rise of 800°C in 38 min followed by losses of 90°C in 50 min

after power shutdown. Power to the coil was set at 175 kW. These results indicated a net efficiency of 25.5 ± 2 percent (45 kW total to the slug) with overall losses of 3.5 kW. Following these power calibration tests, the SURC 4 apparatus was assembled and leak tested. Results of the leak tests using argon gas as the flow medium indicated a cold leak rate of 8.5 std L/min at an inlet flow rate of 165 std L/min (5 percent losses) and an overpressure of 1 psig in the SURC 4 containment vessel.

After the final calibration and pretest checkouts were performed, 98 kW of power were applied to the coil (Figure 1.1-16). This constituted the start of SURC 4 at time = 10.7 min. A summary of the major events in the SURC 4 test is presented in Table 1.1-7. The temperature at the outer edge of the steel slug was monitored (Figure 1.1-17) to confirm that 25.5 percent of the power was being transmitted to the metallic slug. After 33.3 min of heating, the power to the coil was increased to 200 kW at time = 44 min. A second power increase to the maximum allowable level of 245 kW was accomplished at time = 80.5 min. This resulted in a net power of 62.2 kW to the slug. At time = 86 min, the steel slug reached the meltpoint of 1703 K. After nearly 20 min at the meltpoint, the steel became fully molten and concrete attack began. The center line concrete thermocouple at the concrete surface minutes failed at time = 105.4 min. The melt pool temperature at 105.4 min was 1746 K. Shortly after erosion began, the initial aerosol samples were taken. Aerosol filter sample "A" was taken at 113 min and filter sample B was taken at 114 min. The durations of both samples were 1 min. Impactor samples A and B were also taken at these times. A third filter sample (sample C) was taken at time = 115 min, again for 1 min. After nearly 15 min of concrete ablation, the ball valve on top of the SURC 4 containment vessel was opened to deposit the Zr metal. A cursory inspection indicated that the pool was molten with no overlying crusts. The Zr delivery tube was actuated and the full 20-kg charge of Zr entered the melt at time = 119 min. The ball valve was then closed, having been open a total of 96 s. The power supply shut off at 124.1 min because of the failure of an auxiliary cooling line to the containment vessel. Field repairs quickly replaced the line; power, at 245 kW, was applied to the coil at time = 131.7 min. During the power outage, three aerosol filter samples (D, E, and F) and two impactor samples (C and D) were taken at times 124.1, 125, and 126 min. Each sample had a duration of 1 min. Power to the melt pool was held constant at 245 kW for the remainder of the test except for a 30-s excursion at 144.8 min. The final aerosol samples were taken at 155, 156, and 157 min. These were filter samples G, H, and I and impactor samples G and H--these again had durations of 1 min. At time = 161.9 min, there was a pressure spike exceeding 7 psig inside the containment vessel--30 s later, melt was observed flowing out the bottom of the apparatus. The power supply automatically shut off and the SURC 4 experiment was terminated at 162.5 min. Grab samples of gas were taken for the next 28 min.

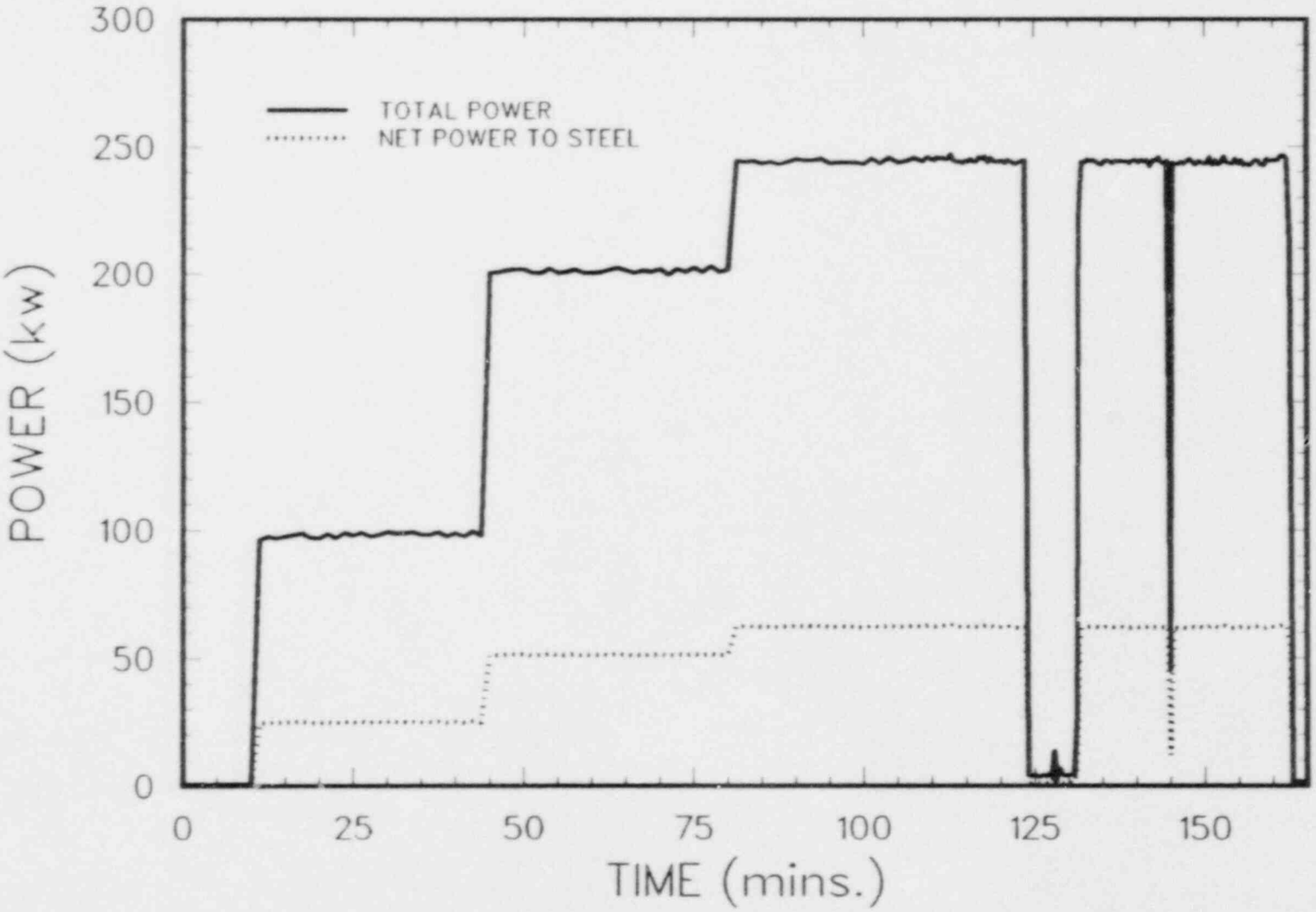

Figure 1.1-16. Power History for SURC 4

Table 1.1-7

Events of Test SURC 4

Time (min)	Events
0.0	Start of data acquisition system
10.7	Power supply on power meter reading 98 kW
18.3	Gas grab sample 10-1 taken from location #3 (inside containment vessel)
44.0	Power increased to 200 kW (power meter)
58.5	Gas grab sample 10-2 taken from location #2 (upstream of gravel filter)
80.5	Power increased to 245 kW (power meter)
102.8	Concrete surface perimeter thermocouple C41 failed (r = 18 cm)
104.3	Gas grab sample 10-3 taken from location #1 (down stream of gravel filter)
105.4	Concrete surface axial center line thermocouple C1 failed (r = 0 cm)
111.9	Concrete surface midradius thermocouple C21 failed (r = 10 cm)
113 - 114	Filter sample A taken
114 - 115	Filter sample B taken Impactor sample A taken Impactor sample B taken
115 - 116	Filter sample C taken
117.6	Ball valve opened to inspect melt
118.0	Ball valve closed - zirconium delivery tube installed
119.0	Zirconium metal delivered to the melt (20 kg)
119.2	Ball valve closed
123.1	Gas grab sample 9-2 taken at location #2
124 - 125	Filter sample D taken

Table 1.1-7 (Continued)

Time (min)	Events
124.1	Power supply off
125 - 126	Filter Sample E taken Impactor sample C taken Impactor sample D taken
125.2	Gas grab sample 9-4 taken at location #2
126 - 127	Filter sample F taken
131.7	Power supply on power meter reading 245 kW
133.2	Gas grab sample 8-2 taken at location #1
135.2	Gas grab sample 8-3 taken at location #2
137.1	Gas grab sample 8-4 taken at location #2
139.3	Gas grab sample 7-2 taken at location #2
141.2	Gas grab sample 7-3 taken at location #2
144.8	Power supply off
145.1	Power supply on power meter reading 245 kW
150.3	Gas grab sample 6-3 taken at location #1
155 - 156	Filter sample G taken
156 - 157	Filter sample H taken Impactor sample G taken Impactor sample H taken
156.1	Gas grab sample 6-4 taken at location #2
157 - 158	Filter sample I taken
158.1	Gas grab sample 5-2 taken at location #2
161.9	Pressure spike inside containment vessel
162.5	Melt flowing from bottom of containment vessel Power supply turned off Test terminated

Table 1.1-7 (Concluded)

Time (min)	Events
169.1	Gas grab sample 5-4 taken at location #1
175.6	Gas grab sample 4-3 taken at location #2
177.0	Gas grab sample 4-4 taken at location #3
185.0	Gas grab sample 3-2 taken at location #3
190.0	Gas grab sample 3-3 taken at location #2

1.1.1.5 Initial Conditions, Boundary Conditions, and Posttest Observations

The SURC 4 test accomplished all of its established pretest goals and was successful in observing and recording all the effects associated with both steady-state concrete erosion as well as the additional effects of Zr addition on steel-concrete attack. These effects were evident in the measured meltpool temperatures, erosion rates, heat losses, gas flow rate, gas composition, and aerosol characterization. A total of nine aerosol filter samples and six impactor samples were taken for posttest analysis. Eighteen grab samples were taken for gas composition analysis and 70 mass spectrometer data points were recorded. Only three of the 166 data channels failed to record properly. The detective channels were M39 and M42 in the MgO sidewall and the melt pool thermocouple at a depth of 10 cm. All of these were redundant measurements so that essentially no information was lost.

- **Initial Conditions**

Initial conditions for the SURC 4 test up to the onset of concrete ablation are shown in Figures 1.1-17 through 1.1-19. Figure 1.1-17 shows the heatup and melting of the steel slug. Complete melting of the slug required approximately 13 min. At the onset of ablation (105 min into the test) the temperature recorded by the thermocouple in the molten steel was 1750 K. Figure 1.1-18 shows the temperature profile in the basaltic concrete substrate prior to concrete ablation. Based on this figure, it is estimated that prior to the onset of concrete ablation evaporable water was released from the first 3 to 4 cm of concrete, bound water was released from the first 1 to 2 cm, and carbon dioxide was released from less than 1 cm. Figure 1.1-19 shows the thermal response of the MgO sidewall at a position

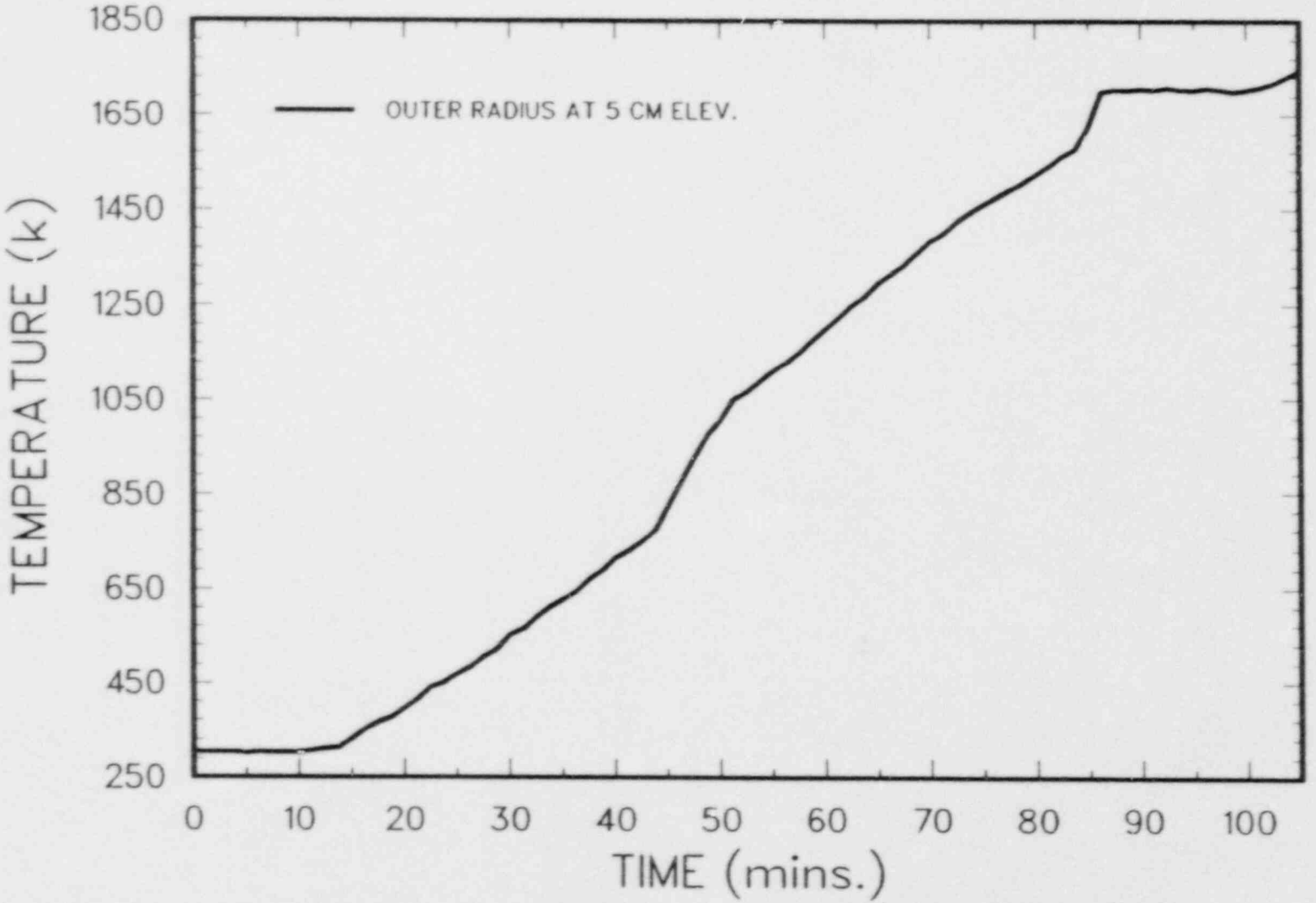

Figure 1.1-17. SURC 4 Initial Steel Temperature

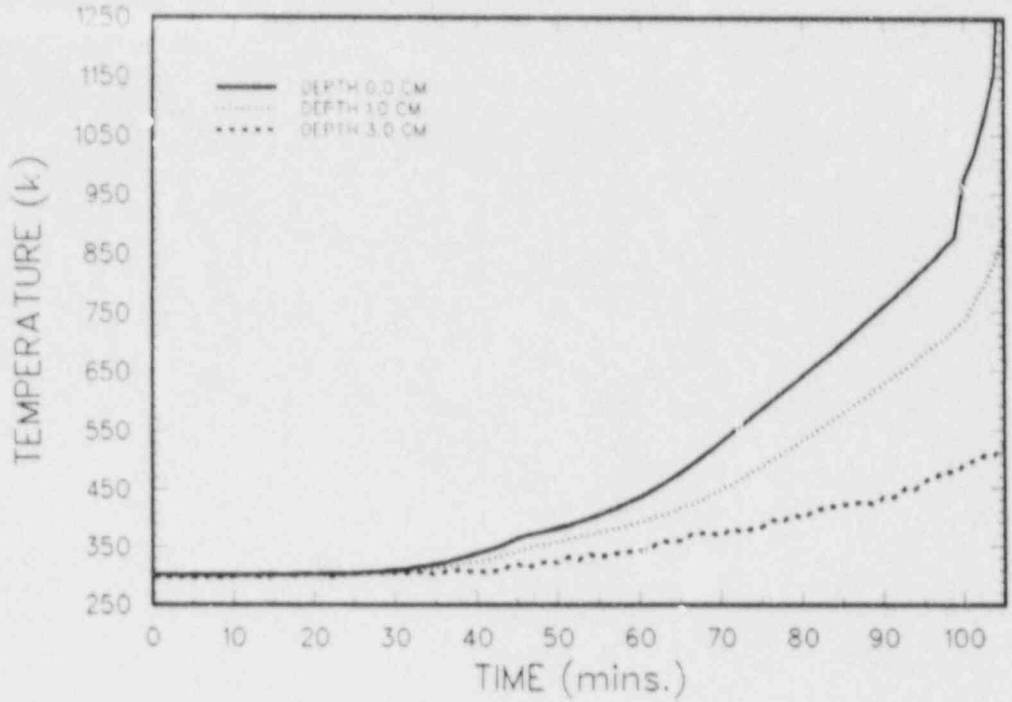

Figure 1.1-18. SURC 4 Initial Concrete Temperatures

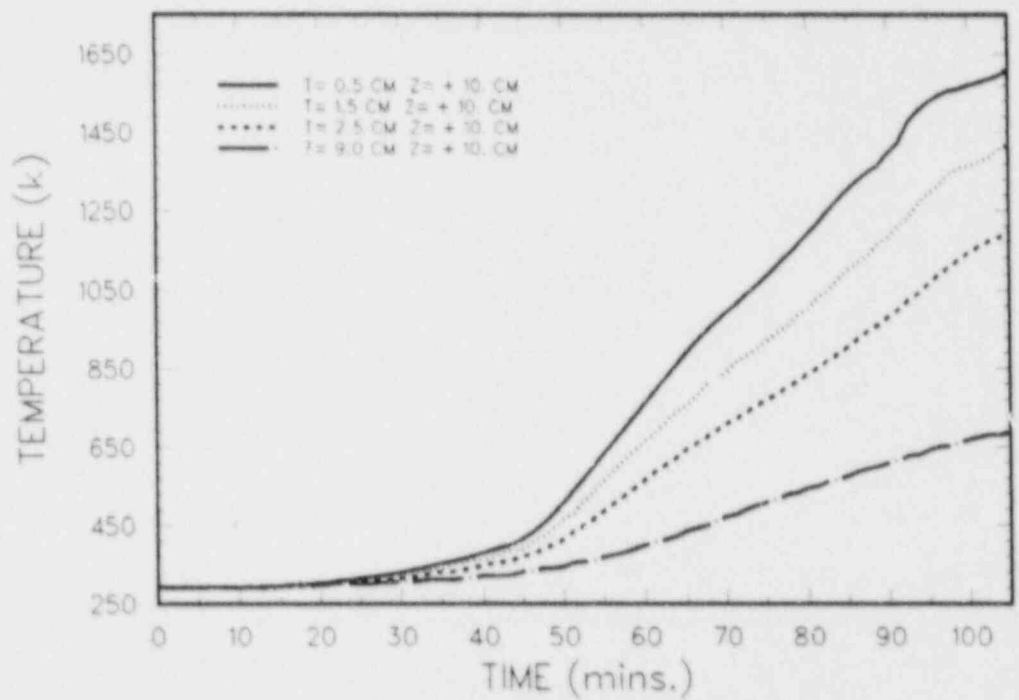

Figure 1.1-19. SURC 4 MgO Sidewall Temperatures

adjacent to the steel charge and 10 cm above the initial concrete interface. When concrete attack started, the MgO sidewall was at a temperature of 1610 K at a depth of 0.5 cm, 1420 K at 1.5 cm, 1200 K at 2.5 cm, and 690 K at 9 cm.

- **Boundary Conditions**

Figures 1.1-20 and 1.1-21 show the thermal response of the MgO walls in the upper region of the crucible--at 35 cm and 50 cm above the original concrete interface. Figure 1.1-22 shows the thermal response of the thermocouples embedded in the MgO cover. Substantial heating of the MgO is evident at each of these locations.

Based on the response of the thermocouples in the MgO walls adjacent to the molten steel during the experiment, the heat flux from the steel melt to the MgO has been calculated. Although minor fluctuations in the heat flux were calculated, for present purposes a constant heat flux of 1.0×10^5 W/m^2 can be assumed.

- **Posttest Observations**

The SURC 4 containment vessel was opened after the test in order to remove and section the interaction crucible. This inspection

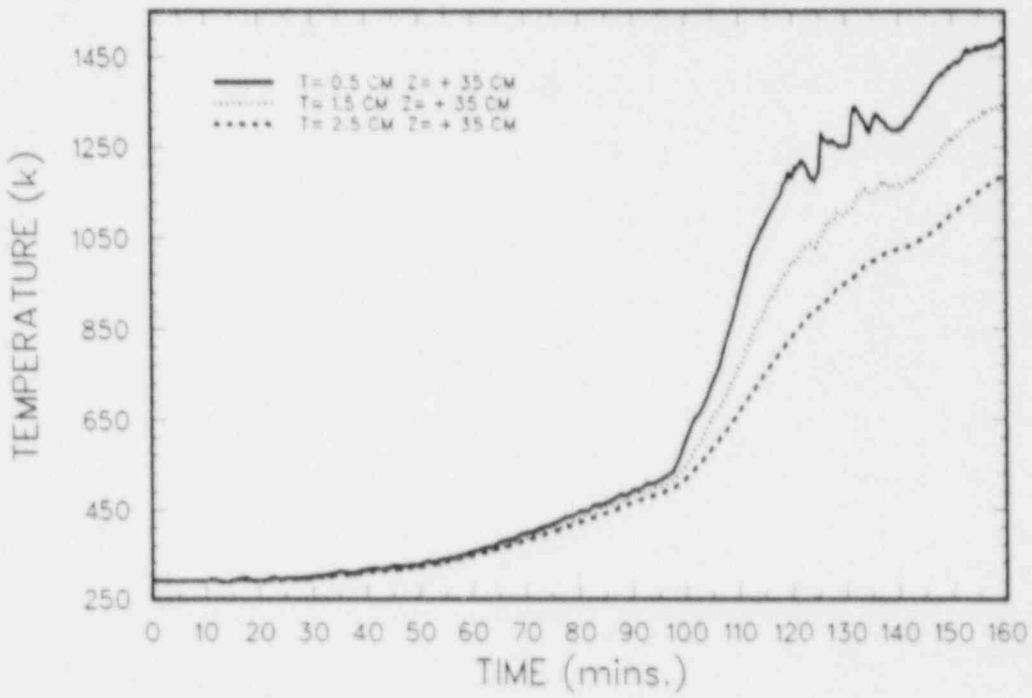

Figure 1.1-20. SURC 4 Middle MgO Temperatures

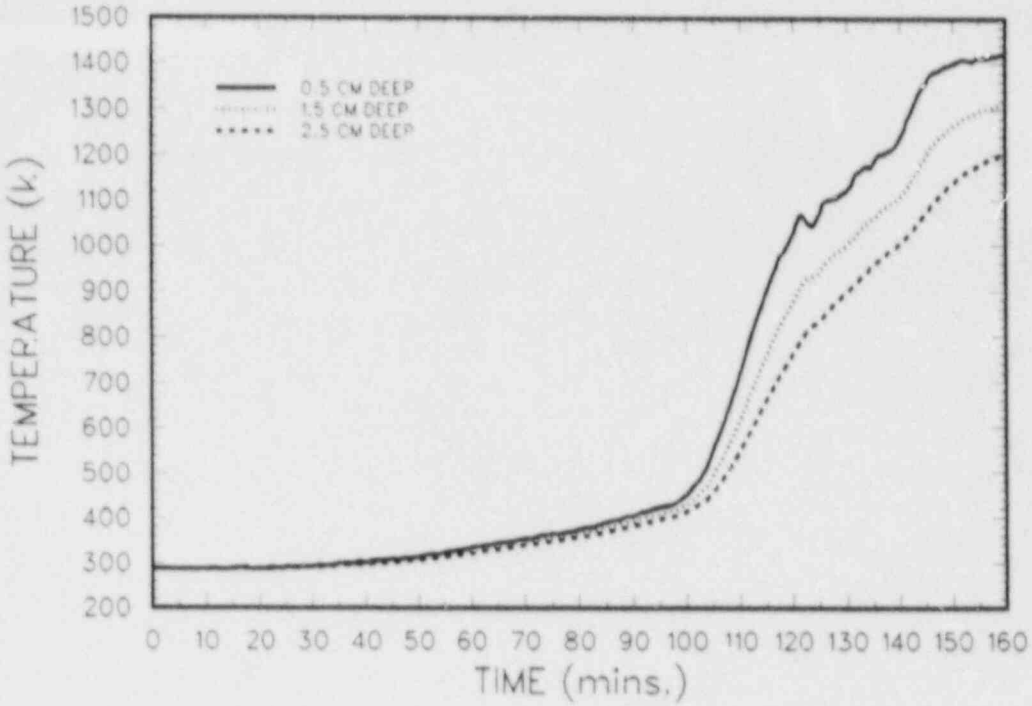

Figure 1.1-21. SURC 4 Upper MgO Temperatures

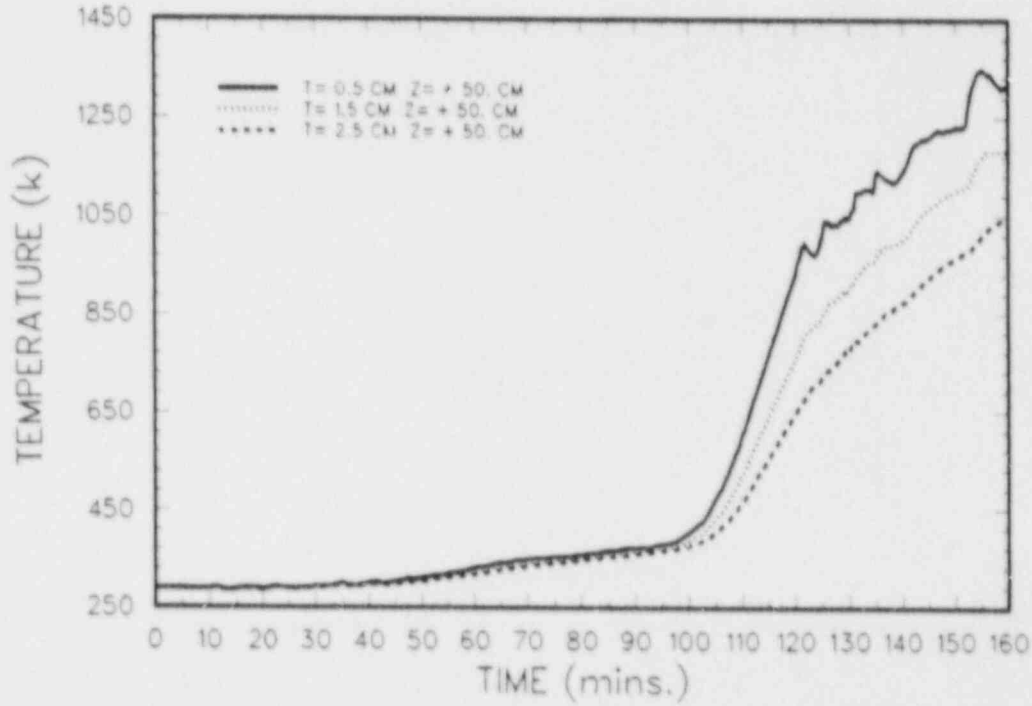

Figure 1.1-22. SURC 4 MgO Cover Temperatures

showed that the MgO sidewalls were intact and that there was no evidence of melt pool-sidewall interaction other than thermal dehydration. The molten steel charge had completely penetrated the bottom of the interaction crucible through a gap between the MgO and the remainder of the basemat. The remainder of the basemat was not cracked and showed no signs of asymmetric erosion. Further inspection of the steel charge and the slag material remaining in the crucible showed that 100 percent of the zirconium metal had been incorporated into the melt.

1.2 High-Pressure Melt Ejection and Direct Containment Heating

(W. Tarbell, J. Brockmann, R. Nichols, and N. Yamano, 6422; M. Pilch 6425)

Accident analyses leading to pressurized ejection of core debris assume a localized failure of the lower head of a reactor pressure vessel (RPV).[7] Typically, the failure is predicted at an instrument guide tube penetration, resulting in a small aperture for debris discharge. Such failures have not been investigated experimentally nor have extensive analyses been performed. A finite element analysis of a pressurized nuclear reactor vessel during core meltdown has been performed by Robert Chambers, Sandia, Div. 1523. He considers that the behavior of the lower head with a prescribed boundary condition represents a degraded core.[8] The results of this analysis are presented here.

1.2.1 Introduction

During a severe accident in which the core of a nuclear reactor has melted, a portion of the bottom of the containment vessel is subjected to extremely high temperatures when directly contacted by the molten material. As the temperature increases through the thickness of the containment vessel, the strength of the steel is dramatically reduced, ultimately leading to failure. Such accident scenarios are often studied using a computer simulation or systems model that neglects the presence of thermal strains produced during heating. Uncertainties surrounding the effect of the resulting thermal expansion in a typical pressurized reactor vessel have warranted further study to determine whether the combined swelling and softening of the heated surface of the vessel aggravate the stress state of the cooler exterior material and thereby expedite the time to failure.

A typical pressurized reactor containment vessel has been analyzed to determine the deformation and time to failure based on the highly nonlinear temperature dependent elastic-plastic response of the steel. Solutions that include thermal strains have been compared to solutions without thermal strains. No material creep or embrittlement was considered.

1.2.2 Problem Definition and Approach

The basic geometry of a section of the lower half of an axisymmetric reactor containment vessel is depicted schematically in Figure 1.2-1. The specific dimensions reflect those chosen for this numerical study. It is assumed that this vessel is subjected to an internal pressure of 2500 psi and operates at a temperature of 440°F (500 K). For purposes of evaluating the significance of thermal strains on the resulting solutions, the presence of molten material was simulated by imposing a sudden temperature boundary condition of 2600°F (1700 K) on the bottom spherical cap subtended by a 60 degree polar angle as shown in Figure 1.2-1. This temperature change was applied after the vessel was equilibrated at 440°F under pressure. Failure was observed by monitoring the sag in the center of the bottom of the vessel.

A solution to this problem was obtained using two separate (uncoupled) finite element procedures: COYOTE[9] and JAC.[10] COYOTE was used to numerically solve the heat conduction problem to determine the transient temperature distribution in the reactor containment vessel. The actual stress analysis was conducted with JAC. The standard temperature solution file written by COYOTE was used to define the transient temperature response needed for the temperature dependent elastic-plastic material model. The finite element meshes were generated with QMESH.[11]

1.2.3 Material Properties

The task of obtaining material properties for a mild steel at extremely high temperatures (near melting point) is nontrivial and somewhat questionable. At these temperatures, the steel undergoes fundamental changes in structure that affect its mechanical response. Although actual property data does exist for the lower temperature domain, it is extremely rare to find such information for temperatures above about half of the melting point. Since the underlying objective of this effort was to at least make a qualitative or semiquantitative comparison between the response of the vessel with and without thermal strains, the precise details of the high temperature material response are not essential. Only reasonable phenomenological behavior is necessary.

Properties for an SA533 Grade B Class I plate, taken from Reference 12, were adopted for use in characterizing the reactor containment vessel. This report contains material data up to a maximum temperature of 1200°F (922 K). Values for temperatures between 1200° and 2600°F were obtained by extrapolation, approximation, and comparison with other high-temperature data.

The temperature dependent elastic-plastic material model in the JAC finite element program is characterized by defining a multitude of material parameters at discrete temperatures. A maximum

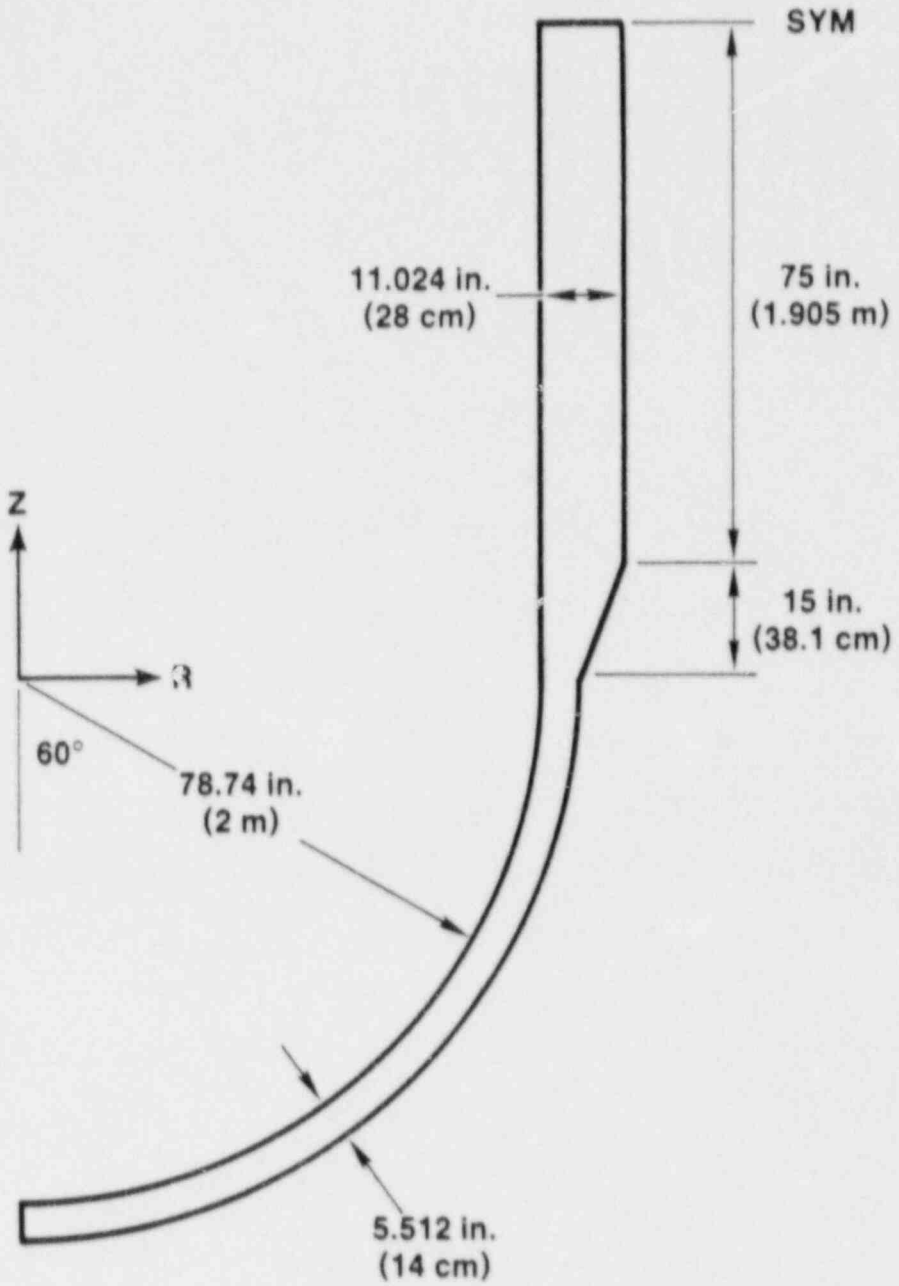

Figure 1.2-1. Schematic Cross Section of an Axisymmetric Nuclear Reactor Containment Vessel

of eight temperatures can be selected with intermediate values defined by interpolation. The material parameters include Young's modulus, Poisson's ratio, yield stress, hardening modulus, hardening parameter (1 denotes isotopic hardening, 0 denotes kinematic hardening), and thermal strain. These parameters were obtained by fitting the available experimental data and extrapolating or approximating, as necessary, to obtain the high-temperature response. A compilation of the inputs used in this study is recorded in Table 1.2-1.

Table 1.2-1

SA533 Temperature Dependent Elastic-Plastic Material Model Data for JAC Finite Element Code

Temp (°F)	Young's Modulus (ksi)	Poisson's Ratio	Yield Stress (ksi)	Hardening Modulus (ksi)	Hardening Parameter	Thermal Strains
70	31000	0.27	70000	374	1	-2.5356×10^{-3}
400	29600	0.27	67400	352	1	-3.0340×10^{-4}
750	27400	0.27	65000	225	1	2.5802×10^{-3}
900	24500	0.27	62200	156	1	3.9731×10^{-3}
1050	21600	0.27	48800	73	1	5.4420×10^{-3}
1200	14100	0.27	32500	48	1	6.9816×10^{-3}
1480	14100	0.33	50	1	1	1.0258×10^{-2}
2600	14100	0.33	50	1	1	2.4706×10^{-2}

Some adjustments to the material data were made solely on the basis of numerical considerations. Although measured data indicate that values for Young's modulus, hardening modulus, and yield stress all virtually go to zero in the 1400° to 1500°F temperature range, nonzero values were adopted. At these temperatures, the material has virtually no stiffness and is in a regime of incompressible plastic flow. This effect was achieved in the JAC finite element formulation of the constitutive equation by defining a relatively small value of yield stress and hardening modulus. Extremely small or zero values of all three of these parameters can adversely affect numerical convergence and make solutions prohibitively expensive or impossible to obtain. Plots of the stress-strain curves defined by the JAC material inputs extracted from Table 1.2-1 are shown in Figure 1.2-2. The 1480 and 2600 degree curves are imperceptible in this

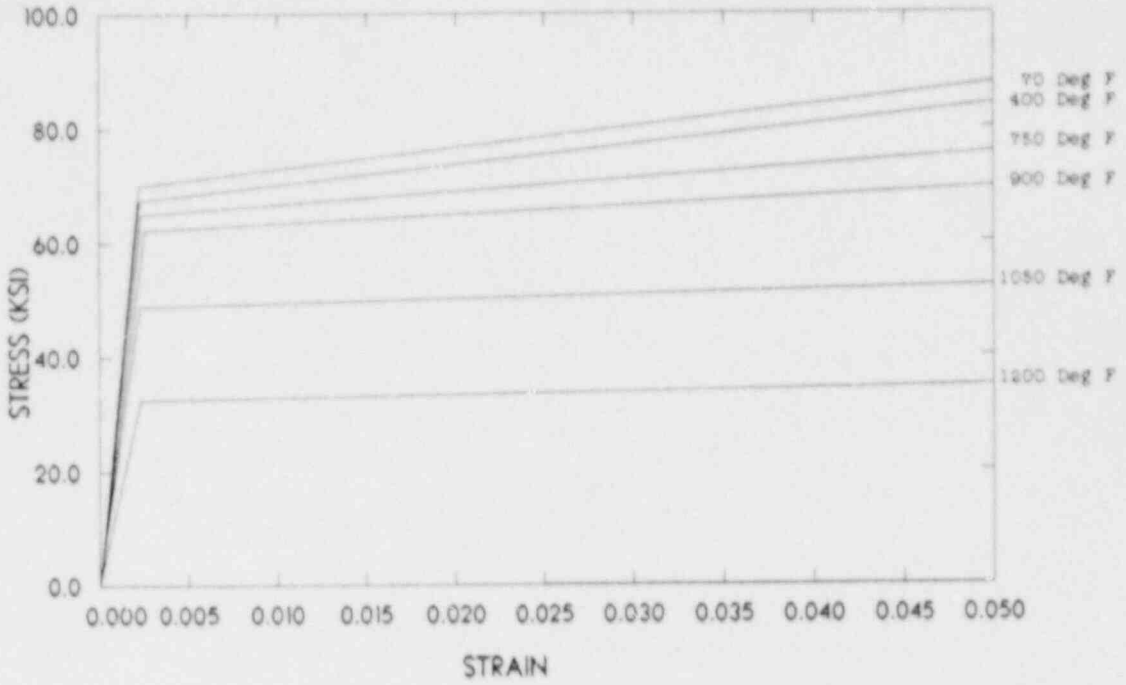

Figure 1.2-2. Temperature Dependent Stress-Strain Curves

figure. The temperature dependence of Poisson's ratio, Young's modulus, the hardening modulus, the yield stress, and the coefficient of thermal expansion is illustrated by the plots in Figures 1.2-3 through 1.2-7, respectively.

Temperature independent properties were designated for input into COYOTE for the numerical solution of the linear heat conduction problem. These values are shown in Table 1.2-2.

1.2.4 Modeling and Numerical Considerations

Because JAC employs exclusively the 4-node quadrilateral element, this element was incorporated into a single finite element mesh that could be used for both the thermal and stress computations. In designing this mesh, attention was given to the minimum number of elements (six) that could be equally distributed through the thickness of the vessel wall in a 2-D axisymmetric model (with one point element integration) while still preserving the radially symmetric deformation expected in a pressurized sphere. Although biasing the mesh toward the interior of the wall would have permitted a more accurate estimate of the steep gradient in short-term temperature fields, this advantage was waived to achieve economy, recognizing the ultimate interest was in comparing long-term time to failure.

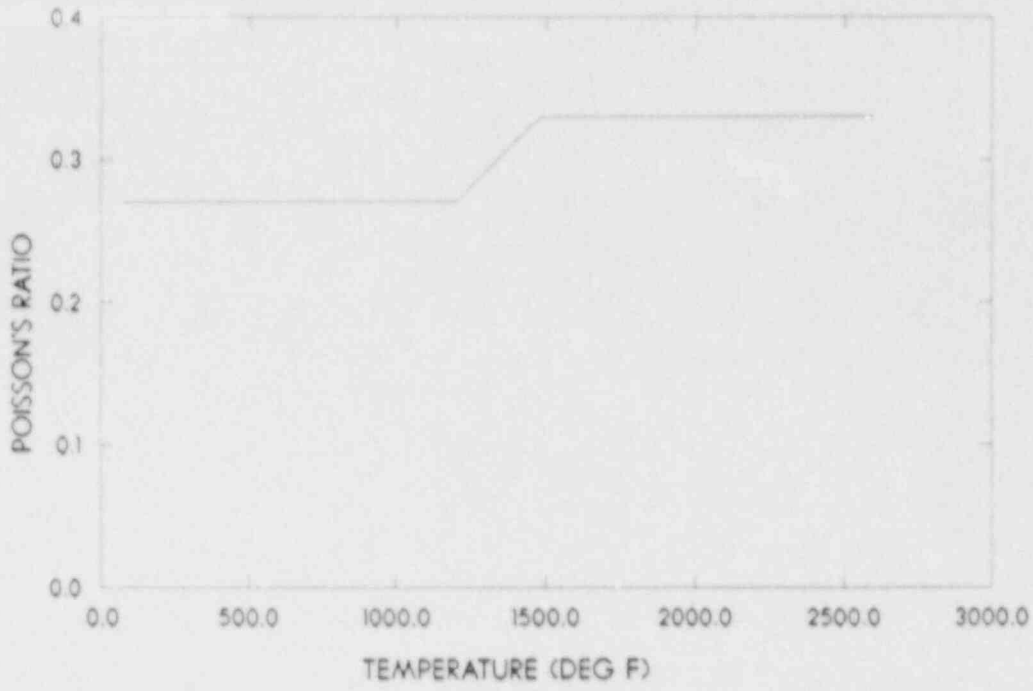

Figure 1.2-3. Temperature Dependence of Poisson's Ratio

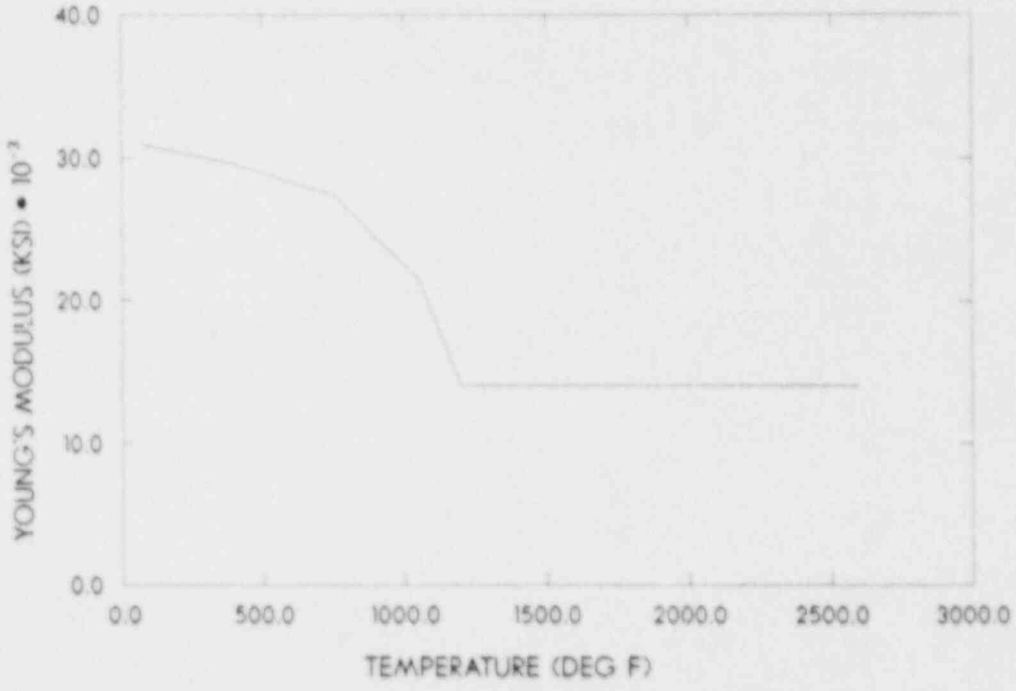

Figure 1.2-4. Temperature Dependence of Young's Modulus

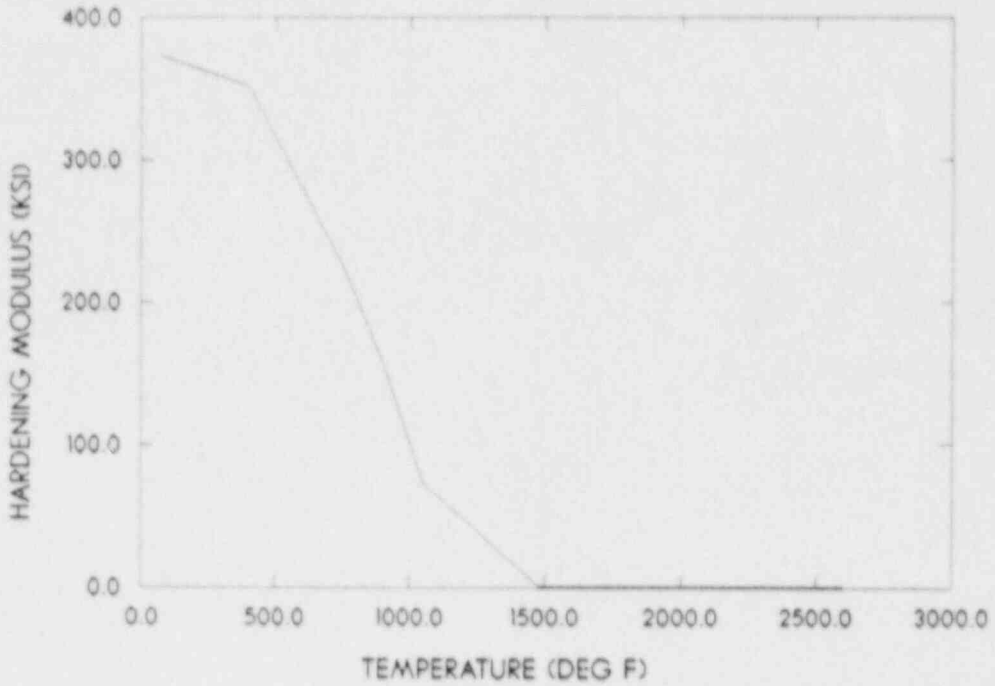

Figure 1.2-5. Temperature Dependence of Hardening Modulus

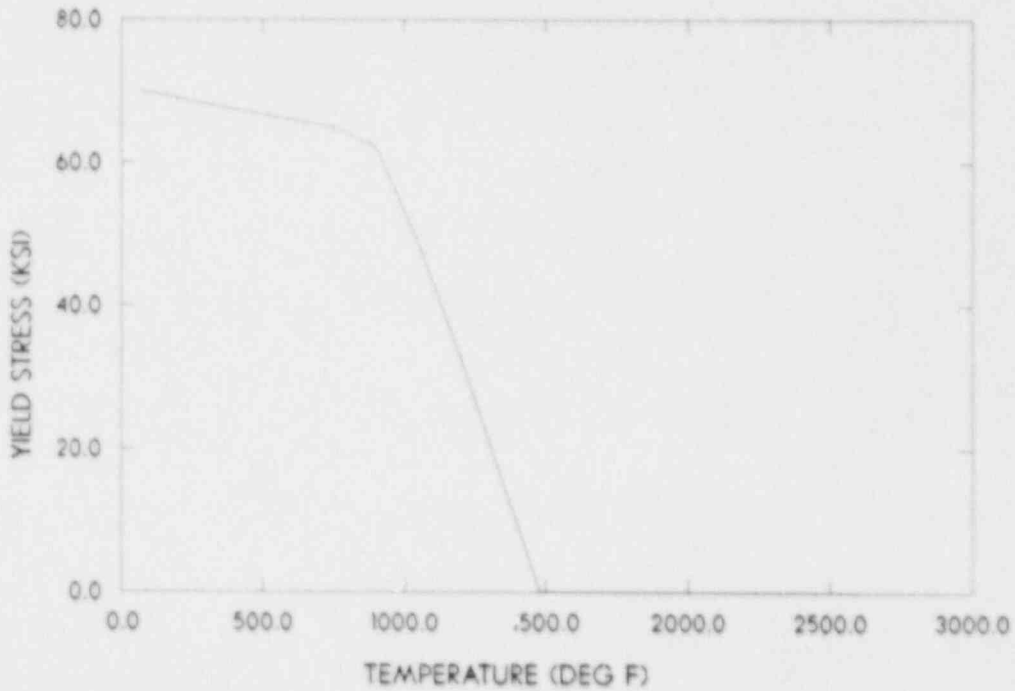

Figure 1.2-6. Temperature Dependence of Yield Stress

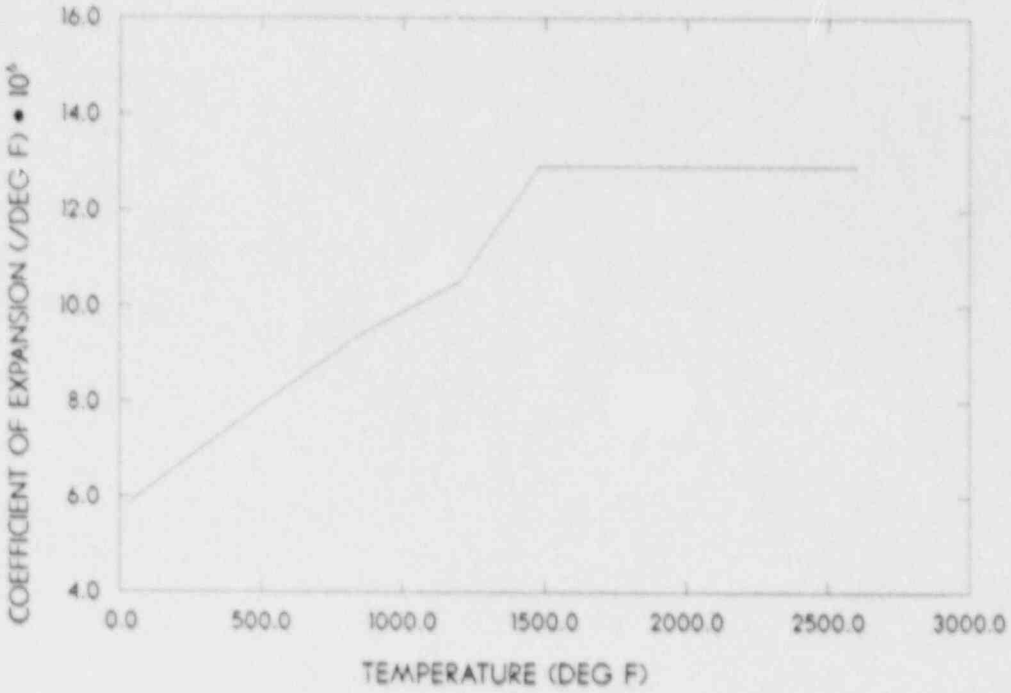

Figure 1.2-7. Temperature Dependence of Thermal Expansion Coefficient

Table 1.2-2

Material Inputs for COYOTE

Density = 0.2736 lbm/in^3
Specific Heat = 0.1457 Btu/lbm•F
Thermal Conductivity = 3.47ł ‹ 10^{-4} Btu/in•s•F

The analysis was started by studying the nonlinear behavior and convergence characteristics associated with obtaining solutions to transient thermal problems with a temperature dependent elastic-plastic material model. For this purpose, the first problem considered was a hollow pressurized sphere subjected to a uniform temperature increase along the interior surface. Due to axisymmetry, this analysis could be conducted by modeling a spherical sector consisting of a single layer of elements through the thickness of the shell. Attempts to obtain a solution with only six elements through the thickness were hindered by the coarseness of the mesh. Because the material softening of individual elements is determined by the temperature at a single integration point, the average temperature difference between adjacent interior elements in the six element mesh was quite substantial. Consequently, vast and abrupt differences occurred between the stiffnesses of connected elements. In addition, as the heated material softened and swelled, the circumferential stress distribution changed from tension to compression. This necessitated the presence of a sufficient number of elements to model reasonably the transition in the stress distribution that occurred through the thickness. The net effect of using this mesh was an inability to obtain convergence. However, this was easily remedied by increasing the number of elements through the thickness. The radial displacements computed from a 24-element model are plotted in Figure 1.2-8 for analyses with and without

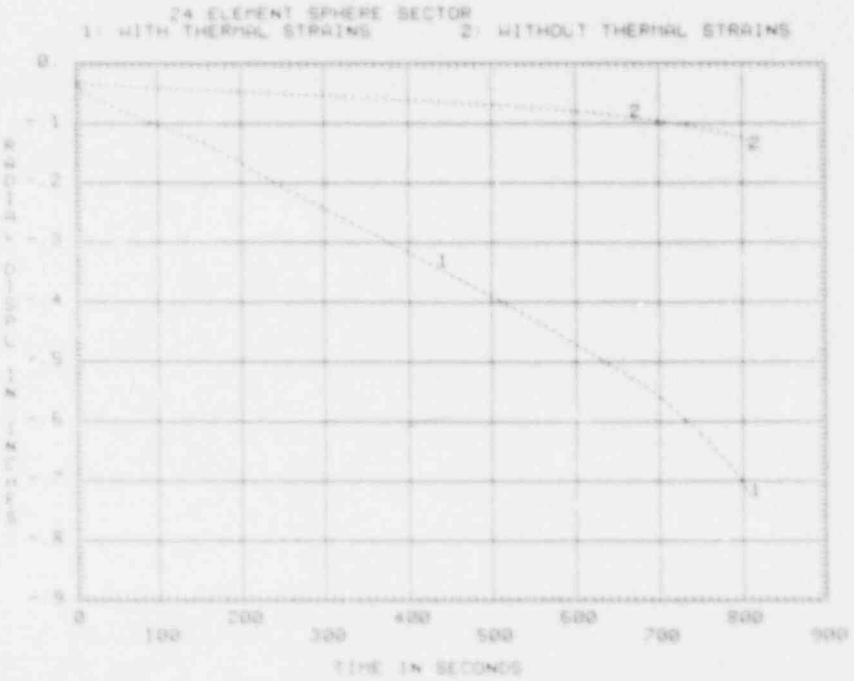

Figure 1.2-8. Displacement (Sag) in Spherical Sector Model

thermal strains. Although there are major differences in the magnitude of the resulting deformation, the times to failure appear to be nearly the same. In solving these problems, it was determined that larger force tolerances can be specified when thermal strains are not present. Both solutions were terminated when convergence was not obtained after several thousand iterations.

In considering the actual problem geometry and thermal boundary condition for the nuclear reactor containment vessel, it was apparent that any model containing 24 elements through the thickness would require an exorbitant amount of computational effort. To overcome this, a finite element mesh was constructed using 10 elements through the thickness, and initially, only the hollow hemispherical portion of the structure was modeled. Geometrically, this hollow half-sphere formed the bottom of the containment vessel and was attached to a thicker circular cylindrical segment. Because the effect of this segment was to partially constrain the edge of the hemisphere, it was expected that this edge condition could be appropriately bounded by performing two analyses, one with a symmetry constraint and another with a totally fixed boundary condition. Furthermore, an attempt was made to design, a priori, an efficient scheme of time integration. Because most convergence impediments were encountered near the times when successive elements achieved the temperature of maximum softening (1480°F), small time steps were taken during these periods. In between, larger time steps were taken.

Two enhancements were made to the JAC source code. The first prohibited the material yield stress that is used during iterative calculations from ever decreasing below the value specified on the material input card. This was implemented after determining that given large time steps with poor estimates of incremental displacements, it is possible to compute unreasonable material parameters, which can inhibit convergence. A second modification was the implementation of an adaptive time step reduction for situations when the specified time step proved to be too large. This allowed the code to reduce the time step and proceed with the analysis rather than abruptly terminating. These time step reductions were carefully restricted within the time limits of the originally specified time step so as to preserve the times designated for writing output, restart, and postprocessing data. This methodology and the incorporated program modifications were highly successful in securing results for this containment study.

1.2.5 Thermal Analysis

To calculate the transient temperature profiles in the bottom of the containment vessel, a 2-D axisymmetric finite element model of the hollow hemisphere was generated. The resulting mesh is shown in Figure 1.2-9. The interior surface over which the

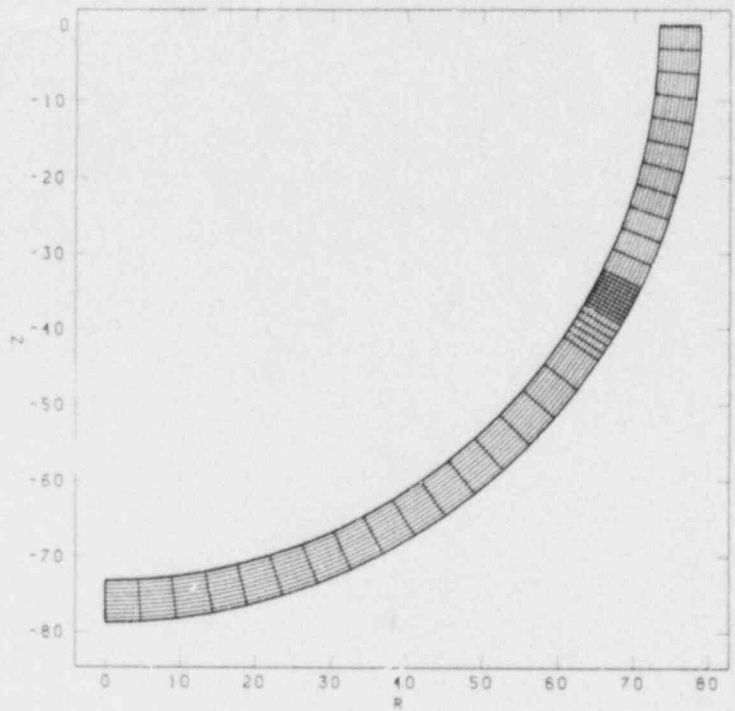

Figure 1.2-9. Hollow Hemispherical Finite Element Mesh

2600°F temperature boundary condition was applied is demarcated by the lower interface between the rectangular elements and the square elements. The square elements were sized to conform with the length of the radial dimension of the elements in the layers through the thickness of the shell. This was done to provide uniformity and consistency in the accuracy of the temperature solution.

The numerical solution to this linear 2-D heat conduction problem was computed by using the generalized Crank-Nicolson integration procedure in COYOTE with a weighting parameter of 0.5. Equal time steps of 15 s each were chosen. This was about the smallest time step that could be taken without producing nonphysical spatial oscillations in the early time temperature field because of limitations in the ability of the finite element mesh to resolve the severe temperature gradients at the boundary. Plots of the temperature variation through the thickness (radial dimension) of the hollow hemisphere, as obtained at different times in the transient response, have been superposed in Figure 1.2-10. The results have been expressed in terms of degrees Fahrenheit (Figure 1.2-10a) and degrees Kelvin (Figure 1.2-10b). It is clear that somewhat more than 4800 s (80 min) are required to reach the steady-state condition.

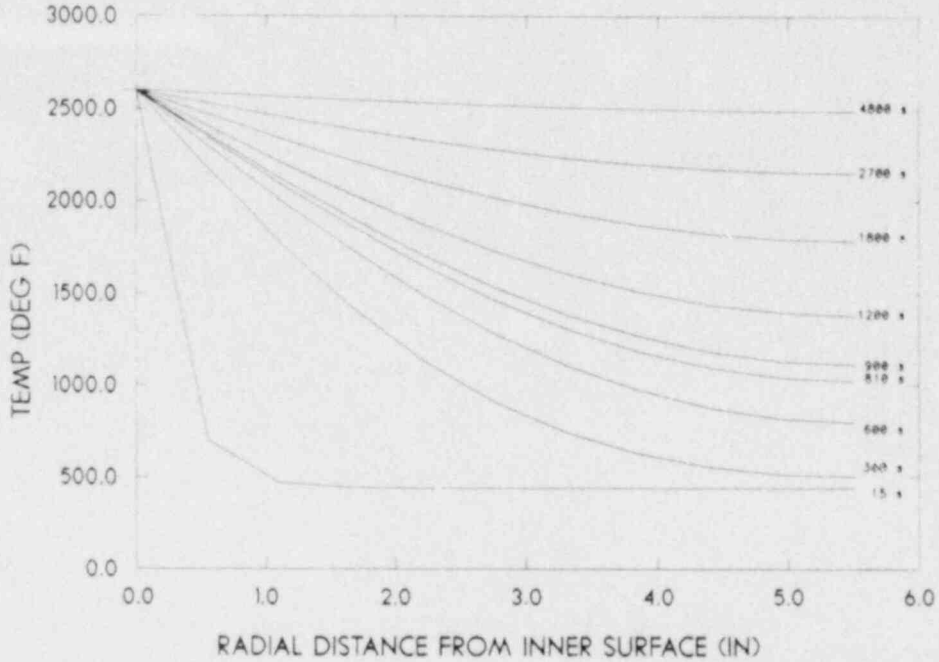

a. Temperature Profiles in Degrees Fahrenheit

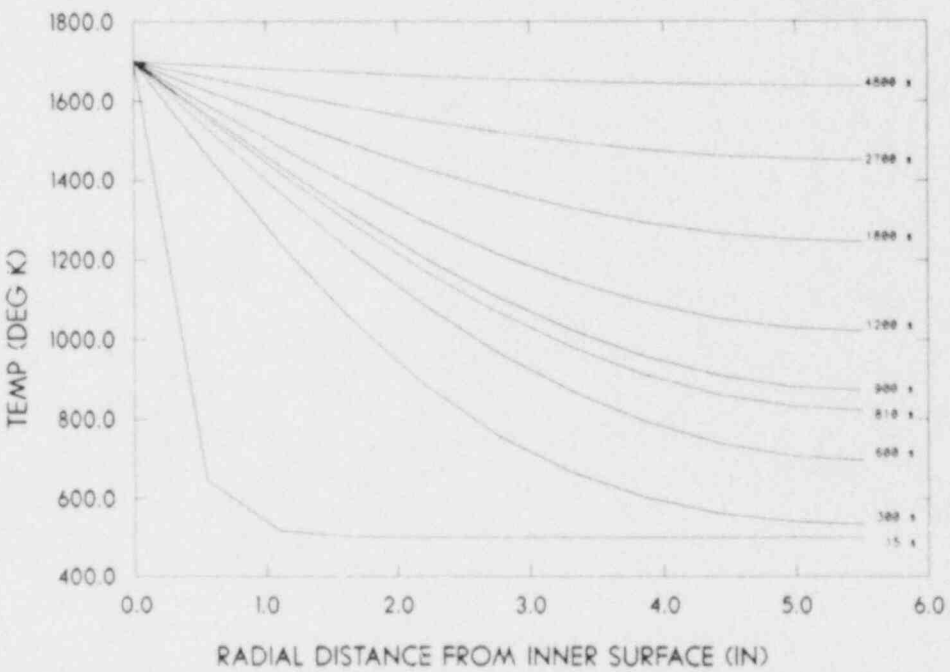

b. Temperature Profiles in Degrees Kelvin

Figure 1.2-10. Temperature Variation Through Thickness of Vessel

1.2.6 Stress Analyses

With the thermal history defined by COYOTE, the stress analyses were performed using the JAC finite element code and the aforementioned program modifications. The finite element mesh in Figure 1.2-9 was also adopted for these computations, and two distinct kinematic boundary conditions were investigated. In the first case, a symmetry constraint was placed on the top edge of the hollow hemisphere. This suppressed vertical displacements but allowed horizontal (radial) motion. In the second case, total fixity was imposed. These two separate problems were analyzed with and without thermal strains.

Plots of the time dependent vertical sag at the bottom of the vessel are shown in Figures 1.2-11 and 1.2-12 for the cases of symmetry and fixed boundary conditions, respectively. Although there are differences in the magnitudes of the displacements associated with the presence or absence of thermal strains as well as type of boundary condition, there is no significant difference in the time to failure. All solutions were terminated when convergence was not achieved after successive adaptive reductions in the size of the originally specified time step. The numerical solutions that lacked thermal strains were computed for a period of about 8 to 10 s longer than those solutions that did include thermal strains. This is apparent in Figures 1.2-11 and 1.2-12 where it is seen that in the absence of thermal strains, it was possible to partially track a portion of the abrupt change in displacement at the time of failure. This computational difference is primarily due to the fact that a larger value in force tolerance could be used to define convergence in the analyses without thermal strains than could be used in analyses with them.

Deformed mesh plots of the problem having a fixed edge condition at the top are illustrated in Figures 1.2-13a and b for solutions obtained with and without thermal strains, respectively. These deformations correspond to the last times for which convergence was achieved, and they have been scaled by a factor of 25 to enhance the failure mode. Figure 1.2-13a clearly shows the effects of thermal swelling over the domain affected by the applied temperature boundary condition, with elements near the interior having greater volumetric strains than those on the exterior. This expansion of the inner layers of the shell is resisted by the outer layers and by the adjacent material, which is still at the initial temperature. Though there is a tendency to straighten or diminish the curvature of the circular shell section near the fixed end, most of the bending necessary to accommodate this expansion is relieved by a hinging that occurs in the hot material. Some of the interior elements near the lower interface between the square and rectangular elements were observed to have taken on an hourglass shape. In the absence of thermal strains, the cooler material near the top of the shell preserved its curvature while the bottom of the vessel sagged due

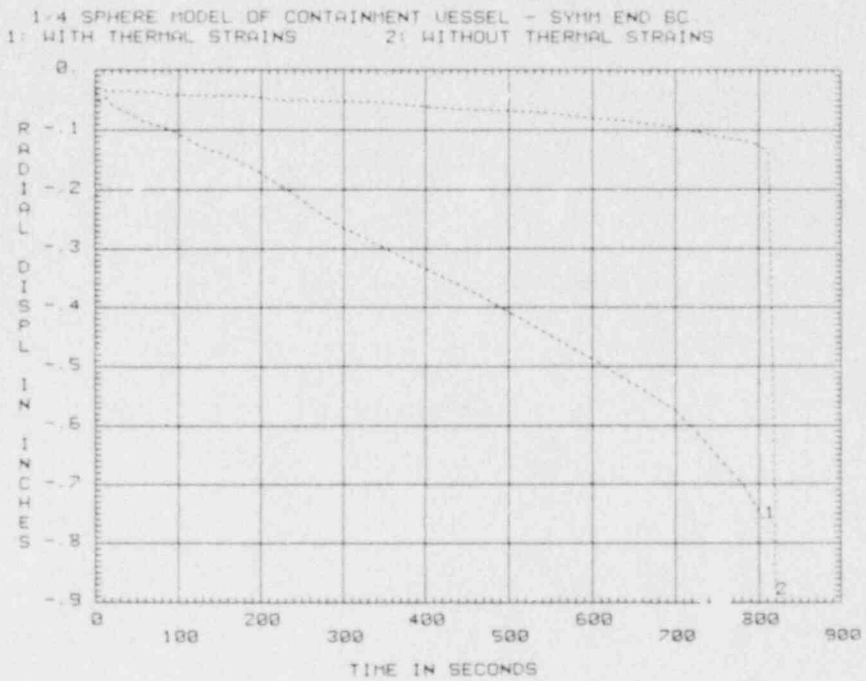

Figure 1.2-11. Displacement (Sag) in Hemisphere - Symmetry BC

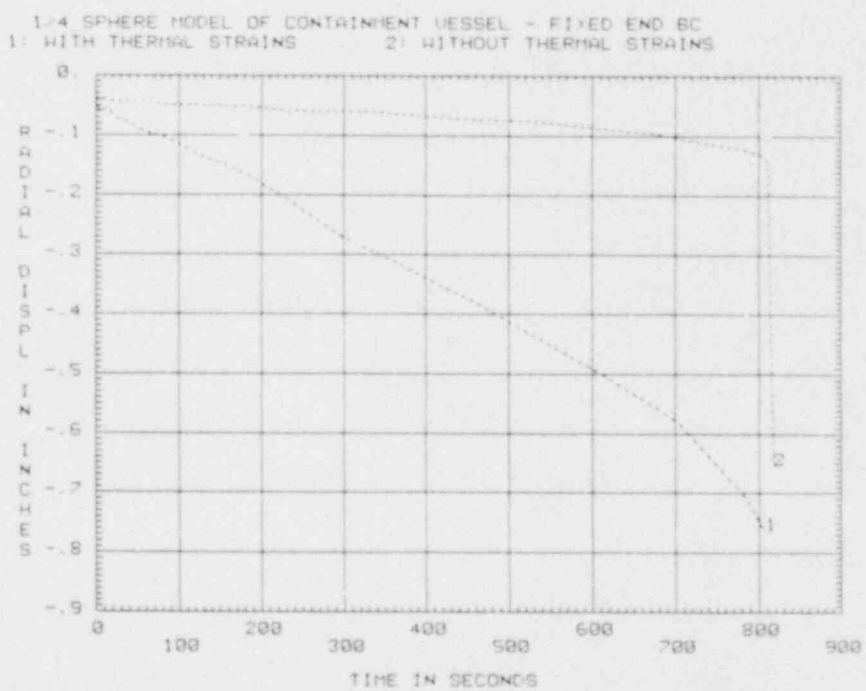

Figure 1.2-12. Displacement (Sag) in Hemisphere - Fixed BC

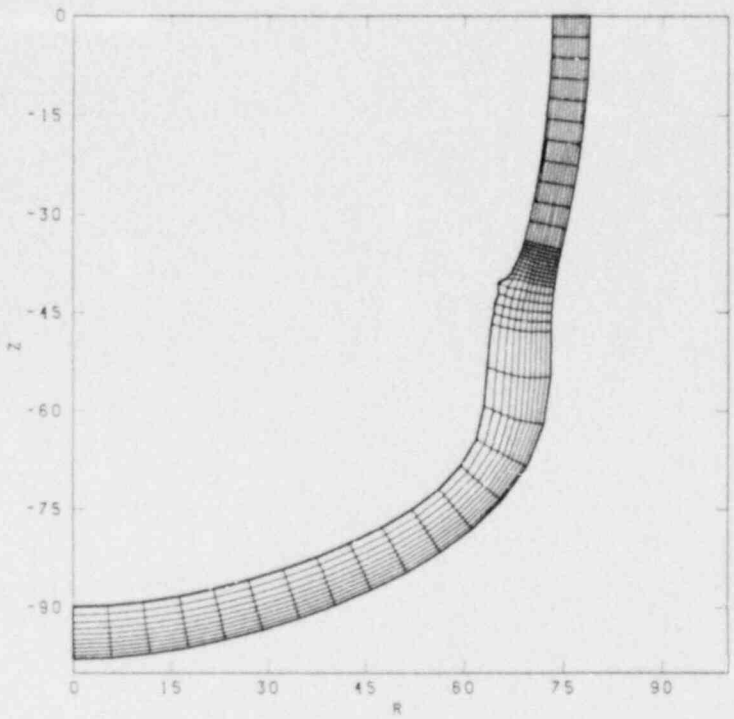

a. Deformation With Thermal Strains

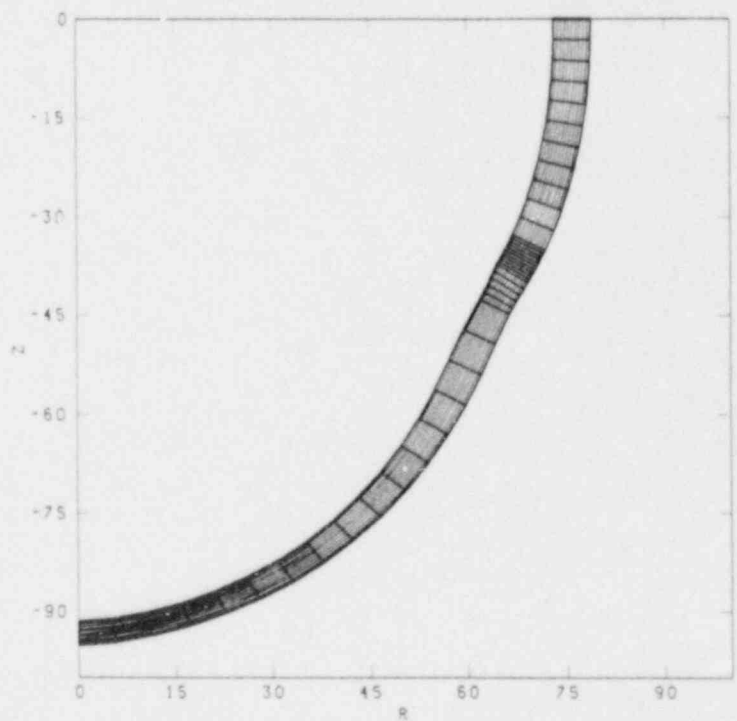

b. Deformation Without Thermal Strains

Figure -1.2-13. Deformed Mesh Plots of Hemisphere With Fixed BC (Magnification Factors of 25)

to the softening under the pressure. Some necking is apparent at the bottom and near the region of mesh refinement at the end of the temperature boundary condition. Although this is also present in Figure 1.2-13a, it is obscured by the dominant volumetric strains. Failure in both instances results when the bottom bursts because of the pressure and material softening under high temperatures.

Of particular interest is the effect of thermal strains on the resulting stresses in the vicinity where the temperature boundary condition discontinues. A plot of the deformed mesh (scaled by a factor of 10) for the case having thermal strains and a fixed top edge condition is shown in Figure 1.2-14. This and all other plots in this section are based on results occurring 807.5 s after imposing the temperature boundary condition. Figure 1.2-15 contains a contour map of the yield stress of the material which reflects the decreases associated with the temperature rise in the steel. The corresponding temperature contours are illustrated in Figures 1.2-16a and b in terms of degrees Fahrenheit and degrees Kelvin, respectively. The thermal gradients and internal pressure combine to produce the high von Mises effective stresses shown in Figure 1.2-17. An indication of material yielding is provided by examining the ratio of the von Mises stress to the yield stress. Unit values denote yielding. Contours of this ratio are shown in Figure 1.2-18. Although unit values denote material yielding, they do not necessarily indicate a free flow condition associated with very little or no strain hardening. This condition is achieved only at temperatures above 1480°F. For comparison, contours of the von Mises stress and the ratio of von Mises stress to the yield stress are plotted in Figures 1.2-19 and 1.2-20, respectively, for results taken at the identical time from the analysis lacking thermal strains. A much simpler stress state exists, but the dominant effect of temperature on the material properties still leads to failure. Numerically, this solution reached the point where yielding had occurred through the entire thickness of the vessel. Further temperature increases serve only to decrease the degree of strain hardening, thereby increasing the deformation.

One final comparison between the analyses with and without thermal strains was made by examining the circumferential stresses at the bottom of the vessel. These results have been plotted in Figures 1.2-21 and 1.2-22. In these figures, the transient variation in stress through the thickness of the vessel has been depicted by the superimposing of stresses from seven distinct times: an initial time (0.001 s) when the pressure was applied, a final time (807.5 s) adopted from prior discussions, and five intermediate times when each of the first five elements (through the thickness of the wall) successively achieved maximum softening (1480°F). At a uniform temperature of 440°F, the classic solution for a pressurized membrane is valid. As the steep thermal gradient appears at the interior surface, the thermal expansion is resisted by cooler outer layers. This

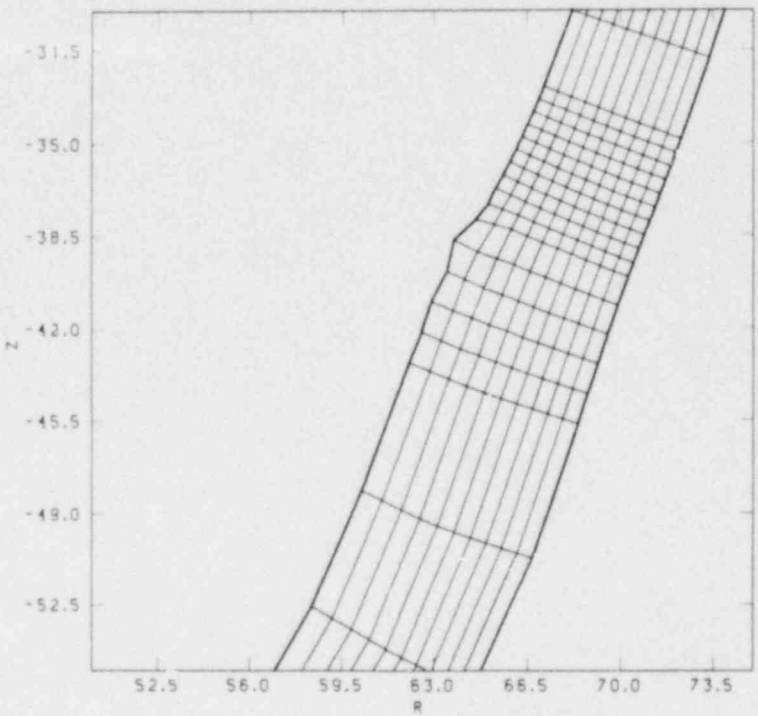

Figure 1.2-14. Deformed Mesh Near Temperature BC Discontinuity (Magnification Factor of 10)

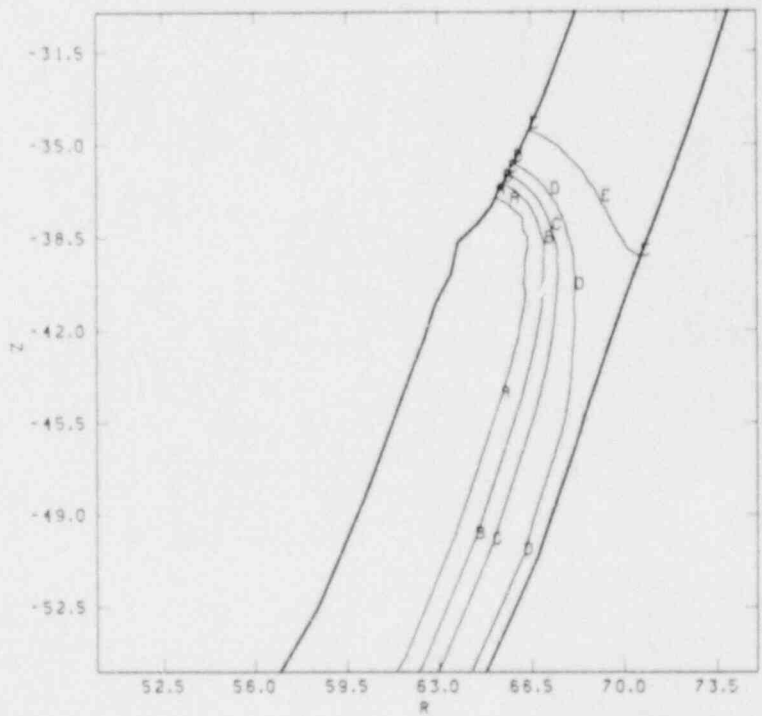

Figure 1.2-15. Yield Stress Contours (psi)

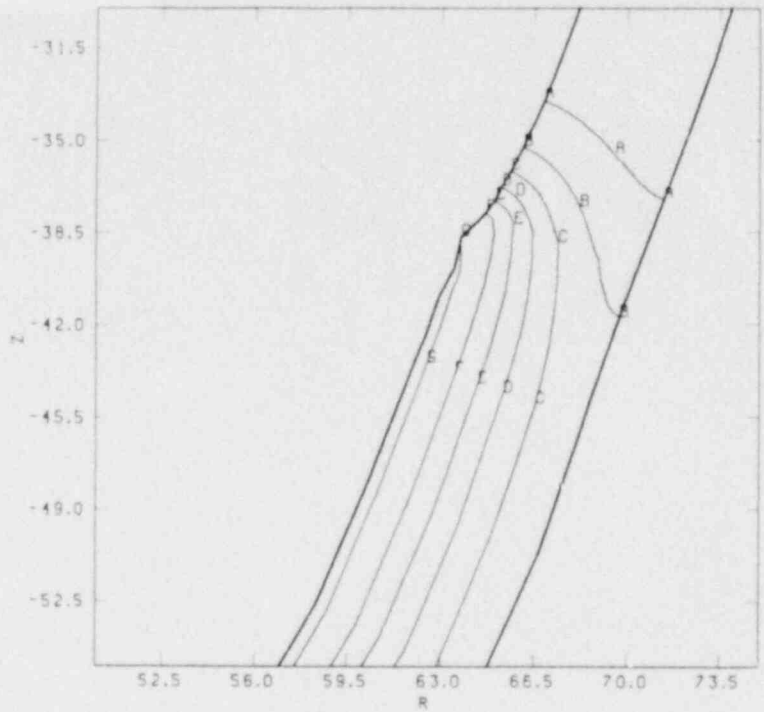

a. Temperature Contours in Degrees Fahrenheit

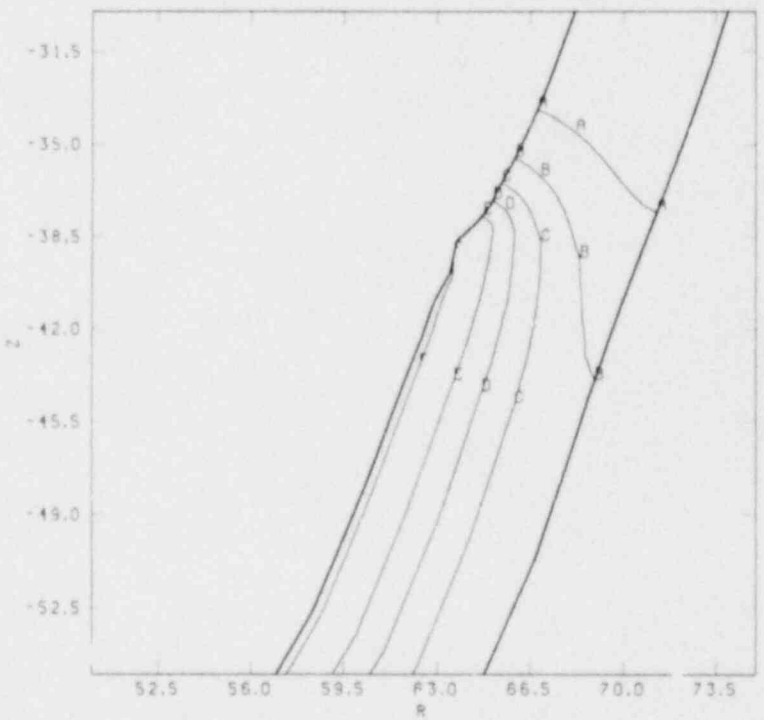

b. Temperature Contours in Degrees Kelvin

Figure 1.2-16. Contours of Average Element Temperature

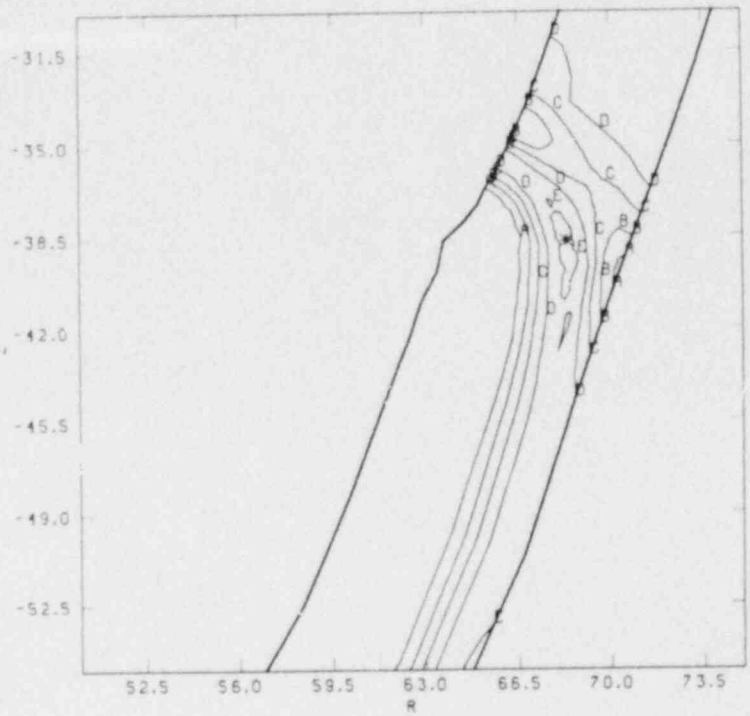

Figure 1.2-17. von Mises Stress Contours (psi) With Thermal Strains

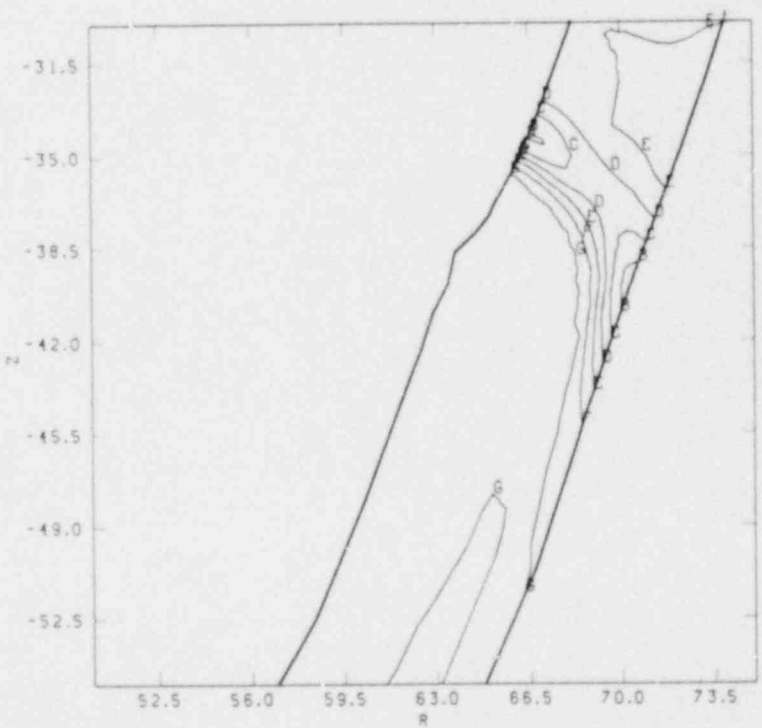

Figure 1.2-18. Contours of Stress Ratio (von Mises/Yield)

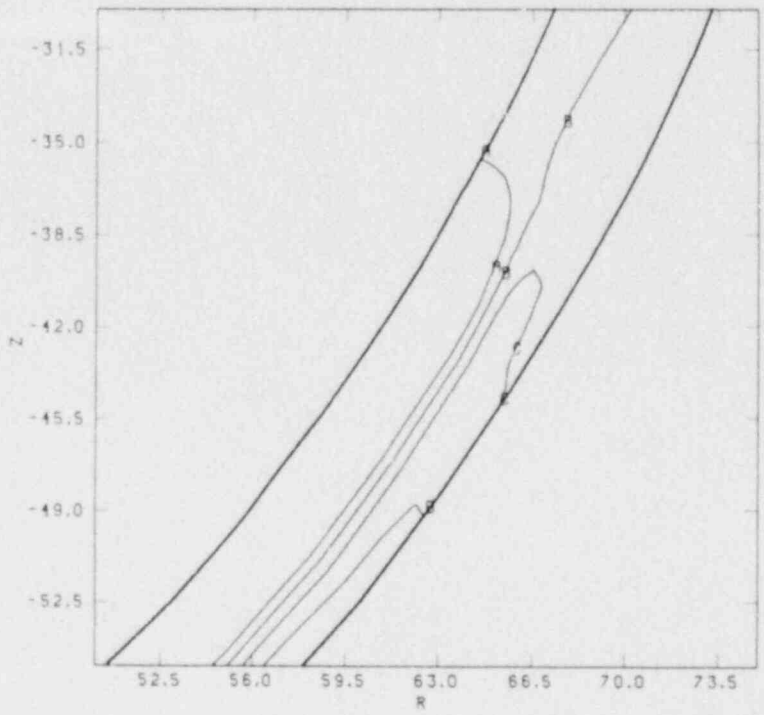

Figure 1.2-19. von Mises Contours (psi) Without Thermal Strains

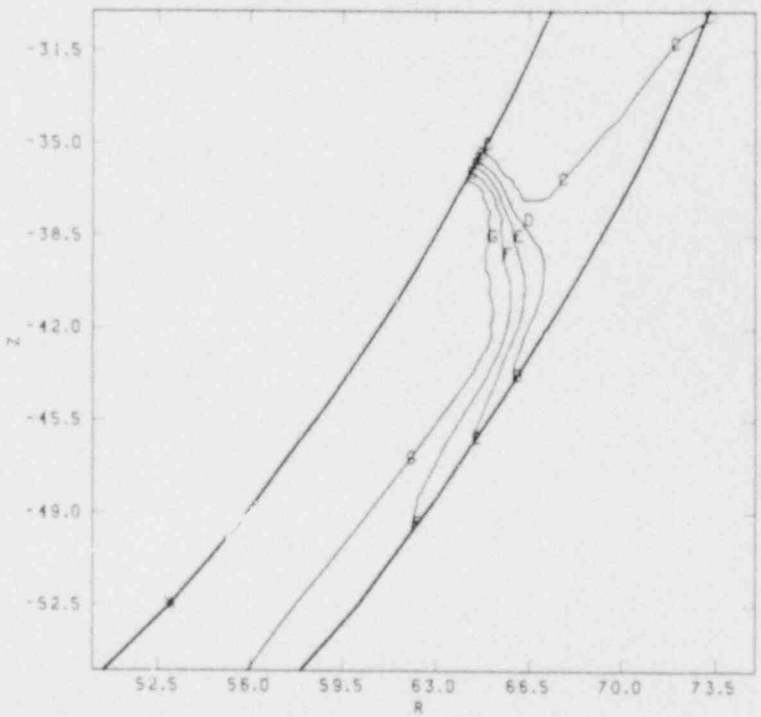

Figure 1.2-20. Contours of Stress Ratio Without Thermal Strains

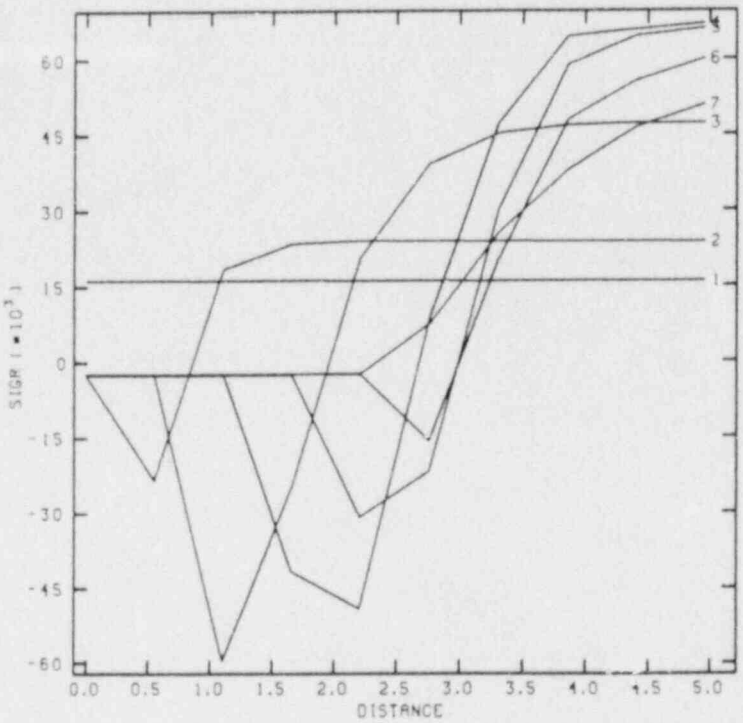

Figure 1.2-21. Circumferential Stress Profiles (psi) With Thermal Stress

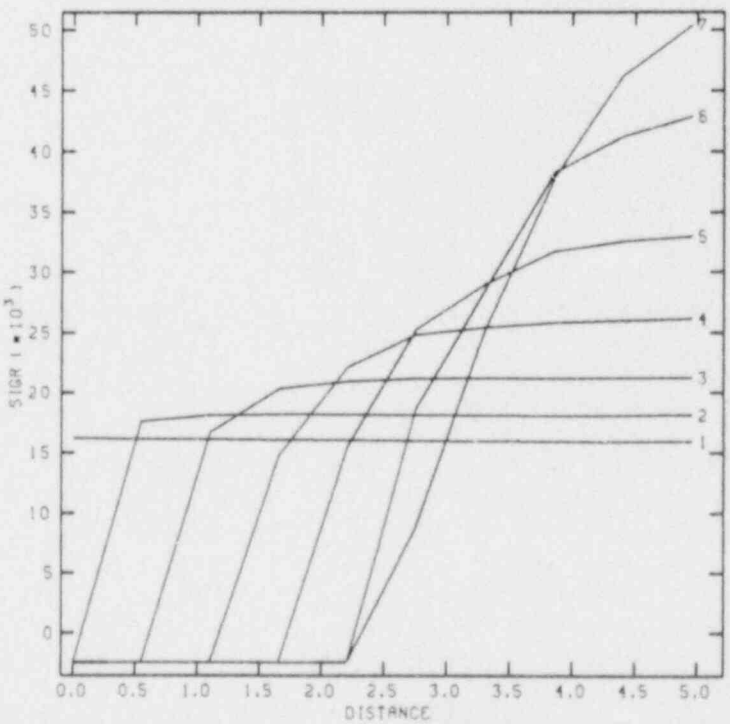

Figure 1.2-22. Circumferential Stress Profiles (psi) Without Thermal Stress

produces the compressive dips in the curves shown in Figure 1.2-21. With increasing temperatures, the leading edge of the thermal gradient propagates through the thickness as evidenced by the shifting of the compressive zone toward the exterior of the shell. In contrast, as the interior elements reach the level of maximum softening, the deviatoric stresses are shed and a hydrostatic stress state is attained and driven by the 2500 psi internal pressure. With the interior elements in compression, the exterior elements must attain higher tensile stresses to provide enough force (represented by the integration of circumferential stresses through the thickness) to sustain the internal pressure being applied to the shell. Ultimately, as the exterior wall temperature increases, the yield stress diminishes to the point at which the material becomes incapable of supporting the load. Then failure ensues. Figure 1.2-22 lacks the compressive spikes found in Figure 1.2-21 because in these analyses, the temperature gradients produce no thermal strains.

Since fixed and symmetry boundary conditions were imposed on this hollow hemispherical mesh as a means of studying and approximating the behavior of a larger and more taxing model of the entire structure, one analysis based on a mesh of the entire structure was undertaken to validate this approach. The corresponding finite element mesh is shown in Figure 1.2-23, and a plot of the calculated sag (including thermal strains) in the bottom of the vessel is depicted in Figure 1.2-24. For purposes of comparison, this sag displacement has been superposed in Figure 1.2-25 with the results obtained from the three other models used in this study. It is seen that the 24-element spherical sector model produces the smallest displacements even though it is based on the highest degree of mesh refinement. Furthermore, it assumes that the temperature boundary condition has been uniformly applied over the entire interior surface of a hollow spherical vessel. The largest displacement is found in the hollow hemispherical model with a fixed edge condition. The identical mesh with a symmetry edge condition has slightly smaller displacements, and the full structure model of Figure 1.2-23 produces a sag that is in fact bounded by these two cases.

1.2.7 Conclusions

An attempt has been made to examine some features associated with the failure of a nuclear reactor containment vessel. In these analyses, the temperature dependent elastic-plastic response of the steel has been considered without regard to any embrittlement or creep phenomena demonstrated by the material. A more detailed analysis cannot be undertaken without determining an appropriate constitutive theory and generating a thorough material characterization. The presence of molten material in the bottom of the containment vessel was simulated by inducing a temperature boundary condition over the spherical cap subtended by a 60-degree polar angle measured from the axis of symmetry. It was assumed

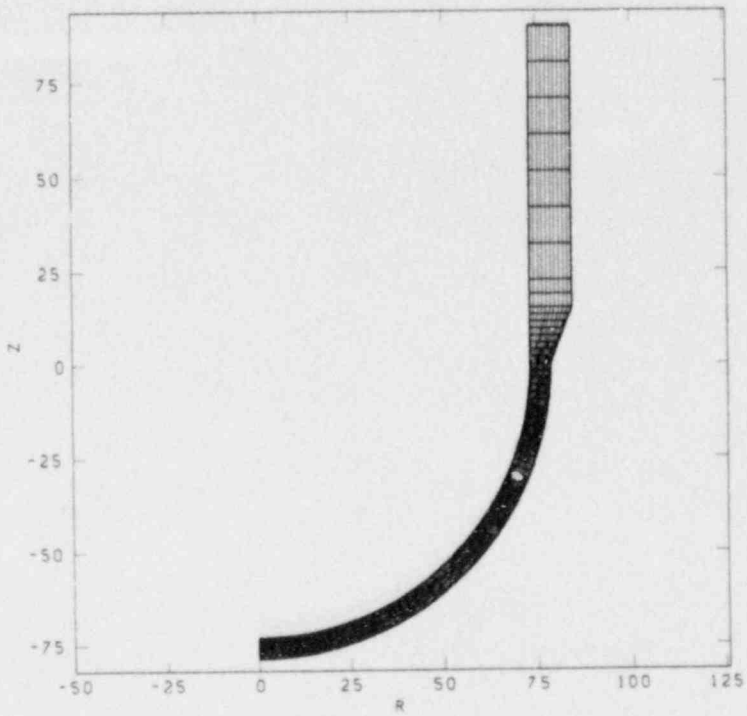

Figure 1.2-23. Finite Element Mesh of Entire Structure

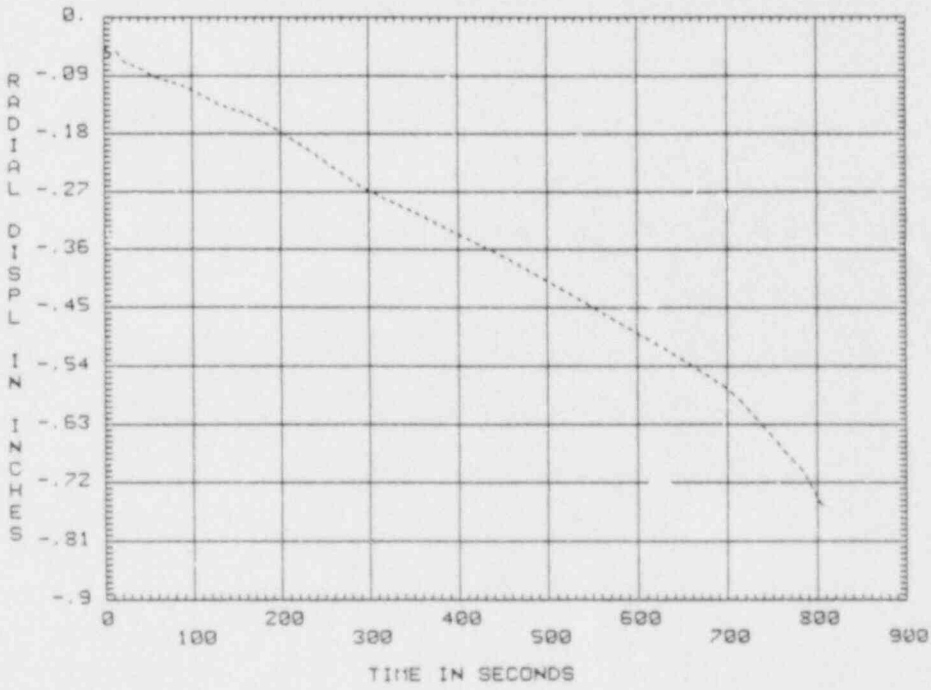

Figure 1.2-24. Displacement (Sag) in Full Structural Model With Thermal Strains

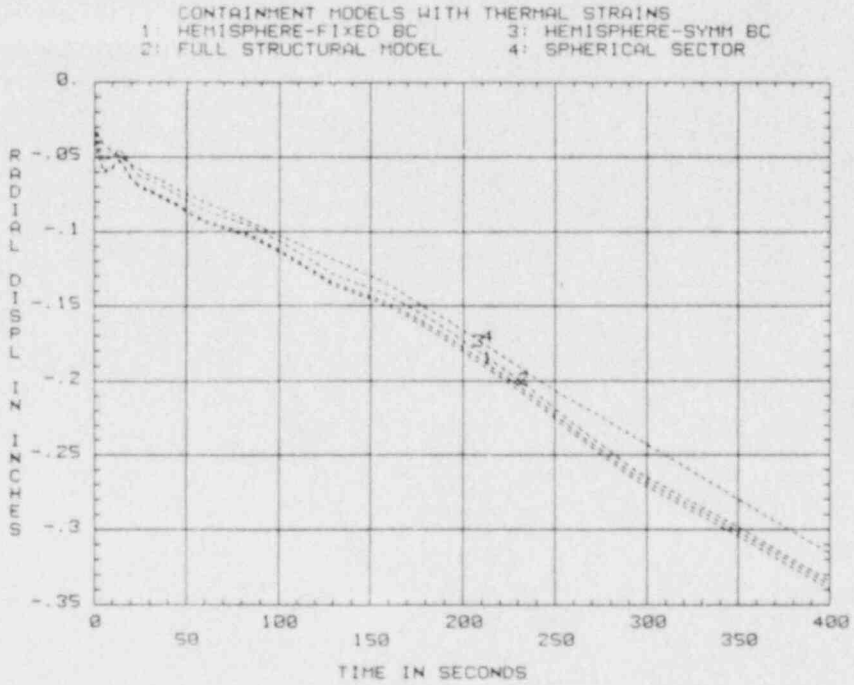

a. Displacements (Sag) During First 400 Seconds

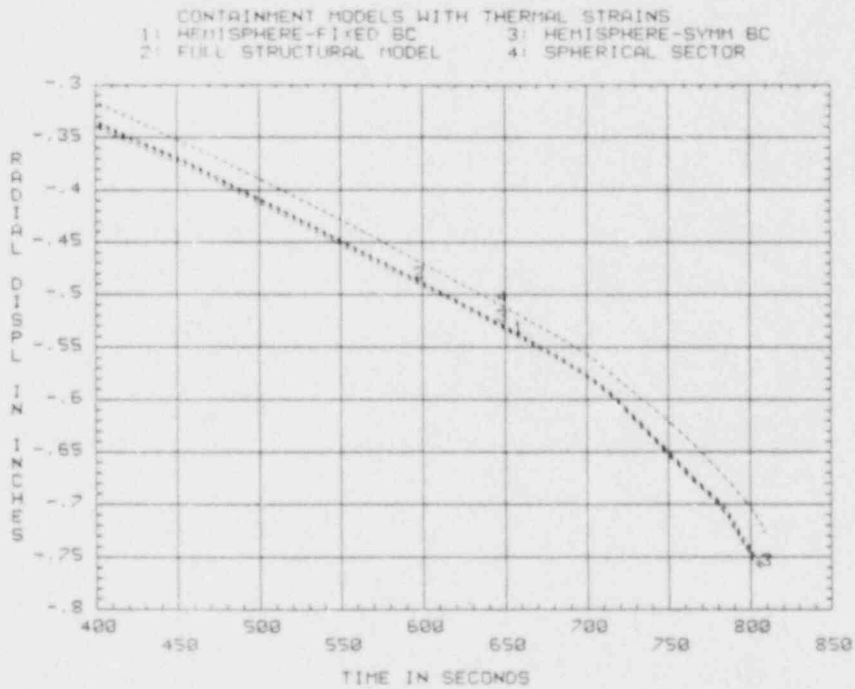

b. Displacements (Sag) During Final Seconds

Figure 1.2-25. Comparison of Sag in Models With Thermal Strains

that the thermal properties were independent of temperature and that the resulting linear heat conduction equation was unaffected by deformation allowing the thermal and mechanical problems to be solved separately.

On the basis of these numerical studies and subject to the limitations resulting from the aforementioned assumptions, several conclusions can be reached:

1. The presence of thermal strains dramatically does increase the magnitude of the sag in the pressurized reactor containment vessel, and it alters the transient stress distribution occurring through the thickness.

2. Thermal strains have no significant effect on the time to failure of the pressurized reactor containment vessel.

3. The failure mechanism consists of a bursting of the bottom of the vessel due to the internal pressure acting on a spherical cap. This bursting occurs after the effective thickness of the cap has been eroded uniformly by the material softening incurred under the propagation of the temperature front through the thickness of the shell.

4. Because of the nature of the failure mechanism, time to failure can be reasonably determined from a simple model of a spherical sector.

5. Models of a hollow hemispherical section with symmetry and fixed edge conditions can be effectively used to bound the mechanical behavior of the full structural model.

The next phase of study will consider the performance of the lower head including the instrument guide tube penetrations.

1.3 CORCON and VANESA Code Development

(D. A. Powers and J. E. Brockmann, 6422; D. R. Bradley, 6425)

The later stages of a severe nuclear reactor accident are marked by the failure of the reactor pressure vessel and deposition of molten core debris into the reactor cavity. This leads to a vigorous interaction between the molten core material and the reactor cavity concrete. Interactions of molten core material with concrete are important for four reasons related to the risks and consequences of the accident: radioactive and nonradioactive aerosol generation, combustible and noncombustible gas generation, degradation of structures and engineered safety features, and penetration of the concrete basemat.

Core-concrete interactions release radioactive and nonradioactive aerosols into the cavity atmosphere. Suspended radioactive aerosols can subsequently be released to the environment if the reactor containment fails. Coincident suspension of nonradioactive aerosols can help to remove radioactive aerosols from the cavity atmosphere through agglomeration and settling.

Steam and carbon dioxide are released from the concrete when it thermally decomposes. These gases chemically react with the core debris and are partially reduced to combustible gases, predominantly hydrogen and carbon monoxide. Generation of combustible and noncombustible gases contributes to pressure in the containment and may result in overpressurization and failure of the containment. The potential for overpressurization is, of course, greatly enhanced by the presence of flammable gas mixtures.

During core-concrete interactions, support structures or engineered safety features may be degraded through direct attack by core debris, thermal radiation from the surface of the core debris, or deposition of aerosols. Of particular concern is the possibility for lateral attack on the drywell liner in boiling water reactors (BWRs) with Mark I containments, or on the reactor pedestal in BWRs with Mark III containments. In either case, significant degradation of these structures can lead to early failure of the containment.

Finally, penetration of the concrete basemat below the reactor vessel can lead to contamination of the ground water around the plant and eventual release to the environment. Although the consequences of basemat penetration are usually not considered to be as severe as some other containment failure modes because radionuclide release is much more gradual, the economic impact on the surrounding community may be quite severe.

Core-concrete interactions have long been recognized as important safety concerns in severe accident source term evaluation.[13] Experimental and analytical research in this area at Sandia has led to the development of two computer codes, CORCON[14] and VANESA,[15] which mechanistically model the salient processes occurring during the interaction. CORCON models the thermal-hydraulic aspect of the interaction, including debris-concrete heat transfer, gas release from the concrete and concrete ablation, chemical reactions between the bubbling gas and core debris, and the effects of coolant boiling. VANESA models radioactive and nonradioactive aerosol generation from vaporization and mechanical processes, and also treats chemical reactions between gas and core debris. Both codes are integral components of NRC severe accident research efforts.

The following discussion outlines recent efforts directed toward the development and validation of improved versions of CORCON and VANESA. Recently released updates to CORCON are described. Next, experiment results from the recent SURC tests are compared

to the results of calculations made using a working version of CORCON. This version of the code contains an improved heat transfer model which is discussed in Reference 16.

1.3.1. Posttest CORCON Calculations for the SURC Tests

A mechanistic model for axial debris-concrete heat transfer has been developed[16,17] and has been incorporated into a working version of CORCON. The phenomena considered in the model and its salient features are:

1. Heat transfer in the bulk melt pool is governed by bubble-driven convection and is modeled using a convective heat transfer correlation by Kutateladze.

2. Except at unrealistically high gas fluxes, a stable gas film is unlikely and there is periodic direct contact between the melt and the concrete.

3. Concrete slag is periodically removed from the interface by buoyancy and bubble motion.

4. Molten core material may solidify as a crust. If the crust is unstable, it will fragment and these fragments will also be removed from the interface.

5. The temperature of the interface between the core melt (or solidified core material) and the concrete slag is constant throughout a bubble cycle. This temperature can be determined by considering transient heat conduction in the four regions of interest: the core melt, the solidified core material, the concrete substrate, and the molten concrete.

6. Analysis of the interface temperature is used in the development of a model for the thermal resistance associated with growth and removal of concrete slag and crust material. This model applies when the crust is unstable.

7. If the crust is stable, slag and gas will flow between the crust and concrete surface. A different heat transfer model is used under these conditions.

In order to test the validity of the new heat transfer model, CORCON calculations were performed for SNL experiments in the TURC[18,19] and SWISS[20] test series, and Kernforschungszentrum Karlsruhe (KfK) experiments in the BETA[21] test series. As reported in References 16 and 17, the comparisons between the calculated and experiment results for these tests were, in general, excellent. The SURC[22] comparisons presented in this section are a continuation of our efforts to validate the new heat transfer model.

Thus far, three experiments in the SURC test series (SURC 3, SURC 3A, and SURC 4) have been completed. All three experiments used stainless steel melts with incorporated fission-product simulants. Fifty-kilogram melts were used in SURC 3 and SURC 3A, while 250 kg were used in SURC 4. The steel was melted in the crucible and was subsequently sustained using induction heating. During each experiment, metallic zirconium was added to the molten steel after several centimeters of concrete ablation. This was done to validate CORCON predictions for the impact of zirconium on core-concrete interactions. Specifically, CORCON predicts that exothermic oxidation of zirconium by gases released from the concrete can contribute a significant amount of energy to the molten core debris. Under some conditions, the energy released during zirconium oxidation is predicted to be several times greater than the energy contributed by decay of radioactive fission products.[23]

The SURC 3 and SURC 4 experiments used a crucible with a concrete base and magnesia sidewalls. This crucible design limits the interaction to the axial (downward) direction. It therefore permits measurement of axial heat transfer without the complicating influence of sidewall interactions between the melt and the concrete. The SURC 3A experiment used a crucible composed entirely of concrete; that is, both the crucible sidewalls and bottom were concrete.

A concrete with limestone as a coarse and fine aggregate was used for the crucibles in SURC 3 and SURC 3A. Concrete with silicious coarse and fine aggregate was used in SURC 4. These two types of concretes differ greatly in composition and thermal properties. The limestone concrete has a high calcium carbonate content, and it, therefore, releases a substantial amount on carbon dioxide when it thermally decomposes. The silicate concrete has a much lower carbonate content so it releases much less carbon dioxide. Both concretes release similar amounts of water as steam during decomposition. The silicate concrete also melts over a much lower temperature range than the limestone concrete. Reference 24 provides an excellent discussion of the thermophysical properties of the limestone and silicate concretes used in the SURC experiments.

The instrumentation used in the SURC experiments was similar to that used in the earlier Sandia experiments; however, several design improvements were made. Most importantly, alumina sheathed thermocouples embedded in the concrete base were used to obtain accurate measurements of the temperature of the molten steel during the interaction. These thermocouples were heated with the concrete and were subsequently exposed to the melt as the concrete was ablated.

In order to model the one-dimensional nature of the melt-concrete interaction in the SURC 3 and SURC 4 experiments using the inherently two-dimensional CORCON code, the radius of the crucible used in the calculations was artificially set to 10 m.

This was done so that radial melt-concrete interactions would have a negligible impact on the calculated results. All masses and input powers were then appropriately scaled to the larger geometry.

Figures 1.3-1 and 1.3-2 show a comparison of the calculated and experimental results for concrete ablation and melt temperature in SURC 3. Prior to the zirconium addition at approximately 132 min, frequent failures of the induction power supply caused the measured ablation rate and melt temperature to fluctuate widely. Despite this, the calculation matched the experiments quite well. Following the zirconium addition, a constant input power was maintained, which allowed an apparent steady state, indicated by a constant ablation rate and melt temperature, to be achieved. The measured ablation rate during zirconium oxidation was 4.6 mm/min, which compares closely to the calculated value of 4.8 mm/min. When oxidation of the zirconium was completed, the ablation rate in the experiment fell to approximately 2.5 mm/min, while in the calculation, the ablation rate declined to 2.7 mm/min. The melt temperature calculated for the last 50 min of the experiment also closely matched the measured values.

Figures 1.3-3 and 1.3-4 present a comparison between experimental and calculated results for the SURC 3A experiment. As shown in the figures, CORCON accurately matches the measured concrete ablation and melt temperature until approximately 90 min into the test. At that point, the melt began to ablate the concrete asymmetrically, burrowing downward at an angle relative to vertical. This unusual erosion behavior, which was also observed in many of the BETA experiments at KfK, makes interpretation of the late time concrete ablation results difficult. Fortunately, sufficient data is available prior to the asymmetric erosion to conclude that the code predictions accurately match the experiment.

A CORCON calculation has been performed for the SURC 4 experiment. However, the results of the experiment cannot be reported here since the SURC 4 test has been chosen by the Committee on the Safety of Nuclear Installations (CSNI) as a sample problem for the validation and testing of existing models for core debris-concrete interactions. The results of the experiment have, therefore, been sequestered until that study is completed. We can report, though, that the code accurately predicted the steady-state melt temperatures and concrete ablation rates observed in the experiment prior to and subsequent to the addition of zirconium.

Based on these comparisons and those presented in References 16 and 17, we conclude that the new heat transfer model offers an approach which is valid for metallic melts and one that, in theory, can be applied to other core debris materials. Unfortunately, no experimental data is currently available for the sustained interaction of prototypic oxide core debris with concrete. Future experiments in the SURC test series at Sandia

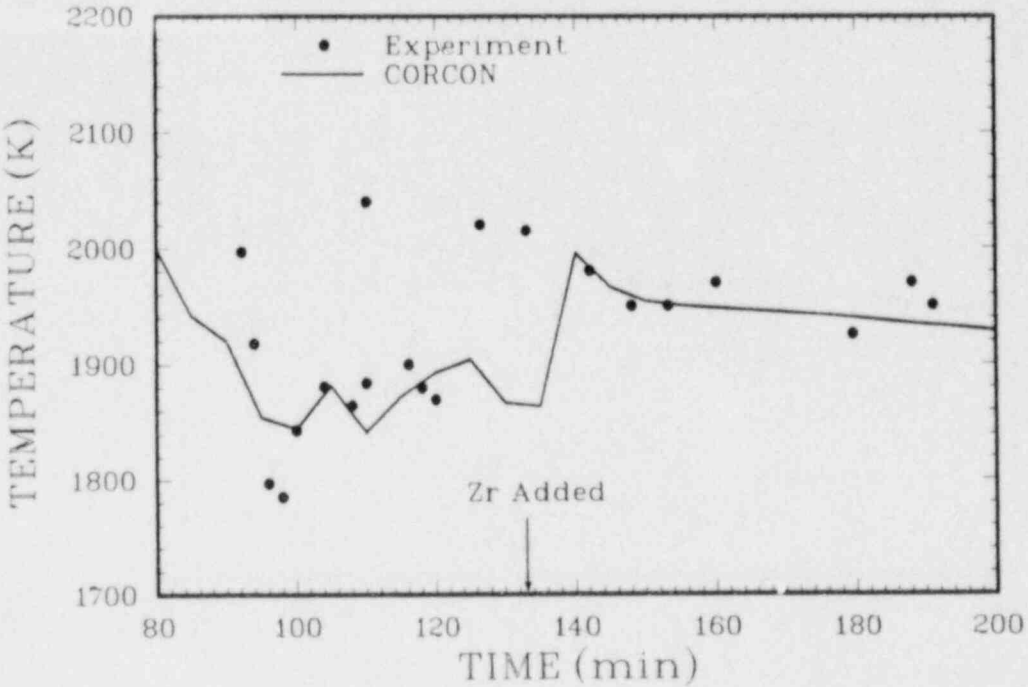

Figure 1.3-1. Comparison of Calculated and Experiment Melt Temperatures for SURC 3.

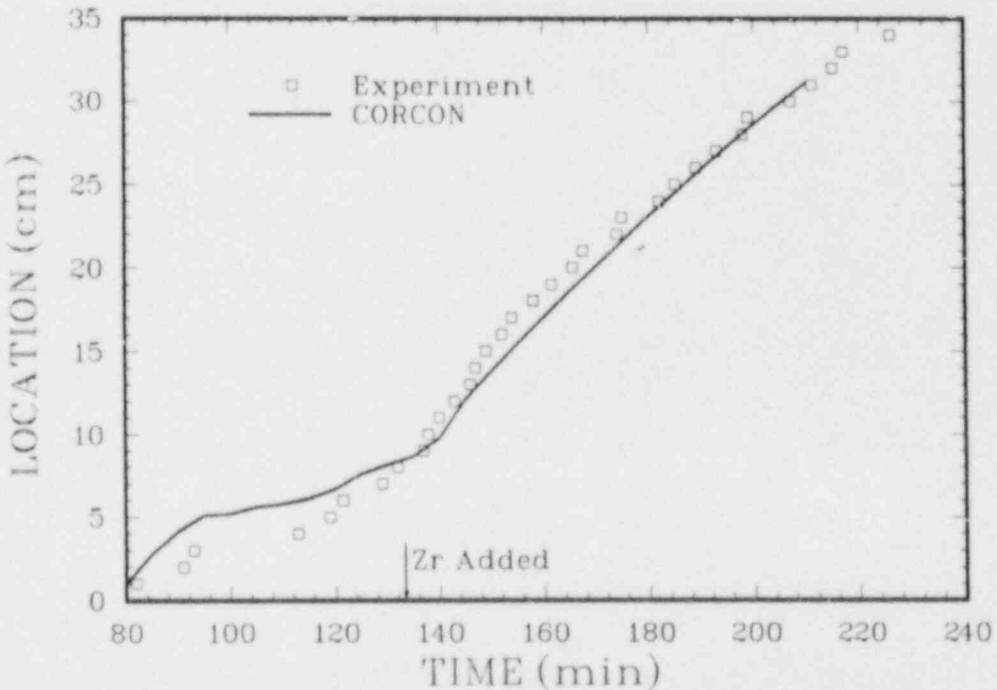

Figure 1.3-2. Comparison of Calculated and Experiment Ablation Distance for SURC 3.

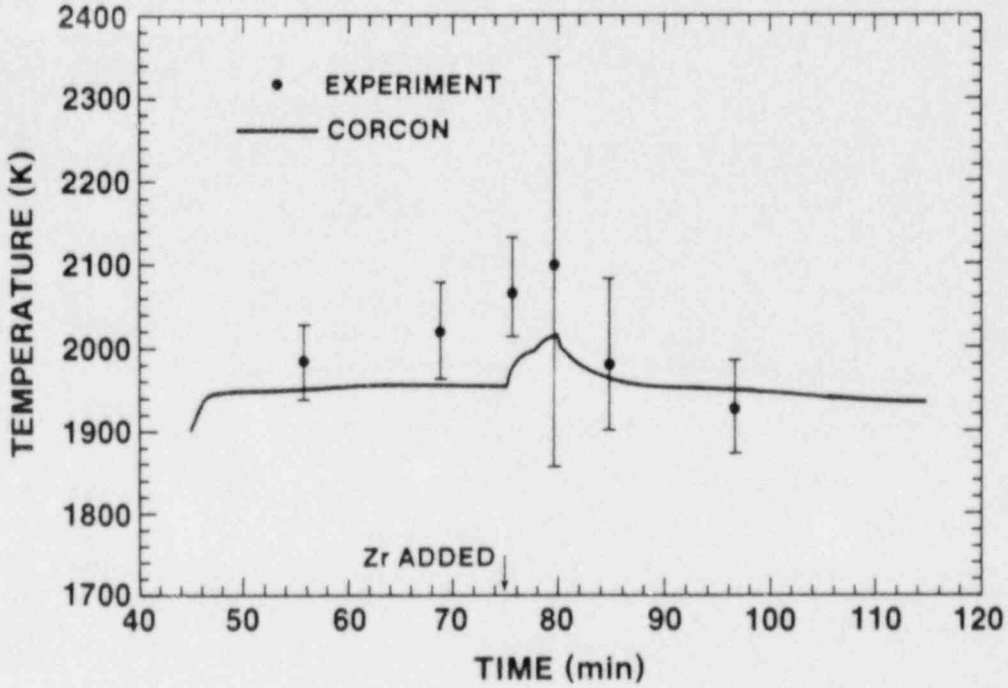

Figure 1.3-3. Comparison of Calculated and Experiment Melt Temperatures for SURC 3A.

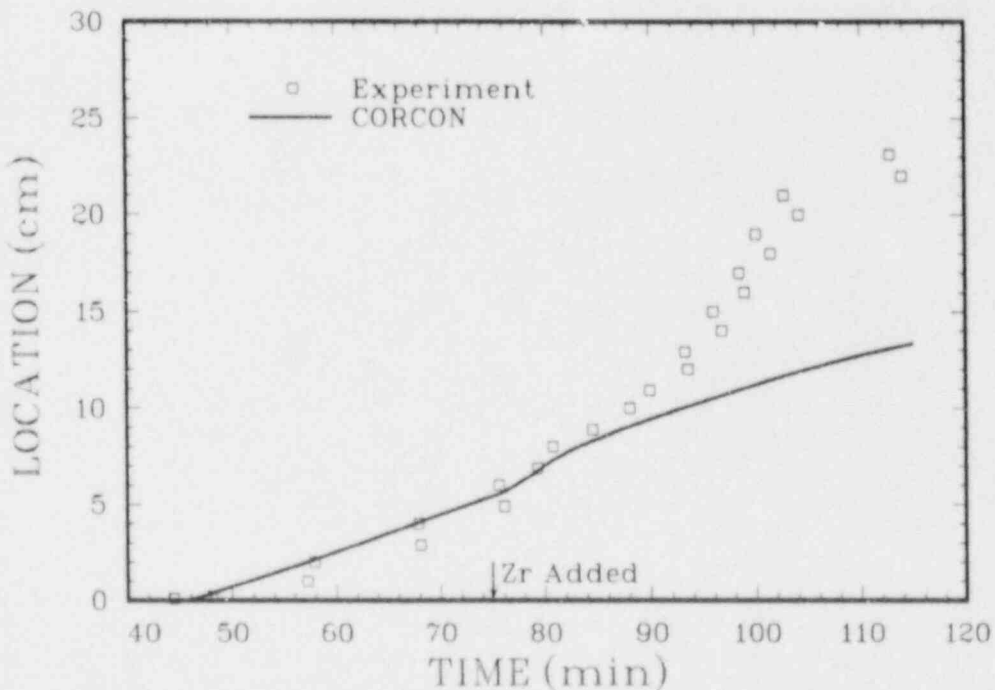

Figure 1.3-4. Comparison of Calculated and Experiment Ablation Distance for SURC 3A.

should provide the data necessary to complete the validation of the model.

1.3.2 Release of the Third CORCON Correction Set

A memo transmitting the third correction set for CORCON Mod2 was distributed to users of the code. CORCON version 2.03 is created by implementation of this update.

This correction set replaces subroutine MLTREA, which performs all calculations of chemical reactions in the code. The new version of MLTREA is a direct replacement for the old. Both versions calculate the equilibrium concentrations of the condensed phase species using minimization of the Gibbs free energy. The old version treated all condensed species as forming mechanical mixtures. That is, the chemical potential of a condensed species was unaffected by the presence of other condensed species. The new version considers two condensed phases, oxidic and metallic, each treated as an ideal solution. That is, the entropy of mixing is considered in the chemical potentials of the condensed species, and each has an activity equal to its mole fraction in the phase.

This change eliminates the strict sequential oxidation of metallic species from the melt. However, the effect is small under most conditions. Essentially all of the zirconium (Zr) is oxidized before any significant amount of chromium (Cr), and essentially all the Cr is oxidized before any significant amount of iron (Fe), etc.

In most calculations with the new chemistry package, oxidation of Zr by carbon dioxide (CO_2) is by the carburization reaction. In other words, Zr is oxidized to ZrO_2 and condensed carbon (C) is produced. Subsequently, when most of the Zr is oxidized, oxidation of the C takes place. The only exceptions to this, in our experience, have been calculations that involve core melts with a temperature exceeding 2700 K. Under these conditions, Zr is oxidized to ZrO_2 and carbon monoxide (CO) is produced.

In every calculation with the old chemistry package, the carburization reaction occurred first. When the Zr was fully oxidized, oxidation of the condensed C began. Once oxidation of the C had been completed, oxidation of the remaining metallic species in the melt began starting with Cr.

Several changes have also been made to the numerics of the solution procedure. Here special attention has been devoted to scaling and round off problems on short-word machines such as IBMs and VAXs. (The original routine had a history of convergence problems on these machines.) The new version has demonstrated much better performance on these machines although it does run somewhat slower than the original.

Occasionally we have encountered cases in which the new chemistry package has had difficulty oxidizing the last bit of Zr from the metallic phase of the melt. This problem is usually eliminated by increasing the ZILCH parameter in MLTREA to a value larger than the default value of 1.E-5. For reactor scale melts, a value as high as 1 can probably be used without creating significant inaccuracies. At this level, only one mole of Zr (0.091 kg) is discarded out of a total Zr mass of 10,000 kg or more and a total core mass of 200,000 kg or more.

Shown in the Figures 1.3-5 through 1.3-10 are comparisons of calculations made using version 2.03 of CORCON and the earlier version, 2.02. Also included are the aerosol source rates predicted by the VANESA code, given the results of the CORCON calculations. Two sets of calculations are presented: the CORCON standard problem and a sample Peach Bottom accident sequence. As the sample calculations illustrate, there is little difference in any of the calculated results. In general, we would expect differences of this magnitude for other accident calculations. The exceptions being calculations with an initial temperature greater than about 2700 K, where coking may occur in version 2.02 but not in version 2.03.

1.3.3 Release of the Fourth CORCON Correction Set

As indicated in Reference 14 (pp. 91-93 and p. 136), CORCON Mod2 was designed to accept time-dependent additions of core material, coolant, and ablated structural material. At the time the code was released, existing models for in-vessel melt progression (e.g., MARCH) predicted accumulation of core debris in the bottom of the reactor vessel, followed by failure of the vessel, and deposition of core material on the floor of the reactor cavity. Subsequent to vessel failure, no additional core debris was calculated to be released into the cavity. As a result, there was no need, at the time CORCON Mod2 was released, to activate the capability for time-dependent addition of material.

Recently, more mechanistic melt progression models such as MELPROG have been developed. These models predict deposition of core material over a period of several hours following failure of the vessel. Hence there is now a need to update CORCON to accept input of time-dependent sources of core material. An update to CORCON, which activates this feature, has been written and has been transmitted to users of the code. Version 2.04 of the code is created by implementation of this update.

The approach taken in the update was slightly different from that suggested in Reference 14. The suggested approach was to (1) read user-specified input in subroutine DATAIN, (2) process this input in subroutine ABLATE to determine the mass added during a time step, and (3) use subroutine MASSEX to include added mass and enthalpy in the CORCON mass and energy balances. In the mass

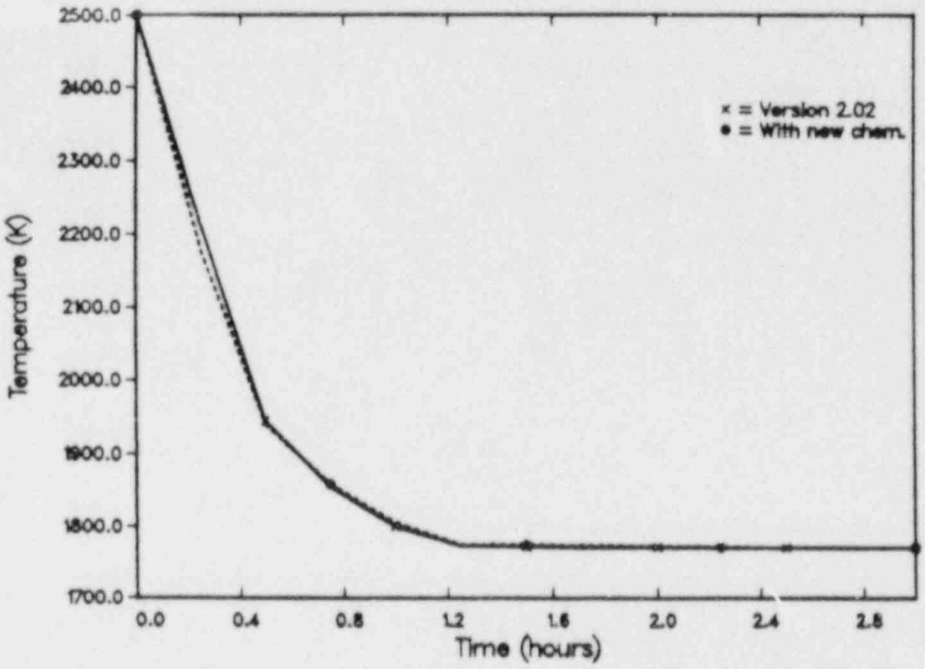

Figure 1.3-5. CORCON Version 2.02 and 2.03 Results for the CORCON Standard Problem - Melt Temperature.

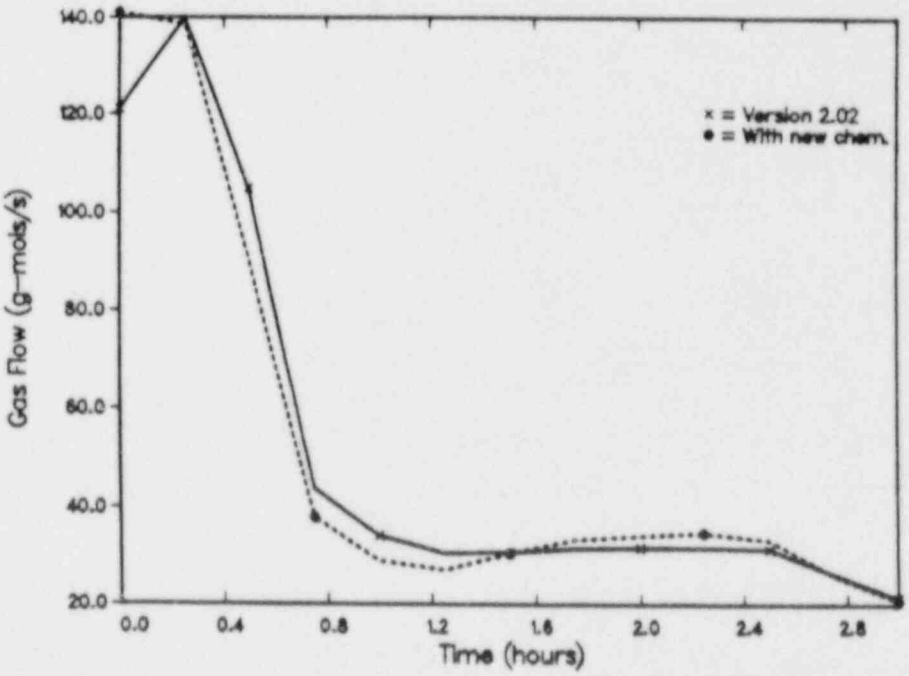

Figure 1.3-6. CORCON Version 2.02 and 2.03 Results for the CORCON Standard Problem - Gas Generation.

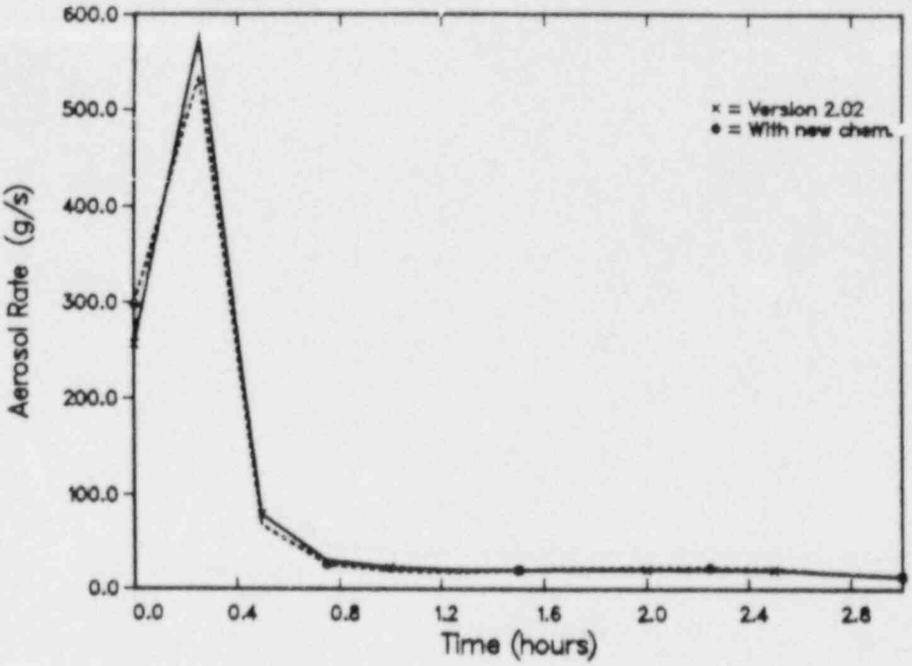

Figure 1.3-7. VANESA Aerosol Source Rates Calculated for the CORCON Standard Problem.

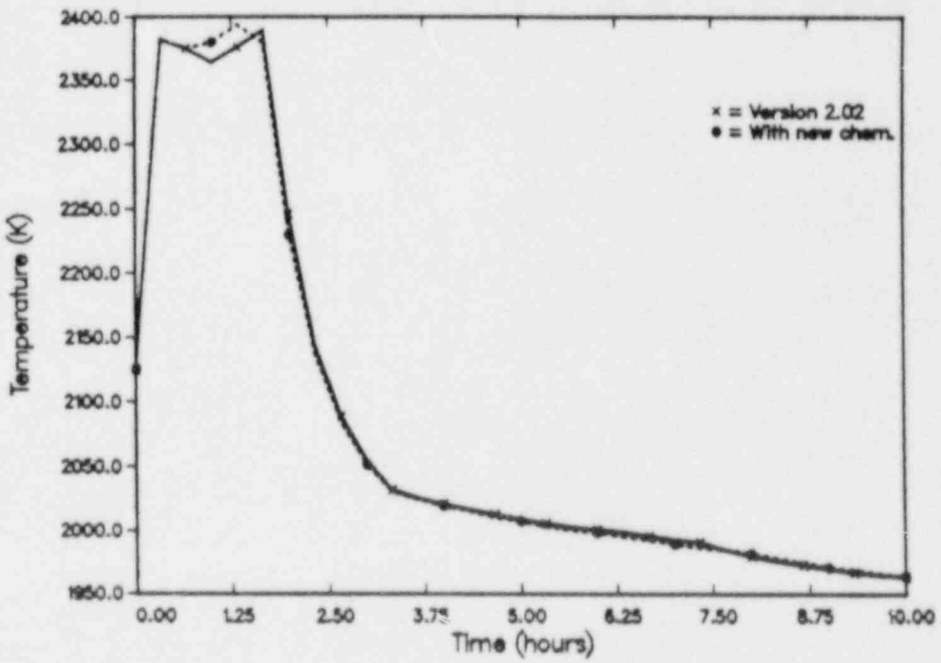

Figure 1.3-8. CORCON Version 2.02 and 2.03 Results for a Peach Bottom Sample Problem - Melt Temperature.

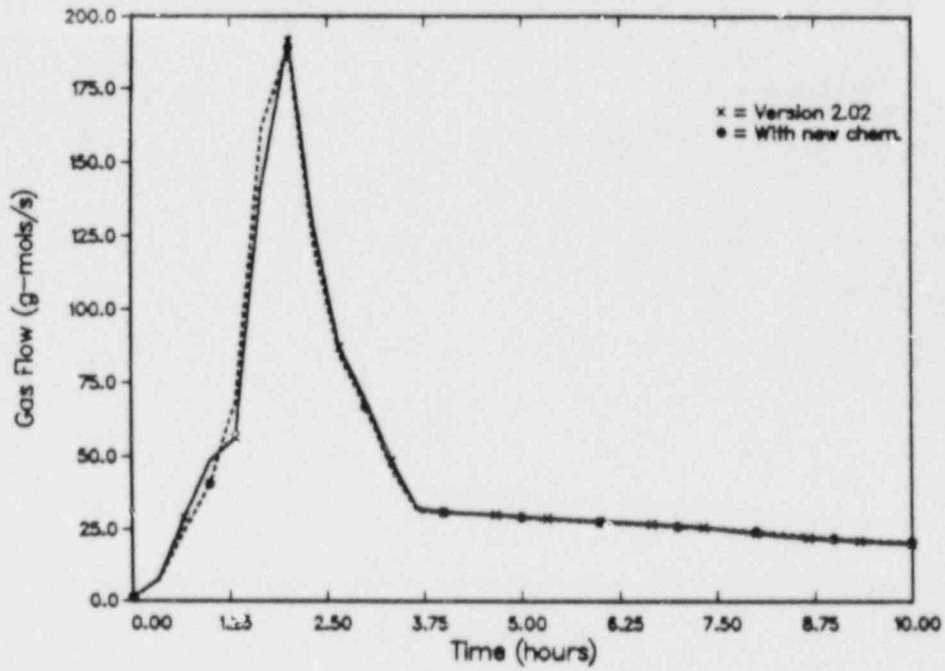

Figure 1.3-9. CORCON Version 2.02 and 2.03 Results for a Peach Bottom Sample Problem - Gas Generation.

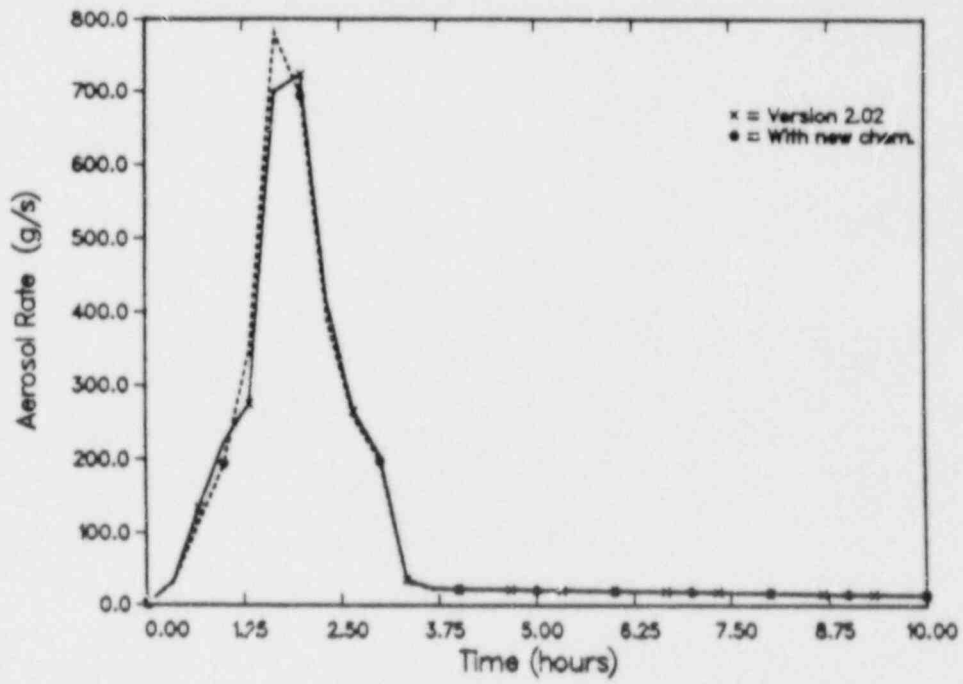

Figure 1.3-10. VANESA Aerosol Source Rates Calculated for the Peach Bottom Sample Problem.

addition update, input is read in DATAIN, but is processed directly by MASSEX. Subroutine ABLATE is not used, but is still maintained within the code. If, in the future, a separate model for ablation of structural concrete above the melt pool surface is developed, it will be included in ABLATE.

In the current update, mass addition is supplied by the user after setting the flags, IABL and ISRABL, equal to 1 (see pp. 81-82 of Reference 14). Mass flow rates of chemical species are then supplied using the modified input format shown in Table 1.3-1. The Table 1.3-1 input format replaces cards 26, 27, 28, and 29 shown in Reference 14 on pp. 91-93. Note that cards 29A-D are additional card groups that were not included in the Reference 14 input guide. These card groups permit the user to specify the temperature of each phase of entering material (oxide, metal, and coolant) as a function of time. Also note that the integer flag, IFPOPT, has been added to card 26. This flag indicates the method for specifying the fission-product composition of the entering material. If IFPOPT = 0, a default fission-product composition is selected. The default composition has the same fission-product content relative to UO_2 mass as in the initial core debris. If IFPOPT = 1, the user must specify the fission-product composition of the entering core material. An error message is printed if IFPOPT = 0 and fission-product species are included in the mass addition tables. The fission-product input is subsequently ignored by the code.

Entering metallic species are added to the metallic layer of the core debris if one is present; if no metallic layer is present, one is created. The addition of coolant is treated in a similar fashion. The situation is somewhat more complicated for the addition of oxidic material since there may be two oxide layers present. If two oxide layers are present, entering oxide species are added to the topmost oxide layer, usually layer ILOX. In some calculations, the addition of dense oxides such as UO_2 or ZrO_2 may cause the topmost oxide to become more dense than the metallic layer below it. When this happens the code initiates an "inverse layer flip", which combines the material in layers ILOX and IHOX into a new IHOX layer and eliminates the ILOX layer. (The coding that initiates the inverse layer flip was written originally by R. K. Cole, Sandia, Div 6418, during the implementation of the CORCON model into the MELCOR code.) As with other material movements in CORCON, mass added to the cavity is assumed to equilibrate thermally with each layer through which it passes or eventually resides.

Sample calculations have been performed using CORCON Version 2.04. Results from five of these calculations are shown in Figures 1.3-11 through 1.3-19. Figures 1.3-11 through 1.3-13 compare results for two calculations: (1) the CORCON Standard Problem[14] and (2) a variation of the Standard Problem in which 0.5 of the core material in (1) is deposited at the start of core-concrete interactions and the remainder is added over the

Table 1.3-1

Modified CORCON Input Format for Mass Addition

Card/ Group No.	Field	Format	Variable Name	Description
26[a]	1-5	I5	NSPG	Number of species in mass addition table; includes only species available in the Master Species List (NSPG ≤ 20)
	6-10	I5	>IFPOPT	Option flag for input of fission product mass addition; IFPOPT = 1 for user-specified fission product addition; IFPOPT=0 for fission product composition of entering material calculated internally.
27[a]	1-	A8	NAMSP	Species names of species in mass addition table (left justified)
			(There will be NSPG cards in group 27.)	
28A[a]	1-5	I5	NMP(1)	Number of points in table of mass flow rate versus time for first species as defined in card group 27.
	6-10	I5	NMP(2)	Same as above expect for second species as defined in card group 27.
	•	•	•	
	•	•	•	
	•	I5	NMP(NSPG)	Same as above exc. pt for species NSPG as defined in card group 27
				NMP(I) ≤ 10, I = 1, NSPG
28B[a]	1-10	E10.0	TMS(1,1)	Tables of mass flow rate of species I, FMS(J,I) (kg/s), versus time, TMS (J,I)(s), for each species I (I=1, NSPG) names in group 27; the number of table entries for each species is NMP(I).
	11-20	E10.0	FMS(1,1)	
	21-30	E10.0	TMS(2,1)	
	31-40	E10.0	FMS(2,1)	
	•	•	•	
	•	•	•	Start a new card for each species.
	•	•	•	
		E10.0	TMS(NMP(1),1)	
		E10.0	FMS(NMP(1),1)	
29A[a]	1-5	I5	NOTS	Number of points in temperature versus time table for added oxide, metal, and coolant NOTS, NMTS, NCTS ≤ 10.
	6-10	I5	NMTS	
	11-15	I5	NCTS	
29B[a]	1-10	E10.0	TIOTS(1)	Tables of time, TIOTS(I)(s), and temperature of added oxide, TOTS(I)(K). I = 1, NOTS
	11-20	E10.0	TOTS(1)	
	21-30	E10.0	TIOTS(2)	
	31-40	E10.0	TOTS(2)	
	•	•	•	
	•	•	•	
	•	E10.0	TIOTS(NOTS)	
		E10.0	TOTS(NOTS)	
29C[a]	Repeat 29B for temperatures of added metal phase TMTS(I)(K) versus time TIMTS(I)(s).			
29D[a]	Repeat 29B for temperatures of added coolant phase TCTS(I)(K) versus time TICTS(I)(s).			

[a]Card 26 and groups 27, 28, and 29 should be included only if IABL ≠ 0.

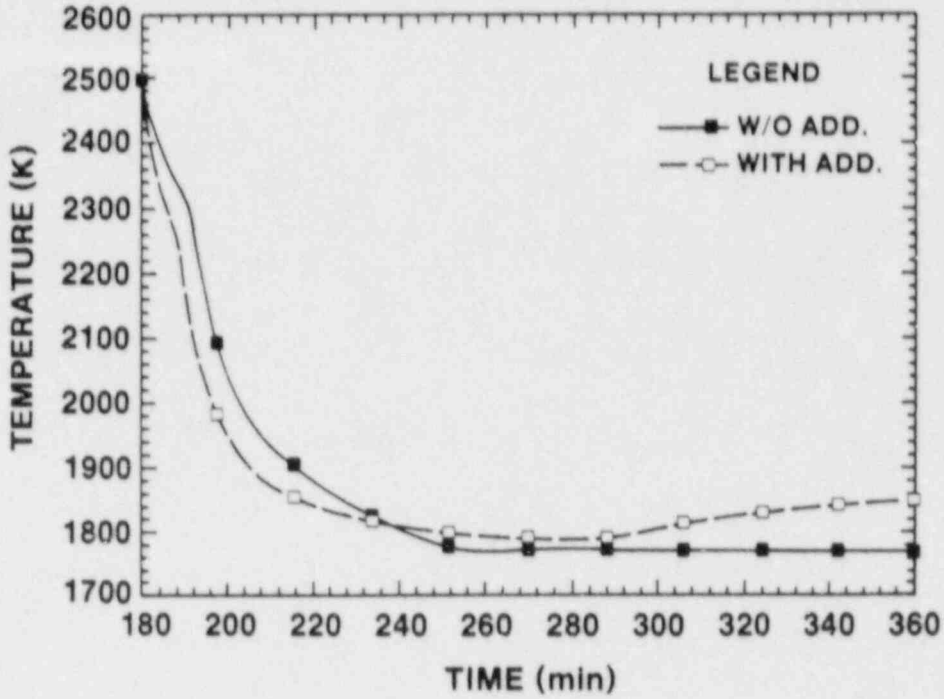

Figure 1.3-11. CORCON Version 2.04 Results for the CORCON Standard Problem With and Without Mass Addition - Melt Temperature.

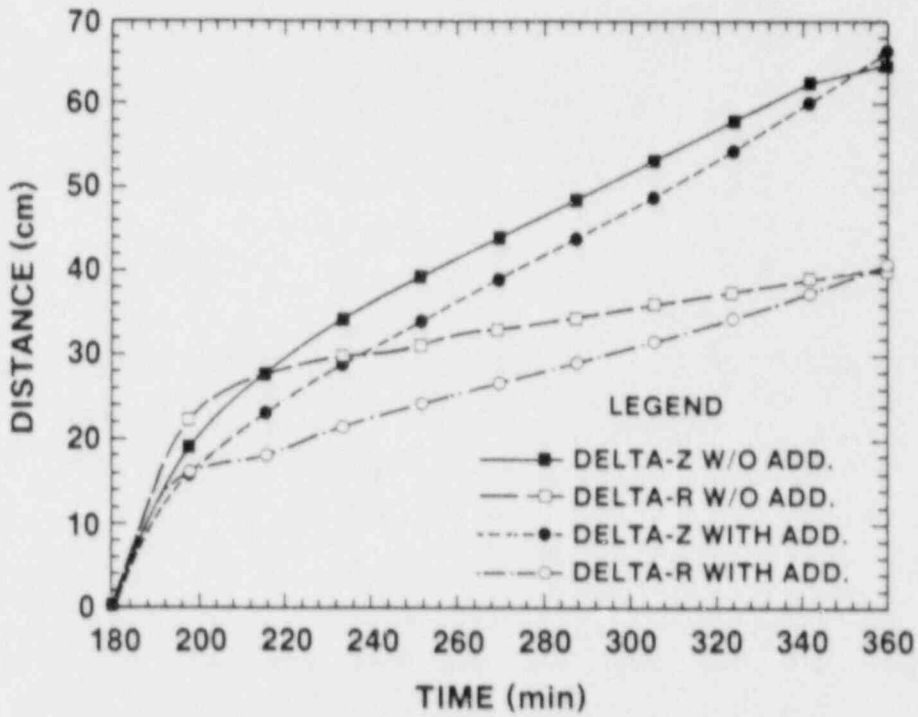

Figure 1.3-12. CORCON Version 2.04 Results for the CORCON Standard Problem With and Without Mass Addition - Ablation Distance.

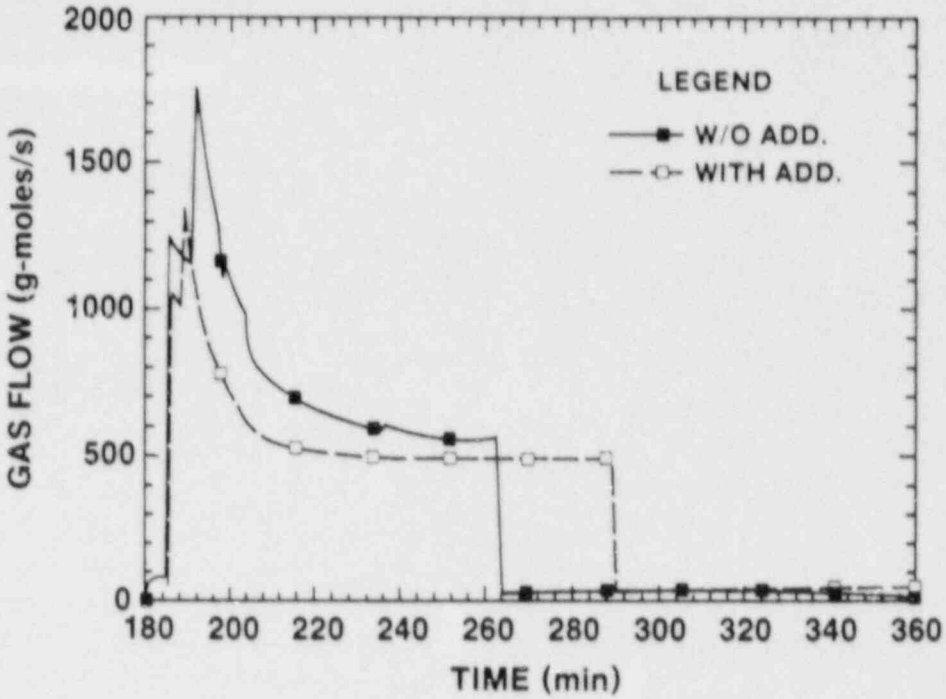

Figure 1.3-13. CORCON Version 2.04 Results for the CORCON Standard Problem With and Without Mass Addition - Gas Generation.

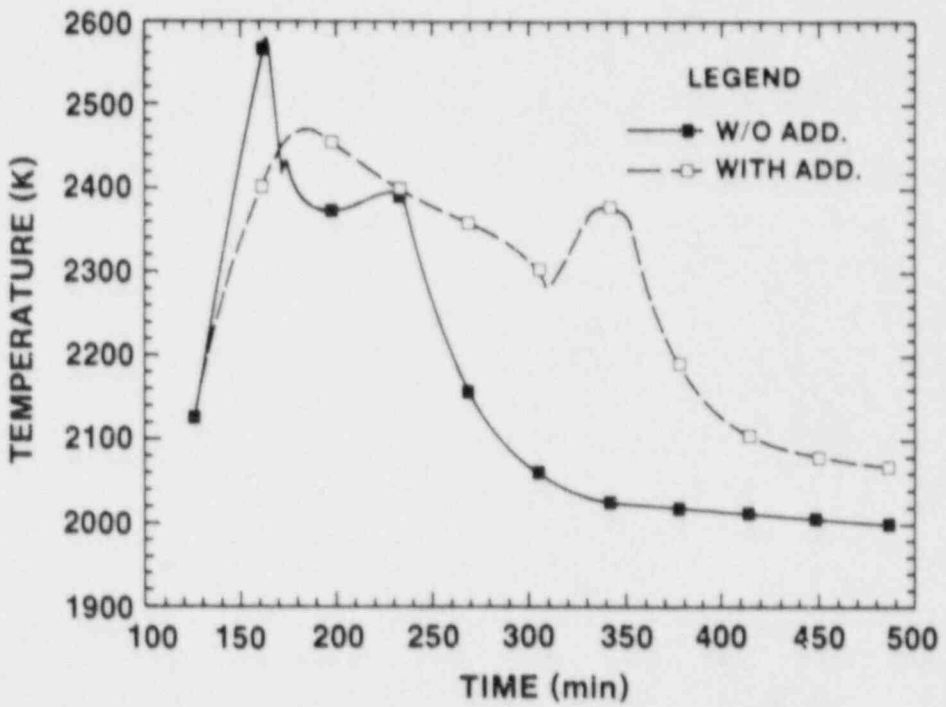

Figure 1.3-14. CORCON Version 2.04 Results for a Peach Bottom Sample Problem With and Without Mass Addition - Melt Temperature.

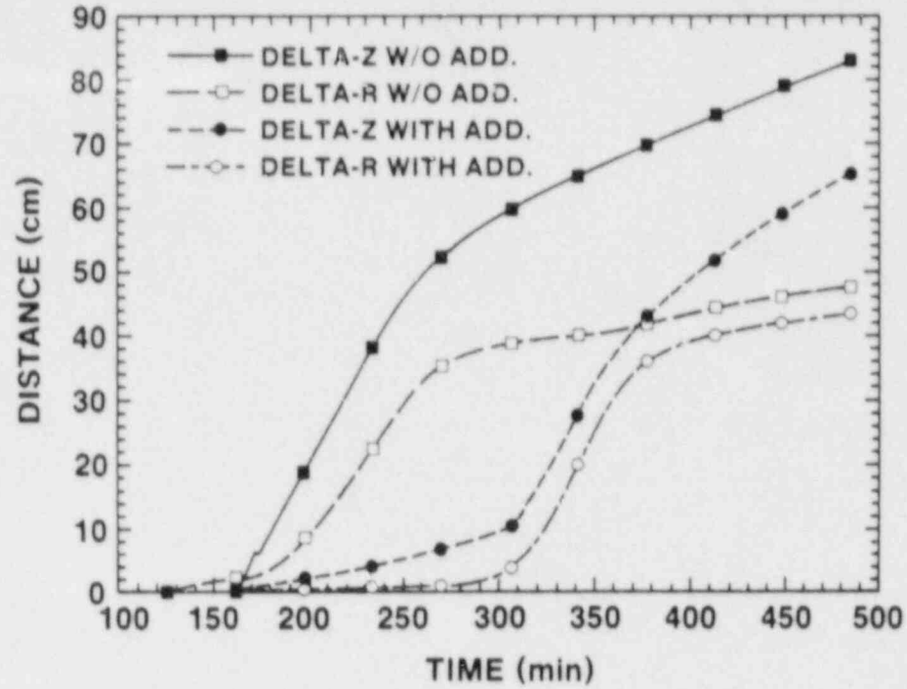

Figure 1.3-15. CORCON Version 2.04 Results for a Peach Bottom Sample Problem With and Without Mass Addition - Ablation Distance.

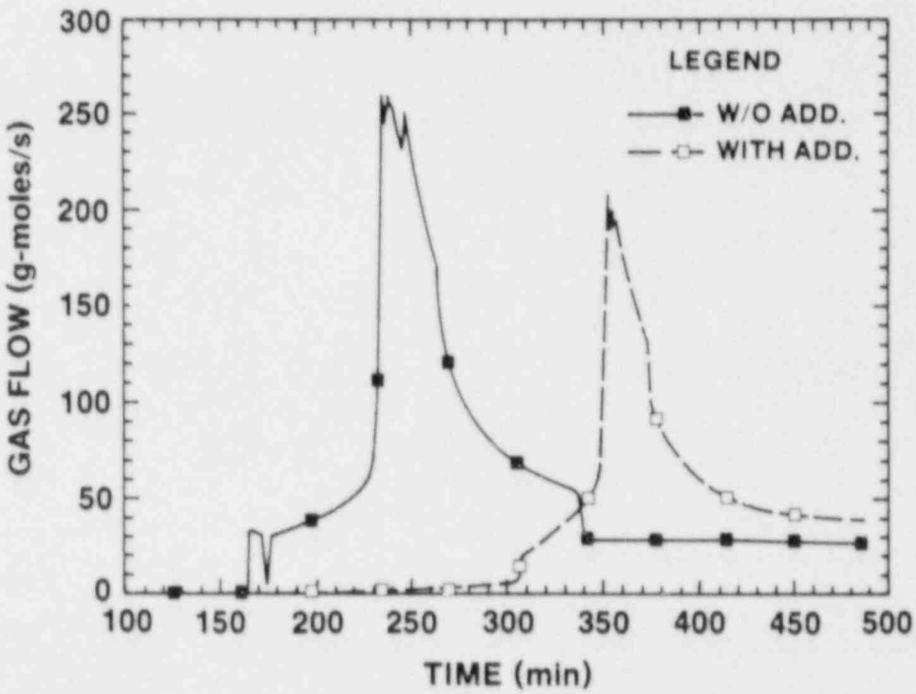

Figure 1.3-16. CORCON Version 2.04 Results for a Peach Bottom Sample Problem With and Without Mass Addition - Gas Generation.

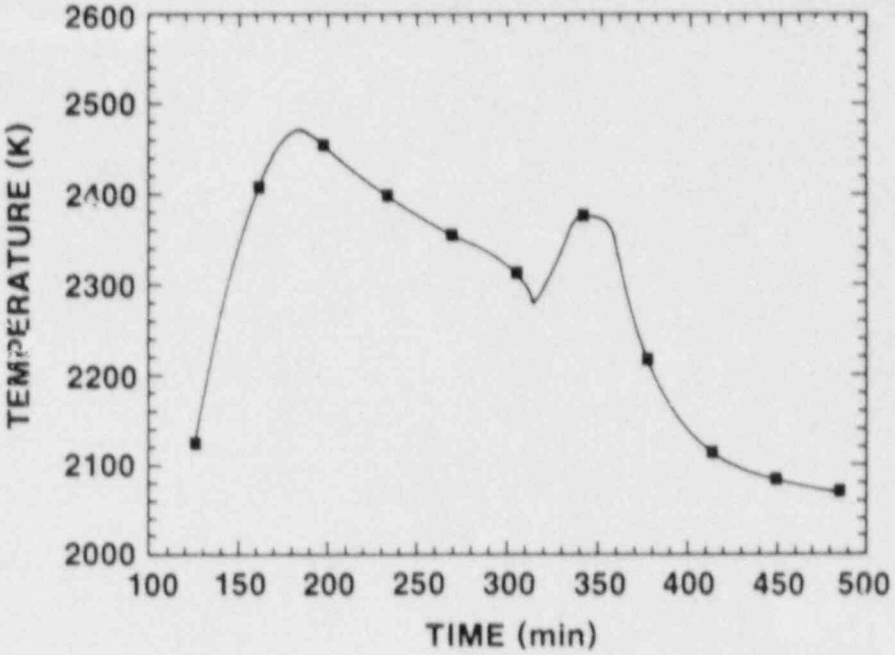

Figure 1.3-17. CORCON Version 2.04 Results for a Peach Bottom Sample Problem With Addition of Core Material and Coolant - Melt Temperature.

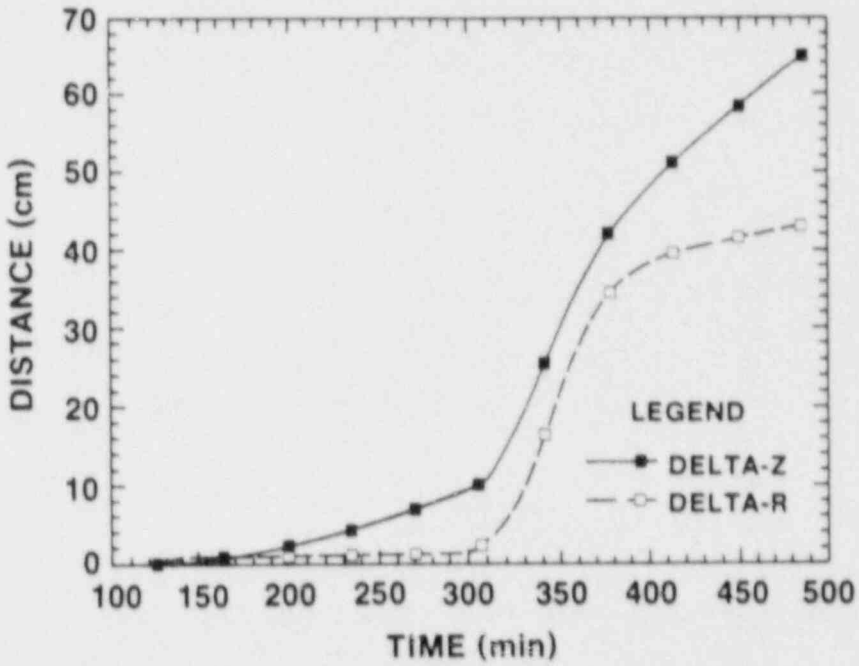

Figure 1.3-18. CORCON Version 2.04 Results for a Peach Bottom Sample Problem With Addition of Core Material and Coolant - Ablation Distance.

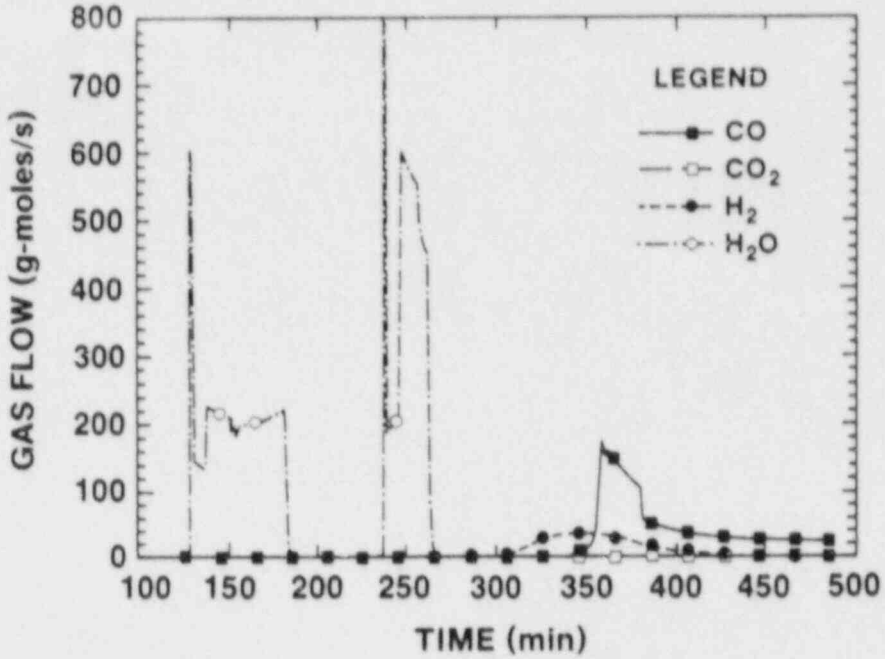

Figure 1.3-19. CORCON Version 2.04 Results for a Peach Bottom Sample Problem With Addition of Core Material and Coolant - Gas Generation.

next 2 h of the accident. The oxidic and metallic material added in (2) enters the cavity at a temperature of 2500 K. The input used for (2) is provided in Table 1.3-2.

The results presented in Figures 1.3-11 through 1.3-13 show that melt temperature, gas flow, and concrete ablation rate are initially higher in the calculation without time-dependent mass addition. This difference is due to the lower surface-to-volume ratio of the full core melt in the Standard Problem calculation. Hence heat losses are lower relative to energy input from decay heat and chemical reactions. After about 1 h, melt temperature, gas flow, and ablation rate are higher in the calculation with mass addition. This is due to the prolonged addition of "fresh" hot core material which continuously adds sensible heat to the core debris in the cavity. At the end of the calculation (3 h after the start of the interaction), axial and radial ablation distances are virtually identical in the two calculations, as is gas flow. Melt temperature is slightly higher in the calculation with mass addition.

Although VANESA calculations have not been run for the case with mass addition (VANESA currently will not accept time-dependent mass sources), we can speculate on what the VANESA results would be. The most important phase of the interaction for aerosol and

Table 1.3-2

Modified Standard Problem Input

```
  CORCON-MOD2 STANDARD PROBLEM - 1/2 CORE INITIAL,1/2 ADDED IN 2 HRS
    0    1    2    2    0    0    1    1    0   30    0    0    1    1    1    1
      30.     10800.    21600.              21601.
   95         0.          .5
       0.      3.000       5.0       0.1     4.000      2.00   10   10
     350.      1550.        .6       .135
    3    4     2500.     2500.
FEO           3000.
UO2          50000.
ZRO2          7000.
FE           35000.
CR            5000.
NI            3000.
ZR            5000.
     90.00     3400.    0
      322.
H2O          60000.
    50000.       0.0      380.    2
H2             0.5
H2O            0.5
    2
   10800.0     1.5E5    21600.     3.0E5
    2
   10800.0     400.0   21600.0     800.0
    7    0
FEO
UO2
ZRO2
FE
CR
NI
ZR
    2    2    2    2    2    2    2
    10800.      0.42    21600.       0.
    10800.      6.94    21600.       0.
    10800.      0.97    21600.       0.
    10800.      4.86    21600.       0.
    10800.      0.69    21600.       0.
    10800.      0.42    21600.       0.
    10800.      0.69    21600.       0.
    2    2    0
    10800.     2500.    30000.    2500.
    10800.     2500.    30000.    2500.
TIMETIMETIME
    1    1    1
       0.        .8
       0.        .8
       0.        .8
       1.
```

fission-product release is the high temperature-high gas flow phase early in the interaction. Since both gas flow and melt temperature are higher in the Standard Problem calculation, we would expect aerosol and fission-product release to be significantly higher. The late time differences between the two calculations are less important since gas flow and melt temperature are much lower and there would be little aerosol and fission-product release. Cumulative aerosol and fission-product release would therefore be higher for the conditions in the Standard Problem calculation.

Figures 1.3-14 through 1.3-16 compare the results from two other calculations: (1) the Peach Bottom sample problem used in previous updates to CORCON Mod2,[18] and (2) a variation from this sample problem in which 1/3 of the core material is deposited at the start of the core-concrete interaction and the remainder is added over the next 4 h of the accident. The material added in (2) is at a temperature of 2000 K when it enters the cavity. The input used for (2) is given in Table 1.3-3.

Because the oxide phase of the core debris in the two Peach Bottom calculations is initially well below its solidus temperature, a lengthy heating period is required before the oxide layer remelts and a vigorous molten core-concrete interaction begins. The heating period is 40 min for (1) and approximately 170 min for (2) (the calculation with time-dependent mass addition). As was the case in the Standard Problem calculations, this difference is due to the higher surface-to-volume ratio of the partial core melt in (2). The plots also show that the maximum temperature and maximum gas flow during the vigorous interaction phase are almost the same in both calculations, and that these maxima are offset in time by approximately 130 min (the same time difference calculated for the heatup phase). Based on these results, we would expect the peaks in aerosol and fission-product release to occur also at different times. However, the magnitude of the peaks in the two calculations should be very similar. We would also expect cumulative release for the two calculations to be nearly the same.

Figures 1.3-17 through 1.3-19 show results for a calculation similar to the Peach Bottom (2) calculation, except with coolant added at two times (at 5 and 120 min) during the interaction. Input for this calculation is given in Table 1.3-4.

Comparison of the results for this calculation with the results from the Peach Bottom (2) calculation shows that coolant addition has little affect on the calculated melt temperature and ablation rate (Figures 1.3-17 and 1.3-18). Figure 1.3-19 shows that except for additional steam generation during coolant boiling, gas flow in the case with water is almost the same as with no coolant. Coolant addition has little effect because boiling heat transfer is in the film boiling regime because of the high

Table 1.3-3

Modified Peach Bottom Input

```
PEACH BOTTOM AE ACCIDENT - 1/3 CORE INITIAL, 2/3 ADDED IN 6 HRS
    0    0    2    3    0    0    1    1    0   20    0    0    1    1    1    0
      60.0      7576.     29176.                70000.
   40          0.0          1.5
        0.0        3.2         5.00         0.1      4.438       3.05   10    6
      300.0      1875.           .6         .135
    3    4      2125.       2125.
UO2              53133.
ZRO2             10997.
FEO               1000.
ZR               13690.
FE               23387.
CR                3700.
NI                2055.
      140.1       3293.     0
      4505.     2.14E+5       525.     3
CO2                0.17
H2                 0.13
N2                 0.70
    5
    7575.0       500.0    11175.0      900.0    14775.0      1300.     18376.     1750.
   60000.        1750.
    7    0
UO2
ZRO2
FEO
FE
CR
NI
ZR
    2    2    2    2    2    2    2
     7575.      4.920     29176.          0.
     7575.      1.018     29176.          0.
     7575.      .0926     29176.          0.
     7575.      0.926     29176.          0.
     7575.      .3426     29176.          0.
     7575.      .1902     29176.          0.
     7575.      1.267     29176.          0.
    2    2    2
     7575.      2000.     80000.       2000.
     7575.      2000.     80000.       2000.
     7575.       350.     80000.        350.
TIMETIMETIME
    1    4    1
       0.0        0.8
     7575.        0.1     14775.          0.1     14800.         0.8     60000.       0.8
       0.0        0.6
```

Table 1.3-4

Modified Peach Bottom Input With Water Added

```
PEACH BOTTOM AE ACCIDENT - 1/3 CORE INITIAL, 2/3 ADDED IN 6 HRS,WATER ADDED
    0    1    2    3    0    0    1    1    0   20    0    0    1    1    1    0
     60.0      7576.     29176.                70000.
   40        0.0        1.5
      0.0        3.2        5.00        0.1      4.438       3.05   10    6
    300.0      1875.          .6        .135
    3    4     2125.      2125.
UO2             53133.
ZRO2            10997.
FEO              1000.
ZR              13690.
FE              23387.
CR               3700.
NI               2055.
     140.1       3293.     0
      350.
H2O               0.00
     4505.    2.14E+5        525.    3
CO2               0.17
H2                0.13
N2                0.70
    5
    7575.0      500.0    11175.0      900.0    14775.0      1300.     18376.     1750.
   60000.      1750.
    8    0
UO2
ZRO2
FEO
FE
CR
NI
ZR
H2OCLN
    2    2    2    2    2    2    2    5
     7575.      4.920     29176.         0.
     7575.      1.018     29176.         0.
     7575.      .0926     29176.         0.
     7575.      0.926     29176.         0.
     7575.      .3426     29176.         0.
     7575.      .1902     29176.         0.
     7575.      1.267     29176.         0.
     7575.         0.      7695.      20.00     8295.         0.     14295.        20.
    14895.         0.
    2    2    2
     7575.      2000.     80000.      2000.
     7575.      2000.     80000.      2000.
     7575.       350.     80000.       350.
TIMETIMETIME
    1    4    1
       0.0        0.8
     7575.        0.1    14775.        0.1    14800.        0.8    60000.        0.8
       0.0        0.6
```

surface temperature of the core debris. Therefore, both before and after coolant addition heat transfer from the top surface of the melt is controlled by thermal radiation.

The five sample calculations just discussed are only a few examples of the vast spectrum of cases which can now be run using CORCON Version 2.04. As the calculations illustrate, prolonged addition of core debris to the reactor cavity may or may not have a significant impact on the calculated results. The effect of time-dependent mass addition depends on the temperature and amount of core debris initially in the cavity, the temperature and amount of core debris entering the cavity later, and the time at which core material is added to the cavity. It is therefore extremely important to have accurate models for in-vessel melt progression and vessel failure. At present, there is still great uncertainty in the modeling of these processes.

1.4 Molten Fuel-Coolant Interactions

(B. W. Marshall, Jr. and M. Berman, 6427)

The objective of this program is to develop an understanding of the nature of fuel-coolant interactions (FCIs) during hypothetical accidents in light water reactors (LWRs). The understanding of FCIs achieved in this program is expected to resolve key reactor safety issues for both terminated and unterminated accidents. Models are being developed to quantitatively determine:

1. The rates and magnitudes of steam and hydrogen generation.

2. The degree of mixing and coarse fragmentation of the fuel.

3. The degree of the fine fragmentation of the individual droplets composing the coarse mixture.

4. The fraction of the available thermal energy that is converted into mechanical energy.

Experiments are being conducted to determine the influence of three classes of important independent variables: thermodynamic conditions (temperatures of the fuel and the coolant and the ambient pressure); scale variables (amount of fuel and coolant initially involved); and boundary conditions (pour diameter and rate, shape and degree of confinement of the interactions region, presence of structures, water depth, and fuel-coolant contact mode). Measurements being made during the experiments include photographic observation of the FCIs, pressures generated in the coolant and the cover gas, steam and hydrogen generation, and the resulting debris characteristics.

1.4.1 FITS-D Experiment

(R. W. Marshall Jr., G. B. StClair, F. Bauer, and W. Teague, 6427)

On May 13, 1987, the final 20-kg experiment for the FITS-D series was conducted. In this experiment, the initial ambient pressure was 0.696 MPa (101 psia), the initial water temperature was 401 K (37 K subcooled), the water chamber had a square cross section with a side dimension of 0.76 m and a water depth of 0.15 m. The fuel was iron/alumina having a temperature of about 2700 K and was dropped from a height of 1.6 m, resulting in an entrance velocity of about 4 m/s.

Due to funding limitations, we have indefinitely postponed the final analysis of this experiment. However, some preliminary results and observations are currently available from this experiment. Following is a summary of these results and observations.

1. As expected from previous experiments with elevated pressure, saturated water, or both, a steam explosion did not occur in this experiment. This observation supports the hypothesis that spontaneously triggered steam explosions are suppressed at elevated pressure and water temperature.

2. We observed rapid generation of hydrogen and steam, pressurizing the FITS chamber to ~1.03 MPa during the first 2 to 3 s. The pressure in the chamber continued to rise, but at a much slower pace, to 1.1 MPa over the next 20 s or so. This type of chamber pressurization was different than observed in any of the previous FITS experiments. We are currently evaluating this result.

3. This was the first experiment in which the mass spectrometers were successfully incorporated into our FITS experiments. The preliminary data show that approximately 70 to 80 percent of the final hydrogen percentage was detected during a 2-s transient. Analysis of the gas-grab samples indicated that the final hydrogen concentration (on a dry-gas basis) was about 11 percent. This translates into almost complete oxidation of the iron (~98 percent) if the FeO reaction is assumed and approximately 65 percent of the iron if the Fe_2O_3 reaction is assumed. These are extremely high oxidation rates compared to past experimental results, which were in the neighborhood of 30 percent for the FeO reaction. Obviously these results are preliminary until and unless further evaluation is performed (e.g., were significant quantities of hydrogen generated from the decomposition of the polysolfone, which is a different chamber material than used in past experiments?). These and other

questions should be addressed before these results are quoted as factual.

1.4.2 Isothermal Liquid-Into-Liquid Jet Studies (IJET)
(D. F. Beck and B. W. Marshall, Jr., 6427)

1.4.2.1 Introduction

Boiling jet experiments conducted under the FCI program led to the observation that the degree and timing of jet breakup are a function of the subcooling of the ambient fluid.[25] Observed behavior was sufficiently complex as to merit further testing designed to separately characterize hydrodynamic and thermal effects. The Isothermal Jet (IJET) test series is the part of the program that is investigating hydrodynamic behavior.

1.4.2.2 Apparatus and Procedure

Plans for conducting an isothermal liquid-into-liquid jet test series proceeded by using TMI-2 core support and flow plates as the guide for scaling. Guidelines included attempts to keep the experiments fairly simple and inexpensive. This allowed a number of tests to be run and analyzed in order to establish overall flow characteristics with a reasonable investment. With these factors in mind, the following parameters and equipment configurations were established.

Primary orifice diameters were set at 4 and 8 cm, which would generate prototypical reactor data in the range of one-quarter to full scale. In addition, tests with orifice diameters of 0.1 and 1 cm were conducted in order to provide a means of correlation with the existing data base. Orifice length-to-diameter ratios (T/D) were selected to span the range of 0.2 to 20 in order to measure the sensitivity of jet behavior to this variable. Such a span more than covered the different T/D ratios found in the TMI-2 design. Square-edged entrances were used throughout.

Orifice exits were located at the surface of a quiescent tank of water. Orientation of the orifices was such that the jets were injected vertically downward into the pool. Flow was driven by gravity head alone, as would exist for a corium melt located on top of a support plate. A 13-cm initial hydraulic head was selected on the basis that it would provide exit velocities representative of TMI-2 conditions. An additional experiment (subsequently referred to as system 1-4) was performed in which test initiation occurred by dropping the jet fluid onto the orifice plate from a height of 30 cm. This was done to simulate any core relocation effects.

The water tank used in the tests was selected from available facilities. With a depth of 1.2 m, sizing approximated the TMI-2

separation distance between the flow distribution plate and the vessel bottom. A spillway was used on one side of the tank in order to maintain water levels fairly constant with respect to the orifice exit. In cross section, the tank was square with each side measuring 0.56 m (interior). Orifice exits were located at the geometric center of this section. A photograph of this facility is provided in Figure 1.4-1. Major components are labeled for identification.

High speed cameras were the primary means used in gathering test data. Several 16-mm cameras and one 70-mm camera provided coverage from several vantage points around the water tank into which the jet was injected. The tank was constructed of a transparent plexiglass on all sides to facilitate photography. Various scaling aids were used in order to allow for refraction correction. Film speeds varied from 30 to 1000 frames per second with the actual setting a function of the camera, subject, and test. Timing signals impressed onto the film allows for correlation between events and elapsed time. Resultant films were projected onto a digitizer to allow for rapid data gathering at reasonable scales.

All tests from which data have been extracted were run with an immiscible liquid pair in order to simulate the hydrodynamic interaction between water and corium. Ideally, the density, viscosity, and interfacial tension values should have been close to that estimated for corium. However, due to safety and economic considerations, the fluid selected was refrigerant 113 (R-113 or trichlorotrifluoroethane). Use of this fluid gave a fully separable system with a density ratio of 1.6 and a viscosity ratio of 1. These ratios are within a factor of 5 of those estimated for a corium into water system and should allow for approximation of resulting hydrodynamic characteristics. Fluid temperature measurements were taken immediately before each test run. This was done in order to determine the actual fluid properties at the time of the test for use in data reduction.

1.4.2.3 Test Parameters

A listing of the initial conditions for the tests conducted can be found in Table 1.4.1. Injection velocities shown represent conditions at test initiation. The values given were first estimated by the use of standard entrance and pipe loss tables given by Olson.[26] Posttest analysis refined these values by use of volumetric flow rate data (reservoir sight tube level versus time) except where not available (systems 1-3 and 1-4). During the short periods that data were taken, volumetric flow rates were found to be constant within experimental accuracy. This allows the injection velocity to be treated as a constant for the purpose of data reduction and analysis.

Figure 1.4-1. Experimental Apparatus

Table 1.4-1

Initial Test Parameters for R-113 Into Water Jet Tests

System Number	Orifice Diameter D(m)	Orifice Aspect Ratio (T/D)	Injection Velocity Uo (m/s)
1-1	0.00119	2.09	1.2
1-2	0.00953	2.00	1.4
1-3	0.0381	0.167	1.4
1-4	0.0381	0.667	3.0
1-5	0.0381	2.00	1.7
1-6	0.0381	24.3	2.0
1-7	0.0762	2.1	1.7

Fluid properties used in calculations were based on standard handbook tables[27] for water and on laboratory measurements for R-113. Interfacial surface tension was set at 0.05 N/m as data accuracy would not support evaluation of the effect of temperature variations. The actual values used for viscosity and density are given in Table 1.4-2 as a function of the system (or test) number. Note that subscript "D" is referencing the dispersed fluid (jet material) while subscript "C" represents the continuous phase fluid (water).

From the data presented in Tables 1.4-1 and 1.4-2, several standard nondimensional groups were determined. Reynolds numbers were calculated in order to provide an indication of the flow regime at the orifice exit. The Reynolds number is given by the ratio of the inertia and viscous forces as follows:

$$Re = \frac{\rho_D \, D \, U_o}{\mu_D} \, ,$$

Table 1.4-2

Density and Viscosity Data

System Number	ρ_D (kg/m^3)	ρ_C (kg/m^3)	μ_D (kg/m•s)	μ_C (kg/m•s)
1-1	1550	998.41	0.00110	0.0011709
1-2	1550	998.60	0.00108	0.0012028
1-3	1550	999.27	0.00106	0.0010299
1-4	1550	999.24	0.00105	0.0010559
1-5	1550	999.38	0.00107	0.0011773
1-6	1570	999.44	0.00118	0.0012895
1-7	1570	999.65	0.00106	0.0012196

where

Re = Reynolds number,

ρ_D = jet material density,

D = orifice diameter,

U_o = orifice exit velocity,

μ_D = jet material dynamic viscosity.

As found in Table 1.4-3, the Reynolds numbers range from 2×10^3 to 2×10^6. Consideration of velocity and buoyancy vector directions then allows the tests to be classified as vertical turbulent buoyant jets.

Froude numbers were determined in order to better characterize buoyancy effects. The densimetric Froude number used in this section is the ratio of the inertia force to the buoyancy force and is given by

$$Fr = \frac{U_o^2 \rho_D}{(\rho_D - \rho_C) g D} ,$$

where

Fr = densimetric Froude number,

ρ_C = continuous phase density,

g = gravitational constant.

Table 1.4-3

Nondimensional Parameter Groups for R-113 Into Water Jet Tests

System Number	Re	We	Fr	Z
1-1	2.0×10^{3}	53	350	4×10^{-3}
1-2	1.9×10^{4}	580	59	1×10^{-3}
1-3	7.8×10^{4}	2.3×10^{3}	15	6×10^{-4}
1-4	1.7×10^{5}	1.1×10^{4}	68	6×10^{-4}
1-5	9.4×10^{4}	3.3×10^{3}	22	6×10^{-4}
1-6	1.0×10^{5}	4.8×10^{3}	29	7×10^{-4}
1-7	1.8×10^{5}	6.9×10^{3}	11	5×10^{-4}

Values obtained range from 11 to 68 for the larger diameters, indicating that these jets are initially operating in a manner that approximates a pure plume (Fr = 0).

Weber numbers were next calculated in order to better understand drop formation and behavior under the test conditions. The Weber number is typically given as the ratio of the inertia force to the surface tension force and was calculated as

$$We = \frac{U_o^2}{\sigma / \rho_D D} ,$$

where

We = Weber number based on exit conditions,

σ = interfacial surface tension.

As shown in Table 1.4-3, the large scale jets exhibited exit Weber numbers on the order of 10^3 to 10^4. Since these values are several orders of magnitude higher than the critical Weber number of 12 typically given for drop breakup,[28] rapid fragmentation would be expected.

The final nondimensional relationship considered under exit conditions was the Ohnesorge number, Z. It is given by

$$Z = \frac{We^{0.5}}{Re} = \frac{\mu_D}{(\rho_D \, D \, \sigma)^{0.5}} \quad .$$

Calculated values ranged from 5×10^{-4} to 4×10^{-3}. When considered in conjunction with the Reynolds number it is found that the large scale jet tests fall into the breakup regime expected for a corium pour. This is shown in Figure 1.4-2, which was taken from Windquist and Corradini.[29] All of the 4- and 8-cm diameter jets are within the range given for expected accident scenarios. This further justifies use of the present experimental system for improving our understanding of hydrodynamic breakup in metal-water jets.

1.4.2.4 Test Observations

This section provides a general qualitative description of observed jet behavior. The main body of the text is devoted to the large diameter jet experiments conducted. However, several observations made during the 1-mm and 1-cm jet tests are worthy of comment.

- **Small and Intermediate Scale Jets**

Initial entry of these jets proceeded in a fairly coherent fashion, with some "mushrooming" evident. Further penetration saw the development of lateral disturbances and limited wave behavior along the jet edges. Camera coverage was not close enough to allow a better description of these disturbances. However, it is thought that the surface disturbances must have been similar to those shown by Ranz and Dreier.[30] Their photographs have been reproduced in Figures 1.4-3 a and b. It is of some interest to note that the behavior shown is not unlike the breakup of Tollmien-Schlichting waves into vortex trusses that can be observed during laminar-to-turbulent boundary layer transitions. For a comparison see Figure 1.4-3 c, which is from the work of Mueller, Nelson, and Kegelman.[31] Other examples for this type of phenomena can be found in the work of Kegelman, Nelson, and Mueller[32] and Brown.[33]

Any solid core region existing early in the jet became fragmented at some depth beyond the initial disturbance point, as evidenced by an ability to see through the surrounding drop or spray field. A "breakup" length could thus be assigned on the basis of observing the location where the fragmented core dispersed to such an extent that a coherent structure was no longer apparent. Observations of the breakup point noted that its location, in

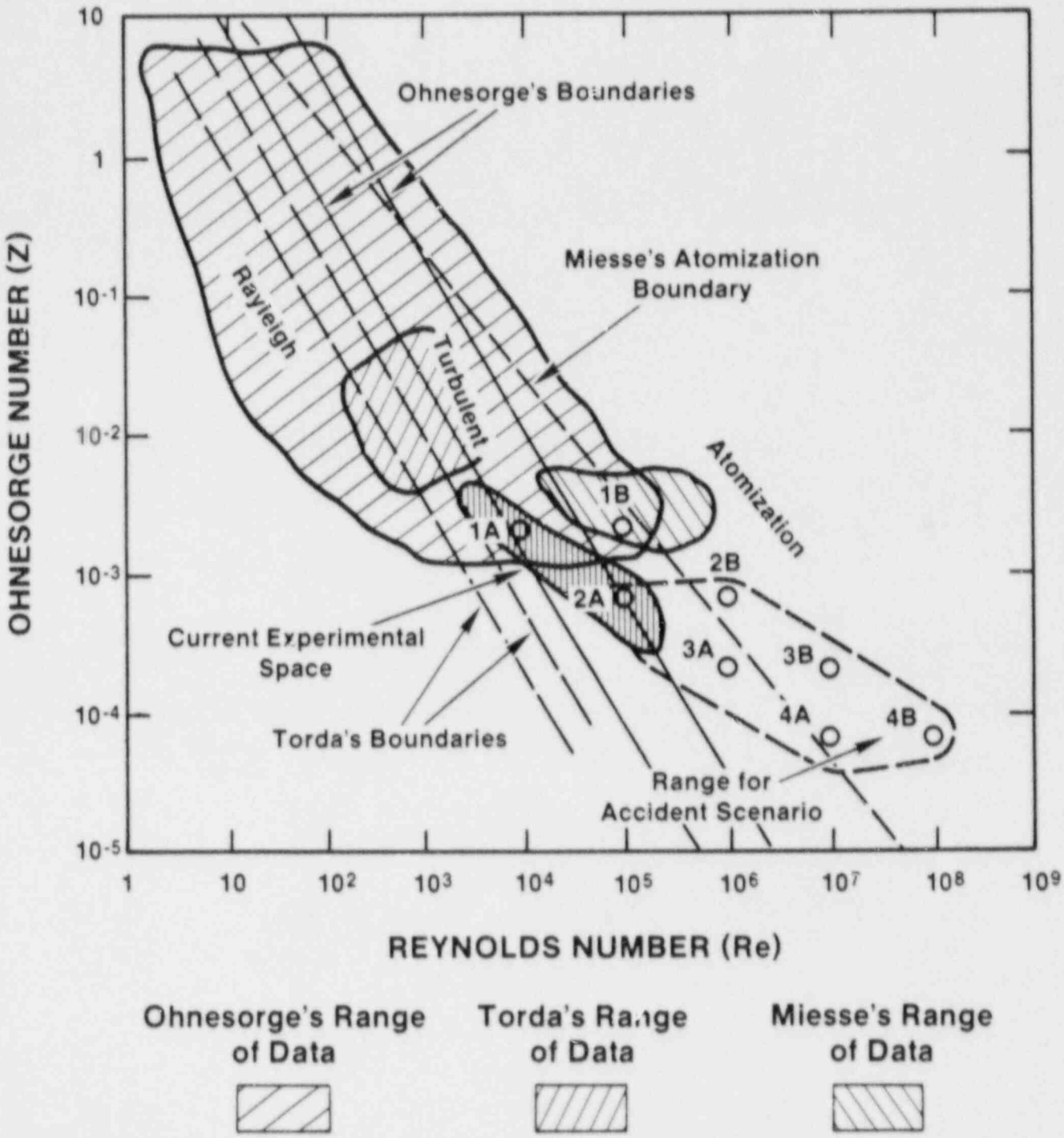

Figure 1.4-2. Liquid Jet Breakup Regime Map[29]

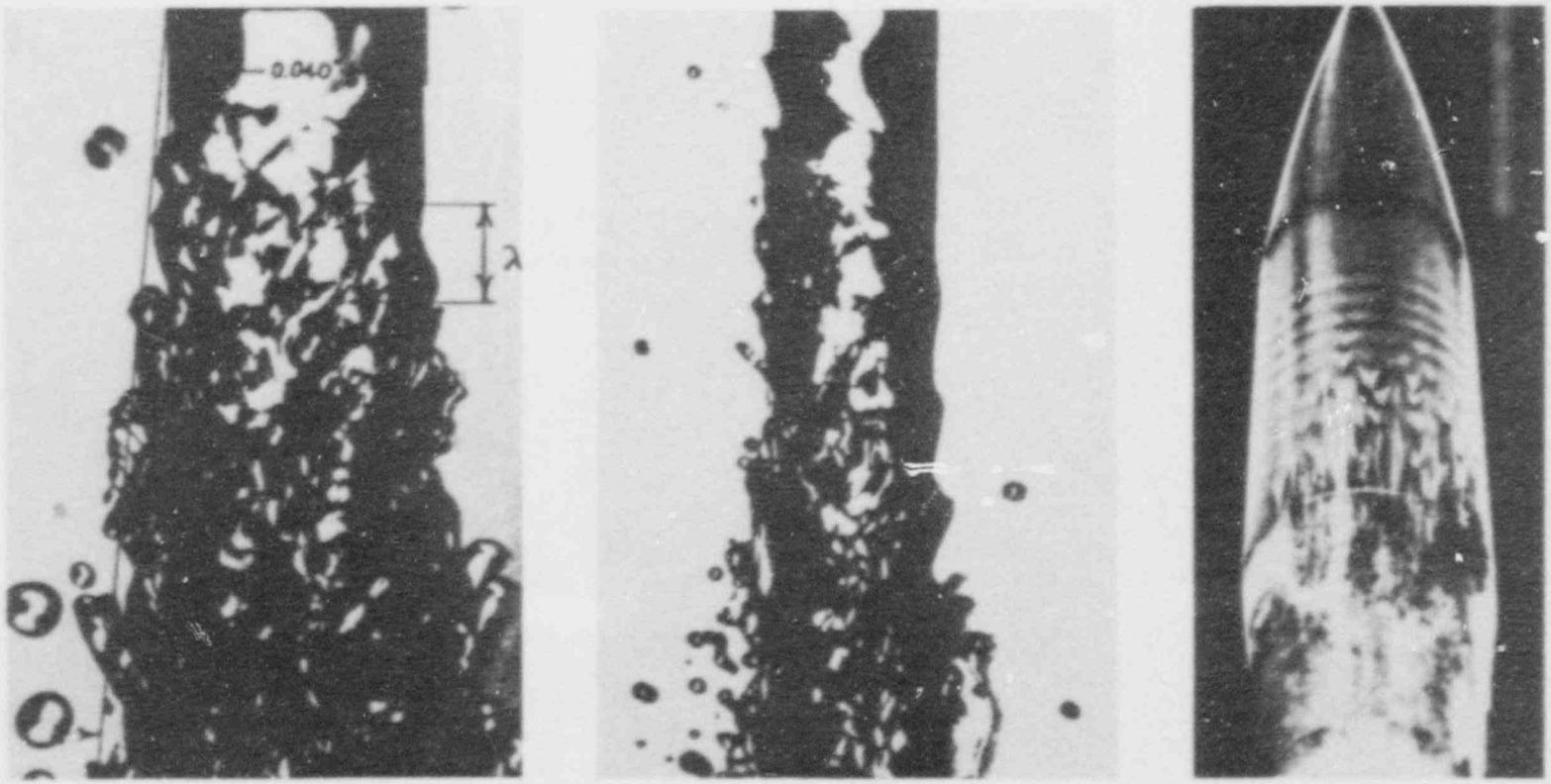

Figure 1.4-3. Comparison of Initial Jet Breakup Behavior for a. Carbon Tetrachloride Into Water and b. Tetrabromoethane Into Water[30] Versus c. Laminar to Turbulent Boundary Layer Transition on an Axisymmetric Body[31]

terms of distance from the orifice, varied by roughly 20 percent over time due to oscillations about some mean point. Reynolds[34] and Sterling and Sleicher[35] have reported observations of similar breakup length oscillations. Sterling and Sleicher also link the amplitude of these oscillations to jet exit velocity. That most authors have not reported this effect is probably a reflection on observation and data reduction methods in use.

Visual classification of the 1-mm and 1-cm jets places them in the initial region of turbulent jet breakup (see for example Tanasawa and Toyoda[36] and Kitamura and Takahashi[37]). This behavior is shown as category d of Figure 1.4-4. However, the observed density of the resultant sprays would certainly place them at opposite ends of the spectrum within this category. Note that Figure 1.4-4 does not imply that the drops are perfectly round nor that the edges of the spray cone are ever straight at any one point in time.

• **Large Scale Jet Penetration**

All 4- and 8-cm diameter jets, regardless of orifice aspect ratio or entrance velocity, followed similar behavior patterns during penetration. As mentioned earlier, these are appropriately classified as vertical turbulent buoyant jets, or forced plumes. During initial formation, the term "starting" plume is also used. The behavior pattern has three phases, or zones, as shown in Figure 1.4-5. This sketch can be compared with the photographs of Figure 1.4-6, which portray most of the features noted. The sequence shown was taken from system 1-7.

Initial jet penetration occurs in zone 1 as a coherent or solid core of material. A rapid expansion or mushrooming of the front occurs as the jet meets with resistance from the continuous phase (water). The material in this flattened face continues to expand and apparently forms a ring vortex. Visually we see the jet expanding to roughly twice its initial diameter within a penetration depth of about one diameter. Zone 2 starts where the newly formed vortex ring begins to penetrate further into the water.

As the vortex ring moves deeper, the main body of the jet tends to penetrate through its center with a higher mean velocity. Thus, as the jet front travels through zone 2, the outer layers of the ring vortex are stripped off of the main flow and left to dissipate on their own. This separated material has been observed to continue to spread and penetrate, all the while undergoing fragmentation until it becomes entirely dispersed. Meanwhile, the interaction of the central core of the jet and the inner regions of the vortex evolve into more of a spherical form.

Turner[38] and Middleton[39] have demonstrated that similarity solutions are possible for a starting plume. Their models are based

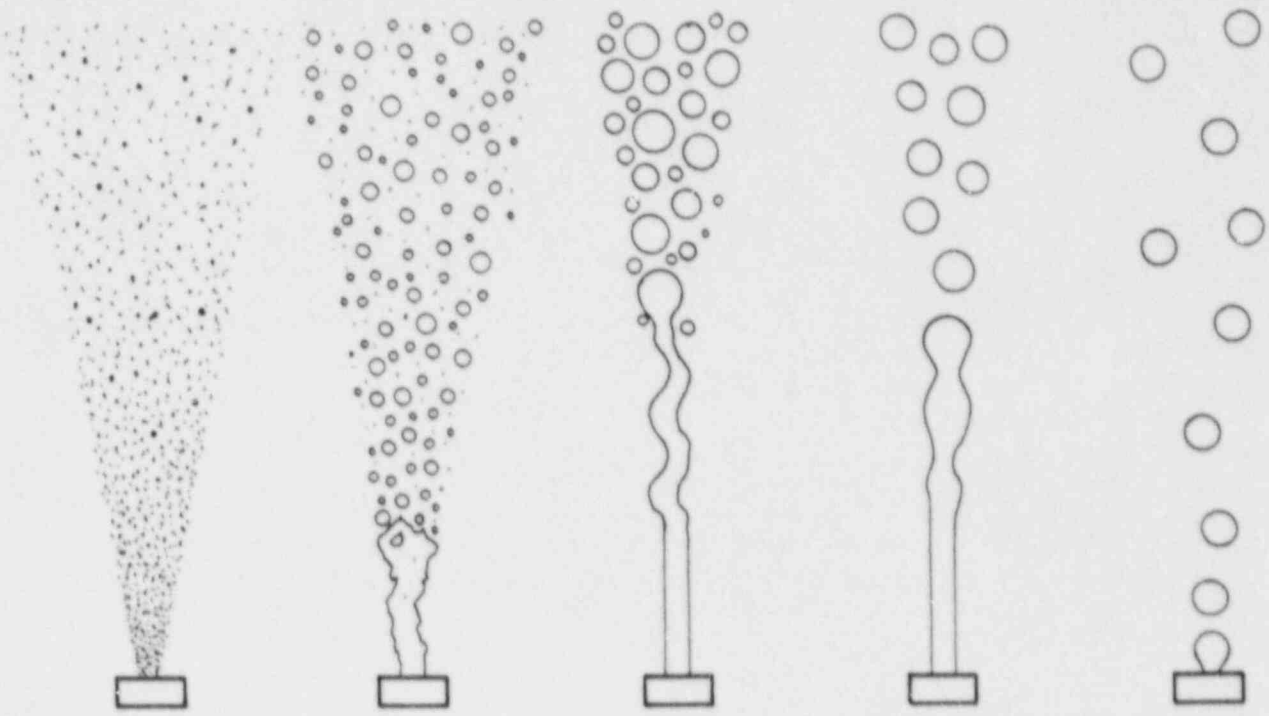

Figure 1.4-4. Modes of Jet Breakup Include a. Dripping, b. Laminar Breakup by Axisymmetric Disturbance, c. Laminar Breakup by Sinuous Wave, d. Turbulent Breakup Because of Lateral Jet Oscillations and Viscous Effects, and e. "Atomizing" Turbulent Breakup Because of Viscous Shearing Effects

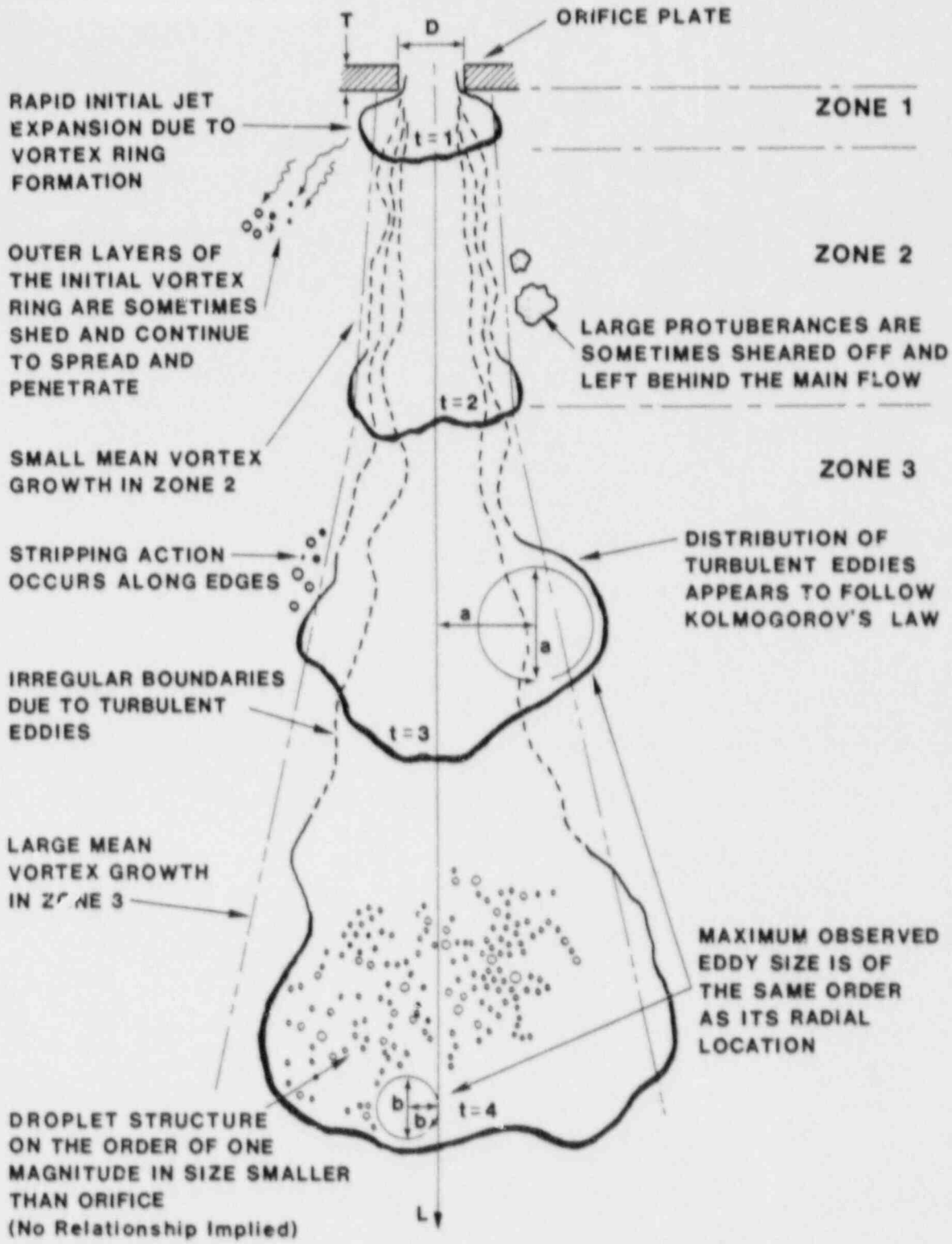

Figure 1.4-5. Composite Description of a Starting Forced Plume

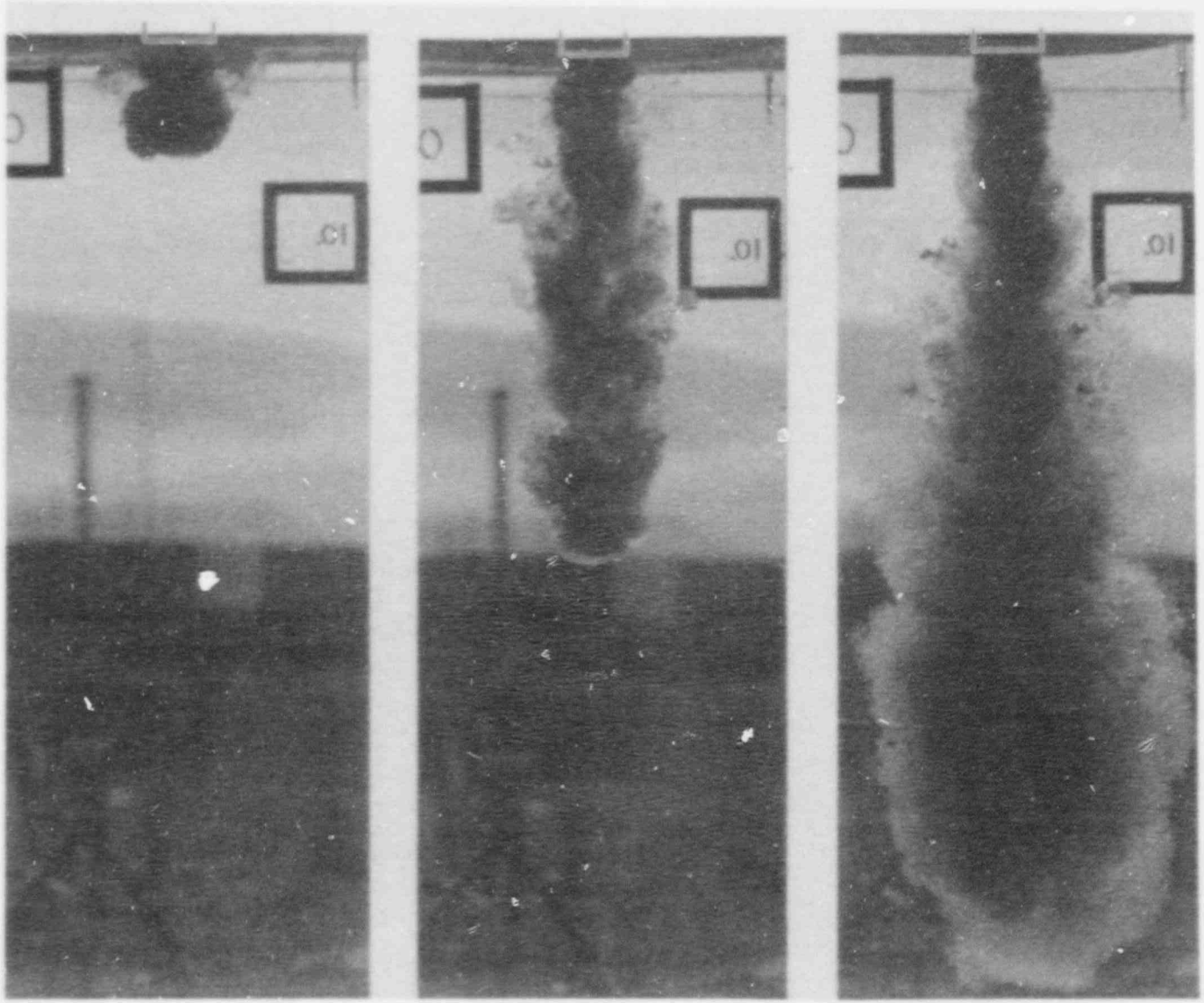

Figure 1.4-6. Typical Penetrating Plume Development

on a steady plume feeding mass, momentum, and buoyancy into a spherical vortex, which will penetrate at velocity u,

$$U \propto t^{-1/4} .$$

This also corresponds to the behavior of a steady plume as shown by the work of Schmidt[40] and Morton, Taylor, and Turner.[41] Morton,[42] on the other hand, has shown that a weakly buoyant vortex ring will have a velocity of

$$U \propto t^{-1/2} .$$

Such a penetration rate is also consistent with solutions presented for a thermal (an isolated buoyant mass) by Scorer.[43] The differences in these velocities gives an indication of why the initial ring vortex gives way to the spherical vortex found at the end of zone 2. The term "spherical vortex" is used to describe a ring vortex that has a ratio of the major to minor radii on the order of 1.5.[38] Middleton's solution[39] indicated that a value of 1.75 is more appropriate from an analytical viewpoint and compares well with Turner's data.

Evidence indicates that zone 2 corresponds with what is commonly called the zone of flow establishment for a stable jet. In this region the mean flow behaves as if a potential core exists that has a constant velocity. Thus, until the jet has penetrated to a depth where mean velocity profiles behind the front reflect an established flow behavior, any vortex at the leading edge is "unstable". Interaction within this zone may also include interplay between a succession of vortex formations, such as documented for a vortex ring pair by Okabe and Inoue[44] and Yamada and Matsui.[45]

The behavior of zone 2 can thus be described as that region where the leading structure or cap of the jet evolves into a stable, albeit turbulent, spherical vortex. It is further characterized by a small mean growth in the visual edge of the maximum diameter of the cap. The mean spread rate is on the order of 0.02 m/m.

The vortex formation in zone 1 and the initial transition of zone 2 can be seen in the photographs of Figure 1.4-7. This sequence was taken from system 1-5. Comparison should also be made with the vortex flow visualization work of Okabe and Inoue[44] and the numerical simulation of Christiansen.[46] Examples can be found in Figure 1.4-8. Other examples of liquid-liquid pair vortex ring visualization can be found in the work of Didden.[47,48] Although these photographs were taken in laminar flow situations, Didden's 1977 work demonstrated that the vortex retained its overall structure even after transition to turbulence occurred.

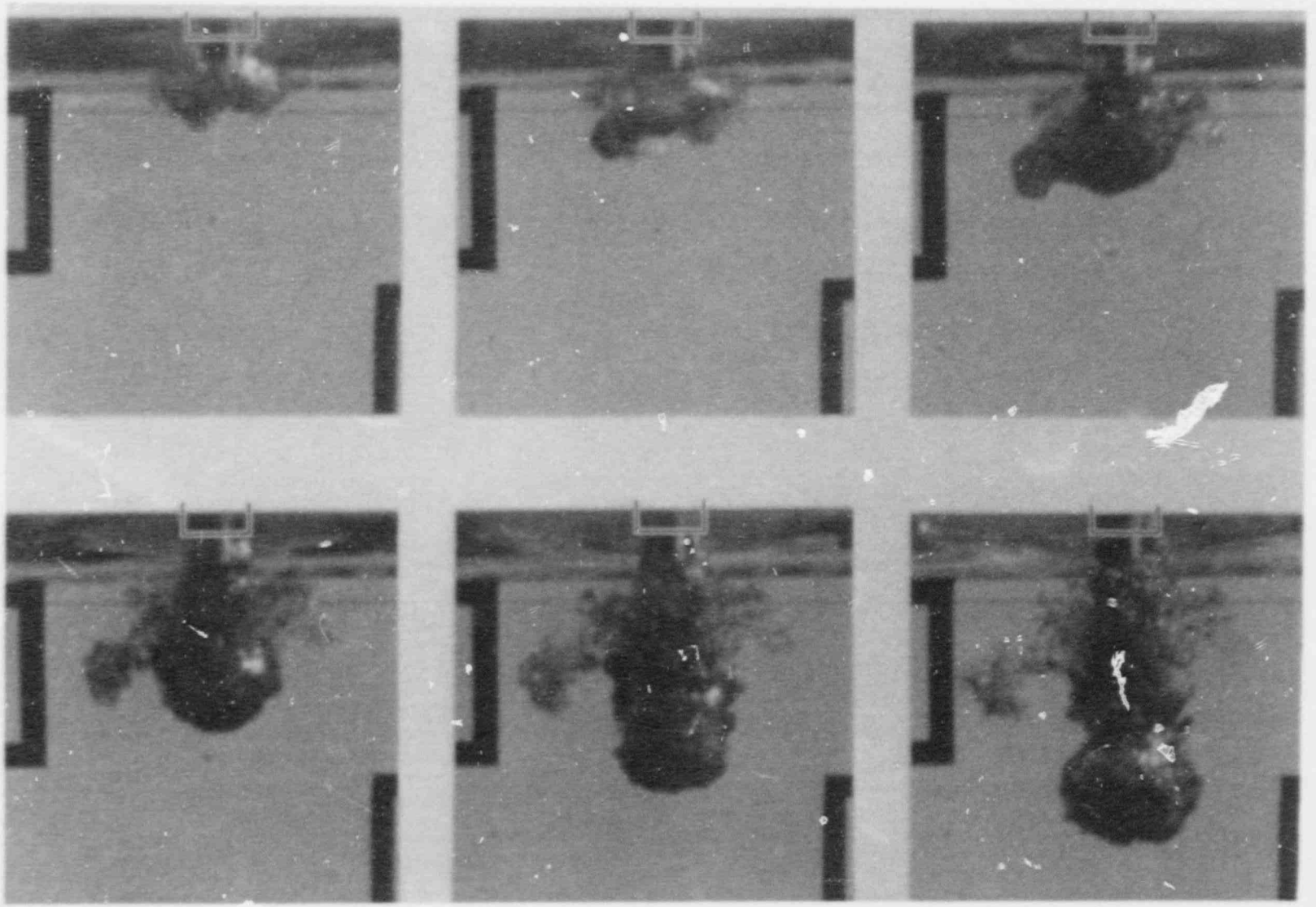

Figure 1.4-7. Typical Initial Penetration Behavior Showing Vortex Formation

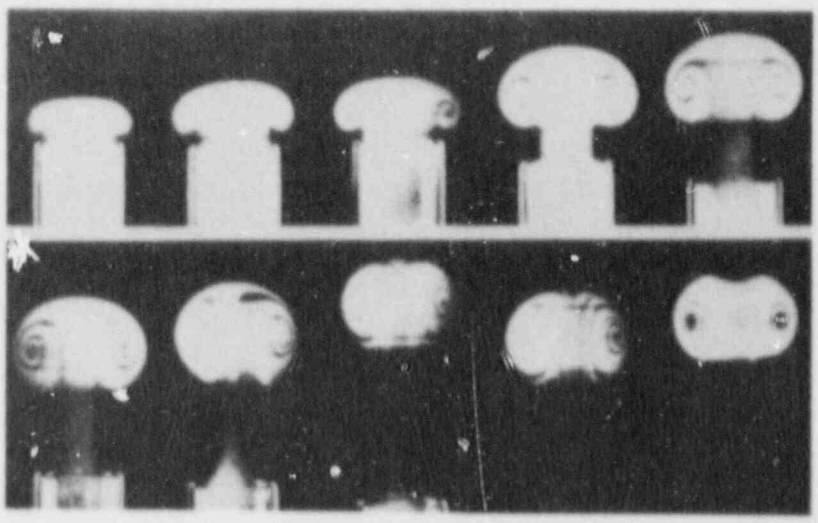

a.

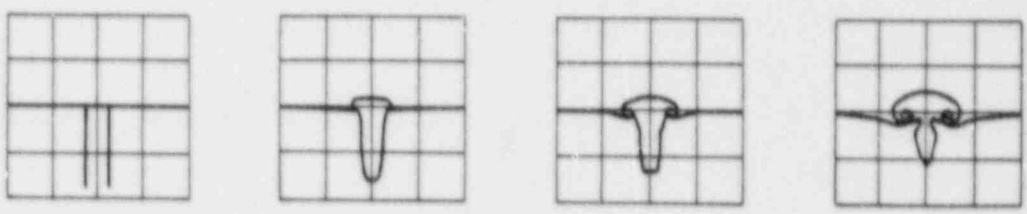

b.

Figure 1.4-8. Vortex Ring Generation as Shown by a. Flow Visualization[44] and b. Numerical Simulation[48]

Zone 3 is characterized by the rapid and near linear mean growth of the leading cap or vortex sphere. In comparison to the small growth rate of zone 2, here we see a mean spread on the order of 0.2 m/m. Overall characteristics follow those described for a starting plume.[38] The observed transition point between zone 2 and zone 3 also corresponds closely with the estimated end of the zone of flow establishment[49] if this had been a steady state jet.

All three zones are characterized by the apparently random appearance of turbulent eddies that protrude from the edges of the jet. At any one point in time this has the effect of giving the jet a very irregular boundary. The majority of these eddies are small when compared to the jet diameter. However, larger protuberances are observed, although their frequency falls off with increasing size. Such a distribution brings to mind the Kolmogorov spectrum law that describes energy content versus wave number for isotopic turbulence (for example, see Reference 50). Some of these large eddies become overextended and lose all forward momentum. As a result they are sheared off of the main flow, stagnate, and slowly dissipate. The maximum observed eddy size was of the same order as its radial location.

The last prominent feature to discuss is the apparent droplet-like structure exhibited by these jets. Close scrutiny of the photographs reveals a myriad of small droplets that form the main visible portion of the jet. Such a structure would be expected based on the experiments of Ranz[51] for carbon tetrachloride sprays into water. It was also noted that turbulence and shearing action along the jet edge tends to strip off outer layers of drops from the main flow region.

As a final note consider the third photograph in Figure 1.4-6. The overall structure of the jet exhibited at this point allows it to be classified under category e of Figure 1.4-4, as might be expected from the high Reynolds and Weber numbers presented in Table 1.4-3. Our attention will now be directed toward quantitative descriptions of the observed behavior described in this section.

1.4.2.5 Breakup Behavior

Discussions in Section 1.4.2.4 classified the breakup of the R-113 into water jets as turbulent on the basis of their visual form, as well as on the values of their orifice exit Reynolds numbers. Although classification based on these observations alone may be adequate, it is also of use to evaluate the data in light of correlations published by other experimenters. For this purpose consider a critical Reynolds number, Re_k, given by

$$Re_k = \frac{\rho_D \, D \, u_k}{\mu_D} ,$$

where u_k is the critical velocity for transition from a laminar to a turbulent jet. The critical Reynolds number is found from the relationship

$$Re_k = a\, Z^n .$$

The values "a" and "n" can be found in Table 1.4-4 for various authors. Since Takahashi and Kitamura's[52,53] work was with liquid-liquid systems, the correlation they present will be used here. The value Z_c, given in their relation, is an Ohnesorge number and is calculated as

$$Z_c = \frac{\mu_c}{(\rho_c\, D\, \sigma)^{1/2}} .$$

Table 1.4-4

Coefficients for Determining the Critical Velocity for Laminar-to-Turbulent Transition in Axisymmetric Jet Breakup

a	n	author
$19{,}000 \left[\frac{\mu_D}{\mu_c}\right]^{0.14} \frac{\sigma}{u_k\, \mu_D}$	1.34	Fujinawa et al.[54]
$98\, Z_c^{-0.11}$	-0.30	Takashasi and Kitamura[52,53]
370	-0.318	Tanasawa and Toyoda[55]
325	-0.28	Grant and Middleman[56]

Using the data presented in the previous section, critical velocities can readily be calculated. The highest value was for the 1-mm diameter orifice (system 1-1), where u_k is 0.86 m/s. In contrast, the 8-cm jet has a critical velocity of only 0.04 m/s. When these calculations are compared to the injection velocities given in Table 1.4-1, we have an indication that all of the

experiments performed should follow turbulent breakup behavior. In a similar vein, Tanasawa and Toyoda[56] recommended use of a "jetting" number, Je, that was of a form equivalent to

$$Je = We \left[\frac{\rho_c}{\rho_D}\right]^{0.55} .$$

Based upon experimental observations, they suggested that laminar-to-turbulent transition occurred at a jetting number of 10. This corresponds to a Weber number of 8 for the present experiments, a number that is well below any values given in Table 1.4-3.

Since these experiments were also shown to be plume-like for the larger diameters (low Froude numbers), plume transition data should also be considered. Such information can be found in the work of Shlien,[57] who demonstrated that in saltwater-into-freshwater systems the critical Reynolds number for laminar-to-turbulent transition had a value of 220. Again we have a criterion that indicates turbulent conditions exist for the experimental systems in use.

Yet another transition criterion is provided by Anwar,[58] who used a freshwater-into-saltwater system. His observations indicated that turbulent plumes exist when the densimetric Froude number is greater than or equal to a value of about 1.12.

Thus by multiple correlations it can be established that we are dealing with turbulent breakup phenomena. However, before further progress can be made our attention needs to be focused on reducing actual breakup data from the tests conducted.

Measurement of breakup length in turbulent jets first requires definition of some physical parameter whose value can be determined. Although this may seem to be a little too obvious, breakup length definitions vary widely for turbulent jets, making data comparisons difficult. Some authors prefer to visually identify the end of a coherent core region as discussed under Section 1.4.2.4. This becomes a difficult task at best because of the clouds of dispersed droplets.[37] Other schemes include the point where surface disturbances are first noted on the jet edge, the distance to where a stable jet expands to twice its initial diameter, the point where surface disturbances grow to a given height, and others. These methods are all suited for visual analysis of steady jets, although widely differing results could be expected.

In light of this, a better definition was sought that would remove some of the ambiguity involved in determining the breakup length. In Figure 1.4-9, we notice that the mean center line flow is expected to have an initially constant velocity core,

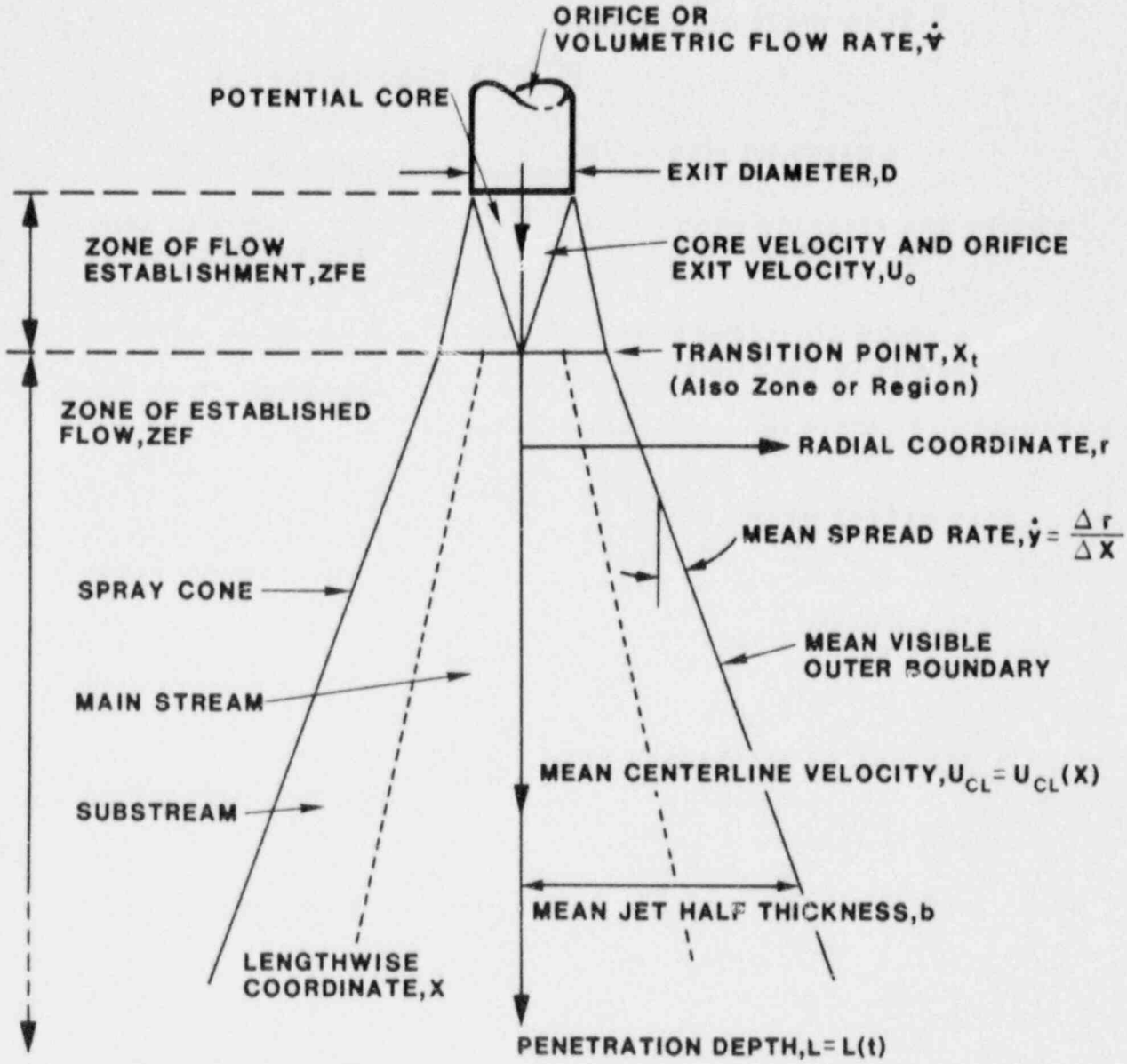

Figure 1.4-9. Schematic Definition of Frequent Terms Used in Jet Flows

followed by an established flow region where velocity decays in an exponential fashion. Thus if center line velocity information is present in some form, breakup length can be identified by observing the location of such a transition point. This method has been used by Abramovich[49] and others.

For a penetrating jet we must now make the assumption that the velocity behavior of the front follows the same trends as found in the steady state jet. If this holds true, reduction of film data on the advancing front will yield velocity data that, in turn, will indicate the location of the breakup point. Turner[38] has shown that the starting plume does, in fact, penetrate at a rate proportional to the mean center line velocity of the steady plume. In his experiments, Turner injected salt water into fresh water and determined that the penetration velocity at any depth was equal to 0.61 (+/- 0.05) of the velocity of the steady plume at the same depth. Demetriou[59] gives velocity data for a starting water-into-water jet that yields the same result.

Based on these observations, we expected our data to show an initially constant penetration rate, followed by an exponential decay. Such behavior was observed. An example is shown in Figure 1.4-10, which was taken from system 1-3. The "knee" of the curve displayed represents the transition point or breakup length as defined here.

Since the flows under discussion are buoyant it is expected that some acceleration may occur upon initial entry if the injection velocity is too low. At some depth the penetration rate would reach a maximum value before beginning the aforementioned deceleration. Close scrutiny of the results for these tests give some indication of this type of behavior. However, as the data all fall within the experimental accuracy for a linear fit, it is treated as a linear phenomena. Under other conditions this may not be appropriate. Demetriou[59] has presented penetration data for starting water-into-water jets that demonstrated such behavior. His penetration profiles exhibited an initial period of acceleration, followed by a fairly constant velocity region that persisted until the expected transition point was reached. After this depth an exponential decay in velocity was observed. The point to be made is that even for initially accelerating flows the present definition for breakup length is appropriate. Table 1.4-5 provides a list of the breakup lengths for our tests as determined in this manner. Both dimensional and non-dimensional forms are given.

It is desirable to compare our results with functional relationships put forth by other authors. Unfortunately, existing correlations for breakup length are restricted primarily to laminar jets or to high speed jets. Examples of the former have been reviewed by Kitamura and Takahashi[37] and do not apply here. High speed breakup lengths have been reported by many authors, and they are typically given as a constant. Of more interest is a

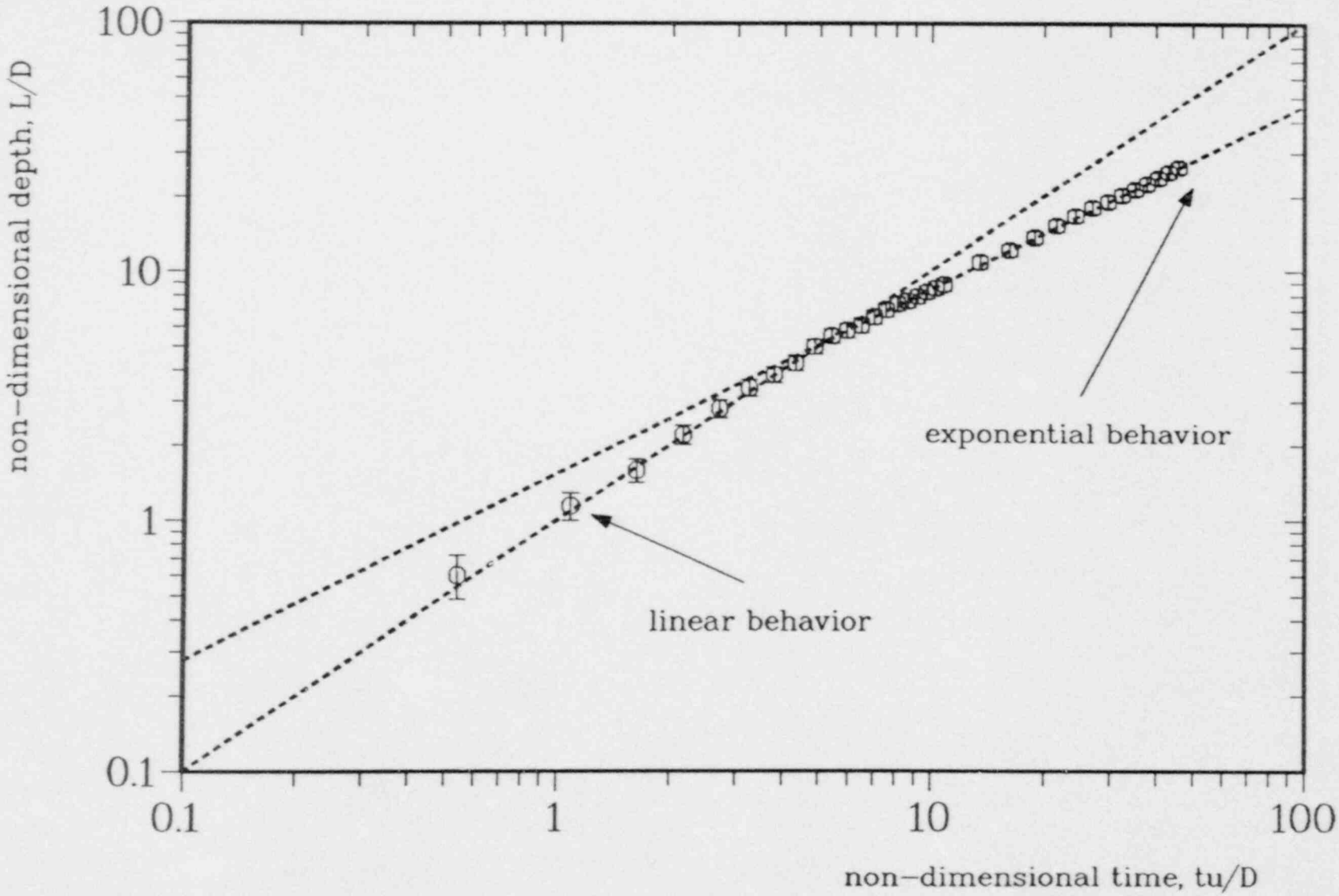

Figure 1.4-10. Typical Penetration Data

Table 1.4-5

Breakup Length Data

System Number	Breakup Length x_t (m)	Non-dim. Breakup Length x_t/D	L^*
1-1	0.036	30.0	24.0
1-2	0.070	7.3	5.9
1-3	0.200	5.2	4.1
1-4	0.240	6.3	5.0
1-5	0.250	6.6	5.3
1-6	0.250	6.6	5.3
1-7	0.480	6.3	5.0

relation put forth by Taylor in 1942[66] that can be written in the form

$$L^* = \left(\frac{\rho_c}{\rho_D}\right)^{0.5} \left(\frac{x_t}{D}\right) ,$$

where L^* is an empirical constant that is to be determined by experiment. This result was an outgrowth of his studies on surface wave generation in 1940[61] from which he determined that the mass loss rate due to stripping of wave tops is a constant function of the density ratio involved, as shown. Other flow parameters, he reasoned, affect only the drop sizes removed. Table 1.4-6 provides a partial listing of breakup data available in this regime, as corrected with Taylor's relationship. Table 1.4-5 also has a column for R-113 breakup data in this format.

Two additional starting length correlations have been found that deal specifically with vertical forced plumes. Abraham[66] presents graphical solutions for the length of the zone of flow establishment (ZFE) for buoyant jets. His solutions indicate that the starting length decreases with a decreasing Froude number. Hirst[67,68] describes a theoretical method for solving for physical properties within the ZFE. His solution for the starting length is quite similar to Abraham's. Both Hirst's and

Table 1.4-6

Typical Transition Points for
Axially Symmetric Jets

L^*	System	Author
7.6	freshwater-saltwater	Anwar[58,62]
6.0	air-air	Albertson et al.[63]
5.0	water-water	Kuethe[64]
5.3	water-air	Oehler[65]
6.0	analytic solution	Abramovich[49]

Abraham's plots for the starting length of a vertical axisymmetric forced plume are reproduced in Figure 1.4-11. Breakup data for the 1-, 4-, and 8-cm R-113 jets are shown for correlation purposes. The starting length for a steady submerged jet as given by Abramovich[49] is also indicated for comparison. Surprisingly, the data are better matched to the starting length for a jet than with the results of Abraham or Hirst. Since these relationships are thus considered unsatisfactory for our purposes, a different correlation is required.

In order to provide some understanding of the breakup behavior in the initial turbulent regime, consider the sketch of Figure 1.4-9. A mass loss mechanism must be present in order to cause the observed mean core behavior. If we consider the classical case of wave growth and crest stripping, a logical point to start would be Taylor's paper of 1940. Mass loss considerations in annular flow typically begin with this paper in developing desired relationships. Tatterson[69] has shown that the mass loss rate can be written in a form similar to

$$\dot{m} \simeq \left[\frac{\rho_D \, u_o^2}{\sigma \, k}\right] (\rho_D \, \rho_c)^{1/2} \, u_o \, f \, ,$$

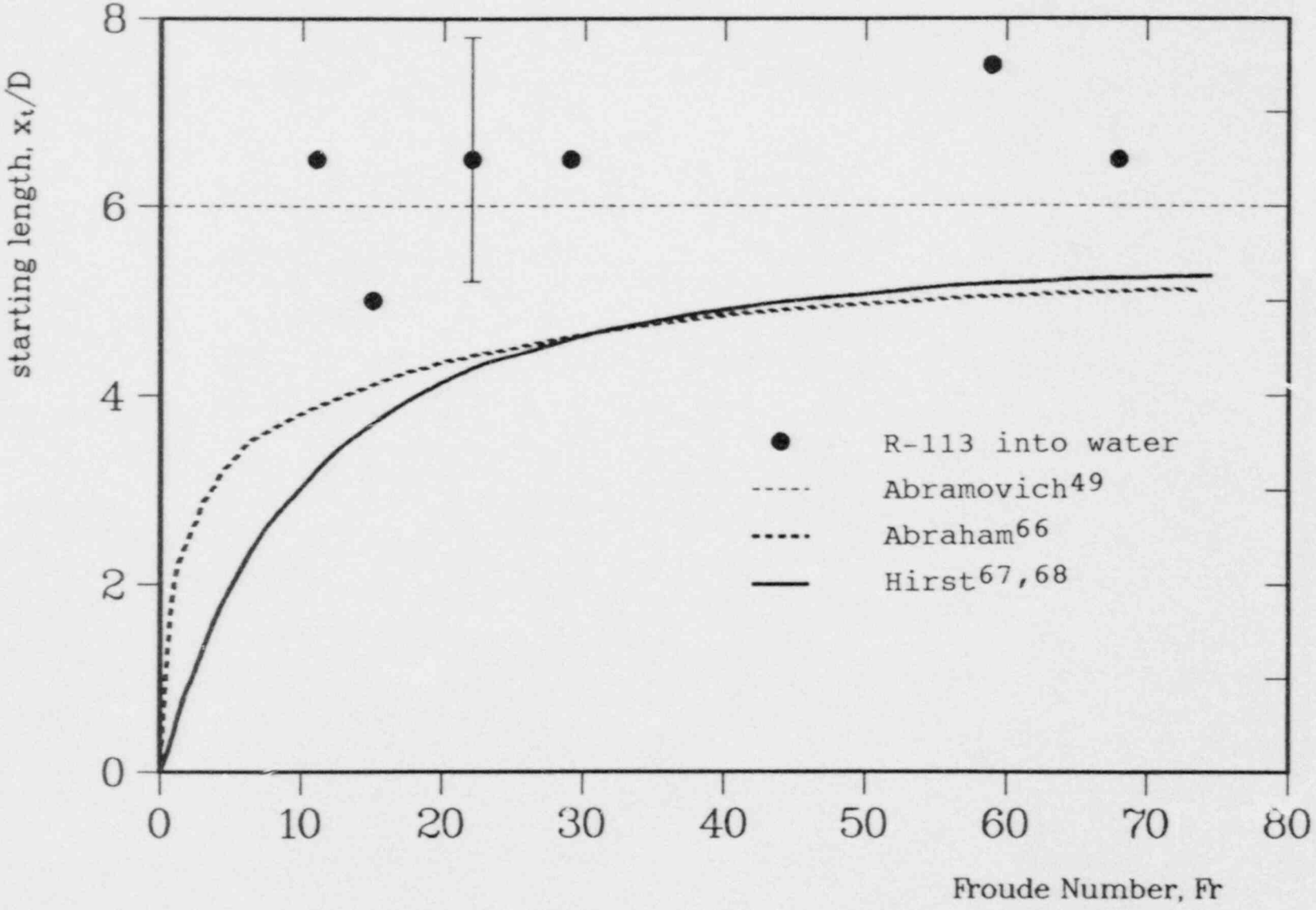

Figure 1.4-11. Test Data Versus Vertical Forced Plume Starting Length Solutions Given by Abraham[66] and Hirst.[67,68]

where

$\dot{m}$ = mass loss rate,

k = disturbance wave number,

f = functional relationship dependent upon k, ρ_D, ρ_c, μ_c, σ, and u_o.

Although Taylor's assumptions that $\rho_D << \rho_c$ and that μ_D can be neglected do not apply here, this equation does provide a useful starting point that will aid in the presentation and interpretation of breakup data. Representing the wave number, k, as

$$k = \frac{k'}{D}$$

allows formation of a Weber number based upon orifice exit conditions, as defined in Section 1.4.2.3. In addition, the mass loss equation can be nondimensionalized by division of the term

$$u_o \left(\rho_D \rho_c\right)^{1/2} .$$

These two steps then yield the relation of

$$\frac{\dot{m}}{u_o \left(\rho_D \rho_c\right)^{1/2}} = We \left[\frac{1}{k'}\right] f .$$

Next consider that if we model the potential core as a cylinder, the mass removal term can be written as

$$\dot{m} \simeq \frac{m}{S\ t_t} ,$$

where

m = mass of potential core,

S = surface area of potential core,

t_t = breakup time,

which are given by

$$m = \frac{\pi D^2}{4} x_t \rho_D ,$$

$$S = \pi D x_t ,$$

$$t_t = \frac{x_t}{u_o} .$$

Combining these terms yields

$$\dot{m} = \frac{\rho_D u_o D}{4 x_t} .$$

Then, using the previous definition of L^*, the mass loss equation reduces to

$$L^* = \frac{k'}{4 We f} = g(We) .$$

In reality the function "g" given here should be considered to include both the dispersed and continuous phase viscosities as terms, each of which could play a role in breakup behavior. Although we are not being specific as to the form of "g" in this report, it should be noted that plots of breakup lengths versus the Weber number should provide behavioral trends that would be useful for a predictive tool in the study of dynamically similar systems.

It is also of interest to note that the nondimensional breakup length, L^*, attributed to Taylor's 1942 work appears here as well. This might be expected in that both results are based upon Taylor's earlier work in 1940.

Following the form set forth above, breakup lengths for the R-113 jets are plotted in Figure 1.4-12 as system number 1. Also shown is the Taylor breakup length for high speed jets where the empirical constant has been given an assumed value of 5. The divisions shown between the laminar breakup, initial turbulent breakup, and high speed breakup regimes are based upon the jetting number correlations presented by Tanasawa and Toyoda[66] for a density ratio of 1.

Also plotted in this figure are all of the available turbulent breakup data for immiscible liquid-into-liquid jets. The liquid

pairs used in the various systems are listed in Table 1.4-7. Where sufficient data was presented on the actual experimental setup it was found that these systems had buoyancy vectors that were pointed in the direction of flow, as for the present experimental setup. The scatter observed in the data is considered to be due to nozzle geometry effects (typical size on the order of 1 mm), inconsistencies in the method of determining breakup length, the oscillatory nature of the breakup length, and evidence of viscosity and other system parameter dependencies.

The estimated trend depicted used the intersection of Taylor's and Tanasaya and Toyoda's correlations as a fixed point because of a lack of data in the Weber number range of 100 to 3000. The slope was set to simply intersect the center point of the data found in the lower Weber number range. The result indicates that the general trend of the data follows the form of

$$L^* = 200\ We^{-0.6},$$

any use of which must be with caution due to the lack of data in the mid-Weber number range.

Consideration of the results presented in Figure 1.4-12 generated the following comments:

1. Breakup of the 1-mm jet of R-113 into water is consistent with data from other experimenters.

2. The breakup data for the 1-cm jet falls near the transition point between the two turbulent breakup regimes. Visually the behavior of the jet had been placed in the upper end of the first turbulent regime. This gives additional support to the placement of transition near a Weber number of 500.

3. The breakup lengths for the 1-, 4-, and 8-cm jets compare favorably with a Taylor breakup length of 5.

4. Breakup behavior for high Reynolds number jets with low Weber numbers may not follow the estimated trend shown. This would be expected in systems with high viscosity and low interfacial surface tension where hydrodynamic effects appear before drip conditions are overcome[51].

1.4.2.6 Conclusions, Plans, and Recommendations

Although data reduction efforts are not complete, some initial conclusions can be drawn on the breakup data presented.

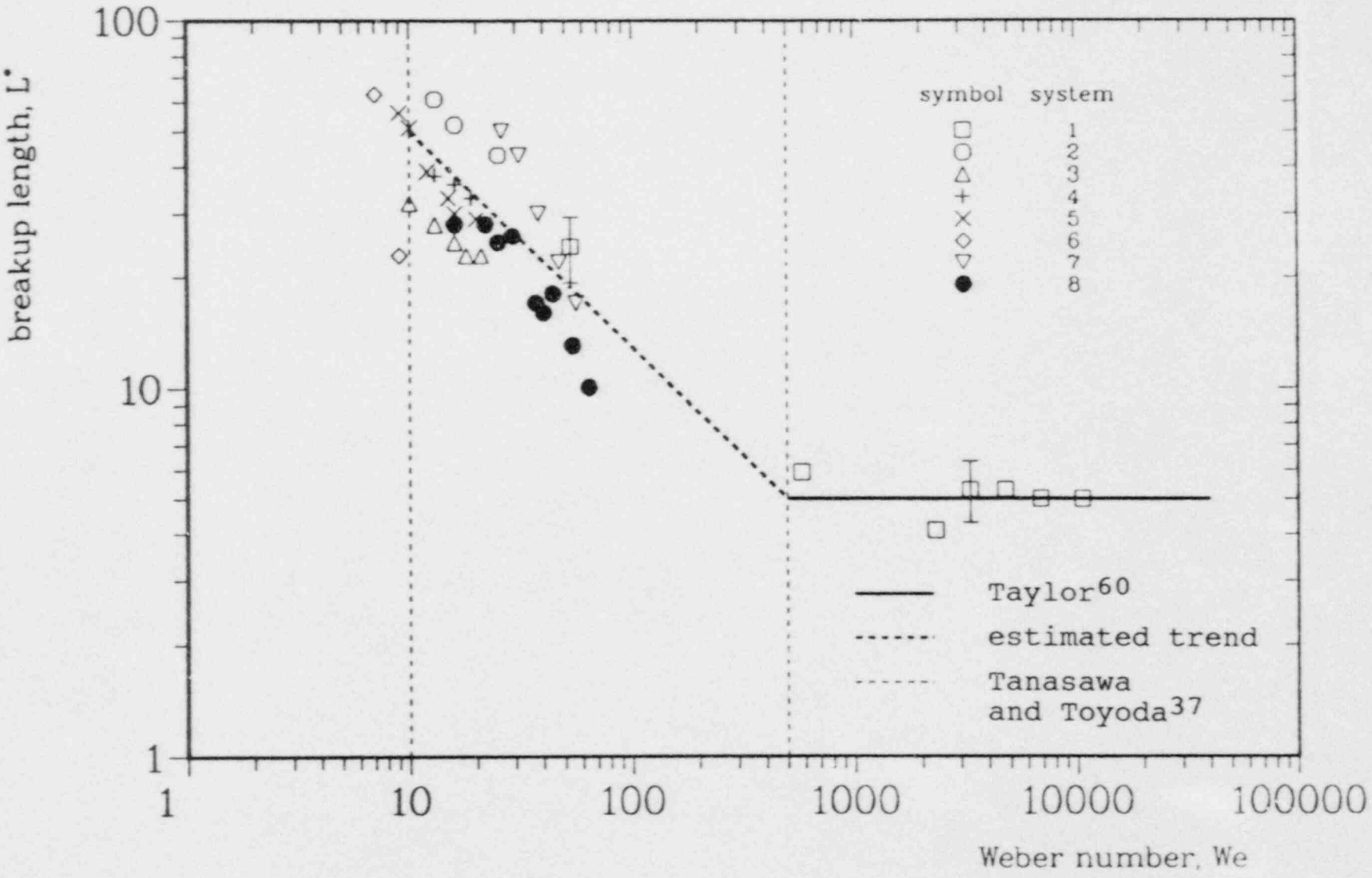

Figure 1.4-12. Immiscible Liquid-Into-Liquid Jet Breakup Data

Table 1.4-7

Immiscible Isothermal Liquid System Pairs for Which Breakup Data Are Available

System Number	Dispersed Fluid	Continuous Phase Fluid	Source
1	R-113	water	Present work
2	benzene + carbon tetrachloride	water	Takahashi & Kitamura[53]
3	water	carbon tetrachloride	Takahashi & Kitamura[53]
4	water	paraffine-gasoline mixture 1	Takahashi & Kitamura[53]
5	water	paraffine-gasoline mixture 2	Takahashi & Kitamura[52]
6	water	paraffine-gasoline mixture 3	Takahashi & Kitamura[52]
7	benzene	water	Meister & Scheele[70]
8	chlorobenzene	water	Dzubur and Sawistowski[71]

1. Immiscible liquid-into-liquid jet breakup data are severely limited in scope.

2. The R-113 into water tests followed breakup behavioral trends as might be predicted based upon the available liquid-liquid data base for the low Weber number range, breakup data for high speed jets, and existing correlations for the laminar-to-turbulent transition point.

3. Hydrodynamic effects for a corium pour will place its behavior well into the turbulent regime. Treatment of such a jet as a capillary breakup phenomenon will give unrealistic results.

4. Scale of tests can be an important parameter. Experimental design must take into account the expected flow regime it is to represent. For example, if it is desired to understand behavior under conditions where the 'Taylor' breakup length, L^*, is a constant, current data

indicate that the exit Weber number must be above a value of 500.

5. Initial jet penetration behavior exhibits a high degree of vorticity. Transient mixing rates are expected to be higher than those found under steady state conditions. Thus transient jet phenomena must be understood and applied properly to predict initial melt-water interactions.

In support of developing a mixing model, data reduction efforts are currently directed at analyzing penetration rates, vortex growth rates, and steady state jet spread rates. When taken together with assumptions about mean flow profiles, these data will provide information on entrainment rates. Coupled with drop size distribution data this will, in turn, enable one to estimate the surface area and volume fraction as a function of penetration depth. Such functional descriptions are important to understand heat transfer rates in thermal jets. Comparisons can then be made with earlier melt-water experiments in an effort to couple hydrodynamic behavior with boiling phenomena.

In terms of recommendations for further testing, one only has to reflect on the dearth of data for liquid-liquid systems. Basic data are needed in all areas of jet phenomena. However, priority would be placed on the following in light of current goals in understanding FCI behavior:

1. Flow visualization should be undertaken to provide data on internal jet structure in an immiscible liquid system. This should include quantification of turbulent eddy size distribution and a description of shear layer thickness behavior.

2. Detailed center line velocity measurements should be made in both starting and steady state jets in order to better link their behavior. This is important to properly understand turbulent breakup in transient jets.

3. A series of tests should be conducted over the mid-Weber number range with several widely different material properties. This will allow definition of the transition point between the initial turbulent breakup regime and the range where the "Taylor" breakup length can be treated as a constant.

1.4.3 Integrated Fuel-Coolant Interaction Code Development (M. F. Young, 6425)

The initial test problem for the IFCI code is intended to demonstrate the capabilities of IFCI and to detect problems in both the numerics and the phenomenological models. The test problem

is a representative FITS experiment, using typical experimental conditions as the input to IFCI.

The following sections describe the setup of the problem on the IFCI computational mesh, the results of the coarse mixing phase, and the results of the triggering and propagation phase. Calculation of the expansion phase was not carried out completely because the expansion phase has already been studied in detail by previous researchers[72,73,74] and because this phase does not present any special calculational problem for IFCI. The main purpose of the test calculation is to demonstrate the operation of the IFCI fragmentation models during the coarse mixing and propagation phases.

1.4.3.1 Problem Setup

The problem conditions are patterned after the FITS "D" series experiments.[75] In this series, roughly 20 kg of molten iron-alumina thermite were dropped into water, 15 to 66 cm deep, contained in a square lucite chamber 61 cm on a side. The velocity of the melt on entry into the water was 5.7 to 7.3 m/s. Water temperature ranged from 368 K (saturation temperature at 0.085 MPa) down to 284 K.

The problem was set up in the IFCI r-z geometry using 5 radial nodes and 10 axial nodes (see Figure 1.4-13); although this mesh is fairly coarse, it is adequate for initial testing of the code. The water chamber is approximated as a cylinder 61 cm high by 69 cm in diameter; the cross-sectional area is thus the same as the square lucite chamber in the experiments. The initial water temperature was 373 K (saturation temperature at 0.1 MPa pressure). The initial melt temperature was 2700 K, and an entrance velocity of 5.9 m/s was used. The initial melt configuration was approximated as a cylinder 20 cm in diameter and 21 cm long, with a total melt mass of 25 kg. These conditions were similar to those in the FITSOD test, except for a higher total melt mass and water depth.

Figure 1.4-13 shows the initial position of the melt and water on the problem grid. As shown, the tail of the melt enters the problem grid through an inlet boundary on the top of the inner two radial nodes. The outlet boundary is a pressure boundary on the outside of the top axial node. All other boundaries are fixed, which means that pressures generated during the propagation phase of the FCI will not be relieved in the same manner as if the chamber were lucite (essentially a free boundary). The calculation is started at the time of initial melt-water contact.

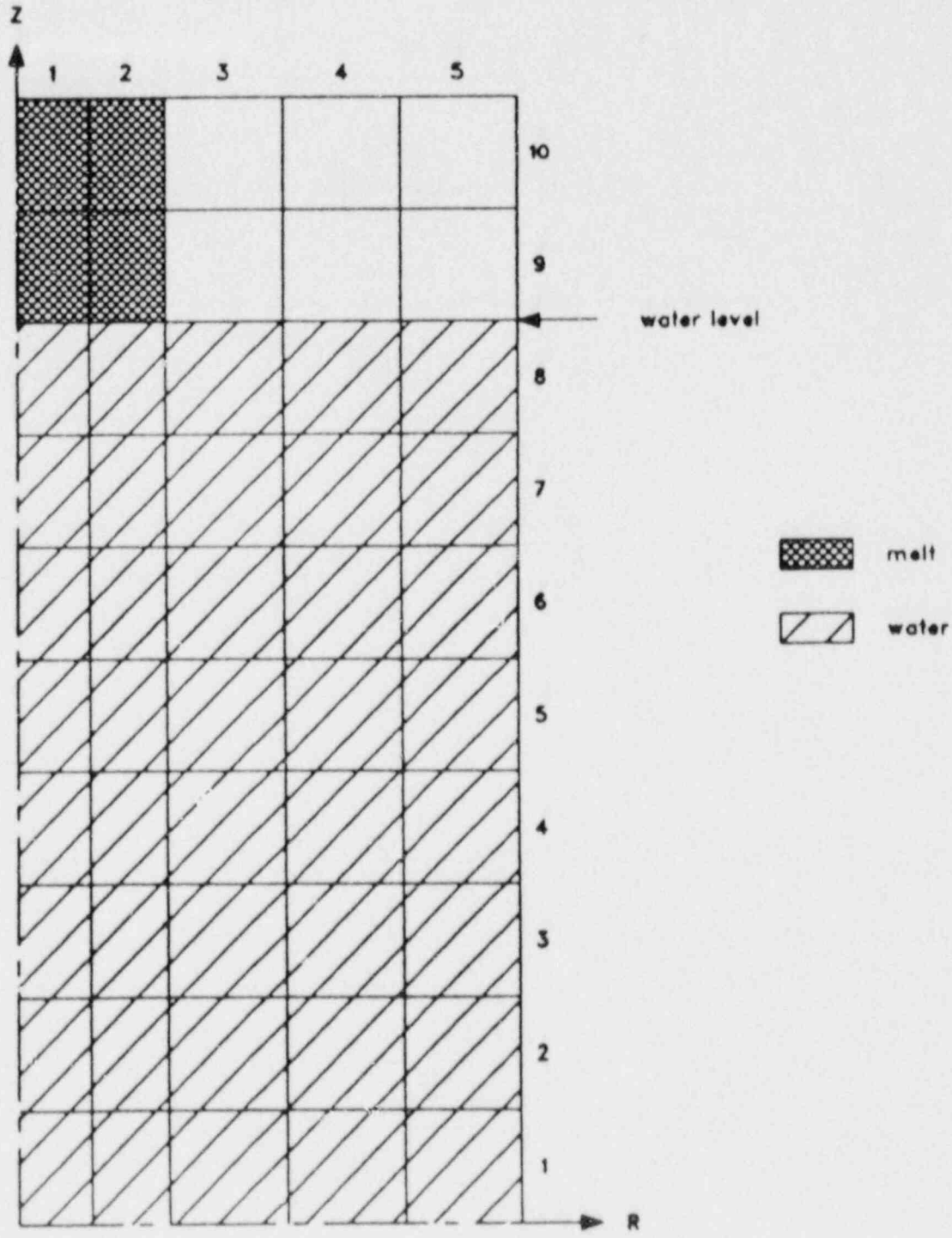

Figure 1.4-13. IFCI Test Problem Mesh Setup

1.4.3.2 Coarse-Mixing Phase

In the coarse-mixing phase, the melt enters the water and falls to the bottom of the water chamber. Heat transfer between the hot melt and the surrounding water is limited by film boiling. The melt fragments and mixes with the surrounding water-steam mixture, spreading out radially as it falls. Experimentally, what is observed is roughly a paraboloid shape for the coarse-mixing region (Figure 1.4-14). This shape forms fairly quickly after melt-water contact and persists as the melt mass falls through the water. The experimental observation is in contrast to a theoretical coarse-mixing correlation by Corradini[78] that predicts an exponential spreading of the mixture region with increasing fall depth.

Two-dimensional slices through the problem, produced by the TRAP graphics postprocessor, are shown at several times during the fall phase in Figures 1.4-15 through 1.4-17. These figures show the melt volume fraction distribution in the problem at various times. (Note: The "quantization" levels on the TRAP 2D slice plots give the shading for five ranges of the dependent variable being displayed, in this case melt volume fraction). It can be seen that there is an immediate spreading in the radial direction as the melt enters the water surface (Figure 1.4-15). The melt then rapidly attains a paraboloid shape as it falls through the water (Figures 1.4-16 and 1.4-17). This is in agreement with the experimental observations. An extremely interesting feature is the appearance of a steam-water chimney in the interior of the paraboloid mixture region; the presence of this chimney has been postulated, but never experimentally observed, because of problems with instrumentation in the hostile FCI environment. This calculation is the first time the presence of the chimney has ever been verified, if only by a numerical simulation.

The volume fractions of steam, water, and melt on the center line as a function of z are shown at 0.3 s in Figure 1.4-18. The average steam volume fraction in the chimney at the time of melt contact with the bottom, 0.3 s, is around 0.25. The absence of steam in the lowest cell is due to the use of the MELPROG bulk boiling model in the present calculation; the water temperature must be greater than the local saturation temperature for boiling to occur in this model, and the hydrostatic pressure is great enough in the lowest cell to temporarily suppress boiling. This bulk boiling model also caused problems in the trigger and propagation phases, and will be replaced by a surface boiling model for future calculations.

The water/melt mass ratio in the mixture region is thought to be an important parameter for characterizing FCIs because the maximum theoretical efficiency of an explosion, for instance, goes through a peak when the water/melt ratio is varied. The peak occurs at a ratio of 0.5 for thermite-water mixtures at atmospheric pressure. The ratio in the present calculation,

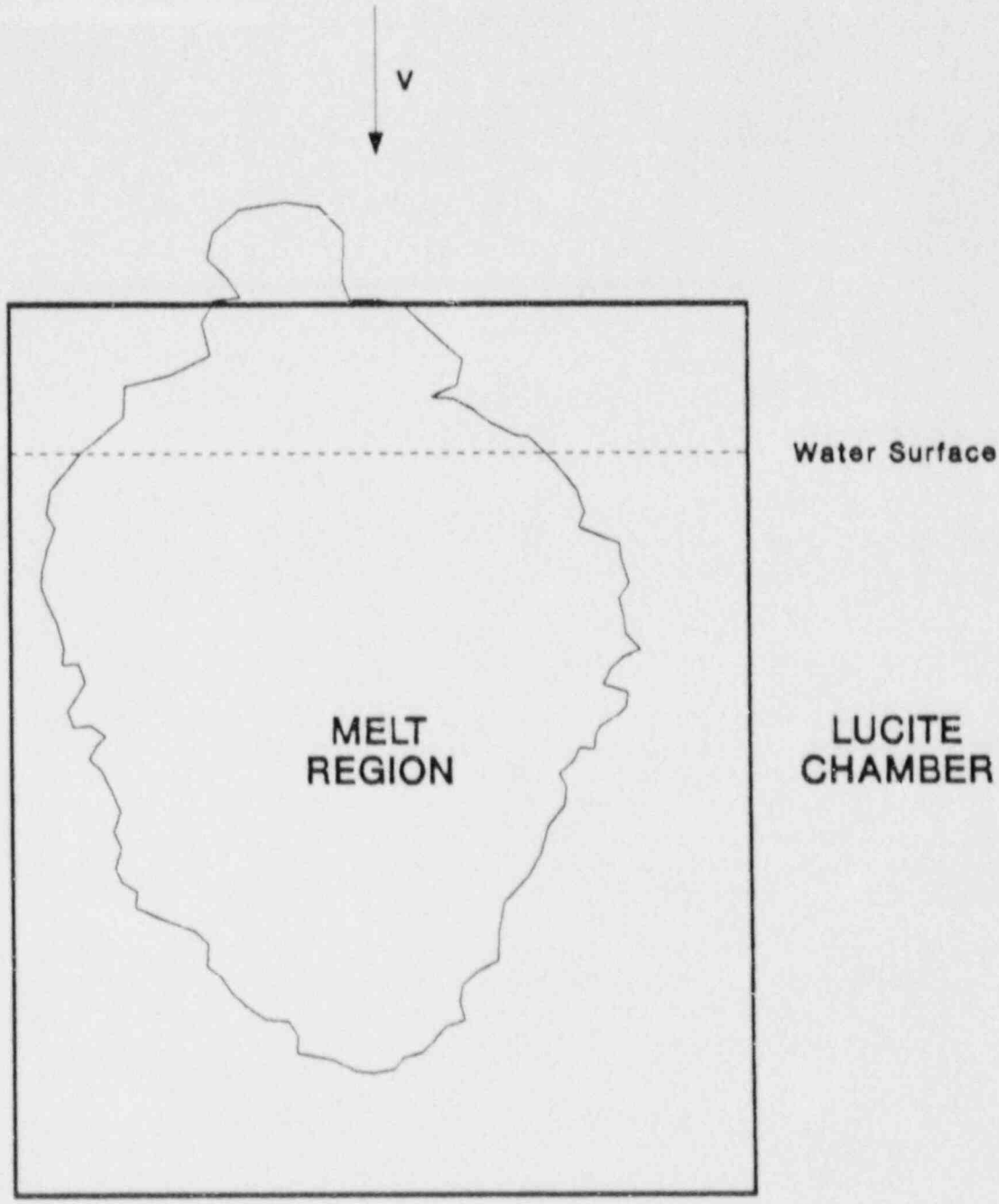

Figure 1.4-14. Melt Outline in FITS Experiment

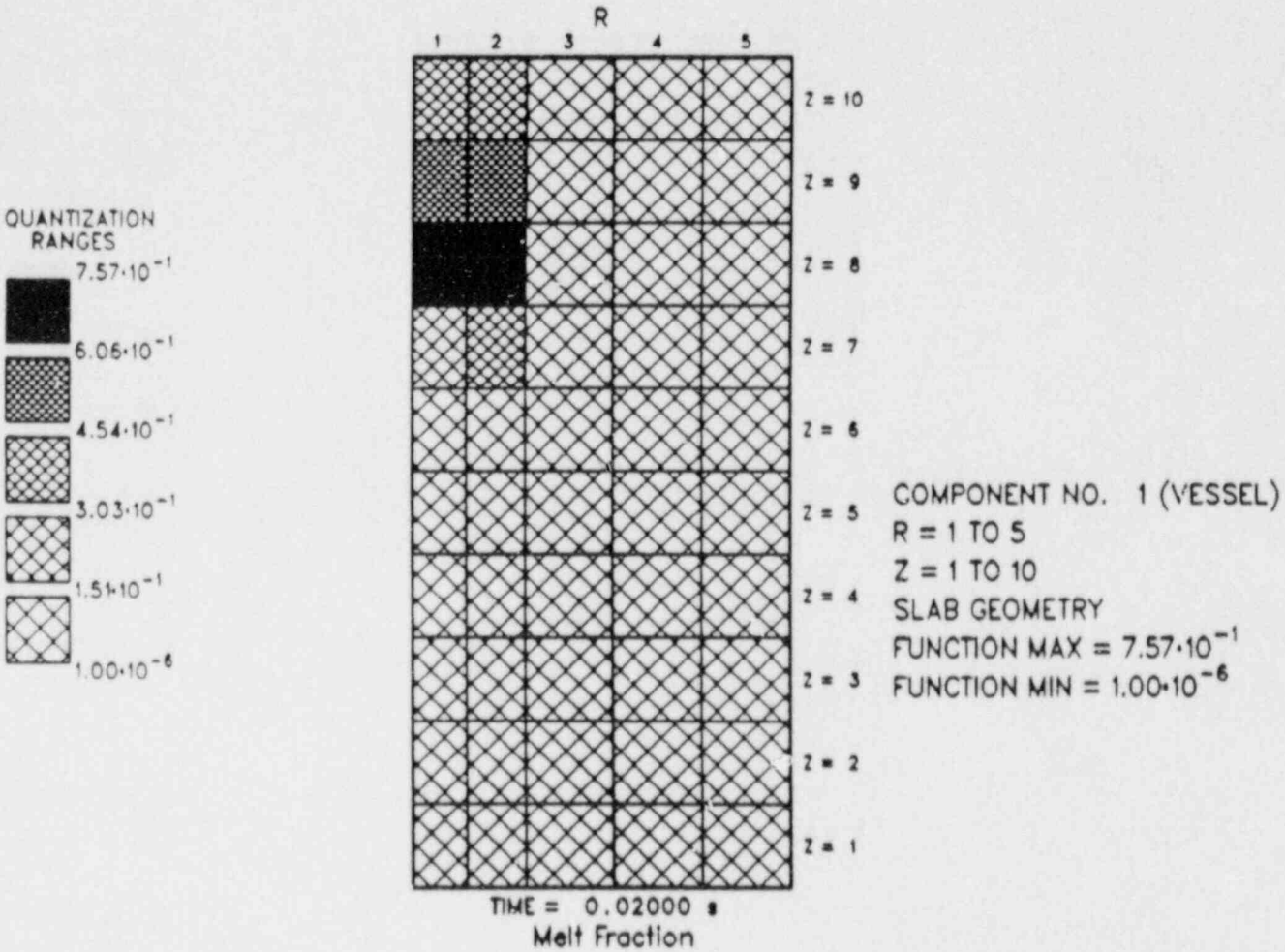

Figure 1.4-15. Melt Volume Fraction at Time 0.02 s

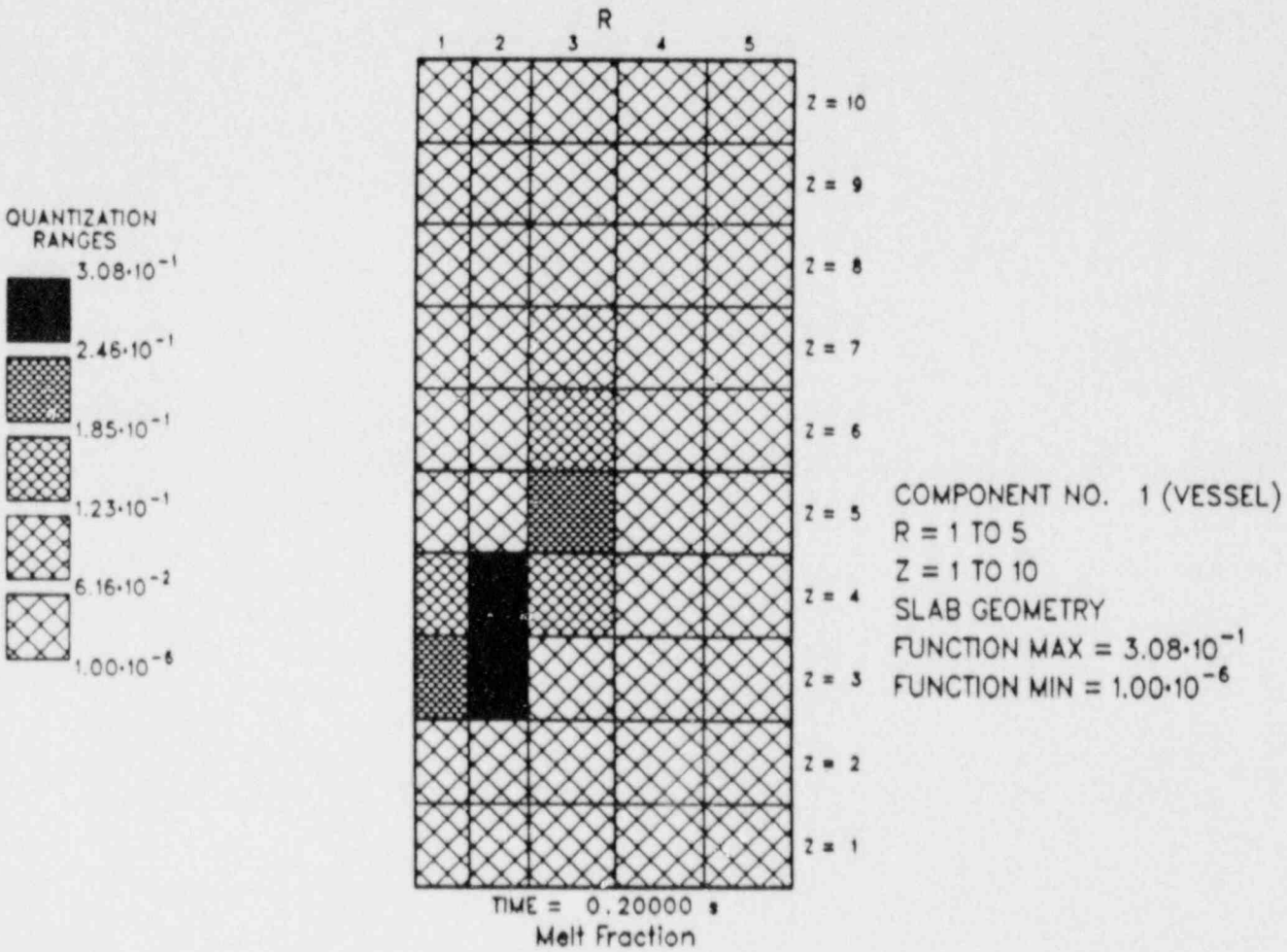

Figure 1.4-16. Melt Volume Fraction at Time 0.2 s

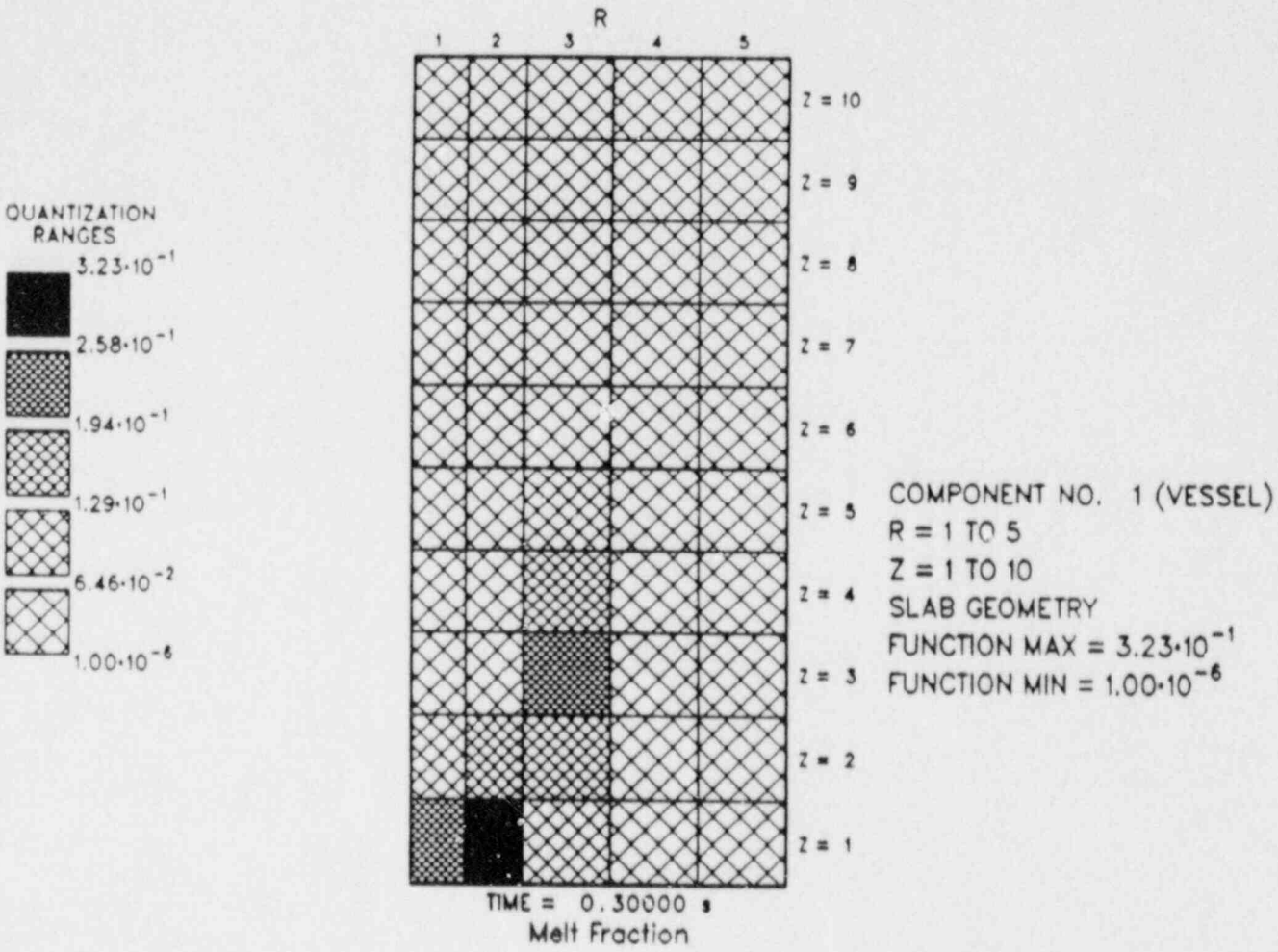

Figure 1.4-17. Melt Volume Fraction at Time 0.3 s

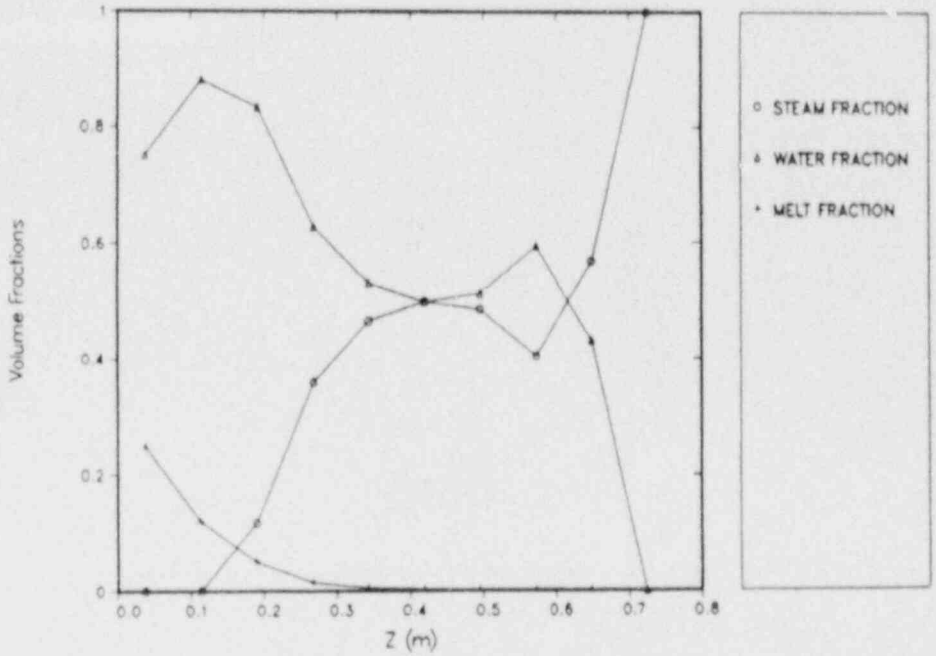

Figure 1.4-18. Volume Fractions of Vapor, Water, and Melt Fields on Problem Center Line Versus Height at Time 0.3 s

determined as the mass-weighted mean of those cells having a melt volume fraction greater than 10^{-6}, is 3. This is in contrast to that calculated experimentally, which sometimes is done by dividing the total water mass in the tank by the total melt mass.[77] (For some experiments, level swell and mixture outline are available from film data, which allows calculation of a more meaningful mass ratio as was done for tests which were analyzed with hydrocodes.[78]) In the present case, this procedure would give a ratio of 8.2. The standard deviation of the mean, also determined using mass-weighting, is ±13.0; the actual range of the mass ratio is from 0.25 to 170. This large range for the FITS-type test problem suggests that the mean mass ratio may not be a very good measure by itself for characterizing the FITS tests.

Another parameter of interest is the steam volume fraction in the mixture region. One common experimental procedure is to use measurements of water level swell to estimate the steam volume fraction in the tank; in the present case, the level swell at 0.3 s is 5.9 cm; this gives a steam fraction of around 0.06 for the entire tank. Estimating the volume of the mixture region from the mixture region outline and then assuming that all of the steam is contained in the mixture is another experimental

approach. For the present case, we get 0.38 for the steam fraction and 0.66 for the water/melt mass ratio when we use Figure 1.4-17 and assume that the cells where the melt volume fraction exceeds 0.07 (the upper limit of the first quantization range) define the mixture outline. The actual mass-weighted steam volume fraction in the mixture region for the test problem is 0.065; the agreement between this value and the level swell measurement is fortuitious because the vapor is, in fact, confined to the mixture region in the IFCI calculation. The volume estimation procedure, while giving a better estimate of the average vapor volume fraction in the observed mixture region, neglects the spatial variation of the mixture components (most of the vapor is contained in the vapor chimney) and results in misleading answers for both the steam fraction and the mass ratio.

The results of the previous paragraph demonstrate the valuable guidance that an integrated code such as IFCI can provide in interpreting experiments. The code results provide an "X-ray" view of the experiment that has proven impossible to obtain solely by instrumentation.

The melt mass mean diameter decreased during the fall from an initial value of 20 cm to a value of around 15 cm at 0.3 s and showed very little spatial variation. This coarse mixing diameter is in agreement with TEXAS predictions of melt breakup using the same initial conditions and the Pilch breakup model. A final mixing diameter of 15 cm is quite large compared to experimental measurements of final debris sizes in the 0.5- to 1-cm range. A diameter of around 1 to 2 cm is sometimes speculated to be the optimum coarse-mixing size to produce strong FCIs during the propagation phase, although this is not actually known.

1.4.3.3 Triggering and Propagation Phase

To simulate the triggering and propagation phase, the mixture was artificially triggered at 0.3 s, roughly when the melt region contacted the bottom of the water chamber. The initial trigger generated high pressures and velocities, which led to a propagating pressure wave through the mixture.

- **Triggering**

The FCI was triggered by introducing a large surface area source in the bottom center node of the problem. The generation rate was such as to decrease the characteristic diameter of the melt in this bottom center node from 10 cm to 100 μm in a time period of 500 μs. The final melt diameter was chosen as typical of observed debris sizes after a FCI. The time period over which fragmentation occurs is based on observed propagation speeds and

reaction zone lengths from FITS tests, but is strictly an estimated number.

Since the trigger appears in the melt transport equation as a surface area source, and the desired effect was a specified change in the melt diameter, some experimentation was necessary to get a source that would give the desired change in diameter. The trigger was set up as a rate of change in the melt diameter:

$$\dot{D}_t = \frac{D - D_f}{\tau} ,$$

where

$\dot{D}_t$ = trigger diameter change rate (m/s),

D_f = final melt diameter (m),

τ = trigger fragmentation period (s).

Thus diameter change rate was applied to the transport equation over a time period of 10 τ, giving roughly an exponential approach to the final diameter over the 10 τ time period.

- **Propagation**

The pressure pulse resulting from the final trigger parameters reached a maximum of about 10 MPa in the trigger cell and nearest neighbors. This level of pressure induced sufficient relative velocity (10 to 20 m/s) to cause very fine fragmentation, resulting in final sizes around 100 μm along the center axis. The pressure and relative velocity died away fairly rapidly with increasing radius, resulting in a distribution of melt diameters that was smallest on the axis and became larger with radius. Figure 1.4-19 shows the radial distribution of melt diameter at a time of 0.31 s (roughly the end of the propagation phase) and an axial level of 19 cm. Although the diameter is around 100 μm on the center axis, the diameters farther away from the axis, in the cells containing the bulk of the melt, are in the 1- to 4-mm range; this diameter is too large to transfer significant heat from the melt to the water over the time scale of the propagation. This relatively low degree of fragmentation suggests that a model for fine fragmentation distinct from the coarse fragmentation model is needed (this is also suggested by some experimental observations[78]). Figure 1.4-20 is a plot of the melt diameter versus radius and axial height at 0.31 s.

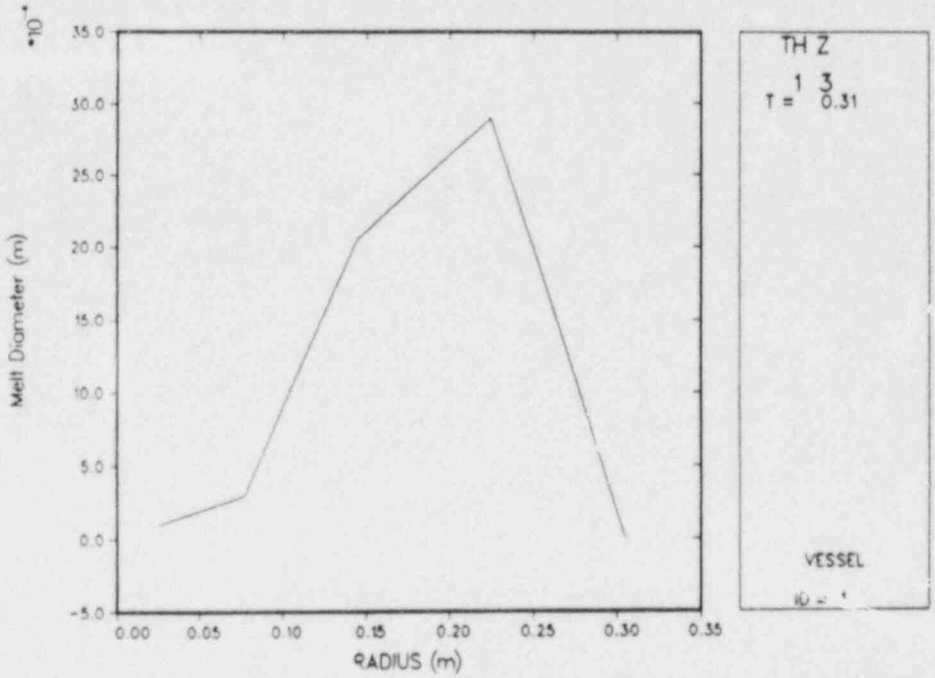

Figure 1.4-19. Melt Characteristic Diameter Versus Radius at Time 0.31 s

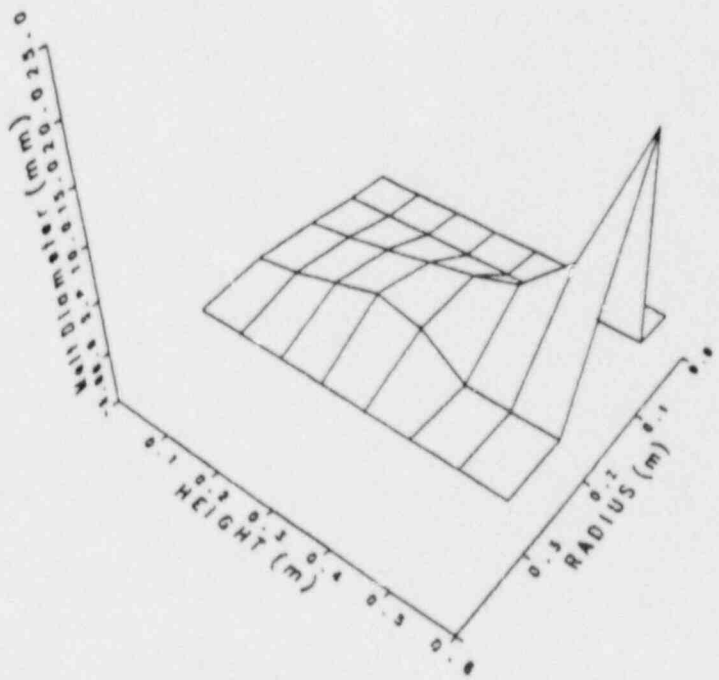

Figure 1.4-20. Melt Diameter Versus Radius and Height at Time 0.31 s

The time at which the propagation phase ended was taken as the time at which the cell farthest from the trigger point and containing a significant amount of melt showed a rapid decrease in melt diameter; this occurred at 0.31 s at the water surface (axial level 8, ring 3), 57 cm from the bottom and 14 cm radially from the center. The speed of propagation varied with local three-phase mixture conditions, ranging from 270 m/s close to the trigger cell (a region containing fairly high volume fractions of melt and liquid water) down to 30 m/s at the top of the steam chimney (a region containing mostly vapor).

Figures 1.4-21 through 1.4-23 are three-dimensional plots of pressure versus r and z, which show the advancing pressure front, at several times during the propagation phase. Note that the level pressure region behind the advancing pressure front is around 2.5 MPa, about one-quarter the magnitude of the initial trigger pulse.

The total internal energy of the melt at 0.3 and 0.31 s was used to determine the energy given up to the water during the propagation phase. From 0.3 to 0.31 s, a period of 10 ms, the energy given up was 2.77 MJ, corresponding to a drop in average melt temperature of 104 K; this amount of energy transfer is not large compared to the theoretical maximum and indicates that a large portion of the melt did not participate in the FCI. These small changes in average melt temperature reflect the large final diameter (1 to 4 mm) for the bulk of the melt. The temperature drop in the melt regions along the center axis, where the final melt diameter was on the order of 100 μm, was 850 K. From 0.31 to 0.32 s, again a 10 ms time period, a further 1.3 MJ was transferred to the water (50 K melt temperature drop).

An estimate of the possible thermal-energy-to-work conversion efficiency of the FCI can be made by assuming that the 850 K drop in melt temperature (which, coincidentally, is about the same as the temperature difference between the initial melt temperature and the arithmetic average of the melting points of the two thermite components, Fe and Al_2O_3) corresponds to the theoretical maximum efficiency of 30 percent. Dividing the average temperature drop of 104 K by 850 K and multiplying by the maximum efficiency then gives an estimated possible conversion efficiency of around 4 percent.

Assuming that all of the melt originally in the trigger cell at time 0.3 s fragmented and experienced an 850 K temperature drop (a good assumption, since convection of melt from the trigger cell over the 500 μs trigger period is only a few percent of the cell mass), the energy given up to the water by the melt in the trigger cell alone was 0.48 MJ, or 17 percent of the total energy transferred, which indicates that the energy of the trigger was only a small fraction of the overall efficiency.

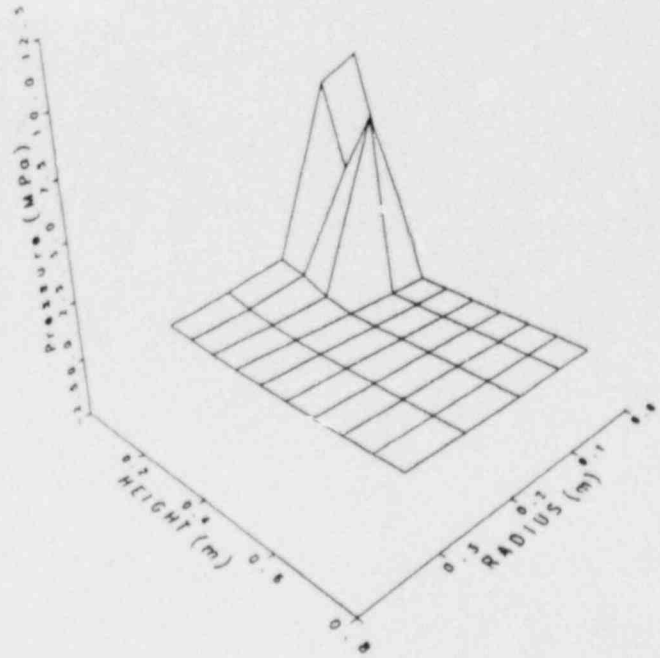

Figure 1.4-21. Pressure Versus Radius and Height at Time 0.302 s

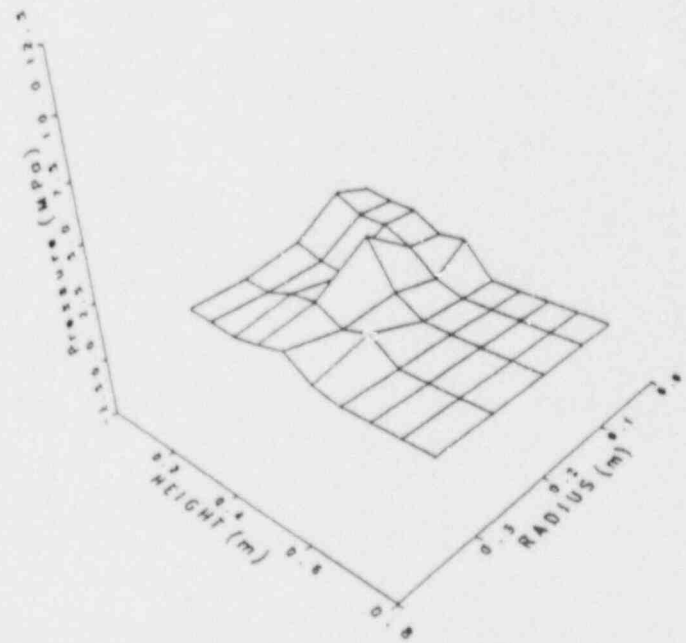

Figure 1.4-22. Pressure Versus Radius and Height at Time 0.304 s

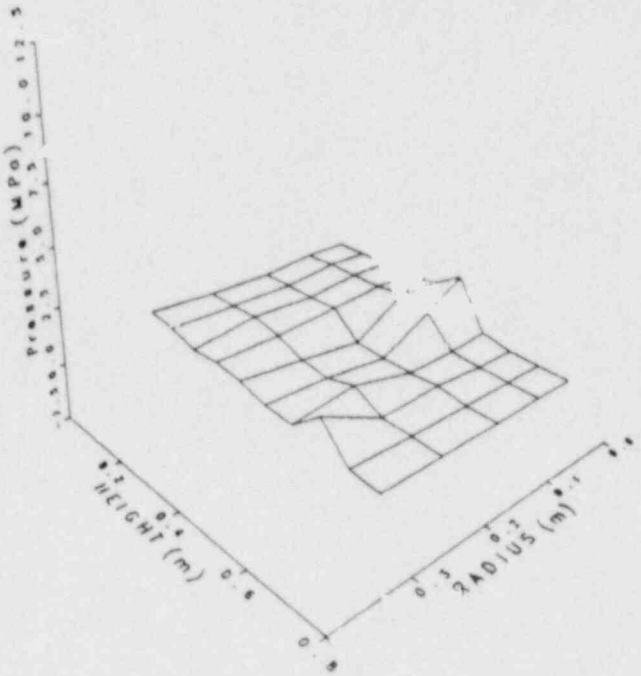

Figure 1.4-23. Pressure Versus Radius and Height at Time 0.306 s

Another estimation method, more in keeping with the procedure used in analyzing the FITS experiments,[77] is to divide the energy given up to the water by the total energy in the melt. Using a specific energy of 2.8 MJ/kg as the thermite melt energy content,[77] a melt mass of 25 kg, and the kinetic energy of the system at 0.31 s,we get we get a thermal-energy-to-work conversion ratio of 0.03 percent, or about one-hundredth of what is found using the thermal estimation procedure. If we consider only the energy available between melt initial temperature and the average melting point (around 1850 K), the conversion ratio is 0.1 percent, which would still be considered a nonexplosion experimentally. The actual energy-to-work conversion ratio lies between the thermal estimation (an upper limit) and the kinetic estimation (a lower limit).

The melt size distribution was derived at 0.31 s, the end of the propagation phase, by binning the melt mass and diameter in each cell into size ranges corresponding to standard sieve sizes used for sieving debris, normalizing with the total melt mass, and dividing by the size range for each bin.[80] The resulting size distribution function is shown in Figure 1.4-24, along with the debris distribution from the FITSOD test, an experiment which did not explode, but did have an "eruption."[75] Since the IFCI problem does not seem to represent a strong FCI, this comparison is more preferable than comparing to a test with a strong explosion.

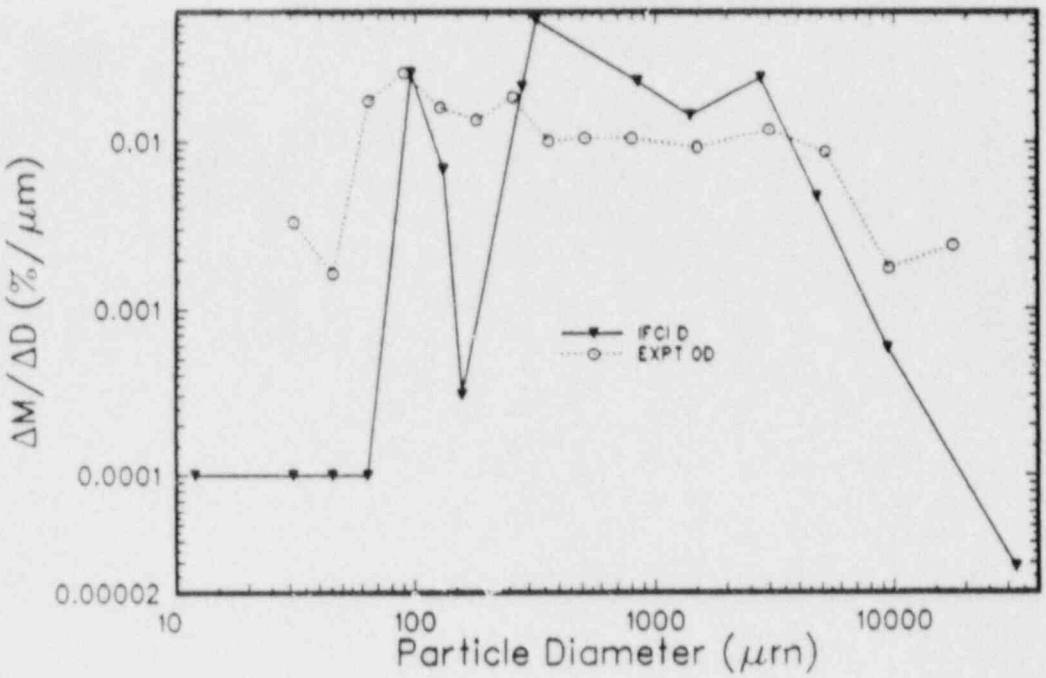

Figure 1.4-24. Melt Size Distributions From IFCI Problem and FITSOD Posttest Debris

The distributions match fairly well over the entire range of debris sizes, although some of the smaller sizes are absent from the IFCI results. The absence of the very small sizes (below 50 μm) is possibly due to the lack of a Kelvin-Helmholtz stripping model in IFCI or a more energetic propagation, which would produce very fine fragments. The lack of sizes between 100 μm and 300 μm probably reflects a need for a fine fragmentation propagation model, distinct from the coarse breakup model. The peak in the IFCI distribution at 100 μm is probably from the trigger event, a judgment which is supported by noting that the amount of mass represented by the peak (sizes below 212 μm) is 1 percent of the total melt mass, which is comparable to the amount of melt contained in the trigger cell at the start of the propagation phase (2 percent). The rest of the particles are in a fairly flat distribution from 300 μm to 2.5 mm. There is a peak in the FITSOD data in the largest bin (2.5 cm and larger) that is not present in the IFCI test; this discrepancy probably means that the main pressure event in the IFCI test (the trigger at the bottom) did a better job of fragmenting the remaining melt than the main event in FITSOD (an eruption at the water surface).

Comparisons of the IFCI results to the other tests in the FITS "D" series are shown in Figures 1.4-25 through 1.4-27. Only test

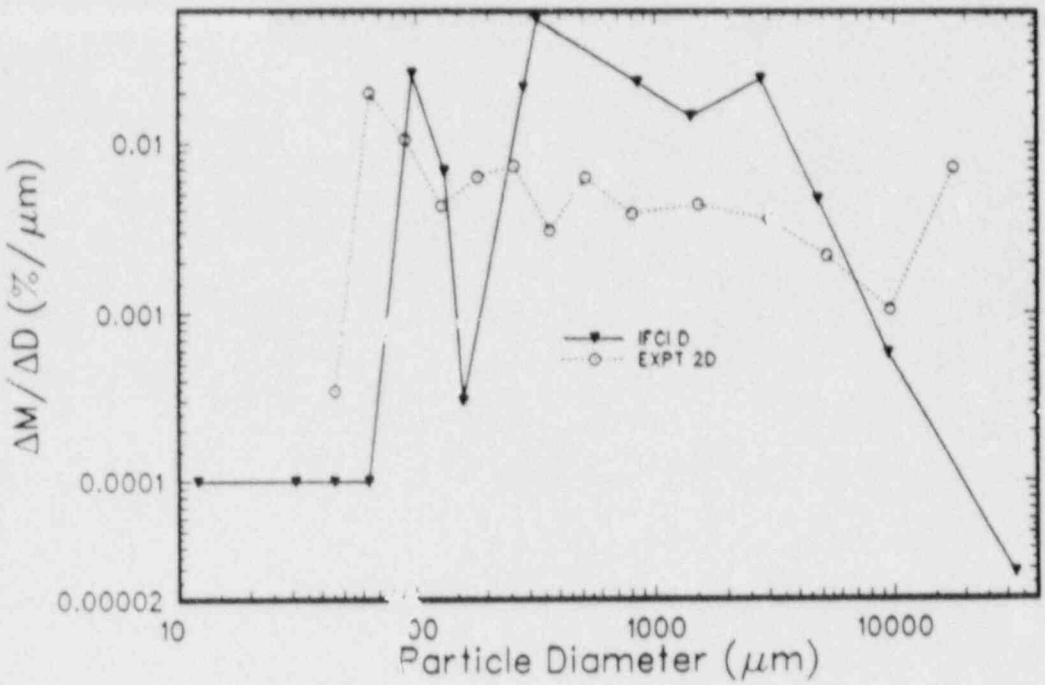

Figure 1.4-25. Melt Size Distributions From IFCI Problem and FITS2D Posttest Debris

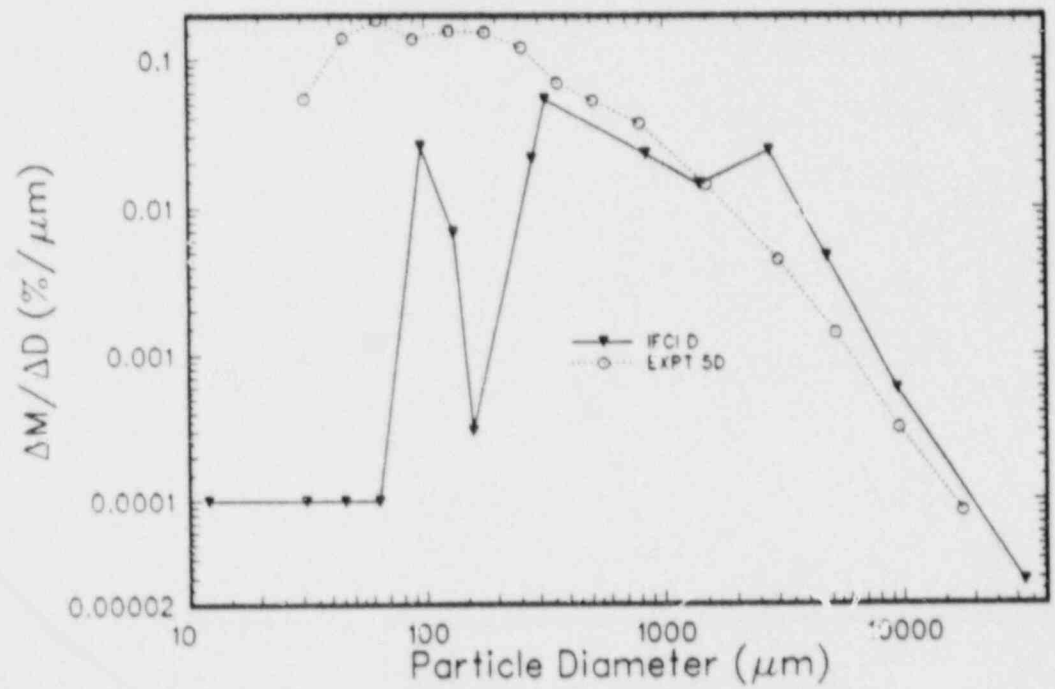

Figure 1.4-26. Melt Size Distributions From IFCI Problem and FITS5D Posttest Debris

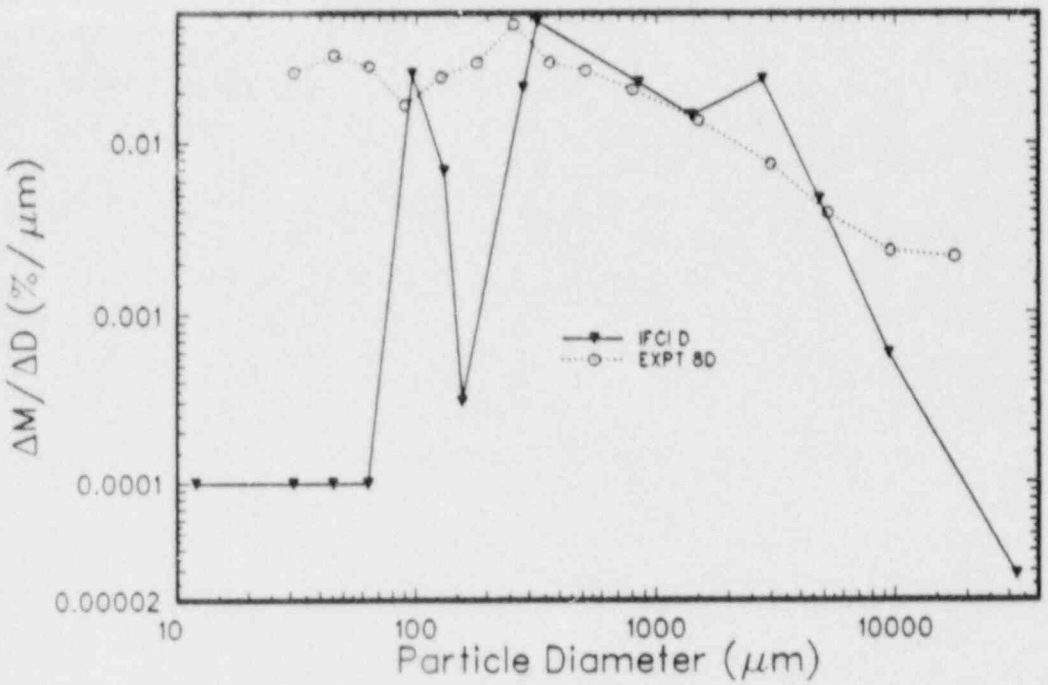

Figure 1.4-27. Melt Size Distributions From IFCI Problem and FITS8D Posttest Debris

FITS5D resulted in a steam explosion; the other tests involved only coarse fragmentation. Inspection of the distributions shows that the IFCI result is most similar to the FITS5D test for the larger particle sizes, although all tests have more very small sizes than were produced by the IFCI calculation.

Another measure of explosion efficiency can be derived from the distribution data as a check on that estimated from the temperature drop data. This is done by using Bird's 280 μm cutoff criterion[81] to estimate that part of a fuel melt that participates in a steam explosion. If we apply this criterion to the IFCI size distribution, 3 percent of the melt mass is below 300 μm in diameter and 9.7 percent is below 425 μm (these are the sizes of two neighboring sieves). Using the smaller diameter as a cutoff would give an overall efficiency of 1 percent (assuming 30 percent as the maximum) compared to the thermal result of 4 percent. Using the next larger sieve size as the cutoff gives an efficiency of 3 percent; this somewhat arbitrary cutoff criterion is in fair agreement with the thermal estimation procedure.

Also derived for the IFCI data were the various length scales normally used to characterize debris experimentally, which include the Sauter mean diameter, mass median, length mean, surface mean, and volume mean[80]. The two most common length

scales are the Sauter mean diameter, which is the diameter of a particle that has the average volume per unit surface area, and the mass median diameter, which is the diameter for which 50 percent of the mass has an equal or smaller diameter. These two length scales for the IFCI data are shown in Table 1.4-8, along with results from the FITS "D" series.

Table 1.4-8

Length Scales From IFCI and FITS "D" Series

Test	Event[a]	Sauter Mean Diameter (mm)	Mass Median Diameter (mm)
IFCI	SE	1.26	4.0
FITS0D	NE(ER)	1.50	4.6
FITS2D	NE(BC)	3.10	16.0
FITS5D	SE	0.25	0.48
FITS8D	NE(ER)	0.81	3.40

[a]NE - no explosion, SE - steam explosion, BC - bottom contact, ER - eruption

Results from the IFCI test are similar to those from the FITS nonexploding experiments, which had an eruption, bearing out the observation that the IFCI result seemed to be a weak steam explosion. The FITS2D experiment, which was nonexplosive, had a Sauter mean twice that of those that "erupted," plus, and probably more significantly, a mass median four times those that erupted. The single steam explosion experiment, FITS5D, had both a Sauter mean and mass median ten times smaller than those that erupted.

1.4.3.4 Discussion of Results

The results of the IFCI test calculation are very encouraging; the IFCI results are similar to the experimental results from the nonexploding FITS-D experiments. The shape of the melt as it falls through the water, the propagation speed of the pressure front through the melt, and the final melt size distribution all match those seen in the experiments. This would seem to indicate that IFCI is doing a good job of simulating the major phenomena

occurring during the FCI process, particularly those operative during the coarse-mixing phase. This gives confidence that IFCI can eventually be used as a predictive tool for FCIs for which no experimental data is available, notably, those which may occur at reactor scale in a reactor geometry. Results are expected to improve for a finer computational grid.

The present calculation represents the first simulation of the complete FCI process in two dimensions, including dynamic fragmentation. Both two dimensions and dynamic fragmentation appear necessary for a code to correctly simulate the coarse-mixing phase, and the presence of these two key features greatly aids the simulation of the propagation and expansion phases without having to make simplifying assumptions.

A steam chimney was observed to form during the coarse-mixing phase, which lends credence to the hypothesis that the steam chimney is also present during actual experiments. This is the first time such a chimney has been observed during a numerical calculation of an FCI.

The ability of IFCI to provide detailed information about experimental features that are difficult or impossible to observe experimentally was demonstrated by, for instance, the calculation of the actual water/melt mass ratio from the IFCI output (3.0), versus that available from experimental observation (8.2).

The IFCI test calculation also revealed some modeling problems; an important one is the bulk boiling model in MELPROG. This model introduces time delays between the introduction of melt into a cell and the commencement of boiling, which is somewhat noticeable during the coarse-mixing phase in the lower cells of the problem, and is probably affecting the results significantly during the propagation phase. There is, for instance, a 1 to 3 ms delay from the time at which the trigger is applied to the time at which the initial pressure spike occurs. The magnitude of the propagated pressure front is, also, not as large as that observed during strong FCIs; this, together with the final particle size distributions, characterize the present calculation as an eruption rather than an explosion.

The bulk boiling model will be replaced at the start of the next phase of IFCI development with a surface boiling model, probably patterned after that used by Bohl[74] in his calculation of FCIs using SIMMER-II.[82] In Bohl's study, the use of a surface boiling model greatly increased the magnitude of the pressure in the FCI region over that seen with a bulk boiling model; the pressure pulse also had a much shorter rise time with the surface boiling model.

Since Bohl did not use a dynamic fragmentation model (the melt was prefragmented) and did determine the heat transfer coefficient between melt and water parametrically, his study does not

give a complete indication of how a surface boiling model would affect the propagation phase results in IFCI. The likely effect will be large propagation pressures, with accompanying finer fragmentation. Whether these effects are enough to duplicate the characteristics of a strong FCI remains to be seen. It also seems likely that a different model must be included for the reaction zone, corresponding to the intimate melt-water contact and different fine fragmentation mechanism postulated for this phase of the FCI process.[79,83,84]

1.4.3.5 Future Work

Future work will, first, repeat the present problem using a surface boiling model; the problem will then be repeated using a finer finite-differencing mesh.

The next major calculation using IFCI will be to calculate jet mixing, probably using the IJET and EJET[85] tests for experimental comparison. The calculation of jet mixing is a crucial step in the eventual use of IFCI as a predictive tool in reactor safety; the jet geometry is the more probable FCI configuration in a reactor accident, rather than that of FITS, which uses a blob of melt dropped into a tank of water. The jet results will be repeated using corium properties in the melt rather than thermite, although it is not expected that the change in melt properties will make any significant difference in the results.

Besides the replacement of the boiling model, a fine fragmentation model for the propagation phase will be added to IFCI. Other enhancements to IFCI will include adding drop entrainment to the coarse fragmentation model, extension of the surface area transport algorithm to allow a melt size distribution within a cell, and adding a hydrogen generation model.

The final goal is to use IFCI as a predictive tool for the calculation of possible FCIs in a reactor geometry. IFCI should be singularly well-suited for this use, since IFCI is based on MELPROG and can thus calculate its own initial conditions for various postulated accidents.

1.5 Hydrogen Behavior

(D. W. Stamps and M. Berman, 6427)

The major concerns regarding hydrogen in LWRs are that the static or dynamic pressure loads from combustion may breach containment or that important, safety-related equipment may be damaged due to either pressure loads or high temperatures. In order to assess the possible threats, it is necessary to understand how hydrogen is produced, how it is transported and mixed within containment, and how it combusts.

The objectives of this program are (1) to quantify the threat to nuclear power plants (containment structure, safety equipment, and the primary system) posed by hydrogen combustion, (2) to disseminate information on hydrogen behavior and control, and (3) to provide programmatic and technical assistance to the NRC on hydrogen-related matters.

1.5.1 Oxidation of Combustible Gases in the Reactor Cavity

1.5.1.1 Introduction

For those severe core-meltdown accidents in which the reactor cavity is dry, the temperatures of the reactor cavity atmosphere and structures following vessel failure may be sufficiently high to promote in-cavity oxidation of combustible gases produced by core-concrete interactions. Specifically, hydrogen and carbon monoxide may react with available oxygen near the heated structures to form steam and carbon dioxide. Complete in-cavity oxidation would prevent any accumulation and subsequent combustion of hydrogen and carbon monoxide in the lower and upper compartments, and the probability of early containment failure due to combustion would be minimal. However, the degree of in-cavity oxidation will be limited by the rate at which oxygen is transported into the reactor cavity region (relative to the rate at which combustible gases are produced), or the oxidation may be precluded by high steam concentrations or low temperatures in the reactor cavity that may exist in flooded-cavity sequences. Most affected by this in-cavity oxidation phenomenon are sequences in large, dry ice-condenser and Mark III containments in which the reactor cavity is dry.

In the IDCOR analysis of the severe accident involving hydrogen combustion using the MAAP code,[86,87] a complete in-cavity oxidation of combustible gases produced from core-concrete interactions was always predicted. This prevented any accumulation and subsequent combustion of combustible gases in the upper and lower compartments. However, in the HECTR analyses of the in-cavity oxidation problem in a PWR ice-condenser containment for a S2HF accident (Figure 1.5-1), we have found that the in-cavity oxidation process is limited by the rate at which oxygen is transported into the reactor cavity region.[88,89] Accumulation and subsequent combustion of hydrogen and carbon monoxide in the upper and lower compartments generate a peak pressure of 384 kPa (56 psig) at 7.4 h. Hence we conclude that assuming a complete in-cavity oxidation is overly optimistic because a variety of phenomena, such as steam inerting and oxygen transport by natural convection, may influence the degree of this in-cavity oxidation that takes place. In the present study in which HECTR calculations have been compared with MAAP calculations, we have performed additional sensitivity studies to better understand the behavior of the combustible gases produced from core-concrete interactions.

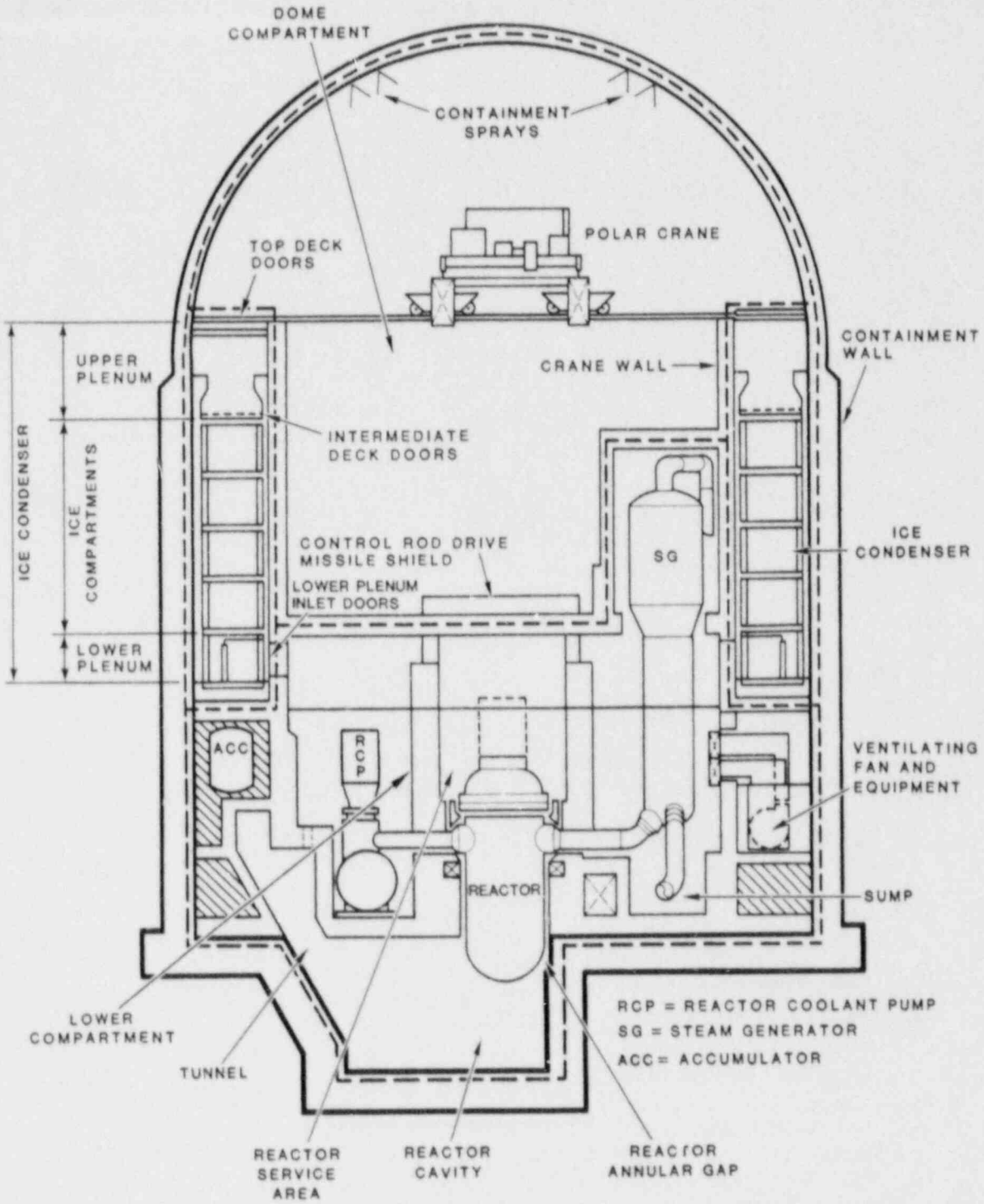

Figure 1.5-1. Simplified Diagram of Ice-Condenser Containment

These new HECTR calculations were performed to analyze the containment responses with respect to each of the following conditions:

1. Oxidation of any combustible gases in the reactor cavity is impossible because of unfavorable situations like flame blowoff or temperature in the cavity below the autoignition temperature.

2. High steam content exists in the cavity and 55 percent steam concentration will prevent any further in-cavity oxidation.

3. For an unexplained reason, the air-return fans have been turned off.

4. The CORCON code is used instead of the MAAP code to predict gas release rates from core-concrete interactions.

1.5.1.2 No Oxidation of Combustible Gases in the Cavity

The oxidation of combustible gases in the reactor cavity is a complex process that requires detailed study of the combustion phenomenon at temperatures above 1000 K. In the past, accident analysts studying containment responses with respect to hydrogen combustion either neglected the in-cavity oxidation process by assuming no reaction as in Reference 90 or simplified the process by assuming a complete reaction as in Reference 87. Under certain circumstances, oxidation of any combustible gases in the cavity may not be possible because of other considerations such as the flame being blown off because of the instability problem, or ignition may not be possible because the bulk gas temperature in the cavity is below the autoignition temperature of the lean hydrogen-air-steam mixture. Autoignition temperature of the hydrogen-air-steam mixture has not been well established at temperatures above 1000 K. Because of this concern, we will look into the situation where oxidation of any combustible gas in the cavity is impossible and study containment responses when burning occurs in the lower and upper compartments. In the other extreme situation, assuming a complete oxidation in the cavity has already proved to be overly optimistic because a variety of phenomena like oxygen transport and steam inerting may influence the degree of in-cavity oxidation[89].

The new HECTR analysis shows that, similar to complete in-cavity oxidation, neglecting any oxidation in the reactor cavity may not be a conservative assumption either, if our concern is the maximum pressure loading on containment. For the S2HF accident in a PWR ice-condenser containment, pressure and gas temperature generated from the global burn in the lower and upper compartments could be higher for the case with partial in-cavity

oxidation than for the case with no in-cavity oxidation (see Figures 1.5-1 through 1.5-5). One explanation for the prediction of a higher pressure for the case with partial in-cavity oxidation is that the oxidation of combustible gases in the cavity will increase the initial pressure before the global burn. Since the peak-to-initial pressure ratios with respect to lean combustion are almost the same for different initial pressures in our range of interest, the peak pressure will be higher when the global burn begins in the lower compartment and completes in the upper compartment. It should be noted that in this accident sequence igniters are working and burns are initiated at the time when the concentration of the combustible gases reaches 7 percent[88].

1.5.1.3 Influence of Steam Inerting

The effect of steam inerting on the oxidation of combustible gases in the cavity could be very important under certain conditions, even though HECTR results of the 12-compartment model did not show it. These two bounding calculations, using the 12-compartment model, show that the degree of in-cavity oxidation is limited by either the oxygen transported into the cavity or the high steam content in the cavity[89]. Both calculations predict that accumulation and global burn of combustible gases will occur in the upper and lower compartment due to insufficient oxygen being transported into the reactor cavity. However, if there is sufficient oxygen being transported into the reactor cavity to support complete oxidation of the combustible gases, the effect of steam inerting would become more important. In order to prove this, we shall consider the HECTR calculation in which a complete oxidation in the cavity is predicted. This calculation uses the 6-compartment model and totally neglects the steam inerting effect. Now we shall repeat the same calculation except to include the steam inerting effect by enforcing a criterion such that a diluent concentration above 55 percent will preclude any in-cavity oxidation. Because of insufficient experimental data on the flammability limits of hydrogen-air-steam-carbon monoxide-carbon dioxide mixtures at temperatures above 1000 K, the flammability limit at the temperature of 400 K is used. This implies that in-cavity oxidation of combustible gases will be suppressed if the diluent concentration is above 55 percent.

For the case neglecting the steam inerting effect, a complete in-cavity oxidation would be predicted and no accumulation and subsequent combustion of hydrogen and carbon monoxide would occur in the upper and lower compartments. However, for the case including the steam inerting effect, an incomplete in-cavity oxidation and a global burn could occur. This would lead to a much higher peak pressure than the case excluding the effect, 399 versus 220 kPa (Figures 1.5-5 and 1.5-6). Thus the steam inerting effect could be substantial.

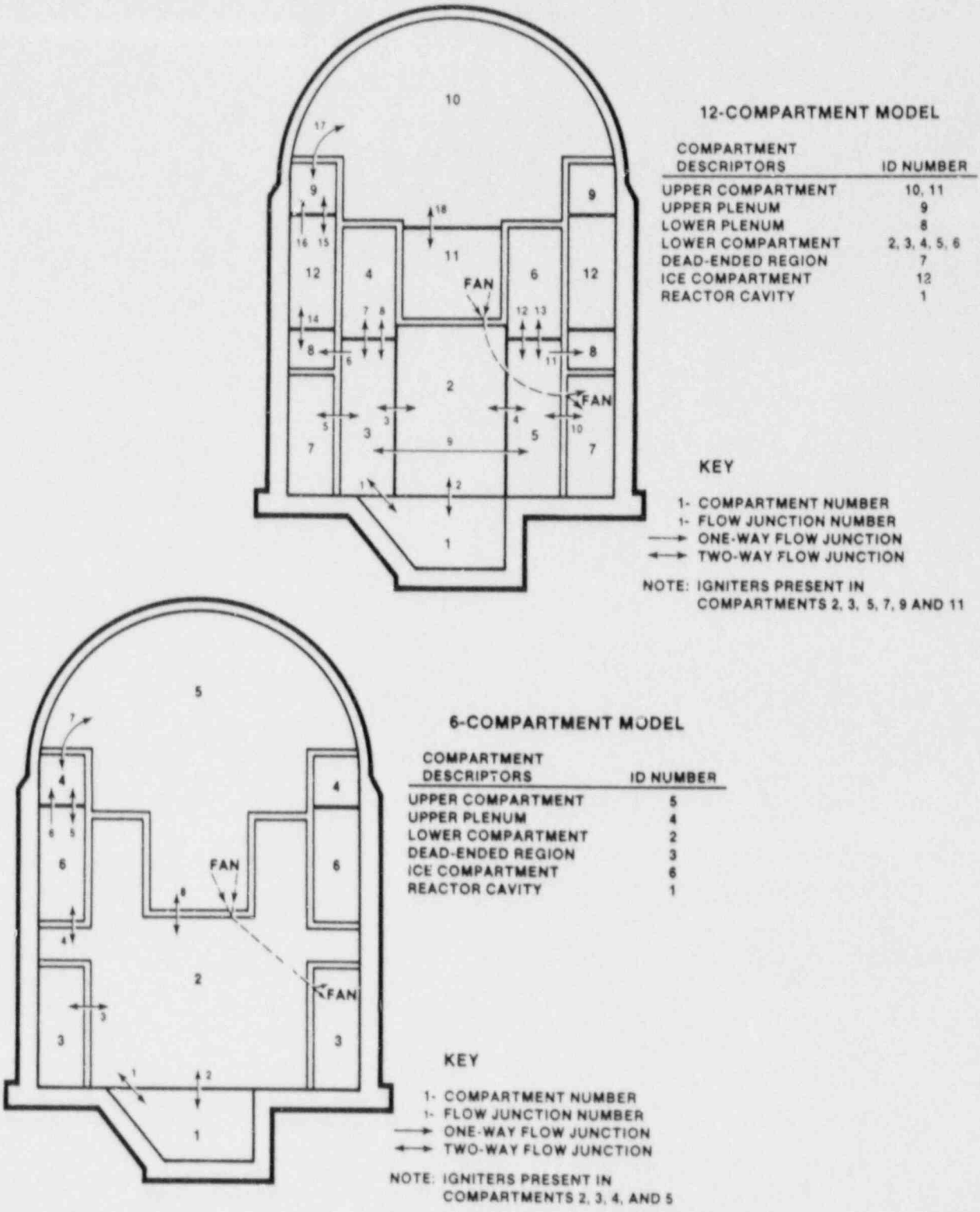

Figure 1.5-2. Containment Noding Systems Used in HECTR Analyses of the In-Cavity Oxidation Problem (12-Compartment Model Versus 6-Compartment Model)

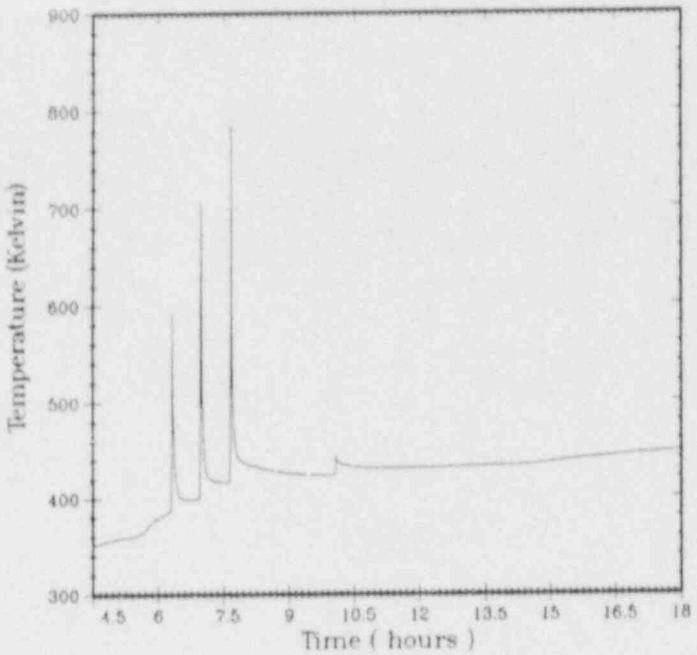

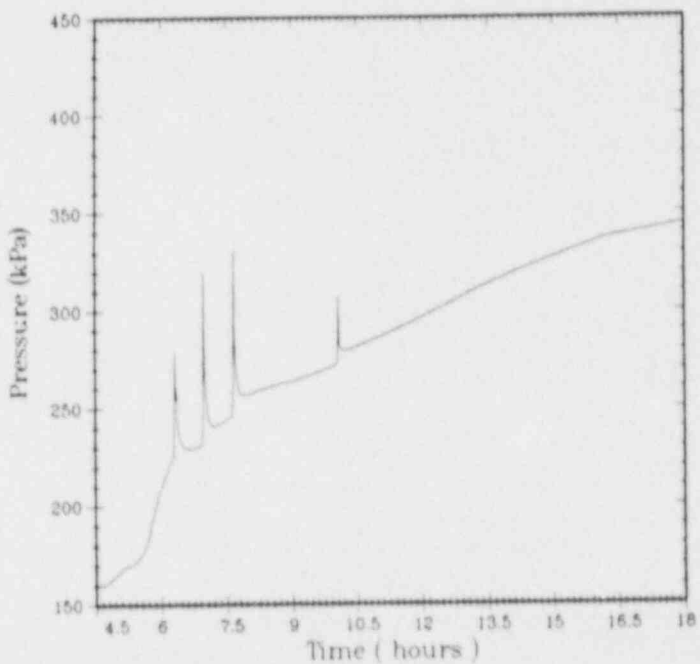

Figure 1.5-3. Pressure and Temperature Responses in the Upper Compartment Predicted by HECTR (Conditions Given: No Oxidation Takes Place in the Reactor Cavity)

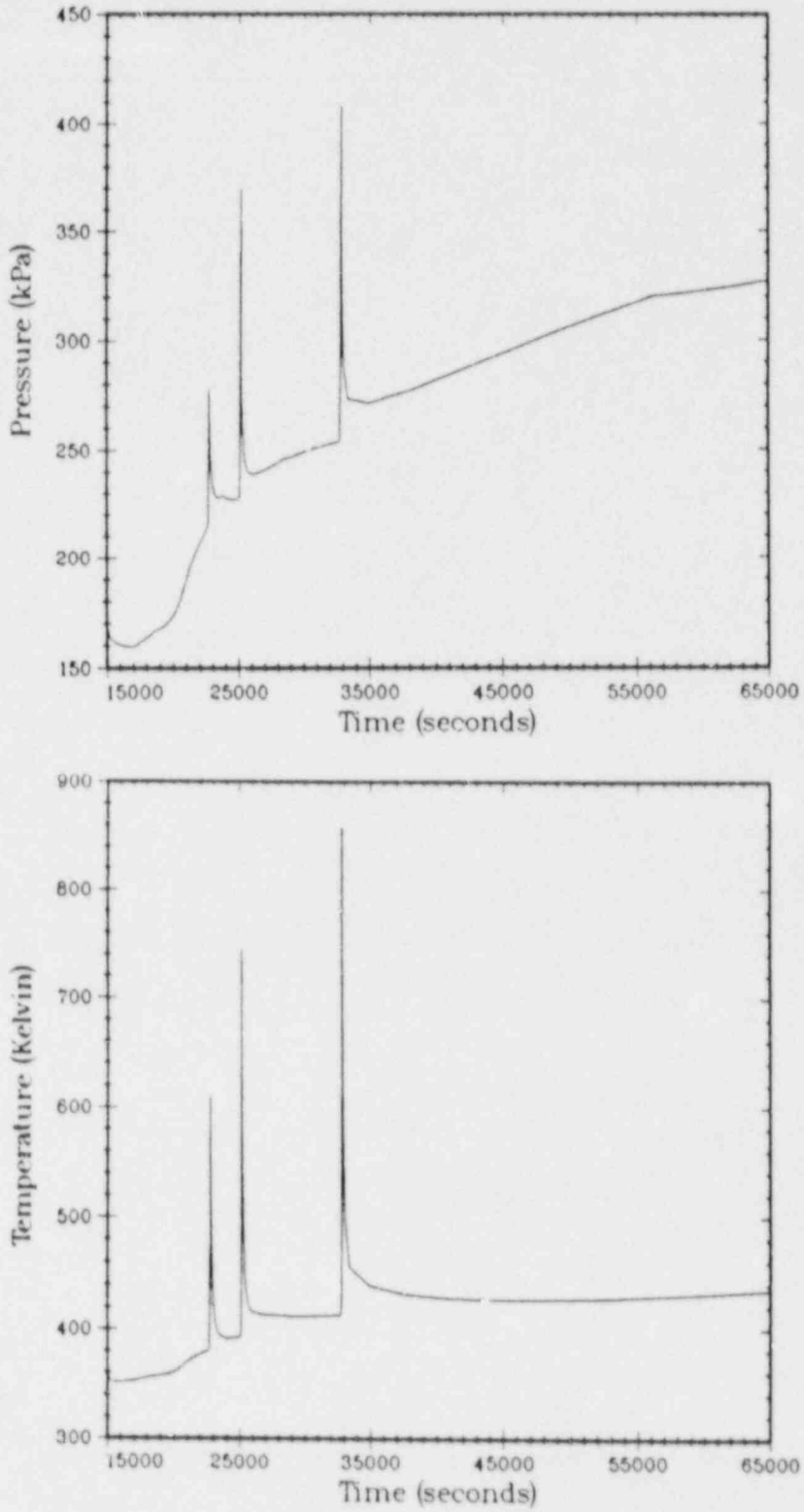

Figure 1.5-4. Pressure and Temperature Responses in the Upper Compartment Predicted by HECTR (Conditions for In-Cavity Oxidation: $O_2 \geq 5$ Percent, Steam ≤ 55 Percent)

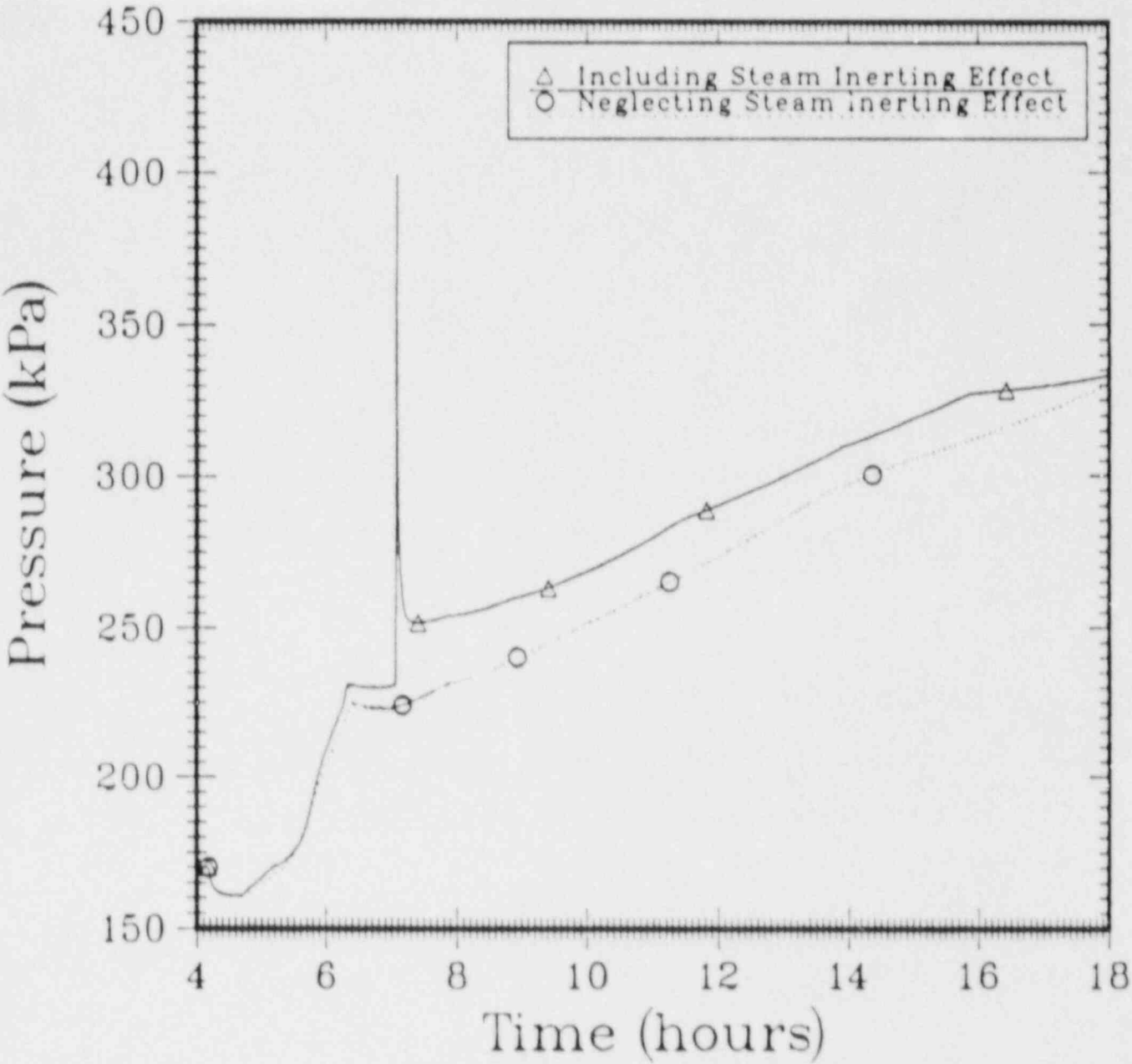

Figure 1.5-5. Pressure Responses in the Upper Compartment Predicted by HECTR (6-Compartment Model)

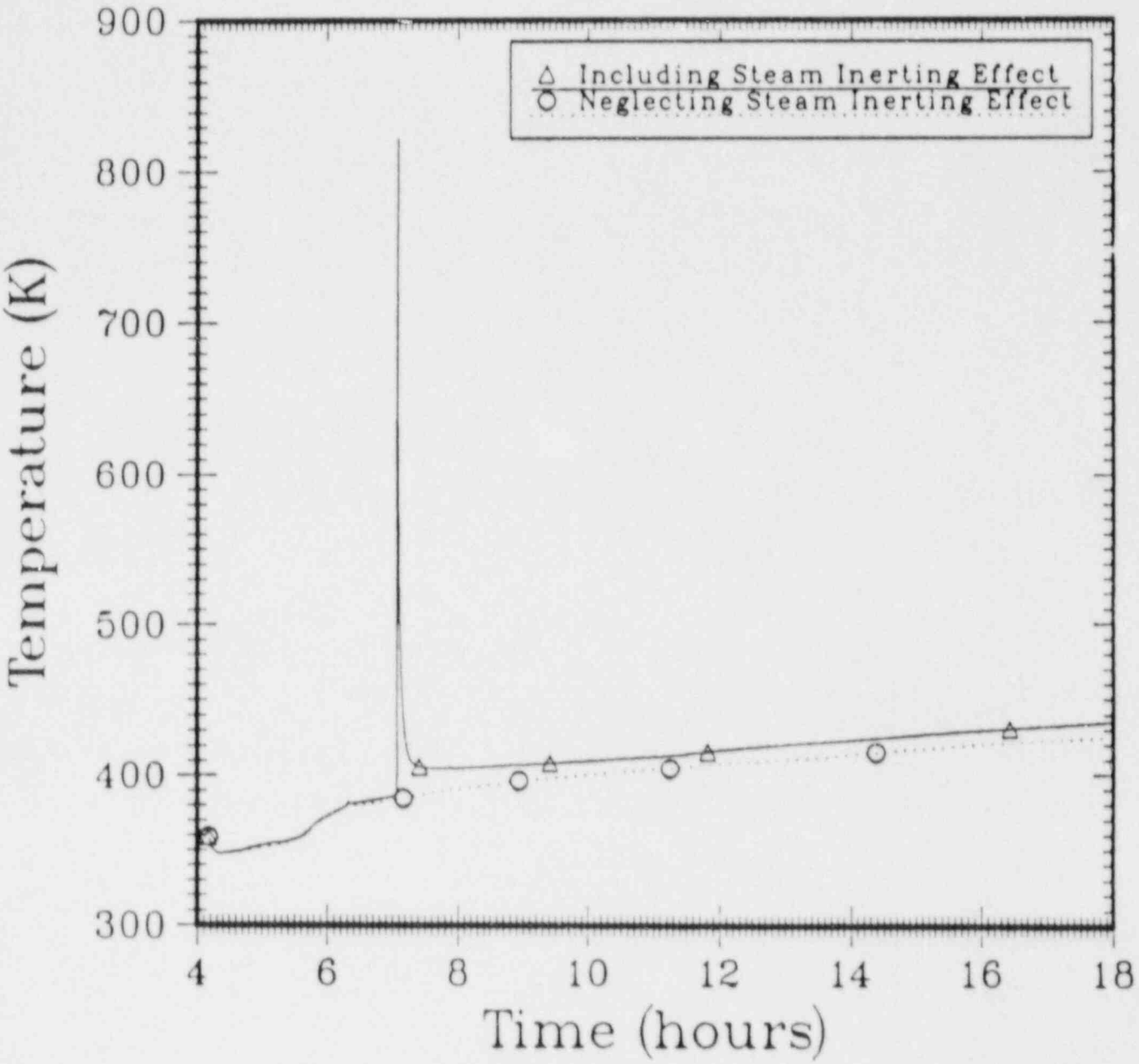

Figure 1.5-6. Temperature Responses in the Upper Compartment Predicted by HECTR (6-Compartment Model)

1.5.1.4 Condition With Air-Return Fans Off

All the HECTR calculations performed so far have the air-return fans operating at a 100 percent capacity. The fans circulate air between the upper and lower compartments. The forced convective flow path is as follows: lower compartment, lower plenum, ice condenser, upper plenum, upper compartment, annular region, and back to lower compartment. When core-concrete interactions are taking place in the reactor cavity, the plume of hot gases, which are convecting out of the reactor cavity into the lower compartment, will be drawn mostly into the upper compartment through the ice condenser by the fans. HECTR predictions show that the hot plume is unlikely to mix well with other gases in the lower compartment. Thus the next sensitivity study will be on the effect of the air-return fans on the mixing process in the lower compartment.

If the air-return fans are turned off during the accident, HECTR predicts that more mixing would take place in the lower compartment. Still the temperature and gas composition distributions within the lower compartments were far from being uniform. Figure 1.5-7. The positive result of switching off the fans is that less combustible gases were predicted to exist in the the upper compartment. Most of the combustible gases remained in the lower compartment. Hence ignition occurred at an earlier time and involved a lesser amount of combustible gases. Only one global burn, which started in the lower compartment and propagated into the upper compartment, and 13 local burns in the upper plenum were predicted. After the completion of the global burn, the lower compartment became steam inerted. Subsequently, only local minor burns appeared in the upper plenum. Eventually, the containment ran out of oxygen to support any more combustion. The peak calculated pressure was 266.2 kPa (38.61 psi) at 9.3 h (Figure 1.5-8).

The above sensitivity study shows that the forced convective current induced by the air-return fans would transport more combustible gases into the upper compartment and enhance less mixing in the lower compartment. Therefore, the burn in the fans-on case is more severe than the fans-off case.

1.5.1.5 Gas Release Rates Predicted by the CORCON Code

In all these analyses of oxidation of the combustible gases in the cavity using the HECTR code, the gas release rates from core-concrete interactions were predicted by the MAAP code as a follow-up work of the standard problem. However, MAAP predictions of the timing and release rate of gases generated from core-concrete interactions for the S2HF accident in a PWR ice-condenser containment were suspect. In order to assess MAAP predictions of gases released from core-concrete interactions, we have used the CORCON code to calculate the gas release rates

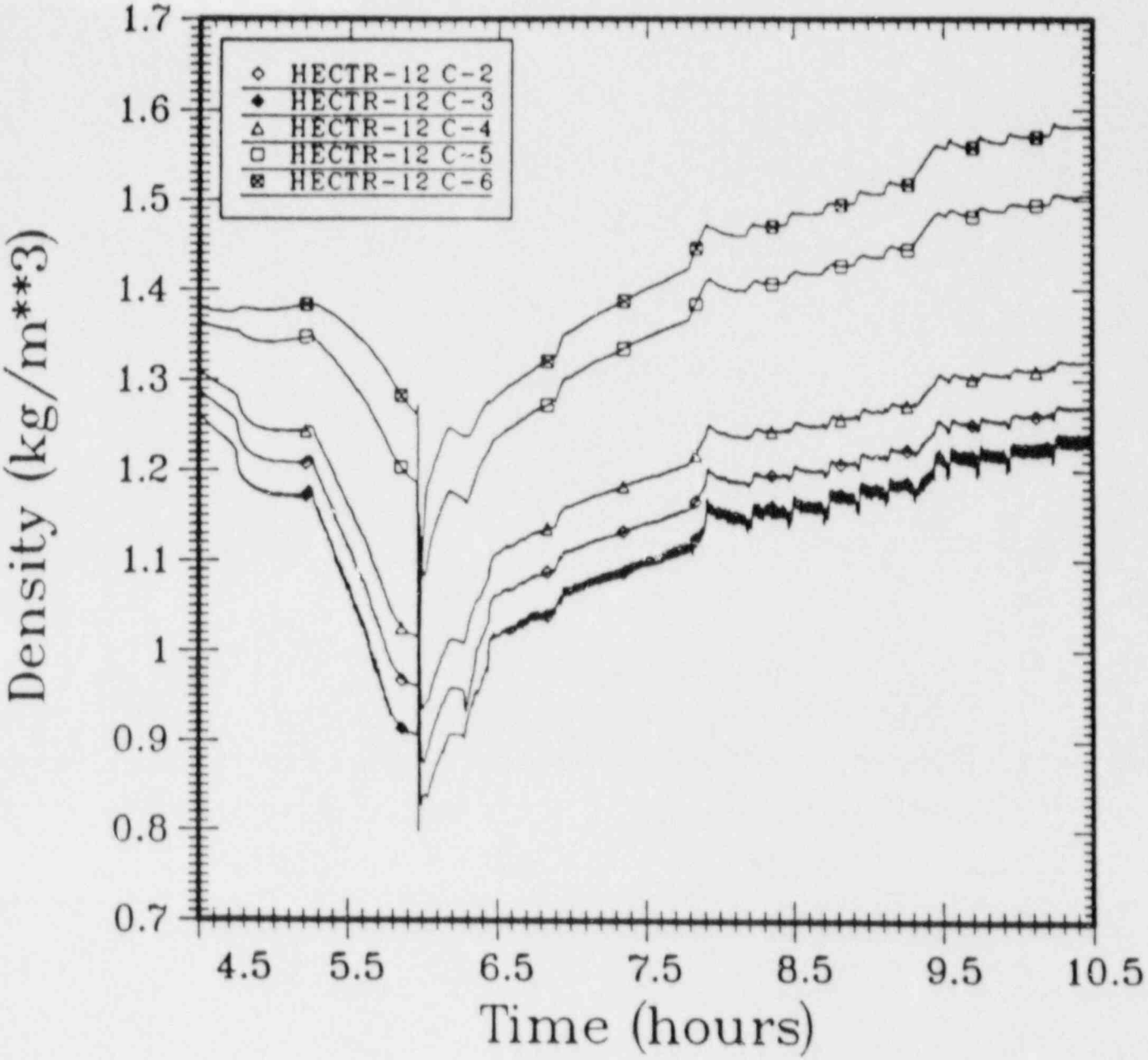

Figure 1.5-7. Density Distributions in the Lower Compartment Predicted by HECTR (12-Compartment Model With Fans-Off; Conditions for In-Cavity Oxidation: $O_2 \geq 0$ Percent, Steam ≤ 100 Percent)

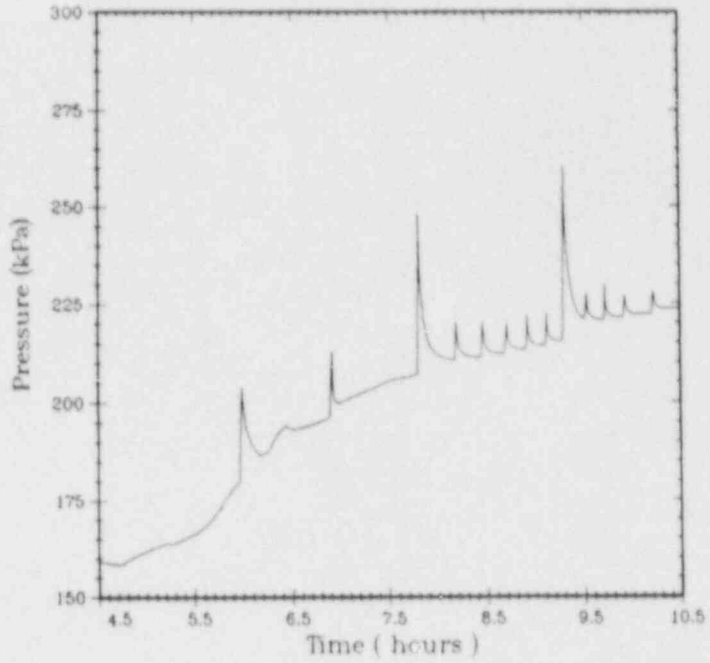

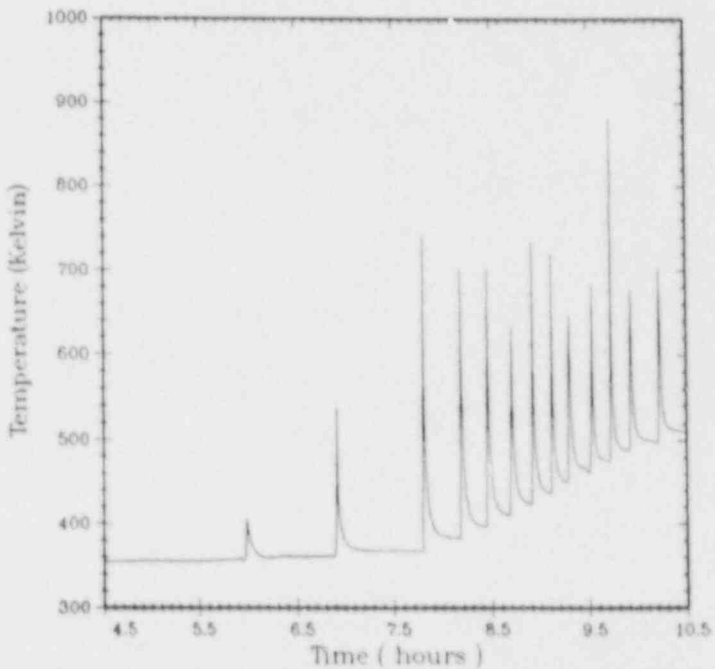

Figure 1.5-8. Pressure and Temperature Responses in the Upper Plenum Predicted by HECTR (12-Compartment Model With Fans-Off; Conditions for In-Cavity Oxidation: $O_2 \geq 0$ Percent, Steam $\leq$ 100 Percent)

under a similar accident condition as specified in MAAP. Substantial differences in the timing and rate of gases released from core-concrete interactions are predicted by both codes. CORCON predicts that hydrogen is generated as soon as core-concrete attack begins (see Figure 1.5-9) while MAAP predicts that only steam is generated for the first hour. No hydrogen is released until the core debris is substantially heated up. However HECTR results using the sources predicted by the CORCON code show that again the oxidation process is limited by the oxygen transport into the cavity (Figure 1.5-10). It predicts an incomplete oxidation of combustible gases in the cavity, which leads to accumulation and combustion of hydrogen and carbon monoxide in the upper and lower compartments. The peak pressure generated from the global burn in the lower and upper compartments is relatively lower than earlier HECTR calculation using the sources predicted by the MAAP code, 313 versus 384 kPa (Figure 1.5-11).

1.5.2 Heated Detonation Tube

(D. W. Stamps and M. Berman, 6427; W. B. Benedick, 1131)

Research conducted has disclosed a new and important area of uncertainty in hydrogen combustion that affects several different accident scenarios. The uncertainty involves the behavior of hydrogen-air-steam mixtures at very high temperatures and high steam concentrations. Three scenarios that may be affected by this uncertainty are the possibility of local and global detonations, the direct containment heating (DCH) hydrogen problem, and the in-cavity oxidation of combustible gases produced by core-concrete interactions.

1.5.2.1 Global and Local Detonations

The possibility of detonations should be reconsidered based on recent theoretical predictions of the sensitivity of hydrogen-air-steam mixtures at elevated temperatures. These predictions were made using a Zeldovich-von Neumann-Doering (ZND) chemical kinetics model developed by J. E. Shepherd.[31] As shown in Figure 1.5-12, a strong increase in the sensitivity of lean hydrogen-air mixtures is predicted as temperature increases from about 300 to 500 K. The detonation cell width for a lean mixture of 15 percent hydrogen in air (equivalence ratio = 0.425) is predicted to decrease by a factor of 18.6 with a 200 K increase in temperature from 300 to 500 K. Since the critical charge depends on the cube of the cell size, this 200 K temperature rise represents an increase of more than a factor of 6000 in detonation sensitivity. Stoichiometric mixtures, however, decrease in sensitivity to detonation as temperature increases. Above about 500 to 600 K, detonation sensitivities are comparable for essentially all mixtures, from lean to rich. The predictions made by the model have

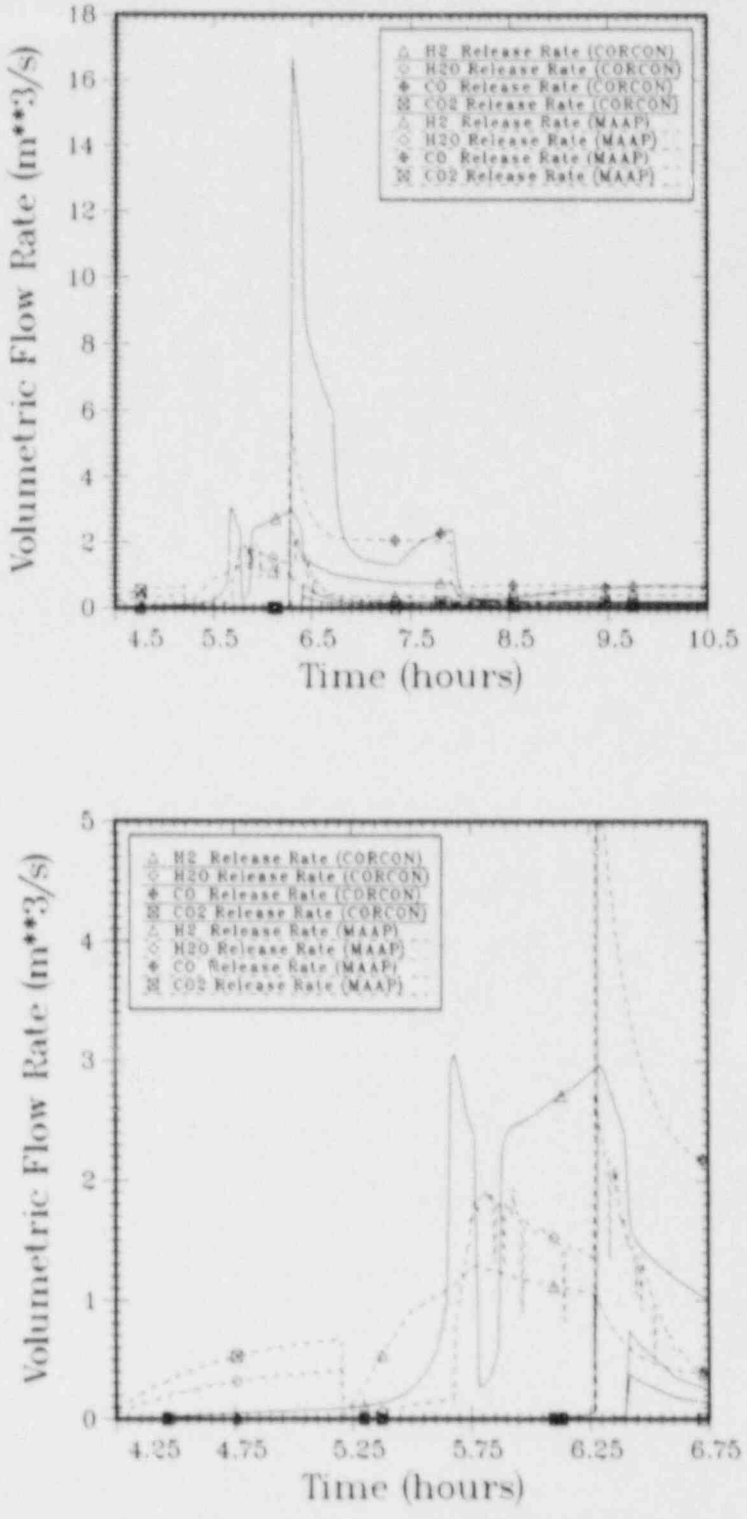

Figure 1.5-9. Comparison of Gas Release Rates from Core-Concrete Interactions Predicted by CORCON and MAAP

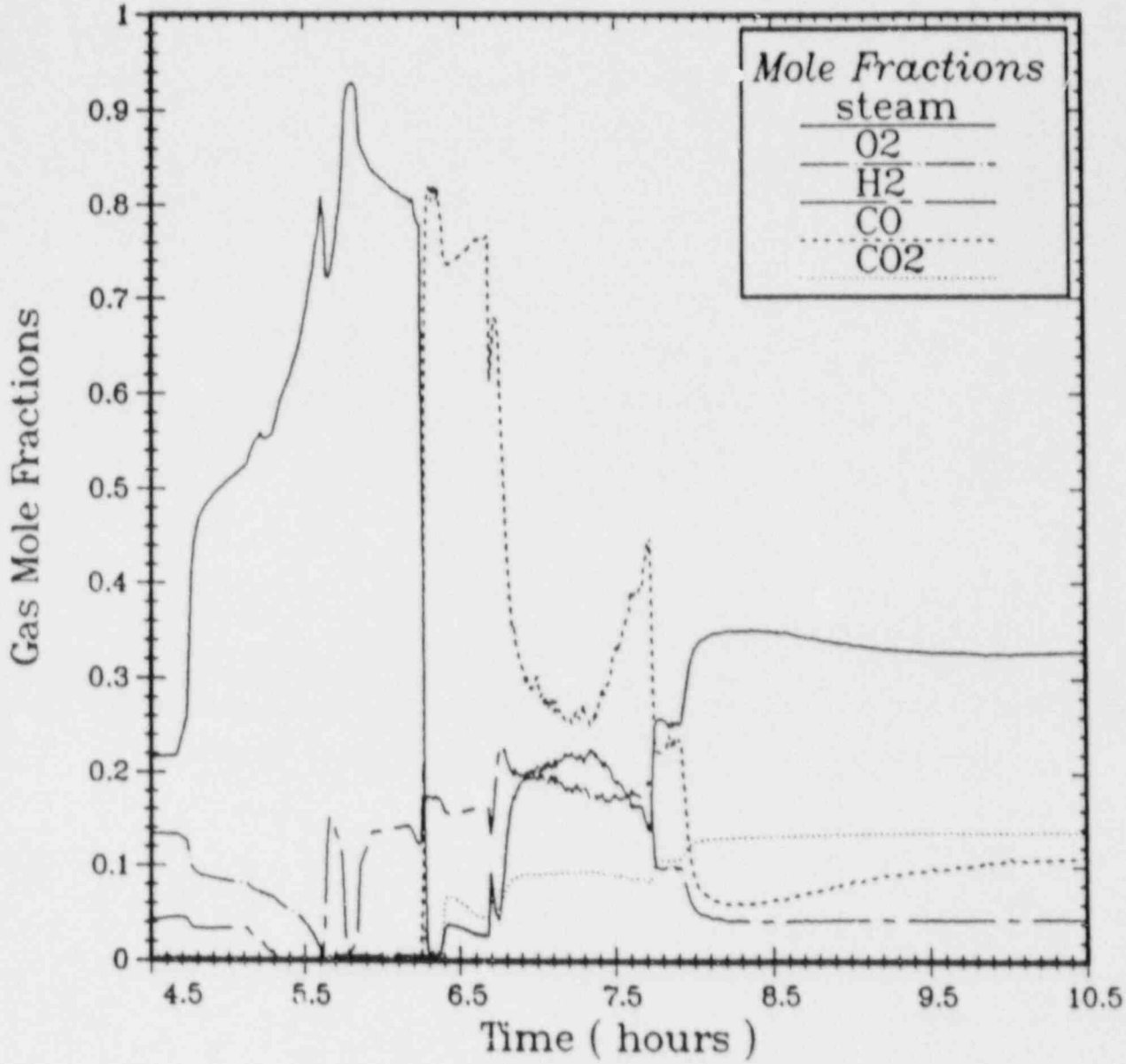

Figure 1.5-10. Mole Fraction of Gases in the Reactor Cavity During Core-Concrete Interactions and In-Cavity Oxidation Predicted by HECTR

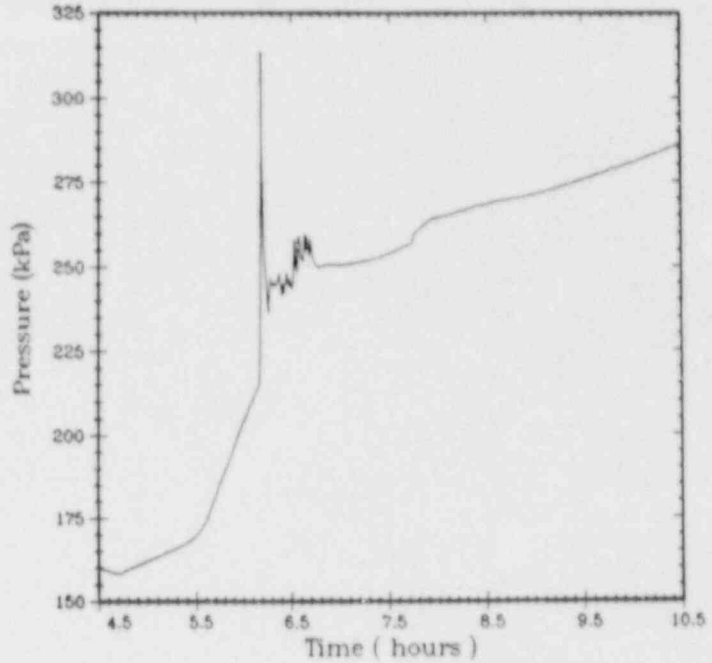

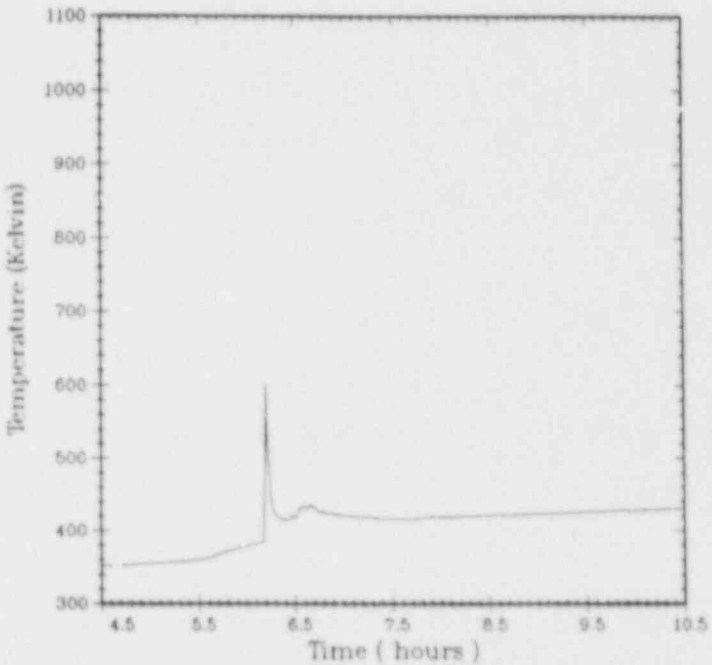

Figure 1.5-11. Pressure and Temperature Responses in the Upper Compartment Predicted by HECTR (12-Compartment Model with CORCON Sources; Conditions for Continuous In-Cavity Oxidation: $O_2 \geq 0$ Percent, Steam $\leq$ 100 Percent).

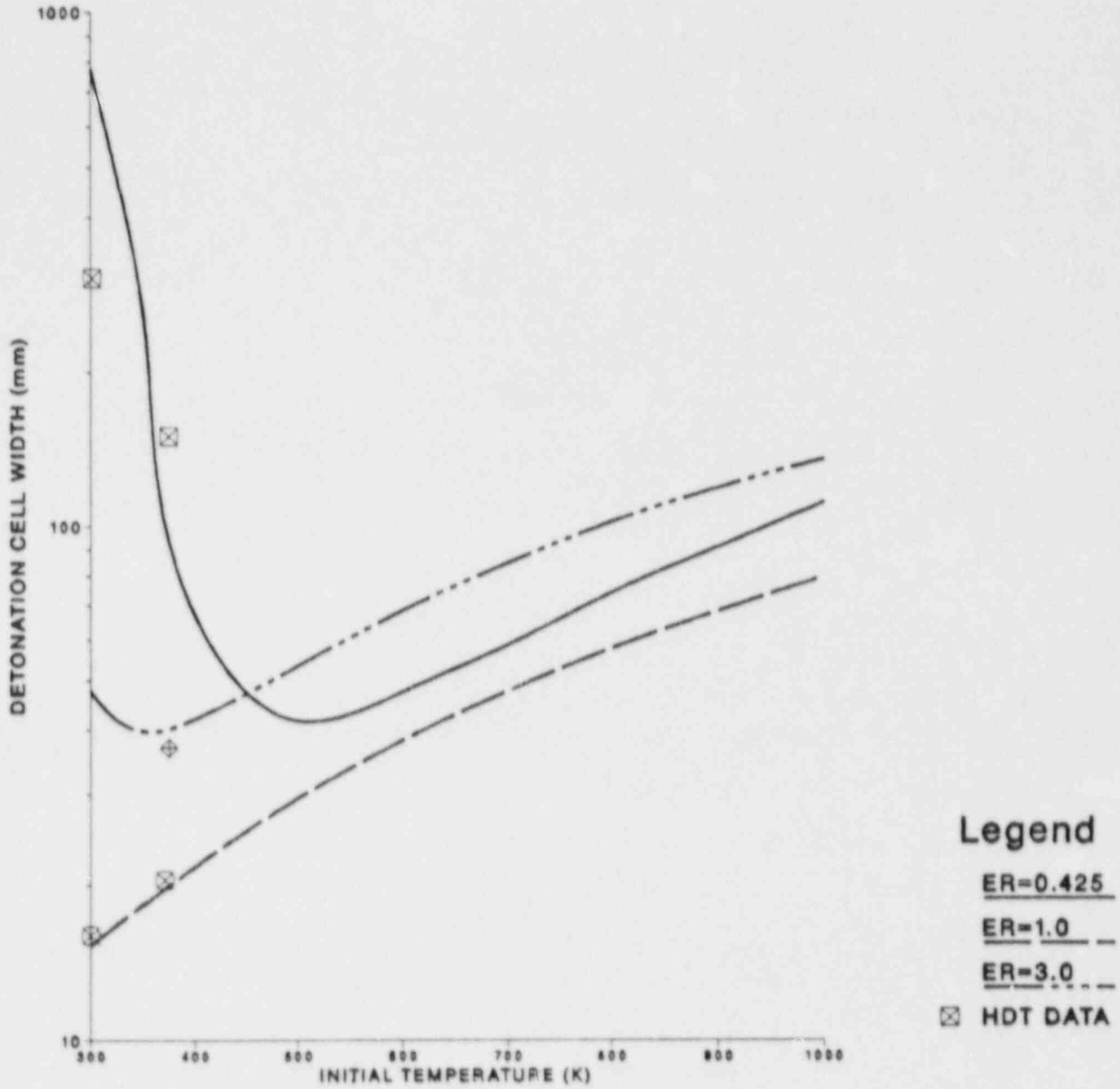

Figure 1.5-12. Detonation Cell Width Dependence on Temperature for Three Equivalence Ratios, No Steam

been verified experimentally only up to 100°C (373 K) as shown by the experimental data points in Figure 1.5-12.

Experiments in the Sandia HDT have shown that steam acts as a detonation inhibitor at relatively low temperatures.[92] However, calculations with the ZND model imply that the inhibiting effect of steam diminishes with increasing temperatures for all hydrogen concentrations. As shown in Figure 1.5-13, the detonation cell width for stoichiometric mixtures diluted with 30 percent steam decreases almost three orders of magnitude for a temperature rise of 400 to 500 K. That translates into a reduction of the required critical charge by a factor of one billion.

Of course, at very high temperatures, the increase in detonation sensitivity becomes moot because the hydrogen-steam-air mixture becomes hyperbolic. Autoignition temperatures depend on mixture concentrations and pressure;[93] past data indicate that temperatures in the range of 800 to 900 K should autoignite most hydrogen mixtures under static conditions.

The addition of steam desensitizes essentially all hydrogen mixtures at any temperature. However, the magnitude of this reduction is greatest at the lower temperatures, as shown in Figure 1.5-14, and decreases rapidly with increasing temperature. The addition of 40 percent steam reduces the detonation cell width for a stoichiometric mixture by about a factor of 200 at 380 K compared to no steam, but only by about a factor of 2 at 800 K.

The increased detonability of hot hydrogen-air mixtures, if confirmed by experiment, could influence several aspects of severe accidents that involve high-gas temperatures. For example, in a small break accident, hydrogen-steam exhaust jet temperatures between 800 and 1000 K are not unreasonable. In this range of temperatures, a wide range of mixture concentrations have similar sensitivities. The jets from breaks will contain varying amounts of steam. As the jet mixes with surrounding air, the potential for transition to detonation could increase dramatically with increasing gas temperatures, even for off-stoichiometric mixtures and high-steam concentrations. It is not inconceivable that a hot hydrogen-steam mixture was created by the fuel-coolant interactions during the Chernobyl accident. This heated mixture may have subsequently undergone a transition to detonation in the building above the reactor compartment.

As mentioned previously, the model has been validated only for hydrogen-air-steam mixtures up to 100°C (373 K). If the model is confirmed experimentally at higher temperatures, the predictions made by the model indicate that detonations may be significantly more probable than previously considered in the vicinity of hot-hydrogen jets released from the vessel or wherever the temperature is high.

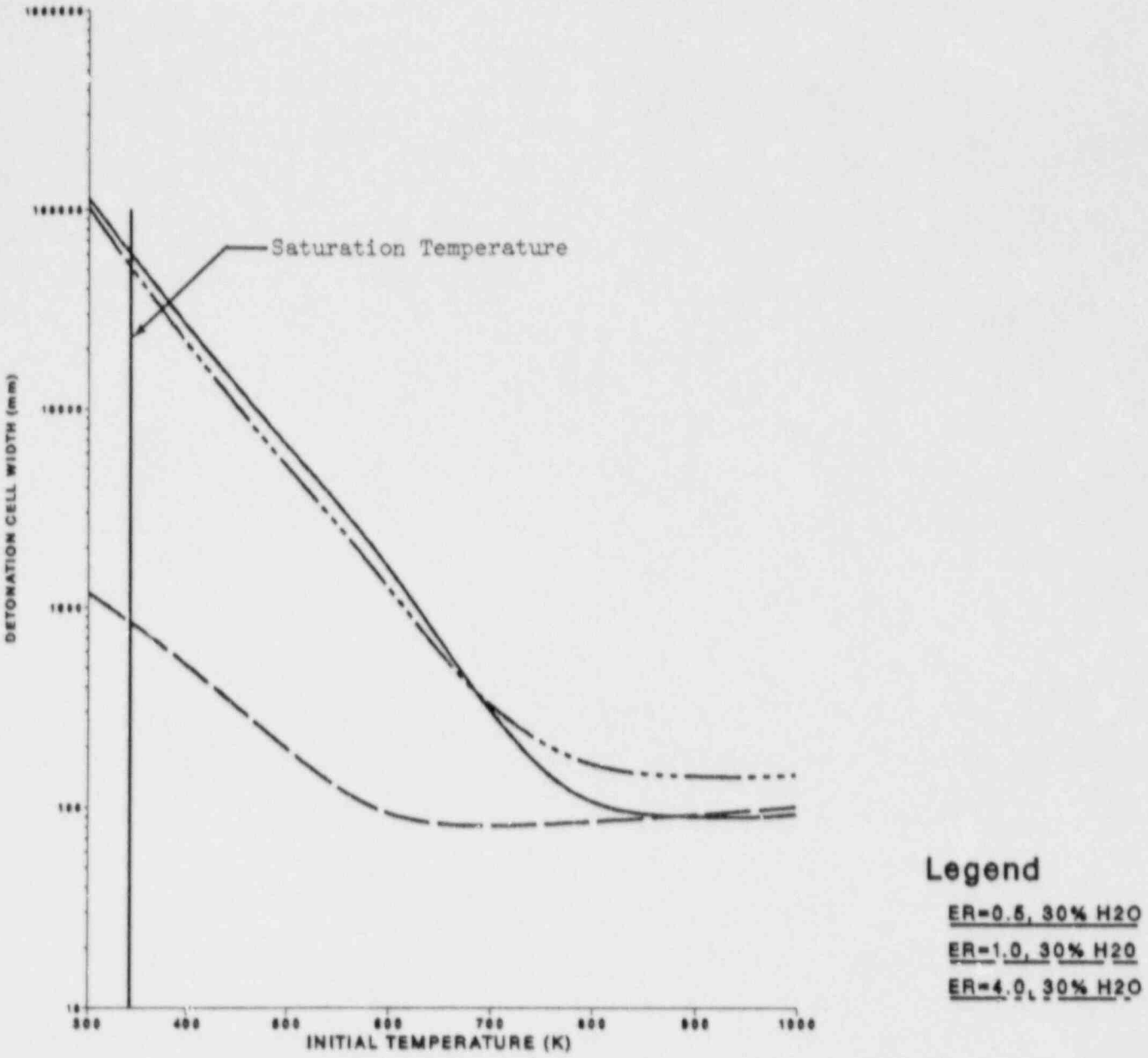

Figure 1.5-13. Detonation Cell Width Dependence on Temperature for Three Equivalence Ratios, 30 Percent Steam

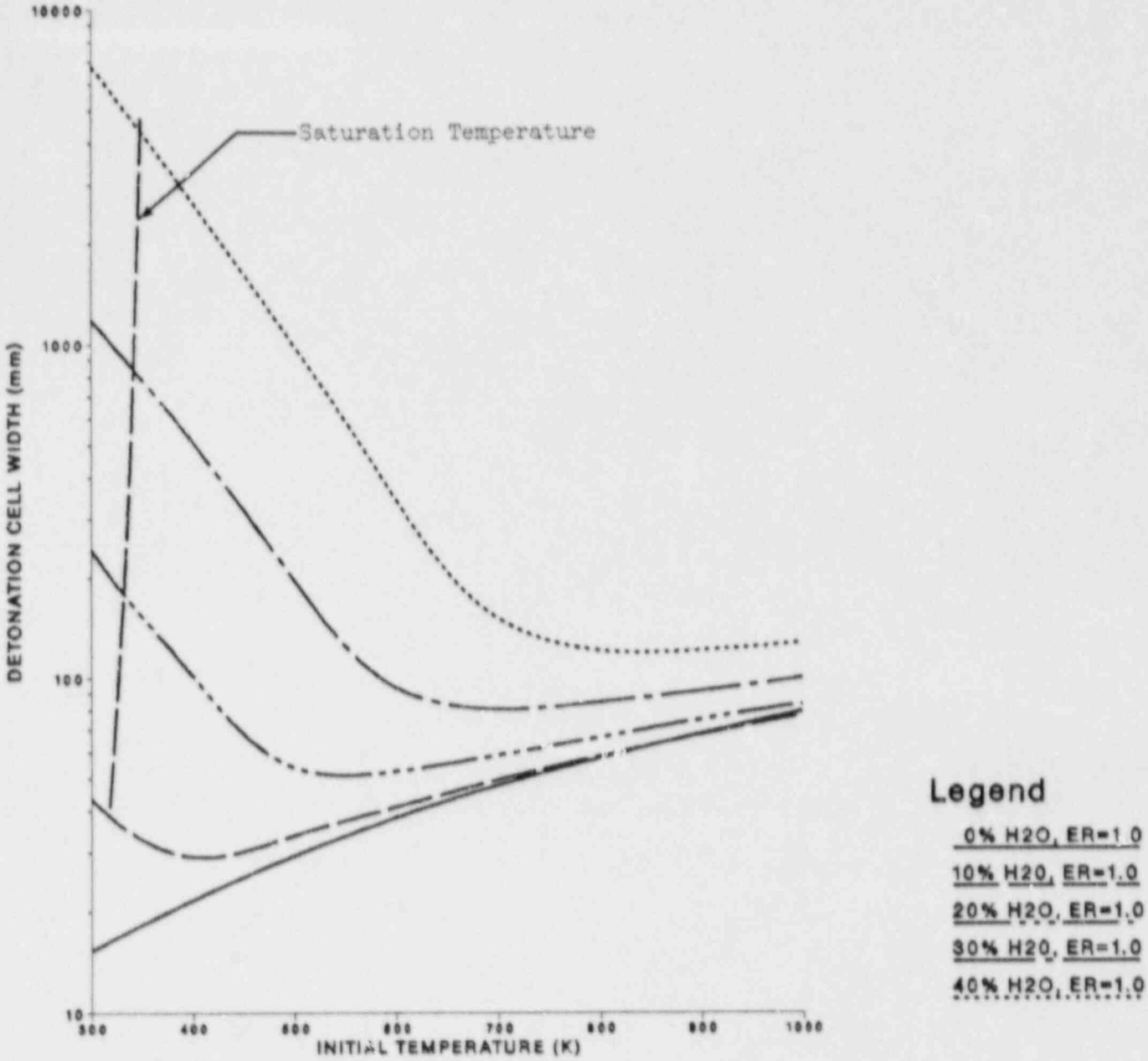

Figure 1.5-14. Detonation Cell Width Dependence on Temperature for Stoichiometric Mixtures (ER=1) and Varying Steam Concentration

The possibility of a local detonation may involve mixtures on the rich side since a pure hydrogen-steam jet will mix with entrained air. A current research effort in the HDT is to determine the limit of detonation propagation of rich hydrogen-air mixtures. Currently, a 75 percent concentration of hydrogen in a hydrogen-air mixture at 1 atm initial pressure and 20°C initial temperature allowed a detonation to propagate in the HDT. (Note that the corresponding oxygen concentration is only 5.3 percent.) The concentration of hydrogen in this detonation is nominally greater than or the same as the 74 percent concentration of hydrogen reported as the rich flammability limit.[93,94] The propagation of detonations near the limits of the HDT may be influenced strongly by the boundaries, but this is not yet understood, either qualitatively or quantitatively.

1.5.2.2 Direct Containment Heating Hydrogen Problem

The direct containment heating hydrogen problem is also influenced by the recent theoretical analysis of the sensitizing effect of high temperature on hydrogen-air-steam mixtures. Preliminary CONTAIN code calculations indicate that rapid metal-steam reactions lead to the production of large quantities of hydrogen at temperatures up to 2000 K during high-pressure melt ejection.[95,96,97] This high-temperature hydrogen ultimately enters the upper compartment containing air, steam, and hydrogen at temperatures up to 900 K. The threat from containment overpressurization can increase significantly for some plants if the hydrogen were to burn in this ostensibly inert environment. The effect of temperature on flammability limits at high temperatures (but below the autoignition temperature) is not well understood. If the mixture of hydrogen, air, and steam is uniformly mixed, will the mixture spontaneously combust, deflagrate, or detonate? If the mixture is not uniformly mixed, at what rate can combustion occur at the boundaries of the hot hydrogen jet or plume, as it enters the relatively cooler upper containment atmosphere? It is also clear that these questions involve dynamic conditions including transport, mixing, and the presence of hot solid or liquid particles moving with the gases.

1.5.2.3 Oxidation of Combustible Gases in the Reactor Cavity

A third accident scenario in which the effect of high temperature is important is the in-cavity oxidation of combustible gases produced by core-concrete interactions following vessel breach. IDCOR calculations with the MAAP code indicate that essentially all of the hydrogen and carbon monoxide generated during the core-concrete interactions will oxidize benignly in the reactor cavity.[87] Wong has shown[98] that these predictions depend strongly on the extent of natural convection and criteria for steam-inerted conditions. Assuming incomplete in-cavity oxidation in the HECTR calculations led to predictions of the transport,

accumulation, and subsequent combustion of hydrogen and carbon monoxide in the lower and upper compartments. The pressure generated from this combustion is much higher than the pressure generated by gradual steam pressurization when there is complete in-cavity oxidation. The ability to predict the degree of in-cavity oxidation is severely limited by the lack of high-temperature data for autoignition and flammability limits.

1.5.2.4 Effects of Diluents on Detonability

The Heated Detonation Tube is also used to quantify the effect of different diluents on hydrogen-air detonations. The two different diluents tested were steam in Test Series 8 and carbon dioxide in Test Series 9.

Twenty-two tests have been completed in the hydrogen-air-steam test series denoted as Test Series 8. The purpose of the current test series is to quantify the effect of steam concentration on hydrogen-air mixtures at 1 atm initial pressure and 100°C initial temperature. These initial conditions are at the lower range of initial conditions calculated by A. C. Peterson, Sandia, for a local detonation study. Test Series 8 is comprised of approximately 25 tests with most tests at 0, 10, 20, and 30 percent steam concentrations on a molar basis. Some tests will be conducted at steam concentrations greater than 30 percent to determine the steam inerting level for the HDT. The range of steam concentrations tested to date varies from 0 percent to 35 percent. A comparison of the experimental results with the theoretical predictions are shown in Figure 1.5-15. All cell-size measurements agree within approximately a factor of 2 with the theoretical predictions. Stoichiometric mixtures with steam concentrations of 10, 20, and 30 percent increase the detonation cell width by factors of 1.5, 6.4, and 32.5, respectively, over a stoichiometric mixture with no steam. To date the maximum steam concentration that has been tested is 35 percent for a stoichiometric mixture. The maximum steam concentration in a stoichiometric mixture that will propagate a detonation in the HDT has not yet been determined. Currently, the lowest concentration of hydrogen in mixtures without steam that will propagate a detonation is 13 percent. The lowest concentration for the HDT has not yet been determined.

Nine tests have been completed in the hydrogen-air-carbon dioxide test series denoted as Test Series 9. The purpose of this test series is to quantify the effect of carbon dioxide as a surrogate for steam for mixtures at 1 atm initial pressure and 100°C initial temperature. Test Series 9 has been completed and was composed of nine tests at 5, 10, 15, and 20 percent carbon dioxide concentrations on a molar basis. A comparison between the experimental results and the theoretical predictions is shown in Figure 1.5-16. All cell size measurements are within approximately a factor of 2 when compared to the theoretical predictions. Stoichiometric mixtures with carbon dioxide concentrations

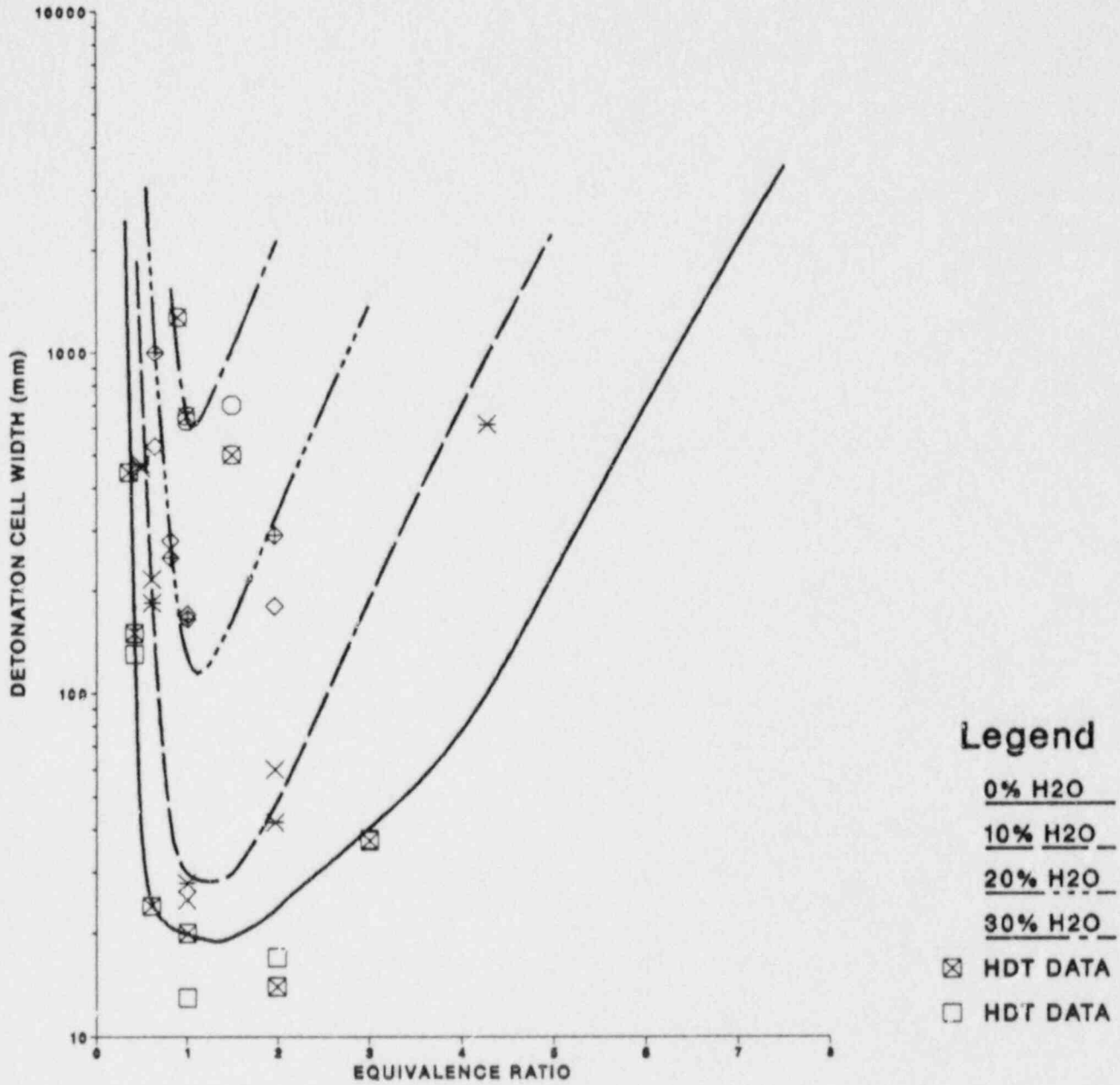

Figure 1.5-15. Detonation Cell Width Versus Equivalence Ratio for Test Series 8 (H_2-Air-Steam at P = 1 atm and T = 100°C)

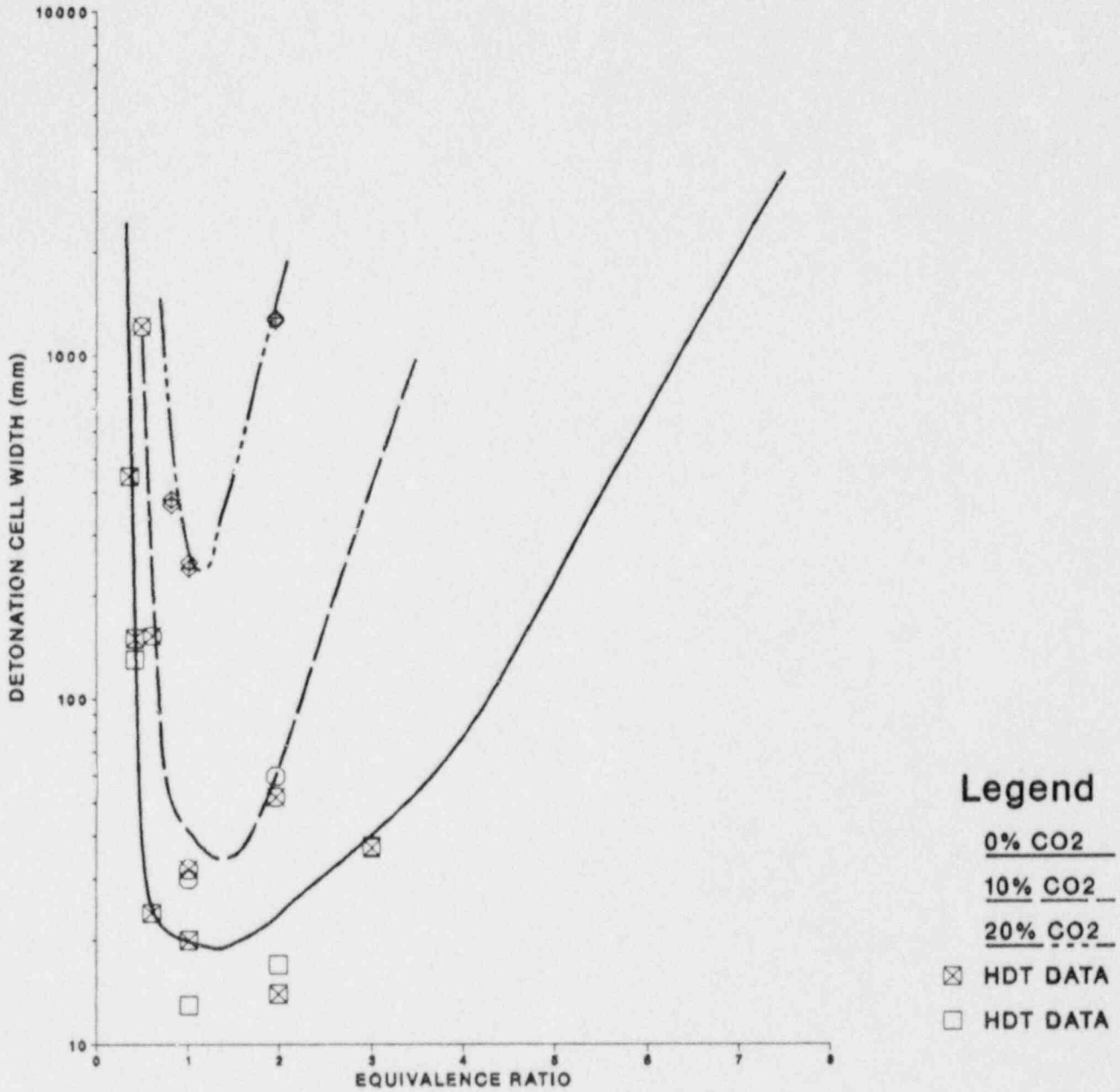

Figure 1.5-16. Detonation Cell Width Versus Equivalence Ratio for Test Series 9 (H_2-Air-CO_2 at P = 1 atm and T = 100°C)

of 10 and 20 percent increase the detonation cell width by factors of approximately 2 and 13.5, respectively, over a stoichiometric mixture with no carbon dioxide. These values should be compared with the previously reported values of 1.5 and 6.4 for 10 percent and 20 percent steam dilution reported earlier. A comparison is made between stoichiometric mixtures diluted with either steam or carbon dioxide in Figure 1.5-17. This comparison indicates that not only is carbon dioxide a better inhibitor than steam, but it becomes more effective with increasing concentration.

Three tests were performed to quantify the effect of temperature on hydrogen-air-carbon dioxide mixtures. These tests represent an extension of Test Series 2 reported by Tieszen, et al.[92]. The mixture initial pressure is 1 atm and initial temperature is 20°C. Stoichiometric mixtures with 5, 10, and 20 percent carbon dioxide on a molar basis were tested. The results indicate that an increase in initial temperature increases the sensitivity of the mixture. As an example, the detonation cell width for a stoichiometric mixture with 10 percent carbon dioxide at 100°C is approximately 75 percent of the same mixture at 20°C. Likewise, a stoichiometric mixture with 20 percent carbon dioxide at 100°C has a detonation cell width approximately 50 percent of the same mixture at 20°C. These examples illustrate that the sensitizing effect of initial temperature is more pronounced with higher diluent concentrations. The theoretical calculations shown in Figure 1.5-14 also indicate this conclusion is valid for steam dilution.

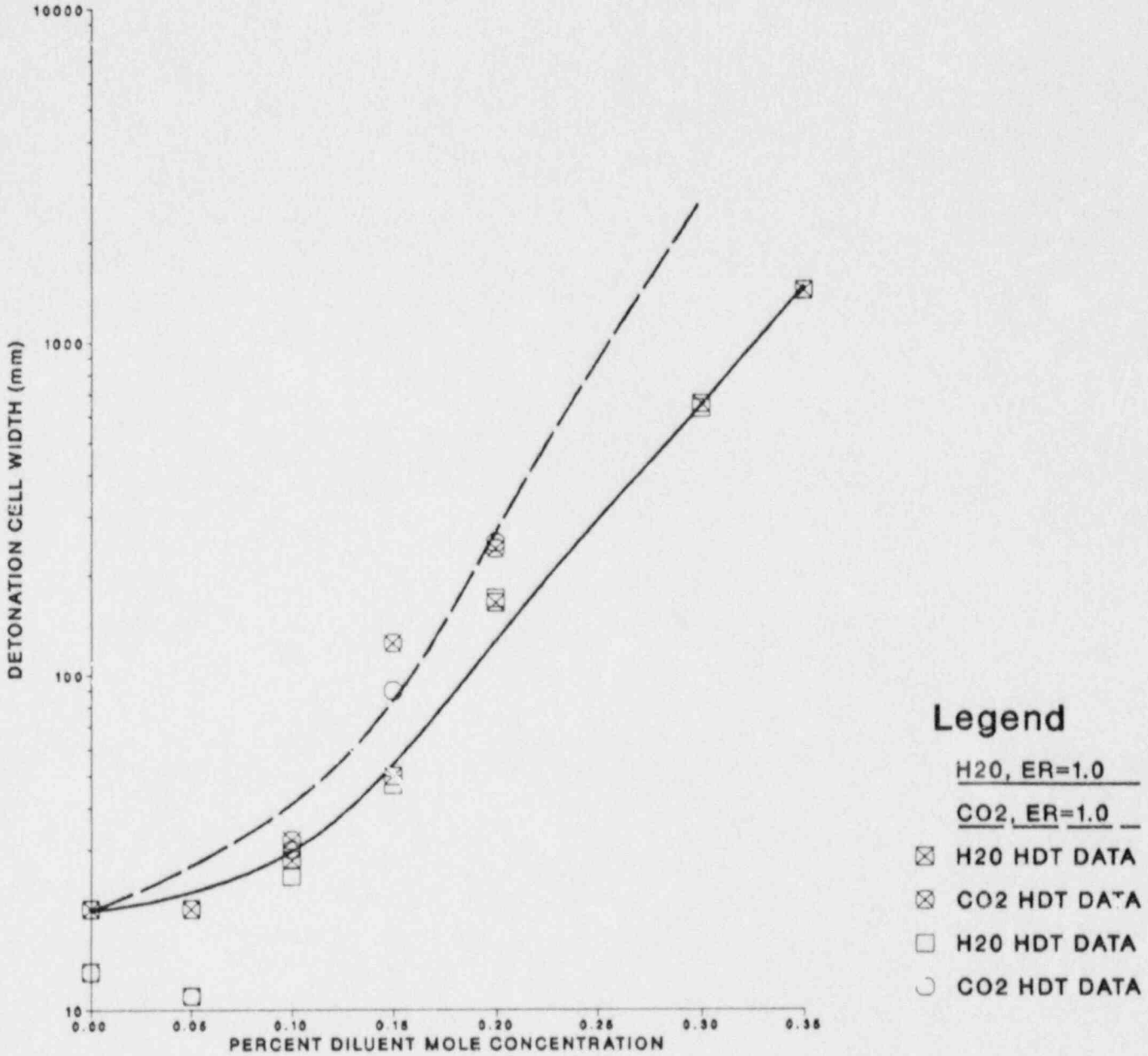

Figure 1.5-17. Comparison of the Inhibiting Effect of Steam and Carbon Dioxide for Stoichiometric Hydrogen-Air-Diluent Mixtures at P = 1 atm and T = 100°C

2. FISSION-PRODUCT SOURCE TERM

Modern reactor accident analyses focus very directly on the mechanistic determination of the release of radionuclides from the fuel and their subsequent behavior--the so-called fission-product source term. This attention is being given to the source term to redress some of the conservatisms and omissions in past analyses. Mechanistic models now available for predicting the release of radionuclides from the reactor fuel under accident conditions and the transport of these radionuclides in the reactor coolant system have yielded substantive insight into the natural processes that attenuate the amount of radioactivity available for release from the plant. Nevertheless, these models are known to be incomplete. Significant uncertainties still exist concerning these release and transport issues. The rates of radionuclide release must be well known to predict deposition in the reactor coolant system. At this juncture, release data may only be correlated against fuel temperature and not correlated against other factors such as system pressure and chemical environment, which are expected to influence strongly the radionuclide release. Chemical forms adopted by released radionuclides--especially iodine and tellurium--will drastically affect the extent to which these radionuclides will deposit and be retained in the reactor coolant system. Chemical transformations of the deposited radionuclides will determine to a significant extent whether these deposited materials revaporize from surfaces and again become a part of the radioactivity that can be released from the plant. These issues require experimental data if the modern accident models are to be upgraded to provide reliable predictions concerning the fission-product source term.

The High-Temperature Fission-Product Chemistry program provides experimental data on the thermodynamics and kinetics of chemical processes affecting the chemical form of released radionuclides, the interactions of these radionuclides with structural and aerosol surfaces, and the revaporization of deposited radionuclides. The ACRR Source Term Experiments are in-pile tests of radionuclide release under high-pressure, high-radiation intensity, and high-hydrogen concentration conditions. They supplement out-of-pile experiments of radionuclide release being conducted elsewhere in the NRC-sponsored research. Both experimental programs provide crucial data needed for accident models. The primary thrusts of the experimental programs are to provide data for the development and validation of the NRC's best-estimate model of fission-product behavior, VICTORIA.

2.1 High-Temperature Fission-Product Chemistry Program

(R. M. Elrick and D. A. Powers, 6422; R. A. Sallach, 1846)

The purpose of the High-Temperature Fission-Product Chemistry and Transport program is to obtain data on the chemistry and processes that affect the transport of fission products under

accident conditions. The program now consists of three tasks related to one another. Baseline thermodynamic and reactivity data are being collected for compounds of fission-product elements of particular interest. An experimental facility has been built to allow the chemistry of fission products in prototypic steam-hydrogen environments to be studied. The interaction of fission products with reactor materials such as stainless steel can be examined in this facility. Results of these experimental studies are compared to predictions of thermochemical models to determine if reaction kinetics play an important role in fission-product transport.

Little of the chemistry of fission products in high-temperature, steam-plus-hydrogen environments is well characterized. The physical and chemical processes taking place can be categorized into those between vapors (gas-phase reactions) and those between a vapor and a condensed-phase surface (heterogeneous reactions). In the latter category are condensation on, adsorption by, and chemical reaction with surfaces. Conversely, should conditions change, the fission-product species may evaporate, desorb, or leave a surface as the result of decomposition of a compound.

If these reaction surfaces are surfaces of structural materials, control rods, cladding, or bulk fuel, then the fission products can be retained in the primary system. However, the same reactions on the same materials in an aerosol form can result in transport out of the primary system.

2.1.1 Introduction

Because boron is a good neutron absorber (poison), its compounds are used extensively in the control of nuclear reactors. The compounds are either dissolved in the reactor coolant or are used in a solid form in clad control rods. In control rods, the boron can be used as an alloy or as boron carbide (B_4C) with either one as a powder, as a pressed pellet, or as a dispersion in a metal. Since boron is a significant component in the core and cooling system, its effect on the high-temperature chemistry in the primary system during an accident could be important. A typical BWR reactor may contain on the order of 7×10^5 g of boron in the control rods. If the boron became exposed, by the cracking or melting of its cladding, to a severe accident environment, the resulting reactions could change the pathway of fission products through the primary system.

To examine these reactions, three tests were performed. The results of these tests, reported in Reference 99, are summarized here. Each of the three tests was conducted in steam at 1270 K in an Inconel 600 system, where the reaction tube was lined with fresh Inconel 600; a flow-through bed of B_4C particles and B_4C coupons were common to all the tests. In the first test (Test 25), the reaction of boron carbide with the steam environment was

examined. By introducing CsOH vapor (Test 26) and CsI vapor (Test 28) into the same environment, the changes in total system response could be studied. Although previous work[100] had been convincing in the identification of CsOH and CsI as the appropriate initial vapor species for cesium and iodine in some primary system environments, the results of these experiments show that the presence of B_4C can produce different species. The cesium in both the CsOH and CsI reacted rather strongly with boric oxide formed in the B_4C-steam reaction to form a less volatile compound, probably cesium metaborate. In the case with CsI, the iodine was released as a volatile, water soluble form, probably HI. Preliminary results of these experiments were reported in Reference 101. Thermodynamic calculations were made to explain these experimental results by assuming first, a vapor phase reaction and second, a heterogeneous reaction. Some of these results were summarized in Reference 102. The results of experiments of this type are used to define and to quantify controlling processes in the fission-product chemistry of severe accidents. These quantities are used in severe accident codes like TRAPMELT and VICTORIA and for the purpose of interpreting the results of large scale tests.

The British have examined, in greater detail, systems consisting of different combinations of CsI and boric acids in the condensed and vapor states in steam-argon mixtures and in a vacuum to temperatures of 1110 K.[103,104,105] Using matrix isolation-infrared spectroscopy and quadruple mass spectroscopy, they observed that in a steam environment substantial decomposition of CsI was observed above 870 K. The reaction products were volatile HI and relatively nonvolatile cesium borates in both the vapor reaction between CsI and boric acid and when either reactant was vaporized and the other condensed.

2.1.2 Summary and Conclusions

From the results of these three scoping tests and a study of the literature, some conclusions can be drawn concerning the influence of boron carbide on severe accident environments.

1. Extensive reaction was observed (Figure 2.1-1) between boron carbide and steam to produce boron oxide and boric acids in a two-step kinetic process that is probably paralinear. Average rates of production for the oxide and acids were calculated for the three tests. These rates are functions of the time, steam partial pressure, partial pressure of acids in the steam, temperature, and surface-to-volume ratio (the size and shape) of the carbide, that is, whether the carbide surface is exposed as in slab geometry or packed as particles in a bed where the steam flows around the bed or through it.

These rates did not appear to be influenced by additions of CsOH and CsI vapors. The two B_4C geometries used were a slab and a flow-through bed of particles. Production rates of the oxides and acids were both on the order of 10^{-4} g (boron)/cm^2·min for the slab geometry and 1 to 2 orders of magnitude less than this for the B_4C particle bed. Our calculated oxide rates are about 10 times faster than those rates found in the literature. These higher rates for B_4C particles could be due in part to differences in flow geometry. In the Reference 106 flow around a pan, the lower rate could be caused by slow formation and removal of acids, which resulted from stagnation flow and saturation conditions just above the bed. The difference in reaction rates for B_4C coupons could be due to the fact that the coupons used in Reference 107 had about 1/16 the amount of boron as our boron carbide.

2. In our experiments, the boric acids condensed at about 370 K, forming a plug porous to the noncondensed gases in the 2.6-cm diameter condenser tube (Figure 2.1-2). Similar blockages might occur in regions of the upper plenum of the reactor where the condensed acids could act as filters for particles and as a reaction medium for vapors and particles. The water soluble acid plugs would probably dissolve upon reflooding.

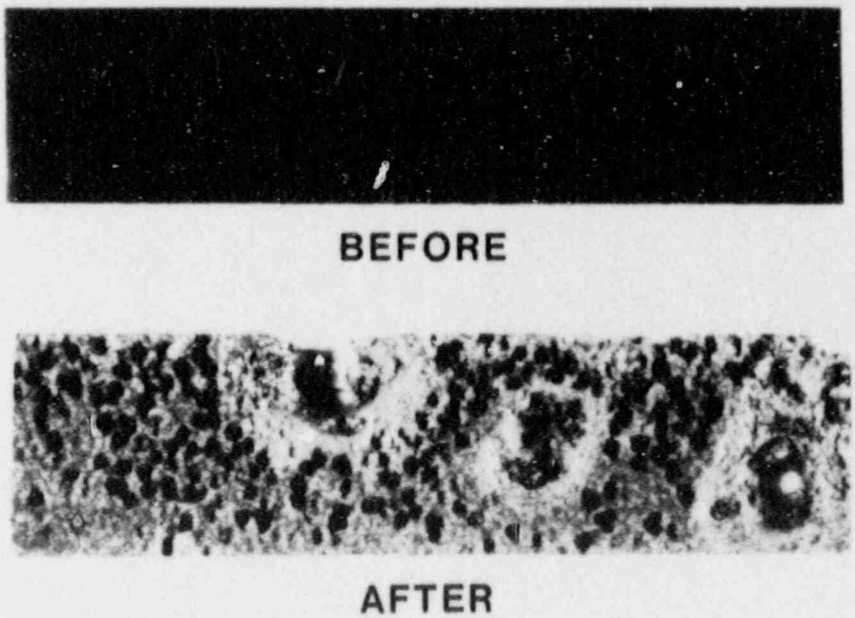

Figure 2.1-1. Coupon of Boron Carbide Before and After Exposure to Steam at 1270 K for About 4.5 Hours - Test 28. Severely pitted surface is shown after water soluble layer of boric oxide was removed.

3. The transition to steady-state oxide production for our conditions is probably less than 1 h but increases with decreasing temperature, according to the literature. Rates during transition would probably not be of interest for accident events lasting much longer than the transition time. During transition, when a layer of boron oxide is developing, the reaction rate is higher than at steady state, thereby generating more hydrogen in the early part of the reaction. The B_4C-steam reaction may, however, be a minor source of hydrogen.

4. The equilibrium state for boric acids in the B_2O_3-steam system depends on the temperature of the system and the partial pressure of the steam. For our conditions, which were shown to approach equilibrium in the reaction tube, the predicted acid mix was 2.5×10^3 Pa (19.2 torr) of H_3BO_3, 5.5×10^2 Pa (4.2 torr) of $(HBO_2)_3$, and 3.8×10^2 Pa (2.9 torr) of HBO_2.

5. Production of boric oxide and acids was measured for two concentration levels of acid in the stream for estimating the influence of the partial pressure of acid on production rates. Rates for the oxide and acids were 8.31×10^{-4} g/min•cm^2 and 2.54×10^{-4} g/min•cm^2 at ~3 torr partial pressure and 3.52×10^{-4} g/min•cm^2 and 1.05×10^{-4} g/min•cm^2 at ~25 torr partial pressure.

6. A significant reaction was observed between CsOH vapor and the boric oxide formed on the B_4C coupons. The reaction product was probably $CsBO_2$. A surface reaction rate constant for the cesium was determined to be about 9.0×10^{-3} m/s. The actual amount of cesium that reacted may have been larger than indicated because some of the $CsBO_2$ may have vaporized after forming.

7. A significant reaction was also observed between the boron oxide and CsI that dissociated the cesium and iodine. Cesium found in the oxide was assumed to be as $CsBO_2$. Iodine was released in the reaction and probably formed volatile and water soluble HI. The calculated surface rate constant for the reaction of the cesium in CsI was about 1.3×10^{-3} m/s.

8. The fact that boron oxide is a flux had an influence, although not a well understood one, on the cesium chemistry. Appreciable amounts of iron and silicon were found in the oxide. The oxide preferentially dissolved the iron from the Inconel. The silicon could be from the Inconel or the contaminant silicon found in the boron carbide. Visual coincidence between some of the cesium and silicon deposits in the oxide suggests the presence of a water insoluble cesium - silicon species. This speculation is supported in part by the analysis.

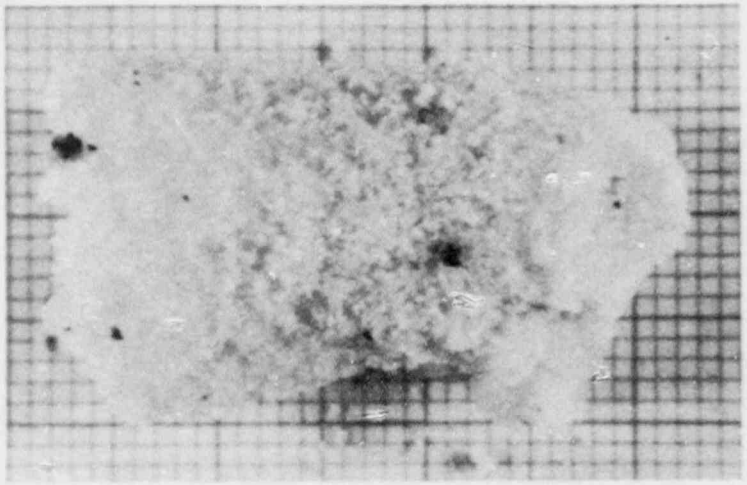

SIDE VIEW

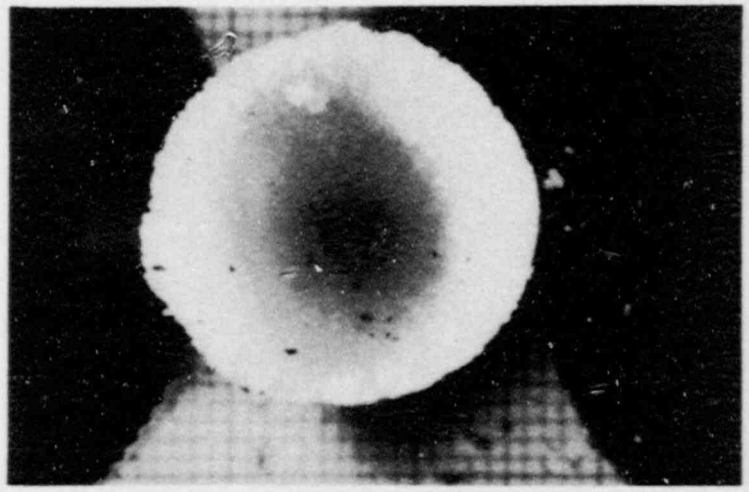

END VIEW

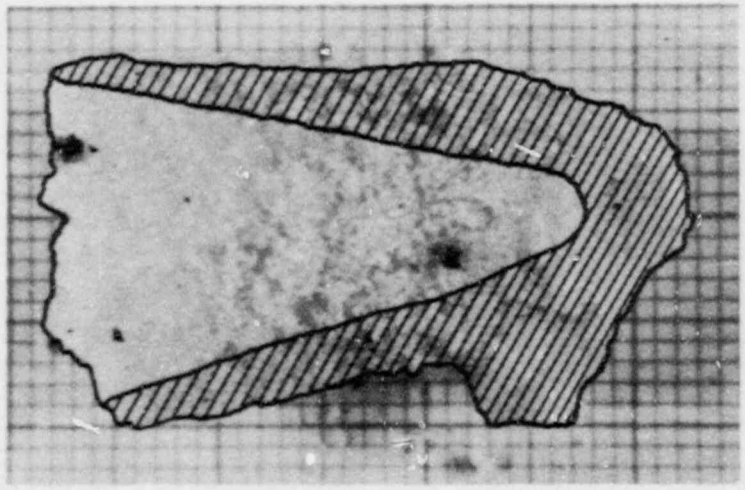

INDICATED CROSS SECTION

Figure 2.1-2. Boric Acids Condensed and Completely Filled the 2.6-cm Diameter Condenser. Removal caused some breakup of the plug. (Smallest grid = 1 mm)

Deposits of cesium in solution and in particles on the Inconel liner surrounding the B_4C coupons might also be attributed to the fluxing behavior of boron oxide.

9. If a vapor phase reaction had occurred between the CsOH and the boric acids, as observed by the British and predicted by equilibrium calculations for a similar system (potassium) to occur, it could not have been detected in the test as it was designed. Similarly, any vapor phase reaction between CsI and the boric acids, observed by the British but predicted by similar (potassium system) equilibrium calculations to not occur, could not have been detected because of the test design. Effects due to the heterogeneous oxide reaction and the vapor phase acid reaction can be identified separately by eliminating the B_4C coupons in the reaction tube, producing acids upstream by the B_4C-steam reaction and identifying the vapor products with a mass spectrometer, sampling from the reaction zone. A comparison of the results from this type of study with results from a test similar to the scoping tests described here, but also using mass spectrometer sampling from the reaction zone, should make it possible to separate the heterogeneous and vapor phase processes. A similar series performed in a stainless steel system would identify processes unique to that system.

2.1.3 Vapor Pressure of Liquid CsOH

2.1.3.1 Introduction

Cesium is one of the more volatile fission product elements that can be released in a nuclear reactor accident. In the high-temperature predominantly steam and hydrogen environment anticipated for the primary systems of light water reactors, much of this cesium can be present as CsOH vapor.[108] Although the JANAF thermochemical tables[109] contain thermodynamic data from which the vapor pressure of CsOH above the pure liquid CsOH can be calculated, there has been no previous measurement of that vapor pressure. This section discusses the first experimental measurements made in the temperature range of 704 to 1133 K.

2.1.3.2 Experimental Section

The equipment used was a modified transpiration apparatus (diagrammed in Figure 2.1-3) with which known quantities of carrier gas were passed over liquid CsOH. The amount of CsOH vapor transported to and condensed in a cooler region was determined, after dissolution in water, by an acid titration for basicity.

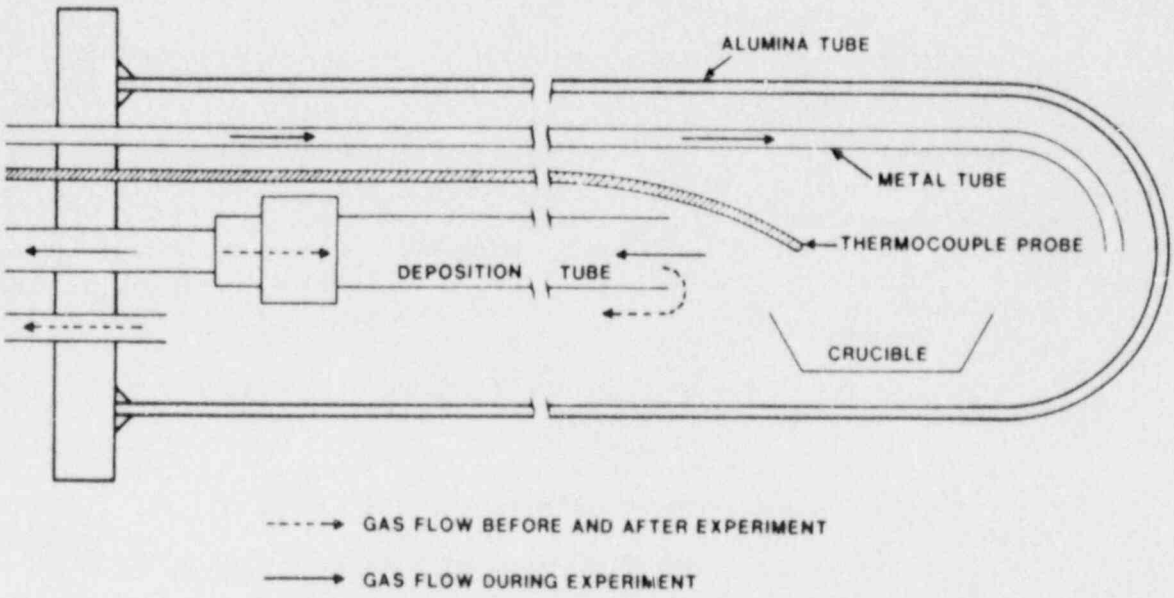

Figure 2.1-3. Sketch of the Transpiration Apparatus

The assumption was made that this basicity was due solely to cesium hydroxide. For verification several solutions were analyzed for their cesium content using atomic absorption methods. The two methods agreed to within ±2 percent.

The basic transpiration apparatus was modified by arranging the ancillary gas handling system so that a reversed gas flow in the condensation tube occurred prior to and subsequent to an experiment. This prevented unwanted diffusional transport of CsOH vapor to the condensation region and permitted accurate timing of the experiments. With this technique, the liquid CsOH was brought to a stabilized temperature before starting an experiment and no corrections for heating and cooling times were needed.

The portions of the transpiration apparatus which came into contact with CsOH vapor were composed of high-purity (>99.5 percent) alumina (Coors, Inc.). No chemical attack of these alumina portions by either liquid or vapor CsOH was evident.

The primary carrier gas was argon. Some experiments were made using argon plus hydrogen or argon plus water vapor mixtures as noted in Table 2.1-1. These gases had no effect on CsOH transport.

Table 2.1-1

CsOH Transpiration Data

Run No.	Carrier Flow mL/min	Time min	Temperature °C	Cesium Transported m mole	Calculated CsOH Pressure torr
1[a]	117	130	599	0.61	0.73
2[a]	130	201	650	4.9	3.4
3[a]	134	265	552	0.89	0.46
4[a]	98	1000	498	0.75	0.14
5[a]	100	65	696	2.9	8.1
6[a]	136	1250	447	0.13	0.014
7	104	300	649	7.5	4.4
8	118	140	597	0.67	0.77
9	100	121	667	3.1	4.9
10	100	125	694	5.5	8.2
11	98	201	626	2.5	2.4
12	102	135	596	0.87	1.2
13	51	326	700	6.7	7.6
14	106	1500	488	0.45	0.054
15	95	160	742	13.1	15.5
16	117	2930	468	0.54	0.03
17	120	2905	501	2.4	0.13
18	70	307	636	3.0	2.6
19	80	205	714	8.6	9.5
20	89	189	710	6.9	7.4
21	97	308	598	1.5	0.90
22	130	1244	450	0.32	0.037
23	216	1215	496	1.6	0.11
24	80	151	799	20.0	29.7
25	70	1005	510	0.79	0.21
26	55	3851	521	3.1	0.27
27	60	1026	540	1.9	0.57
28	89	1020	559	3.2	0.63
29	108	86	859	37.0	66.0
30	97	983	431	0.11	0.022
31	53	999	611	5.0	1.7
32	90	978	474	0.26	0.055
33	65	3879	587	9.0	0.65

[a]Argon carrier gas was saturated with water vapor (ambient laboratory conditions)

The temperature of liquid CsOH was taken to be that registered by an alumina sheathed type K (chromel-alumel) thermocouple positioned above the liquid CsOH.

The CsOH was obtained from Thiokol/Ventron (Alfa Products). The as-received material contained ~10 percent water by mass. Heating this material to 700 K in an argon gas flow expelled the water and introduced no detectable carbonate impurity (detection limit of 0.5 percent by mass). Subsequently, the material was stored in gas-tight containers with minimal gas volume. Transfers in open air were rapid with total exposure time less than 3 min. Heating and cooling were always in dry argon. The major concern was CO_2 pickup to form Cs_2CO_3; incidental H_2O pickup was of no concern since heating before the experiment expelled any H_2O.

2.1.3.3 Results and Discussion

The raw experimental data are shown in Table 2.1-1. From these data, the partial pressure of monomer CsOH vapor was calculated. The presence of the dimer $(CsOH)_2$ molecules was dismissed. Calculation of vapor composition using the JANAF thermochemical data[100] indicates that only at the lower experimental temperatures does the dimer/monomer ratio increase to values approaching 10^{-2}.

The calculated CsOH vapor pressures are plotted in Figure 2.1-4 as a function of the reciprocal absolute temperature. A least squares analysis, fitted to an Arrhenius function, yielded the following equation:

$$\mathrm{Log}_{10}\, P(\mathrm{Pa}) = (9.76 \pm 0.46) - (6611 \pm 397)/T(\mathrm{K}) \quad , \qquad (2.1\text{-}1)$$

where the vapor pressure P is measured in pascals (Pa) and the temperature is measured in kelvins (K). An analogous equation calculated from the JANAF thermochemical data is

$$\mathrm{Log}_{10}\, P(\mathrm{Pa}) = 10.17 - 6514/T(\mathrm{K}) \qquad (2.1\text{-}2)$$

Equation 2.1-2 was obtained by equating the difference of the tabulated ΔG_f for liquid and monomer vapor with the term RTlnP. (The tabulated values have P = 1 atm as the reference point. These data must be corrected to the new reference pressure of 1 Pa.) The calculated values, obtained for 100 K increments between 600 and 1200 K, are plotted in Figure 2.1-4. Equation 2.1-2 is that of a straight line through the calculated points. The slope, of course, is proportional to the average enthalpy of vaporization in this temperature range. Its numerical value (from Equation 2.1-2) is 29.6 kcal/mole whereas the tabulated value of ΔH_v at the tabulated boiling point is 28.6 kcal/mole.

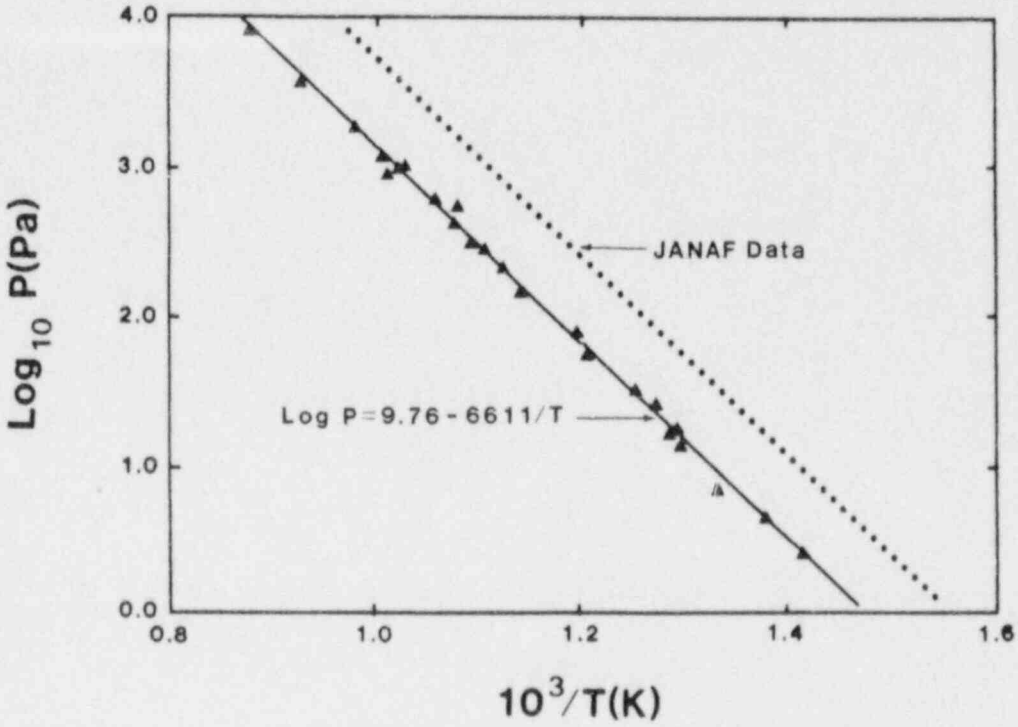

Figure 2.1-4. Vapor Pressure of CsOH

The experimental vapor pressures are approximately a factor of 3 lower than those calculated from the JANAF data. Note that the second terms in Equations 2.1-1 and 2.1-2 are very similar, (-6611/T versus -6514/T). The ΔH_v derived from the experimental data (30.1 ± 1.8 kcal/mole) is in good agreement with the values obtained from the JANAF data.

The difference in vapor pressure as calculated from Equations 2.1-1 and 2.1-2 arises chiefly from differences in the initial constant terms. These terms are related primarily to the entropy of vaporization. A net relative change of ~2 cal deg^{-1} $mole^{-1}$ in the tabulated entropies of CsOH monomer vapor and CsOH liquid is sufficient to resolve this difference.

One additional comment can be made. Based on the JANAF data, the boiling point of liquid CsOH is estimated as 1263 K (990°C). An extrapolation of Equation 2.1-1 would predict a boiling point of 1392 K (1119°C).

2.2 ACRR Source Term Experiments

(K. O. Reil, 6423; M. D. Allen, 6422; H. W. Stockman, 6233; A. J. Grimley, 6425; R. W. Bild, 6454)

Understanding the release of radionuclides during fuel degradation in a core uncovery accident is the first stage in determining the amount and nature of the overall radioactive release from

the damaged nuclear plant. Current estimates of the release of the principal fission products over the range of relevant accident conditions are subject to significant uncertainty. A key element in reducing the uncertainty in predicting the potential releases is an improved understanding of the release of fission products from the fuel under severe fuel damage conditions. Major progress is being made in the development of mechanistic models (e.g., MELPROG's VICTORIA model) to significantly reduce these uncertainties. The ACRR Source Term (ST) program is being conducted to provide a data base for fission-product release over a range of fuel temperatures, system pressures, and fuel damage states. Significantly, these experiments are performed in well-controlled, well-known, in-pile conditions and in the presence of ionizing radiation, where little or no data currently exist, to allow validation of these improved fission-product release models.

2.2.1 Introduction

The ST-1 experiment was successfully conducted on April 28, 1987. This experiment was designed to study the release of fission products in a highly reducing environment at maximum fuel temperatures between 2300 and 2400 K. The goals for the aerosol and vapor sampling system for the ACRR ST-1 Experiment were to (1) measure the mass of specific fission products (primarily Cs, I, Te, Ba, Sr, Kr, and Eu) released from irradiated fuel under severe fuel damage conditions, (2) determine fission-product release rates as a function of temperature and time, and (3) qualitatively establish some of the chemical species that exist close to the fuel bundle under high-temperature accident conditions.

2.2.2 Description of the ST-1 Experiment

The nominal operating conditions for the experiment are listed in Table 2.2-1. The fuel segments used in these experiments were cut from BR-3 rods having a maximum burnup of approximately 47,000 MWd/tonne U. Two rod segments were cut from the center portion of each of two fuel rods. The rods were resealed in a pure argon atmosphere by welding zircaloy end caps on each end. The fuel characteristics for the four irradiated fuel segments and the four fresh fuel pins used as a gas preheater are given in Table 2.2-2.

The computer code ORIGEN was run to calculate the mass of each isotope present in the BR-3 fuel pins. The masses of several important elements present in 310 grams of BR-3 fuel are listed in Table 2.2-3. After posttest analytical methods determine the mass of each element collected in the filters, the values in Table 2.2-3 will be used to calculate the fractional releases, and these numbers will be compared with predictions from VICTORIA

Table 2.2-1

ST-1 Experiment Nominal Parameters

Maximum Temperature	2400 K
Pressure	0.17 MPa
Atmosphere	33% H_2 - 67% Ar
Test Section Flow Velocity	20 cm/s

Table 2.2-2

ST-1 Experiment Fuel Characteristics

• Irradiated Fuel (4 Rod Segments)	
BR-3	(I-44, I-109)
Initial Enrichment	8.26%
Maximum Burnup	47 GWd/tonne U
Maximum Rod Power	273 W/cm
Fuel Length	15 cm
Fuel Mass	310 g
• Fresh Fuel (4 Rod Segments)	
Enrichment	5%
Fuel Length	15 cm
Fuel Mass	320 g

Table 2.2-3

ST-1 Experiment Fission-Product Inventory
(from ORIGEN)

Element	Mass (mg)
Xe	1943
Kr	160
Cs	945
I	67
Te	145
Ba	651
Sr	381
Eu	42

and CORSOR. Segments of the BR-3 fuel rods used in the ST-1 experiment were cut and will be shipped to Carl Alexander at BCL for mass spectroscopic analyses to benchmark the ORIGEN computer code.

A functional diagram of the fission-product gas and aerosol sampling system for the ST-1 experiment is shown in Figure 2.2-1. Seven identical filter thimbles were arranged vertically in a concentric arc over a zirconia mixing plenum. The upstream end of the filter thimbles were located approximately 10 cm above the irradiated fuel bundle. The filter thimbles were plumbed in parallel between the mixing plenum and a gas manifold. The entire exhaust stream carrying fission-product vapors and aerosol flowed through each filter sampler individually. The samplers were changed sequentially using solenoid valves located on the outlet end of the filter thimble.

The final design of the filters that were used in the ST-1 Experiment evolved from a series of seven filter qualification tests that have been described in previous Semiannual Reports. The filter design that was used is shown in Figure 2.2-2. Each filter thimble was made of stainless steel with a nozzle at the upstream end that was about 1 cm in diameter and 5 cm long. The body of each filter thimble had a diameter of approximately 1.6 cm and was about 61 cm long. The first section in the body of the filter thimble was a 32-cm-long thermal gradient tube (TGT), similar in design and function to the one used in the ORNL VI test series. The temperature of the thermal gradient tube at the upstream end was approximately 900 K and decreased to 400 K near

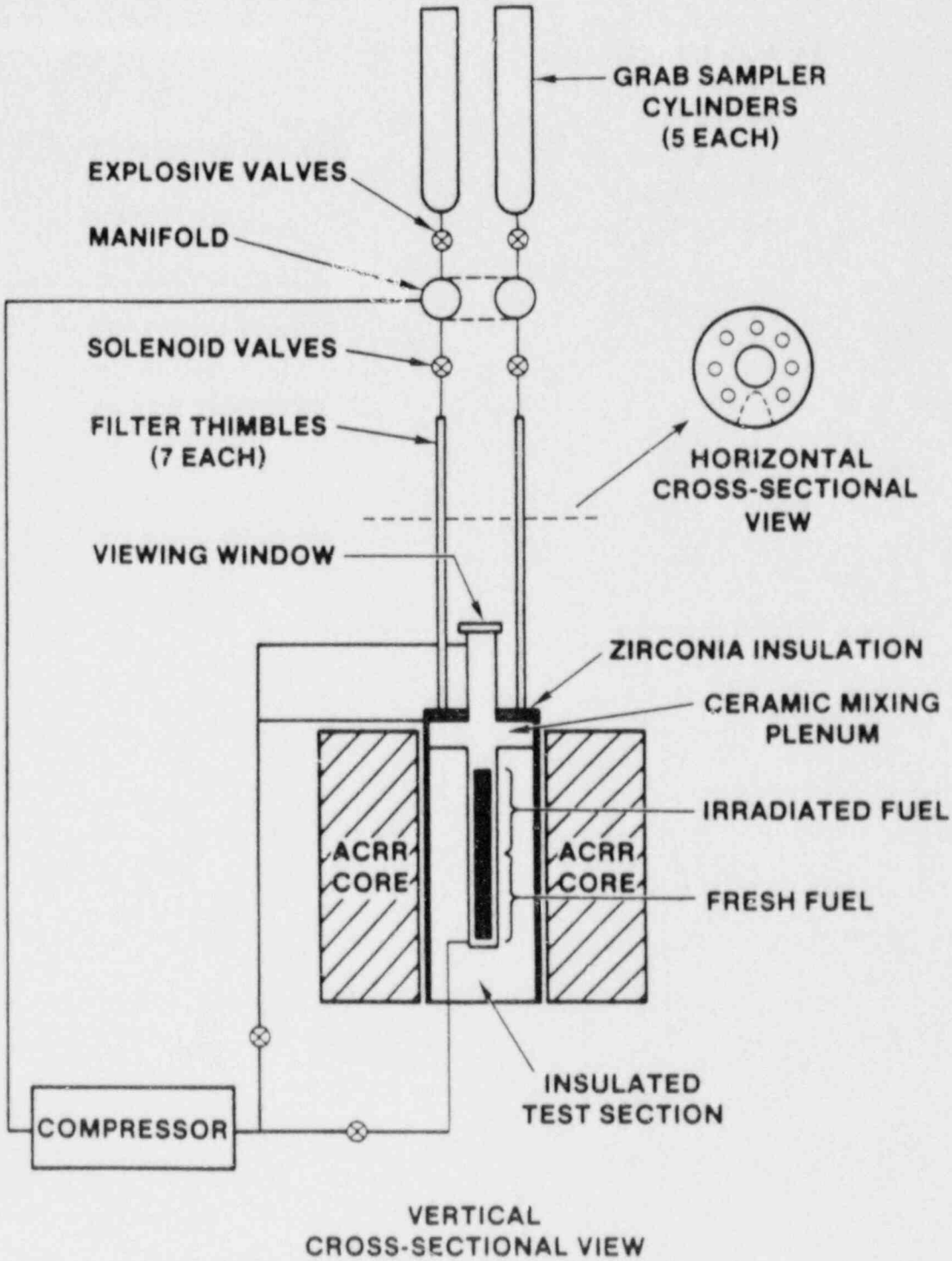

Figure 2.2-1. Functional Diagram of the Gas and Aerosol Sampling System for the Source Term Experiment

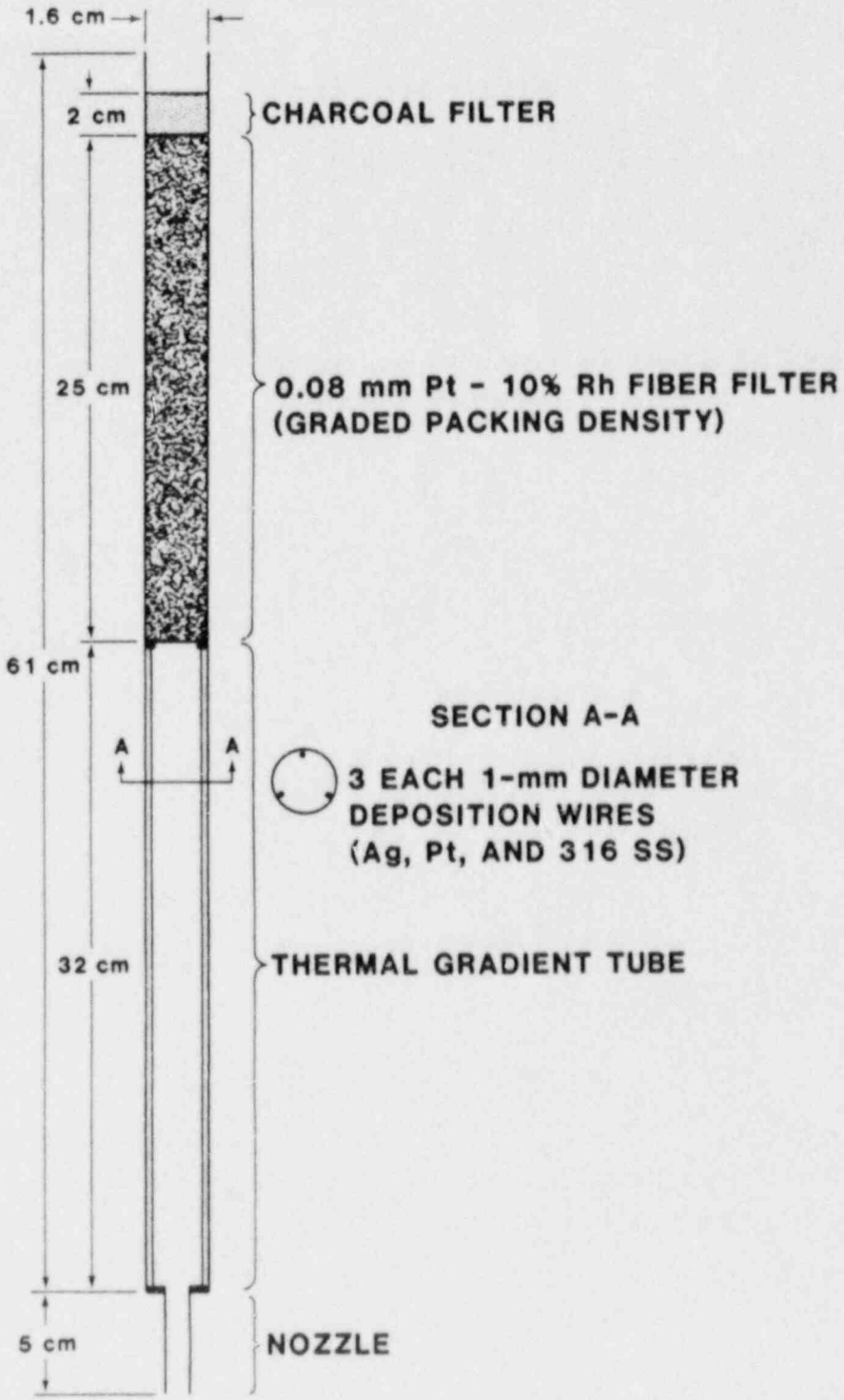

Figure 2.2-2. ST-1 Filter Design

the fiber filter section. The thermal gradient tube had three deposition wires of Ag, Pt, and stainless steel running parallel to its walls. These deposition wires were inserted to provide information on chemical speciation. They were intended to collect fission-product aerosols and chemically reactive vapors that will be analyzed with a SEM by wavelength and energy dispersive analyses. The stainless steel wire was included because it is the same material as the thermal gradient tube and will give an indication of chemical species deposited in the thermal gradient tube; the Pt wire was included because it is chemically inert to most fission products, except possibly Te at high temperatures; and the Ag wire was intended to react with the gaseous iodine species HI and I_2. The flow in each filter sampler passed through a 25-cm-long fiber filter composed of 0.076-mm diameter Pt-10%Rh wire with a graded packing density. The Pt-10%Rh fibers were held in a stainless steel tube by stainless steel screens that were tack welded on each end. The tube had outside O-rings on each end to seal it inside the filter thimble and to prevent the flow of aerosol and vapor around the fiber filter. A graded packing density was used to obtain the necessary filter efficiency and to preclude a high pressure drop and filter plugging. The gas then flowed through a 2-cm-long granular charcoal filter, which was included to collect noncondensed vapors such a HI, I_2, and H_2Te.

After a recirculating H_2-Ar flow was established in the experimental package, the test section was neutronically heated with the ACRR on a temperature ramp of one K/s from room temperature to approximately 1600 K. The fuel bundle was held at 1600 K for about 20 minutes to permit final alignment of the optical systems. The one K/s ramp was then resumed until temperatures in the test section reached approximately 2400 K. The reactor power was then reduced and regulated to maintain the temperature in the irradiated fuel bundle at approximately 2400 K for about 20 min. The experiment was terminated by reactor shutdown. Gas flow was maintained during the cooldown process. The temperature in the test section flow channel versus time is plotted in Figure 2.2-3. The thermocouple labeling scheme shown in the figure legend indicates the general location of the thermocouple (CH indicates channel), the thermocouple type (C indicates a Type-C thermocouple), and the numbers indicate the distance above or below core center line (015 indicates that the thermocouple was located 1.5 in above core center line, while -20 indicates that the thermocouple was located 2 in below core center line).

The axial temperature profiles measured by five Type-C thermocouples in the test section flow channel are plotted in Figure 2.2-4. An axial location of 0 cm marks the interface between the fresh fuel and the irradiated fuel. The negative axial locations correspond to fresh fuel, and the positive axial locations represent distances from the bottom end of the irradiated fuel to the top end. The axial temperature profile that was attained was uniform over the lower two-thirds of the irradiated fuel bundle.

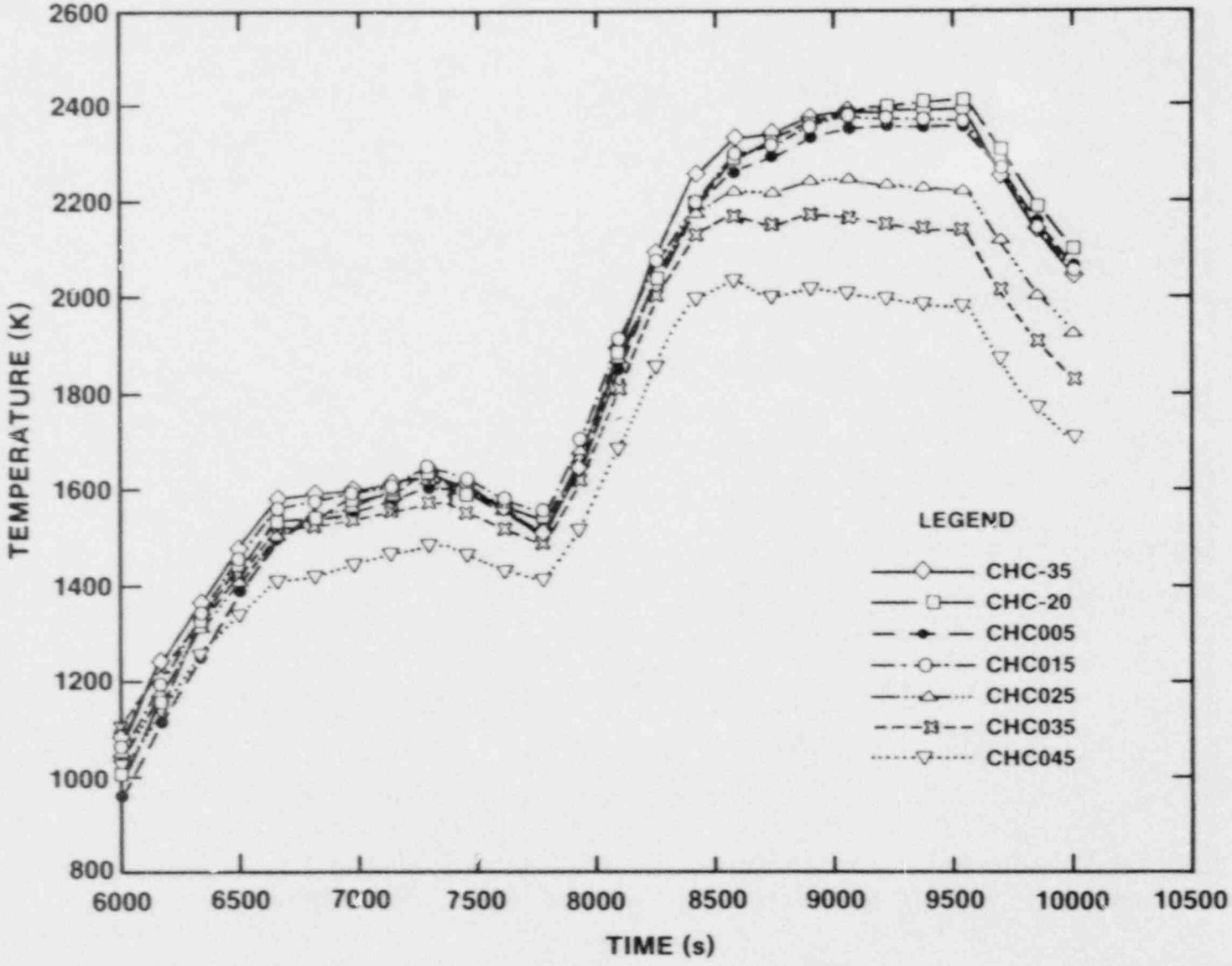

Figure 2.2-3. ST-1: Type C Thermocouples - Channel

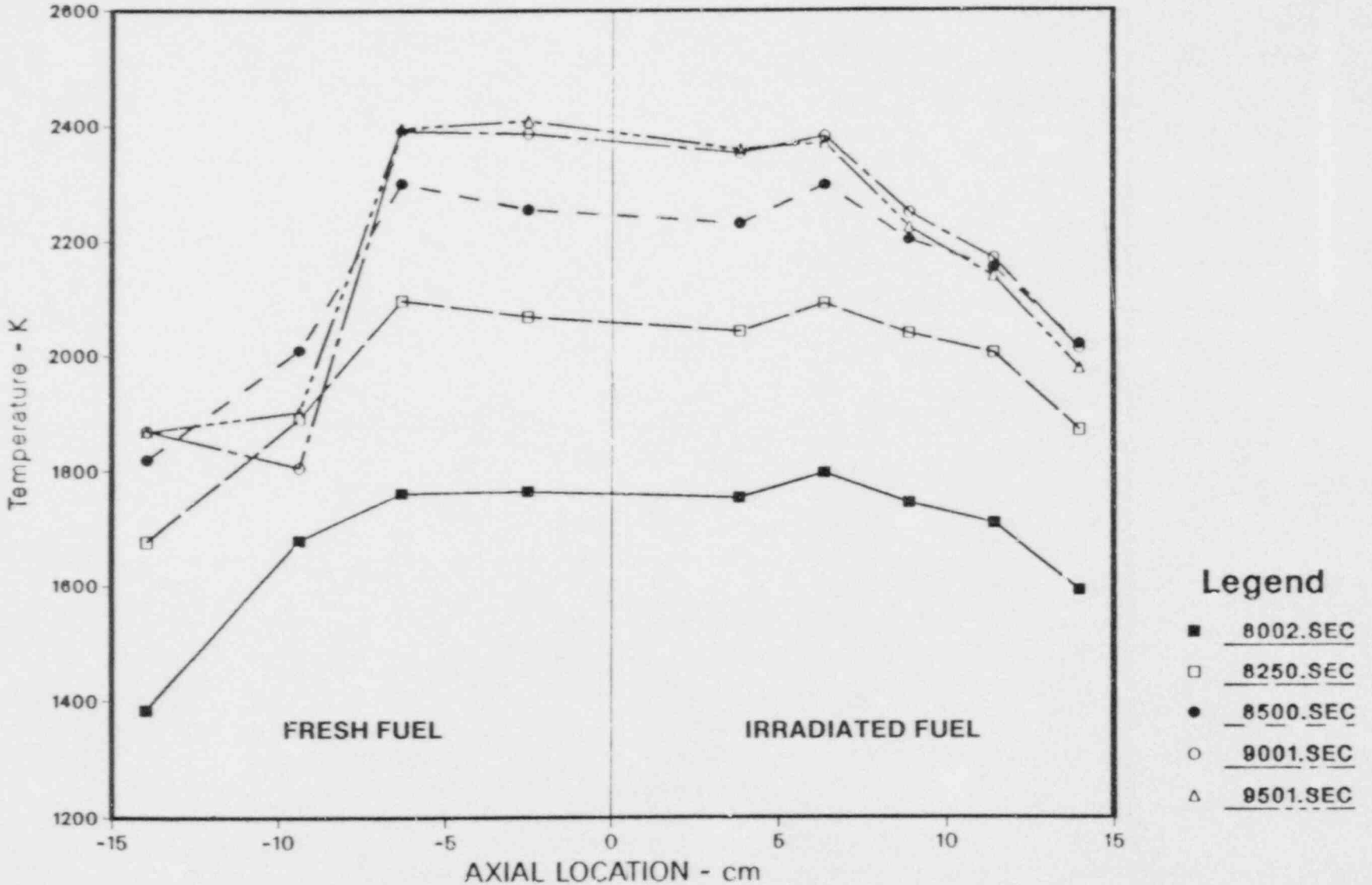

Figure 2.2-4. ST-1: Axial Temperature Profile in Channel

Because of radiation heat losses, the axial temperature profile decreased over the upper third of the rods to a maximum temperature of about 2000 K at the upper end of the rod. Apparently, about two or three cm of the zircaloy cladding on the upper end of the fuel pins may not have reached the melting temperature.

Six of the seven filter samplers were used during the experiment to collect fission-product vapors and aerosols. Filter number 7 was used as a blank, i.e., it was never opened for flow. Flow through each filter was controlled by a solenoid valve on the downstream end of the filter assembly. Each filter had a nozzle that projected into the ceramic mixing plenum above the test section and was therefore open to the mixing plenum even though there was no bulk flow through a filter when its solenoid valve was closed. The blank filter was used to ensure that natural convection caused by large temperature gradients or rapid pressure changes in the system did not cause fission-product contamination in a filter that was not open to bulk flow. Filter number 1 was open on the heat-up ramp and was automatically switched to filter number 2 at 2073 K, just prior to clad melt. At clad melt, a dense cloud of aerosol was observed that obscured the view of the top of the test section and quickly plugged filter number 2. The plugging was indicated by a significant increase in the pressure drop measured across the filter and by a decrease in the gas flow rate through the filter. Filter number 2 was open for 228 s. Filter number 3 was open for 130 s as the temperature in the test section was brought to 2400 K. Filter number 3 also plugged and the flow decreased significantly because of the blocked flow. Filters number 4 and 5 were open during the temperature plateau. Filter number 4 was open for 353 s and filter number 5 was open for 654 s. Filter number 6 was open during the cool-down phase of the experiment. Figure 2.2-5 indicates the time interval and temperature range in which each filter thimble was open. The temperature plotted in this figure was measured by the same Type-C thermocouples located in the test section flow channel that are described in Figure 2.2-3.

2.2.3 Preliminary Results of the ST-1 Posttest Analyses

2.2.3.1 On-line Optical Spectra

An optical multichannel analyzer was used to record the optical spectrum of the ST-1 test at approximately 1 s intervals during the experiment. The light source for the spectra was the blackbody radiation emanating from the hot test section. A full analysis of these absorption spectra could, in principle, be used to identify elements released from the fuel and to quantify this release as a function of time. The environment inside the reactor makes such a task impossible for all species but the spectra do allow a qualitative picture of the release process to be developed for elements whose absorption lines are identified.

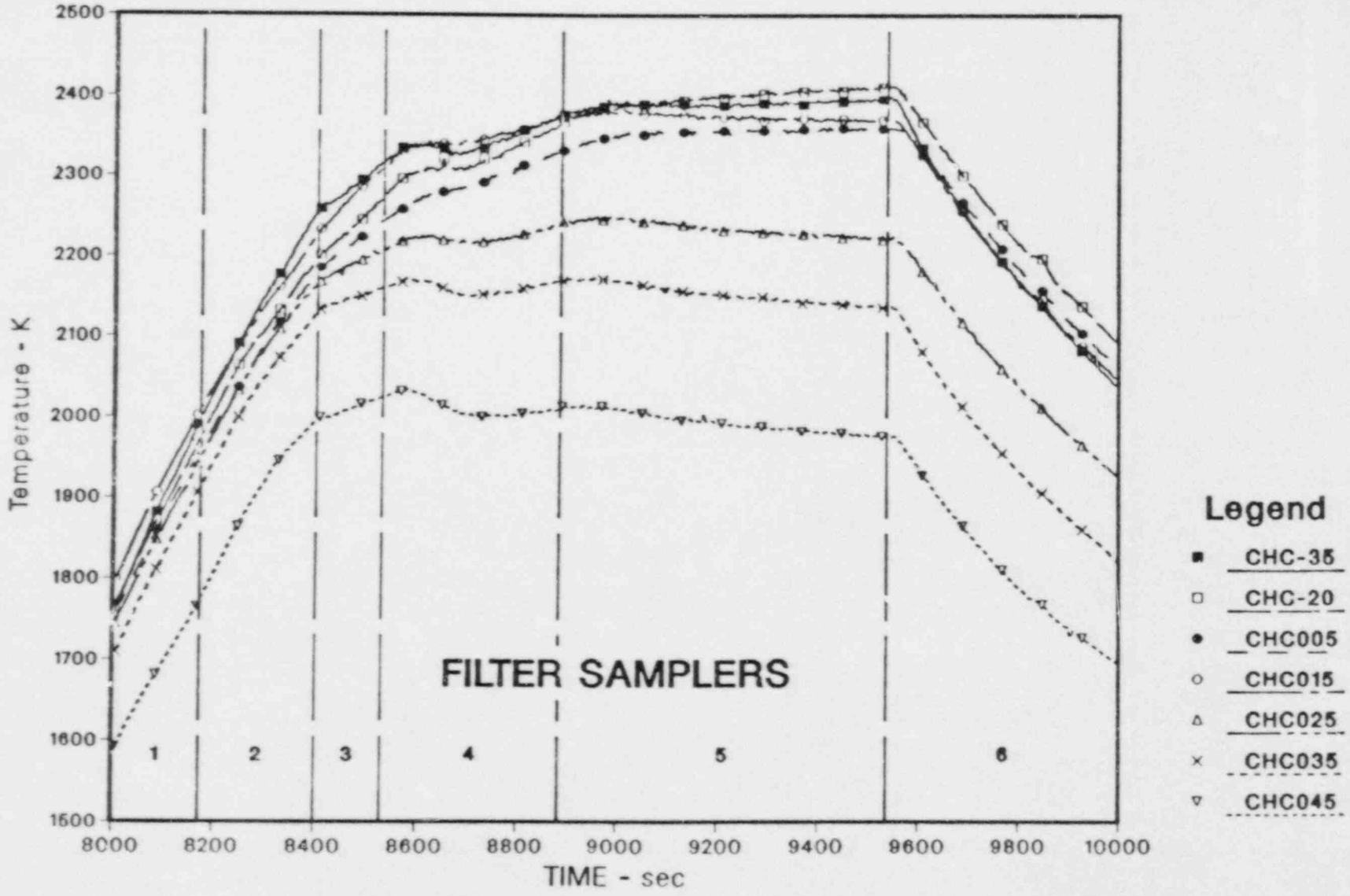

Figure 2.2-5. ST-1: Type C Thermocouples - Channel

In this section three spectra recorded at different times during the experiment are presented and their preliminary analysis discussed.

The temporal locations of the three spectra are shown in Figure 2.2-6. The vertical lines indicate the times at which each spectrum was recorded. The data plotted in the figure are the temperatures indicated by the channel thermocouples. The first spectrum (Figure 2.2-7) was recorded 8282 s into the experiment. The maximum temperature indicated by any of the thermocouples at this time is near cladding melt temperature. There is evidence from other visual sources (the video tape of the test and still photography) that the clad was breached at 8135 s, over 2 min before this spectrum was recorded. The second spectrum (Figure 2.2-8) was recorded at 8973 s. This time comes very near the middle of the isothermal part of the experiment. The third spectrum (Figure 2.2-9) was recorded at 9435 s. This spectrum gives information pertinent to times at the end of the isothermal portion of the test. Shortly after this spectrum was recorded the reactor was shut down and the test section was allowed to cool.

Each of the three spectra (Figures 2.2-7 through 2.2-9) consists of a series of absorbtion (and emission) lines superimposed on a background radiation curve. This background curve is the result of the convolution of a blackbody emission curve due to the hot test section and an optical train detection curve due to the transmission characteristics of the various optical elements in the system and the wavelength sensitivity of the detector. The intensity of the background curve is seen to vary with time. This is brought about by the change in temperature of the test section from one spectrum to the next, which alters the shape and intensity of the blackbody curve, and by a change in apparent aerosol concentration in the optical path, which reduces transmission as the density increases. In examining comparable features in the three spectra, we find the figure of merit is relative light extinction rather than absolute intensity reduction.

The three spectra contain snapshot information at times when the releases of fission products are expected to be quite different. The similarities and differences among the three spectra are pointed out in the next paragraph, concentrating on four features that appear to varying degrees in all three spectra. All the features of interest lie at wavelengths greater than 6000 angstroms. Virtually all features observed at shorter wavelengths are due to the fluorescent lights in the vicinity of the detector. The four features that will be considered are numbered on the spectra in Figures 2.2-7, 2.2-8, and 2.2-9.

Feature number 1 is weakest in the early spectrum, strongest in the middle time spectrum, and dropping in intensity at the late spectrum. This feature has not been identified as due to any

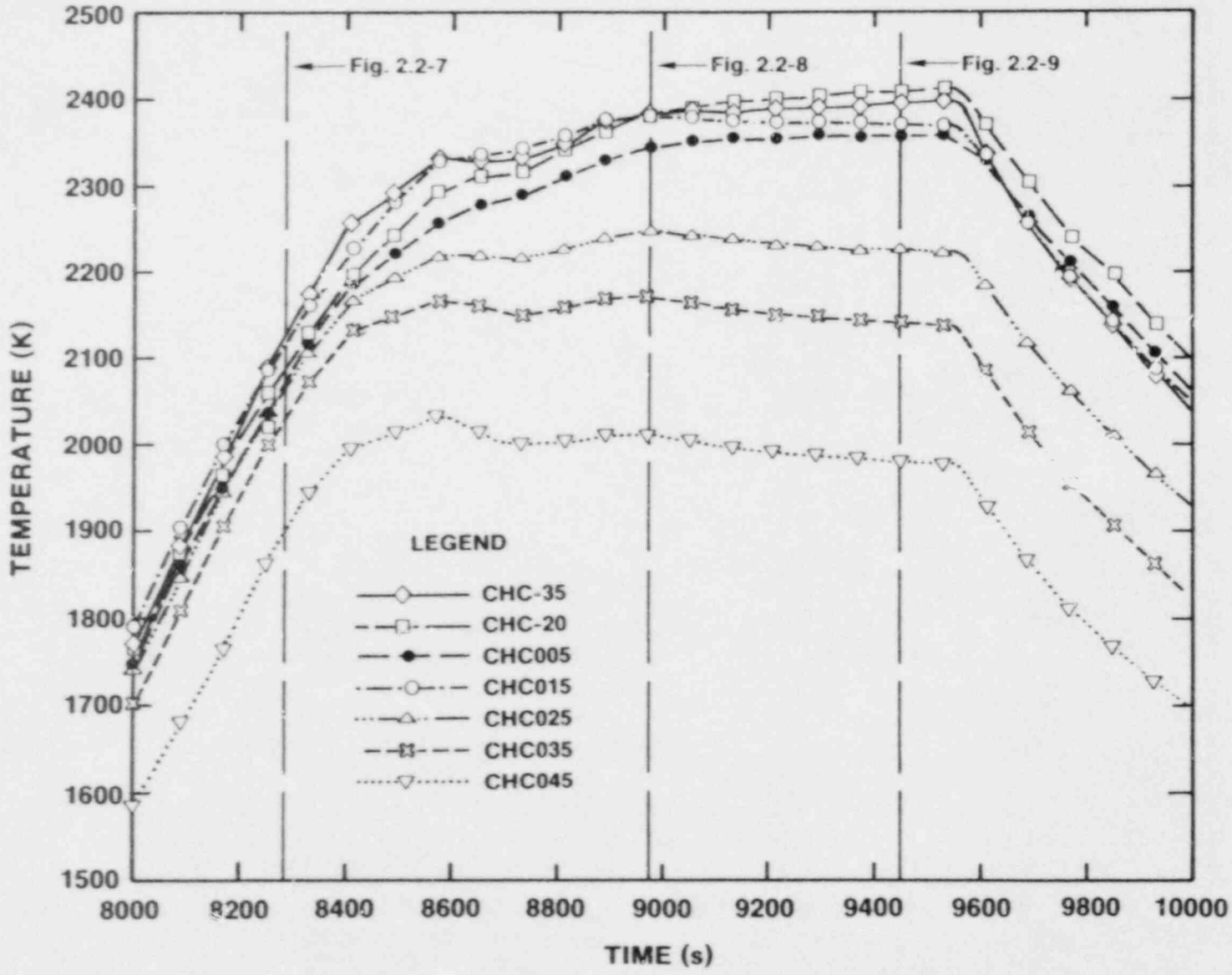

Figure 2.2-6. Selected Optical Spectra Emanating From the ST-1 Test Station

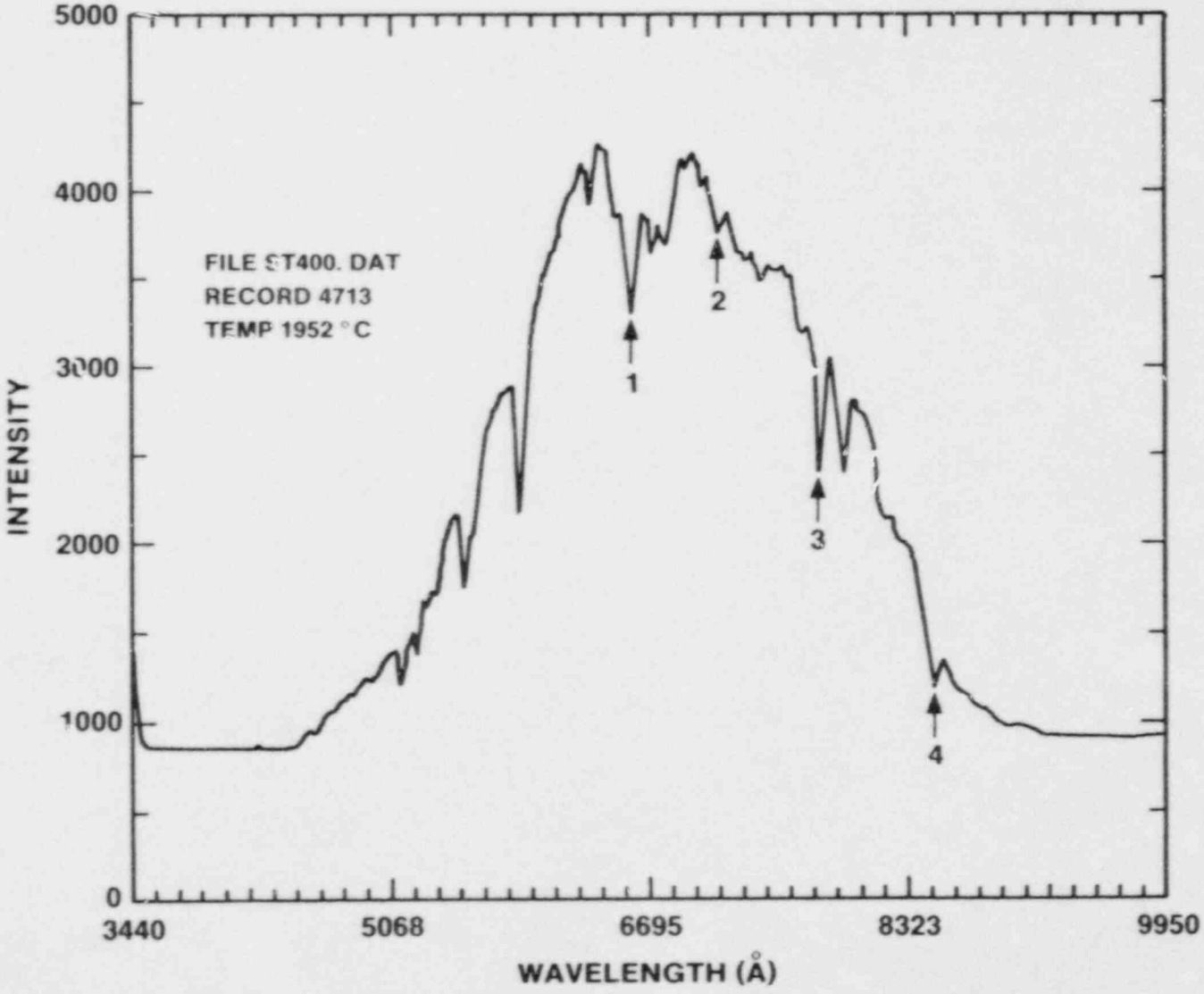

Figure 2.2-7. Optical Spectrum Recorded at 8282 Seconds

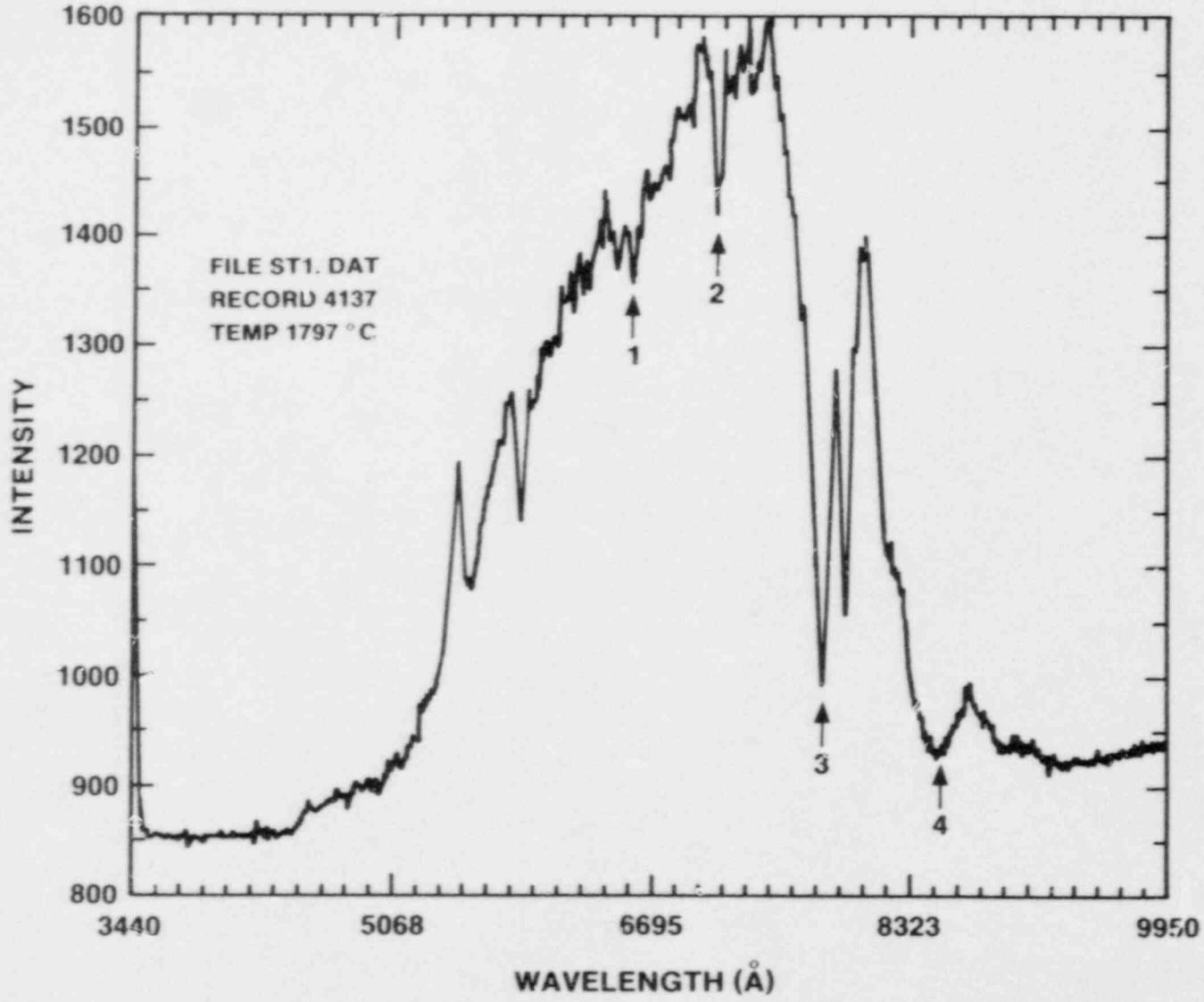

Figure 2.2-8. Optical Spectrum Recorded at 8973 Seconds

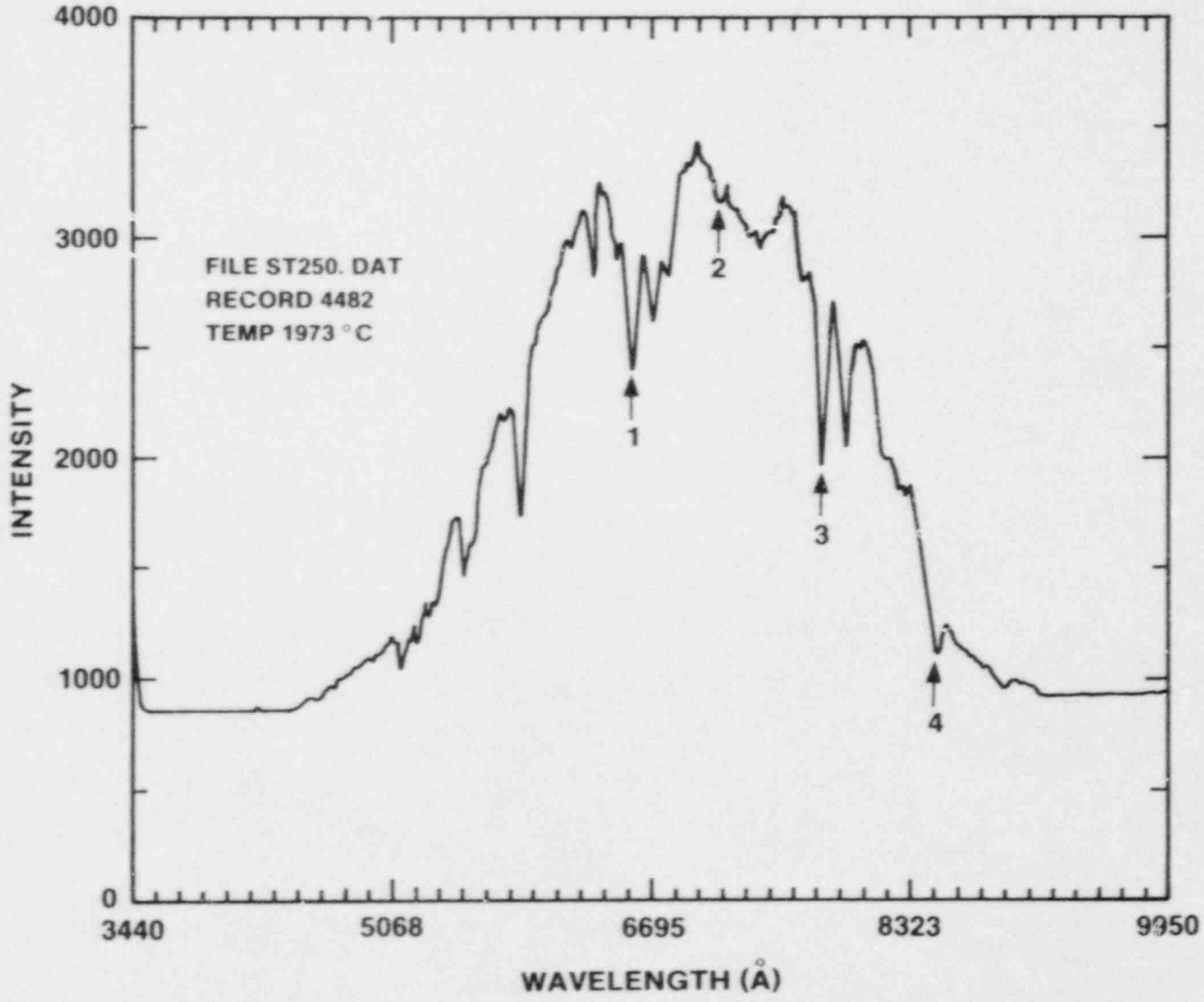

Figure 2.2-9. Optical Spectrum Recorded at 9435 Seconds

particular atom or species. The temporal nature of this feature indicates that it is unlikely to be due to a volatile species or a clad constituent. Feature number 2 is strongest in the earliest spectrum and is very weak in both of the later spectra. An identification of the source of this feature has not been made. The most likely sources, based on the temporal behavior of the absorption, would be a volatile species, i.e., an alkali metal or a halogen, or possibly a clad constituent. Feature number 3 has been identified as a pair of lines due to atomic rubidium. This fission product appears in concentrations about one-fourth that of cesium and should exhibit a very similar chemical behavior. The temporal evolution of this feature shows considerable early release of the rubidium and a steady decline of the intensity, and hence release, as the test proceeds. Feature number 4 is found to be very intense in the earliest time spectrum, giving nearly complete absorption of the background light, and decreases considerably in the later spectra. This feature has been identified as an absorption due to atomic cesium. The temporal behavior of the line agrees quite well with predictions for the temporal release of cesium from the fuel. Efforts are still underway to identify the source of the first and second features in the spectra. The identification of these lines is complicated by the possibilities that they may not be due to atoms, or that the atoms could be in excited states or be ionized by the strong radiation field in the test section. Further analysis of the cesium and rubidium lines will yield more detailed temporal information on the evolution of the neutral atoms of these two species during the test.

2.2.3.2 Gamma Spectroscopy of the ST-1 Package in the Hot Cell

The ST package without the containment canister was gamma scanned in Zone 2A prior to the test. The primary radionuclides observed in the pretest gamma spectra were ^{134}Cs, ^{137}Cs, and ^{154}Eu. The bare ST package was gamma scanned approximately seven days posttest. Figure 2.2-10 compares the pretest and posttest ^{137}Cs activity in the fuel. At the lower end of the irradiated fuel, 98 percent of the cesium was released, whereas at the top end of the fuel, only about 20 percent of the cesium was released. This difference can be explained by the axial temperature profile along the irradiated fuel pins (Figure 2.2-4). The lower end of the irradiated fuel bundle reached temperatures as high as 2400 K, whereas the top end of the fuel probably did not exceed 2000 K. Therefore, zircaloy cladding probably did not melt at the top of the fuel bundle. This affected the fractional releases versus axial location along the irradiated fuel bundle.

Based on posttest gamma spectra of the ST-1 package, the filter samplers were shown to be greater than 98 percent efficient. Most of the radioactivity that permeated the filters was attached to fine charcoal dust that was blown out of the filter assembly and deposited in the solenoid valves just downstream of the filters.

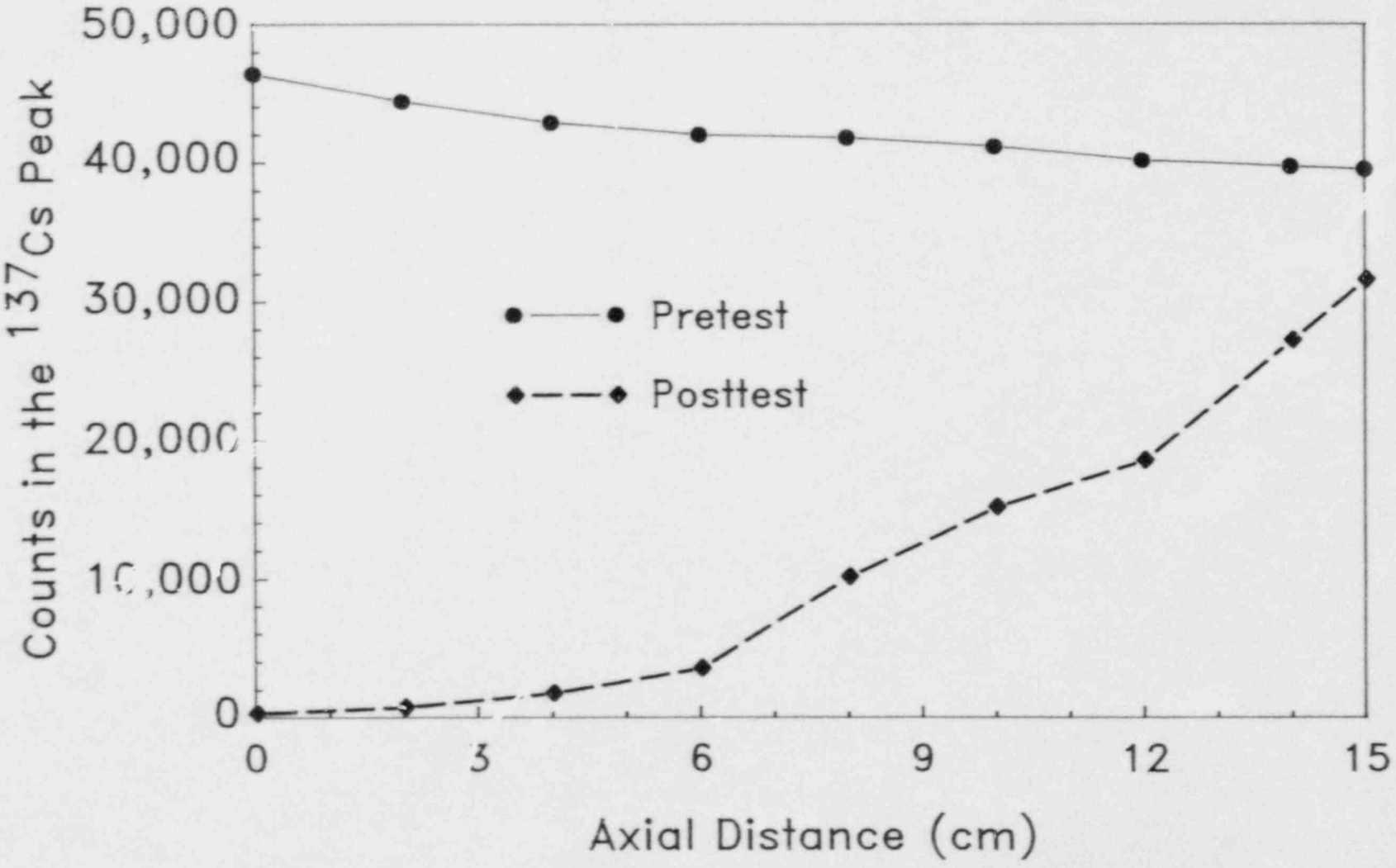

Figure 2.2-10. ^{137}Cs in Fuel -- Before and After ST-1

Gamma spectroscopy was used to determine the europium distribution in the package before and after the ST-1 test. The observed concentrations for the irradiated fuel section both before and after the test are shown in Figure 2.2-11. The pretest concentration is seen to be relatively flat over the entire length of the fuel rods. The posttest scan shows significant migration of europium from the hot end to the cool end of the rods. A plausible mechanism for this migration, in the strongly reducing atmosphere of the test, is the diffusion of atomic europium to the grain surface followed by vaporization into the open porosity. The axial temperature gradient gives rise to an axial concentration gradient that is then a driving force for diffusion through the open porosity from the high-temperature to the low-temperature end of the fuel rod. The low-temperature portion of the fuel is not able to support the same vapor pressure as the high-temperature end, so condensation takes place, which gives the net movement of the europium within the fuel.

The ST-1 package was disassembled in the Hot Cell Facility. Seven filter samplers and five gas grab sample bottles were recovered for analyses. Longitudinal gamma scans of individual filter thimbles were performed in 2-cm increments. As expected, the gamma spectra were dominated by ^{134}Cs and ^{137}Cs. The only other radioisotope that was identified in the gamma spectra of the filter thimbles was ^{154}Eu ($t_{1/2}$ = 16 years). The integral counts in the ^{137}Cs peak are plotted versus distance for filter thimble 1 in Figure 2.2-12. This plot is typical of those for the other five filter samplers that were opened during the ST-1 test. Cesium condensed on the interior surface of the nozzle because it was cooler than the gas in the ceramic mixing plenum. Very little cesium was on the TGT between 6 and 20 cm because it was heated to approximately 900 K. As the fission-product laden gas flowed out of the heated section of the TGT, it condensed on the interior stainless steel surfaces, with a peak at about 26 cm. In all filter thimbles, a large amount of cesium collected on the front of the fiber filter located at 38 cm. The small increase in cesium collection that shows up in the fiber filter at 48 cm was due to an increase in packing density from 5 to 6 percent. An increase in cesium deposition occurred in all filter samplers on the front screen of the charcoal filter and in the charcoal. This cesium was probably collected as CsI.

2.2.3.3 Preliminary Results of Posttest Wet Chemical Analyses

Each filter sampler was divided into five basic components: the nozzle, the TGT, the fiber filter, the deposition wires, and the charcoal. Each component was gamma counted in either 1- or 2-cm increments. After each component was gamma scanned, they were analyzed by other techniques. The deposition wires were transferred out of the Hot Cell for elemental analyses by SEM/WDX. These analyses are incomplete. The charcoal will be rinsed to remove cesium and then neutron activated to quantify the mass of

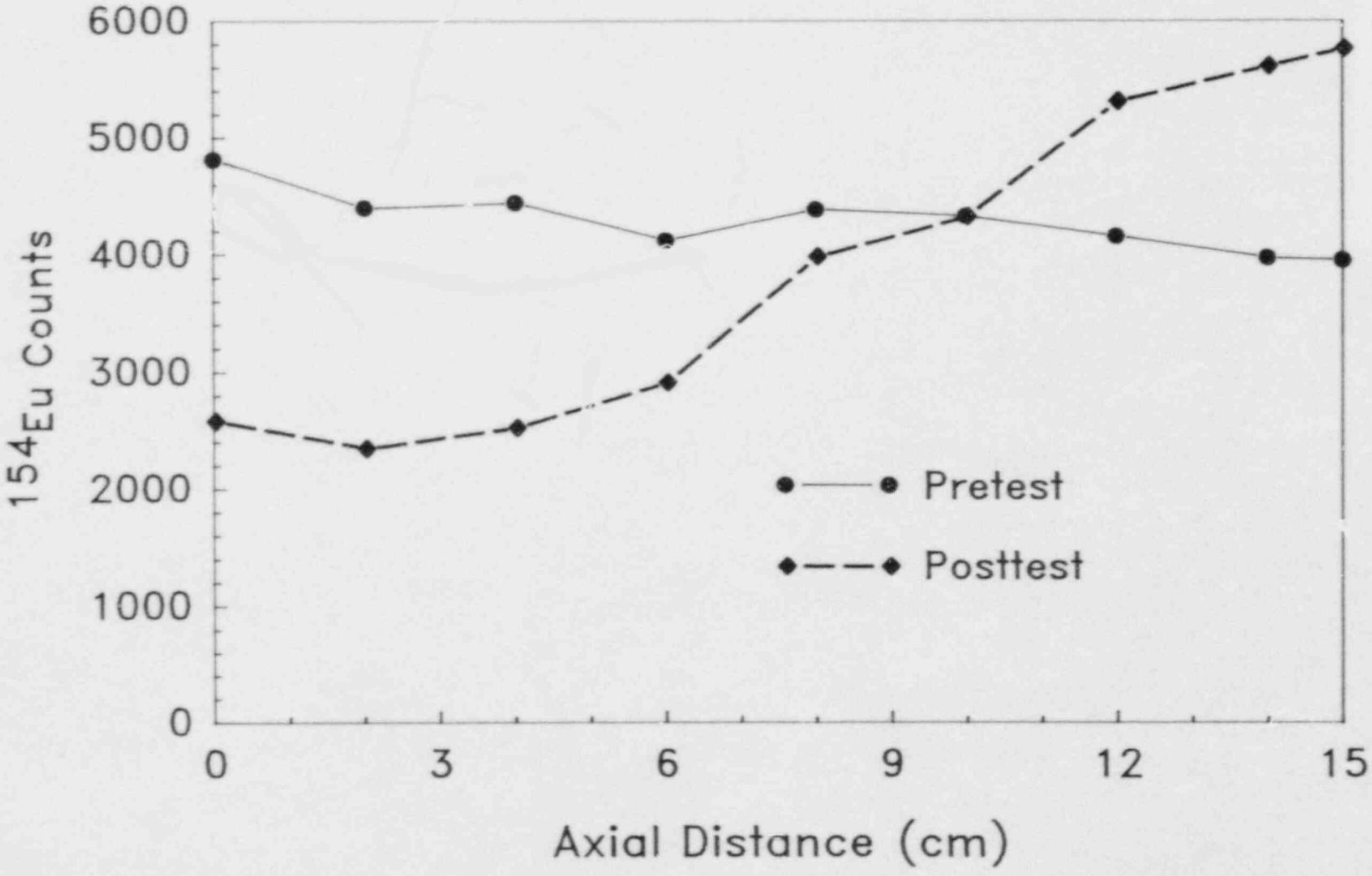

Figure 2.2-11. ^{154}Eu in Fuel -- Before and After ST-1

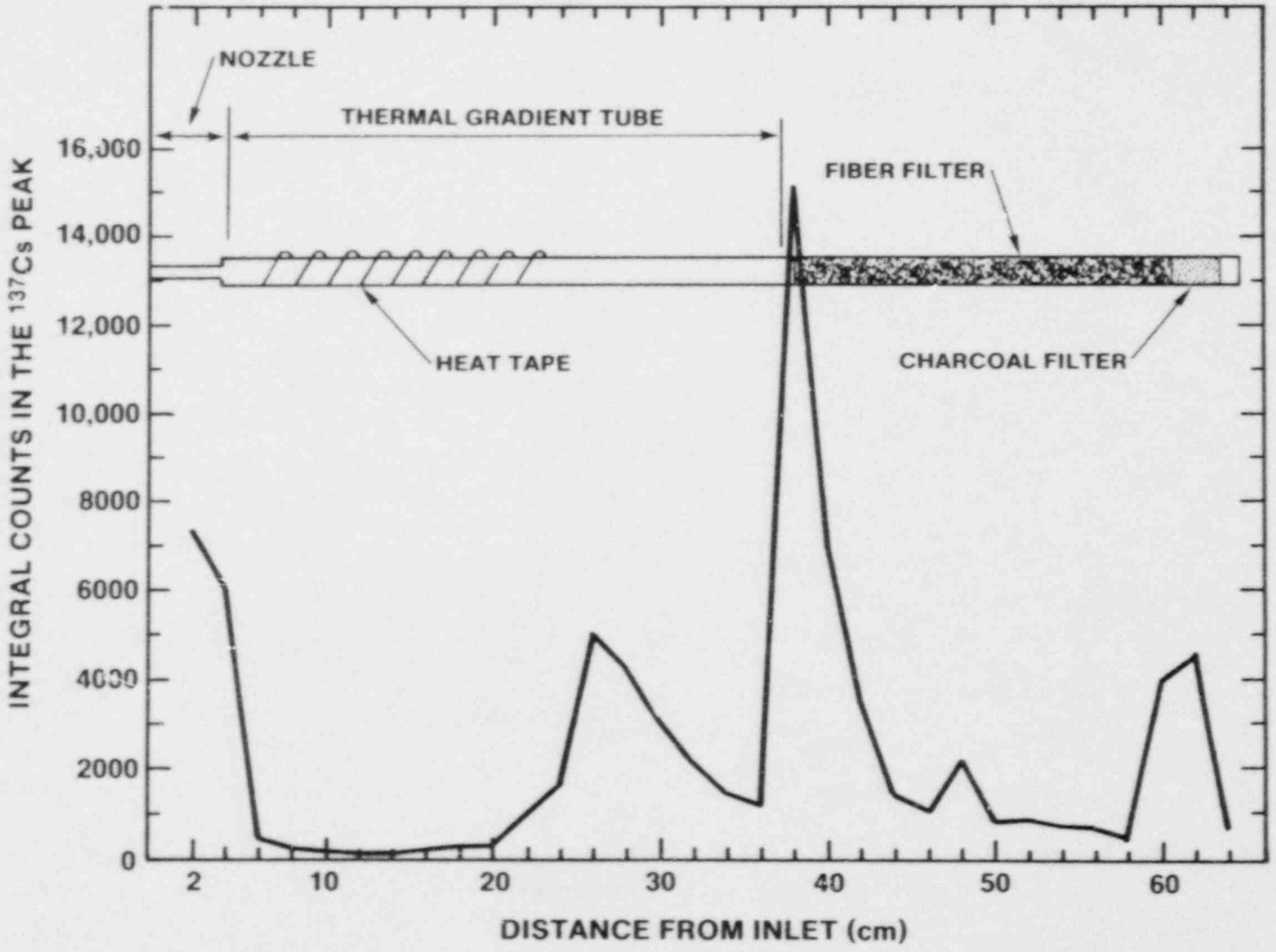

Figure 2.2-12. Source Term Experiment 1 - Filter Thimble 1

iodine collected on it. The nozzle, TGT, and fiber filter were leached with water and then 7.5 M nitric acid to remove soluble species. Aliquots of these leachates were gamma counted. Twelve of the leachate samples had noticeable amounts of insoluble material: the water leachates from fiber filters 1 through 6 and from TGTs 3 through 5, and the acid leachates from fiber filters 3 through 5. Analytical procedures for these insoluble materials are discussed in section 2.2.3.4.

Comparisons of the gamma spectra of aliquots of the water and acid leachates showed that approximately 98 percent of the Cs collected by the filters was soluble in the water leachates. By comparing the gamma spectra for the filter components before and after the leaches, it was calculated that greater than 99.9 percent of all of the Cs was removed from the filter components by the water and acid leaches.

An ion specific electrode (ISE) was used to measure the iodide concentrations in the water leachates. Although the measured release rate matches other volatile species well, e.g., Cs, the total iodine released appears to be low compared with predictions from VICTORIA. The remaining iodine is probably on the charcoal filters. The charcoal filters will be analyzed for iodine by leaching the cesium with water to reduce the gamma activity, analyzing the leachate for iodide by ISE, and analyzing the charcoal for iodine by neutron activation analysis after the Cs has been removed.

Soluble Ba and Sr species have been measured using ion chromatography (IC). The acid leachate samples must be rerun with an additional column that will remove monovalent ions that were added as NaOH to neutralize the acid. However, the majority of the Ba and Sr is in the water leachates. Ion chromatography only measures the Ba and Sr in solution. The black insoluble material found in the water leachates was approximately 10 percent Ba and 10 percent Sr. Insoluble Ba and Sr are not measured by IC, but will be measured by dissolving the water insoluble material in nitric acid and running samples in the IC.

Preliminary results of electrochemical voltammetry indicate that less than 10 μg of Te was present in any of the water and acid leachates of the filter components. Less than 0.1 percent of the Te in the irradiated fuel was transported to the filter samplers in the ST-1 test.

The high beta activity on the deposition wires makes handling them in glove boxes difficult and EDX analyses impossible. Elemental analyses of the deposits on the wires will be obtained by wavelength dispersive analyses (WDX).

2.2.3.4 Black Insoluble Material in Leachates

Some of the water and acid leachates from the fiber filters and thermal gradient tubes had noticeable amounts of black insoluble material, especially the water leachates from fiber filters 3, 4, and 5, which were open during the ST-1 high-temperature plateau (approximately 2000 K). In the water leachates, the black insoluble material was apparently removed by the mechanical action of the water flowing through the filter component; it is not soluble in water. Major elements that have been identified to-date in the black insoluble material in the water leachates are U, Zr, Ba, and Sr, with minor amounts of Pu, Am, I, Y, La, Ce, Sm, Eu, and Cs. The black insoluble material in the acid leachates has been identified by SEM/EDX as primarily AgCl. Samples of the black insoluble material will be sent to BCL and ORNL for quantitative isotopic analyses using mass spectroscopy.

Ten milliliters of the water leachate from fiber filter number 3 was vacuum filtered through a Whatman 42 glass fiber filter. The black insoluble residue collected by the filter contained a strong beta emitter. The filter read about 20 rads/h at 2.5 cm with the Geiger counter beta shield open. It was necessary to prepare weaker samples for alpha and beta counting. Two samples were prepared by transferring a small amount of the original sample to new glass fiber filters. Sample A had a Geiger counter reading of 2.5 rads/h at 2.5 cm with the beta shield open and sample B had a reading of 0.4 rads/h.

Alpha counting was performed using an ORTEC Model 576 Alpha Spectrometer connected to a Canberra Series 40 multichannel analyzer. Alpha standards used for energy calibrations were ^{241}Am, ^{230}Th, and ^{239}Pu. An energy range of 4.0 to 6.5 MeV was used.

The main peak observed was a combination of the 5.49 and 5.44 MeV ^{241}Am alpha peaks. These peaks completely dominated the spectrum up to about 5.5 MeV. Other peaks were seen in the 5.54 to 5.75 MeV range (^{223}Ra from the ^{239}Pu decay series) and in the 5.80 to 6.05 MeV range (^{227}Th from ^{239}Pu or ^{218}Po from ^{238}U or both). There were indications of several other possible peaks. The estimated energies and one or more possible identifications for each are:

1. 4.20 MeV (^{238}U)
2. 4.78 MeV (^{237}Np or ^{233}U from ^{241}Am or both and ^{234}U or ^{222}Ra from ^{238}U or both)
3. 4.81 to 5.05 MeV (^{229}Th from ^{241}Am)
4. 4.95 to 5.06 MeV (^{231}Pa from ^{239}Pu)
5. 5.16 MeV (^{239}Pu or ^{240}Pu)
6. 5.30 MeV (^{218}Po from ^{238}U)
7. 5.9 MeV (^{222}Rn from ^{238}U)
8. 5.54 to 5.75 MeV (^{223}Ra from ^{239}Pu).

None of these latter peaks were large enough to be unambiguously identified, but taken together they are additional evidence that ^{239}Pu or ^{235}U or both are present in the sample. They also provide some evidence for the presence of ^{238}U. Because of the dominance of the ^{241}Am peak, it was not possible to quantitate the amounts of each isotope present. The ^{241}Am activity was estimated to be at least 100 times greater than that of any other alpha emitter. Short counts at higher alpha energy ranges (up to 8 MeV) showed no other alpha peaks.

Filter sample A was beta counted using a Geiger Counter as a detector and a series of graded Al filters between the source and detector to determine the end point energy of the major beta emitter in the sample. The end point energy found was 2.2 MeV. This is a close match to the end point energy of 2.27 MeV for ^{90}Y, indicating that the ^{90}Sr-^{90}Y decay chain is the major beta emitter in the black insoluble material in the water leachates.

2.2.4 Comparison of ST-1 Experiment Results With Predictions From CORSOR and VICTORIA

A stand-alone version of the VICTORIA fission-product release module from the MELPROG code has been used to model the release of fission products in the ST-1 test. In the following paragraphs, VICTORIA predictions are compared to the experimental results and to releases calculated using CORSOR and its various modifications.

The calculations using VICTORIA were performed with the preliminary temperature, pressure, and flow information from the test. These data underestimate the maximum temperature by about 100 K and further refinement of the flow and pressure data is required to determine their accuracy. The underestimate of the temperature affects not only the total release but the timing of the release as well. The strongest temporal effect is brought about by the change in the timing of clad disruption.

The physical parameters used for the VICTORIA and CORSOR calculations are given in Table 2.2-4. The temperature ramp used was a straight linear rise from T_o to the indicated maximum temperature followed by a constant temperature plateau. After a predetermined time at temperature, there was a cool-down period, again at a constant linear rate. The clad was assumed to have failed at its melting point. The pressure and gas flow rate were held constant for the entire calculation.

For the purposes of the VICTORIA calculation, the fueled portion of the test package was divided into five equally spaced axial levels. Each of these nodes had a single temperature for the fuel and clad, another temperature for the coolant gas, and a third for structural materials within that level. There were two additional vertical nodes that did not contain fuel and were

Table 2.2-4

Physical Parameters Used in VICTORIA and CORSOR Calculations

	VICTORIA	CORSOR
T_s (K)	1625	1623
T_{max} (K)	2366	2466
T_{heat} (K/s)	1.1	1.28
T_{cool} (K/s)	0.63	0.63
t_t (s)	1123	1140
profile	(1.0, 1.0, 0.94, 0.91, 0.83)	
P (atm)	1.5	n/a
v (cm/s)	6.0	n/a

designed to model the thermal gradient tube and fiber filter. These two levels had separate temperatures for the gas and structures in each. The pressure and flow parameters were taken to be independent of the spatial location in this calculation.

The CORSOR calculations used only the fueled portion of the test section. The same axial temperature profile was used but the maximum temperature was 100 K higher and the heat-up ramp was steeper to account for this difference. Pressure and flow were not used in the CORSOR calculations.

Table 2.2-5 presents a comparison of the calculated and observed releases for the VICTORIA and CORSOR calculations and the currently available experimental results. It should be noted that the measured release fractions represent preliminary data and are subject to further refinement. The measured data consists of total release and filter fractions for cesium and barium. The barium value is a lower limit and may be quite low due to the incomplete analysis of the black insoluble material. Cesium is also present in this substance but appears to be in a much smaller proportion than the barium.

The total release fractions for cesium show some definite differences in the various calculations. CORSOR-M overpredicts slightly while both modifications underpredict with CORSOR-3 showing much better agreement than CORSOR-D. The VICTORIA prediction lies between CORSOR-3 and the measured value. This result will be improved by the use of the proper temperature

Table 2.2-5

Measured Versus Predicted Releases

CESIUM		
	Observed	71 Percent
	VICTORIA	73 Percent
	CORSOR-M	89.5 Percent
	CORSOR-D	50.6 Percent
	CORSOR-3	69.3 Percent
BARIUM		
	Observed	10 Percent
	VICTORIA	1 Percent
	CORSOR-M	0.4 Percent

profile for the test. It should also be noted that the CORSOR-3 value includes a significant (9 percent) release prior to clad failure. This latter comment is less important for the other versions of CORSOR and does not apply to VICTORIA.

The release data for barium is underpredicted by both CORSOR and VICTORIA. The VICTORIA prediction is suppressed by the low temperature used in the calculation. Further increases in the VICTORIA value will result from improvements in the open porosity transport models, especially the inclusion of an evaporation condensation model.

Figure 2.2-13 shows a comparison of the temporal release profiles of cesium as observed and calculated. The CORSOR calculation uses CORSOR-3. The VICTORIA releases are found to be delayed in time with respect to the experimental data. This is due to the underestimation of the maximum temperature in this calculation and the fact that the clad is only allowed to fail once its melting temperature is reached. A review of the video image of the test shows that the clad was breached before this temperature was indicated. The general shape of the VICTORIA release curve is in good agreement with the experimental results. Refinement of the temperature history, clad dynamics to account for the early breach, and the addition of the improved open porosity transport models will tend to shift the curve to earlier times and broaden it slightly. The CORSOR-3 calculation, while comparing favorably to VICTORIA in terms of total release predicted, can be seen in the figure to have too broad a temporal profile when compared to the experimental results. Further refinements

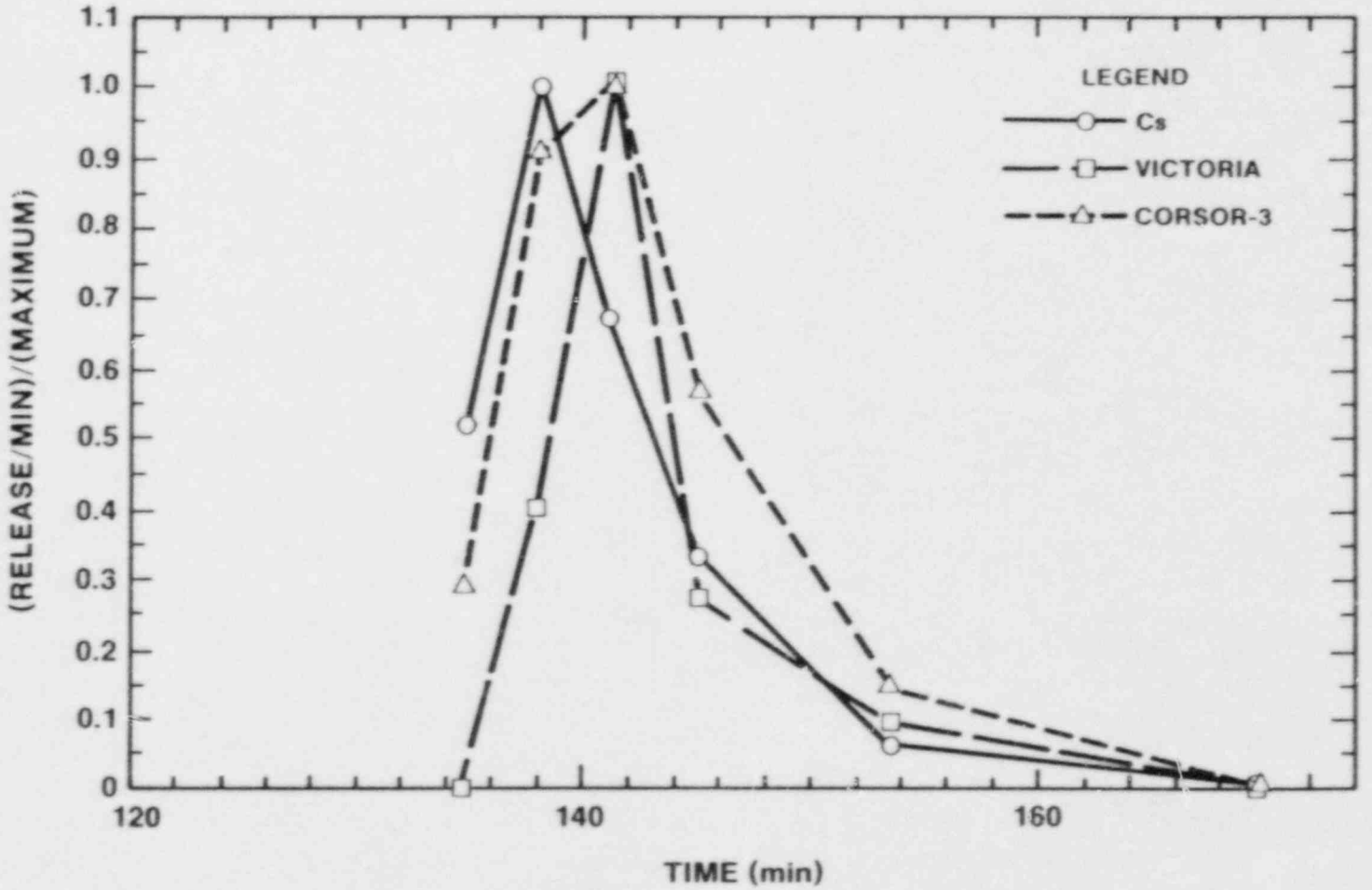

Figure 2.2-13. ST-1 Results (Grams/Minute/Maximum)

to the experimental data are unlikely to alter the shape of this curve.

The comparison of the VICTORIA predictions to the preliminary data has enabled us to identify a few areas needing improvements within the VICTORIA modeling. In particular, an evaporation condensation model needs to be added to the open porosity transport; the clad dynamics models need to be improved to account for clad vaporization and the observed early failure; and the necessity of calculating equilibrium chemistry within the fuel needs to be evaluated further. In addition to the modeling improvements, there is also a need for improvement in the input data. The temperature data, both in terms of slope and maximum value, need to be revamped. The specification of the clad failure point and the mode of failure both require changes in portions of the code that are specific to this test. These changes are being implemented for comparison with the experimental data in a more complete form than is currently available.

2.2.5 Status of ST-1 Posttest Analyses

Posttest examination of the filter components includes gamma spectroscopy for Cs and Eu, ion chromotography for Ba and Sr, ion specific electrode for iodine, and voltammetry for Te. The gamma spectroscopy is complete and the data are being reduced. Data from IC, ISE, and voltammetric analyses are being reviewed. The insoluble material in some of the leachate samples are being sent to other laboratories for quantitative analyses. SEM/WDX analyses of the deposition wires is in progress.

2.2.6 Status of ST-2 Experiment Preparations

The general design of the ST-2 compressor system has been completed. A hardware mockup of that system has been assembled to prove the approach. With the exception of the compressor system, all other components for the package have been delivered. Assembly of the other package systems is now in progress. The ST-2 experiment will be conducted in mid-November.

3. LWR DAMAGED FUEL PHENOMENOLOGY

The Sandia LWR Damaged Fuel Phenomenology program includes analyses and experiments that are part of the integrated NRC Severe Fuel Damage (SFD) Research program. Sandia is investigating, both analytically and in separate-effects experiments, the important in-vessel phenomenology associated with severe LWR accidents. This investigative effort has provided for two related research programs: (1) the Debris Formation and Relocation (DFR) program (ongoing) and (2) the Degraded Core Coolability (DCC) program (completed). The focus of these activities is to provide a data base and improved phenomenological models that can be used to predict the progression and consequences of LWR severe core damage accidents. The DFR experiment program provides unique data on in-vessel fuel damage processes that are of central importance in determining the release and transport of fission products in the primary system. The DCC experiment program, completed early in CY86, provided data on the ultimate coolability of damaged fuel configuration. Models coming from both programs are used directly in the MELPROG and other in-vessel accident codes.

3.1 DF-4 BWR Control Blade/Channel Box Fuel Damage Experiment

3.1.1 Introduction

The DF-4 experiment was the fourth test in the DFR experiment series,[110] which are carried out in the Annular Core Research Reactor (ACRR) at Sandia. These experiments employ prototypic materials (UO_2 fuel, zircaloy clad) in test configurations that are designed to explore the governing phenomenologies pertinent to a LWR undergoing severe damage associated with a core uncovery accident. These experiments together with other in-pile and out-of-pile experimental programs are aimed at providing a data base from which analytical and numerical models of severe core damage may be developed and assessed for subsequent use in reactor accident codes such as MELPROG, SCDAP, and MELCOR. Phenomena participating in the severe fuel damage process include zircaloy oxidation with the associated chemical energy release, clad melting, UO_2 attack and dissolution by molten zircaloy, relocation by candling or slumping of liquefied fuel and clad, and formation of blockage zones from the refreezing of previously molten components. Associated with these damage processes is the production of hydrogen from the oxidizing of zircaloy and UO_2 with steam and the release of fission products and aerosols. The information obtained in the DFR series applies to the early phase of core degradation prior to major geometry changes. As the initial stages of core degradation become better understood through analysis and insights gained from this experiment series, other experimental studies, and the TMI-2 postmortem, follow-on tests subsequently will be required to address the progression of

core melting during the extended accident phase when significant geometry changes have occurred.

The DF-4 experiment addressed the effects of unique BWR geometry upon fuel damage processes. These features are illustrated in Figure 3.1-1 where a cross section through four BWR fuel canisters is shown. The canisters served to isolate each fuel bundle hydraulically so that the coolant flow to each fuel bundle was orficed at the inlet according to the power generated in that location. Because of the use of zircaloy channel boxes in the BWR design, a large BWR (3600 MWt) may contain as much as 60 to 75 x 10^3 kg of zircaloy.[111]

Also shown in Figure 3.1-1 is the cruciform stainless steel/B_4C control blade located in the bypass region between the individual zircaloy flow channel canisters. There is nominally one control blade assembly per four fuel canisters, which is used for reactivity control and power flattening. The blade is formed by numerous stainless steel tubes filled with B_4C powder. There are approximately 550 kg of B_4C powder in the 177 control elements in a large BWR. The tubes are confined in the cruciform array by a thin stainless steel jacket. The jacket is perforated with numerous holes along the length of the blade assembly so that coolant may circulate around the individual tubes and thereby remove heat generated within the blade.

During a core uncovery accident in a BWR, the boildown of coolant occurs principally within the fuel canisters (channel boxes), as this is where the fuel rods reside. For this reason, the major supply of steam for zircaloy oxidation flows within the canister. However, steam does flow to a lesser degree in the interstitial regions external to the channel boxes because of direct heating from decay gamma absorption, conduction from the channel box walls, and by flashing when the vessel depressurizes. Steam is therefore available in differing proportions both to the fuel clad and channel box interior wall as well as to the channel box exterior wall and the stainless steel/B_4C control blade assembly. Additionally, in BWR accident sequences that occur at high pressure, e.g., TQUV (i.e., Station Blackout), the steam flow in the interstitial region between adjacent channel boxes is dominated by the automatic actuation of the safety relief valves (SRVs). The valves have a dead band of about 60 psi between opening pressure and closing pressure, which results in a periodic flashing of steam when the valves are open and a corresponding suppression of steaming in the interstitial region when the valves are closed. Calculations carried out at the Oak Ridge National Laboratory[112] indicate that the time between successive depressurization events is on the order of 3 min. Oxidation in the interstitial zone would then occur in periodic vigorous spurts.

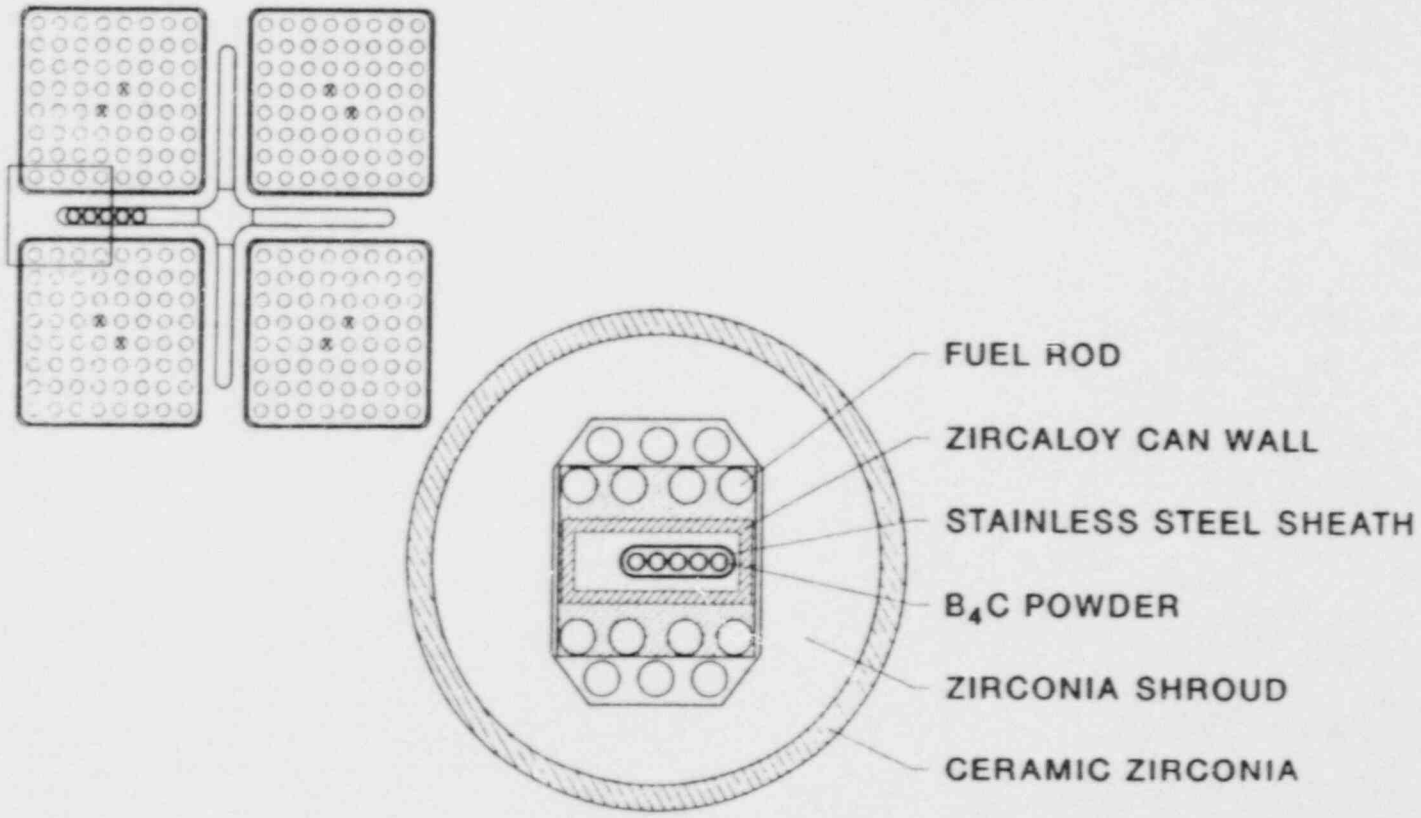

Figure 3.1-1. Cross-Sectional Representation of Key BWR Core Structures (Upper Left) and the DF-4 Experimental Representation (Lower Right)

The key BWR structural features were represented in the DF-4 test section design, a cross section of which also is shown in Figure 3.1-1. As in the BWR core, separate flow regions existed in the DF-4 representation for the fuel rod zone inside the fuel canister and the control blade zone in the interstitial region between adjacent fuel canisters. The rectangular channel box in the DF-4 test bundle prevented cross flow of steam between the two zones. Steam flow rates to each zone were established with consideration given to the differences in steaming rates and hydraulic resistance inside the fuel canister and around the control blade tip of the General Electric "D-Lattice" core design, such as is used in the Browns Ferry plant. The steam flowing inside the control blade region was held constant, however, in the interest of test interpretability and, therefore, represents a time averaging of the periodic flashing events arising from the BWR prototypic SRV actuations.

The chief aim of the DF-4 BWR experiment was to examine the phenomenologies associated with failures of and interactions between the unique control blade and channel box structures in the BWR core. These phenomenologies were explored by initiating high-temperature steam oxidation using nuclear heating in the test configuration (Figure 3.1-1). Important physical processes occurring simultaneously in the damage progression included oxidation by steam of zircaloy (both fuel clad and channel box), stainless steel, and B_4C (control blade); liquefaction and eutectic formation between UO_2 and zircaloy, stainless steel and B_4C, and stainless steel and channel box zircaloy; and refreezing and blockage formation by liquefied components.

One issue currently under debate[113] relates to the Industry Degraded Core Rulemaking Program (IDCOR) position on the behavior of blockages in BWR fuel canisters. The IDCOR MAAP code[114] assumes that a tight coherent blockage forms within the fuel canister when fuel cladding melts. This blockage is assumed to isolate the upper regions of the canister from a source of steam and thereby diminishes the total hydrogen generated. This treatment may be overly simplistic as complete blockage coherency and channel box integrity must exist to completely justify this assumption. Channel box melting or attack by control blade material may jeopardize the integrity assumption. The evidence from DF-4 will be useful in assessing this important modeling treatment.

Another interesting question arises with respect to control blade damage and accident management procedures. Evidence suggests that the stainless steel-B_4C control elements can fail by eutectic reaction at a temperature as low as 1300 C.[115] At this temperature, it is possible that extensive fuel degradation has not yet occurred. The question posed is whether or not the core should be reflooded if the control elements have failed. A likely conclusion is that the core should always be reflooded if possible; however, the possibility of reflooding a largely intact

core with failed control elements adds a new dimension to the accident management aspect.

Beyond these specific issues and questions, a balanced understanding of the important and dominant damage phenomena is necessary for the development of mechanistic modeling of these processes and to aid in the resolution of this and other unresolved issues concerning key damage behaviors.

In the following sections, the details of the experimental procedure used in the DF-4 test are reviewed and important features of test instrumentation and conduct are highlighted. The on-line experimental measurements are presented and discussed, including the thermal response of the fuel rods, channel box, control blade, and the hydrogen recombiner tubes. Comparisons are made between the test data and predictions of a numerical model of the DF-4 experiment test section with the propose of aiding in the interpretation and evaluation of the experimental data.

3.1.2 Description of Experiment

The intent in the DFR experiment design was to represent a short segment (0.5 m) of an uncovered LWR core where severe fuel damage initiates and to provide as well a characterization of environmental conditions as possible. For example, dry steam was introduced to the bottom of the test bundle so that the uncertainties associated with coolant boildown rates were not encountered. The short bundle length was justified since the principal damage process, clad oxidation, tends to localize within an axial zone of 10 to 20 cm in length, and therefore, most pertinent phenomenologies are suitably accommodated. Fuel heating was achieved by fission by means of neutronic coupling with the ACRR. Fission heating in combination with the chemical energy released from zircaloy oxidation generated sufficient power to drive fuel temperatures above 2500 K. Unique diagnostics developed for this test series allowed fuel temperatures as high as 2700 K to be continuously monitored throughout the experiment and allowed accurate time dependent hydrogen production rate measurements to be obtained. In addition, an end-on view of the test bundle was attained using a quartz glass viewing port installed in the experiment capsule; video and film cameras recorded the test progression observed through the viewing port. Postirradiation examination (PIE) was a standard posttest procedure used and included preparation of numerous test bundle cross sections for metallographic characterization.

The experiment was carried out by placing the test capsule in the ACRR central cavity as shown in Figure 3.1-2. Dry steam was supplied to the experiment from a boiler system located beside the ACRR pool. The experiment ex-capsule and in-capsule flow

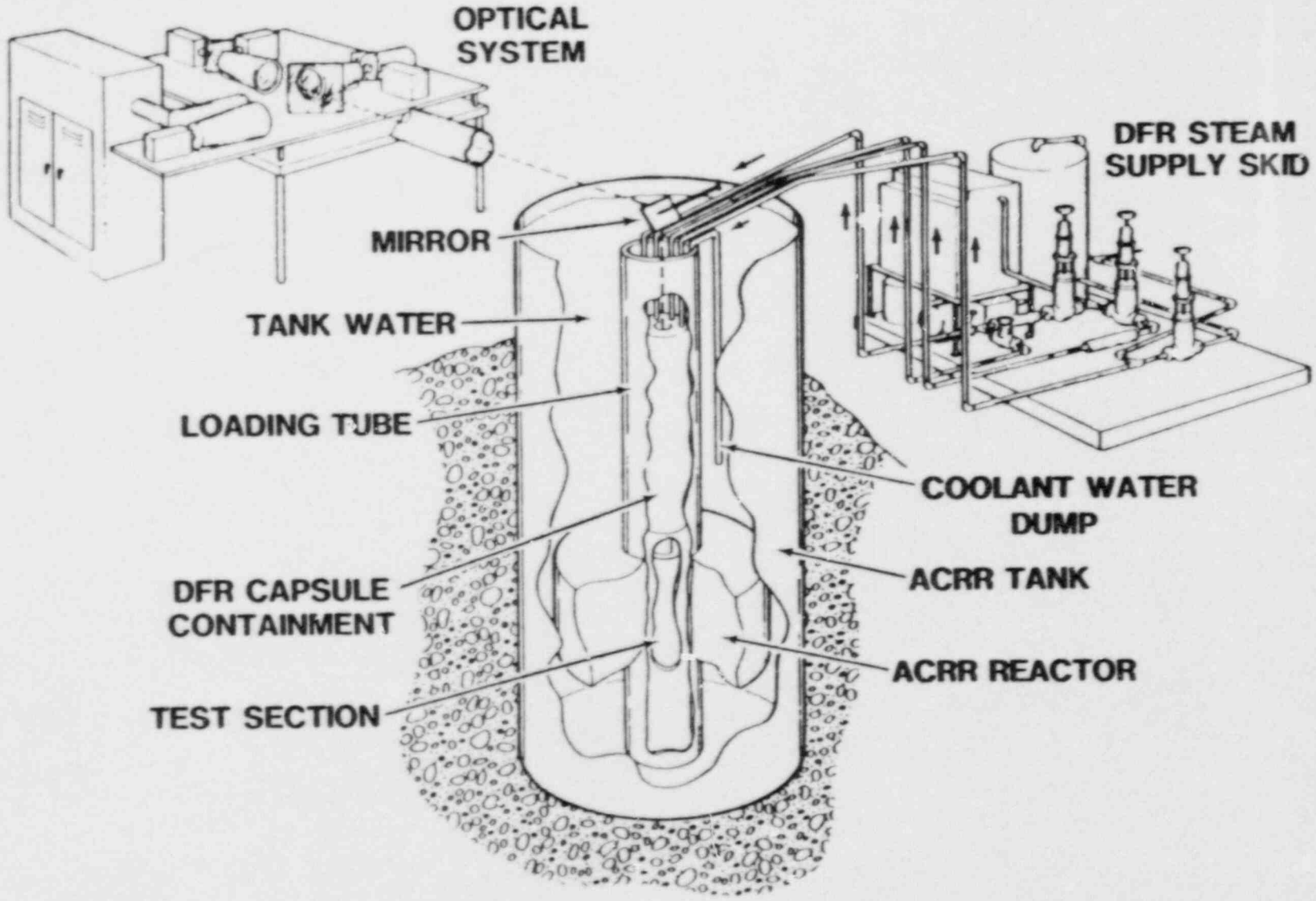

Figure 3.1-2. The DFR Experiment Apparatus Illustrating the Steam Supply Plant, Optical Viewing Station, and the ACRR Loading

system is shown schematically in Figures 3.1-3 and 3.1-4. The steam introduced to the test bundle was ultimately held in the form of liquid water within the test capsule, as no effluents were permitted to exit the package following fuel irradiation (Figure 3.1-4). Isolation valves, explosive shut off valves, and other features (Figure 3.1-3) provided assurance that no effluents or fission products exited the package during the test. A large mirror which directed the visual image to an optical bench where telescopes and cameras recorded the image (Figure 3.1-2), was situated above the central cavity. In excess of 200 data signals in the form of thermocouple, pressure transducer, and other data were extracted from the experiment package and were continuously monitored and recorded by a devoted computer system. These data were used both to characterize the test progression as well as to assure that safe operating conditions were in effect at all times during the test.

3.1.2.1 Experiment Capsule

The test capsule contained a number of notable features (Figure 3.1-4). The principal feature was the test bundle, which was axially centered in the ACRR. Steam introduced to the package entered the bottom of the test bundle and flowed upward around the fission heated fuel rods. Separate steam flows were introduced well above the exit of the test section in order to cool the bundle effluents and to keep the line-of-sight viewing port clear of aerosol, which tended to occlude the view of the test bundle. Each steam flow into the experiment package was individually metered at the steam plant on the ACRR floor level. As zircaloy oxidation occurred, hydrogen was produced and swept out with the bundle effluents. The exiting gases flowed through a parallel bank of eight stainless steel tubes (~2.54-cm ID by 50 cm in length), which were packed with CuO particles (~0.5-mm diameter by 2 mm long). The hydrogen was converted back to steam following the exothermic reaction, $H_2 + CuO \longrightarrow Cu + H_2O + heat$. The heat production from the $CuO-H_2$ reaction was quantified and thus the hydrogen production rate inferred. This was facilitated by a computer model[118] of the reaction tubes that accounts for the heat production and transfer as a function of axial position in the tubes. The steam exiting the reaction tubes passed through a regulating valve, which separated the high pressure side of the flow system from the low pressure-condenser region of the package. The steam passing through the regulating valve was condensed in a counterflow heat exchanger and allowed to holdup and subcool in a tank located at the bottom of the capsule. By measuring the pressure drop across the regulating valve and the valve stem position, the effluents flow rate from the test bundle were calculated and compared against the measured inlet steam flow rates.

Detailed features of the test section are shown in Figure 3.1-5. The test bundle, represented as a single fuel rod in the figure,

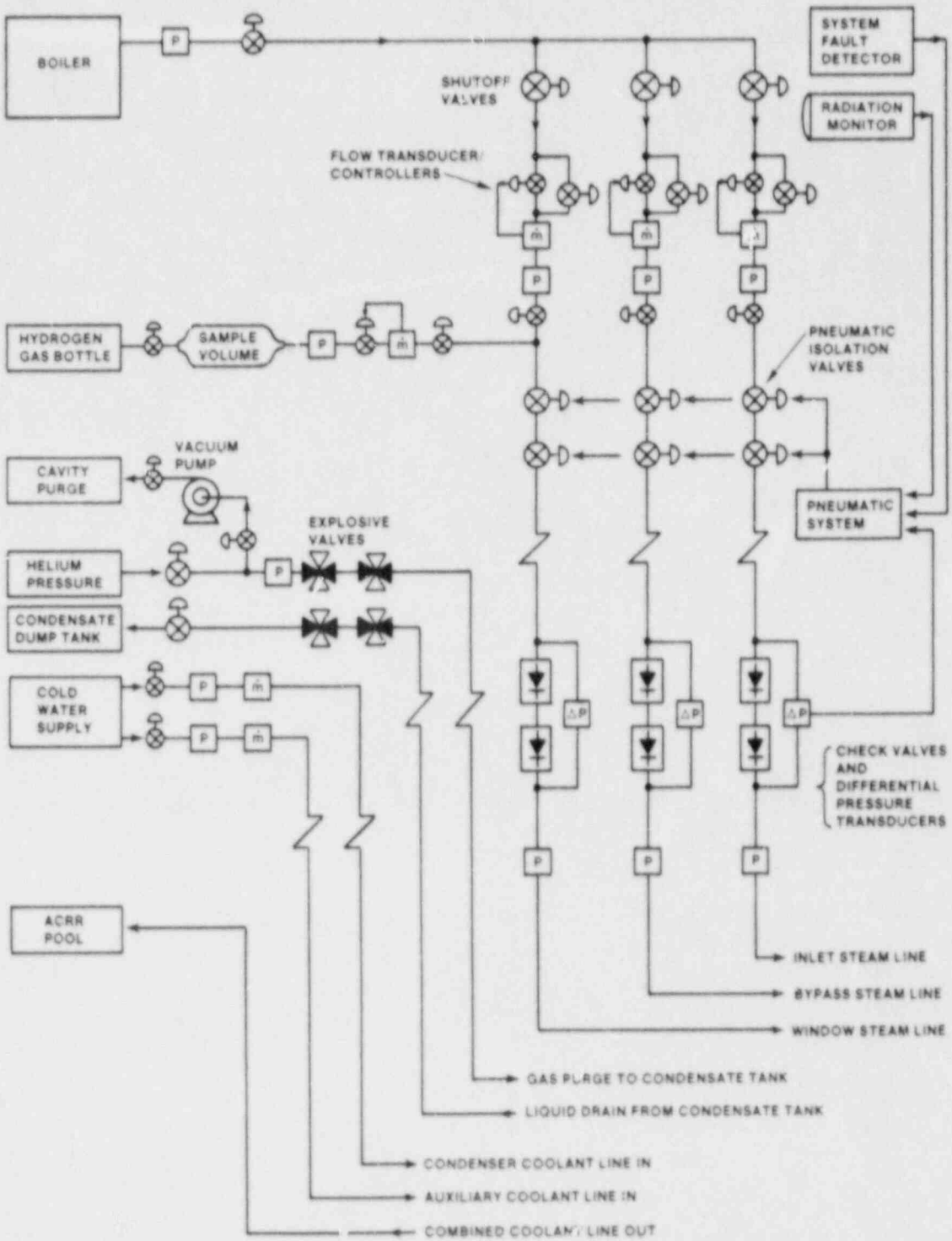

Figure 3.1-3. Schematic Diagram of the Ex-Capsule Flow System Showing the Steam Inlet Lines, Back Flow Preventive Features, and Other Ancillary Plumbing Features

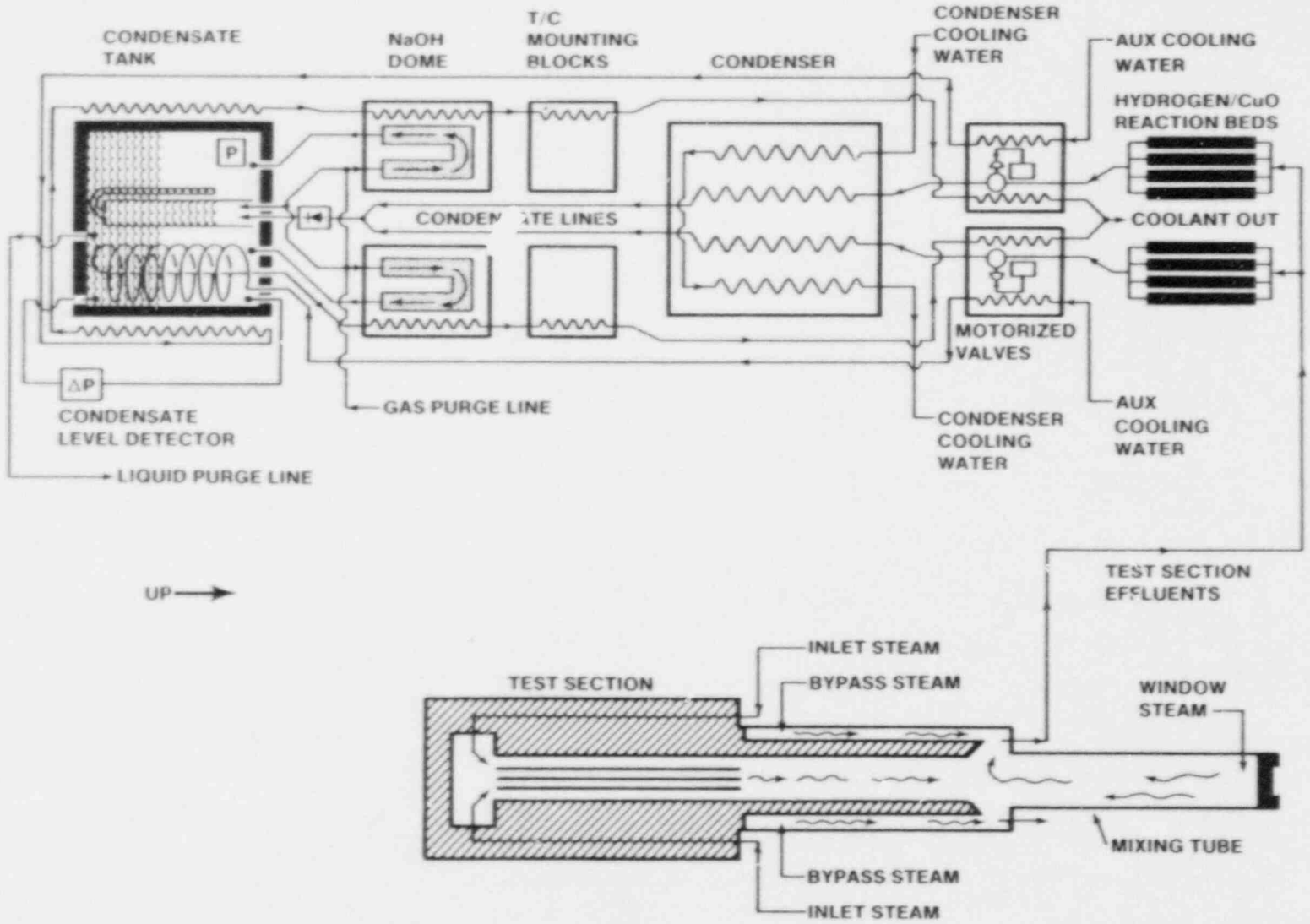

Figure 3.1-4. Schematic Diagram of the In-Capsule Flow System Showing Test Section Flow Circuits, Copper Oxide Tube Manifolds, Condenser, and Holding Tank

could accommodate from 9 to 14 zircaloy clad UO_2 fuel rods in a ~0.5-m assembly. The bundle was insulated radially using a low density ZrO_2 material, which had an open porosity of around 85 percent. Although the insulator performed well thermally, there are two important caveats to note. The first is that a coherent tight fuel bundle blockage, which might have formed during the test, would not have prevented steam from reaching the upper bundle above the blockage zone because steam bypass through the porous insulator would occur. The second point is that liquefied U-Zr-O, which might otherwise have formed a more coherent blockage around fuel rod remnants, instead tended to soak into the insulator, interacting with the material as it migrated radially away from the blockage zone.

3.1.2.2 Test Section Instrumentation

The test bundle was instrumented with various types of thermocouples. The fuel rod cladding was instrumented with Pt-Rh thermocouples where the junction was formed by welding the thermocouple wires to the clad surface. The temperature limit of Pt-Rh instrumentation is ~1800 K, after which failure of the junction occurs. The fuel rod cladding was also instrumented with specially sheathed W-Re thermocouple assemblies. Although considerably more massive and not as well thermally bonded to the clad, these thermocouples survived the high temperature oxidizing environment and monitored bundle temperatures as high as 2700 K. Other temperatures were monitored within the insulator and on the pressure boundary surface to further characterize the thermal behavior of the test bundle. The principal thermocouple instrumentation in the DF-4 test bundle is shown in Figure 3.1-6. In this figure, the axial location of four major instrumentation stations is shown and the lateral positioning of the thermocouples at each station is indicated. The axial locations are relative to the bottom of the fissile zone in the bundle as indicated in Figure 3.1-5. In addition to thermocouples devoted to tracking fuel rod, channel box, and control blade temperatures, two thermocouples were located at the base of the test bundle below the fissile zone. One was located at the base of the control blade within the confines of the channel box and indicated the arrival of molten material draining to the base within the channel box. Similarly, a thermocouple located at the base of the fuel rod zone just outside the channel box indicated the arrival of molten material draining down outside of the channel box.

3.1.2.3 Test Progression

The progression of the experiment proceeded in stages, and a description of the stages of the test is useful in providing insight into the experiment behavior throughout the test. The first phase of the experiment was a heatup phase, where no actual

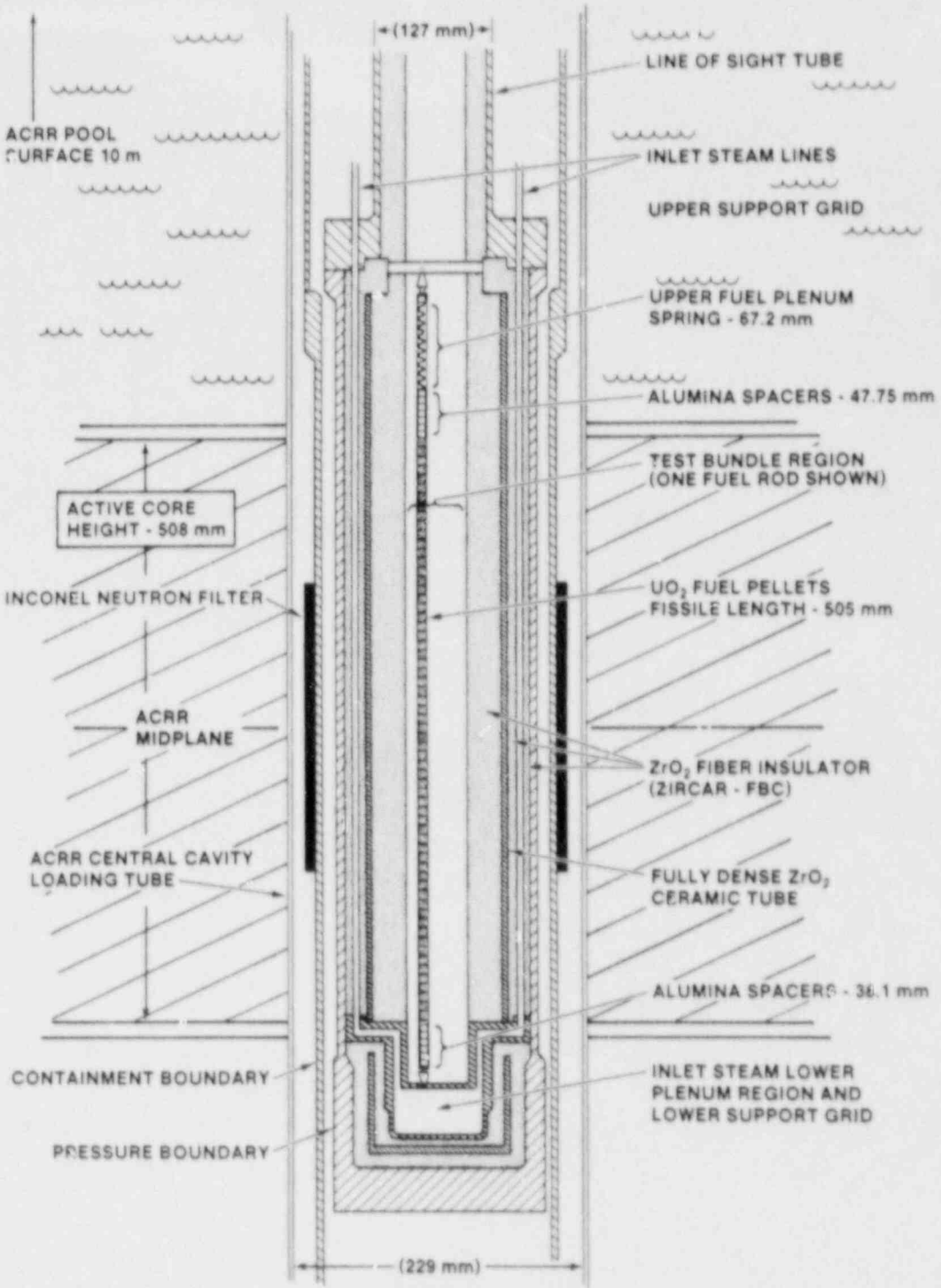

Figure 3.1-5. Schematic of DF-4 Test Showing Test Bundle, Insulation, and Major Boundaries

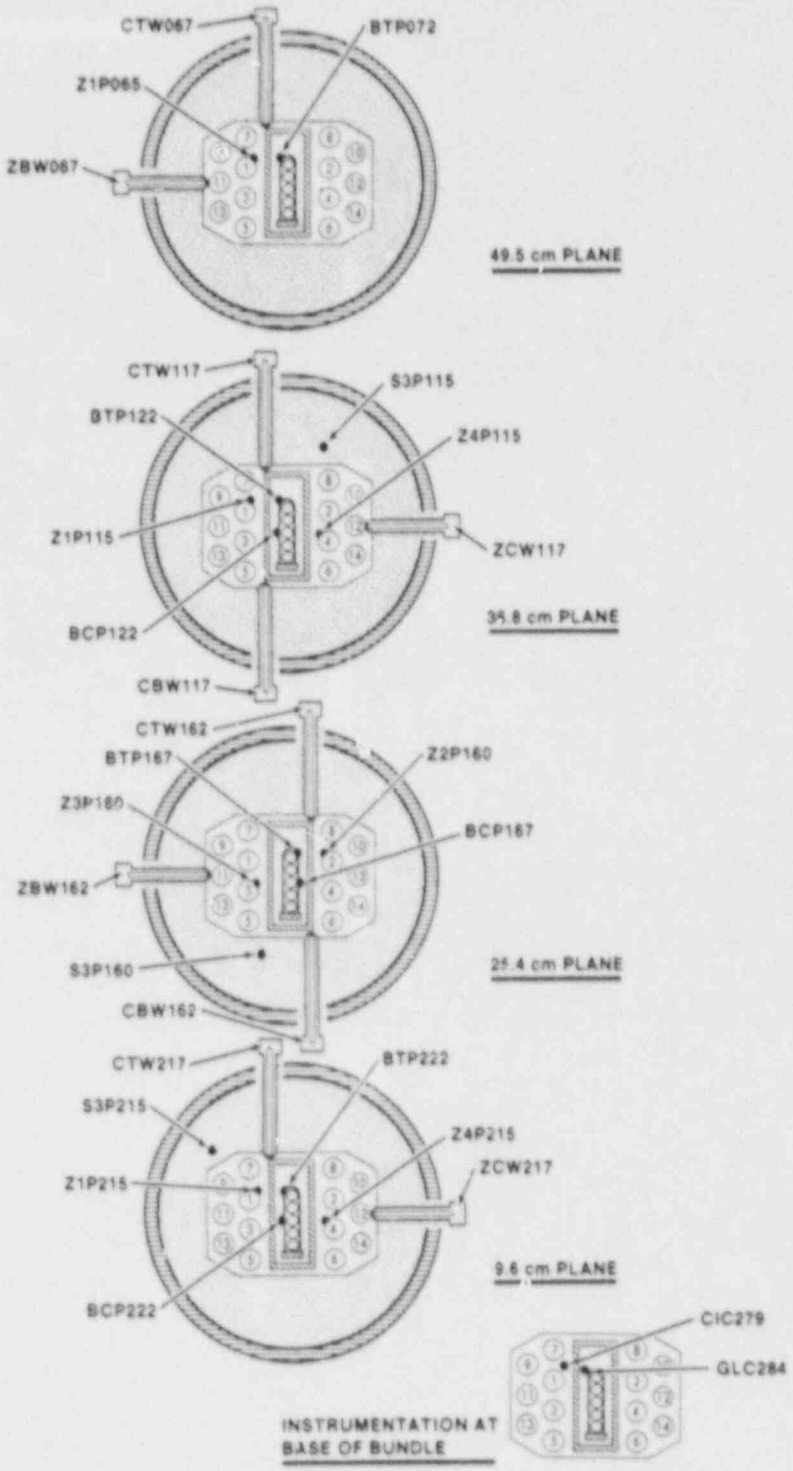

Figure 3.1-6. Diagram of the Principal Test Section Instrumentation

flow of steam into the package occurred. In this stage, the surfaces of the flow boundary were electrically heated to a temperature above the saturation temperature corresponding to the desired operating system pressure. That was to assure that condensation of the steam did not occur; rather the steam had to remain dry as it flowed through the test bundle. After the components of the flow system had been heated sufficiently, including the fuel rods of the test bundle, the flow system was purged of any accumulated noncondensable gases.

The next stage of the experiment involved the introduction of steam into the flow system. This was initiated by first closing off the motor driven pressure regulating valves, which isolated the test section region from the condenser. In this way, as steam was fed into the test section, the system pressure steadily increased. As the system pressure approached the desired operating pressure, the regulating valves were opened in small increments until the pressure stabilized at the desired value. At this point, the total steam inlet flow rate was exactly equal to the steam effluent rate through the regulating valves. The pressure downstream of the regulating valves was determined by the saturation pressure of the condensed water, which was typically at a temperature of ~50°C.

After the test section was fully heated and pressurized with steam flowing through the system, the actual test phase of the experiment began. This phase usually began with selected calibrations being carried out, such as a crosscheck of the condensate tank filling rate against the integrated steam inlet rate and other checks directed towards assuring confidence in the principal instrumentation. One of the most important calibrations done was with the CuO-H_2 reaction tubes. In this check, a known volume of hydrogen was injected into the experiment flow system at a metered rate and allowed to react in the CuO tubes. In doing this the thermal response of the tubes were characterized under carefully controlled conditions, and subsequent analysis of the unknown hydrogen production rate from the test proper was greatly facilitated.

The test bundle was subsequently heated by fissioning by means of ACRR coupling. The usual progression of the test called for approaching the zircaloy oxidation transient regime ($T > 1700$ K) with a bundle heatup rate of from 1 to 2 K/s. This was achieved by augmenting the ACRR power as necessary to offset the increasing radial heat losses experienced with increasing temperature, thereby maintaining a constant fuel heatup rate. As the clad temperatures began to exceed 1800 K, the oxidation power and associated hydrogen evolution rate began to increase dramatically to a point where the chemical power exceeded the fission power in the fuel. At this time, the oxidation reaction was typically in a steam starved state where the reaction zone became highly localized to a region of from 10 to 20 cm in axial extent and gradually migrated downward toward the steam inlet region. Clad

melting with fuel attack and liquefaction quickly followed with molten materials relocating and freezing in the lower cooler portion of the test bundle. The test was terminated by halting steam flow to the bundle inlet and scramming the ACRR. A slow cooldown lasting several hours then followed. After cooldown, the on-line data recorded during the test was made available for examination and characterization.

At some time after completion of the test and before transferring from a vertical state, the test bundle was stabilized with an epoxy resin and removed from the experiment capsule. This prevented any disturbance of the fragile posttest bundle configuration during radiography or during transport to the hot cell facility. In the hot cell, the test bundle was sectioned and examined metallurgically.

3.1.3 Experimental Results

The on-line experimental data provide a principal means of test interpretation. These data, in the form of temperature, pressure, and flow rate measurements for the test section and other regions of the experiment, characterize the test progression. A selection of these data are examined in the following sections, beginning with the ACRR power and bundle steam flow history during the transient phase of the experiment. Subsequently, the thermal response of the fuel rods, channel box and control blade are examined, and interpretations are offered for notable events observed in these temperature traces. Following this, the performance of the CuO-H_2 recombiners are reviewed. All of these data are subjected to careful examination for any evidence of anomalous behavior so that incorrect interpretations may be avoided. Additionally, the final characterization of the experiment demand a consistent interpretation of the on-line measurements with the other experimental evidence such as the video record and metallographic examination.

3.1.3.1 ACRR Power and Steam Flow

The test section inlet steam flow rate is shown in Figure 3.1-7 along with the ACRR power history. Steam flow was initiated well before (~13 min) the ACRR power was brought up. During this time the operating pressure of ~100 psi was established and the ACRR was readied for operation. In this early phase, the steam flow was maintained at one-half of the value desired for the actual oxidation transient so that the condensate tank volume could be conserved. At roughly 6100 s, the ACRR power was brought to 100 kW in a step power change. Three more step increases in reactor power followed, ending with a large boost to ~1 MW just prior to 6400 s. As the ACRR power was incrementally increased during this period, the fuel rod temperatures were seen to increase and at each power boost, the rate of temperature increase was larger.

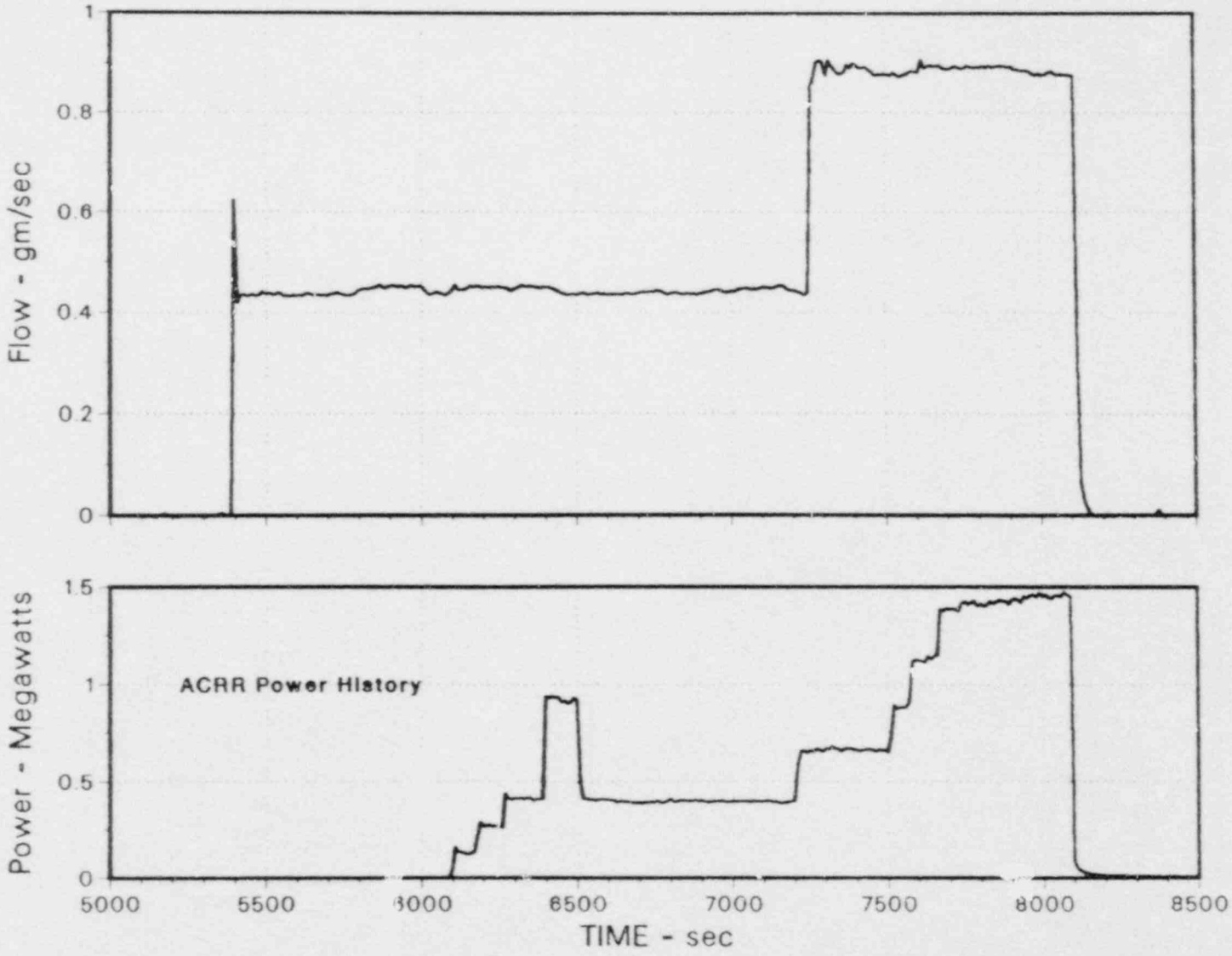

Figure 3.1-7. Test Bundle Total Inlet Steam Flow Rate During the Oxidation Transient Phase of the Test. Also shown is the ACRR power history for comparison

These step changes in temperature rise rate arising from the discrete ACRR power changes will be analyzed to determine the actual reactor power coupling with the test bundle fuel by using a linear regression technique, discussed in Section 3.1.4.1. The power was maintained at the nominal 1 MW value until the test bundle temperature reached between 900° and 1000°C, whereupon the reactor power was sharply decreased to ~400 kW, and the bundle temperature rise ceased. Fuel temperatures were held at ~1100°C for about 12 min during which time the control blade and channel box were allowed to equilibrate thermally with the fission heated fuel rods, and some amount of low level zircaloy oxidation occurred. At 7200 s, a nominal 1 K/s heatup rate was established for the test fuel by bringing the ACRR power up to 650 KW. After the effects of the power boost stabilized, the inlet steam flow rate was increased from the initial 0.025 g/s/rod to 0.050 g/s/rod, where it was held for the duration of the high-temperature oxidation phase of the experiment. Several additional ACRR power increases followed as the bundle temperatures increased and radial heat losses became increasingly larger. The power boosts maintained the bundle heatup rate at ~1 K/s prior to the autocatalytic oxidation transient, whereafter the temperature rise rate was substantially larger. Shortly after 8100 s, both the ACRR power and inlet steam flow were terminated and the cooldown of the test section commenced.

3.1.3.2 Test Bundle Thermal Response

In this section, the test bundle thermal response during the 1 K/s entry to the high-temperature oxidation phase of the test is examined. The W/Re thermocouple data is presented first, as this information persisted throughout the entire high-temperature transient and allows for easier interpretation than the more accurate Pt/Rh instrumentation, which did not survive the high temperatures of the transient. Subsequently, the Pt/Rh thermocouple data is examined; these data provide very accurate temperatures up to failure, and the signature of the thermocouple failure is often indicative of important damage events, such as blade failure and material relocation.

- **Fuel Rod Response**

The fuel rod thermal response to the ACRR fission heating is shown in Figure 3.1-8 along with the ACRR power history. This response is as measured by the specially designed W/Re thermocouple assemblies, which significantly perturbed the actual temperature at the thermocouple location. This perturbation was in the form of a lag in time response as well as a lower indicated temperature (~200° C) and was due to the ceramic ZrO_2 sheath that shielded the rhenium thermocouple body from the oxidizing environment. These nonideal factors can be accounted for analytically; however, no corrections have been applied to the traces shown in Figure 3.1-8. The significant advantage of

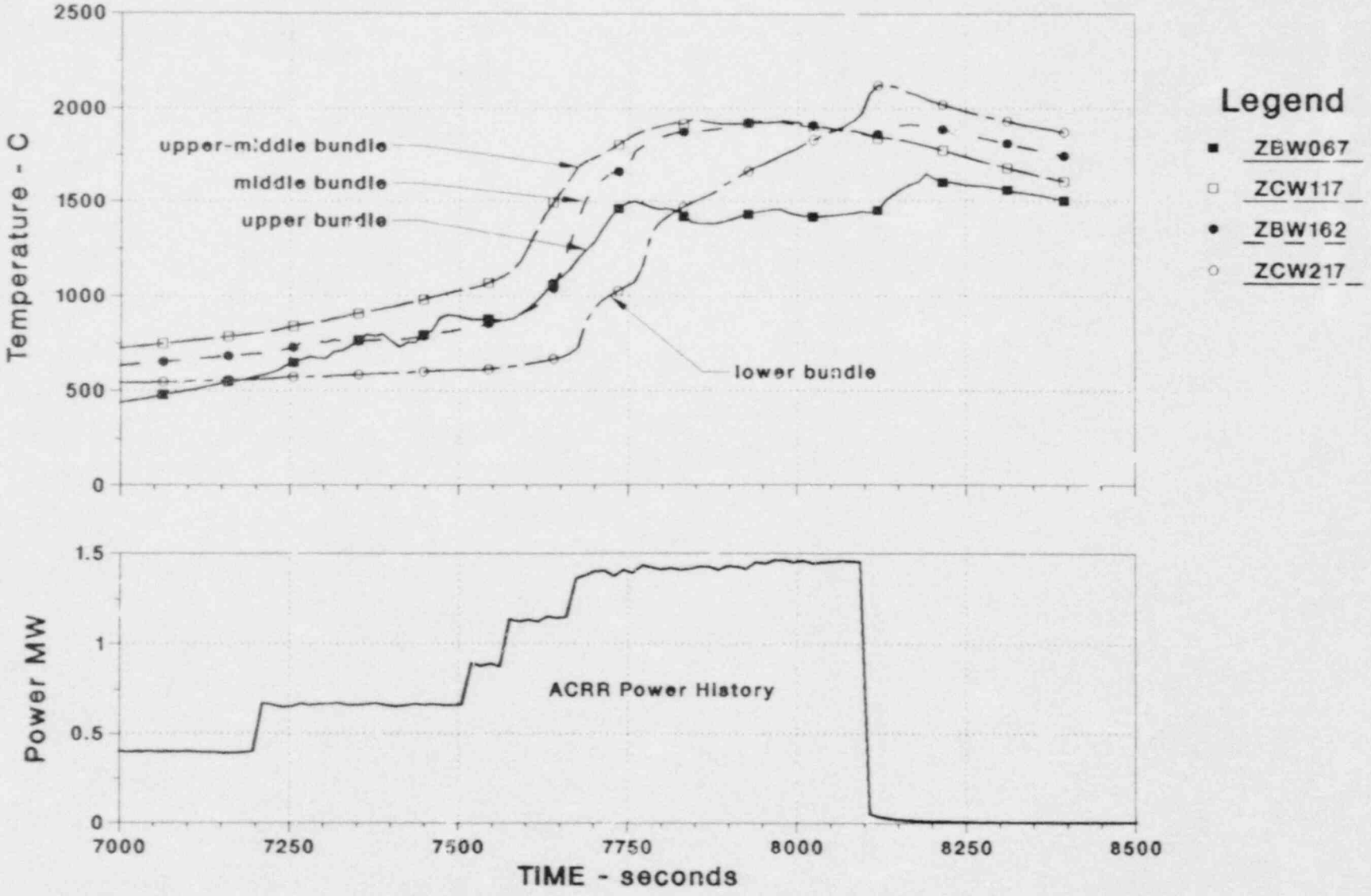

Figure 3.1-8 Tungsten-Rhenium Thermocouple Responses for the Fuel Rod Instrumentation

the thermocouple design is that the measurement is obtained continually throughout the oxidation transient during which conventional diagnostics are destroyed.

As seen in Figure 3.1-8, the upper half of the fuel bundle initially led the lower half owing to the relatively cool steam entering the bottom of the bundle. The top end of the bundle remained cooler throughout the test because of the radiant heat loss out of the top of the bundle and because of steam starvation of oxidation in that region. Between the interval of 7500 and 7750 s, the high-temperature oxidation transient occurred. The thermocouples in the middle and upper third of the bundle (25.4 and 36.8 cm above the bottom of the fissile zone) showed a sudden large increase in heatup rate as the oxidation of the zircaloy clad became significant. The actual clad temperature at the time the rate increase occurred was between 1500° and 1600°C, based on the Pt/Rh intrinsic junction thermocouples. The temperature at the top of the bundle began to follow the transient trends of the 25.4 and 36.8 cm thermocouples but abruptly "flattened out" at 7750 s, while the two next lower thermocouples continued to increase in temperature to a maximum of just under 2000°C. The transient trends of the two midbundle thermocouples are characteristic of high-temperature zircaloy oxidation where the exothermic reaction localizes and migrates downward toward the source of the steam. As the zircaloy melting point was approached, the temperature increase leveled off, presumably because of a slowing or passing of the reaction zone or by melting and relocation of the molten unoxidized zircaloy. The lowest W/Re thermocouple showed a heatup character quite different from the other thermocouples, which were driven principally by oxidation energy release. The lowest thermocouple response appeared to be driven by relocation of molten material to that zone, as evidenced by the abrupt temperature increases between 7650 and 7800 s. It is possible that at later times, oxidation of the accumulated material occurred, generating additional heat locally, but the initial responses strongly suggest arrival of molten material from the much hotter upper bundle regions. The peak temperature measured in the accumulation or blockage zone (9.6 cm above the bottom of fissile zone) was around 2100°C, which would indicate an actual maximum of ~2300°C (above the zircaloy melting point), and suggests that oxidation took place with relocated U-Zr-O.

- Channel Box Response

The channel box thermal response is characterized in much the same way as the fuel rod response, using the W/Re-ZrO_2 sheath thermocouple design. Because of space limitations, the thermocouples could not be situated on the channel box where the highest temperatures were expected. Instead they were located on the sides of the channel box, which did not encounter as much steam during oxidation; the sides also faced the cooler insulation surrounding the test bundle rather than the adjacent hot

radiant fuel rods. Nevertheless, the observed thermocouple response (Figure 3.1-9) was virtually identical to the observed fuel rod response. Based upon a thermal analysis of the bundle heatup (using the experiment analysis code, MARCON-DF4), the portions of the channel box, which faced the radiating fuel rods, led the cooler box sides by 100° to 200°C and, in fact, surpassed the adjacent fuel clad temperatures during a portion of the oxidation transient. Showing a behavior similar to the lower fuel bundle thermocouple (at 9.6 cm), the channel box thermocouple at 9.6 cm indicated the arrival of molten material from the upper bundle regions at ~7700 s, some 30 to 60 s later than that indicated by the fuel thermocouple. The coincidence of these responses indicate the global extent of the material accumulation. Some of this relocating material apparently continued downward to the bottom of the bundle because a thermocouple at the base of the fuel rods ("fuel base" in Figure 3.1-9) also indicated the arrival of molten material, although probably a lesser amount.

• Control Blade Response

Temperatures on the stainless steel control blade were measured at the same four axial stations as were the fuel rods and the channel box (at 9.6 cm, 25.4 cm, 36.8 cm and 49.5 cm). The thermocouples used on the blade, however, were the intrinsic junction Pt/Rh variety, which respond without any appreciable time lag and do not significantly perturb the local temperature. The thermal response indicated by these thermocouples is shown in Figure 3.1-10. Also shown in this figure are the responses of two thermocouples located at the base of the test bundle--one located inside the channel box between the steel control blade and the channel box inner wall, and one located outside the channel box at the base of the fuel rods and the box outer wall. The inner thermocouple was expected to give an indication of the arrival of molten control blade materials flowing downward within the channel box, and the outer thermocouple was intended to indicate arrival of relocating molten fuel cladding or channel box zircaloy. In general, the control blade temperatures lagged the fuel clad temperatures at the same axial location by 50° to 70°C, but showed similar trends during the initial heatup. The first indication of control blade failure (by melting or liquefaction) was evident at ~7470 s when the 36.8-cm thermocouple ("upper-middle" in Figure 3.1-10) abruptly failed. Coincident with this event was a small transient response by the "middle", or 25.4-cm, thermocouple and by the thermocouple located at the base of the control blade. Failure of the control blade progressively continued over the next several minutes as all but the lower most blade thermocouples sequentially failed by blade liquefaction. This progressive blade liquefaction and relocation is vividly observed in the video record of the damage sequence. Note the large response at the base of the control blade at ~7530 s. Finally, at ~7680 s, a very large thermal response was indicated both inside the channel box at the lowest

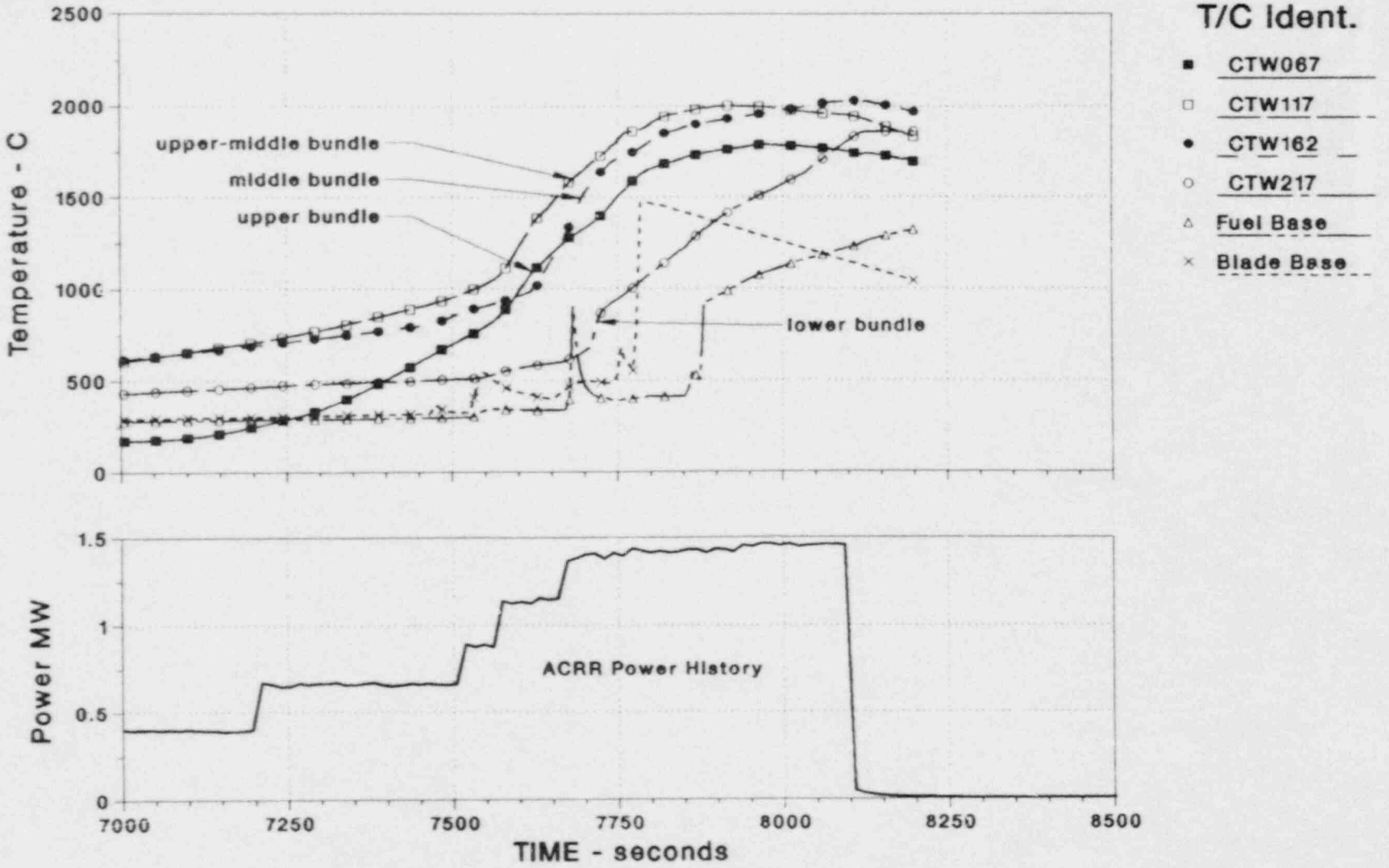

Figure 3.1-9. Tungsten-Rhenium Thermocouples Responses for the Channel Box Instrumentation

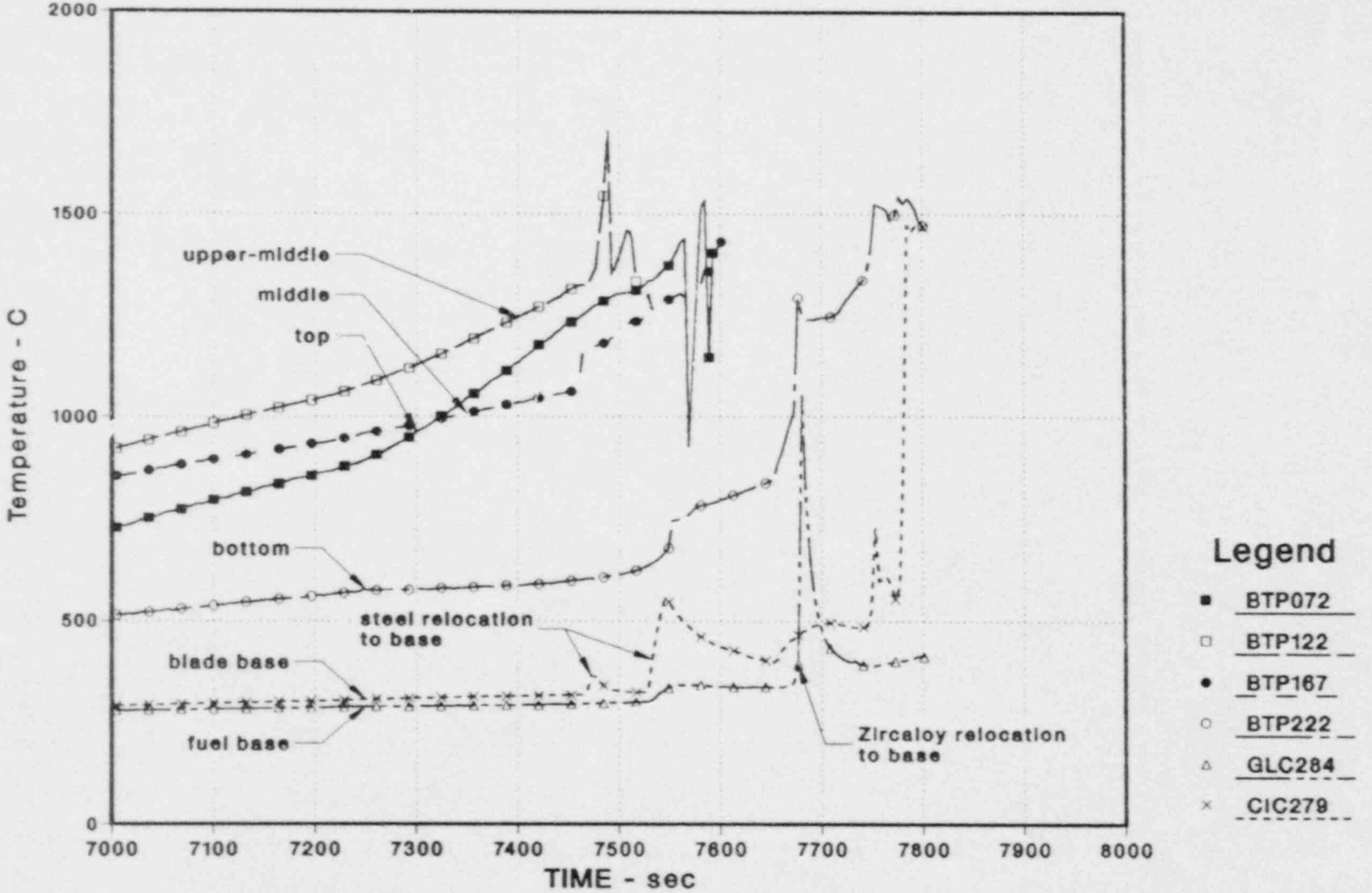

Figure 3.1-10. Platinum-Rhodium Thermocouple Responses for the Control Blade Instrumentation

blade thermocouple, and outside the channel box at the base of the bundle. This might be interpreted as the failure time of the channel box because of the coincidence of these events. This appears also to be coincident with the accumulations of molten material detected by the W/Rh thermocouples at the 9.6-cm station, described in the previous sections.

Oxidation of the boron carbide powder contained within the control blade assembly was not detected. Any substantial B_4C oxidation should have generated CO, CO_2, or CH_4 along with hydrogen. The carbon gases would ultimately have been converted to CO_2 within the CuO reaction beds and appear as a noncondensable gas, which would prematurely pressurize the condensate tank. Such a premature pressurization was not evident when the blade geometry was undergoing severe damage, and on this basis, it cannot be concluded that any significant B_4C oxidation occurred. Rather, it appears that alloying of B_4C with the components of the stainless steel blade was the dominant interaction mode. This conclusion is consistent with observations rendered by Hagen and Hoffman.[115]

3.1.3.3 CuO-H_2 Recombiner Thermal Response

Although not a part of the test section, the thermal response of the CuO-H_2 recombiners provided insight into the events ongoing in the test section. As zircaloy-steam oxidation occurred with the components of the test bundle, hydrogen was evolved. The hydrogen subsequently passed into the CuO particle beds whereupon it was converted back to steam, CuO was reduced to copper, and heat was evolved. The heat released in this reaction was measured by an axial array of thermocouples situated in the CuO bed. The rate of the reaction was determined by performing a heat balance on the instrumented reaction tubes, and in this way, the rate of hydrogen production from the oxidation of zircaloy was made known. The heat balance on the CuO beds is not presented in this section; however, the thermal responses of the bed thermocouples are given for qualitative evaluation.

The eight reaction tubes were manifolded in groups of four, each group channeling the test section effluent, including bypass and window cool steam flows, through two valves and into the steam condenser. Figure 3.1-11 shows the calculated effluent flow through the two reaction tube banks. The calculated flow is based upon measured valve position and valve pressure drop. The reaction of H_2 with CuO in each tube bank was characterized by instrumenting one of the tubes in each bank with an axial array of thermocouples, which penetrate to the center of the CuO bed. The response to the reaction in each tube bank during the oxidation transient phase of the test also is shown in Figure 3.1-11. A heat balance may be performed on each bank to determine the time dependent hydrogen production rate in the experiment.

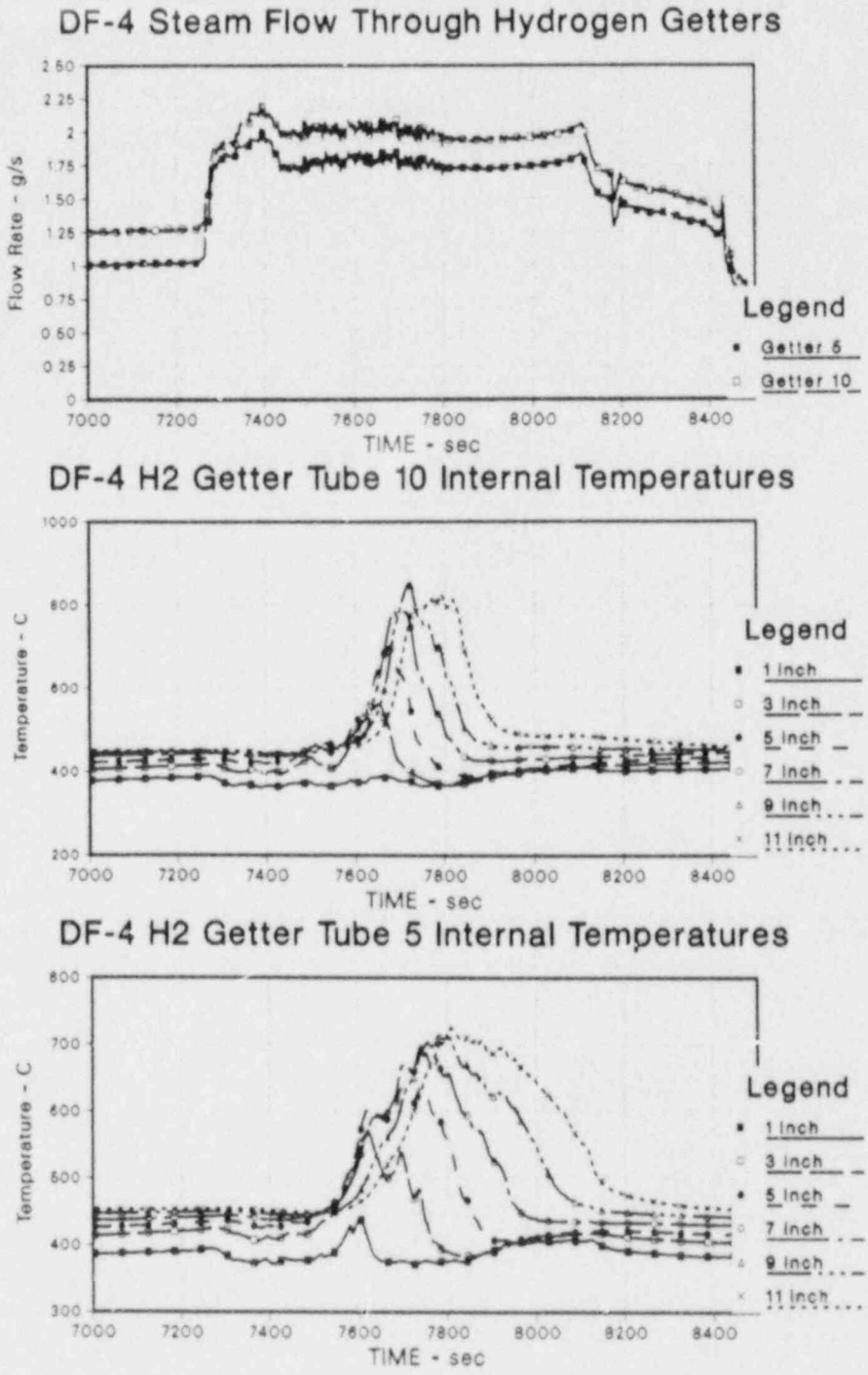

Figure 3.1-11. Copper Oxide Recombiner Tube Behavior for Each Tube Bank. Upper curve shows the effluent flow rate for each bank. The lower two curves show the thermocouple array response in each bank to the hydrogen produced during the oxidation transient phase of the test.

In both recombiner banks, the onset of measurable hydrogen production began at about 7540 s. This onset slightly preceded the rapid temperature transients noted in the previous sections on fuel rod and channel box response. Maximum recombiner temperatures were reached at ~7700 s and persisted at the maximum until 7850 s when the instrumented regions of the recombiner tubes become depleted of CuO. This suggests a period of at least 200 s of hydrogen production at a high and fairly constant level. The apparent maximum hydrogen production rate occurring at 7700 s is coincident with the major relocation events indicated at the 9.6-cm axial stations described previously. For this reason, it is difficult to determine whether the oxidation is limited by steam exhaustion or by gradual relocation of the molten oxidizing zircaloy (U-Zr-O) to the cooler regions of the bundle where the oxidation rate may be much lower. Quantification of the CuO reaction by thermal analysis is required to evaluate this question.

3.1.3.4 Video Record and Test Chronology

The on-line video recording of the test progression provided remarkable visual evidence of key events in the damage sequence. Occurrences observed in the video record have been correlated with the other on-line information and form a more complete picture of the damage sequence. The most clearly observed features in the video record are the control blade damage sequence, occurring over a period of about 2 min, and the onset of dense aerosol release, presumably tin aerosol released from melting zircaloy. A brief chronology of the damage sequence follows wherein notable events from the previously discussed on-line measurements are noted. Two time references are given, one which refers to the time imprinted on the video record and the other relative to the other on-line measurements.

CHRONOLOGY OF DF-4 TEST

Video Time (min)	Exp. Time (s)	
34:33	7193	First power boost after equilibration at 1000° C.
34:40	7200	Fuel heating at 1.1 K/s from ~1000° C.
35:45	7265	Inlet steam doubled from 0.025 g/s/rod to 0.05 g/s/rod
36:40	7320	Alignment lights turned off
37:00	7340	Fuel temp ~1250° C, blade temp ~1200° C.

38:00	7400	Fuel temp ~1310° C, blade temp ~1250° C.
38:42	7442	Onset of steel blade melting (~1300° C). This visual event correlates very well with the control blade thermocouple trends - B_4C alloying with Fe is suspected to have lowered the effective steel melting point.
39:00	7460	TV light attenuator adjusted to full attenuation in gradual steps as light intensity (temperature) increases.
39:40	7500	Several boosts in power follow up to 1.5 MW-ACRR. This marks the start of the rapid oxidation transient phase of the experiment.
40:00	7520	A piece of insulator falls onto the top of the box (video image).
40:20	7540	Onset of measurable hydrogen production. This is evident from the CuO reaction tube temperature behavior (Figure 3.1-10).
40:24	7544	Dark movement across blade tip region visible in the video image (relocation or slumping of steel ?). Temperature traces indicate larger relocation of hot material to bottom control blade region.
41:00	7580	Fuel temperature ~1700° C. Pt/Rh thermocouple instrumentation beginning to fail, leaving only W/Re instrumentation.
41:58	7638	Image darkens somewhat - probably from tin aerosol. This suggests that zircaloy melting temperatures have been attained - most probably for the channel box zircaloy.
42:10	7650	TV attenuator adjusted back to full open as aerosol density increases.
42:35	7675	Large temperature increase at the 9.6-cm thermocouples (blockage region) indicates accumulations of molten materials. Accumulations continue through 7800 s. This may be due to the arrival of large amounts of slumping channel box material to this region.

43:30	7730	Hydrogen production at maximum - probably steam starved.
45:30	7850	Bundle temperatures at maximum indicated value of 2100°C - actual temperature probably ~2200° to 2300°C.
45:45	7865	More insulator falls onto upper fuel grid.
50:00	8120	Steam flow and ACRR power terminated.

When the PIE examinations become available, the sequence of events occurring during this chronology will become more certain. Elemental analysis of the relocated materials should suggest the nature of the relocation. For example, sharply stratified material zones would suggest the temporal sequence of material deposition in the lower blockage regions. Steel components mixed with B_4C would be expected in the lower most region within the channel box. Zircaloy rich zones devoid of dissolved UO_2 would indicate channel box zircaloy, whereas, zircaloy with dissolved UO_2 would suggest fuel cladding as the origin. The way in which the relocated materials are distributed in the lower bundle region will aid in the interpretation of events seen in the on-line data and visual damage record.

3.1.3.5 Posttest X-Radiographic Examination

After the completion of the experiment, an image of the posttest configuration was obtained on X-ray film using a portable ^{60}Co γ-source. This posttest image is compared to a similar image obtained prior to test irradiation in Figure 3.1-12. Observable in the before image are the fuel rods, channel box, and control blade structures. By careful azimuthal alignment, the sharply defined channel box boundaries are easily identified. Notice the interpellet gaps in the fuel rods. In the after image, substantial damage to all of the structures is evident. Most notably, the channel box and control blade structures have largely been destroyed with only a 10-cm remnant discernible in the lowest region of the bundle. The lowest regions of the bundle appear to be filled with previously molten material, presumably stainless steel from the control blade and zircaloy from the channel box. Just above this region of apparently coherent tight blockage, a more diffuse blockage zone is seen. This zone is about 2 cm above the 9.6-cm thermocouple station. Evident here is an intrusion of material into the low density zirconia fiber insulator. The upper half of the bundle is characterized by damaged rods with eroded fuel and oxidized clad remnants. Some rod fracturing and rubblization is observable - this loss of geometry is believed to have occurred during some rough handling the test section received when it was removed from the ACRR.

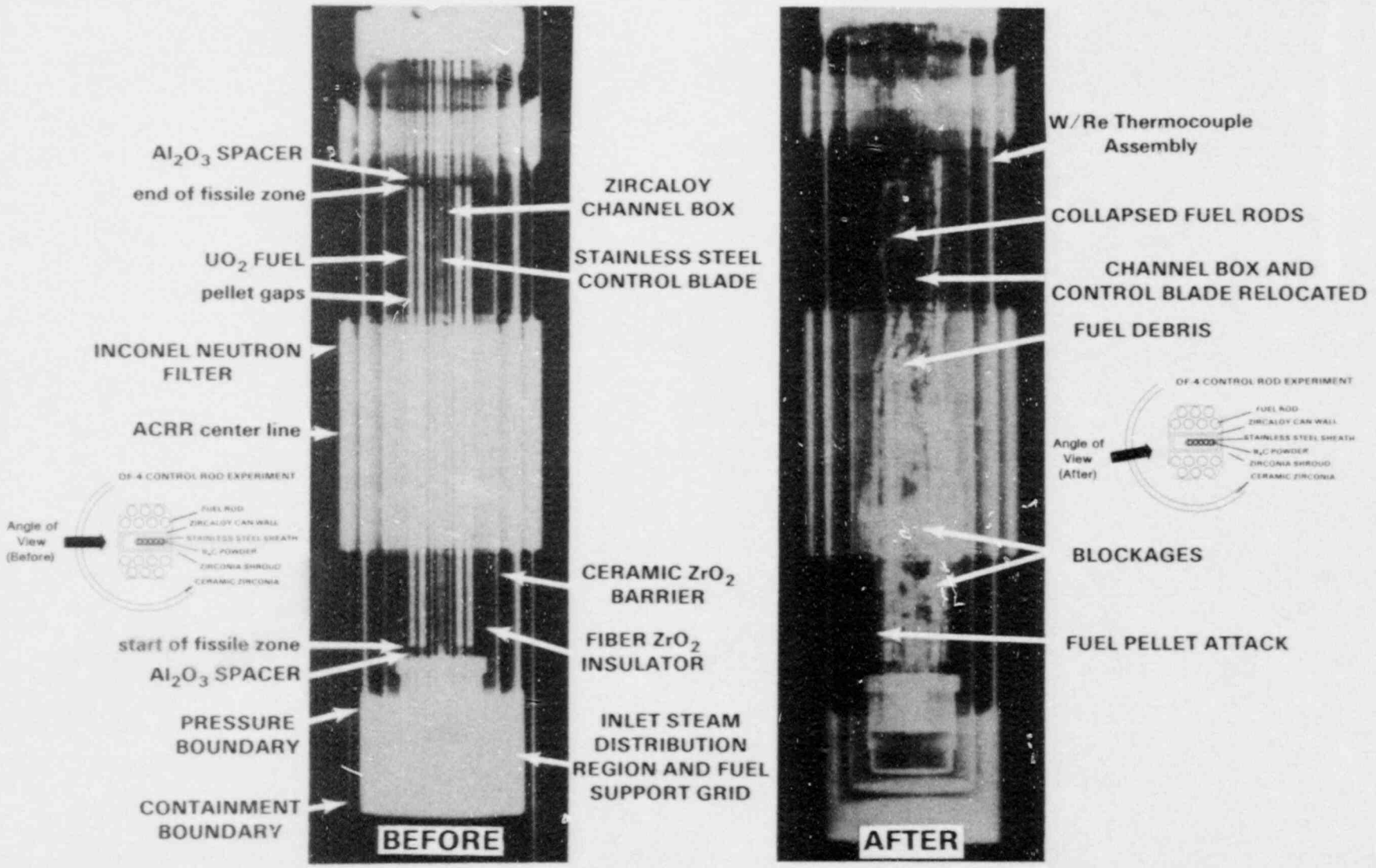

Figure 3.1-12. Pre- and Post- X-Radiographic Images of the DF-4 Test Bundle

3.1.4 Experiment Analysis

A preliminary posttest analysis of the DF-4 experiment has been performed using the MARCON-DF4[117] code as the primary analytical tool. The MARCON-DF4 code was designed to predict the heat transfer rates, chemical reaction rates, and the temperatures in the test section during the DF-4 experiment. The heat transfer processes included conduction in solid structures, convection in the gas phase, and radiation between the interacting surfaces. Metal-water reaction kinetics were modeled to determine the reaction rates of steam with zircaloy in the rods and canister and with steel in the control blade. The hydrogen generation rate and the temporal and spatial distribution of oxide formations were derived from the metal-water reaction calculations. Thus the code is able to produce estimates of the temperature history of the test assembly as well as clad oxidation, hydrogen generation, and the extent of melting of assembly components. The primary limitation of the code is that it does not attempt to calculate the relocation of molten materials and is, therefore, not strictly applicable after significant melting has occurred. The code was initially intended for use as a predictive tool to characterize the various experiment parameters in the pretest mode.

For the posttest analysis, measured information such as the test section inlet flow rates and the reactor power were used as input to the MARCON-DF4 code, and the code was employed in the posttest mode to characterize the test and compare predictions with measured data from the test section instrumentation. Measured thermocouple responses during step reactor power boosts were analyzed and used to calculate the reactor-to-test-section neutronic coupling factors. In turn, the coupling factor information for specific locations in the assembly yielded the axial power shape for the experiment. A check was made to verify the accuracy of the measured steam flow rates by comparing the measured inlet flows to calculated outlet flows. The outlet flows were estimated by utilizing measured temperatures and pressures in the vicinity of the outlet valves together with the measured pressure differentials across the valves. A comparison of the integrated inlet and outlet flows is shown in Figure 3.1-13 and indicates that the steam flows are known quite accurately throughout the experiment. Together with the power and steam flow rates, the code was supplied with the appropriate parameters that describe the DF-4 geometry, initial conditions, and boundary conditions.

3.1.4.1 Coupling Factors

An energy balance on a small section of fuel rod assuming that no chemical reactions are occurring and the rate of heat losses, L, remains constant during a step change in power, yields the following relationship:

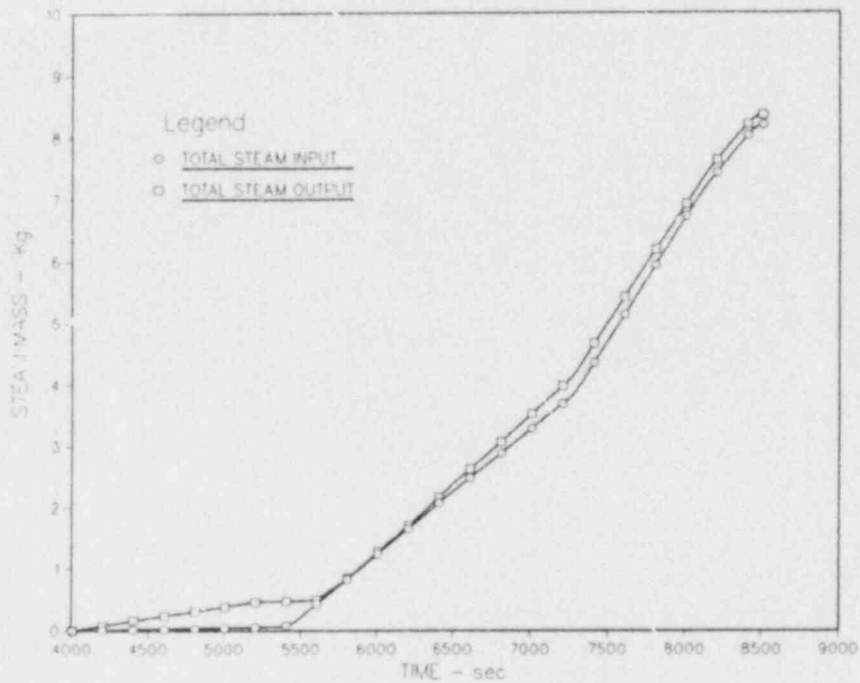

Figure 3.1-13. Comparison of Measured Inlet Steam (Integrated Totals) With Calculated Valve Outlet Flow

$$\int C_p dT = f\int P dt - L\int dt \ , \qquad (3.1\text{-}1)$$

where, f is the coupling factor in watts per gram of UO_2 in the fuel per megawatt of ACRR power. When Equation (3.1-1) is integrated the result is:

$$\Delta H = fP\Delta t - L\Delta t \ . \qquad (3.1\text{-}2)$$

Two sets of data points, one set on either side of a step power change, suffice to calculate the two unknowns in the equation, f and L. To determine the coupling factors for the DF-4 experiment, seven Pt/Rh thermocouples at four different axial positions on the fuel rods were employed. Approximately 30 s of measured thermocouple data, 15 s on either side of a step power adjustment (about 15 data points), were used to obtain a least squares regression of Equation (3.1-2), yielding f and L as correlation constants. This procedure was performed for each thermocouple and each step power adjustment. For each of the thermocouples and power adjustments, a set of 11 delay times was employed to

account for thermal delay between power adjustments and thermocouple responses. The standard errors of estimate of the regressions revealed no indication of a minimum that might have identified a physically preferred delay time, so a delay time of 5 s was assumed.

Of the five power adjustments that were performed before significant oxidation began, three consistently showed the lowest standard errors for the coupling factor. These were the adjustments at 6260, 6400, and 6500 s. Using these three sets of data, we obtained a mean coupling factor at each of the four thermocouple locations. An overall average coupling factor (for the entire test section) of about 1.55 was obtained from this analysis. The spatial variation of the coupling factor yielded a sine shape (away from the axial boundaries of the fissile zone), which can be represented by the relationship

$$f = 1.3 + 0.4\sin[\pi(x - 0.2)/L] \quad , \qquad (3.1\text{-}3)$$

where L is the axial length of the fissile zone. This correlation skews the power slightly higher toward the upper half of the test section, but reflects the general trend observed in the thermocouple responses.

3.1.4.2 Comparison of Calculated and Measured Temperatures

In general, the ability of the codes to predict the temperature histories of the associated structures in the assembly is a good indicator of the accuracy of the modeling and our understanding of the key processes (heat transfer, chemical kinetics). To assess this capability, code-predicted temperatures have been compared with Pt/Rh thermocouple measurements at various locations in the test section. Figures 3.1-14 through 3.1-17 show the results of these comparisons for locations on "hot" fuel rods (MARCON-DF4 nomenclature for rods adjacent to the canister) at axial positions of 9.6, 25.4, 36.8, and 49.5 cm (20, 48, 71, and 95 percent, respectively, from the bottom of the fissile zone).

For the three thermocouples (Z1P215, Z2P160, and Z1P115; Figures 3.1-14 through 3.1-16, respectively) at the lower axial locations, the agreement between measured and calculated temperatures is excellent until melting and relocation begins to occur at about 7700 s. This is the time at which the Pt/Rh thermocouples failed. For these three locations the calculated rod temperatures are nearly identical with the thermocouple measurements, indicating that the rod heatup rates governed by fission power, chemically generated power, and heat losses are accurately determined in the code.

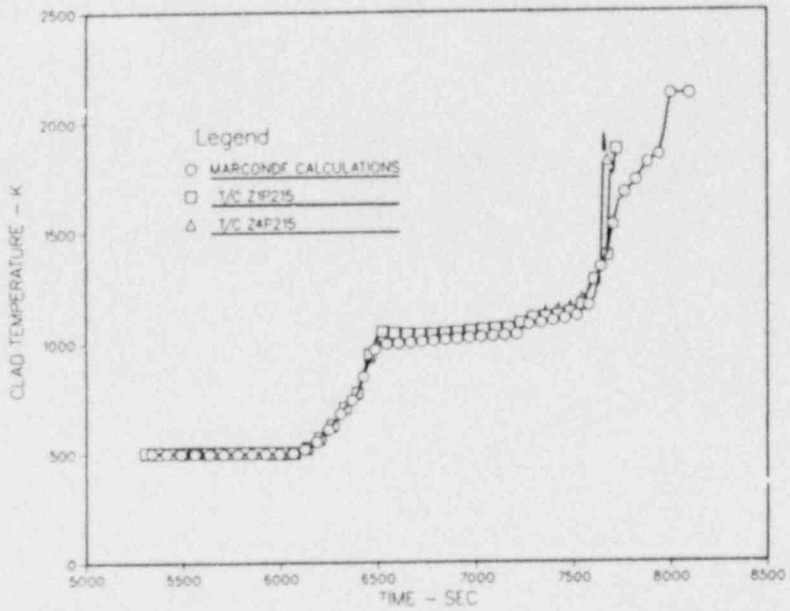

Figure 3.1-14. Comparison of Calculated and Measured Fuel Clad Temperatures at the 9.6-cm Location. Measured values are from Pt/Rh intrinsic junction thermocouples (see Figure 3.1-6 for lateral location).

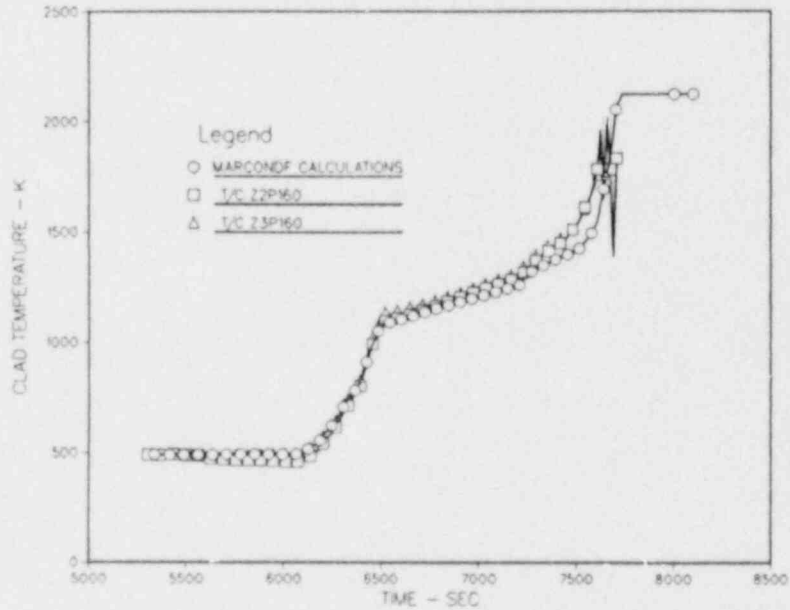

Figure 3.1-15. Comparison of Calculated and Measured Fuel Clad Temperatures at the 25.4-cm Location. Measured values are from Pt/Rh intrinsic junction thermocouples (see Figure 3.1-6 for lateral location).

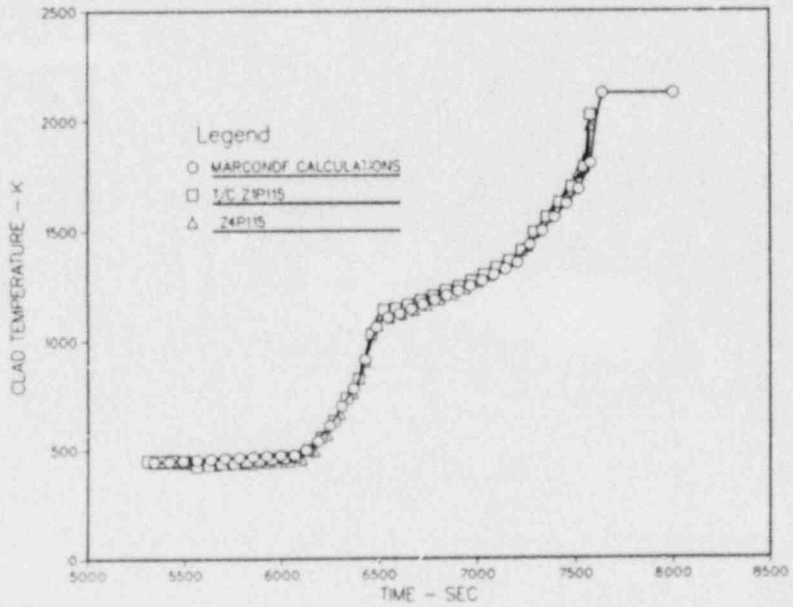

Figure 3.1-16. Comparison of Calculated and Measured Fuel Clad Temperatures at the 36.8-cm Location. Measured values are from Pt/Rh intrinsic junction thermocouples (see Figure 3.1-6 for lateral location).

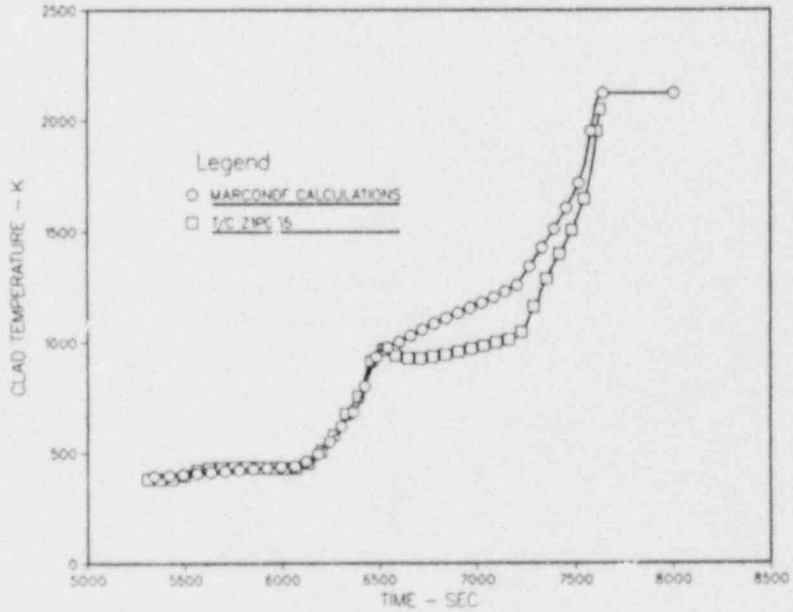

Figure 3.1-17. Comparison of Calculated and Measured Fuel Clad Temperatures at the 49.5-cm Location. Measured values are from Pt/Rh intrinsic junction thermocouples (see Figure 3.1-6 for lateral location).

The calculations for the highest thermocouple location (49.6 cm or 95.5 percent elevation, Figure 3.1-17) show good agreement up to the point at which a power reduction was made from 1 MW to 0.4 MW at about 6500 s. From this time until the power was boosted again at about 7200 s, the code calculates a more rapid heatup rate than is indicated by the thermocouple measurements. If the power shape is altered to reduce the fission power at this location (because of its proximity to the boundary of the fissile zone), the heatup rate during this period can be better simulated, but the result is an underprediction of the initial heatup rate. This procedure is probably not appropriate since the coupling factor for this location was obtained from the same thermocouple and should reflect the relative power level. It is more likely that the heat losses by radiation from the top of the heated zone to the structures above the active region, which are not modeled in the MARCON-DF4 code, are responsible for the overpredicted heatup rate.

The sudden rise in temperature at the bottom of the assembly (thermocouples Z1P215 and Z4P215, Figure 3.1-14) at about 7700 s is probably due to the arrival of molten material from locations higher up in the assembly.

3.1.4.3 Metal-Water Reactions

A maximum hydrogen generation rate of about 0.1 g/s was calculated to occur soon after the final power boost to 1.4 MW. This was reduced to about 0.06 g/s and continued at that level until steam flow to the assembly was terminated at 8100 s. Figure 3.1-18 shows the predicted total hydrogen generated during the experiment. The code estimated that about 43 g of hydrogen were generated during the course of the experiment. Although no measured data is yet available against which to compare this number, it is not out of line with rough estimates made for the amount of copper oxide reacted in the hydrogen getter tubes. In that MARCON-DF4 fails to account for material relocation after melting, the 43 g estimate may be an upper bound, since relocation of molten oxidizing to colder regions would tend to diminish hydrogen generation. Although the code option that extends zircaloy oxidation subsequent to melting was exercised, other modeling contingencies result in only about 20 percent of the channel box being oxidized. This effect is discussed in the following paragraphs.

During the full power phase of the experiment (from 7500 s), the power generated by oxidation of both the rod cladding and the channel box were comparable to fission power (channel box oxidation terminated at about 7800 s). The relative contributions to the energy input to the assembly is shown in Figure 3.1-19. It is seen from Figure 3.1-19 that significant metal-water reaction commenced soon after the power boost at 7200 s, and the total oxidation power actually overtook the fission power at about 7500 s.

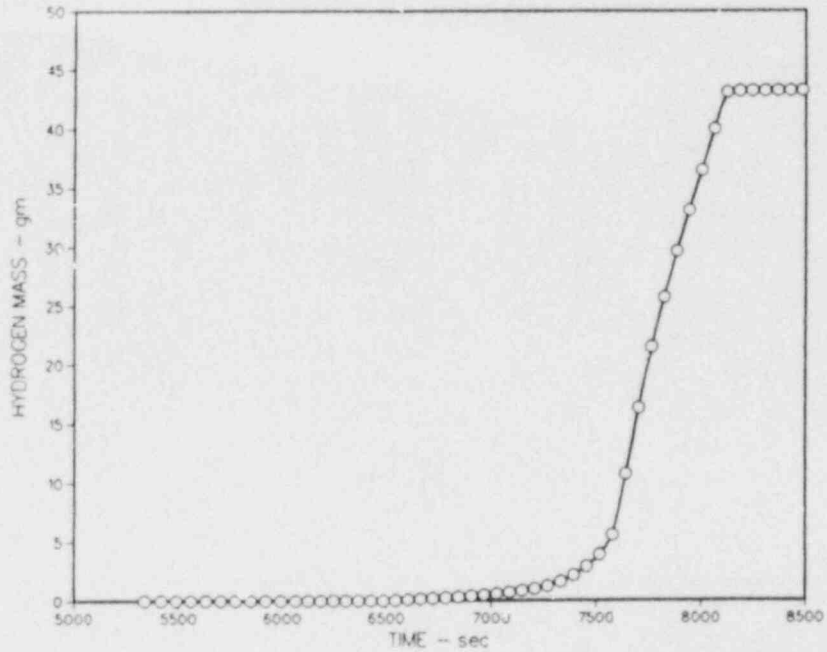

Figure 3.1-18. MARCON-DF4 Predicted Total Hydrogen Produced

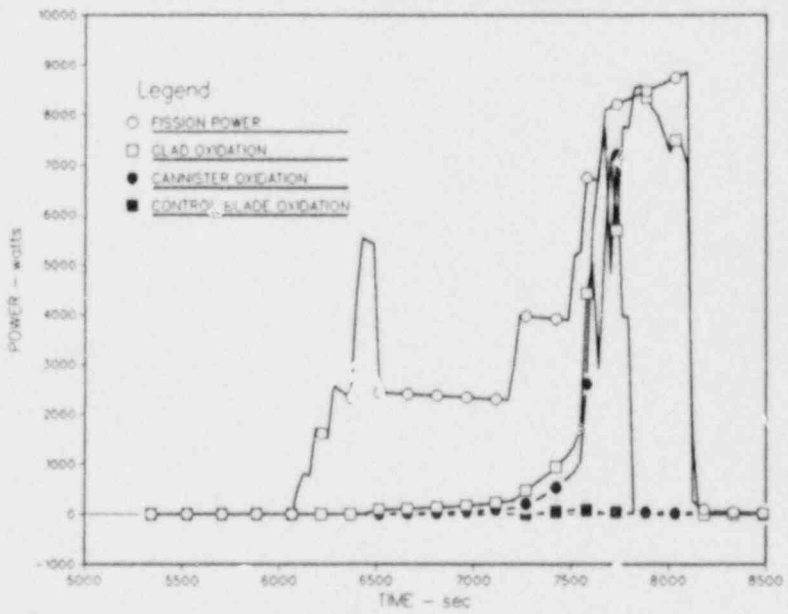

Figure 3.1-19. MARCON-DF4 Predicted Bundle Power Generation. Shown are bundle fission power and chemical power contributions for the fuel cladding, channel box, and control blade structures.

The zone of vigorous oxidation is predicted by the code to begin in the upper half of the bundle (see Figure 3.1-20) and gradually migrate downward. The spatial distribution of oxide at the 7600 s time slice is clearly skewed toward the top half of the bundle while the 7800 s slice shows a flatter profile. By 8000 s the oxidation front had moved to the lower half of the bundle, and in fact, a larger fraction of the cladding had been oxidized in that location. This effect is also seen in the oxidation of the channel box as illustrated in Figure 3.1-21. Here the effect is even more pronounced. Note that the oxidation of the channel box was terminated some time after the 7800 s time slice, whereas oxidation of the rod cladding was not terminated (Figure 3.1-22) until steam flow to the bundle was terminated. There are two code models that are responsible for this behavior. The option that allows continued oxidation subsequent to node melting was used for the rods, the canister, and the blade. However, the option will continue to allow oxidation only until the bottom node in that particular radial region (fuel, channel box, etc.) is melted, at which time oxidation reactions are discontinued in that region. The energy balance model in the code is set up such that the energy that is generated or distributed to an already melted node is redistributed downward to unmelted nodes. The net effect is that the channel box melting quickly propagates downward because of its lower heat capacity in comparison to the fuel rod cladding. As a result, the melt front reaches the bottom node rapidly and oxidation is "switched off". The fuel rods, on the other hand, have significant heat capacity so that the melt front never progresses to the bottom of the assembly and oxidation is not terminated in the rod cladding. Figure 3.1-22 shows this effect graphically--although about 75 percent of the fuel rod cladding has been predicted to be reacted, only about 20 percent of the channel box and 15 percent of the blade have been predicted to oxidize.

3.1.4.4 Melting Attack

The predicted fractions of structures melted during the experiment are indicated in Figure 3.1-23. The code calculates peak melt fractions of 98 percent for the control blade, 87 percent for the channel box, and about 70 percent for the fuel cladding. Clearly, since the code does not relocate melted material, the axial distribution of energy sources from metal-water reactions is not accurately tracked after about 7600 s. Gradual cooling of the assembly after the reactor power and steam flows were turned off (about 8150 s) accounts for the resolidification of rod cladding seen in Figure 3.1-23. The extremely high-melt fractions imply quite massive relocation of clad, canister, and control blade materials. These observations are generally consistent with the sudden temperature excursions in the lower sections of the assembly, as measured by thermocouples in those locations, implying the ingress of molten materials from higher up in the assembly.

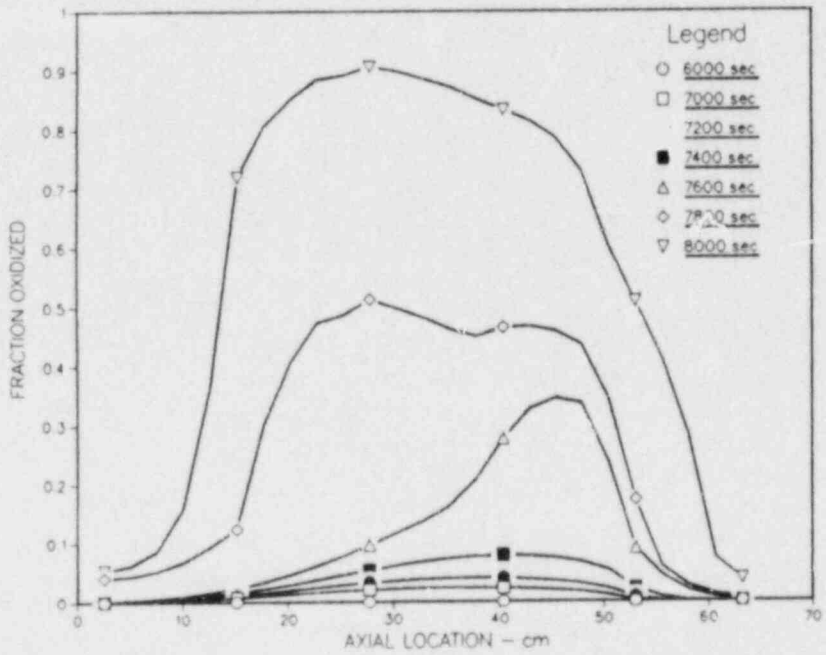

Figure 3.1-20. Predicted Axial Distribution of Clad Oxide Fraction for the Modeled "Hot Rod"

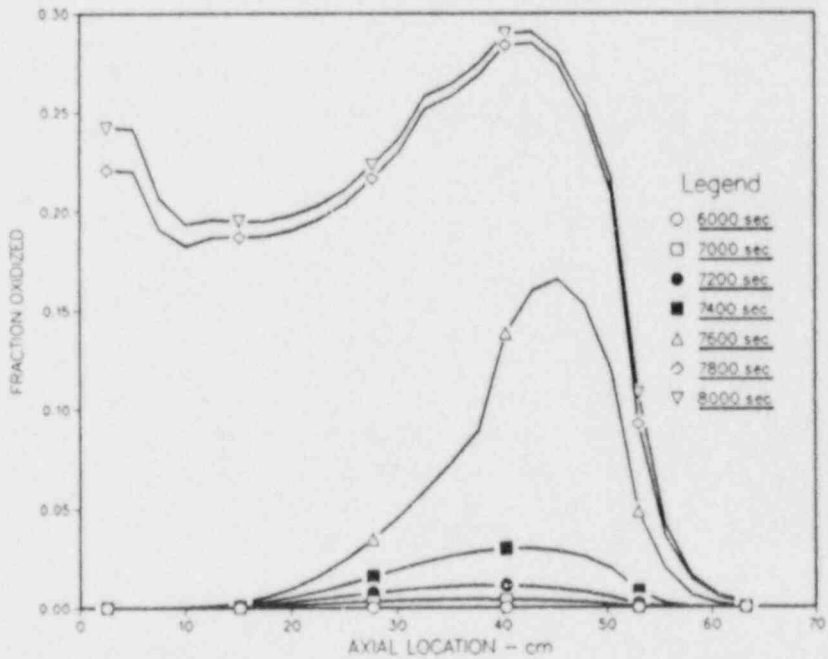

Figure 3.1-21. Predicted Axial Distribution for the Channel Box Oxide Fraction.

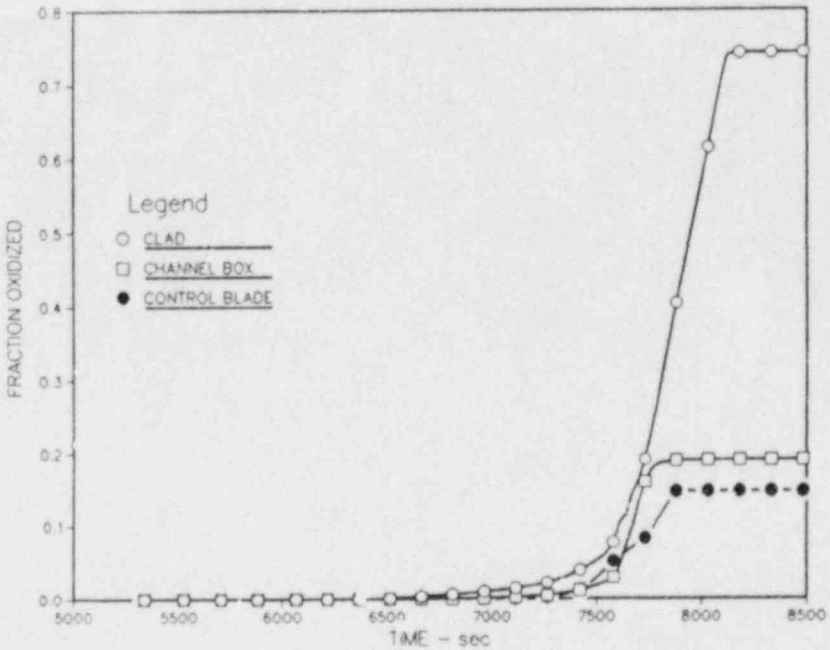

Figure 3.1-22. Predicted Total Oxidation Fraction of Fuel Cladding, Channel Box, and Control Blade.

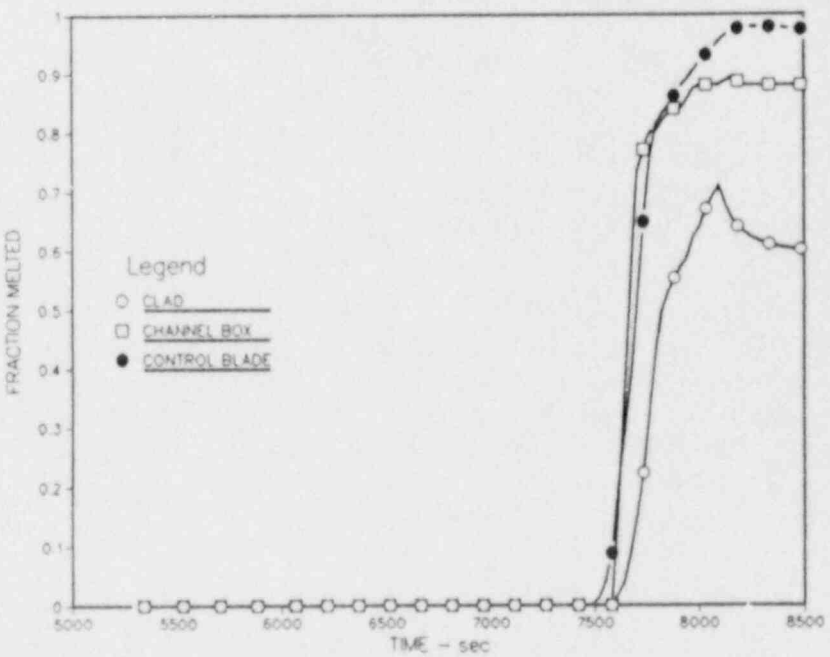

Figure 3.1-23. Predicted Fraction Melted for the Fuel Cladding, Channel Box, and Control Blade

Figure 3.1-23 shows that the control blade began to melt about 100 s before the channel box and rod cladding started to melt. The blade and the channel box melting appears to propagate from the original melt front location in the upper half of the bundle down to the bottom by about 7800 s. Additional melting of these structures was probably from material above the original melt front location.

It seems likely that melting and slumping of the control blade took place before significant melting in the fuel rods and that the B_4C and molten steel from the blade relocated to the lower regions of the assembly without appreciable interaction with the fuel. Interactions between B_4C, steel, and zircaloy from the canister during the period when the blade and canister were melting cannot be ruled out, but there was no indication of a reaction between the B_4C and steam either during or subsequent to the blade melting phase.

3.1.4.5 Thermal Response

The thermal response of the test assembly is illustrated in Figures 3.1-24 and 3.1-25. Figure 3.1-24 gives the axial temperature profile for the hot rods at various time slices during the experiment. It is seen that the fuel temperature predicted by MARCON-DF4 is approaching the fuel melting temperature (2673 K) at the 7750 s time slice. A significant fraction of the energy that heated the fuel rods came from the oxidation of the cladding, and since the cladding had been melted at these temperatures, the code may have artificially held the clad in place while it continued to oxidize adjacent to the fuel. This situation may have supplied too much energy to the fuel and overpredicted the rod heatup rate. The fuel heatup rate as calculated by the code between 7500 and 7750 s ranges from 3 to about 3.6 K/s. Tungsten/rhenium thermocouples indicated heatup rates in the range of 3.1 to about 3.3 in this axial region; this is not out of line with the code. However, peak temperatures measured by the tungsten/rhenium thermocouples did not exceed about 2400 K. Given that these thermocouples may have underestimated the temperatures by perhaps 200 K, the peak temperature does not appear to have exceeded 2600 K. This is somewhat below the eutectic for UO_2-ZrO_2 and below the temperatures reached in the MARCON-DF4 calculations, which imply at least incipient melting in the fuel rods.

A comparison of the calculated temperatures for the fuel, fuel clad, channel box, and control blade are shown in Figure 3.1-25. There exists a distinctively negative temperature gradient from the fuel down to the control blade until about 7600 s. At that time vigorous oxidation on the channel box actually drives its temperature and that of the control blade higher that the fuel temperature. After oxidation is terminated in the control blade, the primary energy sources originate in the fuel and clad and the fuel temperature again exceeds the channel box temperature.

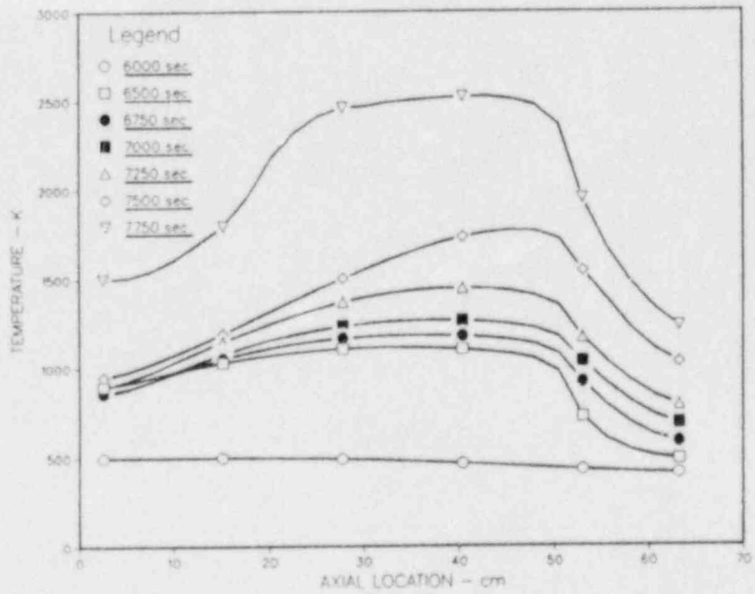

Figure 3.1-24. Predicted Axial Temperature Distribution for the Modeled "Hot Rod"

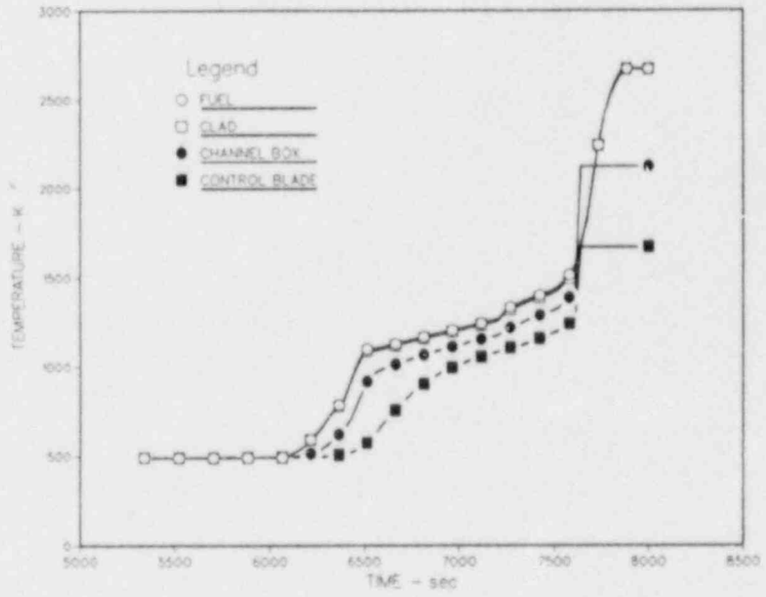

Figure 3.1-25. Predicted Temperatures for the Modeled Structures Corresponding to the 25.4-cm Axial Location

The preliminary analysis of the DF-4 experiment was performed with a view to establishing the general characteristics of the test, and the MARCON-DF4 code proved to be an excellent vehicle for that task. The code exhibits remarkable predictive capabilities despite the major limitation inherent in its inability to relocate melted materials. The preliminary analysis has laid the groundwork for a more rigorous analysis that will use the MELPROG code as the appropriate BWR models become available in that code. The MELPROG code contains a sophisticated set of models for tracking the movement and resolidification of molten materials and, therefore, does not suffer from the same limitations as the MARCON-DF4 code.

In the interim, the DF-4 study is proceeding with the analysis of the high-temperature thermocouple data (tungsten/rhenium thermocouples). These thermocouples were sheathed to protect the junctions from an oxidizing medium and are, therefore, not in good thermal contact with the structures that are being measured. The W/Re thermocouples can extend the temperature history of the experiment considerably past the point at which the Pt/Rh thermocouples fail and are important in that respect. A code, called WRET, has been developed which uses finite difference techniques to calculate the expected thermocouple measurements, given the predicted cladding temperatures produced by the MARCON-DF4 code. The WRET code will supply information regarding delays and biases associated with the W/Re thermocouple measurements.

3.1.5 Discussion

The end state damage sustained by the DF-4 test bundle was severe, with almost complete failure of the stainless steel control element and the zircaloy channel box. Damage to the fuel rods was also substantial, although the end state configuration was largely one of standing rod geometry. In the upper half of the test section, fuel erosion appears to have occurred judging from density comparisons in the X-radiograph posttest image. The lower half of the bundle is much increased in density due to the massive relocation of the control blade and channel box structures. PIE examination should provide evidence as to the sequence of failure of the various components based upon the degree of stratification of materials in the lower bundle.

Of special interest is the degree of interaction between the control blade stainless steel, which was known to fail early in the sequence, and the zircaloy channel box. In addition to failure by melting, the channel box failure could have been initiated or augmented by attack from molten steel at a temperature on the order of 1500°C. This possibility is mentioned because of the potential earlier time of failure of the fuel canister that would be implied. Evidence for such an interaction will be considered in the metallurgical examination of the test

section. The large amount of channel box material, which relocated to the lower bundle regions, refroze around the fuel rods. The channel box material was preferentially directed to the fuel rod regions since the control blade material had previously slumped and refrozen in the channel box interior, thus blocking the path of any subsequent molten channel box zircaloy. The axial freezing behavior and material interaction of the control blade material in the intercanister region of an actual reactor must be considered in order to evaluate the effect of relocating channel box zircaloy with respect to fuel canister blockage. Vigorous interaction between control blade steel and intact canister walls may result in side wall failures even in the event that significant canister blockages form.

Observed and calculated trends in DF-4 suggest that the canister axial failure propagation may occur substantially faster than the fuel cladding failure. This trend was expected because of the lower thermal inertia of the channel box zircaloy in comparison to fuel rod cladding. Based on the massive channel box failure incurred in DF-4, structural failure of the standing fuel canisters should be expected, even if the upper regions of the core are not badly oxidized. This suggests a mode of fuel element breakup and debris layer formation not present in PWR cores. In addition, if large amounts of metallic zircaloy (fuel canister zircaloy) are incorporated into the BWR debris layer, core melt progression could be very different in character from the highly oxidic debris beds postulated for PWR cores.

The entry into the oxidation transient regime of the DF-4 test was characterized by a heatup rate between 1 and 2 K/s, varying somewhat with axial location. Lower heatup rates, e.g. 0.2 to 0.5 K/s, could further separate the control blade failure time from the rapid oxidation-hydrogen production phase of the accident. The effect of core reflood during this interim period should be evaluated in view of the possibility of a reactivity excursion.

Finally, the effect of the BWR prototypic SRV periodic actuations during a high-pressure accident needs to be examined in the context of whole core behavior. One potential behavior of the periodic steam bursts would be that during a period when boiling is suppressed, the control blade and canister walls could be heating to temperatures where oxidation would take place quite readily if steam were available. The subsequent, sudden availability of a large amount of steam upon the SRV opening could then result in a very rapid burst of oxidation accompanied with material melting. It is unclear whether this transient and intermittent behavior would greatly affect the overall melt progression in the core and, therefore, the issue should be examined.

A important step in the application of phenomenological evidence of the type obtained in DF-4 is its implementation into a

mechanistic computer model, i.e., MELPROG. Once this is done, the impact of these phenomena may be evaluated in a context beyond the experiment scale, such that the whole core behavior is considered. For example, the freezeout of the control blade steel and its interaction with the fuel canister walls may exhibit a completely different character from that observed in DF-4 because of the greatly differing axial thermal gradient between the two cases. The mechanistic code can explore these differences. Final conclusions regarding, for example, the appropriateness of the MAAP code treatment of fuel canister blockages cannot be rendered until the mechanistic code embodies these observed experimental phenomena such that a reasonable extrapolation beyond the experiment scale can be affected. In addition, the analytical sophistication provided by the mechanistic code is required in order to logically address the phenomenological uncertainties associated with the extended accident melt progression issues.

4. MELT PROGRESSION PHENOMENOLOGY CODE DEVELOPMENT (MELPROG)

(W. J. Camp and J. L. Tomkins, 6425)

The MELPROG computer code is being developed to provide a mechanistic computer model for the analysis of the in-vessel phases of severe accidents in LWRs. To treat the complete primary coolant system of LWRs, MELPROG has been implicitly linked to the TRAC-PF1 thermal hydraulics code. And to provide a complete treatment of a severe accident from initiation through possible release of fission products to the environment, MELPROG has been linked to the CONTAIN containment analysis computer code.

This work includes both the development of MELPROG and the application of MELPROG to accident scenarios and to the analysis of experiments. MELPROG development includes incorporation of existing models, when appropriate, into the code framework and development of new models when necessary. The applications work includes testing and assessment of individual models and of the interaction of models.

4.1 MELPROG Code Development

(J. L. Tomkins, R. C. Smith, S. S. Dosanjh, and M. F. Young, 6425)

MELPROG has been developed as a set of modules. Each module consists of a set of tightly coupled phenomenological models. The modules are explicitly coupled to each other and share a common data structure. Interfaces between modules are well defined and exist in only one subroutine of each module. The advantages of the MELPROG structure are that it is relatively easy to add or replace specific phenomenological models and that it is also relatively easy to add or replace a complete module.

MELPROG-PWR/MOD0, the first version of the code, has been completed. This version of the code contains five modules and a link to the TRAC-PF1 thermal hydraulics code. The five modules are (1) FLUIDS, a one-dimensional (axial) three-field (steam and hydrogen, water, and corium) treatment model; (2) PINS, a simple fuel rod model and a very simple control rod model; (3) STRUCTURES, heat transfer and mechanical models of in-vessel PWR structures and the PWR vessel; (4) DEBRIS, a one-dimensional debris bed model; and (5) RADIATION, a two-dimensional (radial and axial) net enclosure model that treats absorption and emission in steam, water, and corium.

The second version of MELPROG, MELPROG-PWR/MOD1, is currently under development and includes many significant improvements over the first version. The one-dimensional FLUIDS module has been replaced by a new two-dimensional, four-field fluid dynamics model (FLUIDS-2D). The PINS module has been replaced by a

detailed core structures module (CORE). A fission-product release, transport, deposition, and aerosol formation and transport module (VICTORIA) has been added. A melt-water interactions module (IFCI) and a melt ejection module (EJECT) are also under development. Finally, a new, more detailed debris bed model is under development and will replace all or part of the current DEBRIS module. The new debris bed modeling and a new eutectic dissolution model for the CORE module are discussed here.

4.1.1 DEBRIS Module Development

A model of melt formation and relocation in a one-dimensional core rubble bed has been developed. The analysis includes mass conservation equations for the species of interest (UO_2 and ZrO_2); a momentum equation which represents a balance among drag, capillary, and gravity forces; and an energy equation that incorporates the effects of convection by the melt, radiation, and conduction through the bed and the energy release associated with the decay heat. An equilibrium UO_2-ZrO_2 phase diagram is prescribed and radiative heat transfer through the bed is incorporated using a temperature dependent conductivity. A brief description of the model follows. A few applications are also discussed.

Typical characteristics of a UO_2-ZrO_2 core rubble bed similar to the one found in TMI[118] are given in Table 4.1-1. One hour after reactor shutdown, power generation falls to approximately one percent of peak power.[119] A TMI-2 type plant with an operating power of 2.8×10^3 MW and 93,000 kg of UO_2 in the core[120] has a decay heat, Q, on the order of 300 W/kg of UO_2. Because it takes several days for the decay heat to decrease significantly,[119] it is assumed that Q is constant in the following analysis. A lower limit for the UO_2 volume fraction Y_{s1} is estimated by assuming that all of the roughly 23,000 kg of Zr in a typical core[120] are oxidized, resulting in the formation of 30,000 kg of ZrO_2. Neglecting materials other than UO_2 and ZrO_2 in the core gives a maximum ZrO_2 mass fraction of 0.25. Setting the solid densities of UO_2 and ZrO_2 equal to 9650 and 5700 kg/m^3,[121] respectively, gives a maximum ZrO_2 volume fraction Y_{s2} of 0.36.

Species diffusion is neglected in the following analysis. Typical mass diffusivities for liquids near their melting points are on the order of 10^{-9} m^2/s.[122] For time scales on the order of 10^3 s, the distance characteristic of diffusion, $[Dt]^{1/2}$, is approximately 10^{-3} m. That is, liquid phase diffusion is only important over length scales comparable to the average particle diameter. Balancing the mass stored in a differential control volume, the convective flux flowing into this volume, and production (or depletion) by melting gives, for species j (j=1 and j=2 correspond to UO_2 and ZrO_2, respectively),

Table 4.1-1

Typical Initial Properties of a Core Rubble Bed

Quantity of Interest	Typical Value
decay heat, Q [W/kg of UO_2]	300.0
height of bed, L [m]	1.0[a]
particle diameter, d_p [mm]	0.1-10.0
porosity, ϵ	0.4
UO_2 solid volume fraction, Y_{s1}	$\geq$ 0.64
ZrO_2 solid volume fraction, Y_{s2}	$\leq$ 0.36

[a]Order of magnitude estimate from Reference 118.

$$\frac{\partial}{\partial t}\left[Y_{lj}\rho_{lj}\epsilon S\right] + \frac{\partial}{\partial x}\left[Y_{lj}\rho_{lj}q\right] = -\frac{\partial}{\partial t}\left[Y_{sj}\rho_{sj}(1-\epsilon)\right] , \quad (4.1\text{-}1)$$

where the subscripts, l and s, refer to liquid and solid, respectively. The local porosity, ϵ, is the volume fraction occupied by liquid and gas; the saturation, S, is the fraction of void that is filled with liquid; q is the volumetric flow rate; and Y_{ij} is the portion of phase i that is occupied by species j. The Y_{ij}s are related to each other by $Y_{l1} + Y_{l2} = 1$ and $Y_{s1} + Y_{s2} = 1$.

Assuming that the liquids are miscible, Darcy's Law gives for the momentum equation,

$$\frac{\partial}{\partial t} q \sum_{j=1}^{2} Y_{lj}\rho_{lj} + \frac{\mu}{\kappa_l} q = -\frac{\partial}{\partial x} P_l - g \sum_{j=1}^{2} Y_{lj}\rho_{lj} , \quad (4.1\text{-}2)$$

where μ is the dynamic viscosity of the liquid, g is the gravitational acceleration, and κ_l is the relative permeability. Equation 4.1-2 takes into account viscous drag, which is assumed to vary linearly with q, gravity, and motion as a result of changes in pressure. Capillary forces enter Equation 4.1-2 through the term involving the liquid pressure, P_l. The capillary pressure is defined as the difference between P_l and the gas pressure, P_g (that is, $P_c = P_g - P_l$).[125] Taking the gas flow to be

isobaric, $\partial P_l/\partial x = -\partial P_c/\partial x$. From Equation 4.1-2, it is therefore evident that capillary forces move liquid into regions of high P_c.

Leverett[124] derived the following relation for P_c using dimensional analysis:

$$P_c = J\gamma\left[\frac{\epsilon}{\kappa}\right]^{1/2} , \qquad (4.1\text{-}3)$$

where γ is the surface tension; κ is the permeability; and J is a function of the effective saturation, $S_e = (S - S_r)/(1 - S_r)$, where the residual saturation, S_r, is defined as the threshold value of S below which bulk liquid motion ceases. Bird et al.[125] derive a relation for κ by modeling the porous solid as a bundle of capillary tubes,

$$\kappa = \frac{d_p^2\,\epsilon^3}{150\,(1-\epsilon)^2} , \qquad (4.1\text{-}4)$$

where the factor of 150 is determined empirically. Combining Equations 4.1-3 and 4.1-4 gives

$$P_c = J\gamma\,\frac{\sqrt{150}\,(1-\epsilon)}{d_p\epsilon} . \qquad (4.1\text{-}5)$$

Note that P_c decreases as the particle diameter, d_p, increases. For $\gamma \simeq 0.5$ N/m, capillary forces are only important when d_p is on the order of 1 mm (or smaller). Decreasing ϵ increases P_c, and consequently, capillary forces tend to move liquid into regions of lower porosity.

Empirical correlations are needed for J, the relative permeability, κ_l, and the residual saturation, S_r. Hofmann and Barleon[126] give for J,

$$J = a\,(S_e + b)^{-c} , \qquad (4.1\text{-}6)$$

where a = 0.38, b = 0.014, and c = 0.27. Equation 4.1-6 agrees with the results of Reed et al.[127] except near $S_e = 0$. The primary advantage of Equation 4.1-6 is the absence of a

singularity at $S_e = 0$. Note that J and P_c reach their maximum value in regions of low saturation. Therefore, capillary forces tend to move liquid into regions of low saturation.[123,124]

In fully saturated flow ($S = S_e = 1$), κ_l equals the permeability, κ, while in undersaturated flow, only a fraction of the solid is wetted and κ_l is proportional to κ[127](with the proportionality being a function of S). Reed et al.[127] give for κ_l,

$$\kappa_l = \begin{cases} \kappa S_e^3 & , \text{ for } S > S_r \\ 0 & , \text{ for } S \leq S_r \end{cases} , \qquad (4.1\text{-}7)$$

where $S_e = (S - S_r)/(1 - S_r)$. As discussed earlier, liquid does not begin to flow until the saturation reaches a threshold value, S_r. For $S \leq S_r$, $\kappa_l = 0$, and Equation 4.1-2 requires that $q = 0$. When S is less than S_r, the liquid consists of unconnected pendular rings. Liquid starts to flow when S is increased to the point that these rings touch and coalesce.[124]

Brown et al.[128] give for the residual saturation S_r,

$$S_r = \frac{1}{86.3}\left[\frac{\gamma}{\kappa \rho_l g}\right]^{0.263} . \qquad (4.1\text{-}8)$$

Thus S_r varies with the ratio of surface tension to gravity. The dependence of S_r on the porous matrix is contained in the permeability, κ. Increasing the particle diameter or the porosity raises κ and leads to lower values of S_r. For packed beds consisting of small, tightly packed particles, the saturation must be increased to a high value before bulk liquid motion is observed.

Assuming that all the materials present are in local thermal equilibrium, only one temperature field needs to be determined. Radiation heat transfer in the packed bed is incorporated using a diffusion model with a temperature dependent conductivity. Balancing the energy stored in the solid and the liquid, convection, diffusion and internal heat generation,

$$\frac{\partial}{\partial t}\sum_{j=1}^{2}\left[(1-\epsilon)Y_{sj}\rho_{sj}h_{sj} + \epsilon S Y_{1j}\rho_{1j}h_{1j}\right] + \frac{\partial}{\partial x} q \sum_{j=1}^{2} Y_{1j}\rho_{1j}h_{1j}$$

$$= \frac{\partial}{\partial x} k_{eff} \frac{\partial T}{\partial x} + \left[(1-\epsilon)\rho_{s1}Y_{s1} + \epsilon S \rho_{11}Y_{11}\right] Q , \qquad (4.1\text{-}9)$$

where h_{ij} is the enthalpy of species j in phase i, Q is the decay heat expressed as energy release per mass of UO_2 present, and k_{eff} is an effective thermal conductivity that accounts for both conductive and radiative heat transfer in the porous solid. Note that energy stored in the gas phase is neglected in Equation 4.1-9. This is a reasonable approximation because the densities of materials of interest are very large (typically on the order of 10^4 kg/m^3) compared with the gas density.

Radiation heat transfer in the packed bed is incorporated using a modified gas conductivity, $k_g^* = k_g + k_{rad}$.[129] That is, it is assumed that gas conduction and radiation act in parallel. Several researchers[129] have proposed that $k_{rad} = 4\epsilon_r \sigma d_p T^3$, where ϵ_r is the emissivity of the solid, and σ is the Stefan-Boltzmann constant. Empirical correlations for k_{eff} in solid-gas systems are available in the literature.[129] However, in the current problem, three phases (solid, liquid, and gas) are present. In calculating k_{eff}, the solid and the liquid are treated as a single component with a volume averaged thermal conductivity,

$$k_\sigma = \frac{1}{1-\epsilon+\epsilon S}\left[(1-\epsilon)\sum_{j=1}^{2} Y_{sj}k_{sj} + \epsilon S \sum_{j=1}^{2} Y_{lj}k_{lj}\right], \qquad (4.1\text{-}10)$$

where k_{ij} is the conductivity of species j in phase i. For a single phase i, k_σ depends only on Y_{ij} and k_{ij}. That is, $k_\sigma = Y_{s1}k_{s1} + Y_{s2}k_{s2}$ for $S = 0$ (solid only) and $k_\sigma = Y_{l1}k_{l1} + Y_{l2}k_{l2}$ for $\epsilon = 1$ (liquid only). The following correlation is used to calculate k_{eff}:[129]

$$k_{eff} = \psi\, k_g^* + \frac{1-\psi}{k_\sigma \omega + k_g^*(1-\omega)}\, k_\sigma k_g^* \quad , \qquad (4.1\text{-}11)$$

where

$$\omega = 0.3\, \phi^{1.6}(k_\sigma/k_g^*)^{-0.044} \quad , \qquad (4.1\text{-}12)$$

$$\psi = \frac{\phi-\omega}{1-\omega} \quad , \qquad (4.1\text{-}13)$$

and ϕ $(\epsilon-\epsilon S)$ is the volume fraction occupied by gas. Note that as $\phi \to 0$, $\omega \to 0$, and $\psi \to 0$ and consequently, $k_{eff} \to k_\sigma$. As $\phi \to 1$, $\psi \to 1$, giving $k_{eff} \to k_g$.

Shown in Figure 4.1-1 is a binary phase diagram for a UO_2 - ZrO_2 system. Figure 4.1-1 was constructed from the solidus and liquidus temperatures given in Reference 130. Initially non-homogeneous (over distances comparable to d_p) particulate beds are of primary interest here because the species of interest, UO_2 and ZrO_2, are initially separated in the core. The melting behavior of such composites depends on the rates of both solid phase species diffusion and evaporation-condensation processes at the particulate level. If these processes are fast, Figure 4.1-1 will adequately represent phase changes in the bed, and if they are slow, melt will first form at the minimum solidus temperature (which corresponds to a ZrO_2 mole fraction of 0.5 in the liquid phase).*

4.1.2 CORE Module Development-Eutectic/Mixture Treatment

Pure UO_2 melts at about 3113 K. However, in contact with molten zircaloy at 2200 K, UO_2 will begin to dissolve rapidly. In fact, many materials when in contact with certain other molten materials will begin to dissolve at much lower temperatures than their normal melting points. These so-called eutectic reactions are typically described by equilibrium phase diagrams that indicate the physical state (phase composition) of the materials as a function of their temperature and relative proportions (mole fractions). Eutectic reactions can profoundly affect the course of a severe core accident in a nuclear reactor because there are several materials in a reactor core that form eutectics with one another. The eutectic/mixture model in MELPROG is intended to calculate solid-liquid phase change rates involving eutectic materials.

The model is based on determining the liquidus temperature as a function of composition; the assumption being that solid will continue to dissolve as long as the mixture temperature exceeds the liquidus temperature. The method is limited primarily by the uncertainty in the liquidus temperature when the number of materials exceeds two.

For a binary system the temperature-composition diagram can be represented in two dimensions as in Figure 4.1-2. The liquidus temperatures describe the two curves that meet at the eutectic point E and separate the single phase liquid region L from the two-phase, liquid-solid regions α + L and β + L. Similarly, the solidus temperatures describe the two curves that are joined by the eutectic reaction isothermal, ab, and separate the single phase solid regions α and β from the two-phase regions α + L and β + L. The solvus lines separate single phase solid regions α and β from the two-phase solid region α + β.

---

*Private Communication with D. A. Powers, Sandia, Div 6422, 1987.

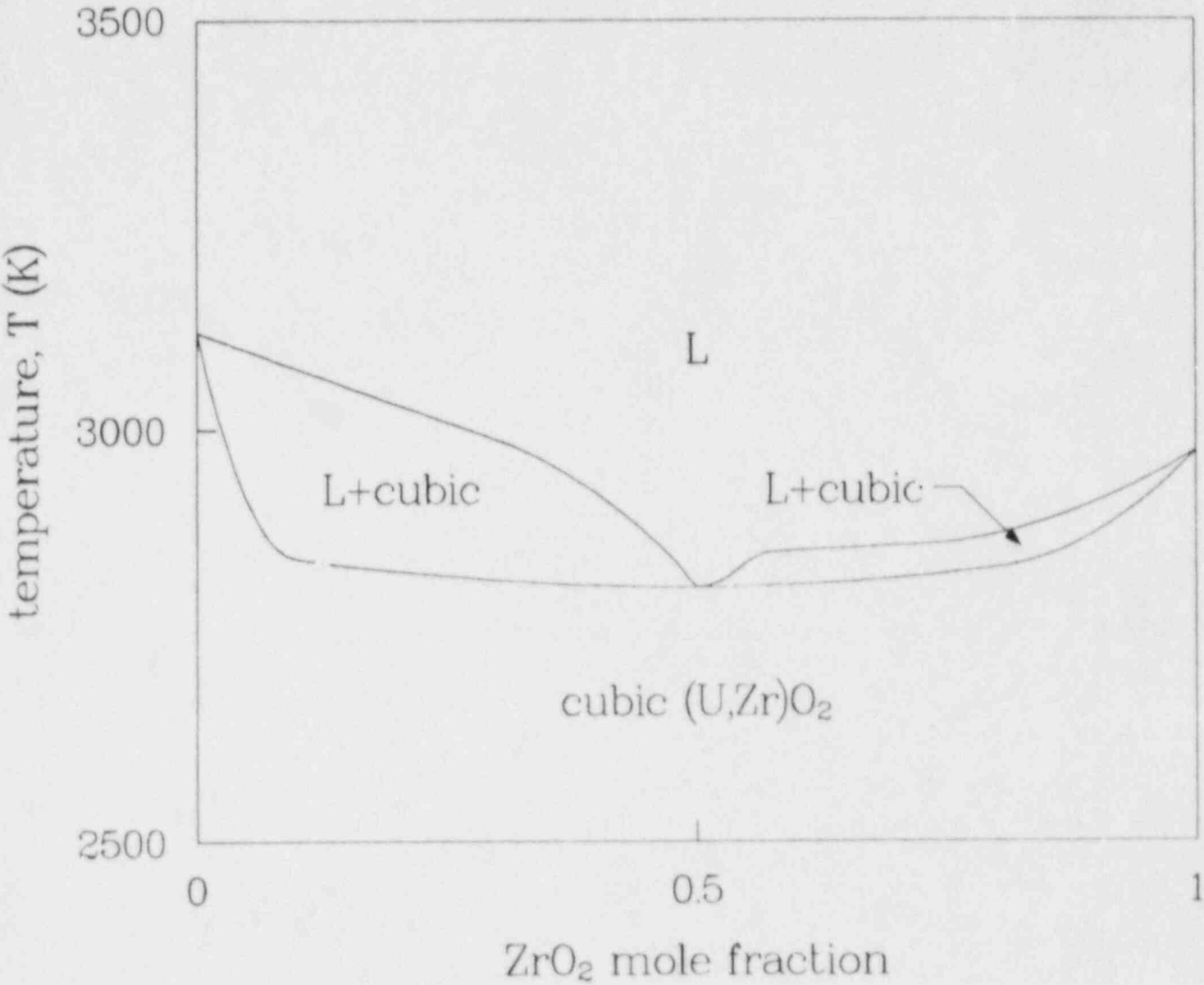

Figure 4.1-1. Phase Diagram for UO_2-ZrO_2

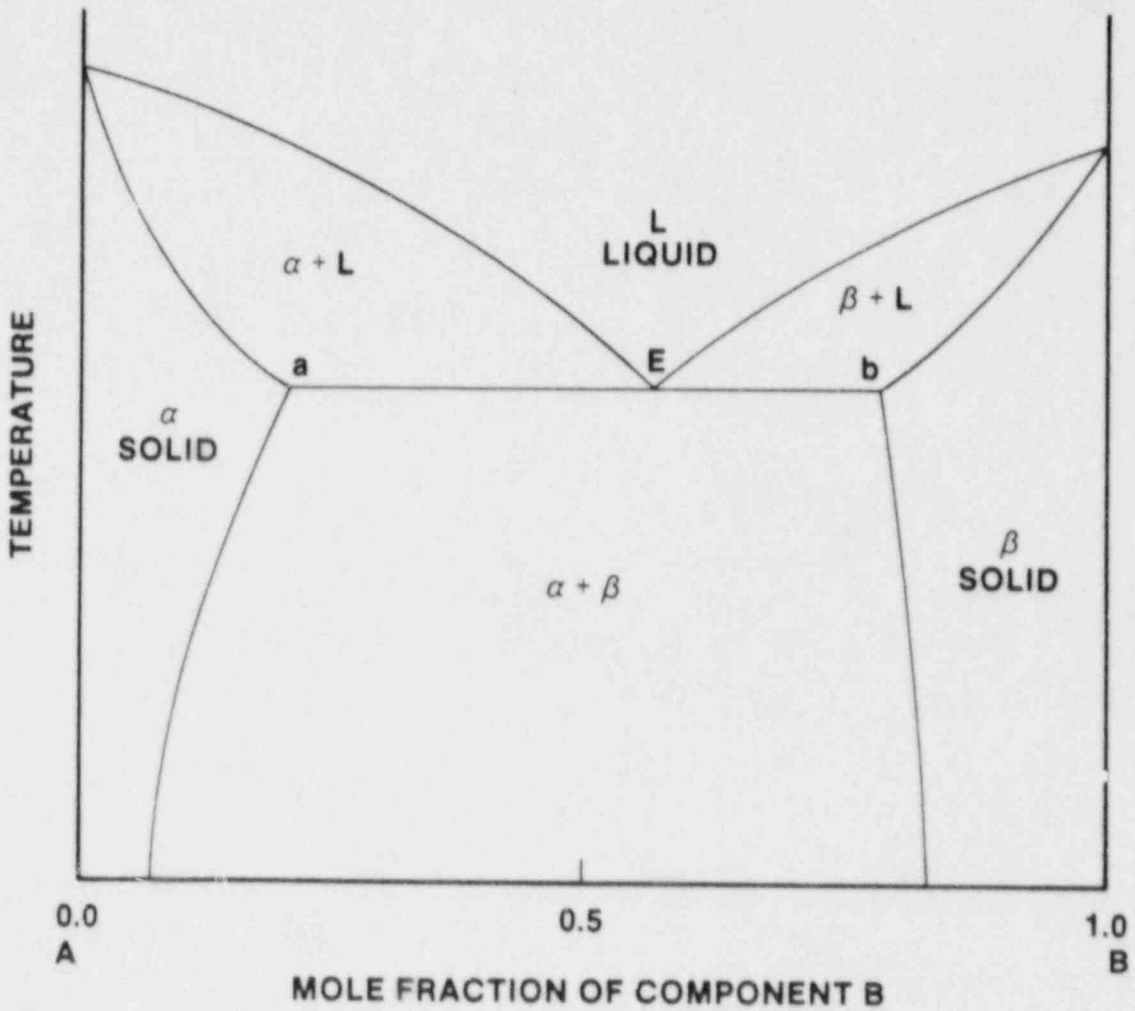

Figure 4.1-2. A Typical Binary Phase Diagram With a Eutectic Reaction

For a ternary system, the temperature-composition diagram can be represented as a three-dimensional region of triangular cross section. The vertices of the equilateral triangle represent pure components, and the temperature axis is projected normal to the plane of the triangle. The faces of the region are two-dimensional binary phase diagrams for the components at each edge. In a ternary system the solidus, liquidus, and solvus temperatures describe surfaces within the region. Because of the obvious difficulty of presenting a three-dimensional region in two dimensions, ternary phase diagrams are typically presented as slices out of the region. Horizontal slices appear as isothermal triangles such as Figure 4.1-3. The solidus, liquidus, and solvus temperatures appear as lines in these isotherms, but unless a specified composition happens to fall on the liquidus line for a given isothermal section, it is necessary to interpolate between isothermal sections to estimate the liquidus temperature for the specified composition. With few isothermal sections near the actual liquidus temperature to work with, the estimate becomes quite uncertain.

Because of the lack of information for systems with more than two components and because often only two components are actually present, the scheme used in MELPROG to determine the liquidus and solidus temperatures as a function of composition uses pseudo-binary phase diagrams rather than isothermal ternary phase diagrams. A pseudo-binary phase diagram is a vertical slice from the three-dimensional temperature--composition region that behaves like a true binary system consisting of the compositions at the two edges of the slice.

The MELPRO model approximates the ternary liquidus temperature as

$$T_L = \frac{\sum_{i=1}^{N} \sum_{j=1}^{N} f_i \, f_j \, T_{Lij}}{\sum_{i=1}^{N} \sum_{j=1}^{N} f_i \, f_j} \quad , \qquad (4.1\text{-}14)$$

where f_i is the mole reaction of the i^{th} component, and T_{Lij} is the liquidus temperature from a pseudo-binary phase diagram for components i and j taken alone. The formula correctly degenerates to $T_L = T_{Lij}$ when only components i and j are present. For mixtures that include components for which these diagrams are unavailable, the liquidus temperature becomes

$$T_L = (1 - f_k) \, T_{BL} + f_k \, T_{Lk} \quad , \qquad (4.1\text{-}15)$$

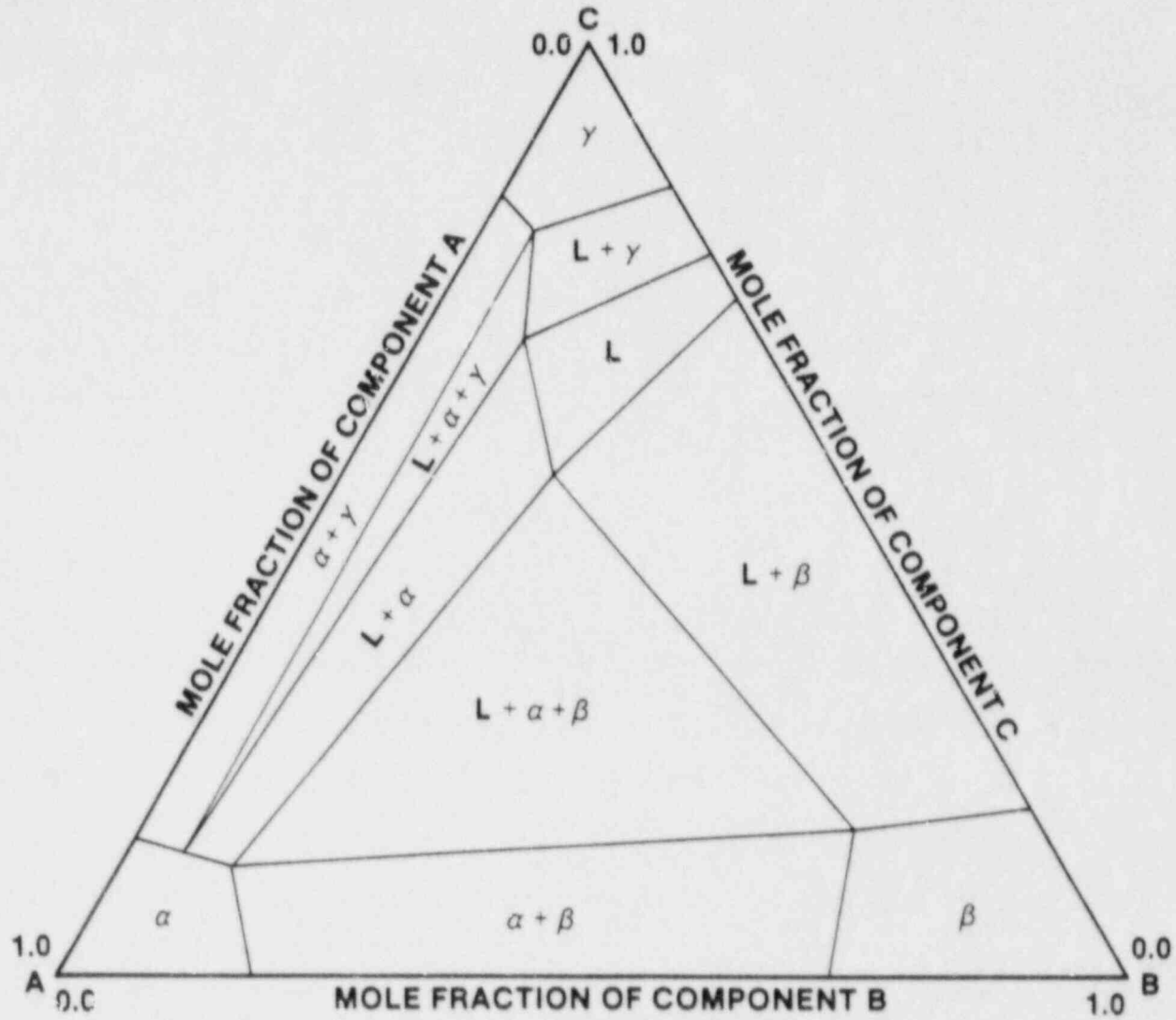

Figure 4.1-3. A Typical Isothermal Ternary Phase Diagram

where f_k is the mole fraction of the k^{th} component (for which phase information is unavailable). T_{Lk} is its normal liquidus temperature and T_{BL} is the liquidus temperature for the components represented by pseudo-binary phase diagrams.

Figure 4.1-4 is a flow chart of the CREUTK subroutine. The routine was initially devised to treat UO_2 eutectic, but the algorithm is general and not limited to those materials. The routine can treat the dissolution of two different solids on opposite sides of the molten material (e.g., UO_2 pellet and ZrO_2 shell separated by molten U-Zr-O); however, because the equilibrium phase diagrams do not provide information on the rate of dissolution and the solids are treated consecutively rather than simultaneously, the comparative rates of dissolution of the two solids may be incorrect. An exact treatment of simultaneous dissolution is not feasible at this time.

Basically, the routine determines how much solid may be added to the mixture before the resulting specific enthalpy equals the liquidus enthalpy of the new composition. The solution algorithm is iterative and unconditionally stable. MCOMP(K) contains the initial masses of the various components that define the mixture, and ISOL is the value of K that refers to the solid component that is being dissolved. The CX(K) array is equal to the MCOMP(K) array plus the mass of new dissolved solid added to MCOMP(ISOL). CREUTK calls MELPRO to determine the initial solid enthalpy and the liquidus enthalpy of the mixture as a function of its changing composition between iterations. The DELM(ISIDE) and DELE(ISIDE) terms are the mass and energy, respectively, of the solid on either side that is dissolved during the time step. The algorithm allows solid dissolution at an interface where the mixture is oxidizing as long as the rate of dissolution of the ZrO_2 is greater than its rate of formation by oxidation. This requirement prevents the simultaneous creation of a new oxide layer and dissolved solid region at the same interface.

4.2 MELPROG Code Applications

(J. L. Tomkins and T. J. Heames, 6425; J. E. Kelly, 6418)

Testing and assessment of MELPROG-PWR/MOD1 are continuing. Currently MELPROG is being used to analyze the DF1 and DF2 experiments. MELPROG/TRAC is currently being used to calculate a TMLB' accident sequence for the Surry PWR. This is the first full reactor calculation to use the CORE module, and this calculation includes a one-way coupling to the CONTAIN code.

The DF1 and DF2 calculations are nearly completed and a complete report on these calculations will be included in the next semi-annual. Preliminary results for these calculations indicate that there is good agreement with the experimental data for the heatup phases and for the hydrogen production. There is also qualitative agreement with the experimental data for material

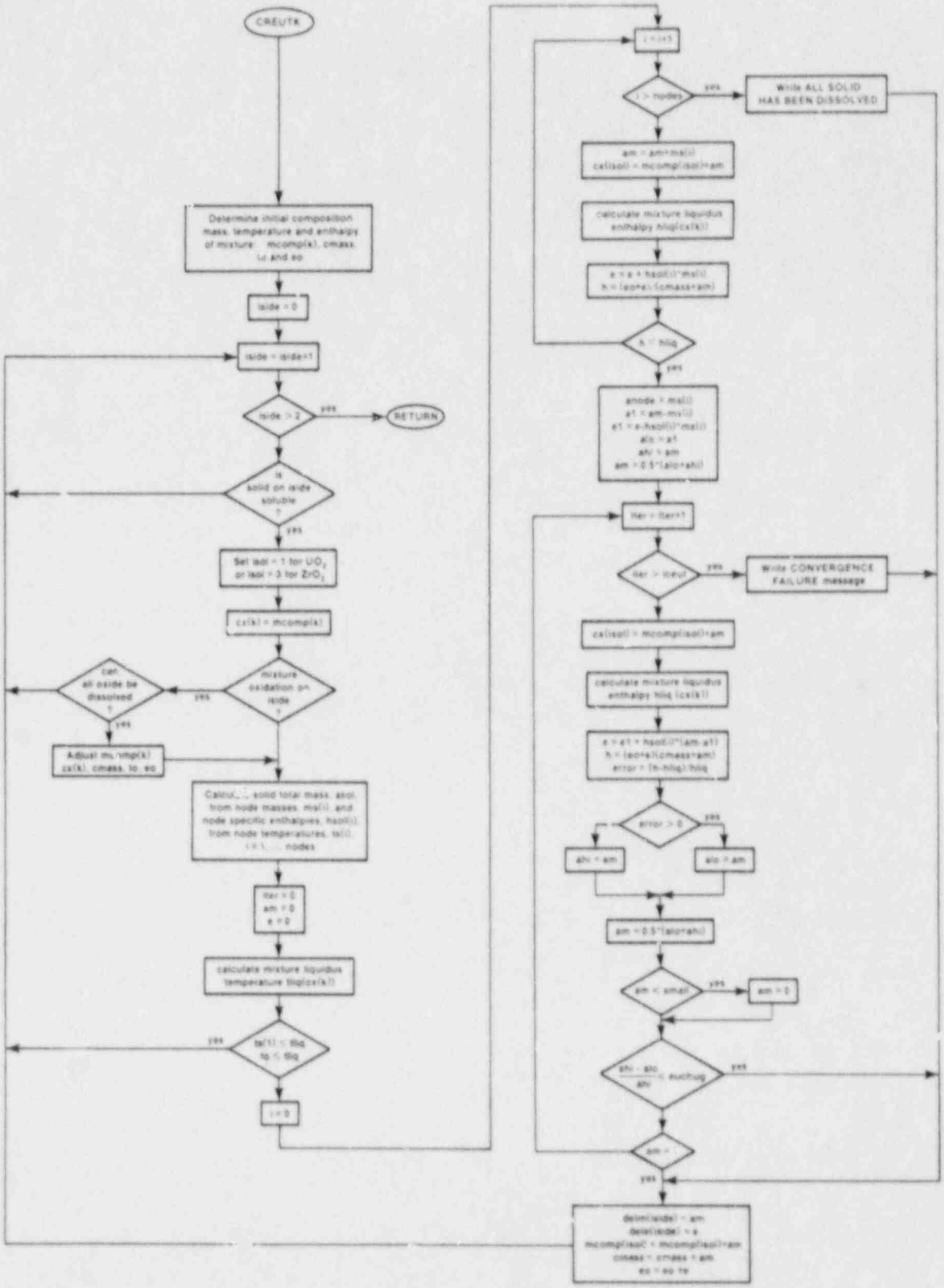

Figure 4.1-4. Flow Chart for the CREUTK Subroutine

relocation. Quantitative experimental data on material relocation are being determined and comparisons to calculated results will be made when this data becomes available.

The Surry TMLB' calculation was begun, but no results are available. This calculation is expected to be completed during the next six months.

4.3 MELPROG Validation Experiments

(W. Tarbell, 6422; A. Reed, 6427; R. Acton and J. Bentz, 7537)

Several experiments have been performed to aid in the design of experiments for the MELPROG program. This program is being conducted to provide experimental verification for the computer codes being developed to predict nuclear reactor accidents.

4.3.1 Introduction

The technique used in making a crust or molten pool of uranium dioxide and zirconium dioxide has been by induction heating; however, these materials do not inductively couple to the induction coil. Consequently, tungsten rings are imbedded in the charge material, and these rings heat the oxides. The crust that held the molten core in the Three Mile Island accident reportedly failed near the top, probably due to convection cells. In MELPROG experiments, the tungsten rings may impede convection cells. Therefore, experiments were performed to see if inductive coupling to uranium dioxide could be achieved. The experiments addressed the following questions:

1. Will uranium dioxide couple at higher temperatures?
2. Will uranium dioxide couple at higher inductive power supply frequencies?
3. Can the tungsten rings be removed once the charge is molten?

Concern has been expressed that the welds holding instrumentation tubes in the wall of the reactor pressure vessel may fail during an accident and thus provide a path for pressurized molten core ejection. A MELPROG experiment has been proposed to test this concept. The test article will consist of a steel plug simulating the reactor vessel in the bottom of a magnesium oxide crucible. The plug will be penetrated by a steel or Inconel tube and will be welded at the upper surface. Above the plug, in the crucible, a molten core charge will be developed. For proper modeling, the steel plug should not be heated by the induction supply. Experiments have been performed to develop techniques to decouple the steel plug from the magnetic field of the induction coils.

4.3.2 Uranium Dioxide Coupling Experiments

The electrical resistivity of a material is an important property in determining if the material will inductively couple to a magnetic field. Highly resistive materials, such as oxides, do not couple. Metallic materials with resistivities of the order of 10^{-6} ohm•cm readily couple. Certain of the oxides have electrical resistivities many orders of magnitude lower than others (see Figures 4.3-1[131,132] and 4.3-2[133]). The resistivities for uranium dioxide and zirconium dioxide are among the lowest values. As seen in Figure 4.3-1, their resistivities decline with increasing temperature. Figure 4.3-2 shows a nomograph of the relationship between resistivity, frequency, and skin depth (the depth at which induced eddy currents have fallen to 1/e of their surface value). The dashed line in Figure 4.3-2 shows that a material with a resistivity of 10^{-2} μohm•cm coupled to a 3-kHz power supply will have a skin depth of 10 cm. The less the skin depth, the more efficient the heating. Figures 4.3-1 and 4.3-2 indicate that it may be possible to inductively couple to the oxide of urania and zirconium, especially at higher temperatures and frequencies.

Three experiments were performed to evaluate the inductive coupling of uranium dioxide. The experimental design is shown schematically for the first two experiments in Figure 4.3-3. Details of all three experiments are listed in Table 4.3-1.

The charge in experiments 1 and 2 were composed of 65, 25, and 10 percent by weight of UO_2, ZrO_2, and Zr, respectively. The third experiment contained no zirconium metal and was 65 and 35 percent by weight of UO_2 and ZrO_2, respectively.

In the first experiment, materials and equipment that were readily available (the experiment was not optimized) were assembled and run. The maximum output of the 125-kW supply was required at the melting point of the charge and no superheat was possible. The imbedded ring susceptor technique is a skull melting technique. Since the charge could not be raised above its melting point, a ring of unmelted, sintered materials existed around the top edge of the pool, and this material prevented the rings from being withdrawn.

The second experiment was designed for better inductive coupling. At the melting point of the charge, only about one-half of the supply power rating was used. However, continued increases in power, up to the maximum, failed to increase the charge temperature above the apparent melting point. Again, an unmelted skull prevented ring removal.

In both of these experiments, the power supply was 125 kW at 3 kHz. A third experiment was conducted with a 30-kW/450-kHz supply to see if a higher frequency would couple to the oxides.

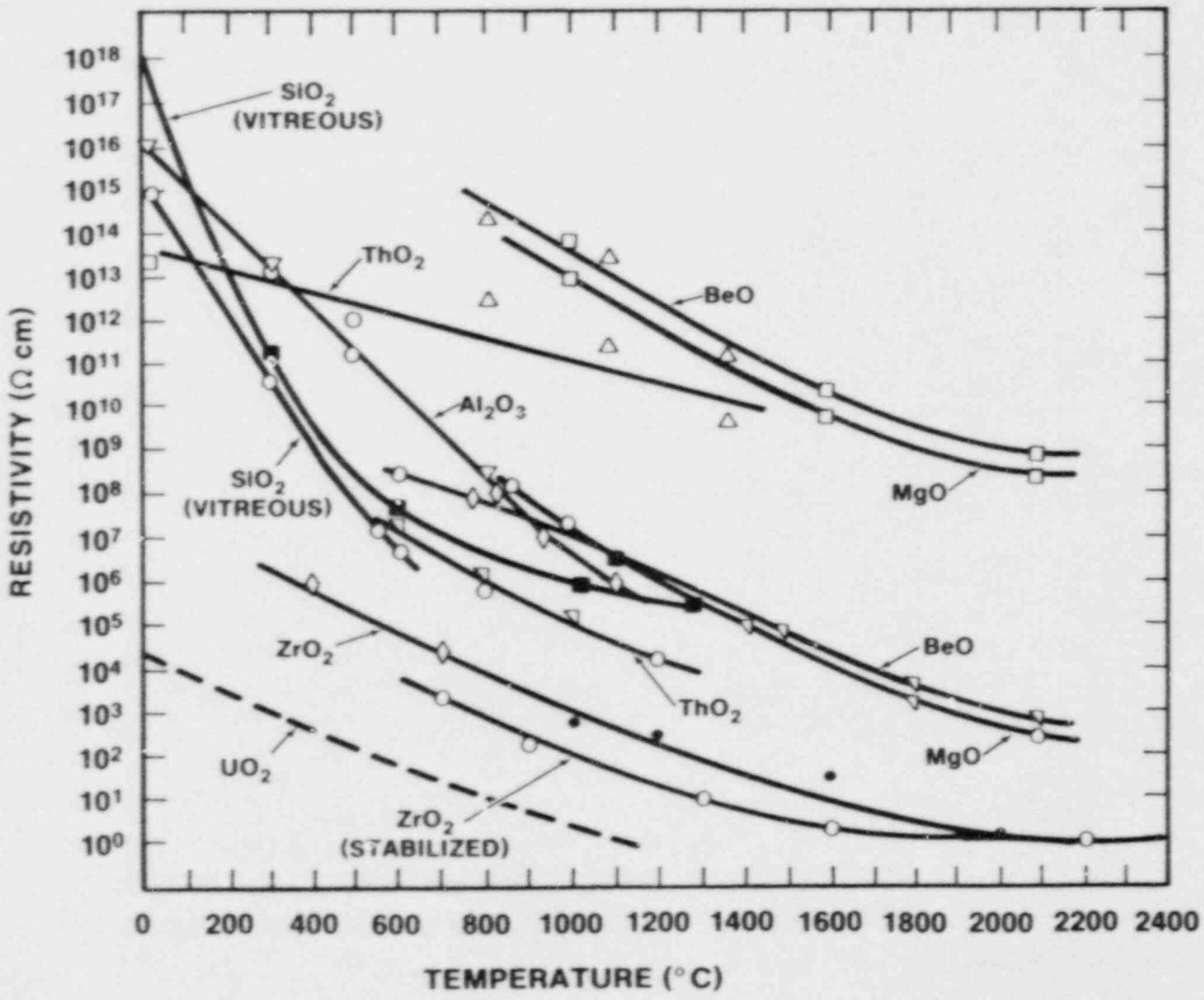

Figure 4.3-1. Electrical Resistivity of Refractory Oxides

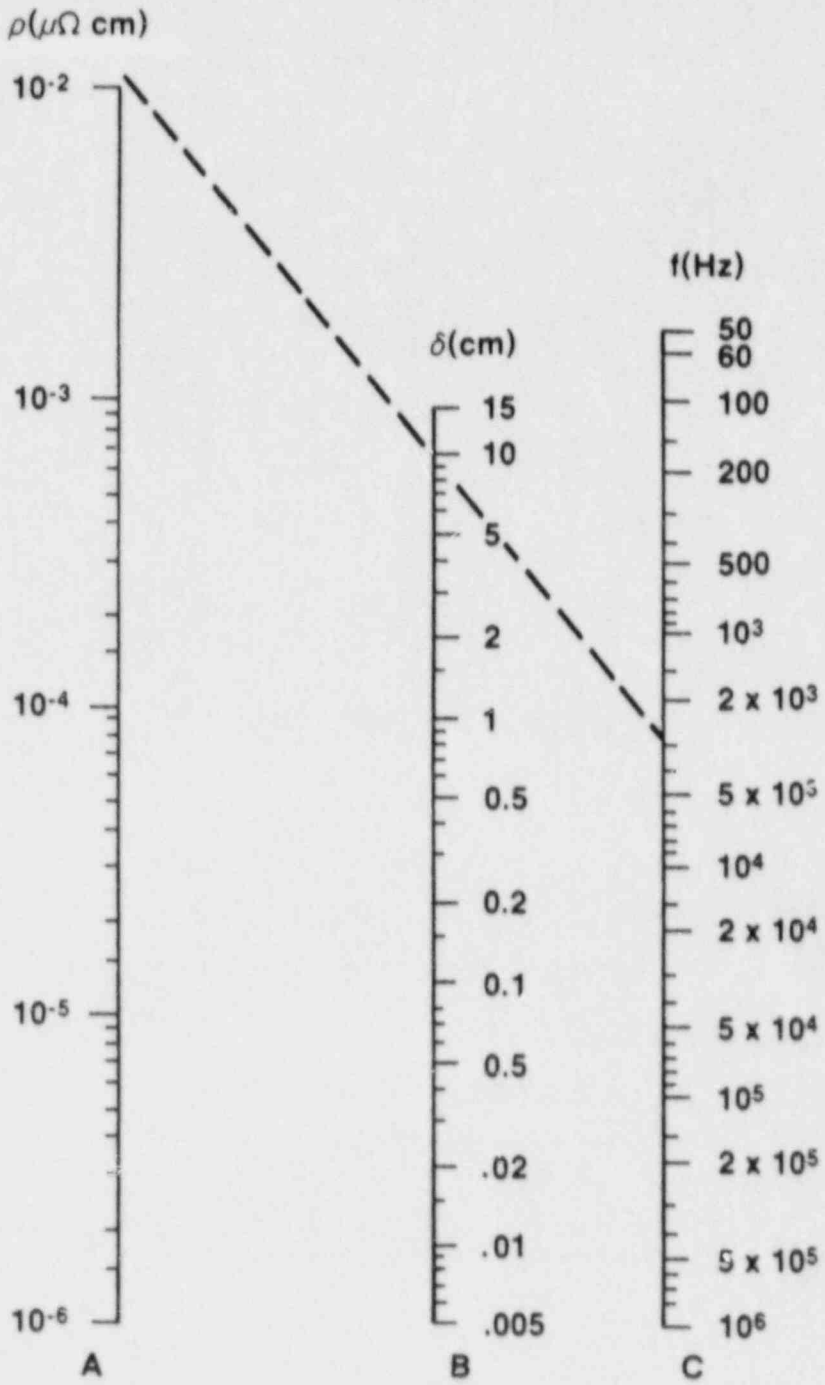

Figure 4.3-2. Nomograph for Induction Heating

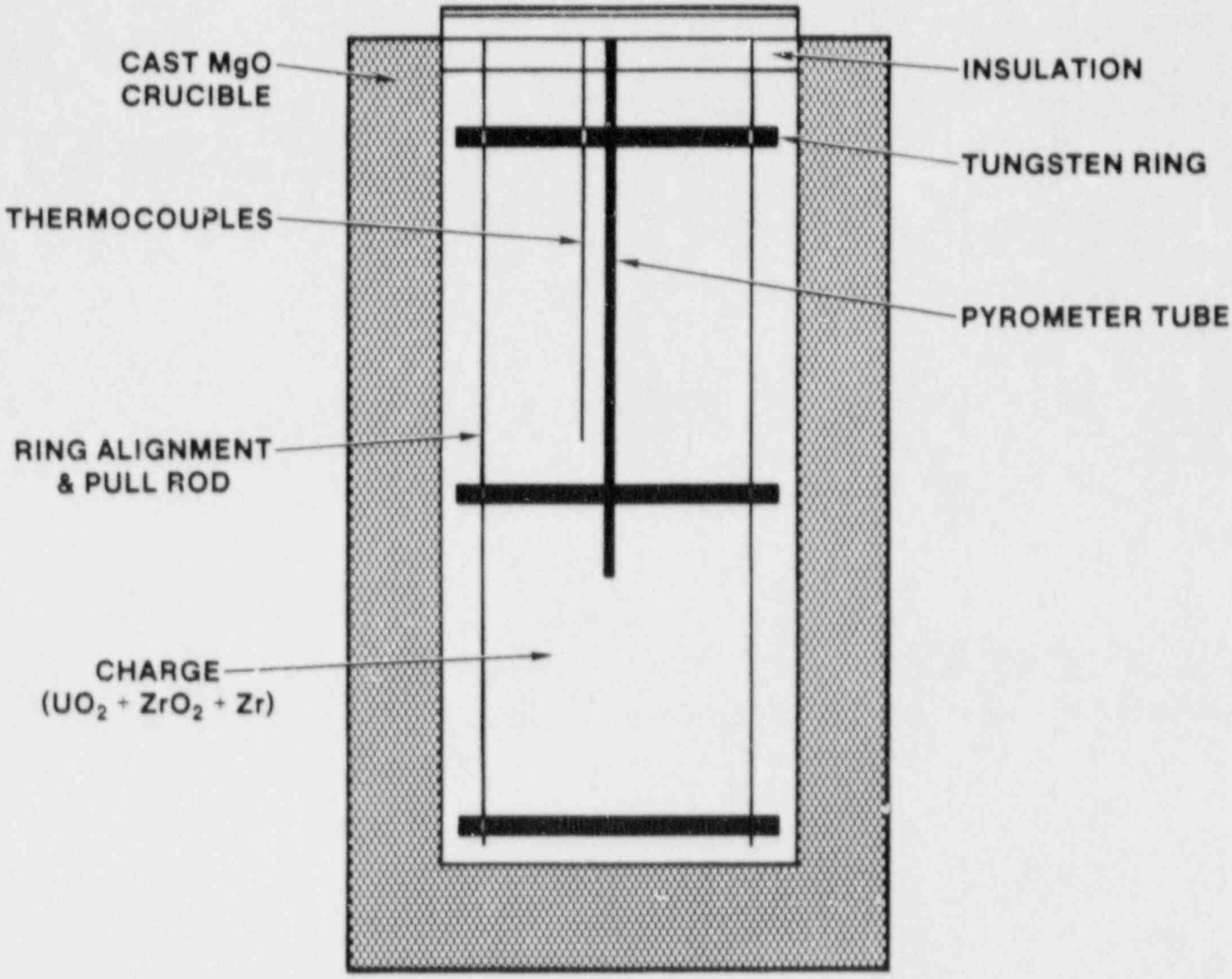

Figure 4.3-3. Schematic of the Experimental Apparatus

Table 4.3-1

Experimental Parameters

Experiment No.	Crucible	Charge (kg)	No. W Rings	Ring Dia. (m)	Supply
1	MgO	8.6	3	0.102 (4 in)	125 kW/3 kH
2	MgO	14.4	4	0.152 (6 in)	125 kW/3 kH
3	Al^2O_3	9.0	0	NA	30 kW/450 kH

No tungsten rings were used and the attempt was made at room temperature. Only a slight increase in the charge temperature was noted.

The time-temperature history of the first experiment is shown in Figure 4.3-4 and the time-power history in Figure 4.3-5. Similar curves for the second experiment are shown in Figures 4.3-6 and 4.3-7. Both experiments indicate that the melting point of the charge is about 2300°C (4172°F). Visual examination of the crucibles after the experiments left no doubt that the material had been molten. The free surface of a liquid was very apparent in both cases. X-ray analyses of the unmelted material above the pool, the sidewall crust, and the frozen pool were made. X-ray flouresence showed no difference in the elemental composition of the three regions. X-ray diffraction analysis of the frozen pool revealed it to be a solid solution of zirconium dioxide in uranium dioxide. While disassembling the second experiment, a light grey, ash-like material was found deposited over the entire inside of the test chamber that contained the crucible. This material was analyzed as magnesium oxide, the crucible material. The mechanism of the ash generation and deposition has not been investigated.

In all three experiments, the charge material was a solution of zirconium dioxide in uranium dioxide, not pure uranium dioxide. Also, the charge was composed of gravel, not a solid cylinder. These factors had a negative effect on the coupling experiments. The zirconium dioxide probably raised the electrical resistivity of the charge. The gravel composition of the bed adversely affected both the coil air gap and the "skin depth" of any induced currents.

Should it be decided that it is mandatory that the molten pool not have the rings because they interfere with pool circulation, then several areas can be investigated. These areas are:

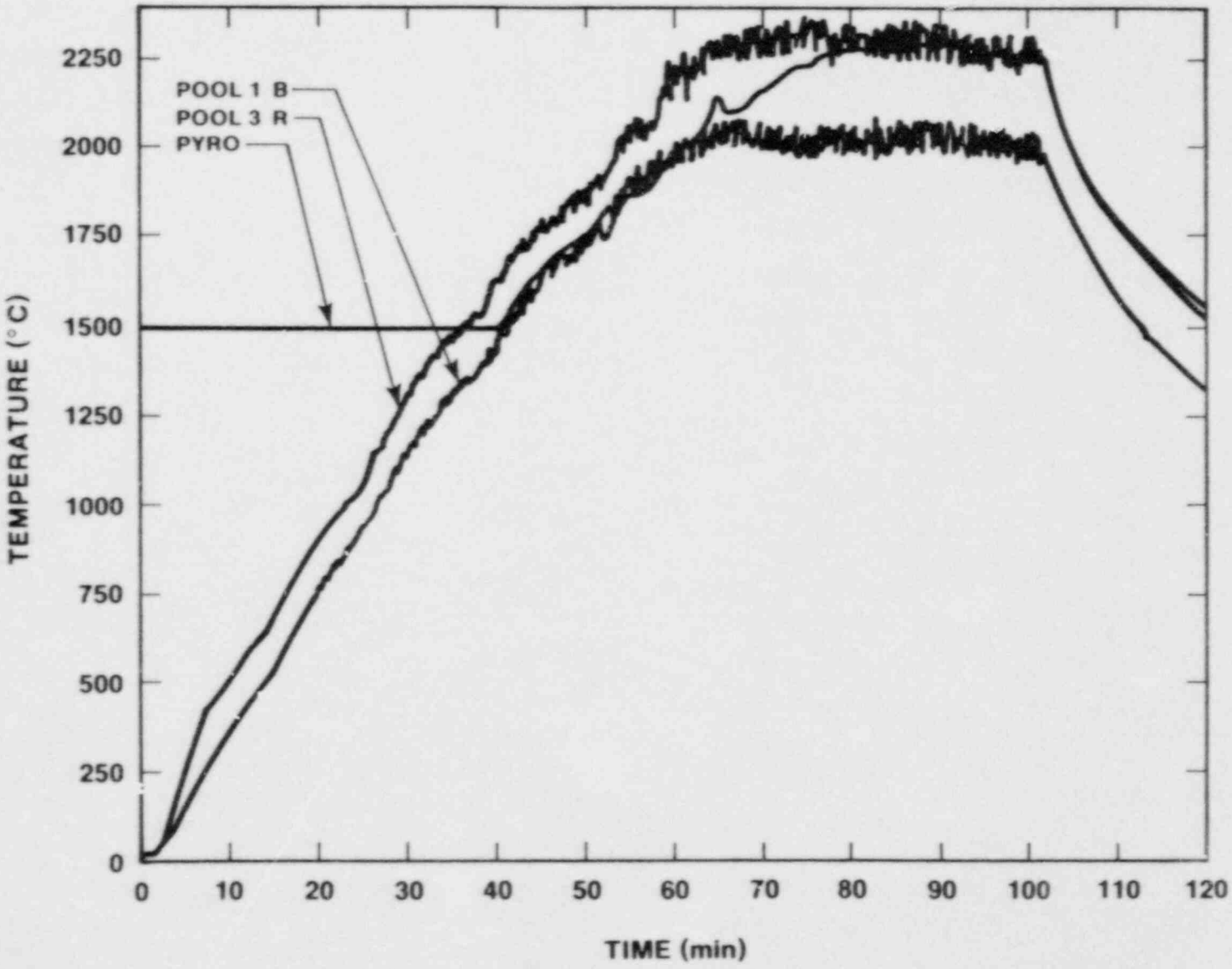

Figure 4.3-4. Temperature History for Experiment Number 1

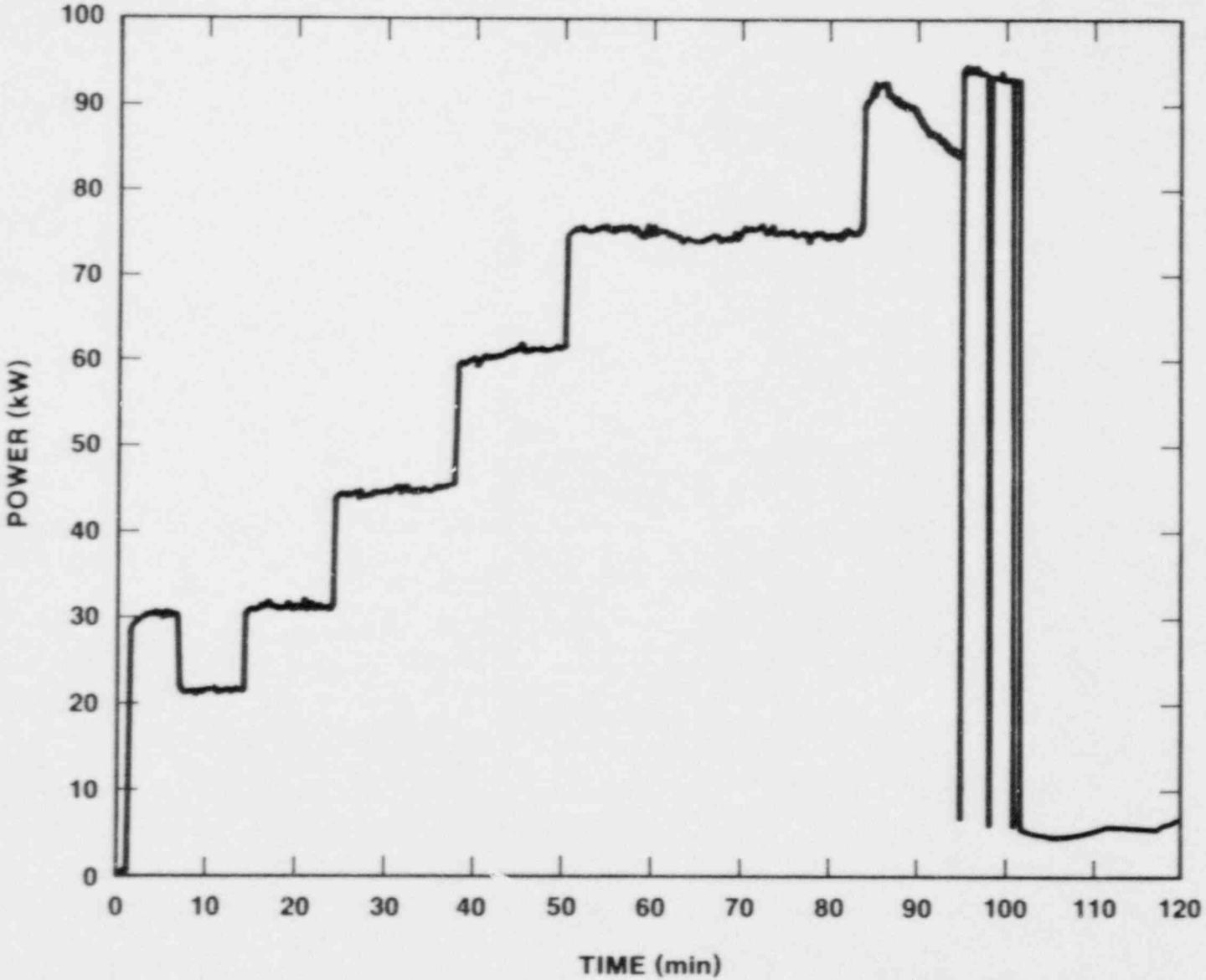

Figure 4.3-5. Power History for Experiment Number 1

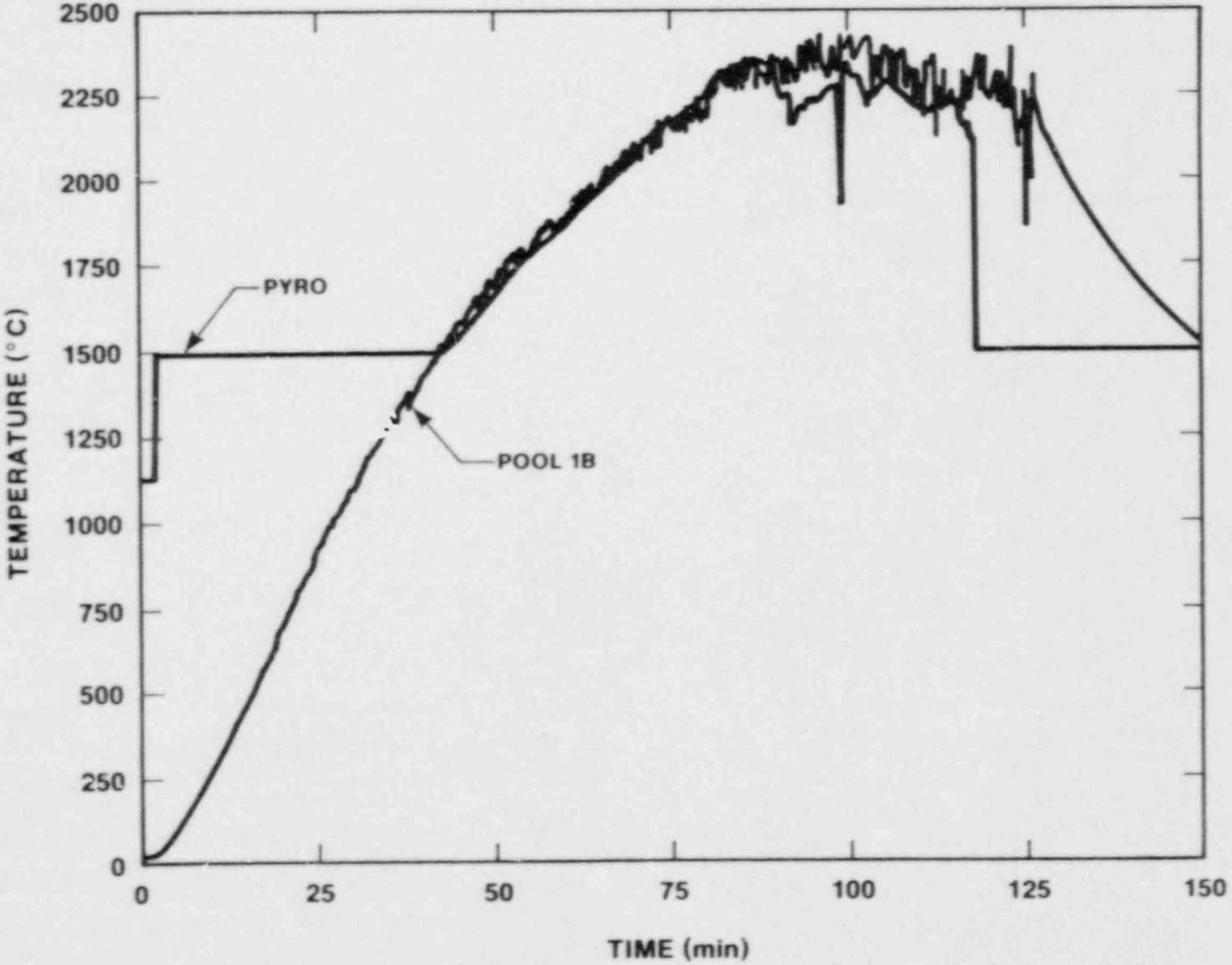

Figure 4.3-6. Temperature History for Experiment Number 2

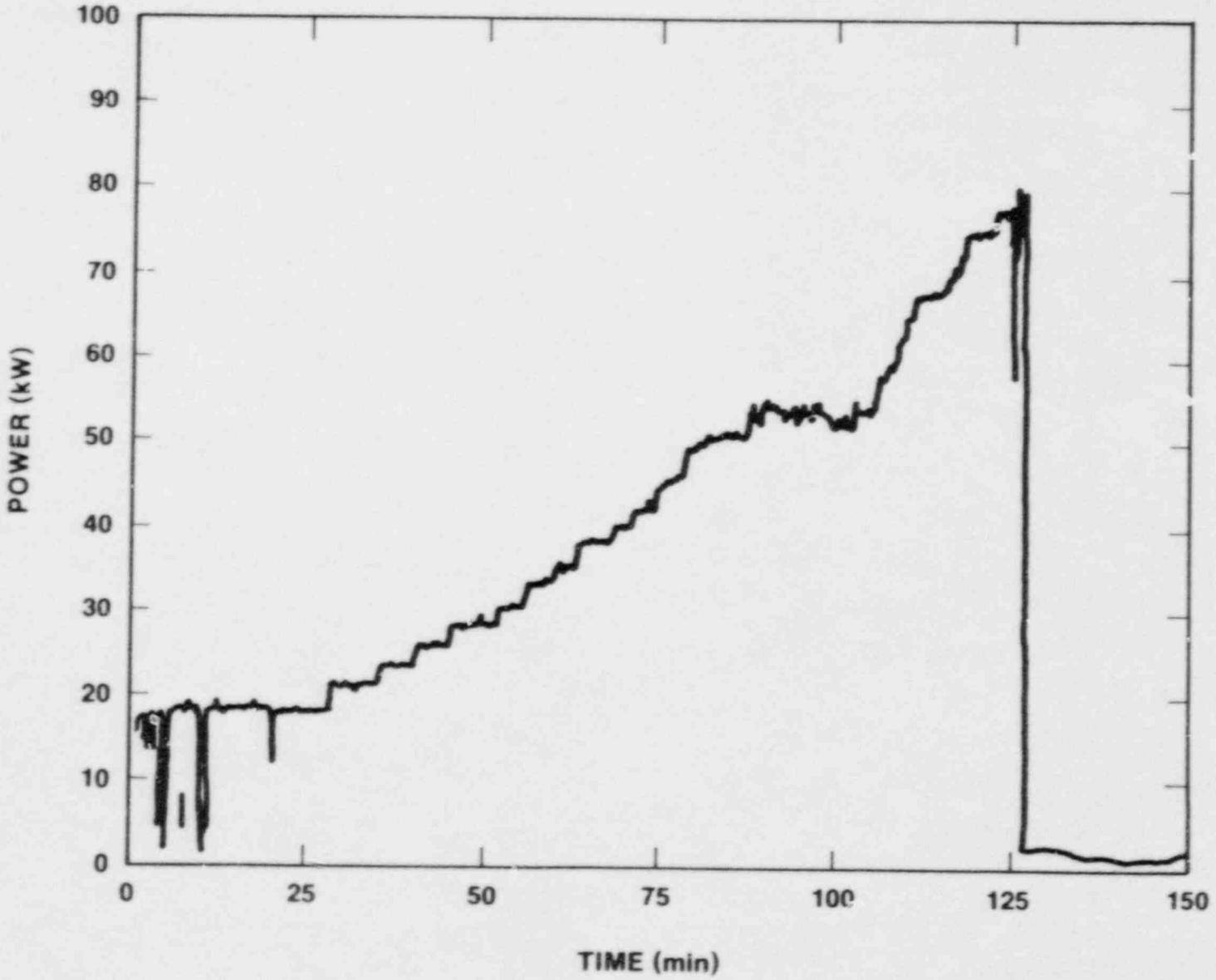

Figure 4.3-7. Power History for Experiment Number 2

1. The charge can be pressed and sintered in the shape of a right circular cylinder to theoretical densities of around 90 percent. This would improve the coil air gap and material skin depth conditions.

2. The charge can be melted in the usual manner with the tungsten rings and then poured into another container that does not have the rings. The success of this operation is doubtful because of past failures to generate any appreciable superheat. The material will probably freeze in the pour stream.

3. Additional tungsten rings can be placed above the charge in an attempt to melt the skull that prevented ring withdrawal in previous experiments. There is no experience for this. The ring or rings setting above the charge may melt themselves.

4. The experiment with the 450-kHz power supply was done at room temperature. Heating the charge to some elevated temperature, say 1000°C, may help the coupling because of the inverse proportionality between electrical resistivity and temperature.

4.3.3 Magnetic Flux Characterization

An evaluation of induction coil magnetic flux density and flux field distribution was needed to predict component heating due to the induction field. This is of interest in several areas of MELPROG experimentation.

1. Crust failure experiments may require sustaining a molten pool on a crust. The sustained temperature of the molten pool will be higher than the sustained temperature of the crust. As currently envisioned, this experiment will require stacked induction coils operating from different power supplies. A study of how the coils interact is required.

2. The instrumentation tube failure experiments will require that the steel plug in the crucible that simulates the reactor pressure vessel wall be isolated from the induction coil.

Iron powder evenly spread over a rigid plastic sheet was used to indicate flux density in a variety of heights and orientations with respect to the induction coil. The flux was strongest within the coil with the flux lines running perpendicular to the coil turns. The flux lines extended as much as 0.5 m past the coil ends. The flux distribution and flux density are a function of the power applied to the coil and the coil geometry.

Flux density readings were taken with a variety of loads in or near the coil. Flux lines were concentrated at the entry and exit points of the load; however, the lines spread to the unloaded flux distribution of the coil shortly past (1 to 2 cm) the load.

A Faraday ring was placed above the coil to distort the flux lines. A Faraday ring is constructed of a highly electrically conductive material with the maximum inside diameter equal to the inside diameter of the induction coil and the minimum outside diameter equal to the outside diameter of the induction coil. The Faraday ring used in the study was 1-cm-thick aluminum with water cooling. The Faraday ring distorted the magnetic field so that less than 10 percent of the original flux lines extended past the ring. The magnetic field above the Faraday ring was compressed to approximately 5 cm.

Interactive effects between induction coils in close proximity were also evaluated. Induction power supplies cannot be frequency synchronized and therefore the magnetic fields will interact in an unpredictable manner. Heating two workpieces revealed the magnetic field effects. The coils were separated by 5 m and a baseline heating profile was established. One coil was then placed on top of the other coil with a 2-cm air gap between the coil assemblies. The power was applied to each coil individually to measure the heating rate of the workpiece within the powered coil. Also, the extended flux lines in the form of heat into the workpiece placed in the other coil were obtained. Both coils had power applied simultaneously to show the interactive effects of the coils. The three coil experiments were duplicated with a Faraday ring placed between the induction coils.

Figures 4.3-8 through 4.3-14 show the temperature histories for the workpieces in each of the two coils for the six tests. The rate of temperature rise represents the power coupled into the object. For these tests, the "10 in" reference is for the steel piece placed in the coil connected to the 1000 Hz (280 kW max) power supply and the "8 in" reference is for the 3000 HZ (125 kW max) power supply. Figure 4.3-8 was obtained when the two power supplies were heating the objects independent of each other. This provides a "baseline" indication of the heating of each workpiece. Figures 4.3-9 and 4.3-10 show the influence of the Faraday ring on the stacked coils when both power supplies were operating.

The temperature history results shown in Figures 4.3-9 through 4.3-14 show that the Faraday ring has minimal influence when power supplies are operating. When either unit was turned off and the ring removed, the magnetic field from the powered coil did not heat the opposing workpiece. Placing the Faraday ring between the coils eliminates this tendency. This indicates that experiments can be conducted where a highly susceptible material

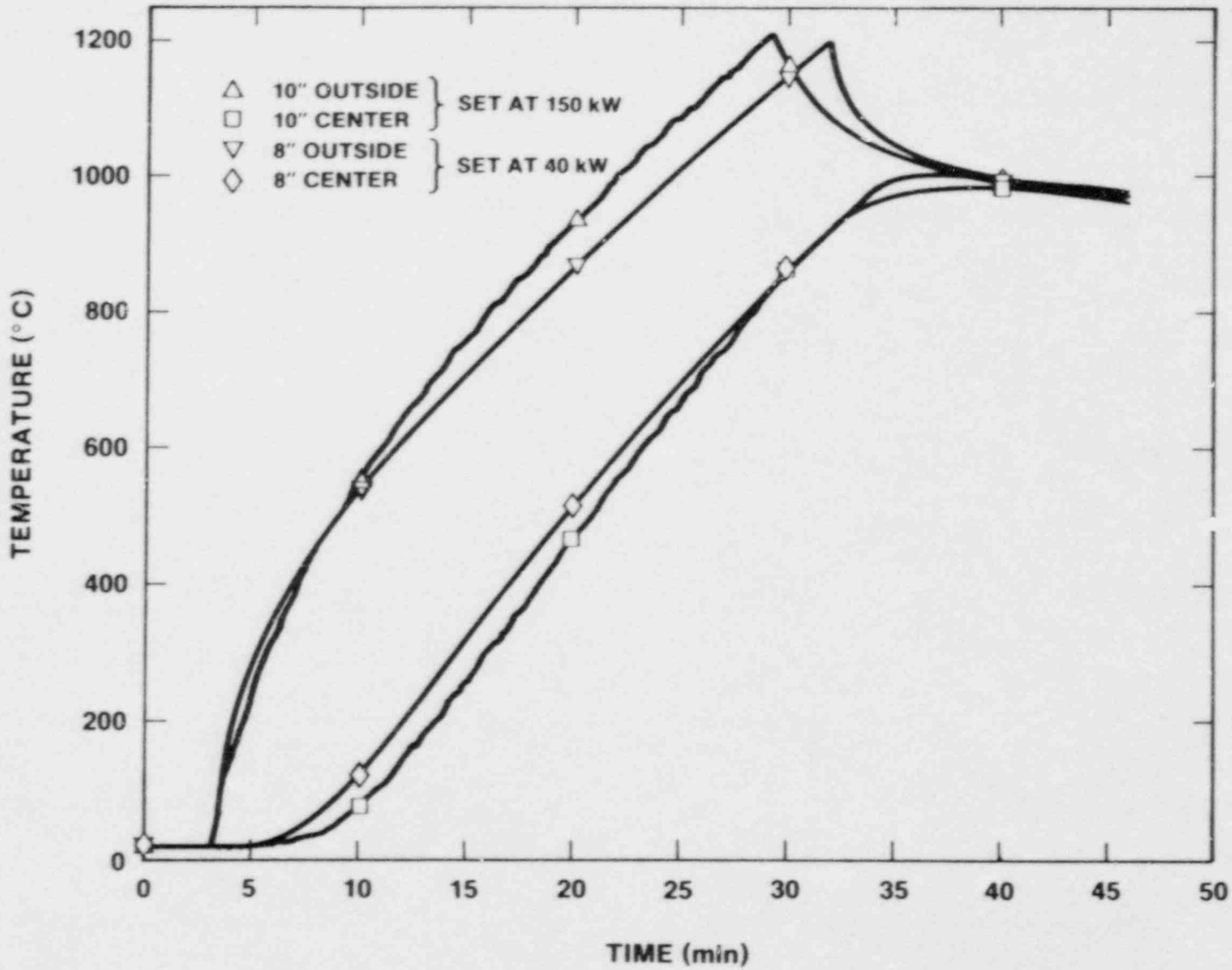

Figure 4.3-8. Temperature Histories for Workpieces Placed In Separated Coil (Both Power Supplies Operating)

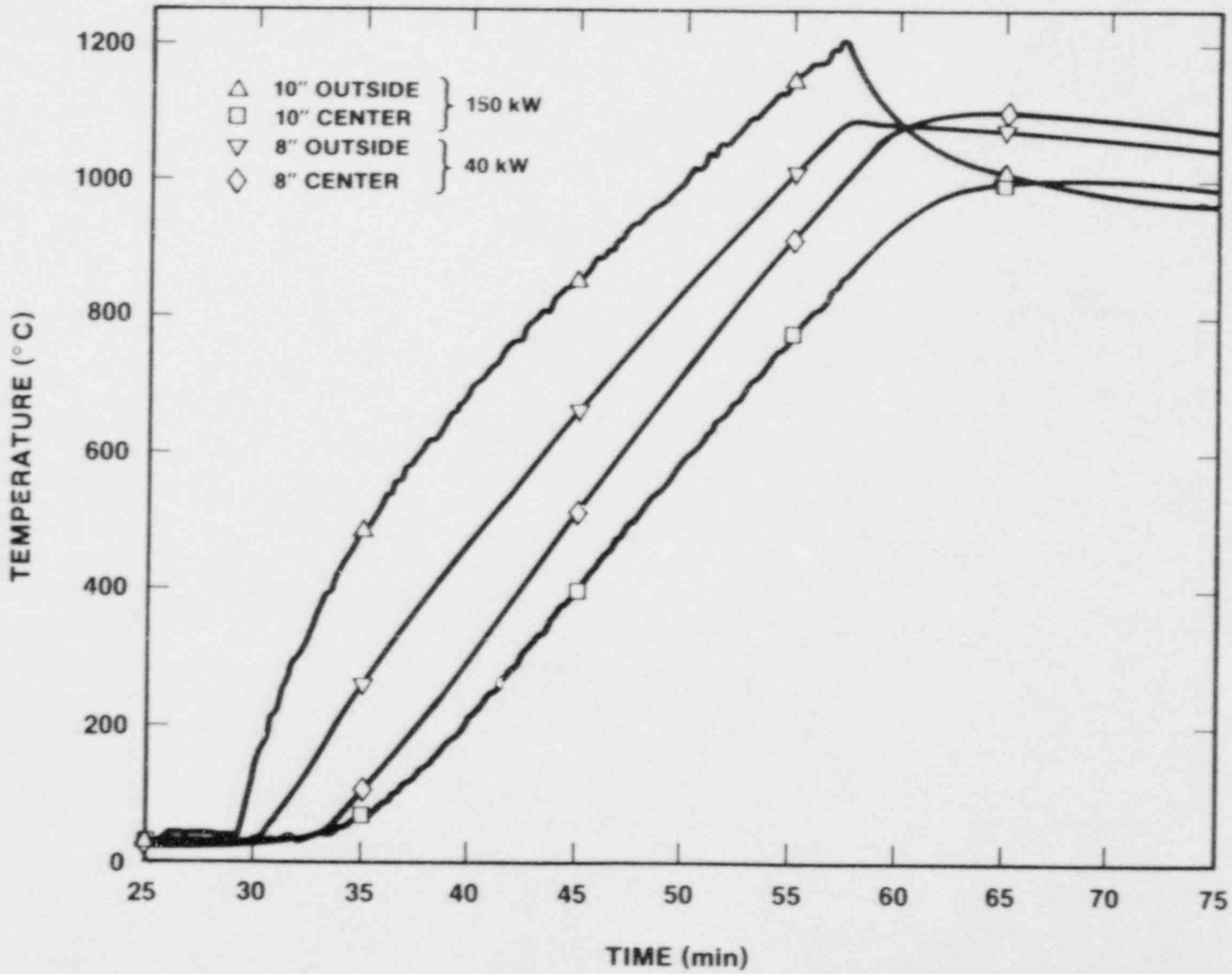

Figure 4.3-9. Workpiece Temperature Histories in Stacked Coil Configuration Without Faraday Ring

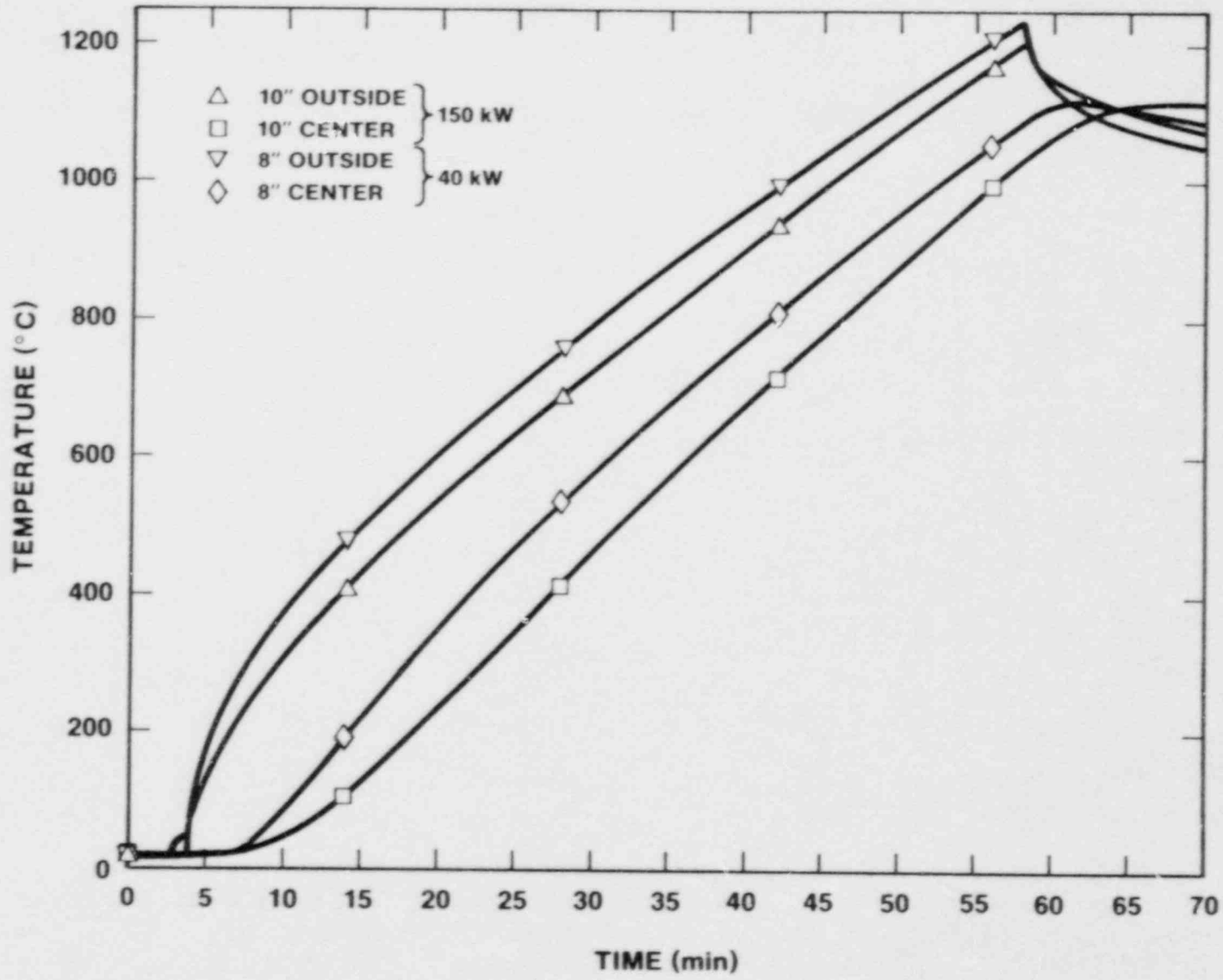

Figure 4.3-10. Workpiece Temperature Histories in Stacked Coil Configuration With Faraday Ring Between Coils

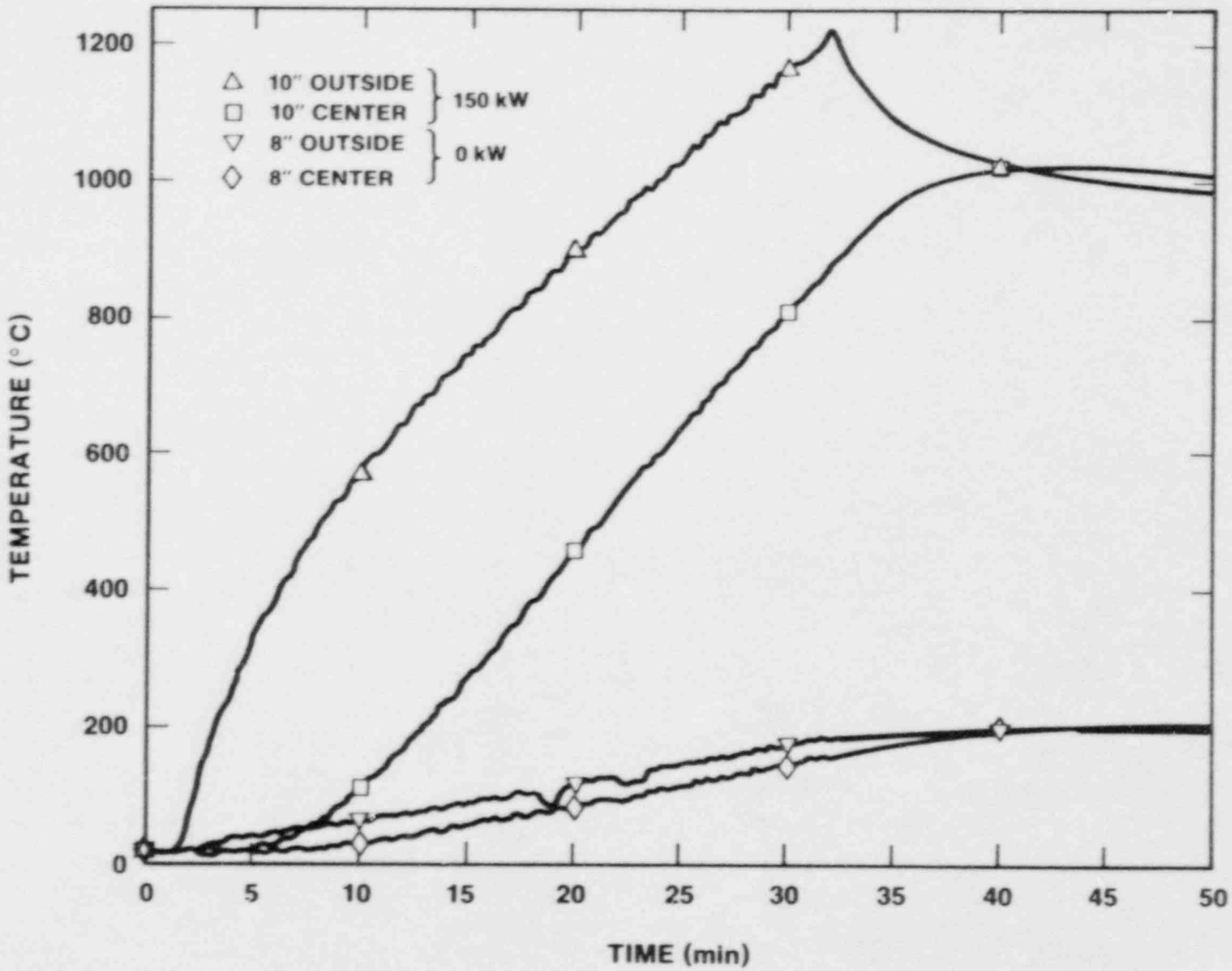

Figure 4.3-11. Workpiece Temperature Histories With Only 250-kW Power Supply Operating and Without Faraday Ring

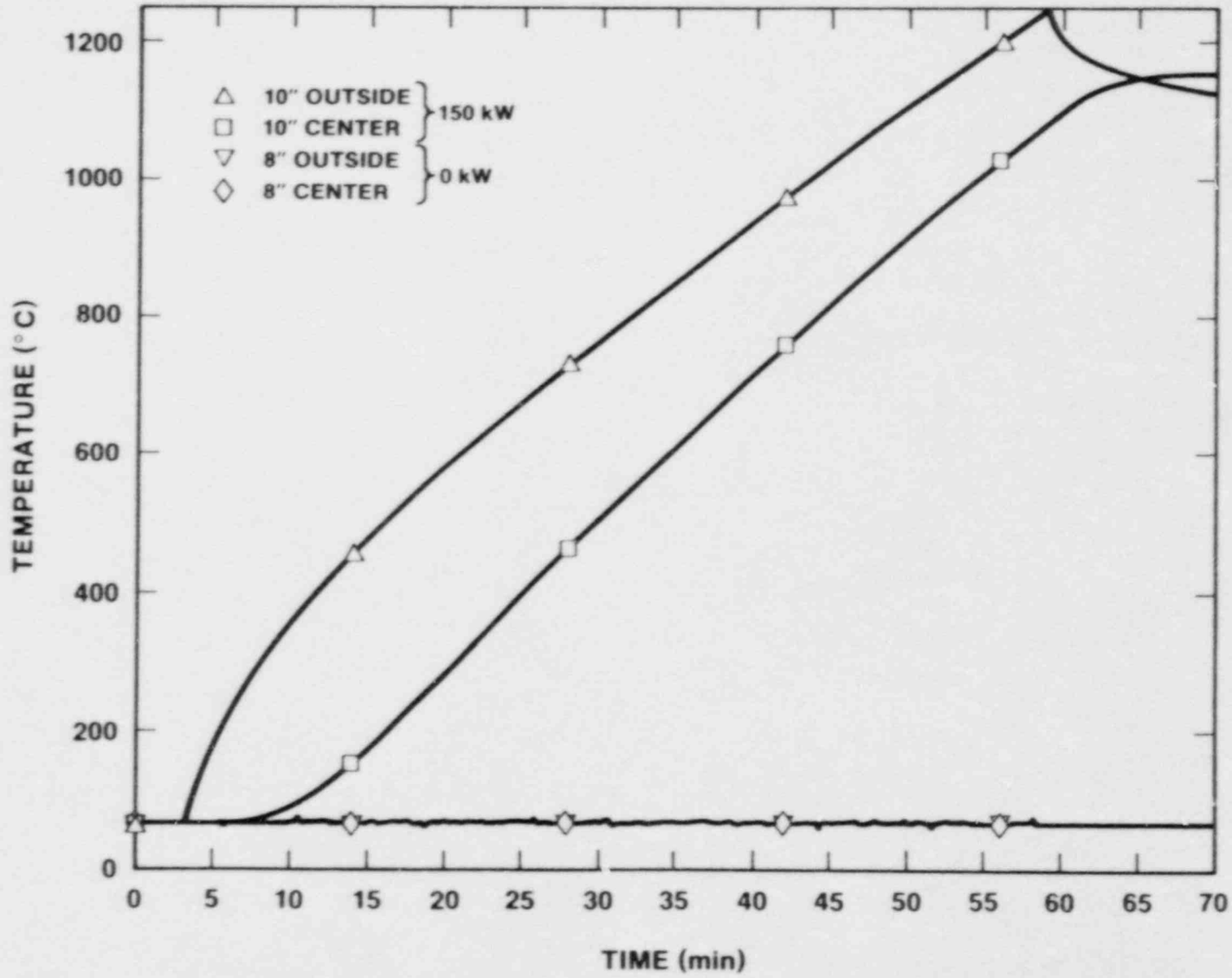

Figure 4.3-11. Workpiece Temperature Histories With Only 250-kW Power Supply Operating and Without Faraday Ring

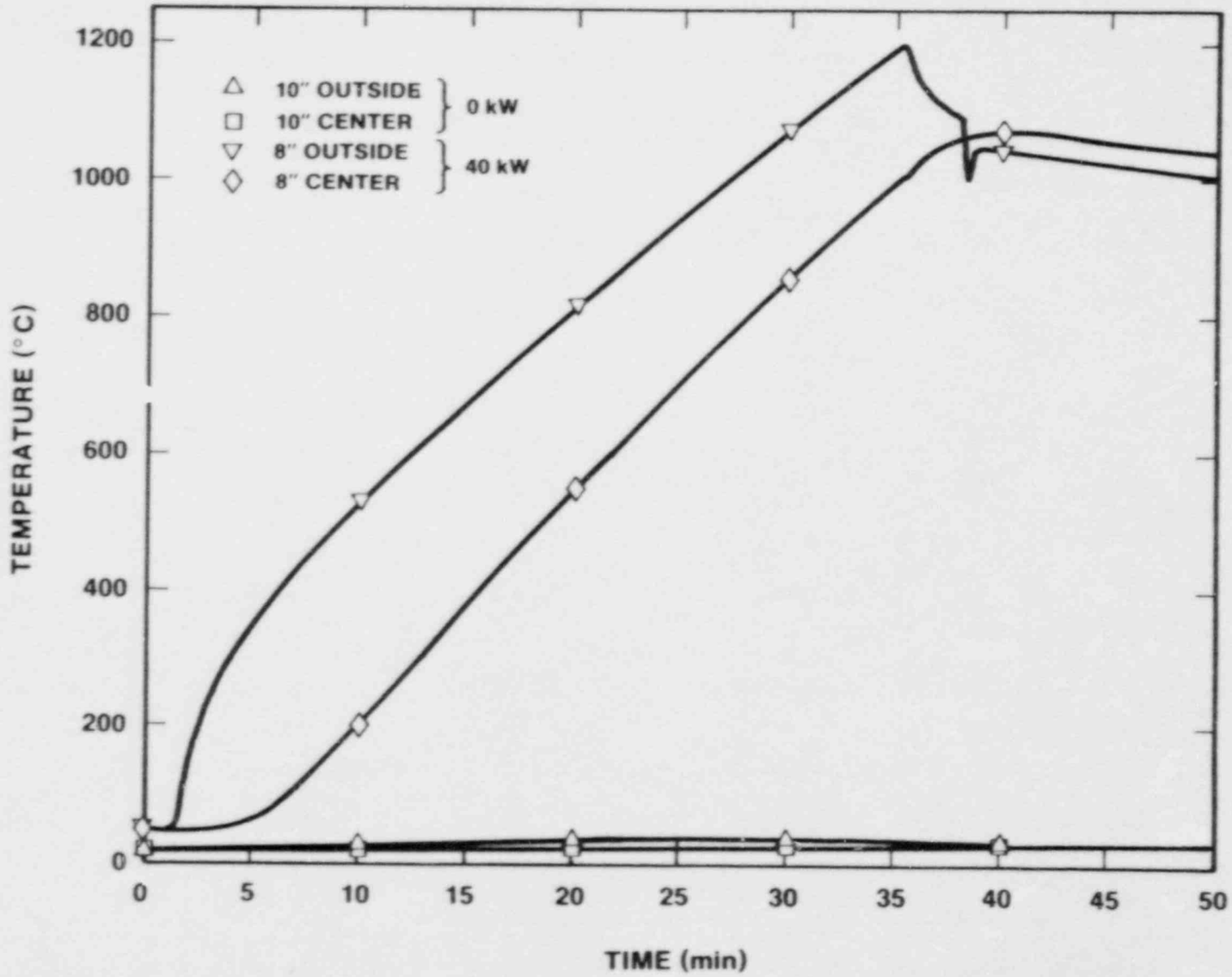

Figure 4.3-13. Workpiece Temperature Histories With Only 125-kW Power Supply Operating and Without Faraday Ring

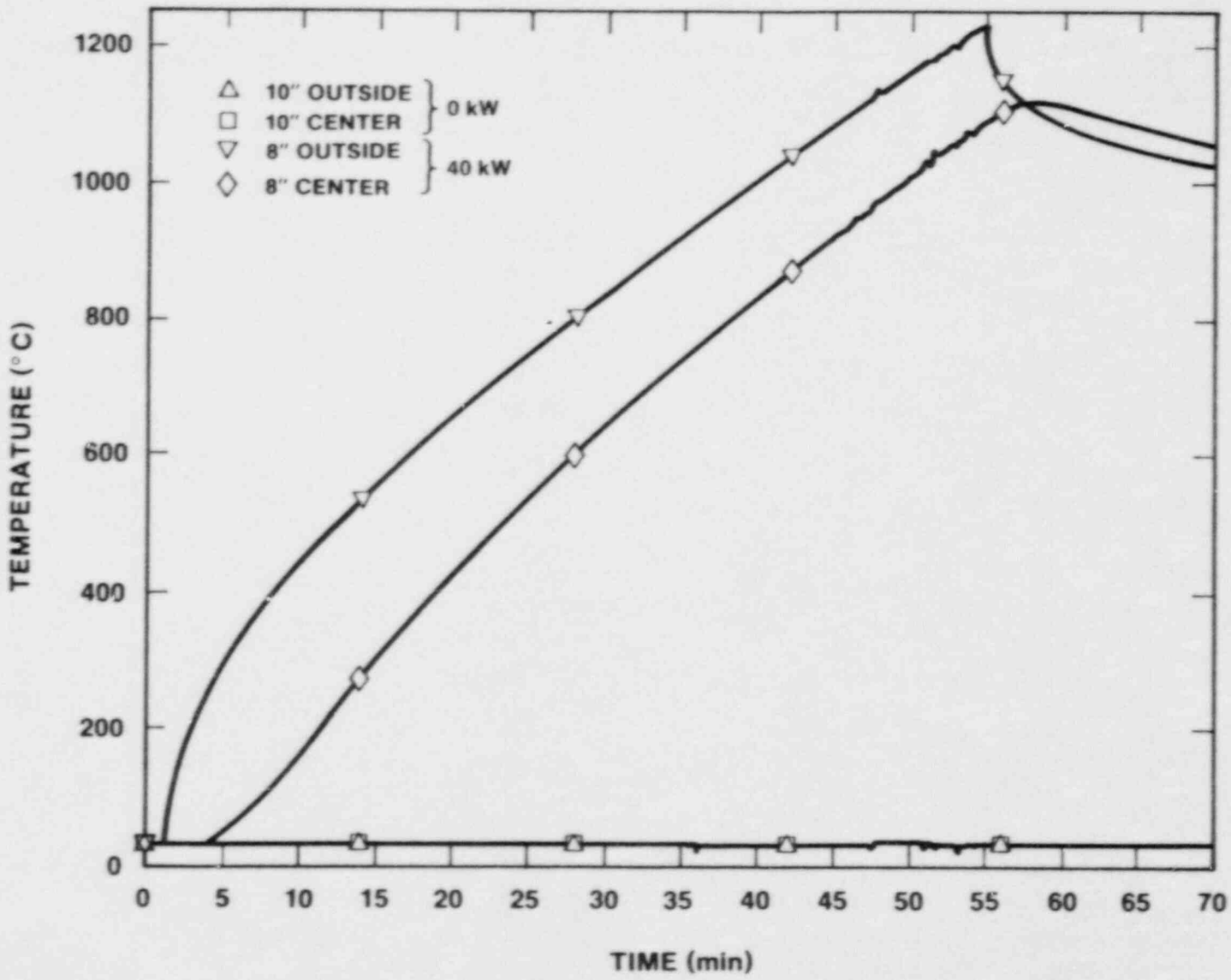

Figure 4.3-14. Workpiece Temperature Histories With Only 125-kW Power Supply Operating and With Faraday Ring Between Coils

can be shielded from the magnetic field. Approximately one-half the available workpiece power is diverted to the Faraday ring in all cases. Therefore, the Faraday ring will decouple the effects of an induction coil upon components external to the coil with a tradeoff of reduced available power.

5. REFERENCES

1. W. C. Baker and J. F. Pouchot, "The Measurement of Gas Flow," Control Technology News, Vol. 33, No. 1, (1983).

2. J. E. Brockmann, "Ex-Vessel Releases: Aerosol Source Terms in Reactor Accidents," Progress in Nuclear Energy, Vol. 19, pp 117-168 (1987).

3. D. A. Powers, J. E. Brockmann, and A. W. Shiver, VANESA: A Mechanistic Model of Radionuclide Release and Aerosol Generation During Core Debris Interactions with Concrete, Sandia National Laboratories, Albuquerque, NM, NUREG/CR-4308, SAND85-1370, 1986.

4. J. E. Brockmann, D. J. Rader, and D. A. Lucero, "Experimental Determination of Dynamic Shape Factors", Paper presented at 1987 Annual Meeting of American Assoc. for Aerosol Research, Seattle, WA, Sept. 14-17, 1987.

5. J. P. Holman, Experimental Methods for Engineers, (New York, NY: McGraw-Hill, Inc., 1966).

6. J. E. Brockmann, B. Y. H. Liu, and P. H. McMurry, "A Sample Extraction Diluter for Ultra Fine Aerosol Sampling," Aerosol Science and Technology, Vol. 3, No. 4, pp 441-451 (1984).

7. Zion Probabilistic Safety Study, Commonwealth Edison Co., Chicago, Il, 1981.

8. R. S. Chambers, A Finite Element Analysis of a Pressurized Nuclear Reactor Containment Vessel During Core Meltdown, Sandia National Laboratories, Albuquerque, NM, SAND87-2183, (to be published).

9. D. K. Gartling, COYOTE--A Finite Element Computer Program for Nonlinear Heat Conduction Problems, Sandia National Laboratories, Albuquerque, NM, SAND77-1332, April 1984.

10. J. H. Biffle, JAC--A Two-Dimensional Finite Element Computer Program for the Non-Linear Quasistatic Response of Solids With the Conjugate Gradient Method, Sandia National Laboratories, Albuquerque, NM, SAND81-0998, April 1984.

11. R. E. Jones, Users Manual for QMESH A Self-Organizing MESH Generation Program, Sandia National Laboratories, Albuquerque, NM, SLA-74-0239, July 1974.

12. High-Temperature Elastic-Plastic and Creep Properties for SA533 Grade B Class I and SA508 Materials, Combustion Engineering, Inc., NP-2763 Research Project 2055-8 and Contract TSA 81-485, December 1982.

13. Reactor Safety Study: An Assessment of Accident Risks in U.S. Commercial Nuclear Power Plants, WASH 1400, U.S. Nuclear Regulatory Commission, Washington, DC, NUREG 75-014, October 1976.

14. R. K. Cole et al., CORCON-Mod2: A Computer Program for Analysis of Molten-Core Concrete Interactions, Sandia National Laboratories, Albuquerque, NM, NUREG/CR-3920, SAND84-1246, August 1984.

15. D. A. Powers et al., VANESA: A Mechanistic Model of Radionuclide Release and Aerosol Generation During Core-Debris Interaction with Concrete, Sandia National Laboratories, Albuquerque, NM, NUREG/CR-4308, SAND85-1370, July 1986.

16. D. R. Bradley and A. J. Suo-Anttila, "Improvements in CORCON Heat Transfer Modelling," Proceedings of the CSNI Specialist Meeting on Core Debris/Concrete Interactions, Palo Alto, CA, September 3-5, 1986.

17. Reactor Safety Research Semiannual Report, January - June 1986, Vol. 35, Sandia National Laboratories, Albuquerque, NM, NUREG/CR-4805 (1 of 2), SAND86-2752 (1 of 2) May 1987.

18. J. E. Gronager et al., TURC 1: Large Scale Metallic Melt-Concrete Interaction Experiments and Analysis, Sandia National Laboratories, Albuquerque, NM, NUREG/CR-4420, SAND85-0707, January 1986.

19. J. E. Gronager et al., TURC2 and 3: Large Scale $UO_2/ZrO_2/Zr$ Melt-Concrete Interaction Experiments and Analysis, Sandia National Laboratories, Albuquerque, NM, NUREG/CR-4521, SAND86-0318, June 1986.

20. R. E. Blose et al., SWISS: Sustained Heated Metallic Melt/Concrete Interactions With Overlying Water Pools, Sandia National Laboratories, Albuquerque, NM, NUREG/CR-4727, SAND85-1546, June 1987.

21. H. Alsmeyer, "BETA Experiments in Verification of the WECHSL Code: Experimental Results on Melt-Concrete Interaction," Nuclear Engineering and Design, Vol. 103, No. 1, (August 1987).

22. E. R. Copus et al., Experimental Results of Core-Concrete Interactions Using Molten Steel with Zirconium, Sandia National Laboratories, Albuquerque, NM, NUREG/CR-4794, SAND86-2638, (to be published).

23. D. R. Bradley and A. W. Shiver, "Uncertainty in the Ex-Vessel Source Term Caused by Uncertainty in In-Vessel Models," Proceedings of the International ANS/ENS Topical Meeting on Thermal Reactor Safety, San Diego, CA, February 2-6, 1986.

24. D. A. Powers and F. E. Arellano, Large-Scale, Transient Tests of the Interaction of Molten Steel with Concrete, Sandia National Laboratories, Albuquerque, NM, NUREG/CR-2282, SAND81-1753, January, 1982.

25. B. W. Marshall, Jr., and M. Berman, "Molten Fuel-Coolant Interactions," Reactor Safety Research Semiannual Report, July - December 1986, Sandia National Laboratories, Albuquerque, NM, NUREG/CR-4805 (2 of 2), SAND86-2752 (2 of 2), October 1987.

26. R. M. Olson, Essentials of Engineering Fluid Mechanics, Third Ed., (New York, NY: Intext Educational Publishers, 1973).

27. R. C. Weast et al., Handbook of Chemistry and Physics, 46th Ed., (Cleveland, OH: The Chemical Rubber Company, 1965).

28. M. Pilch, C. A. Erdman, and A. B. Reynolds, Acceleration Induced Fragmentation of Liquid Drops, Department of Nuclear Engineering, University of Virginia, NUREG/CR-2247, 1981.

29. S. C. Windquist and M. L. Corradini, Modeling the Atomization of a Liquid Jet and Application of the Model to Large Diameter Molten Corium Jets, Reactor Safety Research, Nuclear Engineering Dept., University of Wisconsin, UWRSR Report No. 4, 1986.

30. W. E. Ranz and W. M. Dreier, "Initial Instability of a Viscous Fluid Interface," Industrial and Engineering Chemistry Fundamentals, Vol. 3(1), American Chemical Society, Washington, DC, pp 53-60 (1964).

31. T. J. Mueller, "Flow Visualization by Direct Injection, in Fluid Mechanics Measurements, (Washington, DC: Hemisphere Publishing Corporation, 1983), Ch 7, pp 307-375.

32. J. T. Kegelman, R. C. Nelson, and T. J. Mueller, "Smoke Visualization of the Boundary Layer on an Axisymmetric Body," AIAA Atmospheric Flight Mechanics Conference for Future Space Systems, Boulder, Colo., AIAA paper no. 79-1635, 1979.

33. F. N. M. Brown, "The Physical Model of Boundary Layer Transition," Proceedings of the Ninth Midwestern Mechanics Conference, University of Wisconsin, pp 421-429, 1965.

34. A. J. Reynolds, "Observations of a Liquid-Into-Liquid Jet, Journal of Fluid Mechanics, Vol. 14, pp 552-556 (1962).

35. A. M. Sterling and C. A. Sleicher, "The Instability of Capillary Jets," Journal of Fluid Mechanics, Vol. 68 (3), pp 477-495 (1975).

36. Y. Tanasawa and S. Toyoda, Trans. J.S.M.E., Vol. 20, p 306 (1954).

37. Y. Kitamura and T. Takahashi, "Stability of Jets in Liquid-Liquid Systems," in Encyclopedia of Fluid Mechanics, Vol. 2, Dynamics of Single-Fluid Flows and Mixing, (Houston, Texas: Gulf Publishing Company, 1986), Ch 19, pp 474-510.

38. J. S. Turner, "The 'Starting Plume' in Neutral Surroundings," Journal of Fluid Mechanics, Vol. 13, pp 356-371 (1962).

39. J. H. Middleton, "The Asymptotic Behavior of a Starting Plume," Journal of Fluid Mechanics, Vol. 72 (4), pp 753-771 (1975).

40. W. Schmidt, "Turbulente Ausbreitung Eines Stromes Erhitzter Luft. Z. angew," Math. Mech., Vol. 21, pp 265-278 and 351-363 (1941).

41. B. R. Morton, G. I. Taylor, and J. S. Turner, "Turbulent Gravitational Convection From Maintained and Instantaneous Sources," Proceedings of the Royal Society of London, Series A, Mathematical and Physical Sciences, Vol. 234, pp 1-2, 1956.

42. B. R. Morton, "Weak Thermal Vortex Rings," Journal of Fluid Mechanics, Vol. 9, pp 107-118 (1960).

43. R. S. Scorer, "Experiments on Convection of Isolated Masses of Buoyant Fluid," Journal of Fluid Mechanics, Vol. 2, pp 583-594 (1957).

44. J. Okabe and S. Inoue, "The Generation of Vortex Rings, Reports of Research Institute for Applied Mechanics, Vol. 8, (32), Kyushu University, pp 91-101, 1961.

45. H. Yamada and T. Matsui, Phys. Fluids, Vol. 21, pp 292-294 (1978).

46. J. P. Christiansen, "Numerical Simulation of Hydrodynamics by the Method of Point Vortices," Journal of Computational Physics, Vol. 13, pp 363-379 (1973).

47. N. Didden, "Mitt. Max-Planck-Inst. Stromungsforsch. Aerodyn," Versuchsanst., No. 64, (1977).

48. N. Didden, "Z. Angew," Math. Phys., Vol. 30, pp 101-116 (1979).

49. G. N. Abramovich, The Theory of Turbulent Jets, (Cambridge, Mass: M.I.T. Press, 1963).

50. J. O. Hinze, Turbulence: An Introduction to Its Mechanism and Theory, (New York, NY: McGraw-Hill Book Company, 1959).

51. W. E. Ranz, "Some Experiments on Orifice Sprays," The Canadian Journal of Chemical Engineering, Vol. 36, pp 175-181 (1958).

52. T. Takahashi and Y. Kitamura, Kagaku Kogaku, Vol. 35, p 637-643 (1971).

53. T. Takahashi and Y. Kitamura, Kagaku Kogaku, Vol. 36, pp 912-914 (1972).

54. K. Fujinawa, T. Maruyama, and Y. Nakaike, Kagaku Kogaku, Vol. 21, p 194 (1957).

55. Y. Tanasawa and S. Toyoda, "On the Atomization of Liquid Jet Issuing From a Cylindrical Nozzle," Technology Reports, Vol. 19-21, Tohoku Univ., Sendai, Japan, pp 135-156, 1954 and 1957.

56. R. P. Grant and S. Middleman, "Newtonian Jet Stability," A.I.Ch.E. Journal, Vol. 12, (4), pp 669-678 (1966).

57. D. H. Shlien, "Transition of the Axisymmetric Starting Plume Cap," Phys. Fluids, Vol. 21, (12), pp 2154-2156 (1978).

58. H. O. Anwar, "Appearance of Unstable Buoyant Jet," Journal of the Hydraulics Division, Proceedings of the American Society of Civil Engineers, Vol. 98, (HY 7), Paper 9012, pp 1143-1156 (1972).

59. J. D. Demetriou, "Experiments on Starting Homogeneous Jets," Journal of Hydraulic Engineering, American Society of Civil Engineers, Vol. 109, (7), pp 1039-1044 (1983).

60. G. I. Taylor, "The Dispersion of Jets of Metals of Low Melting Point in Water," in The Scientific Papers of Sir Geoffrey Ingram Taylor, Volume III, Aerodynamics and the Mechanics of Projectiles and Explosions, (Cambridge, England: Cambridge at the University Press, 1963), Paper 32 (1942), pp 304-305.

61. G. I. Taylor, "Generation of Ripples by Wind Blowing Over a Viscous Fluid," in The Scientific Papers of Sir Geoffrey Ingram Taylor, Volume III, Aerodynamics and the Mechanics of Projectiles and Explosions, (Cambridge, England: Cambridge at the University Press, 1963), Paper 25 (1940), pp 244-254.

62. H. O. Anwar, "Behavior of Buoyant Jet in Calm Fluid," Journal of the Hydraulics Division, Proceedings of the American Society of Civil Engineers, Vol. 95, (HY 4), Paper 6688, pp 1289-1303 (1969).

63. M. L. Albertson et al., "Diffusion of Submerged Jet," Transactions of the American Society of Civil Engineers, Vol. 115, Paper 2409, pp 639-697, 1950.

64. A. M. Kuethe, "Investigations of the Turbulent Mixing Regions Formed by Jets," J. Appl. Mech., Vol. 2, (A), p 87 (1935).

65. Oehler, Tech. Mech. u Thermodynamik, 1930.

66. G. Abraham, Jet Diffusion in Stagnant Ambient Fluid, Delft Hydraulics Laboratory, Delft, The Netherlands, Publication No. 29, 1963.

67. E. Hirst, Analysis of Buoyant Jets Within the Zone of Flow Establishment, Oak Ridge National Laboratory, Oak Ridge, Tenn., ORNL-TM-3470, 1971.

68. E. Hirst, "Zone of Flow Establishment for Round Buoyant Jets," Water Resources Research, Vol. 8, (5), pp 1234-1246 (1972).

69. D. F. Tatterson, Rates of Atomization and Drop Size in Annular Two-Phase Flow, University of Illinois, Urbana-Champaign, IL., Thesis, 1975.

70. B. J. Meister and G. F. Scheele, "Prediction of Jet Length in Immiscible Liquid Systems," A.I.Ch.E. Journal, Vol. 15, (5), pp 689-699 (1969).

71. I. Dzubur and H. Sawistowski, "Effect on Direction of Mass Transfer on Break-Up of Liquid Jets," Proceedings International Solvent Extraction Conference, Vol. 1, pp 379-397, 1974.

72. D. V. Swenson and M. L. Corradini, Monte Carlo Analysis of LWR Steam Explosions, Sandia National Laboratories, Albuquerque, NM, NUREG/CR-2307, SAND81-1092, 1981.

73. M. G. Stevenson, Report of the Zion/Indian Point Study, Los Alamos National Laboratory, Los Alamos, NM, NUREG/CR-1411, LA-8306-MS, 1980.

74. W. R. Bohl, An Investigation of Steam Explosion Loadings With SIMMER-II, Los Alamos National Laboratory, Los Alamos, NM, (to be published).

75. B. W. Marshall Jr. and O. P. Seebold, Reactor Safety Research Semiannual Report January - June 1985, Vol. 33, Sandia National Laboratories, Albuquerque, NM, NUREG/CR-4340, SAND85-1606, pp.67-71, October 1985.

76. M. L. Corradini and G. A. Moses, "A Dynamic Model for Fuel-Coolant Mixing," Proceedings of the International Meeting on LWR Severe Accident Evaluation, Cambridge, MA, 1983.

77. D. E. Mitchell and N. A. Evans, Steam Explosion Experiments at Intermediate Scale: FITSB Series, Sandia National Laboratories, Albuquerque, NM, NUREG/CR-3983, SAND83-1057, 1986.

78. D. E. Mitchell, M. L. Corradini, and W. W. Tarbell, Intermediate Scale Steam Explosion Phenomena: Experiments and Analysis, Sandia National Laboratories, Albuquerque, NM, NUREG/CR-2145, SAND81-0124, 1981.

79. L. Nelson et al., "Photographic Evidence for the Mechanism of Fragmentation of a Single Drop of Melt in Triggered Steam Explosion Experiments," Journal of Nonequilibrium Thermodynamics (1986).

80. A. S. Foust et al., Principles of Unit Operations, 2nd Ed., (New York, NY: John Wiley & Sons, 1980).

81. M. J. Bird, "Thermal Interactions Between Molten Uranium Dioxide and Water: An Experimental Study Using Thermite Generated Uranium Dioxide," Fuel-Coolant Interactions, HTD-V19, American Society of Mechanical Engineers (1981).

82. L. B. Luck, SIMMER-II: A Computer Program for LMFBR Disrupted Core Analysis, Rev. 2, Los Alamos National Laboratory, Los Alamos, NM, NUREG/CR-0453, LA-7515-M, September 1986.

83. D. Jakeman and R. Potter, "Fuel-Coolant Interactions," Proceedings of the International Conference on Engineering of Fast Reactors for Safe and Reliable Operation, Karlsruhe, DDR, October 1972.

84. B. Kim, Heat Transfer and Fluid Flow Aspects of Small-Scale Single Droplet Fuel-Coolant Interactions, PhD Thesis, University of Wisconsin-Madison, WI, 1985.

85. B. W. Marshall, Jr. and M. Berman, "An Experimental Study of Isothermal and Boiling Liquid Jets," 14th Water Reactor Safety Research Information Meeting, Gaithersburg, MD, October 1986.

86. MAAP, Modular Accident Analysis Program, User's Manual - Vol. II, IDCOR Technical Report 16.2-3, August 1983.

87. Sequoyah Nuclear Plant - Integrated Containment Analysis, IDCOR Task 23.1 Final Report, December 1984.

88. S. Dingman, A. Camp, C. C. Wong, D. King, and R. Gasser, HECTR Version 1.5 User's Manual, Sandia National Laboratories, Albuquerque, N.M., NUREG/CR-4507, SAND86-0101, April 1986.

89. C. C. Wong, "HECTR Analysis of the Second Part of the Standard Problem," Reactor Safety Research Semiannual Report, July - December 1986, Vol. 36, Sandia National Laboratories, Albuquerque, N.M., NUREG/CR-4805 (1 of 2), SAND86-2752 (1 of 2), November 1987.

90. A. L. Camp, V. L. Behr, and F. E. Haskin, MARCH-HECTR Analysis of Selected Accidents in an Ice-Condenser Containment, Sandia National Laboratories, Albuquerque, N.M., NUREG/CR-3912, SAND83-0501, December 1984.

91. J. E. Shepherd, "Chemical Kinetics of Hydrogen-Air-Diluent Detonations," Progress in Astronautics and Aeronautics, Vol. 106, p 263 (1985).

92. S. R. Tieszen et al., "Detonation Cell Size Measurements in Hydrogen-Air-Steam Mixtures," Progress in Astronautics and Aeronautics, Vol. 106, p 205 (1985).

93. M. P. Sherman et al., The Behavior of Hydrogen During Accidents in Light Water Reactors, Sandia National Laboratories, Albuquerque, NM, NUREG/CR-1561, SAND80-1495, August 1980.

94. Z. M. Shapiro and T. R. Moffette, Hydrogen Flammability Data and Application to PWR Loss-of-Coolant Accident, WAPD-SC-545, Reactors-Power, TID-4500, 13th Ed., September, 1957.

95. K. D. Bergeron et al., "Development and Applications of the Interim Direct Heating Model for the CONTAIN Computer Code," Proceedings of the Fourteenth Water Reactor Safety Research Information Meeting, Gaithersburg, MD, October 27-31, 1986.

96. D. C. Williams, Sandia, memo to M. Berman, Sandia, "Hydrogen Behavior in DCH Scenarios," March 31, 1987.

97. K. D. Bergeron, Sandia, memo to M. Berman, Sandia, "Considerations for Experimental Research on Hot Hydrogen Jet Combustion," April 1, 1987.

98. C. C. Wong, "Natural Convection and In-Cavity Oxidation of Combustible Gases," Paper presented at the National Heat Transfer Conference, Pittsburgh, PA, August 9-12, 1987.

99. R. M. Elrick, R. A. Sallach, A. L. Ouellette, and S. C. Douglas, Boron Carbide-Steam Reactions With Cesium Hydroxide and With Iodide at 1270 K in an Inconel 600 System, Sandia National Laboratories, Albuquerque, NM, NUREG/CR-4963, SAND87-1491, August 1987.

100. Technical Bases for Estimating Fission Product Behavior During LWR Accidents, U.S. Nuclear Regulatory Commission, Washington, DC, NUREG-0772, June 1981.

101. R. M. Elrick and R. A. Sallach, "Fission Product Chemistry in the Primary System," Proceedings of the International Meeting on Light Water Reactor Severe Accident Evaluation Cambridge, Massachusetts, August 28 to September 1, 1983

102. R. A. Sallach and R. M. Elrick, "Chemical Reactions of CsOH, CsI, and Te Vapors With Oxidizing Reactor Materials," Proceedings of the ANS Topical Meeting on Fission Product Behavior and Source Term Research, Snowbird, Utah, July 15 to 19, 1984.

103. I. R. Beattie, B. R. Bowsher, T. R. Gilson, and P. J. Jones, The Interaction of Caesium Iodide With Boric Acid, Atomic Energy Establishment, Winfrith, Dorset, United Kingdom, AEEW-R 1974, June 1985.

104. N. A. Young and B. R. Bowsher, The Interaction of Caesium Iodide With Boric Acid: A Study of the Reaction Products Using Matrix Isolation--Infrared Spectroscopy and Quadrupole Mass Spectrometry, Atomic Energy Establishment, Winfrith, Dorset, United Kingdom, AEEW-R 2042, November 1985.

105. B. R. Bowsher and S. Dickinson, The Interaction of Caesium Iodide With Boric Acid: Vapour Phase and Vapour-Condensed Phase Reactions, Atomic Energy Establishment, Winfrith, Dorset, United Kingdom, AEEW-R 2102, May 1986.

106. L. M. Litz and R. A.Mercuri, "Oxidation of Boron Carbide by Air, Water, and Air-Water Mixtures at Elevated Temperatures," J. of the Electrochemical Society, Vol. 110(8), (1963).

107. R. E. Woodley, "The Reaction of Boronated Graphite With Water Vapor," Carbon, Vol. 7(5), (1969).

108. "Chemistry of Cesium and Iodine," in Technical Bases for Estimating Fission Product Behavior During LWR Accidents, Ch. No. 5, U.S. Nuclear Regulatory Commission, Washington, DC, NUREG-0772, 1981.

109. JANAF Thermochemical Tables, NSRDS-NBS37, 1971, and Supplements, 1974, 1975, and 1978.

110. R. O. Gauntt et al., "Results of the ACRR-DFR Experiments," Program overview presented at the ANS/ENS Topical Meeting on Thermal Reactor Safety, San Diego, Ca., Paper XIX.8-1, February, 1986.

111. Anthony Ness, A Guidebook to Nuclear Reactors, (Berkley, CA: Univ. Calif. Press, 1975).

112. R. M. Harrington and L. J. Ott, The Effect of Small Capacity High Pressure Injection Systems on TQUV Sequences at Browns Ferry Unit One, Oak Ridge National Laboratory, Oak Ridge, TN, NUREG/CR-3179, ORNL/TM-8635, 1983.

113. A. W. Cronenberg and D. J. Osetek, "Assessment of Hydrogen Generation Issues Based on the PBF SFD-ST and SFD 1-1 Data," Presented at the Severe Fuel Damage Meeting, Rockville, MD, October 1986.

114. L. E. Anderson et al., In-Vessel Core Melt Progression Phenomena, IDCOR T15.1A, 1983.

115. S. Hagen and P. Hoffman, "Behavior of B_4C Absorber Rods Under SFD Conditions," Presented at the Severe Fuel Damage Meeting, Rockville, MD, October 1986.

116. Ken Muramatsu, "A Method for Estimating Hydrogen Generation Rate in ACRR Debris Formation (DF) Experiments," JAERI memo 61-442, 1987.

117. L. J. Ott, MARCON-DF4, Oak Ridge National Laboratory, Oak Ridge, TN, 1986.

118. E. L. Tolman et al., TMI-2 Accident Scenario Update, Idaho National Engineering Laboratory, Idaho Falls, ID, EGG-TMI-7489, 1986.

119. M. M. El-Wakil, Nuclear Heat Transport, (New York, NY: International Textbook Company, 1971), pp 94-98.

120. D. W. Golden et al., TMI-2 Standard Problem Package, Idaho National Engineering Laboratory, Idaho Falls, ID, EGG-TMI-7382, 1986.

121. D. L. Hagrman, Material Property Models for Severe Core Damage Analysis, Idaho National Laboratory, Idaho Falls, ID, EGG-CDD-5801, 1982.

122. C. A. Wert and R. M. Thomson, Physics of Solids, Second Edition, (New York, NY: McGraw-Hill Book Co. 1970), pp 71-72.

123. A. E. Scheidegger, The Physics of Flow Through Porous Media, Third Edition, (Toronto and Buffalo: University of Toronto Press, 1974), pp 266-290.

124. M. C. Leverett, "Capillary Behavior in Porous Solids," Pet. Trans. AIME, 142, pp 152-169 (1941).

125. R. B. Bird, W. E. Stewart and E. N. Lightfoot, Transport Phenomena, (New York, NY: John Wiley and Sons, Inc., 1960), p. 199.

126. G. Hofmann and L. Barleon, "Reduced Coolability of Particle Beds as a Result of Capillary Effects at Horizontal Phase Boundaries," Proceedings of the International ANS/ENS Topical Meeting on Thermal Reactor Safety, San Diego, California, February 2-6, 1986.

127. A. W. Reed, K. R. Boldt, E. D. Gorham-Bergeron, R. J. Lipinski, and T. R. Schmidt, DCC-1/DCC-2 Degraded Core Coolability Analysis, Sandia National Laboratories, Albuquerque, NM, NUREG/CR-4390, 1985.

128. G. G. Brown and Associates, Unit Operations, Sixth Edition, (New York, NY: John Wiley and Sons, Inc., 1956), pp 210-228.

129. J. E. Kelly, J. T. Hitchcock, and M. L. Schwarz, "Heat Transfer Characteristics of Dry Porous Particulate Beds With Internal Heat Generation," Proceedings, ASME-JSME Thermal Engineering Joint Conference, Honolulu, Hawaii March 1983.

130. D. L. Hagrman, Materials Properties Models for Zirconium-Uranium Oxygen Melting, (PSOL,PLIQ), Solution, and Precipitation (ZUSOLV), Idaho National Engineering Laboratory, Idaho Falls, ID, 1985.

131. I. E. Campbell and E. M. Sherwood, High Temperature Materials and Technology, (New York, NY: J. Wiley & Sons, 1967), p 269.

132. Y. S. Touloukian, Thermalphysical Properties of High Temperature Materials, Vol 4, Part 1, (New York, NY: Macmillon, 1967), p 493.

133. J. Davies and P. Simpson, Induction Heating Handbook, (London, England: McGraw Hill, 1979).

DISTRIBUTION:

U.S. Government Printing Office
Receiving Branch
(Attn: NRC Stock)
(435 Copies for R3, R5, and R7)
8610 Cherry Lane
Laurel, MD 20707

U.S. Nuclear Regulatory Commission (19)
Division of Accident Evaluation
Office of Nuclear Regulatory Research
Washington, D.C. 20555
Attn: B. W. Morris
D. Ross
C. N. Kelber
G. Marino
W. S. Farmer
P. Worthington
M. Fleishman
B. Burson
M. Silberberg
J. T. Han
L. Chan
T. M. Lee
J. Mitchell
k. Meyer
J. Telford
R. W. Wright
Z. Rosztoczy
W. B. Hardin
F. Eltawila

U.S. Nuclear Regulatory Commission (9)
Office of Nuclear Reactor Regulation
Washington, D.C. 20555
Attn: W. R. Butler
G. W. Knighton
R. Barrett
A. Notafrancesco
R. Palla
K. I. Parczewski
T. M. Su
C. G. Tinkler
D. D. Yue

U.S. Nuclear Regulatory Commission
Office of the Commissioners
Washington, DC 20555
Attn: J. T. Larkins

U.S. Nuclear Regulatory Commission
Advisory Committee on Reactor Safeguards
Washington, D.C. 20555
Attn: G. Quittschreiber

U.S. Department of Energy
Office of Nuclear Safety Coordination
Washington, D.C. 20545
Attn: R. W. Barber

U.S. Department of Energy (2)
Albuquerque Operations Office
P.O. Box 5400
Albuquerque, NM 87185
Attn: J. R. Roeder, Director
Transportation Safeguards Div.
J. A. Morley, Director Energy
Research Technology Division
For: C. B. Quinn
R. N. Holton

Applied Sciences Association, Inc.
P.O. Box 2687
Palos Verdes Pen., CA 90274
Attn: D. Swanson

Argonne National Laboratory (7)
9700 South Cass Avenue
Argonne, IL 60439
Attn: J. Rest
L. Baker
L. Neimark
Dae Cho
R. Anderson
B. Spencer
D. Armstrong

Astron
2028 Old Middlefield Way
Mountain View, CA 94043

Battelle Columbus Laboratory (4)
505 King Avenue
Columbus, OH 43201
Attn: R. Denning
P. Cybulskis
J. Gieseke
C. Alexander

Battelle Pacific Northwest
Laboratory (2)
P.O. Box 999
Richland, WA 99352
Attn: M. Freshley
G. R. Bloom

Brookhaven National Laboratory (5)
Upton, NY 11973
Attn: R. A. Bari
T. Pratt
T. Ginsberg
G. Greene
K. Araj

University of California
Chemical and Nuclear Engineering Dept.
Santa Barbara, CA 93106
Attn: T. G. Theofanous

Duke Power Co. (2)
P.O. Box 33189
Charlotte, NC 28242
Attn: F. G. Hudson
A. L. Sudduth

EG&G Idaho (3)
Willow Creek Building, W-3
P.O. Box 1625
Idaho Falls, ID 83415
Attn: Server Sadik
D. Croucher
R. Hobbins

Electric Power Research Institute (6)
3412 Hillview Avenue
Palo Alto, CA 94303
Attn: W. Loewenstein
M. Leverett
G. Thomas
B. R. Sehgal
R. Vogel
J. Haugh

Fauske and Associates (2)
16W070 West 83rd St.
Burr Ridge, IL 60521
Attn: R. Henry
M. Plys

Factory Mutual Research Corporation
P.O. Box 688
Norwood, MA 02062
Attn: R. Zalosh

General Electric Corporation
Advanced Reactor Systems Department
P.O. Box 508
Sunnyvale, CA 94088
Attn: J. I. Temme, Mgr.,
Probabilistic Risk Assessment

General Electric Corporation
175 Curtner Avenue
Mail Code N 1C157
San Jose, CA 95125
Attn: K. W. Holtzclaw

Institute of Nuclear Power Operation
Suite 1200
1100 Circle 75 Parkway
Atlanta, GA 30339
Attn: Henry Piper

International Technology Corporation
Attn: M. H. Fontana Director, Nuclear
Programs
575 Oak Ridge Turnpike
Oak Ridge, TN 37830

Los Alamos National Laboratory (4)
P.O. Box 1663
Los Alamos, NM 87545
Attn: M. Stevenson
R. Henninger
J. Carson Mark
J. Travis

Massachusetts Institute of Technology
Nuclear Engineering Dept.
Cambridge, MA 02139
Attn: N. C. Rasmussen

University of Michigan
Department of Aerospace Engineering
Ann Arbor, MI 47109
Attn: Prof. M. Sichel

University of Michigan
Nuclear Engineering Department
Ann Arbor, MI 48104

Mississippi Power Light
P.O. Box 1640
Jackson, MS 39205
Attn: S. H. Hobbs

Northwestern University
Chemical Engineering Department
Evanston, IL 60201
Attn: S. G. Bankoff

Oak Ridge National Laboratory
NRC Programs
P.O. Box X. Bldg. 4500S
Oak Ridge, TN 37831
Attn: A. P. Malinauskas

Oak Ridge National Laboratory
NRC Programs
P.O. Box Y
Bldg. 9108, Room 201
Oak Ridge, TN 37831
Attn: T. S. Kress

Power Authority State of NY
10 Columbus Circle
New York, NY 10019

Savannah River Laboratory (3)
E. I. DuPont de Nemours Co.
Aiken, South Carolina 29801
Attn: H. Randolph
M. Lee Hyder
F. Beranek

Stratton & Assoc., Inc.
2 Acoma Lane
Los Alamos, NM 87544
Attn: W. Stratton

Dr. Roger Strehlow
505 South Pine Street
Champaign, IL 61820

Texas A&M University
Nuclear Engineering Dept.
College Station, TX 77843

UCLA
Nuclear Energy Laboratory (2)
405 Hilgaard Avenue
Los Angeles, CA 90024
Attn: I. Catton
D. Okrent

Westinghouse Corporation (3)
P.O. Box 355
Pittsburgh, PA 15230
Attn: N. Liparulo
J. Olhoeft
V. Srinivas

Westinghouse Electric Corporation
Bettis Atomic Power Lab
P.O. Box 79
West Mifflin, PA 15122-0079
Attn: Frances Emert

University of Wisconsin
Nuclear Engineering Department
1500 Johnson Drive
Madison, WI 53706
Attn: M. L. Corradini

Belgonucleaire SA
25 rue de Champ dc Mars
B-1050 Brussels
BELGIUM
Attn: H. Bairiot

Director Research, Science Education
CEC
Rue De La Loi 200
1049 Brussels
BELGIUM
Attn: B. Tolley

Atomic Energy of Canada Ltd. (2)
Chalk River Nuclear Laboratories
Chalk River, Ontario
CANADA KOJ 1J0
Attn: P. Fehrenbach, RSR Div
J. C. Cook

Atomic Energy of Canada Ltd. (2)
Whiteshell Nuclear Research
Establishment
Pinawa, Manitoba
CANADA ROE 1L0
Attn: D. J. Wren
C. K. Chan

Atomic Energy of Canada Ltd.
CANDU Operations
Sheridan Park Research Community
Mississauga, Ontario
CANADA L5K 1B2
Attn: E. Kohn

McGill University
315 Querbes
Outremont, Quebec
CANADA H2V 3W1
Attn: J. H. S. Lee

Ontario Hydro
700 University Avenue
Toronto, Ontario
CANADA M5G 1X6
Attn: J. H. K. Lau

Institute of Nuclear Energy Research
P.O. Box 3
Lung-Tan
Taiwan 325
REPUBLIC OF CHINA
Attn: Sen-I-Chang

Battelle Institute E. V. (3)
Am Roemrhof 35
6000 Frankfurt am Main 90
FEDERAL REPUBLIC OF GERMANY
Attn: Dr. Werner Geiger
Dr. Guenter Langer
Dr. Manfred Schildknecht

Projekt Schneller Brueter (5)
Kernforschungszentrum Karlsruhe GMBH
Postfach 3640
D-7500 Karlsruhe 1
FEDERAL REPUBLIC OF GERMANY
Attn: Dr. Kessler
Dr. Heusener
Dr. S. Hagen
Dr. W. Schock
A. Fiege

Gesellschaft fur Reaktorsicherheit (2)
Forschungsgelande
D-8046 Garching
FEDERAL REPUBLIC OF GERMANY
Attn: Dr. E. F. Hicken
Dr. H. L. Jahn

Gesellschaft fur Reaktorsicherheit (GRS)
Postfach 101650
Glockengasse 2
5000 Koeln 1
FEDERAL REPUBLIC OF GERMANY

Institute fur Kernenergetik und Energiesysteme (2)
University of Stuttgart
Stuttgart
FEDERAL REPUBLIC OF GERMANY
Attn: M. Buerger
A. Unger

Kraftwerk Union
Hammerbacher Strasse 12 14
Postfach 3220
D-8520 Erlangen 2
FEDERAL REPUBLIC OF GERMANY
Attn: Dr. M. Peehs

Departmento Di Costruzioni
Meccaniche E Nucleari
Facolta Di Ingegneria
Via Diotisalvi 2
56100 - ITALY
Attn: M. Carcassi

ENEA Nuclear Energ Alt Disp (2)
Via Vitaliano Brancati, 48
00144 Roma
ITALY
Attn: P. L. Ficara
G. Petrangeli

Japan Atomic Energy Research Institute (3)
Tokai-mura, Naku-gun, Ibaraki-ken, 319-11
JAPAN
Attn: Dr. K. Soda
Dr. T. Fujishiro
Mr. K. Sato

Power Reactor Nuclear Fuel Development Corporation (PNC)
Fast Breeder Reactor Development Project (FBR)
9-13, 1-Chome, Akasaka
Minato-Ku, Tokyo
JAPAN
Attn: Dr. Watanabe

Korea Advanced Energy Research Institute
P.O. Box 7
Daeduk-Danji
Chungnam
KOREA
Attn: H. R. Jun

Netherlands Energy Research Foundation
P.O. Box 1
1755 ZG Petten NH
THE NETHERLANDS
Attn: K. J. Brinkmann

Juan Bagues
Corsejo de Seguridad Nuclear
SOK Angela de la Cruz No 3
Madrid
SPAIN 28046

Royal Institute of Technology
Dept. of Nuclear Reactor Engineering
Stockholm S-10044
SWEDEN
Attn: K. M. Becker

Department of Research
Swedish Nuclear Power Inspectorate
P.O. Box 27106
S-102 52 Stockholm
SWEDEN
Attn: L. Hammar

Studsvik Energiteknik AB
S-611 82 Nykoping
SWEDEN
Attn: K. Johansson

Swedish State Power Board
S-162 Fach 87 Vallingby
SWEDEN
Attn: Wiktor Frid

AERE Harwell (2)
Didcot
Oxfordshire OX11 0RA
UNITED KINGDOM
Attn: J. R. Matthews
Theoretical Physics Division

National Nuclear Corp. Ltd.
Cambridge Road
Whetestone, Leicester, LE83LH
UNITED KINGDOM
Attn: R. May

Simon Engineering Laboratory
University of Manchester
M139PL,
UNITED KINGDOM
Attn: Prof. W. B. Hall

UKAEA, AEA Winfrith, Dorchester (6)
Dorset DT2 8DH
UNITED KINGDOM
Attn: A. Nichols
B. Bowsher
S. Kinnersley
M. Bird
R. Potter
A. Wickett

UKAEA, Culham Laboratory (3)
Abingdon
Oxfordshire OX14 3DB
UNITED KINGDOM
Attn: F. Briscoe
I. Cook
D. Fletcher

Berkeley Nuclear Laboratory (2)
Berkeley
Gloucestershire GL13 9PB
UNITED KINGDOM
Attn: S. J. Board
N. Buttery

UKAEA
Risley Nuclear Power Development
Establishment
Risley, Warrington WA3 6AT
UNITED KINGDOM
Attn: D. Hicks

UKAEA Safety and Reliability
Directorate (9)
Wigshaw Lane
Culcheth, Warrington WA3 4NE
Cheshire
UNITED KINGDOM
Attn: G. Tyror (2)
M. R. Hayns (2)
F. Abbey
P. Barr
B. Cowking
S. F. Hall
A. Taig

SANDIA DISTRIBUTION:

1131 W. B. Benedick
1510 J. W. Nunziato
Attn: 1512 J. C. Cummings
1530 L. W. Davison
Attn: 1534 J. R. Asay
1541 H. C. Hardee
3141 S. A. Landenberger (5)
3151 W. L. Garner
6400 D. J. McCloskey
6410 N. C. Ortiz
6412 A. L. Camp
6415 F. E. Haskin
6418 J. E. Kelly
6420 J. V. Walker
6421 P. S. Pickard
6422 D. A. Powers
6422 M. D. Allen
6422 J. E. Brockmann
6422 E. R. Copus
6422 R. M. Elrick
6422 W. W. Tarbell
6423 K. G. Reil
6423 R. O. Gauntt
6423 B. W. Marshall, Jr.
6425 W. J. Camp
6425 D. R. Bradley
6425 S. S. Dosanjh
6425 M. Pilch
6425 A. W. Reed
6425 R. C. Smith
6425 J. L. Tomkins
6425 M. F. Young
6427 M. Berman
6427 D. Beck
6427 L. S. Nelson
6427 M. P. Sherman
6427 S. Slezak
6427 D. Stamps
6427 S. J. Tieszen
6427 C. C. Wong
6429 K. D. Bergeron
6440 D. A. Dahlgren (1)
Attn: 6442 W. A. Von Riesemann
6447 M. P. Bohn
6450 T. R. Schmidt (1)
Attn: 6451 T. F. Luera
6454 G. L. Cano
7590 T. B. Lane (1)
Attn: 7537 N. R. Keltner
7537 R. U. Acton
7537 T. Y. Chu
7550 T. S. Ellington (1)
Attn: 7551 O. J. Burchett
7552 J. E. Gieske
8024 P. W. Dean
8357 R. J. Carling
8363 B. R. Sanders
Attn: 8363 K. D. Marx

NRC FORM 335 (2-84) NRCM 1102, 3201, 3205

U.S. NUCLEAR REGULATORY COMMISSION

BIBLIOGRAPHIC DATA SHEET

SEE INSTRUCTIONS ON THE REVERSE

1 REPORT NUMBER (Assigned by TIDC and Vol. if any)
NUREG/CR-5039 (1 of 2)
SAND87-2411 (1 of 2)

2 TITLE AND SUBTITLE
REACTOR SAFETY RESEARCH SEMIANNUAL REPORT
January-June 1987

3 LEAVE BLANK

4 DATE REPORT COMPLETED
MONTH: October
YEAR: 1987

5 AUTHOR(S)
Reactor Safety Research Department
Sandia National Laboratories

6 DATE REPORT ISSUED
MONTH: December
YEAR: 1987

7 PERFORMING ORGANIZATION NAME AND MAILING ADDRESS (Include Zip Code)
Sandia National Laboratories
Albuquerque, NM 87185

8 PROJECT/TASK/WORK UNIT NUMBER

9 FIN OR GRANT NUMBER
A1016 etc.

10 SPONSORING ORGANIZATION NAME AND MAILING ADDRESS (Include Zip Code)
U.S. Nuclear Regulatory Commission
Washington, DC 20555

11a TYPE OF REPORT
progress-technical

11b PERIOD COVERED (Inclusive dates)
January-June 1987

12 SUPPLEMENTARY NOTES

13 ABSTRACT (200 words or less)

Sandia National Laboratories is conducting, under USNRC sponsorship, phenomenological research related to the safety of commercial nuclear power reactors. The research includes experiments to simulate the phenomenology of the accident conditions and the development of analytical models, verified by experiment, which can be use to predict reactor and safety systems performance and behavior under abnormal conditions. The objective of this work is to provide NRC requisite data bases and analytical methods to (1) identify and define safety issues, (2) understand the progression of risk-significant accident sequences, and (3) conduct safety assessments. The collective NRC-sponsored effort at Sandia National Laboratories is directed at enhancing the technology base supporting licensing decisions.

14 DOCUMENT ANALYSIS - a KEYWORDS/DESCRIPTORS

b IDENTIFIERS/OPEN-ENDED TERMS

15 AVAILABILITY STATEMENT
GPO SALES
NTIS

16 SECURITY CLASSIFICATION
(This page)
Unclassified
(This report)
Unclassified

17 NUMBER OF PAGES

18 PRICE

© U.S. GOVERNMENT PRINTING OFFICE: 1988—573-048/81201